REPORT SERIES IN AEROSOL SCIENCE
No. 267 (2023)

Abstract Book of the

THE 21ST INTERNATIONAL CONFERENCE ON NUCLEATION & ATMOSPHERIC AEROSOLS

26th-30th June 2023
Brisbane, Australia

Editors: Aino Ovaska and Zoran Ristovski

Aerosolitutkimusseura r.y.
Helsinki 2023

ISBN 978-952-7507-12-4 (print)
ISSN 0784-3496 (print)
ISBN 978-952-7507-13-1 (pdf)
ISSN 2814-4236 (pdf)
Kirjapaino Hermes Oy
Tampere 2023

www.FAAR.fi

Contents

NUMERICAL PREDICTION OF PARTICLE BREATHING ZONE IN A SEMI-OUTDOOR ENVIRONMENT

I. ABOUELHAMD[1], S. J. YOO[2], K. KUGA[2], and K. ITO[2]

[1]*Interdisciplinary Graduate School of Engineering Sciences, Kyushu University, Kasuga-koen, Kasuga, Fukuoka 816-8580, Japan*
[2]*Faculty of Engineering Sciences, Kyushu University, Kasuga-koen, Kasuga, Fukuoka 816-8580, Japan*

Keywords: BREATHING ZONE, AIRFLOW DISTRIBUTION, PARTICLES SIMULATION, COMPUTATIONAL FLUID DYNAMICS

INTRODUCTION

Airborne contagion particles can easily transport to humans in indoor/outdoor/semi-outdoor environments. The infection risk occurs during inhalation, hence the exposure to particle deposition in the respiratory system, which causes pulmonary diseases (Naseri *et al*., 2020). Present research mainly addresses the indoor environment to simulate the breathing zone (Kuga *et al*., 2022; Yoo and Ito, 2022), particle deposition in the respiratory tract (Li *et al*., 2012; Murga *et al*., 2019; Khoa *et al*., 2022), and exposure of the exhaled contaminants (Li *et al*., 2022; Motamedi *et al*., 2022; Bahramian *et al*., 2023). However, few contributions are devoted to outdoor/semi-outdoor environments (Zhang *et al*., 2020; Yang *et al*., 2021), despite the high infection risk occurring in crowded spaces such as train platforms at peak hours. Compared to the indoor environment, the semi-outdoor domains are much more complex in terms of atmospheric characteristics, encountering multiple pollution sources and extreme climate conditions. Thus, residents are exposed to a high concentration of contaminants during their daily commuting. While the studies concerned the indoor environment tend to develop ventilation systems, for the semi-outdoor environment, natural ventilation, appropriate social distancing, space consumption, and public design are crucial interventions to ensure comprehensive public health. The main objective of this study is to investigate the airflow distribution and particle breathing zone in a simplified semi-outdoor environment.

METHODS

The computational fluid dynamics technique (CFD) is employed to predict the airflow patterns and breathing zone in the semi-outdoor environment. It has been widely utilized for numerical simulation to avoid experimental costs. The computational domain is modeled to represent the simplified semi-outdoor environment with the dimension of 30 m length x 30 m width x 15 m height. This study used a computer-simulated person (CSP) produced by Ito (2016) and validated and verified by Yoo and Ito (2022) to simulate the detailed human model. The CSP is placed in the center of the atmospheric domain. Above the CSP, a symmetric ceiling is inserted with a distance of 6.4 m length x 6.4 m width to represent the semi-outdoor environment, such as a bus stop/train platform. The distance from the ground to the lower surface of the ceiling is 3 meters height to neglect the solar radiation (See Fig. 1). A realistic nasal cavity is integrated into the CSP (See Fig. 2) to mark the nasal openings and to set the steady breathing rate at 18.7 L/min (equivalent to 1.73 m/s). The boundary condition of the breathing is velocity inlet starting from the virtual end of the cavity airway. Fanger's model is used to set the thermal conditions of the human with convection heat and 309.55 kelvin for the skin surface temperature to emphasize the effect of the thermal plume. A total of 2.83 million cells is generated via the Polyhedral gridding type with a fine mesh around the CSP and coarse mesh in the outer regions to minimize the computational load (See Fig 3).
The approaching flow is examined in two directions, from the front side (North) and back side (South) of the human. The wind speed is produced by the vertical profiles of the streamwise velocity and turbulence intensity, similarly conducted by Liu and Niu (2016). The constant airflow temperature is 290.15 kelvin. For the setting of particle injection position and generating the probabilistic inhaled particle regions, the nasal openings are used as surfaces to release the particles in the external domain by using the reverse particle tracking method. The shear stress transport model (SST k-ω turbulence model) is selected as it

showed accurate results in the low velocities compared with the other turbulence models, as proved by Li and Ito (2014). The Semi-Implicit Method for Pressure Linked Equations (SIMPLE) algorithm is used to solve the Navier–Stokes equations. The spatial discretization setup changed to a second-order upwind for the momentum, turbulent Kinetic Energy, dissipation rate, and energy.

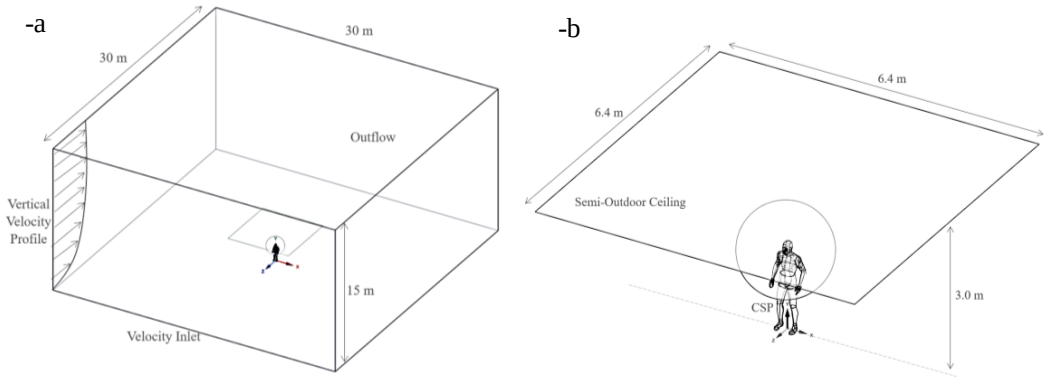

Figure 1. The geometry produced for CFD. (a) the computational domain that represents the semi-outdoor environment, and (b) the inserted ceiling above the computer-simulated person (CSP).

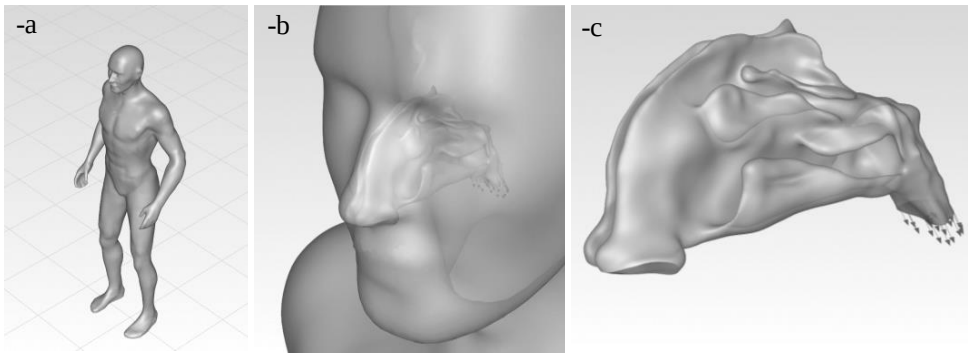

Figure 2. The human and nasal cavity model. (a) the CSP, (b) facial details with an integrated nasal cavity to simulate the breathing airstream, and (c) the nasal cavity and the breathing inlet velocity in the right end.

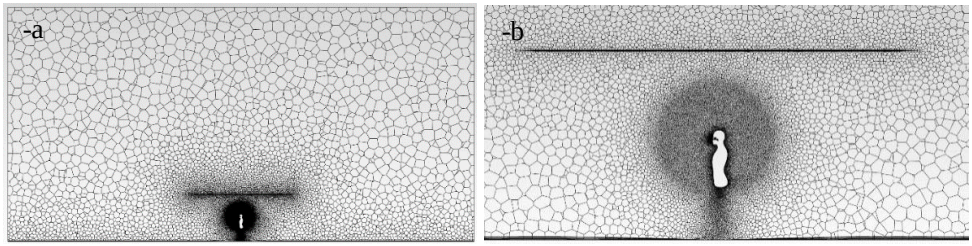

Figure 3. The meshing by using the Polyhedral gridding type with 2.83 million cells. (a) a section in the center of the whole domain and (b) the region under the ceiling where the CSP is placed.

RESULTS AND DISCUSSION

The results of airflow velocity and distribution around the human (Fig 4) indicate notable changes in wind speed and directions close to the CSP due to the impact of the thermal plume and vertical velocity profile of the atmospheric boundary conditions. Moreover, the results highlight the probabilistic size of the breathing zone in two scenarios of wind directions (front and back airflow) and four different particle

sizes (1, 5, 50, and 80μm). Remarkably, the wind direction and particle size have an impact on the inhalation zone. The gravitational characteristics of the particles (due to the change in diameter) have significantly affected the formulation of the breathing region in front of the CSP (See Fig 5). Particles with a diameter of 80 μm, which are relatively large, were strongly affected by gravitational settling. As a result, many particles that settle down from above the head are inhaled.

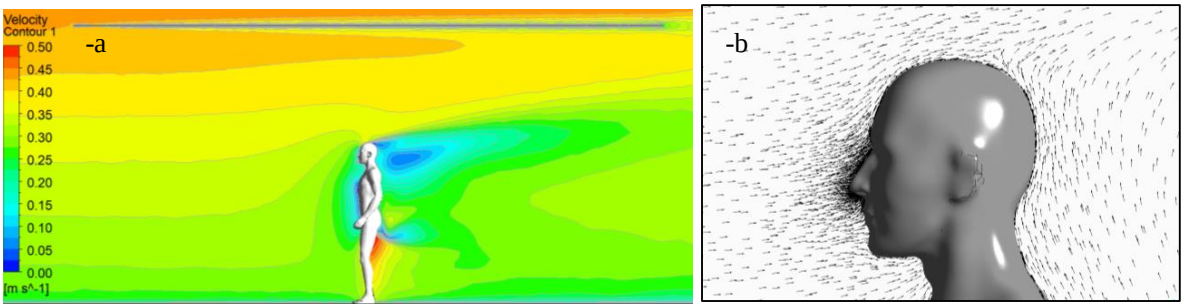

Figure 4. The airflow velocity magnitude and distribution. (a) velocity contour for the north wind scenario and (b) airflow pattern near the CSP.

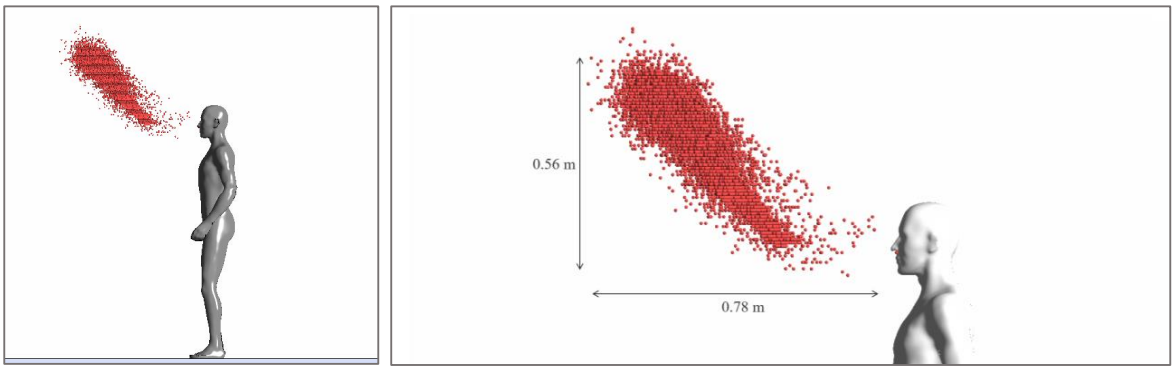

Figure 5. The Probabilistic initial distribution of inhaled particles with a diameter of 80μm by using reverse simulation for the north-wind case. Around 0.78 m in front of the face and 0.56 m in height with a slop as presented.

CONCLUSIONS

This research simulates airflow patterns and particle breathing zone in semi-outdoor environments such as train platforms to identify the probability of infection risk from aerosol contaminants. The breathing zone is identified with the highest possible volume due to the applied steady inhalation. Two wind directions and four-particle sizes were examined to explore the changes in breathing regions in front and around the human. The wind speed is produced by the vertical profiles of the streamwise velocity and turbulence intensity to represent the atmospheric boundary conditions. The results indicate changes in wind velocity and distribution near the CSP due to the impact of the thermal plume and vertical velocity profile. The wind direction and particle size influence the particle breathing zone. Eventually, the findings of this study can be employed for developing actions to control the contagion particle exposure, determine the appropriate social distancing/space consumption, and enhance natural ventilation in semi-enclosed environments.

ACKNOWLEDGEMENTS

This study was partially funded by Japan Science and Technology (JST), CREST Japan (JP 20356547), and JSPS KAKENHI (JP 22H00237, JP 22K18300, JP 20KK0099, JP 22K14371), Health Labour

Sciences Research Grant (JP 21KD2002), and MEXT as “Program for Promoting Researches on the Supercomputer Fugaku” (JPMXP1020210316).

REFERENCES

Bahramian, A., Mohammadi, M. and Ahmadi, G. (2023). Effect of indoor temperature on the velocity fields and airborne transmission of sneeze droplets: An experimental study and transient CFD modeling. Science of The Total Environment, 858, p.159444. doi:10.1016/j.scitotenv.2022.159444.

Ito, K. (2016). Toward the development of an in silico human model for indoor environmental design. Proceedings of the Japan Academy, Series B, [online] 92(7), pp.185–203. doi:10.2183/pjab.92.185.

Khoa, N. D., Phuong, N. L. and Ito, K. (2022). Numerical Investigation of Fine particle Transportation and Deposition in the Human Lower Airway: Impact of airflow and particle size on deposition efficiency. Proceedings of International Exchange and Innovation Conference on Engineering & Sciences (IEICES), 8, pp.366–372. doi:10.5109/5909118.

Kuga, K., Wargocki, P. and Ito, K. (2022). Breathing zone and exhaled air re-inhalation rate under transient conditions assessed with a computer-simulated person. Indoor Air, 32(2). doi:10.1111/ina.13003.

Li, C. and Ito, K. (2014). Numerical and experimental estimation of convective heat transfer coefficient of human body under strong forced convective flow. Journal of Wind Engineering and Industrial Aerodynamics, 126, pp.107–117. doi:10.1016/j.jweia.2014.01.003.

Li, X., Inthavong, K. and Tu, J. (2012). Particle inhalation and deposition in a human nasal cavity from the external surrounding environment. Building and Environment, 47, pp.32–39. doi:10.1016/j.buildenv.2011.04.032.

Li, X., Mak, C.M., Ai, Z. and Wong, H.M. (2022). Airborne transmission of exhaled pollutants during short-term events: Quantitatively assessing inhalation monitor points. Building and Environment, [online] 223, p.109487. doi:10.1016/j.buildenv.2022.109487.

Liu, J. and Niu, J. (2016). CFD simulation of the wind environment around an isolated high-rise building: An evaluation of SRANS, LES and DES models. Building and Environment, 96, pp.91–106. doi:10.1016/j.buildenv.2015.11.007.

Motamedi, H., Shirzadi, M., Tominaga, Y. and Mirzaei, P.A. (2022). CFD modeling of airborne pathogen transmission of COVID-19 in confined spaces under different ventilation strategies. Sustainable Cities and Society, [online] 76, p.103397. doi:10.1016/j.scs.2021.103397.

Murga, A., Kuga, K., Yoo, S.-J. and Ito, K. (2019). Can the inhalation exposure of a specific worker in a cross-ventilated factory be evaluated by time- and spatial-averaged contaminant concentration? Environmental Pollution, [online] 252, pp.1388–1398. doi:10.1016/j.envpol.2019.06.056.

Naseri, A., Emdad, H., Mehrabi, S., Sadrizadeh, S. and Abouali, O. (2020). Inhalability of micro-particles through the human nose breathing at high free-stream airflow velocities. Building and Environment, 179, p.106948. doi:10.1016/j.buildenv.2020.106948.

Yang, X., Yang, H., Ou, C., Luo, Z. and Hang, J. (2021). Airborne transmission of pathogen-laden expiratory droplets in open outdoor space. Science of The Total Environment, 773, p.145537. doi:10.1016/j.scitotenv.2021.145537.

Yoo, S. and Ito, K. (2022). Validation, verification, and quality control of computational fluid dynamics analysis for indoor environments using a computer-simulated person with respiratory tract. Japan Architectural Review, 5(4), pp.714–727. doi:10.1002/2475-8876.12301.

Zhang, X., Ji, Z., Yue, Y., Liu, H. and Wang, J. (2020). Infection Risk Assessment of COVID-19 through Aerosol Transmission: a Case Study of South China Seafood Market. Environmental Science & Technology. doi:10.1021/acs.est.0c02895.

CHARACTERISTICS OF NEW PARTICLE FORMATION EVENTS OCCURRED OVER THE YELLOW SEA IN THE SPRINGTIME FOR 4 YEARS FROM 2019

CHANWOO AHN[1], SEONG SOO YUM[1], MINSU PARK[1] and PYOSUK SEO[1]

[1] Department of Atmospheric Science, Yonsei University, Seoul, Republic of Korea

Keywords: Yellow Sea, ship measurement, aerosol size distribution, new particle formation

INTRODUCTION

Atmospheric aerosols affect climate, human health, and visibility (Charlson 1969; Ramanathan et al., 2001; Apte et al., 2021). Recognizing the importance of aerosols, many observations have been conducted since 2000 in East Asia, where the concentration of the aerosols is high, but observations on air quality over the sea are still scarce. Therefore, it is important to understand the air quality in the Yellow Sea, which is located between the Korean Peninsula and China, to analyze and forecast air quality in the Korean Peninsula. As a way to contribute to such effort, in Korea, a ship measurement campaign has been carried out annually in the springtime since 2018 under the supervision of the National Institute of Meteorological Sciences (NIMS).

A large proportion of the aerosols in the atmosphere are man-made (Streets et al., 2003). However, they can also be formed naturally through a phenomenon called new particle formation (NPF), in which initial clusters are formed from precursor gases and these clusters subsequently grow into larger particles that may act as cloud condensation nuclei (CCN). Therefore, NPF events, which can be regarded as a major source of aerosols and CCN, have been studied steadily because of such importance. Nevertheless, studies on marine NPF events are very scarce, unlike land NPF events that have been extensively studied. As an effort to understand marine NPF events, we conducted research on NPF events occurred over the Yellow Sea using the ship measurement data collected for 4 years (2019-2022). First, an analysis was conducted to confirm whether the already known factors that affect NPF

events are also found for NPF events occurred over the Yellow Sea. We also examined several some parameters closely related to NPF events to compare the condition of the Yellow Sea with that of land (e.g., rural and urban sites) or other seas (e.g., pacific, Aegean, and Barents). Lastly, back trajectory clustering analyses and NPF's area estimation were also conducted to better characterize the NPF events occurred over the Yellow Sea.

METHODS

Three instruments, condensation particle counter (CPC), scanning mobility particle sizer (SMPS), and cloud condensation nuclei counter (CCNC), were installed on the *Gisang 1* research vessel during the four consecutive campaigns. The aerosol size distributions measured by SMPS were used to confirm the occurrence of NPF events according to the classification criteria proposed by Kulmala (2012). To estimate NPF event occurrence area, SMPS data collected from Anmyeondo (36.54°N, 126.33°E) was also analyzed. If NPF occurred both over the Yellow Sea and Anmyeondo, we considered that the NPF event occurrence area was the inner area connecting both ends of the cruise course during the NPF event and the Anmyeondo site.

We calculated formation rate (J_{D_P}) and growth rate (GR), which are the major parameters characterizing the NPF events, using the equations presented by Kulmala (2012). Meanwhile, the duration of NPF events is from the start time of NPF events to the time at which the growth rate of particles is minimized. In addition, we used condensation sink (CS) and coagulation sink (CoagS) as the parameters for pre-existing aerosols. Both parameters indicate how much vapor or particles at a particular size are removed by pre-existing aerosols and were calculated according to the equations presented by Kerminen (2001) and Kulmala (2001), respectively. Back trajectory data for clustering analysis was calculated using the hybrid single-particle Lagrangian integrated trajectory (HYSPLIT) model (Stein, 2015). The contribution of NPF events for CN and CCN was calculated by the formula, $contribution\ (\%) = \frac{N_{NPF\ end} - N_{NPF\ start}}{N_{NPF\ end}} \times 100$.

RESLUTS AND CONCLUSIONS

For 4 years, NPF events occurred 15 times out of 128 observation days and their occurrence areas covered at least $6200\ km^2$ of the Yellow Sea. When compared with the studies conducted over other seas, the occurrence

frequency of NPF events per month was similar despite the difference in the observation season. The average values of formation rate, growth rate, and duration of the NPF events were $2.38 \pm 1.53\ cm^{-3}s^{-1}$, $4.11 \pm 2.81\ nm\ h^{-1}$, and $6.18 \pm 2.87\ h$, respectively. Formation rate and growth rate over the Yellow Sea were higher than those over other seas and ranged between the values for rural and urban sites. Meanwhile, FR and GR tended to decrease steadily, whereas duration tended to increase steadily. This showed that although the concentration of precursor vapor over the Yellow Sea tended to decrease in recent years, the Yellow Sea is still a relatively polluted sea.

The NPF events mainly occurred under the meteorological conditions of low RH and high solar radiation over the Yellow Sea. This result was consistent with some previous studies (Qi et al., 2015; Dada et al., 2017). Also, the NPF events mainly occurred under the conditions of low condensation sink and coagulation sink. That is, NPF events over the Yellow Sea preferred low pre-existing aerosol concentrations. Clustering analysis showed that 10 out of 15 NPF events occurred when air masses came from the Inner Mongolia Plateau. Four NPF events occurred when air masses came from Manchuria and one NPF event occurred when air masses came from the Korean Peninsula. The Inner Mongolia Plateau and Manchuria are continents located to the north of the Korean Peninsula and the air masses had low humidity, which made favorable conditions for NPF events over the Yellow Sea.

Finally, due to NPF events, the number concentration of total aerosol and nucleation mode particles over the Yellow Sea increased by about 61% (numerically $9000\ cm^{-3}$) and 85% (numerically $7000\ cm^{-3}$), respectively. In other words, most of the particles formed by NPF events are nucleation mode particles. On the other hand, the CCN number concentration increased by 27% and 51%, respectively, at supersaturation of 0.2% and 0.6%. The increase in CCN number concentration at 0.6% supersaturation was larger than that at 0.2% supersaturation, since smaller particles can be activated at higher supersaturation.

ACKNOWLEDGEMENTS

This work was supported by the National Research Foundation of Korea (NRF) grant funded by the Korea government (MSIT) (NO.NRF-2021R1A2B5B02002458) and by the Yonsei Signature Research Cluster

Program of 2022-22-0003. The data in Anmyeondo was produced with the support of the Korea Meteorological Administration Research and Development Program “Development of Monitoring and Analysis Techniques for Atmosphere Composition in Korea.” Under Grant (KMA2018-00522).

REFERENCES

Dada, L., et al., 2017. Long-term analysis of clear-sky new particle formation events and nonevents in Hyytiälä. Atmos. Chem. Phys. 17, 6227-6241.

Kerminen, V.-M., Pirjola, L., Kulmala, M., 2001. How significantly does coagulational scavenging limit atmospheric particle production?. J. Geophys. Res. 106, 24119-24125.

Kulmala, M., Dal Maso, M., Mäkelä, J.M, Pirjola, L., Väkevä, M., Aalto, P., Miikkulainen, P., Hämeri, K., O’dowd, C.D., 2001. On the formation, growth and composition of nucleation mode particles, Tellus B. 53, 479-490.

Kulmala, M., Petäjä, T., Nieminen, T., Sipilä, M., Manninen, H.E., Lehtipalo, K., Dal Maso, M., Aalto, P.P., Junninen, H., Paasonen, P., 2012. Measurement of the nucleation of atmospheric aerosol particles. Nat. Protoc. 7, 1651-1667.

Stein, A.F., Draxler, R.R., Rolph, G.D., Stunder, B.J.B., Cohen, M.D., Ngan, F., 2015. NOAA’s HYSPLIT atmospheric transport and dispersion modeling system. Bull. Amer. Meteor. Sci. 96, 2059-2077.

Streets, D.G., et al., 2003. An inventory of gaseous and primary aerosol emissions in Asia in the year 2000. J. Geophys. Res. 108, 8809.

Qi, X.M., et al., 2015. Aerosol size distribution and new particle formation in the western Yangtze River Delta of China: 2 years of measurements at the SORPES station. Atmos. Chem. Phys. 15, 12445-12464.

Apte, J.S., Marchall, J.D., Cohen, A.J., Braure, M., 2015. Addressing global mortality from Ambient PM2.5. Environ. Sci. Technol. 49, 8057-8066.

Charlson, R.J., 1969. Atmospheric visibility related to aerosol mass concentration: review. Environ. Sci. Technol. 3, 913-918.

Ramanathan, V., Crutzen, P.J., Kiehl, J.T., Rosenfeld, D., 2001. Aerosols, climate, and the hydrological cycle. Science. 294, 2119-2144.

EVIDENCE OF THE EFFECT OF WET DEPOSITION ON CCN CONCENTRATION OVER THE SOUTHERN OCEAN

T. ALINEJADTABRIZI[1,2,3], F. LANG[1], L. ACKERMANN[4], Y. HUANG[2,5], S. SIEMS[1,2,3], M. MANTON[1], M. KEYWOOD[6], P. KRUMMEL[6], G. AYERS[7], R. HUMPHRIES[6]

[1]School of Earth, Atmosphere and Environment, Monash University, Melbourne, VIC, Australia

[2]Australian Research Council Centre of Excellence for Climate Extremes (CLEX), Melbourne, VIC, Australia

[3]ARC Securing Antarctica's Environmental Future (SAEF) research centre

[4]Bureau of Meteorology, Observations and Data Science Section

[5]School of Earth Sciences, University of Melbourne, Melbourne, VIC, Australia

[6]Climate Science Centre, CSIRO Oceans and Atmosphere, Melbourne, Australia

Keywords: CAPE GRIM, OPEN MCC, CLOSED MCC, SHALLOW CONVECTION

INTRODUCTION

Southern Ocean (SO) air is amongst the most pristine air anywhere on Earth, particularly during winter when the lowest concentrations of cloud condensation nuclei (CCN) are observed. Historically, there has been an on-going focus on the production of dimethyl sulfide, a precursor gas, as an explanation for the observed seasonal cycle in CCN and in support of the 'CLAW' hypothesis (Charlson et al., 1987). This hypothesis, however, has been found to be incomplete, necessitating the study of other processes that may help determine the CCN budget (e.g., Quinn and Bates, 2011). Coalescence scavenging (drizzle formation) is one such process that may be particularly relevant over the SO (Kang et al., 2022), the region of Earth with the highest frequency of occurrence of drizzle and light rain. However, the impact of wet deposition, which is a direct removal process of aerosols, is still poorly understood, particularly over the SO.

Using a boundary layer cloud climatology based on Himawari-8 observations (developed by Lang et al., 2022), CCN observations from Kennaook/Cape Grim (KCG) and nearby precipitation observations (Station ID: 091331_Bureau of Meteorology), for 6 years (2016-2021), we seek to quantify the difference in the relationship between cloud morphology and precipitation, climatologically, and extend this relationship to CCN concentration as observed at Kennaook/Cape Grim (KCG), Tasmania. The hypothesis is that "highly pristine conditions/low CCN over the SO are associated with periods of relatively high precipitation arising from open mesoscale convective cells MCC".

METHODS

For the 17470 hours of data in baseline sector (refers to local wind direction between 190–280 degrees and the ambient radon concentration of less than 150 $mBeq.m^{-3}$ (Gras & Keywood, 2017)) of KCG, the fractional cloud cover (FCC) of open and closed MCC was calculated from the Himawari-8 imagery (for more information refer to Lang et al., 2022). Two thresholds were used to specify whether a sample was open or closed MCC: 50% was seen as a basic requirement while 80% was seen as a predominant requirement. The median and the 5th and 95th percentiles of CCN were calculated for the times when each cloud class (open or closed MCC) was dominant. The intensity and frequency of precipitation were also calculated for each case. Considering different parameters (shown in Fig. 1) demonstrate that the methodology is robust.

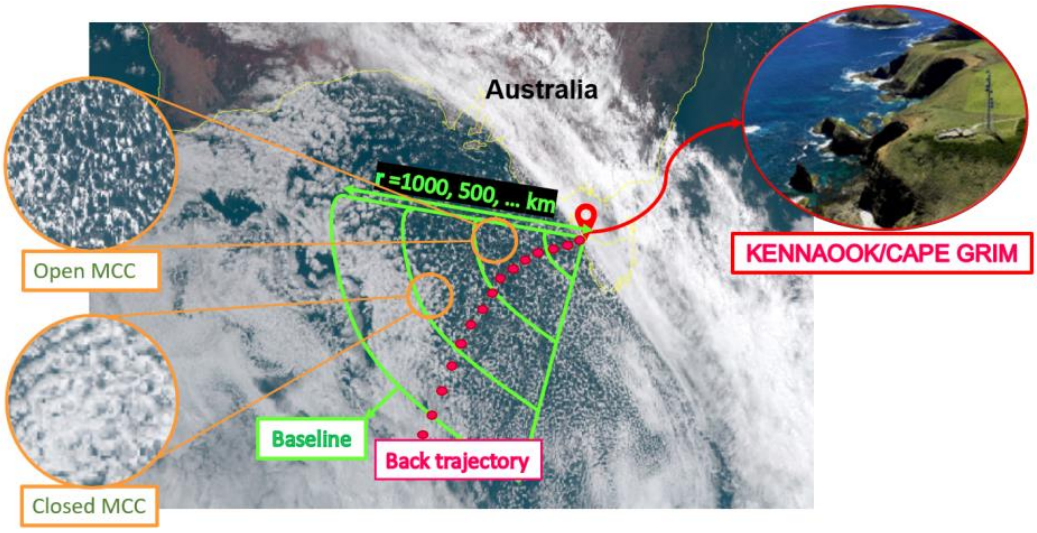

Figure 1. A true colour image of Himawari-8 on 14 January 2016, 00:00 UTC, which demonstrate the study area, the baseline sector defined based on different radii in green colour, a sample back trajectory in red colour started from KCG and also a snapshot of different upwind cloud morphology.

CONCLUSIONS

The result illustrates that for each upwind radius and time, the median CCN is smaller for open than closed MCC, and the differences are statistically significant. consider the 100 km upwind average and 3 hour upwind averaging time, gives a median CCN of 68.9 cm^{-3} from 3285 samples for open MCC and 88.6 cm^{-3} from 1050 samples for closed MCC. The study further shows that the precipitation rate for open MCC (1.72 mm/day) is 6 times greater than for closed MCC (0.29 mm/day), and the frequency of precipitation is also more frequent during open MCC, occurring 16.7% of the time compared to 4.5% for closed MCC. It should be mentioned that this inverse relationship between the precipitation and the CCN concentration is evident at both seasonal and diurnal scale as well.

The top right plot in figure 2 shows that the precipitation from closed MCC is seen to be drizzle (< 15 mm day^{-1}) rather than rain while the precipitation from open MCC exceeds 24 mm day^{-1} ~1% of the time. Further, open MCC has a higher frequency of precipitation at 16.7%, compared with 4.5% for closed MCC. Figure 2, left, shows that very clean air with CCN less than 50 cm^{-3} is much more common under open MCC than closed MCC, suggesting

that smaller CCN are washed out by wet deposition during the heavier rain under open MCC.

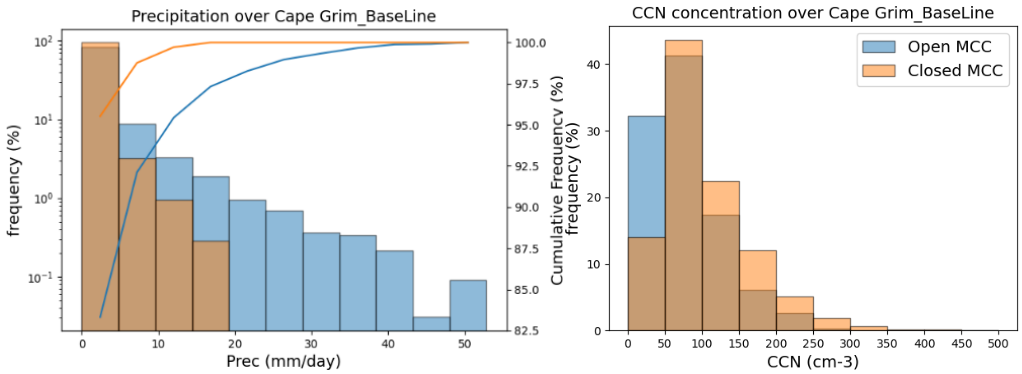

Figure 2. Probability Density Function (PDF) plot and the accumulated frequency for the precipitation (left) and the CCN concentration (right) in open and closed MCC conditions for the 100 km upwind radius and 3 hours upwind averaging time and 80% FCC threshold.

To examine whether the CCN concentration is driving the precipitation rate through an Albrecht mechanism, or precipitation is driving the CCN concentration through wet deposition, we examined their diurnal cycle over the summer season. We found that the diurnal cycle in precipitation leads the diurnal cycle in CCN by ~3 hours, which contradicts an Albrecht mechanism. Wider research suggests that the thinning of these marine boundary layer clouds through solar forcing is driving the diurnal cycle of the precipitation rate. Further research is necessary to establish to what extent, if any, precipitation is driving the CCN concentration.

References

Charlson, R. J., Lovelock, J. E., Andreae, M. O., & Warren, S. G. (1987). Oceanic phytoplankton, atmospheric sulphur, cloud albedo and climate. Nature, 326(6114), 655-661.

Gras, J. L., & Keywood, M. (2017). Cloud condensation nuclei over the Southern Ocean: wind dependence and seasonal cycles. Atmospheric Chemistry and Physics, 17(7), 4419-4432.

Kang, L., Marchand, R. T., Wood, R., & McCoy, I. L. (2022). Coalescence Scavenging Drives Droplet Number Concentration in Southern Ocean Low Clouds. Geophysical Research Letters, 49(7), e2022GL097819.

Lang, F., Ackermann, L., Huang, Y., Truong, S. C., Siems, S. T., & Manton, M. J. (2022). A climatology of open and closed mesoscale cellular convection over the Southern Ocean derived from Himawari-8 observations. Atmospheric Chemistry and Physics, 22(3), 2135-2152.

Quinn, P. K., & Bates, T. S. (2011). The case against climate regulation via oceanic phytoplankton sulphur emissions. Nature, 480(7375), 51-56.

SEAWATER AEROSOL FOGGING TO MITIGATE CORAL BLEACHING: DESIGN AND DEVELOPMENT

P. BAKER[1], J. ALROE[2], A. TAGLIAFICO GUZMAN[3], P. BUTCHERINE[3], S. ELLIS[3], L. HARRISON[4], C. MEDCRAFT[3], D.C. HERNANDEZ-JARAMILLO[3], C. CHEN[1], C. HOLLOWAY[3], J. HORCHLER[2], L. CRAVIGAN[2], M. BAIRD[5], B. KELAHER[3], Z. RISTOVSKI[2] and D. HARRISON[3]

[1] Sydney Institute of Marine Science
[2] Queensland University of Technology (QUT), Brisbane, QLD, Australia
[3] Southern Cross University (SCU),, National Marine Science Centre, Coffs Harbour, N.S.W., Australia
[4] University of Sydney
[5] CSIRO

Keywords: SEAWATER, AEROSOL, FOGGING, CORAL, REEF, BLEACHING

INTRODUCTION

Shading coral reefs to reduce the light stress component contributing to coral bleaching has been well demonstrated at very small scale. However cost-effectively deploying shading materials over entire individual reefs or even larger areas is very challenging both technically and economically. This study investigates replicating natural sea spray with seawater aerosol fog as a scalable technology that can quickly and cost effectively deliver square kilometres of shading to reduce solar radiation stress on corals during thermal bleaching events. The goal is to use seawater fog generators to provide 15-30 % shading which is expected to reduce mortality outcomes in medium level stress events.

Coral bleaching can be intense during 'doldrum' conditions when winds speeds drop below 3 ms^{-1} and typically clearer skies cause the water to warm, thermally stratify, and become clearer allowing light to penetrate further into the water column. These doldrum conditions are the exact conditions where fogging technology can effectively create the densest plume concentrations to shade coral reefs.

Selecting the best aerosol size and quantities of seawater fog to be generated requires key knowledge about when corals bleach and under what weather conditions? How does light affect coral and what wavelengths should be targeted? It is then necessary to design and develop seawater fog generators with the desired aerosol light scattering properties to effectively shade the coral.

BACKGROUND

A multidisciplinary range of methods were employed to answer these key questions; a literature review of prior shading research (Tagliafico et al, 2022) was undertaken to guide our analyses to determine the best approach in terms of target wavelengths, aerosol droplet diameter, and light attenuation.

The coral bleaching literature and recent experiments conducted at SCU indicate that shading up to 30% for 4 to 12 hours a day is beneficial can delay the onset of bleaching up to 3.1 Degree Heating Weeks or more, however the response varies by coral species. The coral shading literature suggests any shading is generally beneficial up to a level of about 75% where low light levels can cause issues.

The key wavelength bands to attenuate are UV-B, UV-A and the blue bands since they cause the most damage to coral via a number of mechanisms leading to bleaching and coral mortality in conjunction with anomalously high water temperatures.

Mie optical modelling of seawater aerosols indicated that particles around 300nm dry diameter offer optimum light scattering per unit mass in the desired wavelengths. The seawater droplet diameter target to attenuate the desired UV and visible light wavelengths was determined to be an aerosol with diameters between 0.5 – 1 µm, which at 80% RH, offers the most efficient attenuation of visible wavelengths.

A technology scan of available fog generator technologies and aerosol laboratory tests identified impact pin fog generators as the lowest energy devices that produce large numbers of seawater droplets in the target size range. High pressure water is forced through a small orifice, upon exiting the orifice the flow of water impacts a pin positioned directly in front of the orifice and is atomized (Chaker et al, 2003). Using only high-pressure seawater, the impact pin nozzles are more economically attractive than other spray technologies considered due to their lower energy consumption, as well as having lower maintenance requirements and easier remote control.

While nozzle industry practice is to typically measure wet droplet size using laser scattering particle measurement technologies, atmospheric aerosol measurement techniques were used to measure both the micron, sub-micron and nanometre scale particles below the wavelengths of visible light.

METHODS

Aerosol sizing instrumentation was set up on a moveable trolley for ease of switching between tent or wind tunnel sampling methods. Aerosol instrumentation included Scanning Electrical Mobility Sizer and Mixing Condensation Particle Counter (Brechtel), Aerodynamic Particle Sizer (TSI), Cloud Condensation Nuclei Counter and Ultra High Sensitivity Aerosol Spectrometer (Droplet Measurement Technologies), DMS500 (Cambustion) with all instruments except for the Cambustion DMS sampling through the installed ejector diluter (Dekati). Ambient background total concentrations were also monitored throughout the tests.

Impact pin nozzles (MeeFog, OzMist) of different orifice sizes were tested at a wide range of pressures. The general trend observed is that increasing pressure increases the performance of the nozzles up to approximately 150 Bar, where there is diminishing returns on particles produced per mL of water pumped. The largest orifice MeeFog nozzle was selected for field trials due to its high production rate of desired droplet sizes.

Initial plume modelling indicates a Prototype nozzle manifold and a multi-pump skid that can pressurize 500 litres of seawater per minute should adequately shade a median sized reef in low wind conditions. Larger reefs will require multiple units arranged across the wind direction to adequately shade larger reefs. Changing wind direction will also require mobile deployment methods to effectively cover the reefs

Both simple 2-D Gaussian modelling and more sophisticated 3-D modelling indicate that seawater fog systems spraying ~10 litre s^{-1} or $10^{15} – 10^{16}$ droplets per second of the right size distribution around 300 nm dry can provide up to 30+ % shading over 2-3 square kilometres in the doldrum low wind conditions. Further model refinement and validation will improve these estimates.

FIELD AEROSOL EQUIPMENT AND TRIALS

A Proof of Concept fog cannon device was custom built in Australia by OZmist with 100 Meefog impact pin type nozzles. Land trials of the fogging apparatus were conducted in 2021 at Kelvin Grove stadium, on the Queensland University of Technology campus (Alroe, 2022). A mast was installed mid-field where aerosol number concentration, three-dimensional wind velocity, air temperature and humidity were measured at heights of 4 and 8 m, allowing investigation of the vertical depth and uniformity of the plume and its impact on local meteorology. Light intensity and aerosol sizing measurements were taken at the base of the mast, to verify the expected distribution of aerosol sizes produced by fog cannon, and to evaluate the amount of shading generated by the plume. For comparison, the ambient light intensity and

meteorological conditions outside the plume were measured at a secondary sampling station located in the corner of the sports field, 40 m to the side of the fog cannon. Drones filmed the fog plume development inside the semi-enclosed stadium with both High Definition RGB and infrared cameras, allowing researchers to study the shape and coverage of the evolving seawater fog. The proof-of-concept device produced $5x10^{13}$ droplets per second with a peak diameter of ~118 nm dry diameter. Field evaluation over the reefs in February 2022 with a similar equipment set showed a similar emission of droplets up to 16% of shading was achieved albeit over a smaller area (~0.5 km).

The Fog Cannon was further developed with a variable speed fan to test the hypothesis that high air flow speeds were reducing the plume concentrations and reducing aerosol sizes. Figure 1 from the land trials near Coffs Harbour in late 2022 shows a sea water fog plume generated with the modified proof-of-concept fog cannon and measured with the aerosol equipment on the tower and tent, fifty metres away.

Figure 1., A sea water fog plume generated with the modified proof-of-concept fog cannon and measured with the aerosol instruments on the tower and tent, fifty metres away.

With the device running at the lowest possible fan speed of 3 ms^{-1} produced denser fog plumes with increased shading from aerosol distributions with a peak dry diameter of ~180 nm. The current hypothesis under investigation is that lower airflows increased local nozzle particle concentrations by an order of magnitude which in turn increased the number of aerosol collisions causing agglomeration into larger droplets and associated satellite droplets (Chaker et al, 2003).

A 10x scaled-up seawater aerosol system for offshore field work Feb-March 2023 has been constructed with a total of 1080 nozzles in a panel of 6 arrays of 1.2 w x 1.6 m high, centre mounted horizontally across rear-most part of the spray boat deck. Custom pump skid filters and pressurizes the seawater to 140 bar. No fans are used so higher plume concentrations resulting in larger average particle sizes are expected. With an increase in the emission rates of at least one order of magnitude, we are optimistic that the desired shading rate of 15-30% might be achieved over a meaningful area of a coral reef. (*latest available results will be reported at the Conference).

\

CONCLUSIONS

Seawater fogging during doldrum conditions as an intervention to mitigate coral bleaching and mortality appears technically feasible. We draw this conclusion based on recent field trials that successfully produced seawater fogs with shading to the level coral stress experiments indicate provides protection from intermediate levels of thermal stress.

Further technical development of seawater fogging systems will aim to improve efficiency by reducing undesired droplet size fractions and reducing overall capital and operating costs. Initial laboratory experiments suggest that large scale fogging operations would be more energy efficient with a greater number of small orifice nozzles operating at lower pressures. Systems engineering, deployment and implementation design will also be required.

To confirm that seawater aerosol fogging will effectively mitigate ecological damage due to coral bleaching will require further bleaching stress experiments over a wider range of species, with better imitation of natural conditions, and ultimately by on-reef field trials with comparison controls.

FUNDING ACKNOWLEDGEMENT

The Reef Restoration and Adaptation Program is funded by the partnership between the Australian Governments Reef Trust and the Great Barrier Reef Foundation.

TRADITIONAL OWNER ACKNOWLEDGEMENT

The authors would like to acknowledge the Traditional Owners of the Great Barrier Reef for permission to conduct seawater fogging experiments on their land and sea Country.

REFERENCES

Tagliafico, A., Baker, P., Kelaher, B., Ellis, S., and Harrison, D. (2022). The Effects of Shade and Light on Corals in the Context of Coral Bleaching and Shading Technologies, *Frontiers in Marine Science* **9**.

Chaker M.A., Meher-Homji, C.B., Mee T., (2003) Inlet Fogging Of Gas Turbine Engines – Experimental And Analytical Investigations On Impaction Pin Fog Nozzle Behavior. *Proceedings of ASME Turbo Expo 2003 Power for Land, Sea and Air*

Alroe, J., (2022) Saltwater Fog Generation Demonstrates Potential as a Coral Bleaching Intervention, 58th annual Australian Marine Science Association Conference 2022

MOLECULAR UNDERSTANDING OF NEW PARTICLE FORMATION IN THE CENTRAL ARCTIC

MATTHEW BOYER[1], LAURIANE L. J. QUÉLÉVER[1], HÉLÈNE ANGOT[2,4], LUBNA DADA[2,5], IVO BECK[2], TIIA LAURILA[1], MARKKU KULMALA[1], TUUKKA PETÄJÄ[1], MIKKO SIPILÄ[1], JULIA SCHMALE[2], and TUIJA JOKINEN[1,3]

[1]*Institute for Atmospheric and Earth System Research (INAR), University of Helsinki, Helsinki, 00014, Finland*

[2] *EPFL, Extreme Environments Research Laboratory, Sion, 1951, Switzerland*

[3]*Climate & Atmosphere Research Centre (CARE-C), The Cyprus Institute, Nicosia, 1645, Cyprus*

[4]*Univ. Grenoble Alpes, CNRS, INRAE, IRD, Grenoble INP, IGE, 38000 Grenoble, France*

[5] *Paul Scherrer Institute, Laboratory of Atmospheric Chemistry, Villigen PSI, Switzerland*

Keywords: CENTRAL ARCTIC, NEW PARTICLE FORMATION, GAS PHASE AEROSOL PRECURSORS.

INTRODUCTION

New particle formation (NPF) is estimated to be a dominant source of cloud condensation nuclei in the central Arctic, thereby it influences climate relevant processes in the region (Gordon *et al.*, 2017). Despite recent advancements (Baccarini *et al.*, 2020; Beck *et al.*, 2021), the mechanism of NPF in the central Arctic remains elusive and poorly understood. The Multidisciplinary drifting Observatory for the Study of Arctic Climate (MOSAiC) expedition, conducted over a full year in the central Arctic, offers a unique opportunity to investigate the mechanisms and processes involved in NPF.

METHODS

In this study, we evaluated NPF mechanisms using a suite of aerosol and gas phase data collected during the MOSAiC expedition. We focus on the time between May – Sep 2020, or the time of year when elevated nucleation mode aerosol is observed (Fig. 1 from Boyer *et al.*, 2023). The chemical composition of growing ion clusters and relevant gas phase precursor concentrations were evaluated.

CONCLUSIONS

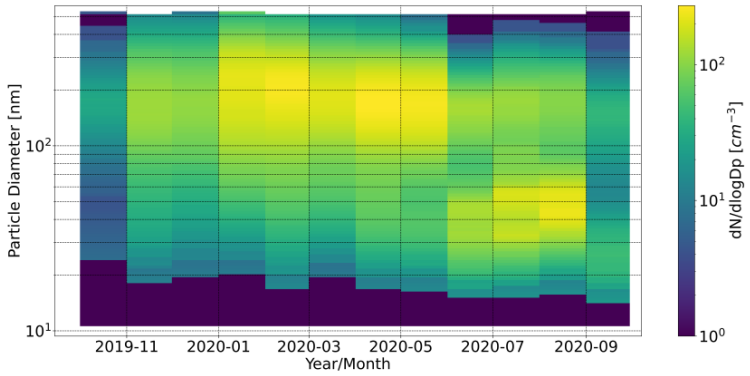

Figure 1. Monthly median aerosol size distributions from the central Arctic.

Our results identify different chemical mechanisms of NPF occurring at different times of the year. During mid-summer (June), we see a much stronger contribution of ammonia in growing clusters, whereas in September, ammonia's contribution is negligible (Fig 2). Such a result suggests that the role of bases is underestimated in NPF in the summertime central Arctic atmosphere. Overall, this analysis offers new insights on the trace gases participating in NPF and growth to atmospherically relevant sizes and highlights the need to consider different particle formation mechanisms during different seasons in the central Arctic.

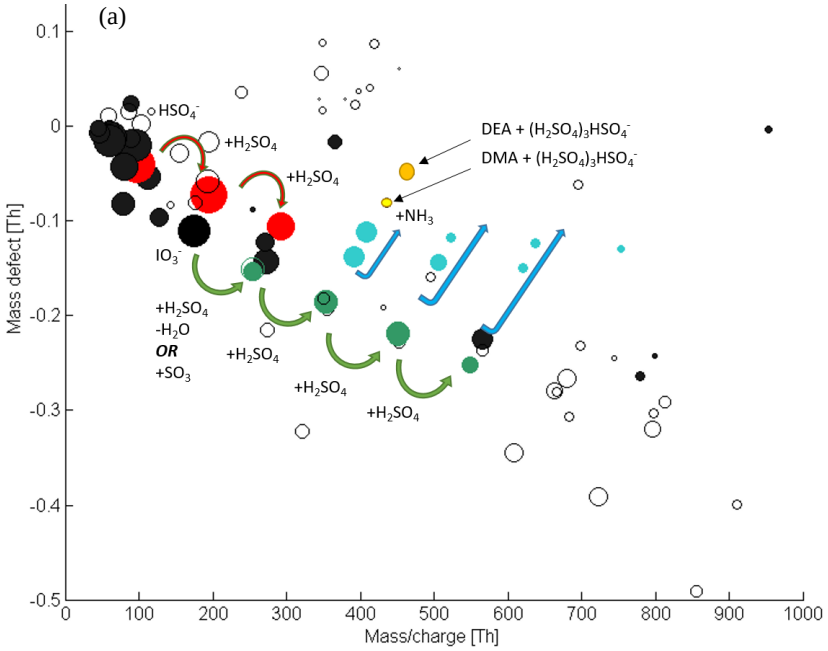

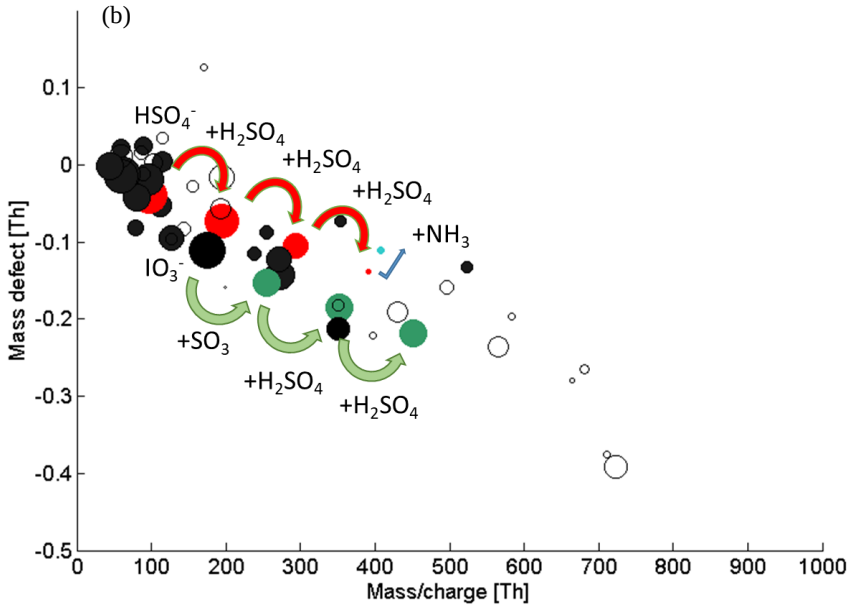

Figure 2. Mass defect plots during NPF events from (a) June 21, 2020 and (b) September 12, 2020.

ACKNOWLEDGEMENTS

We acknowledge funding from the Swiss National Sciences Foundation grant no. 188478 and the Swiss Polar Institute grant no. DIRCR-2018-004, the US DOE grant No. DE-SC0022046, European Union's Horizon 2020 research and innovation programme under grant agreement No. 856612 and the Cyprus Government. JS holds the Ingvar Kamprad Chair, sponsored by Ferring Pharmaceuticals. Part of this project was funded by ERC grant (GASPARCON) and the Academy of Finland.

REFERENCES

Baccarini, A. et al. (2020), Frequent new particle formation over the high Arctic pack ice by enhanced iodine emissions, Nature Communications, 11(1).

Beck, L. et al. (2021), Differing Mechanisms of New Particle Formation at Two Arctic Sites, Geophysical Research Letters (Vol. 48, Issue 4).

Boyer, M., et al. (2023), A full year of aerosol size distribution data from the central Arctic under an extreme positive Arctic Oscillation: Insights from the MOSAiC expedition, Atmospheric Chemistry Physics, 23(1), 389–415.

Gordon, H. et al. (2017), Causes and importance of new particle formation in the present-day and preindustrial atmospheres, Journal of Geophysical Research: Atmospheres, 122(16), 8739–8760.

Cloud parcel model simulations for RRAP Marine Cloud Brightening project

Ramon Campos Braga[1], Daniel Rosenfeld[2], Eva Johanna Horchler[3], Joel Alroe[4], Luke Harrison[5] and Daniel Harrison[1]

[1]*Southern Cross University, National Marine Science Centre, Coffs Harbour - Australia*

[2]*The Hebrew University of Jerusalem, Institute of Earth Science, Jerusalem - Israel*

[3]*Queensland University of Technology, International Laboratory for Air Quality and Health (ILAQH), Brisbane, Australia*

[4]*Queensland University of Technology, School of Earth and Atmospheric Sciences, Brisbane, Australia*

[5]*Sydney Institute of Marine Science, Institute of Marine Science, Sydney, Australia*

Keywords: CCN, Marine Cloud Brightening, effervescent nozzles, Marine Stratocumulus.

INTRODUCTION

We investigated the efficiency of the effervescent atomization technique in generating sea salt aerosol (SSA) particles to act as cloud condensation nuclei (CCN) for Marine Cloud Brightening. The data were collected during Jan-Feb 2022 on the RV Magnetic Research Vessel in the Great Barrier Reef (in the vicinity of Broadhurst and Davies Reefs). The CCN supersaturation spectrum (CCN(S)) for S ranging from 0.1% - 0.7% and aerosol particle size distributions measured for unperturbed/perturbed conditions over the Reef were analysed. An adiabatic cloud parcel model was used to simulate the effect of additional SSA particles on cloud properties, assuming local thermodynamic conditions and particle hygroscopicity (κ) of 0.6 (measured in background conditions). Both models show that the additional SSA particles increase the number concentration of drops by a factor of $\sim$ 2-3 at cloud bases (depending on updraft speeds at cloud bases). Compared with background conditions, the analysed drops have the practical effect of warm rain suppression and an increase to cloud albedo of about 10-20% at cloud depths of 400 m (a height broadly consistent with marine stratocumulus observations from the region).

METHODS

A Marine Cloud Brightening (MCB) project has been implemented in The Reef to prevent or reduce bleaching stress on coral reefs by reducing the amount of incoming solar radiation. Over GBR, the emission of sea salt particles in the marine boundary layer was performed by sprayers that convert seawater into droplets that partially evaporate under ambient humidity conditions to give nano-salty drops. The nozzle type and operating parameters (pressure and flow rates) used during the procedure, as well as meteorological conditions, determine the concentration and size of salt particles emitted. Effervescent nozzles rely on mixing high-pressure gas and liquid seawater to make a large number of tiny droplets, primarily in the nanometer diameter range (dry salt equivalent size). In our analysis, the average size distributions of aerosol particles and CCN spectrum measured for background conditions and perturbed conditions produced by effervescent nozzles are on focus. The cloud microphysical and radiative properties were calculated using two cloud parcel models with the data collected in the field campaign at Davies Reef (18.83 °S, 147.63 °E).

This study presents the analysis of simulations for measurements performed on February 8, 2022.

During this day, the SSA particles were sprayed into the atmosphere on board the RV Guardian Research Vessel. Typically, the aerosol and CCN measurements took place $\sim$ 1.5 km downwind on the RV Magnetic Vessel. Figure 1 shows a schematic figure of measurements and the vesselâs position during the MCB campaign.

The effect of increasing the number concentration of CCN by sprayers using the atomization technique on the simulated cloud properties is shown in Figure 2. The concentration of CCN increased by a factor of $\sim$ 3.5 on average during the spraying period (see Twomey equations (Twomey, 1959) in figure 2a). Fig. 2b shows that the increase in CCN concentrations leads to larger N_d and smaller resulting S_{max} for the same updraft speed. This result is associated with a relatively larger amount of water vapor consumption by a higher number of activated CCN particles (Twomey, 1974). Fig. 2c shows that the values of r_e at a cloud depth (D_c) of 400 m (typical thickness of marine stratocumulus) decrease as a function of w. Warm rain ($r_e \geq 14\,\mu$m) is expected for most of w in background conditions. For perturbed cases, warm rain is suppressed when $w \geq 0.2\,m\,s^{-1}$. The practical effect of increasing the CCN amount on cloud radiative properties is an increase in the cloud albedo (as shown in Fig.2d) since the cloud reflectivity increases due to the larger surface area of droplets in the cloud parcel. Fig. 2d shows that the cloud albedo is $\sim$ 20% larger for lower w ($\leq 0.4\,m\,s^{-1}$), when SSA was released and about 10% for $w \geq 0.5\,m\,s^{-1}$.

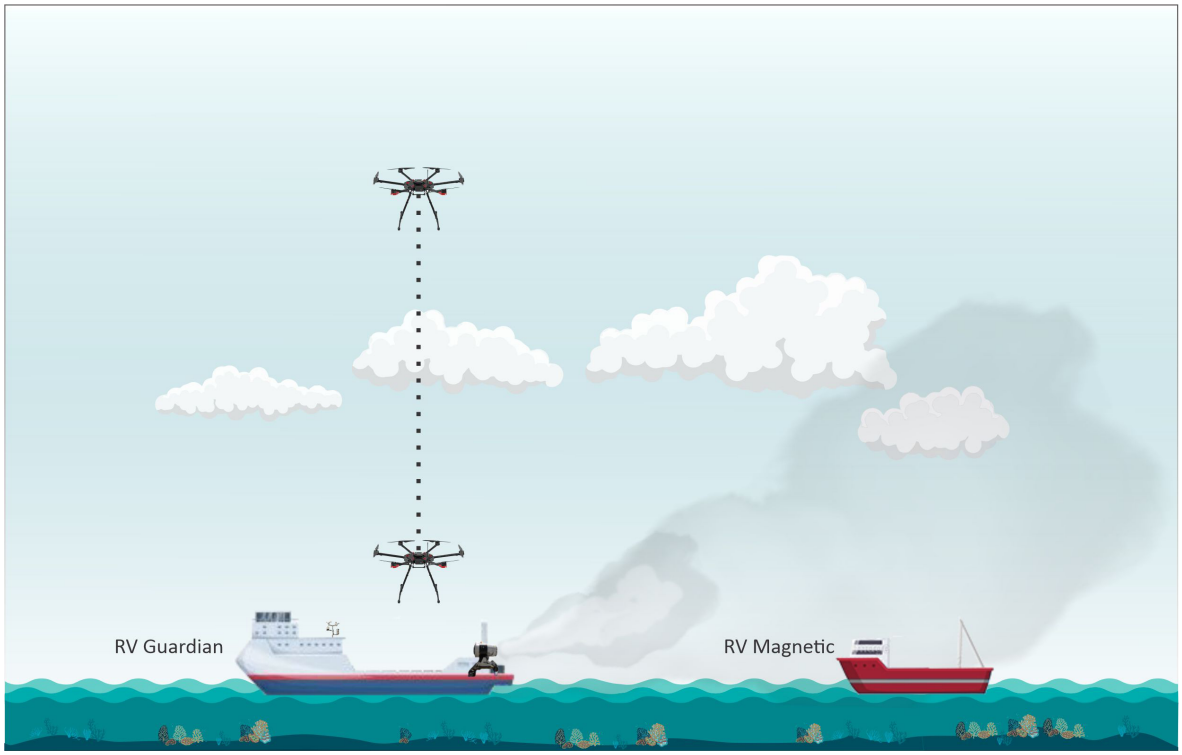

Figure 1: Positions of RV Guardian and RV Magnetic vessels during the Marine Cloud Brightening campaign on Jan-Feb 2022. SSA particles were released during the campaign on board the RV Guardian while CCN and aerosol, measurements were performed on board the RV Magnetic. The distance between the vessels was typically about 1.5 km. During spraying time, measurements of the atmospheric thermodynamic conditions (T, P, RH) above RV Guardian were performed by drones up to heights of $\sim$ 1-2 km.

CONCLUSIONS

This study investigated the effect of additional SSA particles generated by effervescent nozzles released in the vicinity of Davies and Broadhurst Reefs on simulated cloud microphysical and radiative properties of clouds. To this end, a cloud parcel model using the CCN spectrum input was used. Data collected on February 8, 2022, at the RV Magnetic Vessel were used in the analysis. Our preliminary results show that the additional SSA particles released over the Reef increase droplet number concentration by a factor of $\sim$ 2-3 at cloud bases. The practical effect on warm clouds is a smaller resulting cloud droplet effective radius and larger cloud albedo for cloud depths up to 400 m ($\sim$ 10-20% depending on cloud bases updraft speed) in comparison with background conditions. Furthermore, the increase in droplet activation leads to warm rain suppression, potentially further increasing the net cloud albedo.

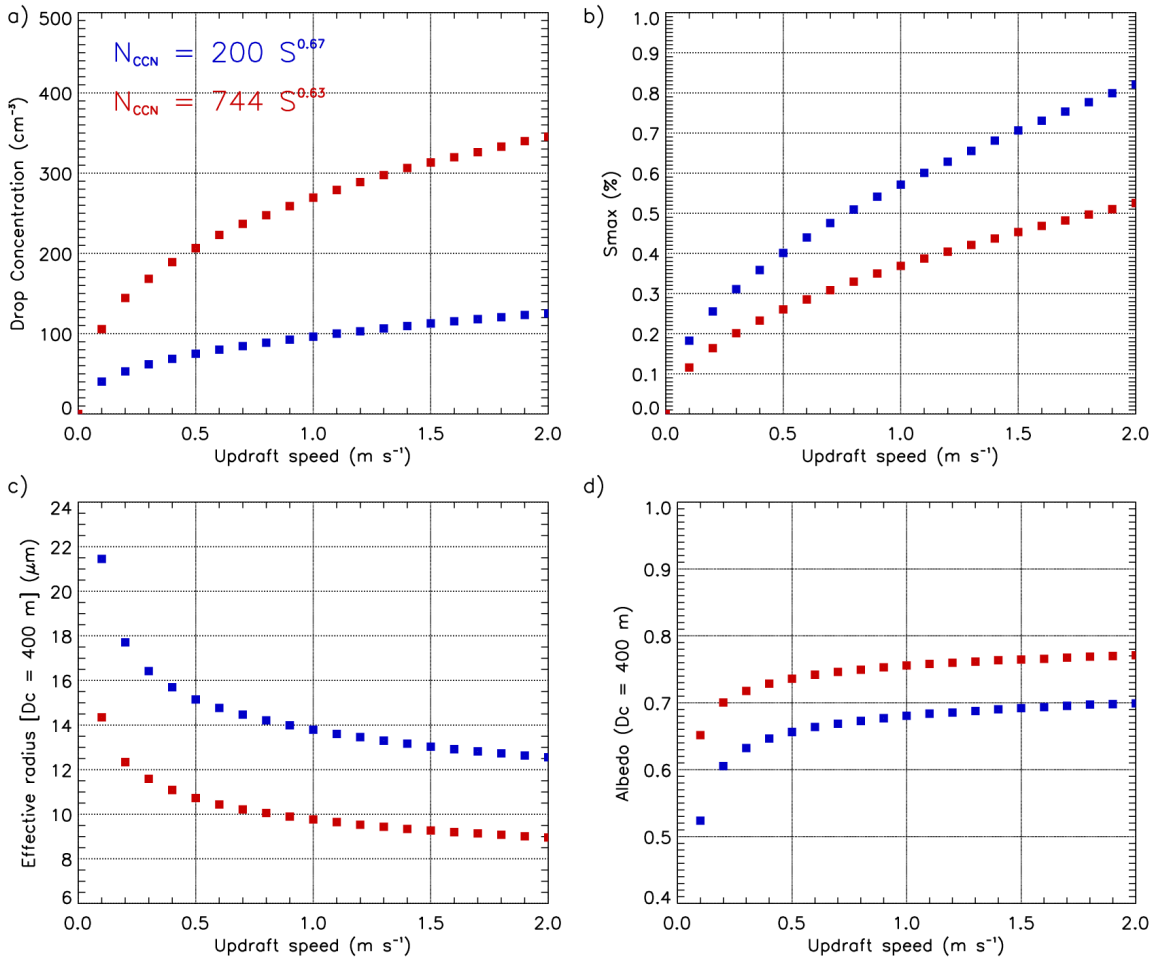

Figure 2: a) Number of droplet concentrations simulated at the cloud bases as a function of updraft speed. b) Similar to a) for the maximum supersaturation at cloud bases. c) Cloud droplet effective radius at 400 m (D_c = 400 m) above Smax level (cloud base). d) Cloud albedo at D_c = 400 m. The colors indicate the CCN spectra used in the simulation (shown on the upper left side of panel a). Blue (red) dots show results for simulations of background (perturbed) conditions. Twomey equations (Twomey, 1959) are shown in the upper-left corner of Fig.2a

ACKNOWLEDGEMENTS

This work was supported by the National Council for Aerosol Research under grant A1/001.

This work was undertaken as part of the Reef Restoration and Adaptation Program, funded by the partnership between the Australian Governments Reef Trust and the Great Barrier Reef Foundation.

REFERENCES

Twomey, S. (1959). *The nuclei of natural cloud formation part II: The supersaturation in natural clouds and the variation of cloud droplet concentration.* Geofisica Pura e Applicata.

Twomey, S. (1974). Pollution and the planetary albedo. Atmospheric Environment.

IMPROVING THE SENSITIVITY OF FOURIER TRANSFORM MASS SPECTROMETER (ORBITRAP) FOR MEASURING NUCLEATION AND GROWTH OF ATMOSPHERIC AEROSOLS

R. CAI*, W. HUANG, F. BIANCHI and M. EHN*

Institute for Atmospheric and Earth System Research/Physics, Faculty of Science, University of Helsinki, Helsinki, Finland

Keywords: FOURIER TRANSFORM MASS SPECTROMETER, ORBITRAP, NUCLEATION, VOLATILE ORGANIC COMPOUNDS

INTRODUCTION

Measurements of newly formed particles and their gaseous precursors are fundamental to understanding the mechanisms of atmospheric nucleation and growth, which require analytical techniques with high resolving powers, low limits of detection (LOD), and sufficient temporal resolution. As a new-generation technique for online analysis in nucleation studies, Orbitrap Fourier transform (FT) mass spectrometry (MS) coupled with chemical ionization (CI) can greatly improve the identification of atmospheric vapors. The mass resolving power of a Q Exactive™ Orbitrap MS at a mass-to-charge ratio (m/Q) of 200 Th can be in excess of 100,000, whereas the resolving power of time-of-flight based MS rarely exceeds 15,000 for typical online atmospheric measurements. This high resolving power of the Orbitrap MS indicates a promising advantage in the identification of numerous vapors in complex atmospheric conditions (Riva *et al*., 2019), yet it has been compromised by the relatively low sensitivity of the Orbitrap MS to trace compounds in complex gaseous mixtures.

The online detection of trace precursors such as oxidized organic molecules (OOMs) poses a significant challenge to the mass spectrometric approaches, as the precursor concentrations are often too low to produce signals with sufficient signal-to-noise ratios (SNR) or even to go over the limit of detection (LOD). At elevated noise levels, all the reported values tend to deteriorate. The intensity-based correction for the Orbitrap MS due to underestimations in inferred concentrations does improve the fidelity of the approach (Riva *et al*., 2020); however, it has no effect on the LOD, and does not address the uncertainties in the obtained results due to the corruption of the mass spectra by noise.

In this study, we aim to optimize the sensitivity of a CI-Orbitrap (Q Exactive Plus). First, we sample gas-phase OOMs from chamber experiments to investigate different governing parameters, e.g., the number of ions in the Orbitrap analyzer via adjusting the auto gain control (AGC) target and the number of microscans for signal averaging. Other parameters influencing the sensitivity and the LOD of the spectra such as spectral averaging, the temperature of the inlet capillary, radio frequency amplitude of the stacked-ring ion guide, and the measured mass range, are also investigated. After optimizing these parameters, we use the CI-Orbitrap to measure OOMs in the urban atmosphere of Helsinki, Finland. Based on these investigations, we give recommendations on the operations of CI-Orbitrap in measuring trace vapors.

METHODS

The data reported in this study were acquired with a research-grade Q Exactive Plus Orbitrap MS (Thermo Fisher Scientific Inc.). The mass resolution setting of the Orbitrap at m/Q = 200 Th was 280,000. The sample air containing trace vapors such as OOMs entered an Eisele-type CI-inlet. Neutral gas-phase OOMs were charged in the inlet using NO_3^- and $HNO_3 \cdot NO_3^-$ as reagent ions, which were generated from gas-phase HNO_3 using a soft X-ray ion source (Figure 1). The Orbitrap was operated in negative ion mode. The sampling flow rate (15 L min^{-1}), sheath flow rate (30 L min^{-1}), and voltages for the CI-inlet (−144 and − 131 V) were optimized to improve the signal and then kept constant during the experiments.

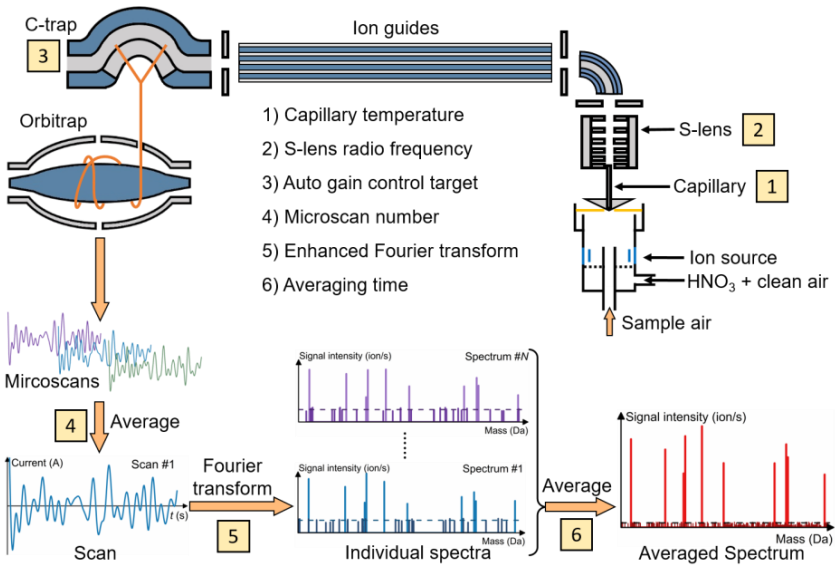

Figure 1. Illustrative schematic of the chemical ionization Orbitrap Fourier transform mass spectrometry. The influencing parameters investigated in this study are indicated by the numbers.

We investigated and optimized the sensitivity of the CI-Orbitrap to the measured OOMs and its influencing parameters with chamber experiments, then tested its performance in atmospheric measurements. The volume of the chamber was 2 m^3 and the total flow rate of clean air entering the chamber was 40 L min^{-1}. Background OOM residues composed of C, H, O, and possibly N were used for testing the CI-Orbitrap sensitivity for their low and stable concentrations (~5 × 10^8 cm^{-3}). To further minimize the influence of potential temporal variations of OOM concentrations during the experiments, the sensitivity as a function of each influencing parameter was determined twice during the increase (upscan) and the decrease (downscan) of the varying parameter. The sampling site for atmospheric measurements was located on the fourth floor of the Physicum building on the Kumpula campus of the University of Helsinki, Finland. A road with a bus stop is right below the sampling inlet (on the ground level). The nearest main road was ~100 m away. The ambient air was sampled through a 1.2 m long 3/4 inch Teflon tube. The parameters for the CI-Orbitrap were switched every half an hour between two parameter settings when they were tested in atmospheric measurements.

The raw mass spectra reported by the CI-Orbitrap were analyzed using Orbitool (Cai *et al.*, 2021), which was designed for analysis of long-term online atmospheric data sets measured by Orbitrap MS.

RESULTS

Here we mainly focus on the governing parameters for the LOD and the SNR, namely the AGC target and the microscan number. Some other influencing parameters can be found in Cai *et al*. (2022).

The mean noise of individual spectra decreased almost linearly with an increasing AGC target, which determines the number of ions in the Orbitrap analyzer during the detection event. With relatively constant OOM concentrations in the chamber, the measured peak intensities generally increased with an increasing AGC target. This increase was significant when the SNR for individual spectra was close to one. However, a high AGC target may cause some ion losses in the C-trap, which decreased the signal when AGC target was raised above 10^5. We chose 10^6 as an optimal AGC target for OOMs measurements in this study as a balance of improvement of the sensitivity to low signals and the increased ion losses in the C-trap.

The SNR can be boosted by increasing the number of observations in addition to increasing the AGC target. One way to increase the number of observations is to extend the residence time of ions in the Orbitrap analyzer, which is known not only to boost the resolution but also the SNR. However, with an insufficient number of ions, the ion statistics will not improve significantly. Alternatively, averaging multiple microscans addresses the SNR issue as each microscan is an independent FTMS experiment, and it is known to be an efficient tool in the analysis, characterization, and sequencing of biological macromolecules and their complexes (e.g., Fornelli *et al*. 2014).

Spectral averaging can further decrease the noise of the averaged spectra to facilitate the identification of the trace OOMs. However, unlike the time domain data, FT mass spectra are strictly non-negative. Consequently, averaging FT mass spectra mainly affects the outliers above the noise threshold, which does not result in as strong of a de-noising effect as that on the microscan level.

We further use the measured isotope abundances to indicate the sensitivity of the CI-Orbitrap. Molecules with less abundant isotopes (e.g., ^{13}C) are expected to show a lower signal than the value predicted using natural abundances (e.g., ^{13}C:^{12}C = 1.12 %) if sensitivity is a function of concentration. As shown in Figure 2, the relative abundance of measured isotopic OOMs compared to theoretical isotopic abundance does indeed decrease with decreasing intensity, while increasing the AGC target and the microscan number improves the sensitivity of CI-Orbitrap for trace compounds. A 50 % sensitivity threshold is herein taken as the normalized intensity at which the sensitivity is reduced by half (i.e., the measured abundance of an isotope is 50 % of the theoretical abundance). Compared to a setting with AGC target = 10^5 and microscan number = 1, increasing the AGC target to 10^6 and the microscan number to 100 decreases the 50 % sensitivity threshold from 1.7×10^{-4} to 3.6×10^{-6}, the latter corresponding to a concentration of no higher than 7.2×10^4 cm^{-3}.

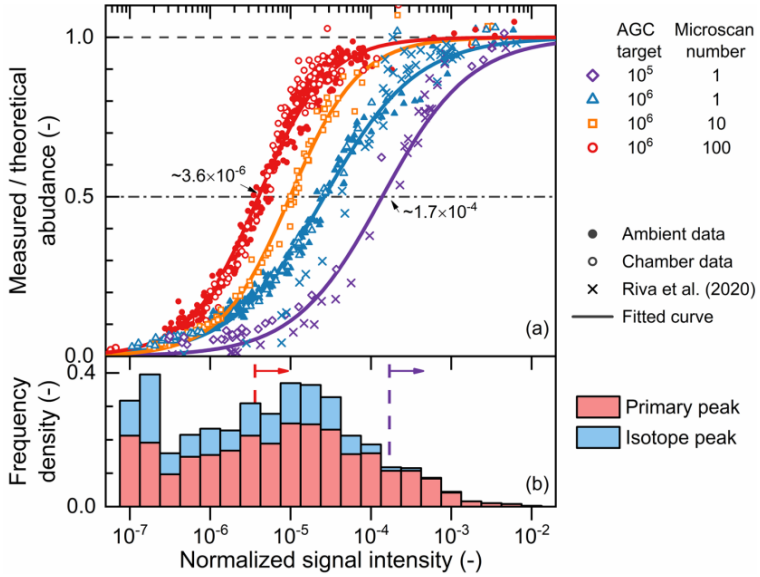

Figure 2. The Orbitrap sensitivity (a) and the intensity distribution of measured signal of ambient gaseous compounds (b). The horizontal axis is the signal intensity normalized by dividing it by the total intensity of the reagent ions ($[NO_3^-]$ + $[HNO_3 \cdot NO_3^-]$). The vertical axis in (a) is the measured abundance of ions containing less abundant isotopes divided by the theoretical abundance calculated from the primary peak. The frequency in (b) gives the number of all unique peaks in the intensity range and it is characterized by the area (rather than height) of each bar. "Primary peak" refers to ions where each atom is the most abundant isotope (e.g. ^{12}C, ^{16}O, etc), while all other ions are termed "isotope peaks". The dashed lines and arrows indicate the 50 % sensitivity thresholds for the two different settings.

The CI-Orbitrap with optimized parameters was used to measure atmospheric OOMs in the city of Helsinki from June to July in 2021. As shown in Fig. 3, we detected a total of 935 ions and retrieved their

molecular formulae. Most of the detected ions were OOMs, and a large fraction of those OOMs were nitrogen-containing OOMs due to the reactions between RO_2 radicals and NO_x in the urban atmosphere.

In accordance with the chamber experiments, the signal of trace OOMs measured in the ambient increased as the microscan number increased. The measured atmospheric OOM signals emphasize the necessity to improve the sensitivity of the CI-Orbitrap. With AGC target = 10^5 and microscan number = 1, only 12 % (129 ions) of the measured peaks were above the 50 % sensitivity threshold. In contrast, by improving the sensitivity with AGC target = 10^6 and microscan number = 100, the fraction of the peaks above the 50 % sensitivity threshold was increased to 58 % (644 ions). A scan with a mass resolution setting of 280,000 takes ~2 min in this study, which meets the demand of most OOM measurements in atmospheric conditions.

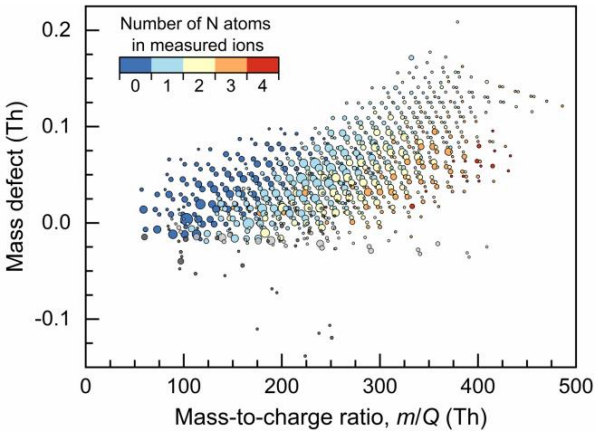

Figure 3. Gaseous compounds measured with CI-Orbitrap in urban Helsinki. Only the peaks with assigned molecular formulae are shown. The reagent ion (NO_3^-) has not been subtracted from the measured NO_3^--clustered ions. The sizes of markers indicate the concentrations of the measured compounds after the sensitivity correction.

ACKNOWLEDGEMENTS

This work was supported by the European Research Council (ERCStG CHAPAs grant no. 850614; ERC-StG MAARvEL grant no. 852161), the Academy of Finland (project no. 332547 and 337549). We thank Yihao Li for his efforts in improving the software tool for data analysis and Alexander Makarov for the experimental support and insightful discussions.

REFERENCES

Cai, R., Huang, W., Meder, M., Bourgain, F., Aizikov, K., Riva, M., Bianchi, F., and Ehn, M. (2022). Improving the sensitivity of Fourier transform mass spectrometer (Orbitrap) for online measurements of atmospheric vapors. *Analytical Chemistry* **94**, 15746-15753.

Cai, R., Li, Y., Clément, Y., Li, D., Dubois, C., Fabre, M., Besson, L., Perrier, S., George, C., Ehn, M., Huang, C., Yi, P., Ma, Y., and Riva, M. (2021). Orbitool: A software tool for analyzing online Orbitrap mass spectrometry data. *Atmospheric Measurement Techniques* **14**, 2377–2387.

Fornelli, L., Ayoub, D., Aizikov, K., Beck, A., and Tsybin, Y.O. (2014). Middle-down analysis of monoclonal antibodies with electron transfer dissociation orbitrap fourier transform mass spectrometry. *Analytical Chemistry* **86**, 3005-3012.

Riva, M., Ehn, M., Li, D., Tomaz, S., Bourgain, F., Perrier, S., George, C. (2019). CI-Orbitrap: an analytical instrument to study atmospheric reactive organic species. *Analytical Chemistry* **91**, 9419-9423.

Riva, M., Bruggemann, M., Li, D., Perrier, S., George, C., Herrmann, H., and Berndt, T. (2020). Capability of CI-Orbitrap for gas-phase analysis in atmospheric chemistry: a comparison with the CI-APi-TOF technique. *Analytical Chemistry* **92**, 8142-8150.

MARINE AEROSOL HYGROSCOPICITY, STATE OF MIXING AND CLOUD NUCLEI OVER THE WESTERN ANTARCTIC PENNINSULA

D. CEBURNIS[1], W. XU[1,2], HJ, KANG[3], YT. GIM[3], CE. KIM, K. FOSSUM[1], R. KREJCI[4], C. O'DOWD[1], YJ. YOON[3]

[1]*Center of Climate and Air Pollution Studies, University of Galway, Galway, Ireland*

[2]*College of Ocean and Earth Sciences, Xiamen University, Xiamen, China*

[3]*Korean Polar Research Institute (KOPRI), Incheon, South Korea*

[4]*Department of Environmental Science, Stockholm University, Sweden*

Keywords: marine aerosol, Antarctica, cloud condensation nuclei, hygroscopicity, number size distribution

INTRODUCTION

Marine aerosol is a critical component of the global climate system due to Earth Ocean's 70% coverage. The complexity of marine aerosol in terms of sources, hygroscopicity, state of mixing and ultimately cloud condensation nuclei potential necessitates long-term observations at globally relevant locations. Western Antarctic Peninsula, embedded in Circumpolar Antarctic Circulation, is particularly susceptible to global climate change where aerosol-cloud interactions play a key role in mitigating greenhouse gas induced warming. Highly resolved aerosol measurements are required to guide climate models and future projections.

METHODS

Long-term observations of aerosol concentrations, hygroscopicity, mixing state and cloud nucleating potential have been initiated at the King Sejong station off the Western Antarctic Peninsula. By utilising hygroscopicity tandem differential mobility analyser (HTDMA) and size discriminated cloud condensation nuclei potential (Xu et al., 2021) along with the more established aerosol measurements we expand understanding of the overall mixing state of polar marine aerosol as well as the anthropogenic impact of the research facilities to the otherwise pristine marine environment.

CONCLUSIONS

Our results have shown that marine aerosol population over the Western Antarctic Peninsula exhibits consistent high degree of external mixing across the size range where distinct chemical species coexist independently (Figure 1). There is, however, an internally mixed mode of marine organic matter, ammonium sulphate and sea salt most likely arising from cloud processing. Combining hygroscopicity measurements with the size segregated cloud condensation nuclei measurements further elucidates complexity of marine aerosol population. Size segregated particles measurements combined with the total CCN measurements enables the inference of the cloud supersaturation by considering characteristic Hoppel minimum.

Highly resolved aerosol physico-chemical measurements let us estimate the impact of anthropogenic emissions from the research bases which can at times be very significant, however, clearly discernible, short lasting and contrasted by pristine marine polar aerosol.

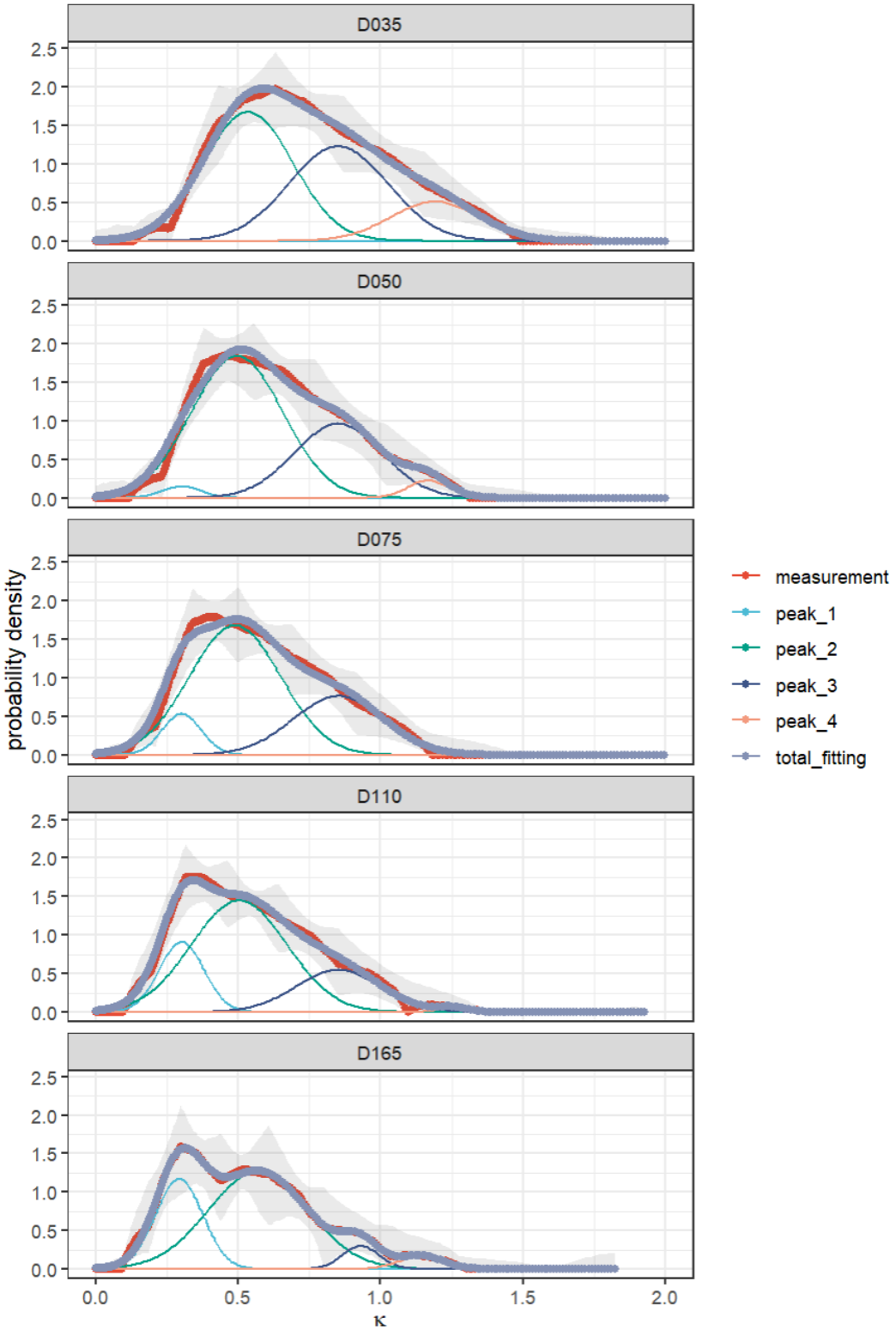

Figure 1. Deconvolved hygroscopicity distribution of kappa values at 90% relative humidity for 35, 50, 75, 110 and 165 nm particles revealing four distinct modes characteristic of marine organic matter (peak_1), ubiquitous and dominant ammonium sulphate (peak_2), internal mixture of organic matter, sulphate, and sea salt (peak_3) and pure sea salt (peak_4).

ACKNOWLEDGEMENTS

This work was supported by the KOPRI Antarctic Research programme (Project No. PE23030).

REFERENCES

Xu, W. et al. Seasonal Trends of Aerosol Hygroscopicity and Mixing State in Clean Marine and Polluted Continental Air Masses Over the Northeast Atlantic. J. Geophys. Res. Atmos. vol.126(11) (2021).

SIMULATING WINTERTIME OROGRAPHIC CLOUD SEEDING OVER THE SNOWY MOUNTAINS

S. CHEN[1], L. XUE[1], S. TESSENDORF[1], T. Chubb[2], A. PEACE[2], L. ACKERMANN[3], A. GEVORGYAN[3,5], Y. HUANG[4,6], S. SIEMS[3], J. WOLFF[1], R. RASMUSSEN[1], S. KENYON[2], J. SPEIRS[2]

A.A. AUTHOR[1], B.B. BAUTHOR[2]and C.C. CAUTHOR[2]

[1]*NCAR, Boulder, Colorado, USA.*

[2]*Snowy Hydro Ltd., Cooma, NSW, Australia.*

[3]*Monash University, Melbourne, Victoria, Australia.*

[4]*University of Melbourne, Melbourne, Victoria, Australia*

[5]*Hydrometeorology and Monitoring Center, Climate Service Division, Yerevan, Armenia*

[6]*Australian Research Council (ARC) Centre of Excellence for Climate Extremes, Melbourne, Victoria, Australia*

Keywords: Cloud Seeding, WRF-WxMod, Orographic Clouds, Snowy Mountains.

ABSTRACT

This study presents the first numerical simulations of glaciogenic cloud seeding over the Snowy Mountains, Australia using the WRF-WxMod® model. WRF-WxMod is a novel glaciogenic cloud seeding model that can track the evolution of silver iodide (AgI) nuclei in clouds, precipitation, and clear air over complex terrain, and can be utilized to simulate and quantify the cloud response to winter orographic seeding.

Three winter orographic seeding cases during the 2018 seeding periods were simulated and validated against the intensive observation campaign data. Model-observation comparisons show that the model realistically represents the cloud structures, liquid water path, and precipitation, with the sensitivity of the results to different model configurations and large-scale meteorology being tested. The results reveal that the nucleation of AgI particles and the seeding impact on precipitation are sensitive to aerosol concentrations, initial/boundary condition datasets, ice nucleation schemes, and large-scale meteorology.

In particular, we found that model sensitivities are not consistent across all three cases, and no single optimized model configuration was found to best represent all cases. Therefore, an ensemble approach is needed in the future to better assess the seeding impact. This study provides valuable insights into the complex interactions between seeding, meteorology, and cloud microphysics, highlighting the significance of accounting for model uncertainties when evaluating the seeding impact of past cases and planning for future seeding operations.

ICE GROWTH IN MIXED-PHASE CLOUD-TOP GENERATING CELLS

S. CHEN[1], L. XUE[1], S. TESSENDORF[1], K. IKEDA[1], C. WEEKS[1], J. WOLFF[1], R. RASMUSSEN[1], M. KUNKEL[2], D. BLESTRUD[2], S. PARKINSON[2], M. MEADOWS[2], and N. DAWSON[2].

[1]*NCAR, Boulder, Colorado, USA.*

[2]*Idaho Power Company, Boise, Idaho, USA.*

Keywords: Direct Numerical Simulation, Generating Cells, Mixed-Phase Clouds.

ABSTRACT

The simulation of ice growth in mixed-phase clouds is always a challenging task in cloud and weather models due to a poor understanding of the microphysical processes at fine scales (<< 100 m). Lagrangian-particle-based direct numerical simulations (DNS) offer a solution to fill the knowledge gap at fine scales by accurately resolving turbulence and particle trajectories.

This presentation introduces a mixed-phase DNS model, and the model is used to study the impact of turbulence and environmental conditions on ice growth and the potential mechanism of efficient ice growth in cloud-top generating cells (GCs). GCs are fine-scale features frequently observed in winter orographic clouds, midlatitude cyclones, and mixed-phase clouds in the southern ocean. They are hypothesized to provide favorable conditions for the formation and growth of natural ice, which is crucial for precipitation formation in mixed-phase clouds.

We performed a set of DNS experiments to examine the favorable conditions for ice growth. The influential factors such as relative humidity (RH), liquid water content (LWC), ice number concentration, vertical motions, and turbulent fluctuations are investigated. Measurements from the SNOWIE (Seeded and Natural Orographic Wintertime Clouds: The Idaho Experiment) campaign were utilized to set up the critical initial conditions that resemble those inside and outside GCs. Results show that GCs with high LWC or high RH are critical to maintaining effective ice growth. The study also found that supersaturation fluctuations substantially broaden the size spectra, which can affect the subsequent size spectral tail development and thus accelerate the formation of precipitating hydrometeors.

High Number Concentration of Atmospheric Sub-3 nm Particles in Polluted Environment of East China: three years' Observation at SORPES Station

Liangduo Chen[1], X. Qi[1, 2 *], G. Niu[1], Y. Li[1], C. Liu[1], S. Lai[1], Y. Liu[1, 2], W. Nie[1, 2], C. Yan[1, 2], J. Wang[1, 2], X. Chi[1, 2], P. Paasonen[3], K. Lehtipalo[3], V. Kerminen[3], T. Petäjä[3], M. Kulmala[3], and A. Ding[1, 2]

[1]Joint International Research Laboratory of Atmospheric and Earth System Sciences, School of Atmospheric Sciences, Nanjing University, Nanjing, China.

[2]Jiangsu Provincial Collaborative Innovation Center for Climate Change, Nanjing University, Nanjing, China.

[3]Institute for Atmospheric and Earth Systems Research/Physics, Faculty of Science, University of Helsinki, Helsinki, Finland.

Keywords: sub-3 nm particles, new particle formation, primary emission

INTRODUCTION

Atmospheric aerosols are of great concern due to their impacts on human health, visibility, and climate (Wu et al., 2019; Atkinson et al., 2014; Chen et al., 2016). New particle formation (NPF), proceeding via gas-to-particle conversion to form sub-3 nm particles and subsequently grow to large size, is a worldwide phenomenon (Nieminen et al., 2018). NPF is one of the main sources of atmospheric aerosols and cloud condensation nuclei (CCN) in the global atmosphere, thus influencing the Earth's radiative balance (Kulmala et al., 2004; Lee et al., 2019). In order to understand the gas-to-particle conversion and initial growth of NPF, the in-situ observation of sub-3 nm particles are essential.

In urban areas, in addition to NPF, primary emissions are one of the significant sources of sub-3 nm particles (Ronkko et al., 2017). In some instances, their contribution can be equal to, or even greater than, that from NPF(Olin et al., 2020). High concentrations of sub-3 nm particles have been reported in several studies conducted in megacities of eastern China. Nevertheless, a comprehensive understanding of the overall characteristics of sub-3 nm particles in polluted environments remains elusive due to the lack of long-term in situ observations, and the sources and contribution of sub-3nm particle populations are not well quantified.

This work conducted a three-year measurement of particle number size distribution down to 1 nm particles from 2018 to 2020 in the YRD region of eastern China. The sulfuric acid in each season was observed during the intensive observation campaign, and other supporting atmospheric parameters were simultaneously observed. This work aims to investigate the general characteristics of sub-3 nm particles in polluted environments of eastern China, the sources of sub-3 nm particles, including the characteristics of NPF events and primary

emissions, and the contribution of primary emissions and NPF to sub-3 nm particles and their synergetic effects.

METHODS

Field measurements were conducted at Station for Observing Regional Processes of the Earth System (SORPES) (118°57′10″E, 32°07′14″N), located in the west of the Yangtze River Delta, East China. A nano-Condensation Nucleus Counter (nCNC, Airmodus A11) system was used to observe the size distribution of sub-3 nm particles. This system consists of two major parts: A Butanol Condensable Particle Counter (bCPC, Airmodus A20) and a Particle Size Magnifier (PSM, Airmodus A10).

The nitrate-based Chemical Ionization Atmospheric Pressure interface Time-of-Flight mass spectrometer (nitrate CI-APi-ToF, Aerodyne Research Inc., and Tofwerk AG) was used to measure the concentration of sulfate acid (SA). The meteorological conditions (e.g., solar radiation, temperature, relative humidity, wind speed, and wind direction) were observed by meteorology sensors and radiometers (e.g., a weather station and 4 component net radiometer; Campbell) at the height of 9 m; trace gases (e.g., O_3, SO_2, NO, NO_2, and CO); and $PM_{2.5}$ were simultaneously observed at SORPES.

RESULTS AND CONCLUSIONS

In this study, we present observations of a high concentration of sub-3 nm particles in eastern China, with magnitudes ranging from 10^3 to 10^5 cm^{-3}, which is approximately two orders of magnitude higher than that observed in the boreal forest environment, specifically Hyytiälä, where the median sub-3 nm particle concentration was approximately 4×10^2 cm^{-3}(Sulo et al., 2021). Figure 1a shows the diurnal variation of sub-3 nm particle concentration, with the highest concentration occurring at noon when the photochemical formation is most intense. During nighttime sub-3 nm particle concentration still reaches 10^4 cm^{-3}, when primary emissions can be the dominant source. Additionally, seasonal variations of sub-3 nm particle concentration were observed, with higher concentrations occurring in spring and autumn, due to the higher frequency of NPF events.

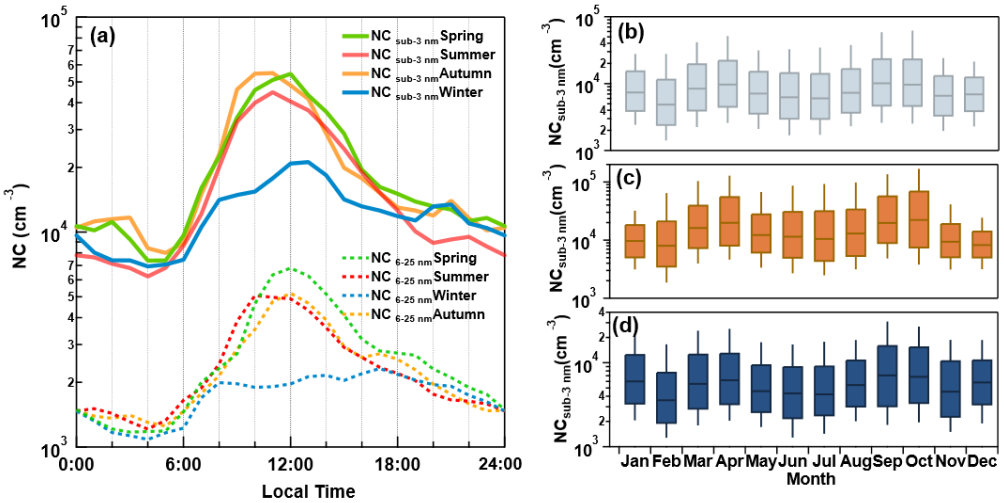

Figure 1. (a) Median diurnal variation of sub-3 nm particle concentration (solid line) and the number concentration in the size range from 6 nm to 25 nm (dashed line). The seasonal cycle of sub-3 nm particle concentration in (b) the whole day (00:00-24:00 L.T.) (c) daytime (09:00-15:00 L.T.), (d) nighttime (21:00-03:00 L.T.).

Primary emission and secondary formation were found as two major sources of sub-3 nm particles by analyzing daytime and nighttime separately. To quantify the contribution of these sources, SA and NO_x concentration were used as tracers for indicating the strength of the secondary formation and primary emission, respectively. The sub-3 nm particle concentration was estimated using multiple linear regression, as illustrated in Fig.2a. The results showed that in addition to the secondary formation, primary emission is surprisingly an unneglectable contributor to sub-3 nm particles. As indicated in Fig.2b-d, the contribution of primary emissions was found to be up to 13% on NPF days and 50% on non-NPF days during the daytime, and up to 70% during nighttime. Our study also highlights the significance of measuring the smallest particles in the atmosphere and stresses the importance of considering the primary source of sub-3 nm particles in regional and global air quality models for areas affected by anthropogenic pollution.

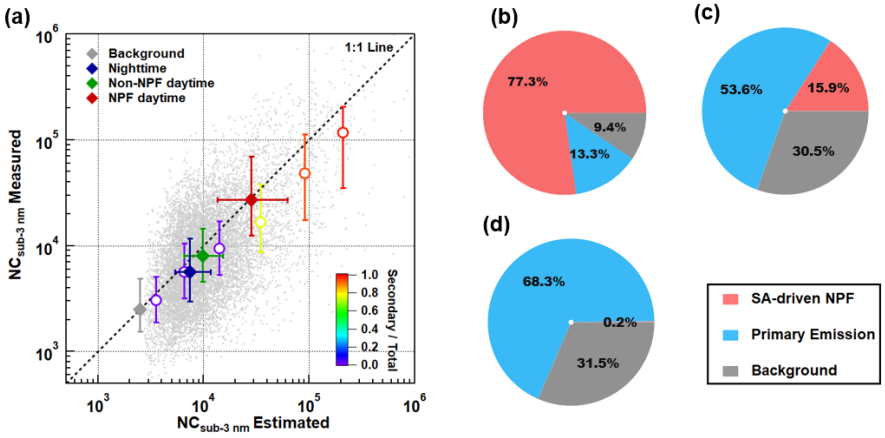

Figure 2. (a) Estimated sub-3 nm particle concentration versus measured data, the proportion of sub-3 nm particles from primary emission and secondary formation at (b) NPF day daytime, (c) Non-NPF day daytime, and (d) nighttime.

ACKNOWLEDGEMENTS

This work was supported by the Chinese Scholarship Council (CSC).

REFERENCES

Atkinson, R. W., Kang, S., Anderson, H. R., Mills, I. C., and Walton, H. A.: Epidemiological time series studies of PM2.5 and daily mortality and hospital admissions: a systematic review and meta-analysis, Thorax, 69, 660-665, 10.1136/thoraxjnl-2013-204492, 2014.

Chen, D., Liu, Z., Fast, J., and Ban, J.: Simulations of sulfate-nitrate-ammonium (SNA) aerosols during the extreme haze events over northern China in October 2014, Atmospheric Chemistry and Physics, 16, 10707-10724, 10.5194/acp-16-10707-2016, 2016.

Kulmala, M., Vehkamaki, H., Petaja, T., Dal Maso, M., Lauri, A., Kerminen, V. M., Birmili, W., and McMurry, P. H.: Formation and growth rates of ultrafine atmospheric particles: a review of observations, Journal of Aerosol Science, 35, 143-176, 10.1016/j.jaerosci.2003.10.003, 2004.

Lee, S. H., Gordon, H., Yu, H., Lehtipalo, K., Haley, R., Li, Y., and Zhang, R.: New Particle Formation in the Atmosphere: From Molecular Clusters to Global Climate, Journal of Geophysical Research: Atmospheres, 124, 7098-7146, 10.1029/2018jd029356, 2019.

Nieminen, T., Kerminen, V.-M., Petaja, T., Aalto, P. P., Arshinov, M., Asmi, E., Baltensperger, U., Beddows, D. C. S., Beukes, J. P., Collins, D., Ding, A., Harrison, R. M., Henzing, B., Hooda, R., Hu, M., Horrak, U., Kivekas, N., Komsaare, K., Krejci, R., Kristensson, A., Laakso, L., Laaksonen, A., Leaitch, W. R., Lihavainen, H., Mihalopoulos, N., Nemeth, Z., Nie, W., O'Dowd, C., Salma, I., Sellegri, K., Svenningsson, B., Swietlicki, E., Tunved, P., Ulevicius, V., Vakkari, V., Vana, M., Wiedensohler, A., Wu, Z., Virtanen, A., and Kulmala, M.: Global analysis of continental boundary layer new particle formation based on long-term measurements, Atmospheric Chemistry and Physics, 18, 14737-14756, 10.5194/acp-18-14737-2018, 2018.

Olin, M., Kuuluvainen, H., Aurela, M., Kalliokoski, J., Kuittinen, N., Isotalo, M., Timonen, H. J., Niemi, J. V., Rönkkö, T., and Dal Maso, M.: Traffic-originated nanocluster emission exceeds H₂SO₄-driven photochemical new particle formation in an urban area, Atmospheric Chemistry and Physics, 20, 1-13, 10.5194/acp-20-1-2020, 2020.

Ronkko, T., Kuuluvainen, H., Karjalainen, P., Keskinen, J., Hillamo, R., Niemi, J. V., Pirjola, L., Timonen, H. J., Saarikoski, S., Saukko, E., Jarvinen, A., Silvennoinen, H., Rostedt, A., Olin, M., Yli-Ojanpera, J., Nousiainen, P., Kousa, A., and Dal Maso, M.: Traffic is a major source of atmospheric nanocluster aerosol, Proc Natl Acad Sci U S A, 114, 7549-7554, 10.1073/pnas.1700830114, 2017.

Sulo, J., Sarnela, N., Kontkanen, J., Ahonen, L., Paasonen, P., Laurila, T., Jokinen, T., Kangasluoma, J., Junninen, H., Sipilä, M., Petäjä, T., Kulmala, M., and Lehtipalo, K.: Long-term measurement of sub-3 nm particles and their precursor gases in the boreal forest, Atmospheric Chemistry and Physics, 21, 695-715, 10.5194/acp-21-695-2021, 2021.

Wu, G., Brown, J., Zamora, M. L., Miller, A., Satterfield, M. C., Meininger, C. J., Steinhauser, C. B., Johnson, G. A., Burghardt, R. C., Bazer, F. W., Li, Y., Johnson, N. M., Molina, M. J., and Zhang, R.: Adverse organogenesis and predisposed long-term metabolic syndrome from prenatal exposure to fine particulate matter, Proc Natl Acad Sci U S A, 116, 11590-11595, 10.1073/pnas.1902925116, 2019.

Aviation emissions and their contrail formation based on QAR database

Zhu Meiyin[2], Yu Zhenghong[2], Xu Zheng[2], Zhong Shenghui[2], Pan Kang[2], Zhao Yiwei[1], Zhang Qian[1], Gao Mengyun[1] and Longfei Chen[1]
[1]School of Energy and Power Engineering, Beihang Univestiy, Beijing 100191, China.

[2]Beihang Hangzhou Innovation Institute Yuhang, Xixi Octagon City, Yuhang District, Hangzhou 310023, China.

Keywords: Aviation particulate and gaseous emissions, contrail formation, Convolutional Neural Network, Quick Access Record.

INTRODUCTION

With the continuous growth of air traffic and aviation activities, the impacts of aviation emitted particulate and gaseous pollutants on airport local air quality and global climate have received much attention within the international research community (ICAO, 2023; Schumann, 2021). As almost the only anthropogenic emission source at cruise altitudes, aviation emissions can cause positive global radiative forcing through contrails and induced cirrus, even greater than aviation CO_2 emissions (Schumann, 2021; Schumann, 2013; Kärcher, 2018; Fahey, 1999; Kärcher, 2018; Kärcher, 2015). However, current estimate or models are still suffering several uncertainties including: 1) as the important input parameters for contrail prediction model, the aviation emission inventory is normally based on the planned flight data with the assumption of the great-circle route, while the actual flight route could be quite different from the great-circle route. In addition, fuel flow rate of the aircraft at cruise is considered to be constant, but the actual fuel flow rate of aircraft may deviate from the designed value at times; 2) most of the current contrail prediction models are developed based on the Schmidt-Appleman criterion, which is based on thermodynamic theory and does not consider the influence of aviation nvPM emissions. This assumption could also bring uncertainty to the prediction of contrails; 3) the ambient air parameters (e.g. temperature, humidity, pressure, wind etc.) used in the prediction of contrail formation are mostly come from meteorological satellite data. The low spatial resolution and poor accuracy of meteorological satellite data may inevitably bring great uncertainty to contrail prediction. In this study, we used the real flight data to calculate flight trajectory, fuel consumption, on-board meteorological parameters, and combined the latest AI-based aviation emission index prediction model to calculate global aviation emission inventory, so as to eliminate the aforementioned uncertainties. Furthermore, the Schidt-Appleman criterion was verified by using the experimental data of cloud wake simulation in a high-altitude simulation chamber, to justify the accuracy of the contrails prediction model. The purpose of this study is to provide experimental and theoretical supports for accurate assessment of the impact of aviation emissions on climate change.

METHODS

This study use the latest predictive model of aviation non-volatile particulate matter (nvPM) emissions, called APMEP-CNN (Ge et al, 2022), and the real flight data obtained from Quick Access Record (QAR), to predict aviation emission inventory with high accuracy. QAR means quick access recorder, which is an important data collection equipment for civil aircraft. It can record a large number of parameters in the aircraft operation, including crew operation, aircraft status, engine status, fuel consumption, environment parameters around the aircraft, etc. The model is established with data sets from the newly published aviation emission databank and measurement results from several field studies on the ground and during cruise operation. The model also takes the influence of sustainable aviation fuels (SAFs) on nvPM emissions into account by considering fuel properties. At present, based on the APMEP-CNN, the ICAO, 2021 Aircraft Engine Emissions Databank (EEDB) (ICAO, 2021), and the global scheduled flight dataset in 2005, we predicted the nvPM number emission inventory in 2005 as shown in Figure 1. In addition, based on the Schidt-Appleman criterion, emission index, engine emission data, meteorological satellite data, and the global scheduled flight dataset in 2005, we predicted the number distribution of contrail formation in 2005 as shown in Figure 2. This study is still ongoing, and we will

combine the real flight data to further improve the prediction accuracy of aviation emission inventory and contrail formation

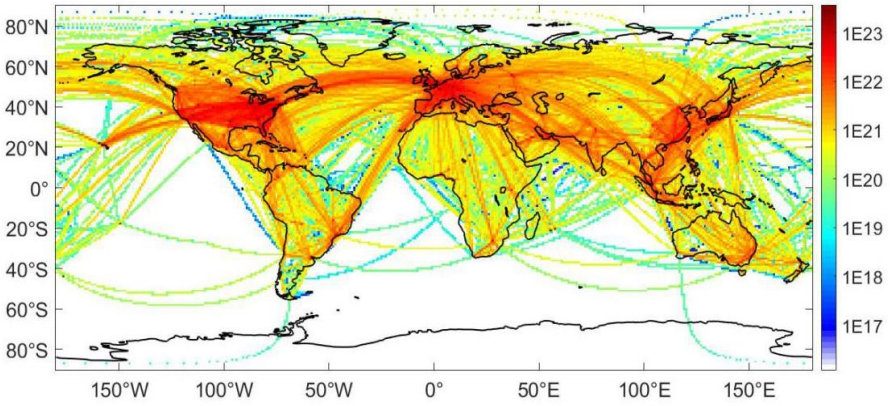

Figure 1. The prediction of nvPM number emission inventory in 2005 by using the APMEP-CNN, the ICAO, 2021 EEDB (ICAO, 2021), and the global scheduled flight dataset in 2005.

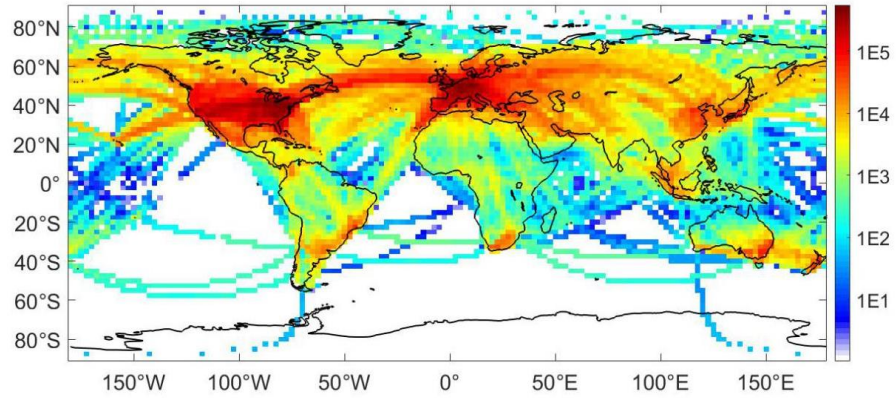

Figure 2. The number distribution of contrail formation in 2005 by using the Schidt-Appleman criterion, emission index, engine emission data, meteorological satellite data, and the global scheduled flight dataset in 2005.

CONCLUSIONS

Some preliminary conclusions are as follows:

In conclusion, With the newly published APMEP-CNN, a new prediction of nvPM number emission inventory in 2005 was proposed. The calculation results show that the nvPM number emissions at cruise phase accounts for 76.7% of the total number emissions. According to the prediction of contrail formation in 2005, the contrails was mainly generated in the northern hemisphere, where air traffic was large, especially in North America, western Europe and eastern Asia. In the future, with the real flight data, we will further improve the prediction accuracy of aviation emission inventory and contrail formation.

ACKNOWLEDGEMENTS

This work was supported by Zhejiang Provincial Natural Science Foundation of China under Grant No. LQ23E060007.

REFERENCES

ICAO. (2023). Economic Impacts of COVID-19 on Civil Aviation. https://www.icao.int/sustainability/Pages/Economic-Impacts-of-COVID-19.aspx.

Schumann, U., and Bugliaro, L. et al. (2021). Aviation contrail cirrus and radiative forcing over Europe during 6 months of COVID-19. *Geophysical research letters* 48(8), e2021GL092771.

Schumann, U., and Graf, K. (2013). Aviation-induced cirrus and radiation changes at diurnal timescales. *Journal of Geophysical Research: Atmospheres* 118(5), 2404-2421.
Fahey, D.W. and Schumann, U. (1999). Aviation-produced aerosols and cloudiness. In Aviation and the Global Atmosphere. A Special Report of IPCC Working Groups I and III. Intergovernmental Panel on Climate Change (ed. Penner, J.E.), (Cambridge University Press, Cambridge, U.K.).
Kärcher, B. (2018). Formation and radiative forcing of contrail cirrus. *Nature communications* 9(1): 1-17.
Kärcher, B. and Burkhardt, U. et al. (2015). The microphysical pathway to contrail formation. *Journal of Geophysical Research: Atmospheres* 120(15): 7893-7927.
ICAO, 2021. EASA ICAO Engine Emissions Databank. The European Union Aviation Safety Agency.
Ge, F.D. and Yu, Z.H. et al. (2022). Predicting aviation non-volatile particulate matter emissions at cruise via convolutional neural network. *Science of the Total Environment* 850, 158089.

Particle size distributions and semi-VOC analysis of a miniature aero-engine

LEI LIU[1], ZHIRONG LIANG[1], LONGFEI CHEN[1,2],

[1]Beihang Hangzhou Innovation Institute Yuhang, Hangzhou, 310023, China.

[2]School of Energy and Power Engineering, Beihang University, Beijing, 100191, China.

Keywords: Miniature aero-engine, Emission characterization, Particle size distribution, VOC, GC-MS.

INTRODUCTION

Aircraft emit both particulate and gaseous emissions (Unal et al., 2005; Hudda et al., 2014). The global-scale impacts of civil aviation are heavily debated and are principally attributed to the climate forcing of exhausts emitted at cruising altitudes. In the lower troposphere, civil aviation has more local effects on the deterioration of air quality and thus human exposure and health due to airport operations (Masiol et al., 2016). Recent studies have demonstrated that aviation emissions can increase particle number (PN) concentrations for long distances downwind from runways (Hudda et al., 2014; Keuken et al., 2015). Especially, the impacts of aviation emissions on the ground-level ambient ultrafine particle (UFP; aerodynamic diameter < 100 nm) concentrations were found to extend over unexpectedly large areas near airports and in particular along flight paths (Stacey, B., 2019). Besides, Miracolo et al. (2011) found that the aging of aircraft semi-VOCs produced substantial amounts of secondary aerosol exceeding primary emissions severalfold.

Although many studies have been conducted to analyze the particle size distributions and semi-VOC speciation of aviation emissions, most of them have been limited to ambient observations within a few hundred meters of airports or were measured in individually intercepted plumes, primarily from takeoffs or idling. In addition, the high background concentrations of atmospheric particles from other sources (i.e., vehicular emission, coal combustion, industrial activities) may significantly interfere with the measurement of particle size distributions from aircraft in the airport.

In this study, we built a miniature aero-engine mimicking CMF56 in lab scale, which could simulate aircraft emissions under various operating conditions. Therefore, we can directly measure the particle size distributions and chemical compositions of semi-VOCs of aircraft emissions by eliminating the influence of external factors. Both the gaseous and particulate semi-VOCs including n-alkanes, cyclic alkanes, ketones, aldehydes, PAHs can be characterized using the high-resolution GCxGC/MS methodology. Their relationships with the nucleation mode and accumulation mode particulate matter (PM) emissisions are identified for revealing the compositional particulate structures. Besides, various fuels including kerosene, and bio-get fuels towards carbon neutrality can be burned in this engine to examine the impact of sustainable aviation fuels on emissions. We mainly focus on the effectiveness of alternative fuel on varying the particulate size distributions with compositional variations, which would be further resolved in combination with comprehensive morphological analysis. This can help us better estimate the local and global influence of aircraft emissions on the climate and human health.

METHODS

Exhaust measurements were conducted to characterize the particle size distributions and the semi-VOC speciation from the self-built miniature CFM56 variant turbofan (Figure 1) in the lab. The test engine was operated at several engine loads, selected to represent aircraft activities during a typical landing–take-off (LTO) cycle and the cruising condition. The turbine engine exhaust was sampled by a multi-point probe with an inner diameter of 8 mm, located 0.7m downstream of the engine exit plane. The particle size distributions under different conditions were measured by a fast particulate analyzer (DMS500, Cambustion Ltd., UK) with signal acquisition frequency of 10 Hz, which could realize transient measurements. The DMS500 system as supplied for engine sampling incorporates two stages of dilution.

During the measurements, the 1st stage dilution factor was set to 5 by using dry compressed air to avoid condensation. The 2nd dilution stage uses a rotating disc to provide a variable dilution factor which may be varied to maintain good signal to noise ratio, while minimizing the cleaning requirements. In this study, the 2nd stage dilution factor was set to 70.

A two-dimensional Gas Chromatography-Time of Flight Mass Spectrometry (GCxGC-ToF-MS, Figure 2) was adopted to characterize the gaseous and particulate semi-VOC emissions including aliphatics, aromatics, ketones, aldehydes etc from the aero-engine emissions. The initial samples were analyzed using gas chromatography (GC, 7890 B, Agilent Technologies, USA) which was equipped with a Zoex ZX 2 cryogenic modulator (Houston, TX, USA). The first dimension was comprised of a SGE DBX5, non-polar capillary column (5% phenyl polysilphenylene-siloxane) and it was equipped within the primary oven. The secondary dimension polar column was equipped with a SGE DBX50 (50% phenyl polysilphenylene-siloxane), which was arranged in an internal oven. Both dimensions were adopted to attain better compositional separation.

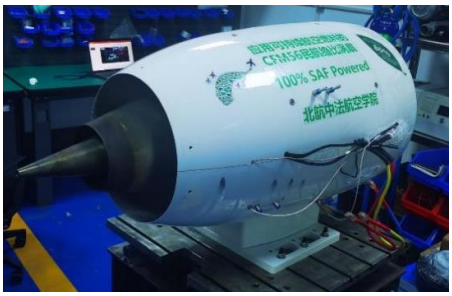

Figure 1. Photo of the miniature aero-engine in the lab.

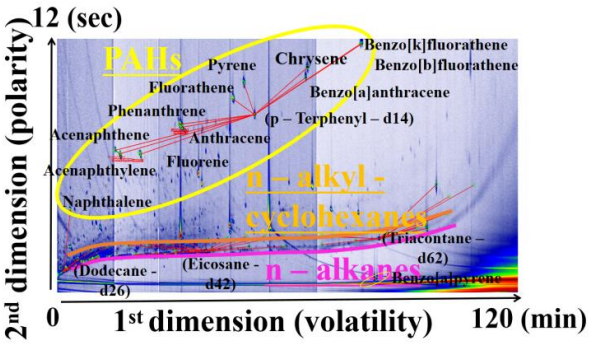

Figure 2. The eluting semi-VOC distributions interpreted by multi-dimensional GC/MS technique.

CONCLUSIONS

Our experiment is still ongoing, only some preliminary results are presented here. Figure 3 shows the particle size distributions under different thrust conditions using the kerosene fuel. Furthermore, we calculate the variations in the geometric mean diameter (GMD) and total particle concentration as a function of thrust as shown in Figure 4a and b. Moreover, the semi-VOCs were preliminarily speciated using the multi-dimensional GC/MS technique.

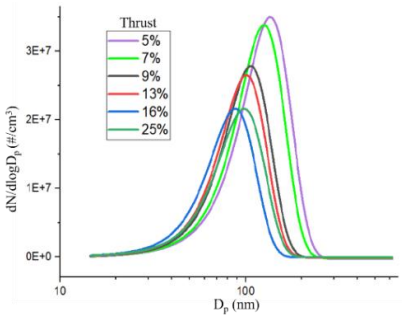

Figure 3. Particle size distributions at different engine thrust.

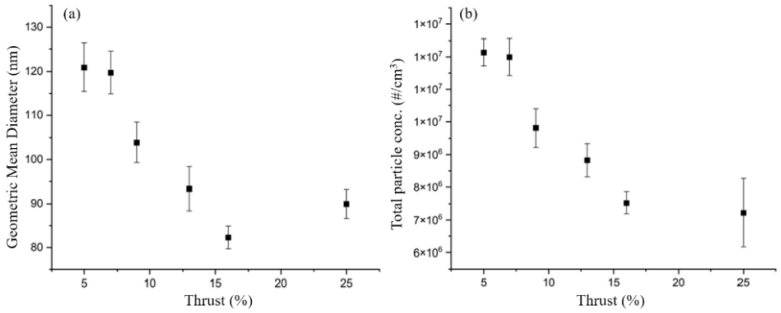

Figure 4. Variations in geometric mean diameter (a) and total particle concentration (b) as a function of thrust.

In summary, we can conclude that within the measurement range, when the relative thrust is less than 20%, particulate matter GMD gradually decreases with the increase of thrust, which is caused by an increase in the air-fuel ratio resulting in fuller fuel combustion. When the relative thrust is higher than 20%, the GMD increases with the increase of thrust. With the increase of engine thrust, the total particle concentration decreases firstly and then gradually increases. It should be noted that the GMD of particles emitted by aviation turbofan engines represented by CFM56 is usually within the range of 30-100 nm, while the GMD of particles emitted by the self-built miniature engine measured during the experiment is between 80-130 nm. This is because the combustion efficiency of the engine used in the experiment is lower than that of the civil aviation turbofan engine, fuel combustion is insufficient, and the existence of semi-volatile substances leads to higher GMD.

ACKNOWLEDGEMENTS

This work was supported by the National Science Foundation of China.

REFERENCES

Unal, A., Hu, Y., Chang, M. E., Odman, M. T., and Russell, A. G.: Airport related emissions and impacts on air quality: Application to the Atlanta International Airport, Atmos. Environ., 39, 5787–5798, 2005.

Hudda, N., Gould, T., Hartin, K., Larson, T. V., and Fruin, S. A.: Emissions from an international airport increase particle number concentrations 4-fold at 10 km downwind, Environ. Sci. Technol., 48, 6628–6635, 2014.

Masiol, M., Vu, T. V., Beddows, D. C. S., Harrison, R. M.: Source apportionment of wide range particle size spectra and black carbon collected at the airport of Venice (Italy), Atmos. Environ., 139, 56–74, 2016.

Keuken, M. P.; Moerman, M.; Zandveld, P.; Henzing, J. S.; Hoek, G. Total and size-resolved particle number and black carbon concentrations in urban areas near Schiphol airport (the Netherlands). Atmos. Environ. 2015, 104, 132−142.

Stacey, B. Measurement of Ultrafine Particles at Airports: A Review. Atmos. Environ. 2019, 198, 463−477.

Miracolo, M. A., Hennigan, C. J., Ranjan, M., Nguyen, N. T., Gordon, T. D., Lipsky, E. M., Presto, A. A., Donahue, N. M., and Robinson, A. L.: Secondary aerosol formation from photochemical aging of aircraft exhaust in a smog chamber, Atmos. Chem. Phys., 11, 4135–4147, 2011.

SEASONAL VARIATIONS OF N_2O_5 AND $CLNO_2$ IN URBAN BEIJING

Xin Chen[1], Wei Ma[1], Junlei Zhan[1], Zongcheng Wang[1], Yiran Li[2], Chenjie Hua[1], Feixue Zheng[1], Rujing Yin[3], Yongchun Liu[1], Jingkun Jiang[2], Markku Kulmala[1,3], Men Xia[3], Chao Yan[1,3,4]

[1]Aerosol and Haze Laboratory, Advanced Innovation Center for Soft Matter Science and Engineering, Beijing University of Chemical Technology, Beijing, China

[2] State Key Joint Laboratory of Environment Simulation and Pollution Control, School of Environment, Tsinghua University, Beijing, China

[3]Institute for Atmospheric and Earth System Research, Faculty of Science, University of Helsinki, Helsinki, 00014, Finland

[4]Joint International Research Laboratory of Atmospheric and Earth System Research, School of Atmospheric Sciences, Nanjing University, Nanjing, China

Keywords: Nocturnal Chemistry, N_2O_5, $ClNO_2$, nitrate formation

INTRODUCTION

Air pollution is a major environmental problem in China due to its adverse effects on human health (Cai, W. et al). With the decrease of sulfur dioxide (SO_2) in the Atmosphere, sulfate in particulate matter begins to decrease, while the proportion of nitrate gradually increases (Zhou et al., 2022; Xie et al., 2022). High concentrations of NO_3^- will contribute to the formation of haze and reduce visibility (Hu et al., 2021; Xie et al., 2020). Therefore, it is important to understand the mechanism of nitrate formation for PM2.5 reduction and air pollution mitigation in China.

It is well known that there are two main production ways of nitrate formation: one is that nitrogen dioxide (NO_2) reacts with hydroxyl radicals (OH) to form nitric acid (HNO_3), which can react with ammonia and contribute to pNO_3^- in the daytime. Another is nocturnal chemistry reaction that heterogeneous reaction of N_2O_5 on aerosol (Chen et al., 2020; Fan et al., 2021). And then N_2O_5 can produce nitryl chloride ($ClNO_2$) on chloride-containing aerosols, which can be photolyzed into NO_2 and atomic chlorine (Cl) after sunrise, resulting in significant impacts on daytime photochemistry (Simpson et al., 2015; Tham et al., 2018; Xia et al., 2021). It shows that N_2O_5 and $ClNO_2$ have important roles in nitrate production and atmospheric oxidation, respectively (Thornton et al., 2010; Wang et al., 2016).

Observations of N_2O_5 and $ClNO_2$ in the troposphere have been reported worldwide, mostly in North America (Osthoff et al., 2008; Thornton et al., 2010; Mielke et al., 2013; Kim et al., 2014; Mielke et al., 2016), Europe (Phillips et al., 2012; Bannan et al., 2015), and China (Tham et al., 2014; Tham et al., 2016; Wang et al., 2016, Wang et al., 2017, Wang et al., 2020, Xia et al., 2019, Xia et al., 2021).These studies have shown that they are widely distributed in the troposphere of which concentrations ranging from a few hundred ppt to several ppb.

From the above, N_2O_5 are strongly influenced by meteorological conditions and precursors such as temperature, relative humidity, NO_x, O_3, etc. This variance will be more noticeable in different seasons. many studies have proved that the lower temperature and dark environment facilitates the occurrence of nocturnal chemistry during winter (Wagner et al., 2013). Meanwhile, nocturnal nitrate formation was comparable to or even higher than that formed via the daytime pathway (Wang et al., 2017; Wang et al., 2019; Alexander et al., 2020). For example, the heterogeneous reaction of N_2O_5 is the main nocturnal NO_3^- formation in winter, with contributions of 44%~97% at night (Fu et al., 2020; He et al., 2018). Li et al. (2021) reported that the nighttime pathway can account for 40% in cold seasons in the YRD. And in the NCP, the nitrate contribution of heterogeneous pathways was about 30.8 % (Liu et al., 2020). This shows that diverse regional conditions can lead to discrepancy in nocturnal chemical reactions and in turn lead to differences in nitrate formation. However, intensive seasonal measurements about N_2O_5 in china, to our knowledge, have not been performed so far. More detailed studies are needed to broaden our knowledge of

their seasonal behavior, and variation in different chemical conditions especially in polluted metropolis such as Beijing.

In this study, long-term observations of N_2O_5 were performed in four seasons in urban Beijing. It aims to obtain a comprehensive understanding of the seasonal variations in the nocturnal chemistry as well as the key precursors, and chemical pathways in Beijing. And it can provide a scientific basis for designing effective emissions policy implications to control the urgent fine particulate pollution in the NCP region.

METHODS

Field observations

Sampling site description

The measurements were conducted carried out at Aerosol andHaze Laboratory, Beijing University of Chemical Technology (AHL/BUCT Station, 39º56'31" N, 116º17'50" E) from October 1, 2021, to March 16, 2022 and June 6, 2022, to September 30, 2022. All instruments were on the rooftop of the corresponding main teaching building (~18 m above the ground surface). The station is a typical urban observation station, surrounded by main roads, residential, and commercial areas. More details can be found in previous work (Liu et al., 2020).

Measurement of main Species

N_2O_5, $ClNO_2$, and Cl_2 were measured with a high-resolution Time-of-Flight chemical ionization mass spectrometer using iodide as the reagent ion (I-CIMS).

Meteorological parameters including UVB radiation, temperature, pressure, relative humidity (RH), wind speed, and direction are measured with a weather station (AWS310, Vaisala Inc.).

Trace gases, including NO_x, SO_2, CO, and O_3, were measured with the corresponding analyzer (Thermo Scientific, 42i, 43i, 48i, and 49i).

The number size distributions of particles were measured by a diethylene glycol scanning mobility particle spectrometer (DEG-SMPS), which was corrected to the wet particle-state Sa with a hygroscopic growth factor (Liu et al., 2013).

VOCs were detected by proton transfer reaction time-of-flight mass spectrometry (PTR-ToF-MS 8000, IONICON) with a hydronium ion (H_3O^+) source.

The bulk composition, including chloride, nitrate, sulfate, ammonium, and organics of nonrefractory PM2.5 (NR-PM2.5), was measured with a time-of-flight aerosol chemical speciation monitor (ToF-ACSM, Aerodyne) at the

AHL/BUCT station. All the measurement techniques above mentioned, are summarized in Table 1.

Species	Instruments
N_2O_5, $ClNO_2$	I-CIMS
meteorological parameters (T, RH, UVB, ect.)	Weather station
trace gas (CO, SO_2, NO_x, and O_3)	Thermo Environmental Instruments
sizes of aerosols	SMPS
VOCs	PTR
aerosol chemical composition (NR-$PM_{2.5}$, including Org, SO_4^{2-}, NO_3^-, NH_4^+, and Cl^-)	ACSM

Table 1. Instruments used for measurement in BUCT.

Calculation of uptake coefficient (γ)

To derive the uptake coefficient of N_2O_5, NO_3 and N_2O_5 were deemed as ($[NO_3] + [N_2O_5]$). It is in pseudo-steady state rather than balance state, suggested by McLaren et al (2010).

$$\frac{\mathrm{d}([\mathrm{N_2O_5}]+[\mathrm{NO_3}])}{\mathrm{d}t} = P_{\mathrm{NO_3}} - L_{\mathrm{N_2O_5+NO_3}} (1)$$

$$L_{\mathrm{NO_3+N_2O_5}} = L_{\mathrm{NO_3}} + L_{\mathrm{N_2O_5}} = k_{\mathrm{x}}[\mathrm{NO_3}] + k_{\mathrm{y}}[\mathrm{N_2O_5}] (2)$$

$$P_{\mathrm{NO_3}} = k_1[\mathrm{NO_2}][\mathrm{O_3}] (3)$$

where k_{x} and k_{y} are the overall pseudo first order rate constants for $\mathrm{NO_3}$ and $\mathrm{N_2O_5}$ respectively.

$$k_{\mathrm{y}} = 0.25 \cdot \gamma_{\mathrm{N2O5}} \cdot C \cdot \mathrm{Sa} \cdot K_{eq}[\mathrm{NO_2}] \quad (4)$$

where C denotes the mean molecular speed of N_2O_5, Sa is the surface-to-volume ratio of aerosols, γ_{N2O5} is the uptake coefficient of N_2O_5 and K_{eq} represents the thermal equilibrium constant between NO_3 and N_2O_5.

Chemical box model

To estimate the concentration of OH radical in the daytime, a chemical box model was developed with the latest version of the MCM (v3.3.1) (Wolfe et al., 2016) and an updated chlorine (Cl) radical chemistry module (Xue et al., 2015). The integrated production of nitric acid during daytime was then calculated based on the simulation results. The input data included the data relating to N_2O_5, $ClNO_2$, HONO, O_3, NO, NO_2, SO_2, CO, C_2 to C_{10} NMHCs, OVOCs (formaldehyde, acetaldehyde, acetone, and MEK), temperature, aerosol surface area, BLH, and J(NO_2). The resolution of the date in this model was 10 min.

RESULTS AND CONCLUSIONS

Based on long-term observations, seasonal data of N_2O_5 and $ClNO_2$ seasons were obtained in BUCT station. The highest value of N_2O_5 was observed in autumn with 1.5 ppbv, while the highest value of $ClNO_2$ occurred in winter with 2.2 ppbv. The levels observed at BUCT are comparable with measurements at YRD region, but slightly higher than the previous Beijing data. Even though it is lower than the polluted areas of southern China, like Hong Kong and Guangdong province, it indicates more intense nighttime chemical reactions than before in Beijing and a more serious air pollution in NCP area. Therefore, it is particularly important to enforce policies to curb the increase of nitrates.

In diurnal profiles of N_2O_5, $ClNO_2$, both N_2O_5 and $ClNO_2$ exhibited typical diurnal variations, increasing during the night and decreasing during the day. And nocturnal chemistry exhibits obvious seasonal characteristics. N_2O_5, $ClNO_2$ had a higher concentration at night during the spring and winter Olympics. It was associated with few NO, lower temperature and longer reaction times, which can contribute to the conversion and accumulation of N_2O_5. And in the autumn and winter, high NO concentrations prevented nocturnal chemistry because NO can deplete NO_3 radical rapidly regardless of their weather conditions. In summer, meteorological conditions including humidity, solar radiation and precursors such as high concentrations of O_3 and low concentrations of NO are conducive to nocturnal chemical reactions. However, the most important influence factors are high temperature, facilitating the conversion of N_2O_5 to NO_3 radical and it also inhibited N_2O_5 production.

In summary, we report on the seasonal concentration characteristics of N_2O_5 in urban Beijing. Analyzing the long-term observation data, the chemistry of N_2O_5 is influenced by precursors and meteorological factors, and this dominant factor varies in different seasons. We hope this study will help to implement different policies to mitigate the environmental pollution more effectively in different seasons.

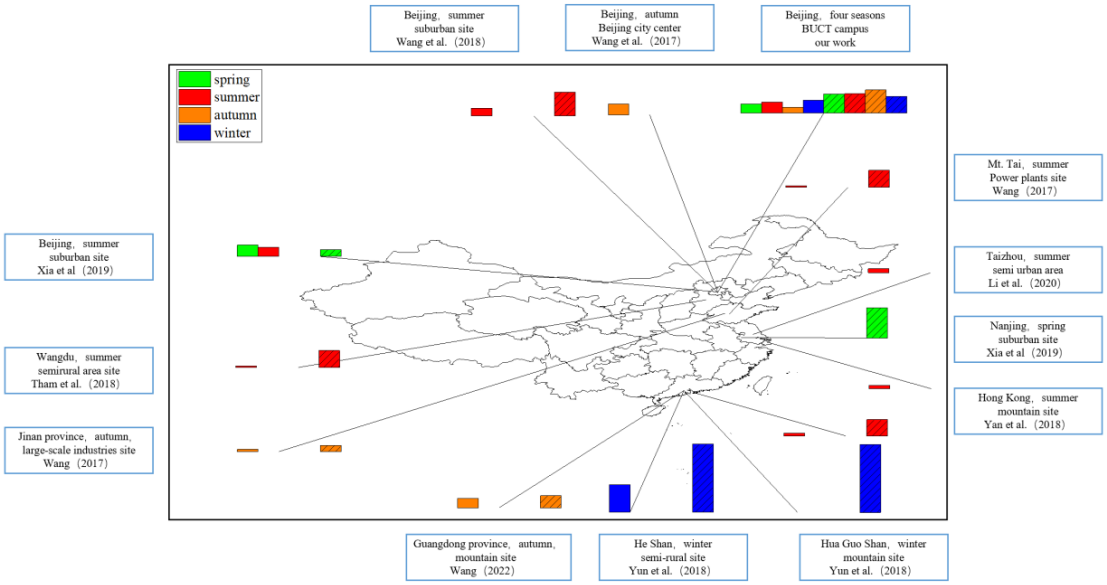

Figure 1. The observational data of N_2O_5 and $ClNO_2$ levels in China in recent five years. Color stands for different seasons. green: spring; red: summer; orange: autumn; blue: winter. The slanted line fill represents $ClNO_2$, while the blank fill represents N_2O_5.

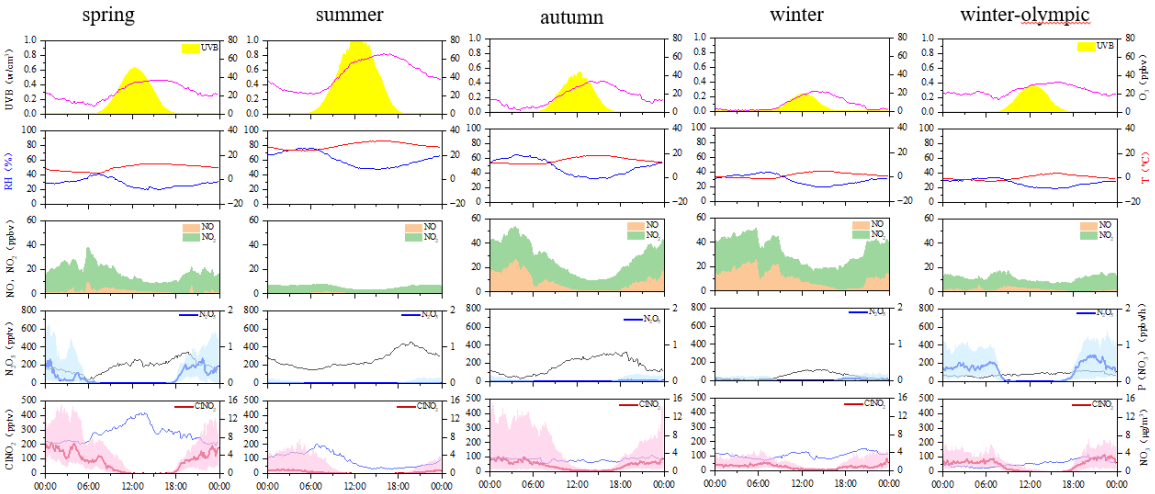

Figure 2. Mean diurnal profiles of N_2O_5, $ClNO_2$ and relevant parameters in the four seasons.

ACKNOWLEDGEMENTS

Heikki Junninen is acknowledged, for providing the tofTool package used for processing I-CIMS data.

REFERENCES

1. Alexander B., Sherwen T., Holmes C. D., et al. Global inorganic nitrate production mechanisms: comparison of a global model with nitrate isotope observations[J]. Atmospheric Chemistry and Physics, 2020, 20(6): 3859-3877.
2. Bannan T. J., Booth A. M., Bacak A., et al. The first UK measurements of nitryl chloride using a chemical ionization mass spectrometer in central London in the summer of 2012, and an investigation of the role of Cl atom oxidation[J]. Journal of Geophysical Research: Atmospheres, 2015, 120(11): 5638-5657.
3. Cai, W. et al. The 2020 China report of the Lancet Countdown on health and climate change. The Lancet Public Health 6, e64-e81, (2021).

4. Chen X., Wang H., Lu K., et al. Field Determination of Nitrate Formation Pathway in Winter Beijing[J]. Environ Sci Technol, 2020, 54(15): 9243-9253.
5. Fan M. Y., Zhang Y. L., Lin Y. C., et al. Important Role of NO_3 Radical to Nitrate Formation Aloft in Urban Beijing: Insights from Triple Oxygen Isotopes Measured at the Tower[J]. Environ Sci Technol, 2022 56 (11), 6870-6879.
6. Fu X., Wang T., Gao J., et al. Persistent Heavy Winter Nitrate Pollution Driven by Increased Photochemical Oxidants in Northern China[J]. Environ Sci Technol, 2020, 54(7): 3881-3889.
7. He, P., Xie, Z., Chi, X., Yu, X., Fan, S., Kang, H., Liu, C., and Zhan, H.: Atmospheric $^{17}O(NO_3^-)$ reveals nocturnal chemistry dominates nitrate production in Beijing haze, Atmos. Chem. Phys., 2018, 18, 14465–14476.
8. Kim M. J., Farmer D. K., Bertram T. H. A controlling role for the air-sea interface in the chemical processing of reactive nitrogen in the coastal marine boundary layer[J]. Proc Natl Acad Sci U S A, 2014, 111(11): 3943-3948.
9. Li Q., Fu X., Peng X., et al. Halogens Enhance Haze Pollution in China[J]. Environ Sci Technol, 2021, 55(20): 13625-13637.
10. Liu L., Bei N., Hu B., et al. Wintertime nitrate formation pathways in the north China plain: Importance of N2O5 heterogeneous hydrolysis[J]. Environ Pollut, 2020, 266(Pt 2): 115287.
11. Liu, Y. et al. Continuous and comprehensive atmospheric observations in Beijing: a station to understand the complex urban atmospheric environment. Big Earth Data 4, 2020, 295-321.
12. Liu X., Gu J., Li Y., et al. Increase of aerosol scattering by hygroscopic growth: Observation, modeling, and implications on visibility[J]. Atmospheric Research, 2013, 132-133(91-101).
13. McLaren R., Wojtal P., Majonis D., et al. NO3 radical measurements in a polluted marine environment: links to ozone formation[J]. Atmospheric Chemistry and Physics, 2010, 10(9): 4187-4206.
14. Mielke L. H., Furgeson A., Odame-Ankrah C. A., et al. Ubiquity of ClNO2 in the urban boundary layer of Calgary, Alberta, Canada[J]. Canadian Journal of Chemistry, 2016, 94(4): 414-423.
15. Mielke L. H., Stutz J., Tsai C., et al. Heterogeneous formation of nitryl chloride and its role as a nocturnal NO_x reservoir species during CalNex-LA 2010[J]. Journal of Geophysical Research: Atmospheres, 2013, 118(18).
16. Osthoff H. D., Roberts J. M., Ravishankara A. R., et al. High levels of nitryl chloride in the polluted subtropical marine boundary layer[J]. Nature Geoscience, 2008, 1(5): 324-328.
17. Phillips G. J., Tang M. J., Thieser J., et al. Significant concentrations of nitryl chloride observed in rural continental Europe associated with the influence of sea salt chloride and anthropogenic emissions[J]. Geophysical Research Letters, 2012, 39(10): L10811.
18. Simpson W. R., Brown S. S., Saiz-Lopez A., et al. Tropospheric halogen chemistry: sources, cycling, and impacts[J]. Chem Rev, 2015, 115(10): 4035-4062.
19. Tham Y. J., Wang Z., Li Q., et al. Significant concentrations of nitryl chloride sustained in the morning: investigations of the causes and impacts on ozone production in a polluted region of northern China[J]. Atmospheric Chemistry and Physics, 2016, 16(23): 1-34.
20. Tham Y. J., Wang Z., Li Q., et al. Heterogeneous N_2O_5 uptake coefficient and production yield of $ClNO_2$ in polluted northern China: roles of aerosol water content and chemical composition[J]. Atmospheric Chemistry and Physics, 2018, 18(17): 13155-13171.
21. Thornton J. A., Kercher J. P., Riedel T. P., et al. A large atomic chlorine source inferred from mid-continental reactive nitrogen chemistry[J]. Nature, 2010, 464(7286): 271-274.
22. Wang T., Brown S. S., Dubé W. P., et al. Observations of nitryl chloride and modeling its source and effect on ozone in the planetary boundary layer of southern China[J]. Journal of Geophysical Research: Atmospheres, 2016, 121(5): 2457-2475.
23. Wang H., Lu K., Chen X., et al. High N_2O_5 Concentrations Observed in Urban Beijing: Implications of a Large Nitrate Formation Pathway[J]. Environmental Science & Technology Letters, 2017, 4(10): 416-420.
24. Wang H., Chen X., Lu K., et al. Wintertime N_2O_5 uptake coefficients over the North China Plain[J]. Science Bulletin, 2020, 65(9): 765-774.
25. Wagner N. L., Riedel T. P., Young C. J., et al. N_2O_5 uptake coefficients and nocturnal NO_2 removal rates determined from ambient wintertime measurements[J]. Journal of Geophysical Research: Atmospheres, 2013, 118(16): 9331-9350.
26. Wang X., Wang H., Xue L., et al. Observations of N_2O_5 and $ClNO_2$ at a polluted urban surface site in North China: High N_2O_5 uptake coefficients and low $ClNO_2$ product yields[J]. Atmospheric Environment, 2017, 156(125-134).
27. Wolfe G. M., Marvin M. R., Roberts S. J., et al. The Framework for 0-D Atmospheric Modeling (F0AM) v3.1[J]. Geoscientific Model Development, 2016, 9(9): 3309-3319.
28. Xue L. K., Saunders S. M., Wang T., et al. Development of a chlorine chemistry module for the Master Chemical Mechanism[J]. Geoscientific Model Development, 2015, 8(10): 3151-3162.
29. Xie, X., Hu, J., Qin, M., Guo, S., Hu, M., Wang, H., Lou, S., Li, J., Sun, J., Li, X., Sheng, L., Zhu, J., Chen, G., Yin, J., Fu, W., Huang, C., and Zhang, Y.: Modeling particulate nitrate in China: current findings and future directions, Environ. Int., 2022,166, 107369,
30. Xia M., Peng X., Wang W., et al. Winter $ClNO_2$ formation in the region of fresh anthropogenic emissions: seasonal variability and insights into daytime peaks in northern China[J]. Atmospheric Chemistry and Physics, 2021, 21(20): 15985-16000.
31. Xia M., Wang W., Wang Z., et al. Heterogeneous Uptake of N_2O_5 in Sand Dust and Urban Aerosols Observed during the Dry Season in Beijing[J]. Atmosphere, 2019, 10(4), 204.
32. Zhou, M., Nie, W., Qiao, L., Huang, D. D., Zhu, S., Lou, S., Wang, H., Wang, Q., Tao, S., Sun, P., Liu, Y., Xu, Z., An, J., Yan, R., Su, H., Huang, C., Ding, A., and Chen, C.: Elevated formation of particulate nitrate from N_2O_5 hydrolysis in the Yangtze River Delta region from 2011 to 2019, Geophys. Res. Lett., 2022, 49, e2021GL097393.

Multiphase Chemical Processes Influencing Atmospheric Aerosols, Air Quality, and Climate in the Anthropocene

Yafang Cheng[1], Ulrich Pöschl[1], and Hang Su[1]

[1]Max Planck Institute for Chemistry, Mainz, 55128, Germany.

Keywords: aerosol, air quality, climate, haze chemistry.

INTRODUCTION

Atmospheric aerosols and fine particulate matter (PM2.5) are strongly affecting human health and climate in the Anthropocene, that is, in the current era of globally pervasive and rapidly increasing human influence on planet Earth. Poor air quality associated with high aerosol concentrations is among the leading health risks worldwide, causing millions of attributable excess deaths and years of life lost every year. Besides their health impact, aerosols are also influencing climate through interactions with clouds and solar radiation with an estimated negative total effective radiative forcing that may compensate about half of the positive radiative forcing of carbon dioxide but exhibits a much larger uncertainty. Heterogeneous and multiphase chemical reactions on the surface and in the bulk of solid, semisolid, and liquid aerosol particles have been recognized to influence aerosol formation and transformation and thus their environmental effects. However, atmospheric multiphase chemistry is not well understood because of its intrinsic complexity of dealing with the matter in multiple phases and the difficulties of distinguishing its effect from that of gas phase reactions.

Recently, research on atmospheric multiphase chemistry received a boost from the growing interest in understanding severe haze formation of very high PM2.5 concentrations in polluted megacities and densely populated regions. State-of-the-art models suggest that the gas phase reactions, however, are not capturing the high concentrations and rapid increase of PM2.5 observed during haze events, suggesting a gap in our understanding of the chemical mechanisms of aerosol formation. These haze events are characterized by high concentrations of aerosol particles and high humidity, especially favoring multiphase chemistry.

METHODS

Here, I reviewed recent advances that my group has made as well as current challenges and future perspectives for research on multiphase chemical processes involved in atmospheric aerosol formation and transformation. We focus on the following questions: what are the key reaction pathways leading to aerosol formation under polluted conditions, what is the relative importance of multiphase chemistry versus gas-phase chemistry, and what are the implications for the development of efficient and reliable air quality control strategies? In particular, we discuss advances and challenges related to different chemical

regimes of sulfate, nitrate, and secondary organic aerosols (SOAs) under haze conditions, and we synthesize new insights into the influence of aerosol water content, aerosol pH, phase state, and nanoparticle size effects. Overall, there is increasing evidence that multiphase chemistry plays an important role in aerosol formation during haze events. In contrast to the gas phase photochemical reactions, which are self-buffered against heavy pollution, multiphase reactions have a positive feedback mechanism, where higher particle matter levels accelerate multiphase production, which further increases the aerosol concentration resulting in a series of record-breaking pollution events. We discuss perspectives to fill the gap of the current understanding of atmospheric multiphase reactions that involve multiple physical and chemical processes from bulk to nanoscale and from regional to global scales. A synthetic approach combining laboratory experiments, field measurements, instrument development, and model simulations is suggested as a roadmap to advance future research.

CONCLUSIONS

Overall, there is increasing evidence of the importance of multiphase chemistry in aerosol formation during haze events. It is more efficient in producing inorganic aerosols than organic aerosols. The high ionic strength and distinct pH in aerosol water can either increase or reduce the rate of certain reactions compared to that in cloudwater. While most studies agree that the N2O5 reaction is the main pathway producing nitrate, a consensus has not been reached for sulfate and SOA formation. Model calculation and a few studies suggest that aerosols mostly stay in a liquid phase during severe haze events, but the range of RH and T to maintain the liquid phase in the presence of organic aerosols is not clear.

To further advance understanding of atmospheric multiphase chemistry, we have the following suggestions:

(1) To effectively identify the atmospherically relevant reactions and to validate laboratory-determined kinetics in the presence of other gases or mixtures of other aerosols, it is desirable to extend the current kinetic studies from a relatively simple reaction system to a system reflecting the complexity of the real atmosphere, for example, an environment chamber filled with real atmospheric gases and aerosols.

(2) New techniques and design of experiments are needed, especially for the effect of aerosol pH, high ionic strength and aerosol phase sate.

(3) We need to promote the establishment of a 3-D comprehensive observation network at a global scale through international collaborations and initiatives.

(4) We suggest more comparative studies of multiphase chemistry during hazy days with that at nighttime and in fogs.

ACKNOWLEDGEMENTS

This work was supported by the Max Planck Society.

REFERENCES

Cheng, Y.; Zheng, G.; Wei, C.; Mu, Q.; Zheng, B.; Wang, Z.; Gao, M.; Zhang, Q.; He, K.; Carmichael, G.; Pöschl, U.; Su, H. Reactive nitrogen chemistry in aerosol water as a source of sulfate during haze events in China. Sci. Adv. 2016, 2, e1601530.

Zheng, G. J.; Duan, F. K.; Su, H.; Ma, Y. L.; Cheng, Y.; Zheng, B.; Zhang, Q.; Huang, T.; Kimoto, T.; Chang, D.; Pöschl, U.; Cheng, Y. F.; He, K. B. Exploring the severe winter haze in Beijing: the impact of synoptic weather, regional transport and heterogeneous reactions. Atmos. Chem. Phys. 2015, 15, 2969−2983.

Cheng, Y.; Su, H.; Koop, T.; Mikhailov, E.; Poeschl, U. Size dependence of phase transitions in aerosol nanoparticles. Nat. Commun. 2015, 6, 5923.3

Mu, Q.; Shiraiwa, M.; Octaviani, M.; Ma, N.; Ding, A.; Su, H.; Lammel, G.; Pöschl, U.; Cheng, Y. Temperature effect on phase state and reactivity controls atmospheric multiphase chemistry and transport of PAHs. Sci. Adv. 2018, 4, eaap7314.4.

Su, H.; Cheng, Y.; Pöschl, U. New Multiphase Chemical Processes Influencing Atmospheric Aerosols, Air Quality, and Climate in the Anthropocene. Acc. Chem. Res. 2020.

Zheng, G.; Su, H.; Wang, S.; Andreae, M.; Pöschl, U. and Cheng, Y. 2020. "Multiphase buffer theory explains contrasts in atmospheric aerosol acidity." Science 369 (6509):1374-1377.

MODELING OF PURE BIOGENIC NUCLEATION WITH WRF-CHIMERE OVER NEPAL

G. CIARELLI[1], A. CHOLAKIAN[2], B. VITALI[1,3], and F. BIANCHI[1]

[1] Institute for Atmospheric and Earth System Research/Physics, Faculty of Science, University of Helsinki, Helsinki, Finland

[2] Laboratoire de Météorologie Dynamique (LMD), Ecole Polytechnique, IPSL Research University, Ecole Normale Supérieure, Université Paris-Saclay, Sorbonne Universités, UPMC Univ Paris 06, CNRS, Route de Saclay, 91128 Palaiseau, France.

[3] University of Trento, Trento, Italy

Keywords: HOMs, Nucleation, Extreme environments, WRF-CHIMERE

INTRODUCTION

We present an application of the state-of-the-art atmospheric chemical transport model WRF-CHIMERE over the South Asia domain, i.e., Nepal. The model was recently implemented at the Institute for Atmospheric and Earth System Research (INAR) with the aim to investigate the formation and transportation processes of biogenic aerosol particles in extreme environments.

METHODS

The WRF-CHIMERE chemical transport model (Menut et al., 2013) was deployed over the Himalayan Range and specifically over the Nepal Climate Observatory Pyramid (NCO-P) in the eastern part of the Himalaya for the whole month of December 2014. The model was set up with a 4 domains nested configuration, and with the high-resolution domain, i.e. at 1 km, centered over NCO-P. Biogenic emissions were prepared using the Model of Emissions of Gases and Aerosols from Nature (MEGAN) (Guenther et al., 2012) and combined with organic chemical schemes parametrized using the volatility basis set scheme. For this specific application, formation and nucleation of highly oxygenated molecules (HOMs) arising from the oxidation of biogenic precursors such as alpha-pinene and isoprene (among others) where parametrized based on latest smog chamber experiments (Kirkby et al., 2016). Model results were evaluated against a comprehensive set of measurements available during an intensive campaign performed at NCO-P during the December 2014 period. Observational data included Neutral cluster and Air Ion Spectrometer (NAIS), Scanning mobility particle sizer (SMPS) as well as ozone (O_3) and black carbon (BC) data. Additionally, a detailed comparison with local meteorological measurements was also performed to investigate the capability of the model in reproducing the valley-wind mechanism, which are typical of the Himalayan valleys. Various sensitivity tests were carried out with altered biogenic emissions fluxes to investing their potential role on model performance.

CONCLUSIONS

Preliminary simulations indicated a substantial increase in the number of modeled biogenic particles when formation and nucleation of HOMs processes are included in the model, and below the 10 nm size. In line with the observations, the model indicated that biogenic particles formed in the Himalayan valleys located directly south of the NCO-P site, can be ventilated out of the valleys via thermally driven winds, and eventually reach the NCO-P site. A sensitivity test with increased biogenic emissions indicated that such mechanism could potentially increase the number of could condensation nuclei (CCN).

ACKNOWLEDGEMENTS

This work was supported by the European Research Council with the project CHAPAs no. 850614.

REFERENCES

Bianchi, F., Junninen, H., Bigi, A., Sinclair, V.A., Dada, L., Hoyle, C.R., Zha, Q., Yao, L., Ahonen, L.R., Bonasoni, P., Buenrostro Mazon, S., Hutterli, M., Laj, P., Lehtipalo, K., Kangasluoma, J., Kerminen, V.-M., Kontkanen, J., Marinoni, A., Mirme, S., Molteni, U., Petäjä, T., Riva, M., Rose, C., Sellegri, K., Yan, C., Worsnop, D.R., Kulmala, M., Baltensperger, U., Dommen, J., 2021. Biogenic particles formed in the Himalaya as an important source of free tropospheric aerosols. Nat. Geosci. 14, 4–9. https://doi.org/10.1038/s41561-020-00661-5

Guenther, A.B., Jiang, X., Heald, C.L., Sakulyanontvittaya, T., Duhl, T., Emmons, L.K., Wang, X., 2012. The Model of Emissions of Gases and Aerosols from Nature version 2.1 (MEGAN2.1): an extended and updated framework for modeling biogenic emissions. Geosci. Model Dev. 5, 1471–1492. https://doi.org/10.5194/gmd-5-1471-2012

Kirkby, J., Duplissy, J., Sengupta, K., Frege, C., Gordon, H., Williamson, C., Heinritzi, M., Simon, M., Yan, C., Almeida, J., Tröstl, J., Nieminen, T., Ortega, I.K., Wagner, R., Adamov, A., Amorim, A., Bernhammer, A.-K., Bianchi, F., Breitenlechner, M., Brilke, S., Chen, X., Craven, J., Dias, A., Ehrhart, S., Flagan, R.C., Franchin, A., Fuchs, C., Guida, R., Hakala, J., Hoyle, C.R., Jokinen, T., Junninen, H., Kangasluoma, J., Kim, J., Krapf, M., Kürten, A., Laaksonen, A., Lehtipalo, K., Makhmutov, V., Mathot, S., Molteni, U., Onnela, A., Peräkylä, O., Piel, F., Petäjä, T., Praplan, A.P., Pringle, K., Rap, A., Richards, N.A.D., Riipinen, I., Rissanen, M.P., Rondo, L., Sarnela, N., Schobesberger, S., Scott, C.E., Seinfeld, J.H., Sipilä, M., Steiner, G., Stozhkov, Y., Stratmann, F., Tomé, A., Virtanen, A., Vogel, A.L., Wagner, A.C., Wagner, P.E., Weingartner, E., Wimmer, D., Winkler, P.M., Ye, P., Zhang, X., Hansel, A., Dommen, J., Donahue, N.M., Worsnop, D.R., Baltensperger, U., Kulmala, M., Carslaw, K.S., Curtius, J., 2016. Ion-induced nucleation of pure biogenic particles. Nature 533, 521–526. https://doi.org/10.1038/nature17953

Menut, L., Bessagnet, B., Khvorostyanov, D., Beekmann, M., Blond, N., Colette, A., Coll, I., Curci, G., Foret, G., Hodzic, A., Mailler, S., Meleux, F., Monge, J.-L., Pison, I., Siour, G., Turquety, S., Valari, M., Vautard, R., Vivanco, M.G., 2013. CHIMERE 2013: a model for regional atmospheric composition modelling. Geosci. Model Dev. 6, 981–1028. https://doi.org/10.5194/gmd-6-981-2013

AEROSOL FORMATION AT TE WAEWAE BAY: FIRST RESULTS FROM THE GOSOUTH / LOSTECCA CAMPAIGN

FRANK STRATMANN[1] GUY COULSON[2], SILVIA HENNING[1], THOMAS CONRATH[1], SEBASTIAN DÜSING[1], JULIAN HOFER[1], JULIANE KALLA[3], DANIEL MORRISH[2], SALLY GRAY[2], TONY BROMLEY[2], WADINGA FOMBA[1], HOLGER SIEBERT[1], BIRGIT WEHNER[1], HEIKE WEX[1], RICHARD QUEREL[1], GUSTAVO OLIVARES[2], GUNTHER SECKMEYER[3]

[1] Leibniz Institute For Tropospheric Research (Tropos)
[2] National Institute Of Water And Atmospheric Research (Niwa)
[3] Institute Of Meteorology And Climatology (Imuk)

Keywords: Aerosol formation, southern ocean, clouds,

Clouds over the Southern Ocean are a large source of error in the current generation of climate models. Comparisons with satellite observations shows that they are regularly underestimated in models, allowing increased sunlight to reach the ocean surface, altering sea surface temperatures and hence, circulation patterns. This is partly due to an incomplete picture of Southern Ocean cloud properties (e.g. droplet sizes, phase state) and the factors (aerosol particles, thermodynamics, boundary layer dynamics, atmospheric and cloud turbulence) that influence them.

goSouth is an international collaboration between the Leibniz Institute for Tropospheric Research (TROPOS), the Institute for Meteorology and Climatology (IMUK) at the Leibniz University of Hannover, the University of Auckland, the University of Canterbury and NIWA. Rejoicing in the full title of *"Model assisted vertical in-situ investigation of aerosols, and aerosol-cloud-turbulence interactions in the Southern Hemisphere marine boundary layer (goSouth)"* it has two main purposes:

- Characterisation of climate relevant aerosol processes in the turbulent boundary layer over the Southern Ocean
- Proof of concept for collaboration between Germany and NZ with a view to a larger ship and air-borne programme to follow

A measurement campaign was carried out in November 2022 at a site overlooking Te Waewae Bay near Pahia (46.31°S, 167.71°W, 10 m a.s.l.), about 50 km west of Invercargill (Figure 1). Five researchers from TROPOS and one researcher from IMUK joined the NZ contingent for three weeks of aerosol and turbulence measurements from ground level to 1 km.

The campaign focused on the vertical distribution of aerosol physicochemical properties, turbulence and meteorological variables in the marine boundary layer. A combination of ground-based and balloon-borne measurements of aerosol, thermodynamic and turbulence properties was carried out. The goSouth measurement campaign will be jointly realized with a remote-sensing campaign of the LOSTECCA project (Hofer et al., 2022).

Methods

Measurements were made of aerosol physicochemical properties and concentrations. The instrumental suite consists of:

- Filter samples for aerosol chemical analysis
- Aethalometer
- Condensation Particle Counters
- Cloud Condensation Nuclei Counter
- Mobility Particle Sizers
- Hemispherical Sky Imager

There was also a complete suite of meteorological measurements. Aerosol particle and meteorological – including turbulence – measurements were made from tethered balloons up to a height of 1000 m.

The partner project LOSTECCA will in addition contribute continuous observations of the vertical distribution of aerosol, clouds and atmospheric dynamics from multi-wavelength Raman polarization lidar and Doppler lidar, as well as integrated measurements of atmospheric water vapour, liquid water, and aerosol optical thickness from microwave radiometer and Sun-photometer. The instruments deployed are listed in Tables 1 and 2.

Figure 1: The sampling site at Te Waewae Bay

Table 1: Ground-based in-situ instrumentation

Property	Instrument	Institution
temperature, pressure, humidity, wind	meteorological stations	NIWA
Aerosol particles	Mast and aerosol inlet system	NIWA and TROPOS
particle size distribution	MMPS and SMPS	TROPOS and NIWA
coarse aerosol	OPC and APS	TROPOS and NIWA
CN	CPC CN>7 nm	TROPOS
CCN	DMT CCN-100	TROPOS and NIWA
Scattering	Nephelometer Ecotech Aurora 4000	TROPOS
Attenuation	Aethalometer AE22	NIWA
INP	LVS-sampler (polycarbonate filters)	TROPOS
Chemical composition	LVS-sampler (quarz fibre filters)	TROPOS

Table 2: Air-borne instrumentation:

Property	Instrument	Platform	Institution
temperature, pressure humidity	meteorological sonde	sonde	TROPOS
Meteorology and turbulence	meteorological and turbulence sondes	Helikite	TROPOS/NIWA
Particle size distribution	POPS (0.15 – 3 um)	Helikite	TROPOS
Ice nucleating particles	HALFBAC (polycarbonate)	Helikite	TROPOS
chemical composition	(quarz fiber)	Helikite	TROPOS

Despite severe logistical difficulties, due mainly to international shipping and local power problems, a potentially interesting ground-based and vertically resolved in-situ aerosol, meteorological and turbulence dataset, was acquired. First indications are that particle formation events were observed but due to the circulation patterns in the bay, we hypothesize that formation came from gaseous precursors emitted from New Zealand terrestrial sources. However, thorough data evaluation is needed to confirm - or otherwise - this hypothesis.
The project successfully met its second objective of demonstrating the feasibility of joint field campaigns in NZ and that due to the complex terrain and flow conditions, Te Waewae Bay is not the best place for investigating undisturbed Southern Ocean air-masses.

This talk will give an overview of the measurement campaign and present preliminary results, focussing on two case study events on the 18th and 20th November when particles formed under similar conditions but with different growth behaviour.
The results will be used to develop or improve models of Southern Ocean ocean/aerosol/cloud interactions which are currently a source of error in climate projections.

Acknowledgements

Go South is funded by BMBF (German Federal Ministry for Education and Research, project 01LK2003A), TROPOS, the Deep South Challenge and NIWA through SSIF.

References:

Hofer et al., 2022. Lidar observations of spatiotemporal contrasts in clouds and aerosols (LOSTECCA) in New Zealand. *Proceedings of the Hydrometsoc22 meeting (Our water: a taonga in an ever-changing world)*

MOBILE MONITORING OF URBAN ULTRAFINE PARTICLES IN NOVI SAD, SERBIA

MILOŠ D. DAVIDOVIĆ[1], DUŠKA KLEUT[1], SAVERIO DE VITO[2], ALENA BARTONOVA[3] and MILENA JOVAŠEVIĆ-STOJANOVIĆ[1]

[1]Vinča Institute of Nuclear Sciences, University of Belgrade,
National Institute of the Republic of Serbia, P.O.B. 522, 11001 Belgrade, Serbia.

[2]ENEA Italian National Agency for New Technologies, Energy and Sustainable Economic Development, Centro Ricerche Portici, Portici, Italy.

[3]NILU – Norwegian Institute for Air Research, PO Box 100, 2027, Kjeller, Norway

Keywords: mobile monitoring, ultrafine particles, scanning mobility particle sizer, optical particle sizer

INTRODUCTION

Level of atmospheric aerosols and related air pollution in urban areas are most commonly characterized by measuring and reporting mass concentration of certain aerosol fractions, such as PM1, PM2.5 and PM10. However, aerosols are more precisely characterized by using their size distribution, which can range in size from a few nanometers to a few micrometers. Furthermore, health effects of aerosols are also strongly size dependent (Oberdörster *et al.*, 2005; Gurr *et al*., 2005), thus raising an important issue of insufficient information often provided by the regulatory monitoring networks, which are in addition to that typically spatially very sparse. Additional monitoring tools are thus needed. Here we describe results of a recently conducted mobile monitoring campaign that covered heating (winter) and non-heating (summer) periods in 2022 in the city of Novi Sad, which was at the time European Capital of Culture, especially focusing on urban aerosol aspects not typically available in traditional monitoring, such as number concentration of ultrafine particles. Several examples of obtained results are shown in the form of thematic maps illustrating ultrafine particles concentration on workdays and weekends in the heating and non-heating season.

METHODS

How can we increase the spatial resolution of air pollution data, and furthermore increase the quality of air pollution information? For the measurement and characterization of particulate matter pollution, which for aerosols in general, and of course aerosols in urban areas, consists of particles of different diameters, in a very wide range of particle diameters (from a few nanometers to 10 um), usually several instruments are used, so that their spectra (measured particle size distributions) combine. The necessity of using several instruments, with fundamentally different measurement methods, stems from the impossibility of covering the entire relevant range with only one method, as for example the optical method cannot be used for the smallest nanometer particles. Therefore, for such comprehensive measurements and characterization of aerosols, methods based on different physical principles must be used, such as optical methods, methods based on electrical mobility measurements, and others.
In this work we have used a large number of measurements obtained with high quality equipment (laboratory grade equipment) located in a moving vehicle. Instrumentation consisted of laboratory grade instruments: TSI NanoScan SMPS Model 3910 (13 channels from 10 nm to 420 nm with 1 minute resolution) and TSI Optical particle sizer 3330 (17 channels from 0.3 um to 10 um with 1 second resolution). Each measurement point was geolocated. During one part of the campaign, a dashcam recorded the view through the vehicle's front windshield, allowing for later analysis, source identification and explanation of sudden spikes in air pollution. The aerosol inlet was conical, placed on the right side of the vehicle, and two sampling tubes led the ambient air from the conical inlet to the instrumentation located in the passenger cabin. Data on particulate matter pollution were collected during 2 weeks of March 2022, in Novi Sad (heating season), and 2 weeks of August 2022 (non-heating season). Each day, one vehicle with a gasoline engine and

instrumentation performed measurements on 4 predetermined routes, 2 routes in the morning/afternoon period and 2 two routes in the afternoon/night. Instrument maintenance was performed between runs (cleaning the inlet, charging the battery, zero testing, data collection). Table 1 shows the metadata summary statistics of the acquired mobile monitoring campaign data.

	2022 HEATING SEASON (MARCH 4-16)			**2022 NON-HEATING SEASON (AUGUST 18-30)**		
ROUTE NUMBER	No. of runs along a route	No. of samples using TSI Nanoscan 3910 (10nm-420nm)	No. of samples using TSI OPS 3330 (300nm-10um)	No. of runs along a route	No. of samples using TSI Nanoscan 3910 (10nm-420nm)	No. of samples using TSI OPS 3330 (300nm-10um)
1	13	1011	58932	12	1056	62839
2	13	753	44825	12	691	40841
3	12	861	51597	14	1058	63011
4	12	951	56447	12	1126	64655
TOTAL	50	3576	211801	50	3932	231346

Table 1. Summary statistics of the acquired data during the mobile monitoring campaign.

Color of the marker	**Datapoint of number concentration is belonging to percentile (both seasons)**	**Range of measured number concentration values in [#/cm^3]**
green	0-25%	0 - 5617
yellow	25-50%	5617 - 10972
orange	50-75%	10972 - 21025
red	75-100%	21025 - max

Table 2. Legend of the markings used to depict the measurement of ultrafine particles.

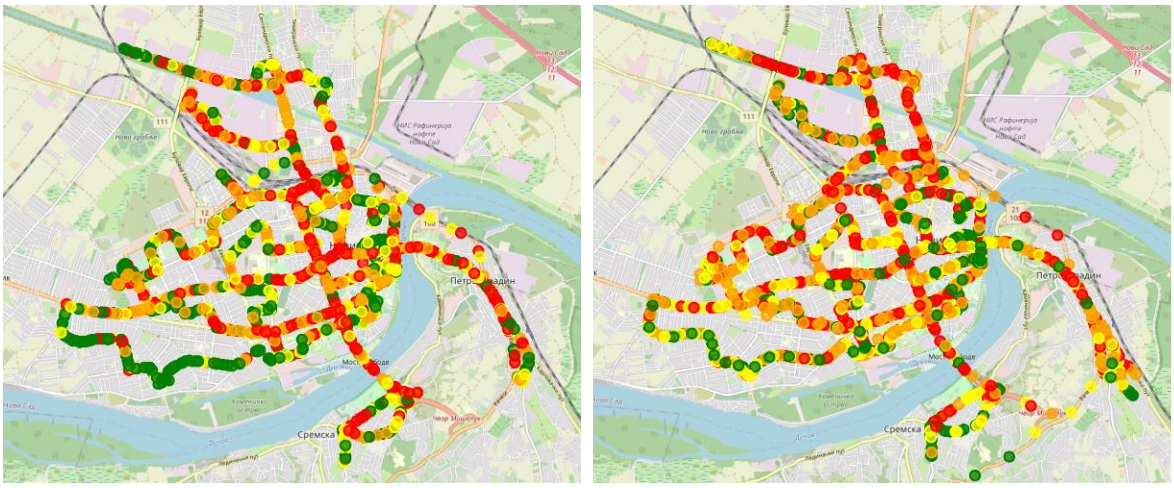

(a) (b)

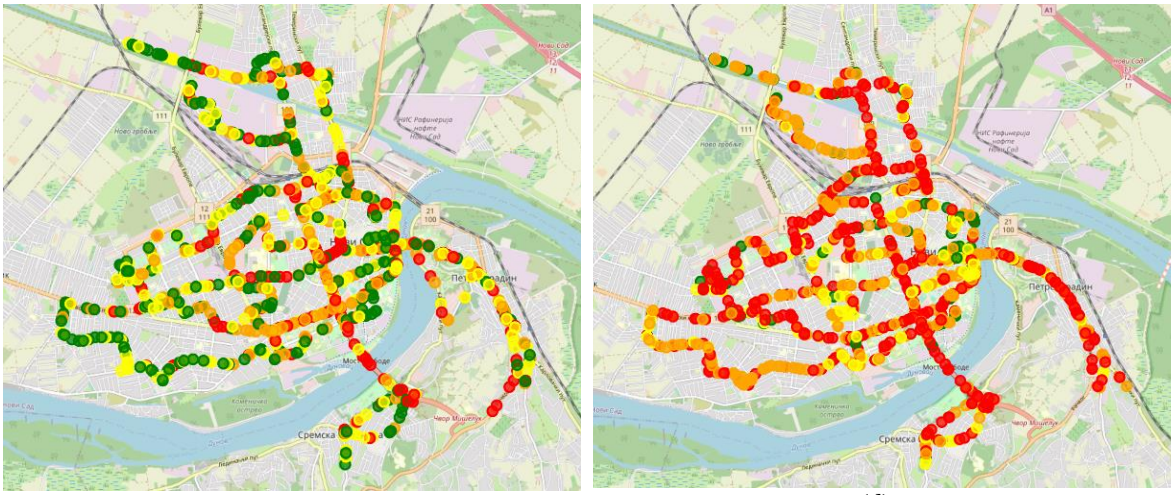

(c) (d)

Figure 1. Distribution of number concentration of ultrafine particles measured on: a) weekdays during the summer campaign, b) weekdays during the winter campaign, c) weekends during the summer campaign, d) weekends during the winter campaign.

Table 2 and Figure 1 show a map of concentration of ultrafine particles, which enables simple visual insight into differences between work day/week day in heating vs non-heating season. Project website (H2020 VIDIS, 2023) features clickable maps, with popups detailing measurement point (timestamp and concentration).

CONCLUSIONS

A lower number of datapoints in the upper percentile ranges can be observed in the summer along major roads due to a reduced level of pollution, most likely due to reduced traffic intensity. From all four panels in Figure 1, it is clearly visible that the highest concentrations in all parts of the city were measured during the winter campaign on weekend days when residential buildings with individual fireplaces are heated throughout the day. During workdays, differences between winter and summer were less pronounced.

This work showcased use of mobile monitoring to increase spatial resolution of PM air pollution information. Lab grade monitors operating based on two different principles were used, namely optical method based instrumentation for 300nm - 10um size range, and scanning mobility particle sizers for 10nm – 420nm size range. Even without additional modelling effort, geostamped and plotted data points can be used to explore the urban area in the context of PM pollution, which is not possible using conventional sparse monitoring. Further analysis will include analysis of more fine temporal patterns, reference station comparisons and geostatistical modelling.

ACKNOWLEDGEMENTS

The researchers acknowledge the funding of the project “Spatio-temporal variations of the level of respirable particles in the urban area of Novi Sad - mobile monitoring, modelling and creation of high-resolution maps” (City Administration for Environmental Protection Novi Sad project no. VI-501-2/2021-19в-19), “Mapping particulate matter air pollution in near-real time in Novi Sad using data from sensor networks and statistical/physical modeling” (City Administration for Environmental Protection Novi Sad project no. VI-501-2/2022-35в-11), Ministry of Science, Technological Development and Innovation of the Republic of Serbia under contract number 451-03-47/2023-01/ 200017 which is being realized in Vinca Institute of Nuclear Sciences, as well as the VIDIS project funded by the European Union’s Horizon 2020 Research and Innovation programme under grant agreement No 952433.

REFERENCES

Oberdörster G, Oberdörster E and Oberdörster J (2005), Nanotoxicology: an emerging discipline evolving from studies of ultrafine particles. *Environ Health Perspect*, **11**: 823-839.
Gurr, J.R., Wang, A.S.S., Chenb, C-H. and K.Y. Jan (2005), Ultrafine titanium dioxide particles in the absence of photoactivation can induce oxidative damage to human bronchial epithelial cells. *Toxicology*, **213**: 66-73.
H2020 VIDIS project website, https://vidis-project.org/index.php/about/vidis-synergistic-projects/novi-sad-mobile-monitoring-project/, last accessed 15 February 2023

LOW TEMPERATURE ICE NUCLEATION OF PRIMARY AND SECONDARY MARINE AEROSOLS

PAUL J DEMOTT, RYAN J. PATNAUDE, KATHRYN A. MOORE, RUSSELL J. PERKINS, THOMAS C. J. HILL, and SONIA M. KREIDENWEIS

Department of Atmospheric Science, Colorado State University, Fort Collins, CO, USA.

Keywords: ICE NUCLEATING PARTICLES, ICE NUCLEATION, CIRRUS

INTRODUCTION

Cirrus clouds are high altitude tropospheric ice clouds present at below 235 K that cover 25 – 45% of the globe. Their influence on the balance of radiation reaching the Earth depends on their microphysical properties (DeMott et al., 2016). These properties depend on the action of two freezing pathways that help to determine the size and number of ice crystals and even the sign of radiative effect: homogeneous and heterogeneous ice nucleation (Jensen et al., 1994). The homogeneous (or spontaneous) pathway is controlled by the water activity of dissolved aerosol components in highly supercooled solutions (Koop et al., 2000), while heterogeneous nucleation is controlled by the specific nature of ice nucleating particles (INPs) (Vali et al., 2015). The two processes compete, in dependence on the lower threshold relative humidity (RH) required for a specific INP, INP concentrations, and the vertical motions that drive RH increases and ultimately cirrus formation (Kärcher et al., 2022). A host of aerosol types may be relevant for heterogeneous ice nucleation at cirrus levels. Field studies of cirrus ice crystal residual compositions have indicated an occurrence of sea salt at levels up to 25% of collected ice crystals for flights over ocean regions (Cziczo et al., 2013). This is strong evidence that sea spray aerosols (SSA) can be lofted from the marine boundary layer in deep convection, participate in formation of cirrus anvils via ice nucleation, and be detrained from evaporating clouds to be present as potential cloud nuclei for subsequent formation of in situ cirrus.

In prior laboratory studies, high fractions (~10%) of SSA were confirmed to freeze heterogeneously below 220 K (Wagner et al., 2018; Patnaude et al., 2021), attributed to the salts in SSA. These particles could represent a significant source of cirrus INPs in competition with mineral dust in some regions of the world (Patnaude et al., 2021). Studies have not previously examined the action of atmospheric oxidation on the freezing properties of these same INPs, nor the potential low temperature freezing of secondary marine aerosols (SMA) produced due to oxidation of oceanic gas phase emissions. We address these subjects and explore the low temperature behavior of non-sea-salt components of SSA that are known to initiate heterogeneous immersion freezing at mixed-phase (liquid and ice) cloud temperatures (McCluskey et al., 2018).

METHODS

Studies used a Marine Aerosol Reference Tank (MART) (Stokes et al., 2013) designed to generate a realistic atmospheric distribution of SSA via plunging water and the consequent bubble bursting process, an oxidation flow reactor (OFR) (Peng et al., 2020), and a low temperature continuous flow diffusion chamber (Patnaude et al., 2021; Kasparoglu et al., 2022). The MART was filled with 120 L of either 1) artificial seawater (ASW), 2) real seawater (SW) collected at the Scripps Institution Pier in La Jolla, CA, or 3) deionized (DI) water. After generation, the polydisperse particles were passed through the OFR. When the OFR was operating to induce oxidation, two 90/10 lamps (90% 254 nm, 10% 185 nm) were

used to generate O_3 and OH radicals to oxidize particles, and OFR exposure was set to resemble ~4-6 days of atmospheric aging. Relative humidity (RH) was controlled to > 60% inside the OFR to ensure OH chemistry, rather than singlet oxygen. Comparative nascent SSA experiments were performed by passing particles through the OFR without operating the lamps. For SMA freezing studies, the plunging was turned off in the MART and clean air was passed from the MART headspace to the OFR for all water types. These various experimental configurations are summarized in Table 1. We note that in defining the types the way we do herein, the "aged" category means that organic aerosol composition has likely been altered both by production of particles that are secondary organic only (called SMA here) and alteration of the organic component composition of nascent SSA particles. Thus, for experiments termed "SMA-only", we are only isolating the impact of newly formed organic particles in ice nucleation experiments.

Generated aerosol types (Water type)	**OFR lamp operation**	**MART plunging**
Nascent SSA (ASW, SW)	OFF	ON
Aged SSA+SMA (ASW, SW)	ON	ON
SMA only (ASW, SW, DI)	ON	OFF

Table 1. Experimental matrix for nascent SSA, aged SSA and secondary marine aerosol freezing studies.

Aerosol particle distributions were constructed via merging data from a scanning mobility particle sizer and an aerodynamic particle sizer. As discussed in detail in Patnaude et al. (2023), passage through the OFR when lights were activated produced a bimodal distribution for the aged SSA+SMA cases, with a smaller size mode dominated by secondary organic aerosols augmenting (3 - 4 orders of magnitude by number) primary SSA (lamps off) at sizes below 200 nm for both ASW and SW. No large mode was present for SMA only cases. However, when DI water was tested with an active OFR, it was also found to lead to the formation of secondary aerosol, likely due to VOCs emitted from the acrylic that composes the MART walls. Hence, it was not possible to easily determine the proportion of total secondary material that was contributed as true SMA versus other organics in the aged aerosol cases. This issue will need to be resolved in future studies via use of non-plastic materials, but we believe that the experiments still allow for interpretation of the role of SMA alone, as discussed in the results.

Ice nucleation measurements used the Colorado State University Continuous Flow Diffusion Chamber (CFDC) to expose continuously generated particles to a range of relative humidity (RH) conditions for temperatures from 233 to 190 K (Patnaude et al., 2021, 2023). Experiments constituted RH "scans" wherein initially very dry particles entered the chamber, temperature at the aerosol lamina is held constant, and RH is slowly increased until a high frozen fraction of particles, as detected optically, is achieved over the ~25 s chamber residence time. After each cycle, RH is lowered and a stepwise change in temperature is used to ultimately span the full range of temperature and RH space. Using these methods, heterogeneous ice nucleation characteristically produces gradually increasing ice crystal concentrations as RH is increased, while homogeneous freezing results in a strong discontinuity in ice concentrations equating to a high fraction of total particles freezing over a narrow range of RH.

RESULTS

A summary of selected ice nucleation results is shown in Figure 1, focusing on the SW results. Ice nucleation results shown are only for a fraction of 1% of particles freezing. Full results are elaborated in Patnaude et al. (2023) and will be described at conference time. At the 1% freezing level shown, results at temperatures higher than 220 K suggest alignment with the homogeneous freezing process, regardless of aging. A heterogeneous nucleation process is inferred to ensue at temperatures colder than 220 K, based on ice formation ensuing at RH well below the conditions required to be predicted for homogeneous freezing. This behavior has been previously attributed to the nature of the surfaces of crystallized salts (Wagner et al., 2018; Patnaude et al., 2021) as they begin to take up water. This is shown by the fact that

the onset of freezing occurs at near the RH conditions where deliquescence of the initially dry particles is predicted, as well as near the conditions where condensation freezing may also ensue if freezing starts in pores on particles. Interestingly, no significant difference in heterogeneous freezing conditions is noted after particle aging (SSA+SMA). This suggests that the inorganic (salt) component is likely involved in the freezing process, and thus the alteration by organics has little or no influence on this lower temperature freezing process. In contrast, freezing conditions for the SMA only experiment require RH close to water saturation, suggesting that these particles were hydrophobic and/or very slow to plasticize, if glassy, and thus required water saturation to drive water uptake and freezing. These freezing conditions also typify most secondary organic aerosol freezing conditions at cirrus temperatures (Kasparoglu et al., 2022).

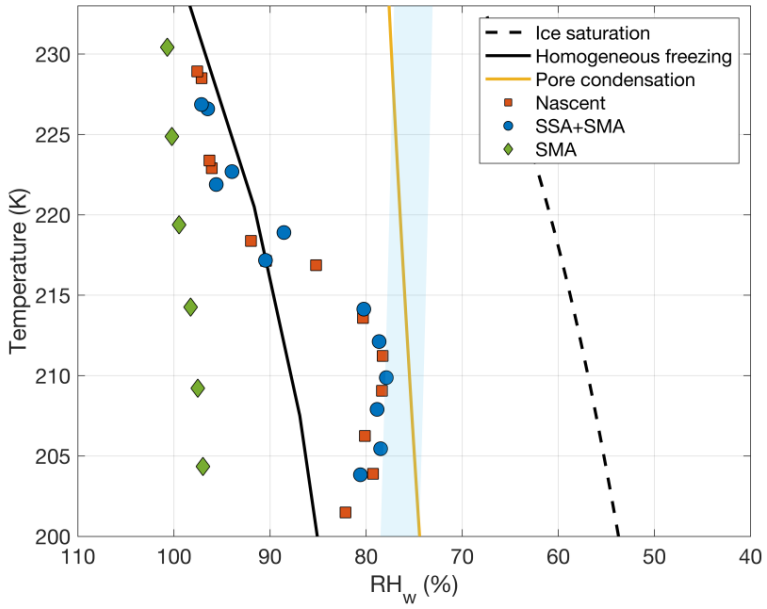

Figure 1. Summary of conditions needed to freeze 1% of all SW particles for nascent, aged (SSA+SMA) and SMA-only particles. Reference lines and shading indicate ice saturation (black dashed), the parameterized water relative humidity (RH_w) for pore condensation in a 11 nm pore (Marcolli, 2014) (solid yellow), and the threshold for the onset of homogeneous freezing (Koop et al. 2000) (solid black). The blue shaded region represents possible deliquescence RH for NaCl and SSA (see Patnaude et al., 2023).

Not shown in Figure 1 is an additional heterogeneous freezing process that was observed to occur at lower ice active fractions for SW produced particles, present even at temperatures >220 K and presumably on the INPs known to be present within SSA and active at mixed-phase cloud conditions (McCluskey et al., 2018). This process, evident at a freezing fraction of 0.1%, parallels conditions for homogeneous freezing but requires several percent lower RH, as expected for heterogeneous immersion freezing.

CONCLUSIONS

The ice nucleating behavior of SSA generated from a MART in this study is like that found in previous laboratory measurements of low temperature ice nucleation of monodisperse SSA (Patnaude et al., 2021) in denoting a transition from a homogeneous to heterogeneous nucleation process for a large proportion of salt-containing particles at temperatures near and below 220 K. These onset conditions were relatively unperturbed when particles were exposed to atmospheric oxidation. We thus infer little influence of oxidized marine organics on these major freezing processes. When sub-200 nm SMA (and co-generated SOA) were tested in isolation, these showed very poor ice nucleating ability, similar to previous works on other secondary organic aerosols in the cirrus regime. An additional heterogeneous freezing process was

found to occur at lower ice active fractions that was consistent with expectations for heterogeneous immersion freezing of the most active INPs emitted in SSA, those also active at higher temperatures. Further results and implications will be presented.

ACKNOWLEDGEMENTS

This work was largely supported by NSF through the NSF Center for Aerosol Impacts on Chemistry of the Environment (CAICE), an NSF Funded Center for Chemical Innovation (CHE-1801971). Any opinions, findings, and conclusions or recommendations expressed in this material are those of the author(s) and do not necessarily reflect the views of the National Science Foundation (NSF). Special thanks to Matt Pendergraft and Raymond Leibensperger III for assistance in seawater collections and shipping.

REFERENCES

Cziczo, D. J., K. D. Froyd, C. Hoose, E. J. Jensen, M. Diao, M. A. Zondlo, J. B. Smith, C. H. Twohy, and D. M. Murphy (2013). Clarifying the Dominant Sources and Mechanisms of Cirrus Cloud Formation, *Science*, **340** (6138), 1320–1324.

Jensen, E. J., O. B. Toon, D. L. Westphal, S. Kinne, and A. J. Heymsfield (1994). Microphysical modeling of cirrus: 2. Sensitivity studies, *J. Geophys. Res*., **99** (D5), 10443–10454.

Kärcher, B., P. J. DeMott, E. J. Jensen, and J. Y. Harrington (2022). Studies on the competition between homogeneous and heterogeneous ice nucleation in cirrus formation. *Journal of Geophysical Research: Atmospheres*, **127**, e2021JD035805.

Kasparoglu, S., R. Perkins, P. J. Ziemann, P. J. DeMott, S. M. Kreidenweis, Z. Finewax, B. L. Deming, M. P. DeVault, and M. D. and Petters (2022). Experimental determination of the relationship between organic aerosol viscosity and ice nucleation at upper free tropospheric conditions. *Journal of Geophysical Research: Atmospheres*, **127**, e2021JD036296.

Koop, T., B. Luo, A. Tsias, and T. Peter (2000). Water activity as the determinant for homogeneous ice nucleation in aqueous solutions. *Nature*, **406**, 611–614.

Marcolli, C. (2014). Deposition Nucleation Viewed as Homogeneous or Immersion Freezing in Pores and Cavities, *Atmos. Chem. Phys.*, **14** (4), 2071−2104.

Patnaude et al. (2023). Low temperature ice nucleation of sea spray aerosols and secondary marine aerosols under cirrus cloud conditions, in preparation.

Patnaude, R., R. J. Perkins, S. M. Kreidenweis and P. J. DeMott, (2021). Is ice formation by sea spray particles at cirrus temperatures controlled by crystalline salts? *ACS Earth and Space Chemistry*, **5** (9), 2196–2211.

Peng, Z., and J. L. Jimenez (2020). Radical chemistry in oxidation flow reactors for atmospheric chemistry research. *Chem. Soc. Re*v., **49** (9), 2570−2616.

Stokes, M. D., G. B. Deane, K. Prather, T. H. Bertram, M. J. Ruppel, O. S. Ryder, J. M. Brady, and D. Zhao (2013). A marine aerosol reference tank system as a breaking wave analogue for the production of foam and sea-spray aerosols. *Atmos. Meas. Tech*., **6**, 1085–1094.

Vali, G., P. J. DeMott, O. Möhler, and T. F. Whale (2015). Technical Note: A proposal for ice nucleation terminology, *Atmos. Chem. Phys.*, **15**, 10263–10270.

Wagner, R., J. Kaufmann, O. Möhler, H. Saathoff, M. Schnaiter, R. Ullrich, and T. Leisner (2018). Heterogeneous Ice Nucleation Ability of NaCl and Sea Salt Aerosol Particles at Cirrus Temperatures. *J. Geophys. Res.: Atmos.*, **123** (5), 2841−2860.

DEGRADATION OF NANOPLASTICS IN THE AQUEOUS ENVIRONMENT

J. DOU[1], P. A. ALPERT[2], P. CORRAL ARROYO[2,a], B. WATTS[2], M. AMMANN[2], U. K. KRIEGER[3], A. Bianco[1,b], D. Vione[4], and M. PASSANANTI[1,4]

[1]*Institute for Atmospheric and Earth System Research/Physics, Faculty of Science, University of Helsinki, 00014 Helsinki, Finland*

[2]*Laboratory of Environmental Chemistry, Paul Scherrer Institute, 5232 Villigen, Switzerland*

[3]*Institute for Atmospheric and Climate Science, ETH Zürich, 8092 Zürich, Switzerland*

[4]*Dipartimento di Chimica, Università di Torino, Via Pietro Giuria 5, 10125 Torino, Italy*

[a]*now at: Varian Medical Systems, Inc., Switzerland*

[b]*now at: Laboratoire de Météorologie Physique, UMR 6016, CNRS, Université Clermont Auvergne, 63178 Aubière, France*

Keywords: Nanoplastics, Photochemistry, Ozone oxidation, Weathering

Plastic pollution of the oceans has become a major environmental problem. This marine plastic debris has a size ranging from nm to cm. Only recently, the presence of nanoplastics (NPs) in oceans has been demonstrated (Halle et al., 2017), and their environmental impact has remained unclear. Due to their low density, NPs can float at the surface of the oceans and interact with both the atmosphere and the seawater. Therefore, aqueous NPs can react with oxidants in the gas phase (e.g., ozone) and light, thus interfering with other (photo)chemical degradation processes in the atmosphere. In order to understand the degradation processes of NPs in the aqueous environment, we firstly investigated chemical composition changes of standard polystyrene (PS) particles before and after the exposure to light or ozone, with the technique of scanning transmission X-ray microscopy coupled to near-edge X-ray absorption fine structure spectroscopy (STXM/NEXAFS). The presence of oxygenated functions was observed in PS particles after light or ozone exposure, indicating that these plastic particles dispersed in water can react with both light and ozone. The results can be applied to both surface and atmospheric waters, like cloud and fog droplets.

In addition, simulated weathering was done by exposing a suspension of standard PS in the real environment for one year. This suspension turned yellow upon exposure, and STXM/NEXAFS results showed a significant amount of organic matter with ketone and carboxylic functions being released to the aqueous phase. We also collected particle samples from the Baltic Sea (Gulf of Finland) and analyzed them by STXM/NEXAFS. Potential NPs were found in the environmental sample, which is a motivation for us to further study the reactivity, transformation, and fate of NPs in the environment.

Reference

Alexandra Ter Halle, Laurent Jeanneau, Marion Martignac, Emilie Jardé, Boris Pedrono, Laurent Brach, and Julien Gigault: Nanoplastic in the North Atlantic Subtropical Gyre. *Environ. Sci. Technol.*, 51 (23), 13689–13697, 2017.

PMOA AS A SOURCE OF INPS IN THE NZESM

N. J. EDKINS[1,2], O. MORGENSTERN[1], L. E. REVELL[2], A. U. VENUGOPAL[2], Y. BHATTI[2], and J. WILLIAMS[1].

[1]*National Institute of Water and Atmospheric Research (NIWA), Wellington, New Zealand.*

[2]*School of Physical and Chemical Sciences, University of Canterbury, Christchurch, New Zealand.*

Keywords: ICE NUCLEATION, PRIMARY MARINE ORGANIC AEROSOL, EARTH SYSTEM MODELLING.

INTRODUCTION

The problem that this work aims to address is the shortwave radiation bias over the Southern Ocean (SO). In climate models, the downwelling shortwave radiation at the top of the atmosphere is significantly lower than in observations (IPCC, 2013). This bias has been linked to a deficit in supercooled liquid over the SO in models (Fan et al., 2011).

This deficit in supercooled liquid could be caused by using parameterisations of ice nucleation tuned to northern hemisphere observations, where mineral dust is much more prevalent. In the pristine atmosphere over the SO, however, primary marine organic aerosol (PMOA) is in fact the dominant source of INPs (Vergara-Temprado et al., 2017; Zhao et al., 2021).

PMOA has recently been implemented in UKESM1 (Mulcahy et al., 2018), from which the NZESM is derived. The purpose of this work is to allow PMOA to function as a source of ice nucleating particles (INPs) within the NZESM. This will be an extension to earlier work by Varma et al. (2021), which enabled dust particles to function as INPs in the NZESM.

METHODS

Because the NZESM has no explicit INP functionality, Varma *et al.* (2021) instead replaced the globally uniform heterogeneous freezing temperature with a three-dimensional distribution that is a function of the dust number density. This increases the freezing temperature for high dust densities, mimicking the function of dust INPs.

A similar approach will be used in this work, but with PMOA. Different parameterisations of INP number density for PMOA exist in the literature, representing PMOA INPs as a function of temperature and total organic carbon mass concentration (Wilson *et al.*, 2015) or temperature and sea spray aerosol mixing ratio (McCluskey *et al.*, 2018). These will be implemented within the NZESM and assessed for their ability to reduce the SW radiation bias over the SO.

ACKNOWLEDGEMENTS

This work was supported by the Deep South National Science Challenge.

REFERENCES

Fan, J., Ghan, S., Ovchinnikov, M., Liu, X., Rasch, P. J., & Korolev, A. (2011). Representation of Arctic mixed-phase clouds and the Wegener-Bergeron-Findeisen process in climate models: Perspectives from a cloud-resolving study. Journal of Geophysical Research: Atmospheres, 116(D1). https://doi.org/10.1029/2010JD015375

McCluskey, C. S., Hill, T. C. J., Humphries, R. S., Rauker, A. M., Moreau, S., Strutton, P. G., Chambers, S. D., Williams, A. G., McRobert, I., Ward, J., Keywood, M. D., Harnwell, J., Ponsonby, W., Loh, Z. M., Krummel, P. B., Protat, A., Kreidenweis, S. M., & DeMott, P. J. (2018). Observations of Ice Nucleating Particles Over Southern Ocean Waters. Geophysical Research Letters, 45(21), 11,989-11,997. https://doi.org/10.1029/2018GL079981

Mulcahy, J. P., Johnson, C., Jones, C. G., Povey, A. C., Scott, C. E., Sellar, A., Turnock, S. T., Woodhouse, M. T., Abraham, N. L., Andrews, M. B., Bellouin, N., Browse, J., Carslaw, K. S., Dalvi, M., Folberth, G. A., Glover, M., Grosvenor, D. P., Hardacre, C., Hill, R., … Yool, A. (2020). Description and evaluation of aerosol in UKESM1 and HadGEM3-GC3.1 CMIP6 historical simulations. Geoscientific Model Development, 13(12), 6383–6423. https://doi.org/10.5194/gmd-13-6383-2020

Stocker, T.F., D. Qin, G.-K. Plattner, M. Tignor, S.K. Allen, J. Boschung, A. Nauels, Y. Xia, V. Bex and P.M. Midgley (eds.). 2013. Climate Change 2013: The Physical Science Basis. Contribution of Working Group I to the Fifth Assessment Report of the Intergovernmental Panel on Climate Change. Cambridge University Press, Cambridge, United Kingdom and New York, NY, USA, 1535 pp.

Varma, V., Morgenstern, O., Furtado, K., Field, P., & Williams, J. (2021). Introducing Ice Nucleating Particles functionality into the Unified Model and its impact on the Southern Ocean short-wave radiation biases. Atmospheric Chemistry and Physics Discussions, 1–22. https://doi.org/10.5194/acp-2021-438

Vergara-Temprado, J., Murray, B. J., Wilson, T. W., O'Sullivan, D., Browse, J., Pringle, K. J., Ardon-Dryer, K., Bertram, A. K., Burrows, S. M., Ceburnis, D., DeMott, P. J., Mason, R. H., O'Dowd, C. D., Rinaldi, M., & Carslaw, K. S. (2017). Contribution of feldspar and marine organic aerosols to global ice nucleating particle concentrations. Atmospheric Chemistry and Physics, 17(5), 3637–3658. https://doi.org/10.5194/acp-17-3637-2017

Wilson, T. W., Ladino, L. A., Alpert, P. A., Breckels, M. N., Brooks, I. M., Browse, J., Burrows, S. M., Carslaw, K. S., Huffman, J. A., Judd, C., Kilthau, W. P., Mason, R. H., McFiggans, G., Miller, L. A., Nájera, J. J., Polishchuk, E., Rae, S., Schiller, C. L., Si, M., … Murray, B. J. (2015). A marine biogenic source of atmospheric ice-nucleating particles. Nature, 525(7568), 234–238. https://doi.org/10.1038/nature14986

Zhao, X., Liu, X., Burrows, S. M., & Shi, Y. (2021). Effects of marine organic aerosols as sources of immersion-mode ice-nucleating particles on high-latitude mixed-phase clouds. Atmospheric Chemistry and Physics, 21(4), 2305–2327. https://doi.org/10.5194/acp-21-2305-2021

MODELLING MARINE AEROSOL IN THE AUSTRALIAN REGION: CORAL-REEFS TO SEA-ICE

S.L. FIDDES[1,2], M.T., WOODHOUSE[2,1], L.J. LAMPREY[1], R.S. HUMPHRIES[2,1], M.D. MALLET[1], R. SCHOFIELD[3]

[1]*Australian Antarctic Program Partnership, Institute for Marine and Antarctic Studies, University of Tasmania, Hobart, Australia*

[2]*Climate Science Centre, Commonwealth Scientific and Industrial Research Organisation, Melbourne, Australia*

[3]*School of Geography, Earth and Atmospheric Sciences, University of Melbourne, Melbourne, Australia*

Keywords: Marine aerosol, modelling, dimethyl sulfide, clouds.

INTRODUCTION

Measurements of aerosol and their precursors in key marine environments in the Australian region have been the focus of several important field campaigns over the last few years. Many of these campaigns have made significant contributions to our understanding of aerosol abundance and processes. In this work, we present a range of modelling projects that learn from and compliment several recent field campaigns (eg. McFarquhar et al. 2021, Trounce et al. 2023). In particular, we focus on an overarching study of aerosol number concentrations in the Australian and Southern Ocean regions (Figure 1), as well as some specific regional studies, including a major campaign over the Great Barrier Reef.

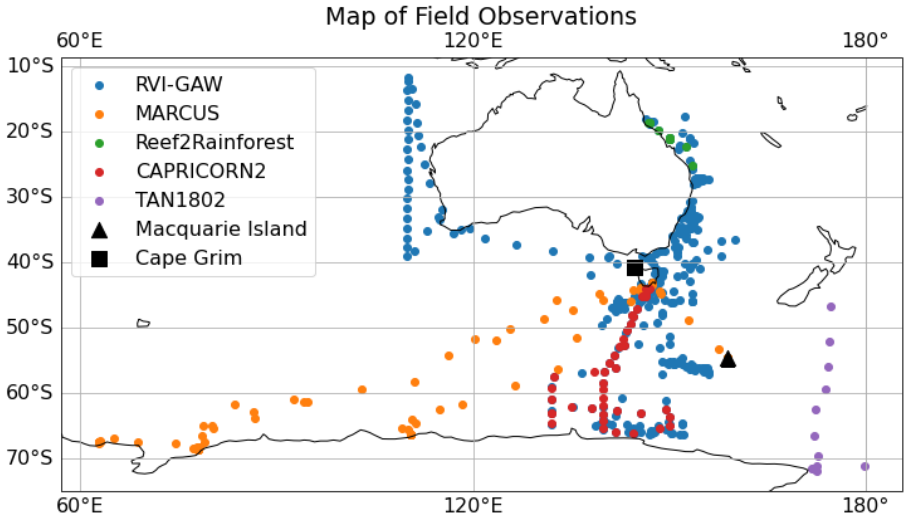

Figure 1: A map of all field observations taken from ship campaigns (coloured circles) and at stations on Macquarie Island (black triangle) and at Cape Grim (black square) analysed in Lamprey et al. (2023, in prep).

METHODS

Two models will be discussed in this presentation: the global atmosphere Australian Community Climate and Earth System Simulator – Atmosphere Model 2 (ACCESS-AM2), which includes the United Kingdom Chemistry and Aerosol (UKCA) scheme (Lamprey et al. 2023 in prep), and the Weather Research and Forecast model coupled to the Carbon Bond Mechanism Z - Model for Simulating Aerosol Interactions and Chemistry) chemistry-aerosol scheme (WRF-Chem, Fiddes et al. 2022). While WRF-Chem has been run over the Great Barrier Reef domain only, ACCESS has been tested over multiple domains, from the reef down to the sea ice. Statistical comparisons have then been performed to compare the modelled aerosol concentrations to the observed.

CONCLUSIONS

Our studies show that aerosol number concentrations and cloud condensation nuclei are underpredicted by a factor of approximately four in the Australian region within the ACCESS-AM2 model. The inclusion of boundary layer nucleation processes reduced this bias around the Australian coastline, but not in the remote marine environments. This work indicates that there may be a missing source of aerosol, or missing aerosol processes within the model, which is being investigated further.

More specifically, we have found that dimethyl sulfide concentrations are overestimated by the standard climatology over the Great Barrier Reef. By halving these concentrations, the WRF-Chem model is able to capture the dimethyl sulfide-aerosol processes with good accuracy. Unfortunately, no other campaign in this data set included DMS observations, presenting a gap for model testing of other regions.

ACKNOWLEDGEMENTS

This work was supported by the ARC Discovery Project: Great Barrier Reef as a significant source of climatically relevant aerosol particles (DP150101649) and the Antarctic Science Collaboration Initiative program, under the Australian Antarctic Program Partnership, ASCI000002. This research was undertaken with the assistance of resources and services from the National Computational Infrastructure (Project jk72 and hh5), which is supported by the Australian Government.

REFERENCES

Fiddes, S. L., Woodhouse, M. T., Utembe, S., Schofield, R., Alexander, S. P., Alroe, J., Chambers, S. D., Chen, Z., Cravigan, L., Dunne, E., Humphries, R. S., Johnson, G., Keywood, M. D., Lane, T. P., Miljevic, B., Omori, Y., Protat, A., Ristovski, Z., Selleck, P., … Williams, A. G. (2022). The contribution of coral-reef-derived dimethyl sulfide to aerosol burden over the Great Barrier Reef: a modelling study. *Atmospheric Chemistry and Physics*, *22*(4), 2419–2445. https://doi.org/10.5194/acp-22-2419-2022

Lamprey. L., Fiddes, S., Humphries, R. & Woodhouse, M. (2023). Evaluating the Australian Climate Model ACCESS-AM2 against Southern Hemisphere marine aerosol observations. *Atmospheric Chemistry and Physics, In prep.*

McFarquhar, G. M., Bretherton, C. S., Marchand, R., Protat, A., DeMott, P. J., Alexander, S. P., Roberts, G. C., Twohy, C. H., Toohey, D., Siems, S., Huang, Y., Wood, R., Rauber, R. M., Lasher-Trapp, S., Jensen, J., Stith, J. L., Mace, J., Um, J., Järvinen, E., … McDonald, A. (2021). Observations of Clouds, Aerosols, Precipitation, and Surface Radiation over the Southern Ocean: An Overview of CAPRICORN, MARCUS, MICRE, and SOCRATES. *Bulletin of the American Meteorological Society*, *102*(4), E894–E928. https://doi.org/10.1175/BAMS-D-20-0132.1

Trounce, H., Ristovsky, Z., Miljevic, B., Cravigan, L., Alroe, J., Osuagwa, C., Harvey, M., Bromley, T., Grey, S., Dunne, E., Humphries, R., Keywood, M., Ward, J., Lawson, S., Protat, A., Alexander, S.,

Schofield, R., Ryan, R., Fiddes, S., … Tanimoto, H. (2023). Great Barrier Reef aerosol and cloud data from the Reef to Rainforest campaign. *Earth System Science Data*, *In prep*.

EXTRACTING A SHIPPING-RELATED SOURCE FROM AIR POLLUTION AROUND DUBLIN PORT

K.N. FOSSUM[1], N. O'SULLIVAN[2], C. LIN[1,3], D. CEBURNIS[1], S. JAIN[2], S. HELLEBUST[2], C. O'DOWD[1], J. WENGER[2] and J. OVADNEVAITE[1]

[1]The Ryan Institute's Centre for Climate & Air Pollution Studies (C-CAPS), University of Galway, Galway, H91 CF50, Republic of Ireland.

[2]School of Chemistry and Environmental Research Institute, University College Cork, Cork, T12 YN60, Republic of Ireland.

[3]CAS Center for Excellence in Quaternary Science and Global Change & State Key Laboratory of Loess and Quaternary Geology, Chinese Academy of Sciences, Xi'an 710061, China.

Keywords: SOURCE APPORTIONMENT, PMF, DUBLIN PORT, AIR QUALITY.

INTRODUCTION

Air pollution contributes to human-related climate change while being simultaneously harmful to human health. Identifying different sources of air pollution through long-term study and state-of-the-art techniques can inform policymakers and aid in efficient mediation of poor air quality. Ports are of particular interest they have a range of emissions sources and are often near populous cities. Dublin Port is Ireland's biggest port and grossed about 34.9M tonnes of imports and exports in 2021 (Dublin Port Company Annual Report, 2021). The Port itself is adjacent to Dublin City, which is the largest city in Ireland, with an estimated 1.43M people in 2021 (28.5% of Ireland, Central Statistics Office). Dublin Port is located at the head of the river Liffey, a few kilometers east of the city center (Figure 1).

There are many port related activities, e.g. shipping traffic, road traffic, industrial works, and the transfer of goods between land and sea, that cause emissions of air pollutants through primary or secondary processes. These emissions pose a health risk to people downwind and may affect the overall emission burden of Ireland. Dublin port plans to increase trade traffic significantly over the next ten years and, the impact of port-related activities on local air quality needs quantification. In general, Dublin City experiences strong wintertime pollution events due to the burning of solid fuels for residential heating (Lin *et al.*, 2018). Historically, these local PM_1 pollution events were driven by organic aerosol (OA) in excess of 200 μg m^{-3}. Recently, a ban on the sale of smoky solid fuels (October 2022) was introduced that could lessen the significance of the pollution episodes or alter the composition of the PM_1 pollution over the next decade. Since port related emissions are set to rise, a yearlong monitoring campaign was established as part of a research project titled Source Apportionment of Air Pollution in the Dublin Port Area (PortAIR)

.

METHODS

The measurement campaign ran from December 2021 through February 2023. The scientific objective was to quantify both port-related and city-center emissions in terms of impact on air quality, as well as be able to assess regional sources of pollution and the impact on Dublin air quality. To do this, PortAIR ran a full suite of instrumentation to monitor PM and pollutant gases in the port for over a year. The state-of-the art instruments were operated inside a portable cabin at a location carefully selected within the port (Figure 1) to capture the full range of emission sources. Additionally, an intensive 1-month ran from December 2022 through January 2023, which added online elemental analysis and higher time resolution aerosol filter measurements. A simultaneous long-term measurements site at University College Dublin (UCD) also provided PM_1 online aerosol composition measurements throughout the campaign (Figure 1).

Figure 1. Picture of the Dublin city area with the PortAIR site shown in the red arrow marked 1, the Dublin Port area highlighted in bright green, and the UCD site shown with the red arrow marked 2, and the distance from the PortAIR site to the main city-center area of Temple Bar in blue (< 5 km).

Source apportionment was performed on online aerosol composition using a quadrupole aerosol chemical speciation monitor (Q-ACSM, Aerodyne Research Inc.). Primarily positive matrix factorization (PMF) was run using the ME-2 engine in the SoFi software package compatible with Igor Pro (Paatero, 1997; Conanoco *et al.*, 2013). Dublin city-center emissions have been well-studied (Ovadnevaite *et al.*, 2021) yielding well-documented fingerprints of emissions from different Irish fuel types. The source apportionment of PM in the port can be constrained using these well-documented primary emissions (Lin *et al.*, 2017). However, in terms of extracting different port related emissions, the picture is less clear as the fingerprints of ship-related emissions from marine fuels and other port sources are yet to be constrained by this project

CONCLUSIONS

Westerly winds are most common in Dublin, which held true for the PortAIR measurement campaign, although wind came from almost all directions during the year. The emissions from the city (upwind) have a significant impact on air quality measured in the port, especially in the colder months of the year around winter when residential heating emissions are at a maximum. Source apportionment was run on the Q-ACSM data, for which an initial analysis showed difficulty in extracting a ship-related factor using free PMF alone. Many techniques of extracting a ship-related source were applied to the data. The most successful attempt involved the use of mass spectral profiles of pollution plumes identified from the ships as a-priori information, an example is shown in Figure 2 where it is compared to a ship profile in the literature. Then PMF was run on a rolling-basis across the year of data, giving a seasonally linked source apportionment of the factors in the organic aerosol component of the online measurements. Presented here is the PMF solution as a set of factors, which include ship-related emissions, and are represented by the corresponding mass spectra and time series. Results from a relatively novel source apportionment approach involving the combined inorganic and organic chemical components are also presented from the intensive campaign.

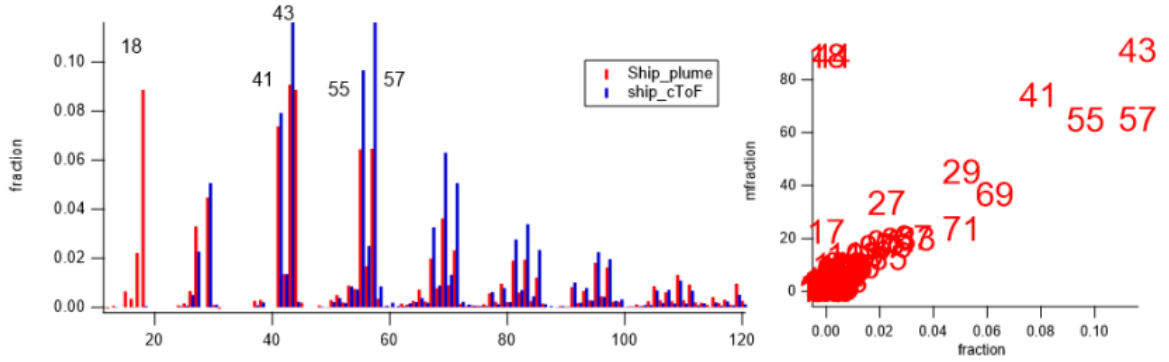

Figure 2. Comparison between a PortAIR ship plume Q-ACSM organic aerosol mass spectral profile and a cToF-AMS Ship profile from the literature (Chang *et al.*, 2011).

ACKNOWLEDGEMENTS

This work was supported by EPA-Ireland (Port-Air, 2020-CCRP-LS.6), the Department of the Environment, Climate and Communications. The online elemental analysis instrumentation and data provided by D. Green and A. Tremper of Imperial College London.

REFERENCES

Canonaco, F., Crippa, M., Slowik, J. G., Baltensperger, U., Prévôt, A. S. H (2013). SoFi, an IGOR-based interface for the efficient use of the generalized multilinear engine (ME-2) for the source apportionment: ME-2 application to aerosol mass spectrometer data. *Atmos. Meas. Tech*. **6**, 3649−3661.

Chang, R. Y. W., Leck, C., Graus, M., Müller, M., Paatero, J., Burkhart, J. F., Stohl, A., Orr, L. H., Hayden, K., Li, S. M., Hansel, A., Tjernström, M., Leaitch, W. R., and Abbatt, J. P. D. (2011). Aerosol composition and sources in the central Arctic Ocean during ASCOS, *Atmos. Chem. Phys*., **11**, 10619-10636.

Lin, C., Ceburnis, D., Hellebust, S., Buckley, P., Wenger, J., Canonaco, F., Prévôt, A. S. H., Huang, R.-J., O'Dowd, C., and Ovadnevaite, J. (2017). Characterization of Primary Organic Aerosol from Domestic Wood, Peat, and Coal Burning in Ireland, *Environmental Science & Technology*, **51**, 10624-10632,

Lin, C., Huang, R.-J., Ceburnis, D., Buckley, P., Preissler, J., Wenger, J., Rinaldi, M., Facchini, M. C., O'Dowd, C., and Ovadnevaite, J. (2021). Extreme air pollution from residential solid fuel burning, *Nature Sustainability*, **1**, 512-517.

Ovadnevaite, J., Lin, C., Rinaldi, M., Ceburnis, D., Buckley, P., Coleman, L., Facchini, M. C., Wenger, J., and O'Dowd, C. (2021). *Air Pollution Sources in Ireland; 2016-CCRP-MS.31*, National University of Ireland Galway, Istituto di Scienze dell'Atmosfera e del Clima and University College Cork, www.epa.ie.

Paatero, P. (1997). Least squares formulation of robust non-negative factor analysis, *Chemometrics and Intelligent Laboratory Systems*, **37**(1), 23-35.

OBSERVATIONS OF AEROSOL HYGROSCOPICITY AND ACTIVATION OVER REMOTE OCEANS

K.N. FOSSUM[1], W. XU[2], D. CEBURNIS[1], C. O'DOWD[1] and J. OVADNEVAITE[1]

[1]The Ryan Institute's Centre for Climate & Air Pollution Studies (C-CAPS), University of Galway, Galway, H91 CF50, Republic of Ireland.

[2]CAS Center for Excellence in Quaternary Science and Global Change & State Key Laboratory of Loess and Quaternary Geology, Chinese Academy of Sciences, Xi'an 710061, China.

Keywords: MARINE AEROSOL, CCN, MIXING STATE, HYGROSCOPICITY.

INTRODUCTION

The oceans are a dark absorbing surface covering the surface of the earth. The addition of haze or cloud layers close to the ocean surface can significantly enhance reflectance and lead to net cooling effects. Marine aerosol play a key role in the formation of these low-level clouds and are made of up particles called cloud condensation nuclei (CCN). These particles can be emitted as primary sea-spray or formed through secondary formation from gas-to-particle conversion. Sulfate is both the most common secondary marine aerosol and the most abundant marine aerosol by number concentration. While sulfate often dominates CCN number concentration, sea-spray acts more efficiently as CCN and activate into cloud droplets more readily, so the relative importance of either species to act in cloud formation can vary.

METHODS

North East Atlantic aerosol measurements spanning several years from Mace Head Research Station (MHD GAW) were used to evaluate aerosol hygroscopicity in marine air (Xu *et al.*, 2021a; Xu *et al.*, 2021b). These long-term investigations primarily focused on data from a humidified tandem differential mobility analyzer (HTDMA), which gives information of subsaturated aerosol hygroscopicity, alongside CCN measurements, which give information on the supersaturated aerosol hygroscopicity.
Aerosol measurements from the PEGASO cruise (2015) in the Southern Ocean were used to investigate marine aerosol physico-chemistry (Fossum *et al.*, 2018). Refractory black carbon measurements were used to create a statistical method to assess the degrees of pollution in Southern Ocean air and separate out polluted measurements (Fossum *et al.*, 2022). Using cases of clean marine air and only sea-salt and sulfate as CCN species, a simple cloud parcel model (Pyrcel) was used to recreate the cloud activation conditions (Fossum *et al.*, 2020).

CONCLUSIONS

The Southern Ocean PEGASO campaign captured two clean air mass types, marine polar and continental Antarctic. Of these air masses, several periods greater than 4-hours of pseudo-steady-state conditions were identified and used for analysis. The aerosol was shown to be composed of mainly secondary sulfate and sea-salt with some distinct number-size distribution characteristics between the two air mass types, appearing to be owed to the differences in sea-salt influence, even though sea-salt CCN concentration was ten times less than that of sulfate. Detailed investigation showed that the CCN in the clean air showed a systematic inverse relationship between the concentration of sea-salt CCN and the estimated boundary layer cloud peak supersaturation even at these low relative fractions of sea-salt to sulfate aerosol concentrations. Further investigation by modelling confirmed that this sea-salt effect could be accounted for using realistic external mixtures of aerosol-number concentrations of sea-salt, sulfate, and environmental conditions. The sea-salt effect on cloud activation could theoretically lead to an albedo difference of as much as 30% for low-level marine clouds (Figure 1).

Long-term investigations into North East Atlantic marine aerosol hygroscopicity shows characteristic clean, polluted, wintertime, and summertime aerosol. Growth factors are more dependent on the extent of pollution, with an average growth factor of 1.67 for the clean marine air. While the mixing state of the

aerosol is seasonally dependent, with external mixtures ubiquitous in winter and more internal mixing in summer. It was also shown, by coupling CCN measurements, that in clean marine air the mixing state of the aerosol is more important to estimation of CCN by growth factor at low supersaturations rather than higher supersaturations. However, when dealing with higher supersaturations, size-dependent hygroscopicity matter more to the estimation. This is relevant as it is common practice in growth factor CCN estimations to make the assumption that the aerosol in internally mixed and to neglect size-dependent growth factor. In terms of the sea-salt effect, it is most pronounced at low supersaturations where the mixing state of the aerosol is important for CCN estimation.

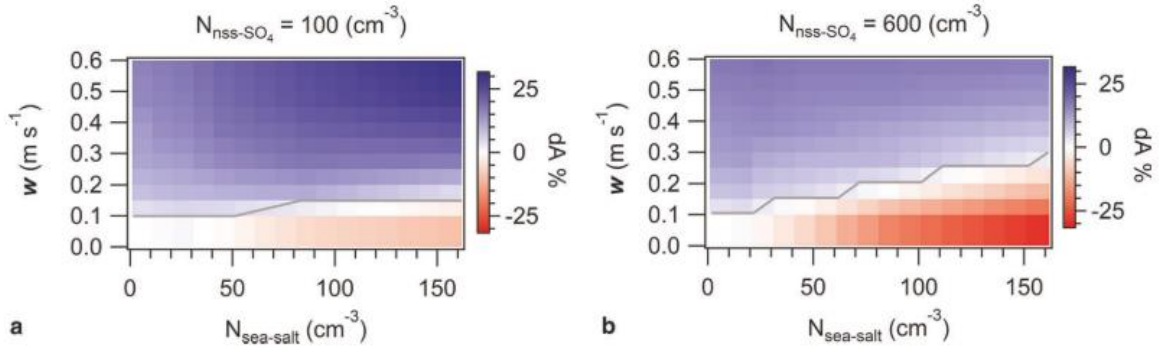

Figure 1. (Reproduced from Fossum *et al.*, 2020) Changes in cloud albedo (dA) as a function of updraft velocity (*w*) and sea-salt aerosol concentration. The sulfate number concentration is fixed at wintertime concentrations of 100 cm^{-3} (**a**) and summertime of 600 100 cm^{-3} (**b**) and simulated as a monomodal distribution (CMD ~ 60nm). The percent dA is calculated relative to the base case of low wind speed (*w*= 0.1 m/s) and sea-salt concentration (1 cm^{-3}). In the graph, blue represent a positive albedo change, red represents a negative albedo change and the grey line shows no change in dA.

ACKNOWLEDGEMENTS

This work was supported by the EPA Research Programme 2021-2030 (AEROSOURCE project 2016-CCRP-MS-31), Science Foundation Ireland (SFI) through MaREI, the SFI Research Centre for Energy, Climate, and Marine, the European Union's Seventh Framework Programme (FP7/2007–2013) project BACCHUS under grant agreement n_603445, Spanish Ministry of Economy and Competitiveness (MINECO) as part of the PEGASO (Ref.: CTM2012-37615) and BIONUC (Ref: CGL2013-49020-R) projects. The EPA Research Programme is a Government of Ireland initiative funded by the Department of Environment, Climate and Communications. The Antarctic cruise that led to this study was organised by R. Simo and M. Dall'Osto from the Institut de Ciéncies del Mar (CSIC), Barcelona, Catalonia, Spain.

REFERENCES

Fossum, K. N., Ovadnevaite, J., Ceburnis, D., Dall'Osto, M., Marullo, S., Bellacicco, M., Simó, R., Liu, D., Flynn, M., Zuend, A., and O'Dowd, C. (2018). Summertime Primary and Secondary Contributions to Southern Ocean Cloud Condensation Nuclei, *Scientific Reports*, **8**, 13844.

Fossum, K. N., Ovadnevaite, J., Ceburnis, D., Preißler, J., Snider, J. R., Huang, R.-J., Zuend, A., and O'Dowd, C. (2020). Sea-spray regulates sulfate cloud droplet activation over oceans, *npj Climate and Atmospheric Science*, **3**, 14.

Fossum, K. N., Ovadnevaite, J., Liu, D., Flynn, M., O'Dowd, C., and Ceburnis, D. (2022). Background levels of black carbon over remote marine locations, *Atmospheric Research*, **271**, 106119.

Xu, W., Fossum, K. N., Ovadnevaite, J., Lin, C., Huang, R. J., O'Dowd, C., and Ceburnis, D. (2021b). The impact of aerosol size-dependent hygroscopicity and mixing state on the cloud condensation nuclei potential over the north-east Atlantic, *Atmos. Chem. Phys.*, **21**, 8655-8675.

Xu, W., Ovadnevaite, J., Fossum, K. N., Lin, C., Huang, R.-J., O'Dowd, C., and Ceburnis, D. (2021a). Seasonal Trends of Aerosol Hygroscopicity and Mixing State in Clean Marine and Polluted Continental Air Masses Over the Northeast Atlantic, *JGR Atmospheres*, **126**, e2020JD033851.

AEROSOLS IN THE WESTERN NORTH ATLANTIC OCEAN REGION DURING THE NASA NORTH ATLANTIC AEROSOLS AND MARINE ECONSYSTEMS STUDY (NAAMES)

FRANCESCA GALLO[1,2], KEVIN J. SANCHEZ[2], BRUCE E. ANDERSON[2], MATTHEW D. BROWN[2,3], EWAN C. CROSBIE[2,3], CAROLYN JORDAN[2,4], CLAIRE E. ROBINSON[2,3], TAYLOR J. SHINGLER[2], MICHAEL A. SHOOK[2], KENNETH L. THORNHILL[2,3], ELIZABETH B. WIGGINS[2], EDWARD L. WINSTEAD[2,3], LUKE D. ZIEMBA[2], AND RICHARD H. MOORE[2]

[1]NASA Postdoctoral Program, [2]NASA Langley Research Center, Hampton, VA, [3]Science Systems and Applications, Inc., Hampton, VA, [4]National Institute of Aerospace, Hampton, VA

Keywords: North Atlantic Ocean, Aerosol-cloud interactions, marine environment.

INTRODUCTION

The complex interactions among aerosol and low clouds in marine remote environment represent one of the major sources of uncertainty in future climate projections. The reason of this uncertainty stems from the incomplete representation of the aerosol state in natural pristine conditions where clouds are highly sensitive to perturbations in aerosol properties. Aiming to improve the understanding of ocean ecosystem drivers on aerosol properties and key processes, as well as the competing influence of long range-transported aerosols in remote marine regions, between the years 2015 and 2018, NASA deployed the North Atlantic Aerosols and Marine Ecosystems Study (NAAMES) over the western subarctic Atlantic (Behrenfeld *et al*., 2019). Simultaneous ship- and aircraft-based measurements of aerosols, trace gases, and clouds were collected during three field campaigns targeting specific phases of the annual phytoplankton cycle: NAAMES-1 (November 2015) – winter transition, NAAMES-2 (May 2016) – bloom climax transition, and NAAMES-3 (September 2017) – declining phase. Here, we leverage NAAMES ship and aircraft datasets to provide a quantitative understanding of aerosol seasonal variations in the atmospheric column over the Western North Atlantic, in relation to different aerosol emission sources, and synoptic conditions.

METHODS

During NAAMES, the NASA C-130 aircraft flew over the Western North Atlantic performing 10 hours standard flight patterns. The flight patterns included vertical spirals where the C-130 transitioned from high to low altitude collecting measurements as a function of altitude. Here, we examine NASA C-130 aircraft aerosols, trace gasses and meteorological measurements collected during 37 vertical spirals. Additionally, we integrate the C-130 datasets with ship-based aerosol measurements to link aerosol property observations in the vertical column and at the surface ocean. Finally, we assess aerosol measurements collected in the free troposphere during periods in which the C-130 intercepted biomass burning plumes from Canadian wildfires.

CONCLUSIONS

Aerosol properties and vertical distribution over the Western North Atlantic Ocean exhibit strong seasonal variability. The occurrence of pristine marine conditions and new particle formation is prevalent in the winter (NAAMES-1) due to reduced biogenic emissions from the surface ocean and minimal contributions from continental sources. In the spring (NAAMES-2), the concentrations of submicron aerosol particles are higher as the result of strong phytoplankton activity at the surface ocean and the arrival of continental plumes in the free troposphere. In the summertime (NAAMES-3), the aerosol budget in marine boundary layer and free troposphere is largely driven by biomass burning aerosols from boreal wildfires (Gallo *et al*., 2023). Preliminary results of the influence of aged biomass burning plumes on the regional aerosol regime will also be discussed.

AKNOWDLEDGEMENTS

This research has been supported by the National Aeronautics and Space administration.

REFERENCES

Behrenfeld, M. J., Moore, R. H., Hostetler, C. A., Graff, J., Gaube, P., Russell, L. M., Chen, G., Doney, S. C., Giovannoni, S., Liu, H., Proctor, C., Bolaños, L. M., Baetge, N., Davie-Martin, C., Westberry, T. K., Bates, T. S., Bell, T. G., Bidle, K. D., Boss, E. S., Brooks, S. D., Cairns, B., Carlson, C., Halsey, K., Harvey, E. L., Hu, C., Karp-Boss, L., Kleb, M., Menden-Deuer, S., Morison, F., Quinn, P. K., Scarino, A. J., Anderson, B., Chowdhary, J., Crosbie, E., Ferrare, R., Hair, J. W., Hu, Y., Janz, S., Redemann, J., Saltzman, E., Shook, M., Siegel, D. A., Wisthaler, A., Martin, M. Y., and Ziemba, L. (2019). The North Atlantic Aerosol and Marine Ecosystem Study (NAAMES): Science Motive and Mission Overview, Front. Mar. Sci., 6, 122.

Gallo, F., Sanchez, K. J., Anderson, B. E., Bennett, R., Brown, M. D., Crosbie, E. C., Hostetler, C., Jordan, C., Yang Martin, M., Robinson, C. E., Russell, L. M., Shingler, T. J., Shook, M. A., Thornhill, K. L., Wiggins, E. B., Winstead, E. L., Wisthaler, A., Ziemba, L. D., and Moore, R. H. (2023). Measurement report: Aerosol vertical profiles over the western North Atlantic Ocean during the North Atlantic Aerosols and Marine Ecosys- tems Study (NAAMES), Atmos. Chem. Phys., 23, 1465–1490.

AEROSOL CHARACTERIZATION UPWIND OF A MEGACITY IN THE INDO-GANGETIC PLAIN: ROLE OF SOURCES, SINKS, AND METEOROLOGY

S. GANI[1,2*], J. RATHORE[1], R. C. THAKUR[2], S. SHUKLA[1], V. SINGH[1], S. DEY[1,3], R. KUNCHALA[1], P. PAASONEN[2], T. PETÄJÄ[2], D. GANGULY[1*], K. ACHUTARAO[1,3*], M. KULMALA[2*]

[1] Centre for Atmospheric Sciences, Indian Institute of Technology Delhi, New Delhi, India

[2]Institute for Atmospheric and Earth System Research/Physics, University of Helsinki, Helsinki, Finland

[3]School of Public Policy, Indian Institute of Technology Delhi, New Delhi, India

Keywords: atmospheric observatory, air pollution, aerosols, India, new particle formation

INTRODUCTION

A quarter of the global population lives in South Asia, and its cities and villages have some of the worst air quality in the world. Advances in atmospheric measurement and analysis techniques over the last few decades have drastically improved the ability to understand the sources and processes that drive air pollution and effective ways to reduce it. Unfortunately, local capacity in these state-of-art techniques is still extremely limited in South Asia. The Institute for Atmospheric and Earth System Research, University of Helsinki (INAR-UH) and the Centre for Atmospheric Sciences, Indian Institute of Technology Delhi (CAS-IITD) are collaborating to setup an advanced atmospheric observatory in India and perform state-of-art atmospheric measurements and analysis. We aim to advance air pollution science with implications for evidence-based policy to reduce air pollution in a highly polluted and populated region, with climate co-benefits.

METHODS

INAR-UH and CAS-IITD are collaborating to setup and operationalize the atmospheric observatory at IITD's Sonipat campus in the Indo-Gangetic Plain (IGP; population: 400 million). The measurement site is located 10 km northwest (upwind) of the Delhi-National Capital Territory, the world's most polluted megacity, and also acts as a gateway of pollutants from upwind locations in the middle east, Pakistan, and northern states in India. This measurement station is envisioned to become the most advanced atmospheric observatory in South Asia which will help to answer questions pertaining to air pollution and climate change. Table 1 shows the list of instrumentation already installed at the site and those that are upcoming. We will present preliminary results from these measurements at ICNAA-2023. We will focus on the findings related to aerosol size (2nm–10μm) and composition, and interpret them in the context of sources, sinks, and meteorology.

Parameters	Instrument
Number size distribution of ions and particles	Neutral cluster and Air Ion Spectrometer: positive and negative ions 0.8– 42 nm; particles: 2.5–42 nm
	Scanning Mobility Particle Sizer + Optical Particle Sizer: 5 nm –10 μm
$PM_{2.5}$ composition	Aerosol Chemical Speciation Monitor
Black Carbon	Aethalometer (upcoming)
Aerosol scattering coefficients	Nephelometer (upcoming)
Particulate matter (mass concentration): PM_1, $PM_{2.5}$, PM_{10}, Total PM	Real time Environmental Monitor (upcoming)

Greenhouse gas measurements: CO_2, CH_4, H_2O	Cavity Ring-Down Spectroscopy Gas analyzers
Trace gas concentrations: NO_x, CO, O_3, SO_2	Gas analyzers (upcoming)
Meteorological parameters; Global, direct, and diffuse radiation	Automatic Weather Station with Pyranometer and Pyrheliometer
Aerosol optical depth	Aerosol Mass and Optical Depth sampler
PBL turbulence, mixing layer height, cloud height, aerosol profile	LiDAR Ceilometer

Table 1. List of measurements which are operational (or will be installed soon) at the atmospheric observatory in Sonipat, India.

CONCLUSIONS

Considering the multicomponent nature of air pollution, an integrated approach is needed to tackle air pollution in the Indo-Gangetic Plain and across India. A holistic scientific understanding of atmospheric phenomena associated with air quality, or the connection between air quality and climate, is currently lacking. Long-term, continuous, and comprehensive observations of atmospheric aerosol properties, trace gases and atmospheric oxidants as well as greenhouse gases and meteorological conditions, such as those being planned at the Sonipat atmospheric observatory, will be crucial to India's understanding of atmospheric phenomenon related to air pollution and climate change.

ACKNOWLEDGEMENTS

SG, RT, TP, PP, and MK acknowledge the support of the Academy of Finland ACCC flagship (grant no. 337549). SD acknowledges funding from IIT Delhi for the Institute Chair position and the office of the Principal Scientific Advisor to the Government of India through a project on 'Delhi cluster-Delhi research implementation and innovation' (DRIIV, Prn.SA/DelhiHub/2018(C)).

AEROSOL NUCLEATION - CCN AND PARTICLES GENERATOR OF SSA

R.D. GOENAWAN[1], M.KUDSY[2] and E. ADRIAN[3]

[1,2,3] *Cloud Physics Group and Application, Center of PRIMA Reasearch, BRIN, Indonesia*

Keywords: AEROSOL, CCN, PARTICLE, SSA.

INTRODUCTION

Measurement of Concentration Distribution and smoke particles from the ignition SSA (Sistem Semai Awan) conducted in TMC-Lab Puspiptek Serpong (West Java). Measurement tool used in both large, the distribution and concentration of particles is using Light-House (LH) which can display directly in the device monitor screen which is directly readable in monitoring large particles and LH is the number of particles per unit volume (m3). LH range of gauges can measure the smallest particles 0.3 microns to 5 microns with the details 0.3, 0.5, 1.0, 2.5 and 5 microns. Light House (LH) is the only tool used to measure air and environment of the Aerosol Laboratory, PTKMR BATAN in Jakarta. Have performed measurements ofthe smoke particles SSA as much as 21 times the sampling. Once pegambilan sampling smoke take as many as 5 minutes and air measurements in the sampling container also takes about 5 minutes as well. In additionto measurements by using LH, also be measured by using the cascade Impaktor Type Anderson with 12 levels that allow measurement of 0.1 microns to 9 microns. It takesquite a long time, which is between 13:15 to 18:15 hrs ie 5 hour. Impaktor can not directly read the results of measurements of the particles but must be in process later in kondiskan and sediment particles weighing is done at every level, so they can know the distribution of particles of 0.1 microns each level until the largest particles is 9 microns. Interim results of measurements using as many as 21 samples of LH is for 0.3 micron particles have the greatest number of particles reaching 495 partikel/cm^3 495.466.815/m^3 or as much smoke and the smallest 52 partikel/cm^3 51.767.763/m^3 or smoke. While, for the measured particles 0.5 microns or 9 the highest reaches 8.969.923/m3 partikel/cm3 smoke and smallest partikel/m^3 84,755,200 or 85 partikel/cm^3. Whereas, particles measured 1.0, 2.5 and 5.0 microns in LH is not monitored or none at all, aka Zero. Looks peak distribution estimated to be less than 0.1 microns, as the "tail" distribution right (if itis considered normal) is 0.5 microns. The estimate will be proved by using Impaktor that can measure the smallest particles of 0.1 microns.

METHODS

As a reference and analogy in the formation of aerosols and clouds, the presence of aerosol particles in the atmosphere (as a back ground) will affect climatic conditions on earth, especially in the process of cloud formation [1, 2]. Aerosol particles from seawater evaporation not only contain the dominance of NaCl but also contain Calcium Cloride (CaCl2) and ammonium sulfate ((NH4)2SO4) with a diameter between 10 – 40 nm (0.01 – 0.04 □m) in Aitken mode believed to be the source of cloud condensation nuclei (CCN) [3, 4, 5]. These very small particles are highly hygroscopic and easily condensed [6]. There is a linear correlation between condensation nuclei (CN) and cloud condensation nuclei (CCN) Above sea level, condensation nuclei concentrations (CN) range from 100 – 400 particles/cm3 [7]. According to research and simulation of cloud models, if aerosol particles in the air are less than 100 particles per cm3 and the particle size is more than 2 microns then the cloud easily forms into rain otherwise if the dominant particles are smaller than 2 microns and the number of aerosols as CCN ranges from 100-400 particles / cm3 then there will be competition for the formation of ccn in the air, The absorption of moisture from aerosol to CCN occurs evenly and the air becomes stable so that it becomes clouds for a long time and it is difficult to form rain. Based on the foregoing, it is necessary to understand the process of cloud formation and its characteristics. Therefore, it is necessary to research aerosol particles as a background and we engineer by injecting as many particles as possible and with a size of less than 2 microns so that there will be competition in the air so that clouds are difficult to develop into rain. By utilizing the equipment owned by the Aerosol Lab – PTKMR BATAN. Cooperation between UPT Artificial Rain and BATAN. The collaboration between UPT Artificial Rain and BATAN in this study is

expected to be able to provide information on the characterization of smoke particles coming out of the GPG chimney, so that cloud seeding with a competition system from GPG particle smoke can take place optimally.

Figure 1. Left is Light House and Right is Impactor Cascade Anderson Sampling or sampling using Light House is done in stages.

First the sample bag is opened, then flow the GPG particle smoke with a metal pipe and connect it to the Templar plastic bag and connected to an air suction generator. After the smoke containing the particles is fully filled into the sample bag, immediately stop the suction pump and close the bag channel so that the smoke sample does not escape. Next, connect Lihgt House with the sample bag channel containing the GPG particle smoke. Up to about 5 minutes, slowly until the smoke in the smoke sample bag begins to flow in and out of the Light House (LH) and begins to see the number of particles and the measured size of particles on the LH screen.

CONCLUSIONS

Interim results from measurements using Light House (Figure 2b) of as many as 21 samplings carried out that smoke particles from GPG with a diameter of 0.3 microns have a particle count of 495,466,815 m-3 (the most) or 495 cm-3 particles and 51,767,763 m-3 or 52 cm-3 particles (the smallest). Meanwhile, for particles of 0.5 microns reached 84,755,200 cm-3 particles or 85 cm-3 particles (the most) and 8,969,923 m-3 or the smallest 9 cm-3. So that the total particles [0.3 & 0.5] of microns amount to 547 (the most) and 94 (smallest) particles of cm-3. Meanwhile, particles measured with diameters of 1.0, 2.5 and 5.0 microns in the Light House were not significantly monitored in the order of volume (cubic [m-3] and cc[cm-3]) even ZERO or none at all (2.5 and 5) microns. The results of measurements of the tool with the Anderson Cascade Impactor, as of this writing, have not been completed. If depicted on the distribution diagram (if considered) Normal, from the measurement results above it appears that the peak of the distribution is estimated to be less than 0.3 microns (between 0.1 – 0.05 microns), as the right "tail" of the "normal distribution" is 1.0 and 2.5 microns. These estimates and assumptions will be proven using the measurement and calculation results of the Anderson Cascade Impactor which can measure the smallest particles of 0.1 microns, while the smallest Light House can only measure particles with a diameter of 0.3 microns.

ACKNOWLEDGEMENTS

Very Thanks the National Laboratory for Weather Modification - Indonesia http://wxmod.bppt.go.id/

REFERENCES

BREED, D., R. BRUINTJES, V. SALAZAR, and T. JENSEN, Research Aplication Laboratory, NCAR, Boulder, Co. 80307USA, 2002.

PUDJADI, E., TAKEDA, K., NAKANE, K., Measurement of Lead Isotope Ratios in Tree Ring Width of the *P. jamaskura* as a Biomonitor of Air Pollution, *48th AnnualMeeting of The Ecological Society of Japan*, p.268, 2001.

PUDJADI, E., ROU, C., NAKANE K., Decline of *P. mume* and Change in Tree Ring Width and Heavy Metal Concentration, *J. Journal of Conservation Ecology*, Vol. 9 No.1, p.13-24, 2004.

HARYANTO, U., Penambahan Curah Hujan Melalui Modifikasi Awan: Basis Ilmiah danPerkembangannya, Workshop TMC-BPPT, Jakarta, 13 maret 2007.

PHYSICOCHEMICAL PROPERTIES OF RESPIRATORY AEROSOL AND IMPLICATIONS FOR AIRBORNE VIRUSES

ROBERT GROTH[1], SADEGH NIAZI[1], KIRSTEN SPANN[2], GRAHAM R. JOHNSON[1], and ZORAN RISTOVSKI[1]

[1]School of Earth and Atmospheric Sciences, International Laboratory for Air Quality and Health, Faculty of Science, Queensland University of Technology, Brisbane, QLD 4000, Australia

[2]School of Biomedical Sciences, Centre for Immunology and Infection Control, Faculty of Health, Queensland University of Technology, Brisbane, QLD 4000, Australia

Keywords: respiratory aerosol, aerosol physicochemistry, virus transmission

INTRODUCTION

The global burden of respiratory viruses on human health is of great concern, exacerbated by the severe acute respiratory syndrome coronavirus 2 (SARS-CoV-2) pandemic. Along with SARS-CoV-2, other viruses such as influenza virus, human rhinovirus, and measles virus are known to spread through the air by means of respiratory aerosols or droplets. These viruses are not naked in the air but instead are embedded in particles composed of the fluid in which they propagate – respiratory fluid. Therefore, the chemical and physical properties of the respiratory aerosol microenvironment are paramount for determining the infectivity of airborne respiratory viruses. The solute concentration in the aerosol phase will increase as these respiratory particles are expired into the ambient environment which will generally have lower relative humidity (RH) than within the respiratory tract. This increasing solute concentration is concomitant with a reduction in particle size through evaporation of liquid water in the particle. It is therefore clear that particle composition determines both virus infectivity and transmission routes of airborne respiratory viruses.

METHODS

Porcine respiratory fluid (PRF) was recovered from deceased piglets. PRF was recovered separately from the trachea and the lungs by washing with Milli-Q water and recovering with a pipette. Due to differences in organ geometry and physiology, it is not simple to determine the amount of dilution for each PRF sample. A cell culture medium (Dulbecco's Modified Eagle Medium, DMEM) was also analysed in comparison to PRF to assess the representativity of cell culture media to real respiratory fluid. Elemental analysis of PRF was performed using inductively coupled plasma optical emission spectroscopy (ICP-OES). The total protein concentration of PRF was measured using a BCA Protein Assay kit (ThermoFisher Scientific) and was used as directed by the manufacturer. The hygroscopicity of PRF and DMEM aerosols was measured using hygroscopicity tandem differential mobility analysis (H-TDMA), as discussed in previous publications (Cravigan et al., 2020; Duplissy et al., 2009; Groth et al., 2022; Gysel et al., 2009; Johnson et al., 2008). PRF and DMEM particle morphology was investigated using transmission electron microscopy (TEM) on Cu/formvar grids and atomic force microscopy (AFM) on Si wafers. Crystallography of PRF and DMEM particles were investigated using select area electron diffraction (SAED) in TEM

and crystallography of DMEM particles was investigated using grazing incident X-ray diffraction (GID) on (522) Si. Compositional analysis of PRF and DMEM aerosols was analysed using energy dispersive X-ray spectroscopy (EDS) and functional group analysis of DMEM aerosols was performed using Fourier transform infrared spectroscopy (FTIR) on Si.

RESULTS

Compositional analysis of bulk PRF and DMEM was compared as the mass ratio of sodium to potassium (Na:K), and the mass ratio of protein to sodium (Pr:Na) (Figure 1a). The Na:K ratio of lung fluid (~2:1) was statistically different from trachea fluid (~3:1). The Na:K ratio of DMEM (from manufacturers description) was ~16:1, which is an ~8-fold increase over PRF. The ratio protein content of DMEM (limited to only amino acids) to Na was ~100-fold lower than in PRF (Figure 1b). This indicates that there is less potassium and less protein in DMEM than in PRF.

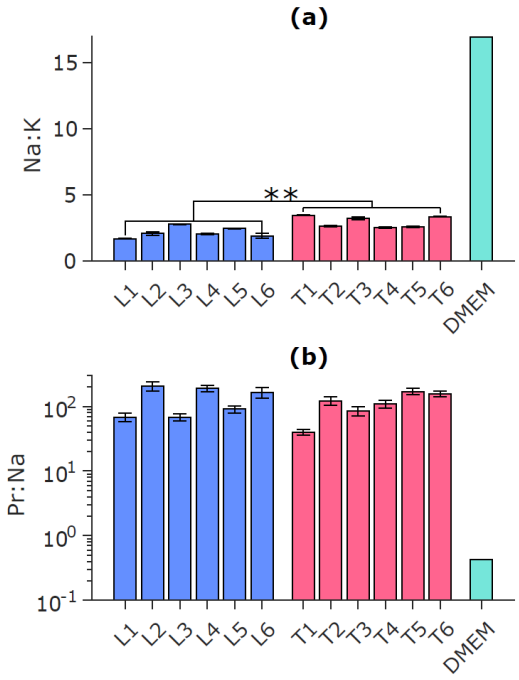

Figure 1. Mass ratio of sodium to potassium (Na:K) for porcine lung (L) and trachea (T) fluid (a) and mass ratio of proteins to sodium (Pr:Na) (b).

Hygroscopic growth factor (GF) analysis and modelling provides estimates that the protein volume fraction in the aerosol phase of PRF was 0.93±0.02. The protein volume fraction of bulk PRF was 0.97, which indicates that the composition of the aerosols differed from the bulk, or that the hygroscopicity model was not suitable or too simplified to adequately estimate the composition. Aerosol phase organic enrichment has been reported in sea spray aerosol, with organic mass contributing for higher fractions of small submicron particles (Facchini et al., 2008; Quinn et al., 2014). Given that the bulk measurement is higher than the aerosol phase estimate, it is more likely that the model does not adequately capture the behaviour of the particles. The average GF at 90% RH (GF_{90}) of PRF was 1.3, which is similar to the GF_{90} of in situ human respiratory aerosol reported previously, indicating that they are likely similar in composition (Groth et al., 2021).

EDS mapped electron micrographs show clustered Na, K, and Cl counts which correspond to spatially resolved crystals as confirmed by electron diffraction. In trachea particles, (Figure 2, top panel) numerous spatially distinct crystals were observed. In lung particles, (Figure 2, bottom panel) crystals were typically observed touching. The reason for this distinction is unclear, but may be due to rheological properties of the particles which vary with fluid site of origin. The total crystal surface area in particles with numerous crystals is larger than for single crystals and may be unfavourable for viruses localised at the interface of the crystals prior to efflorescence.

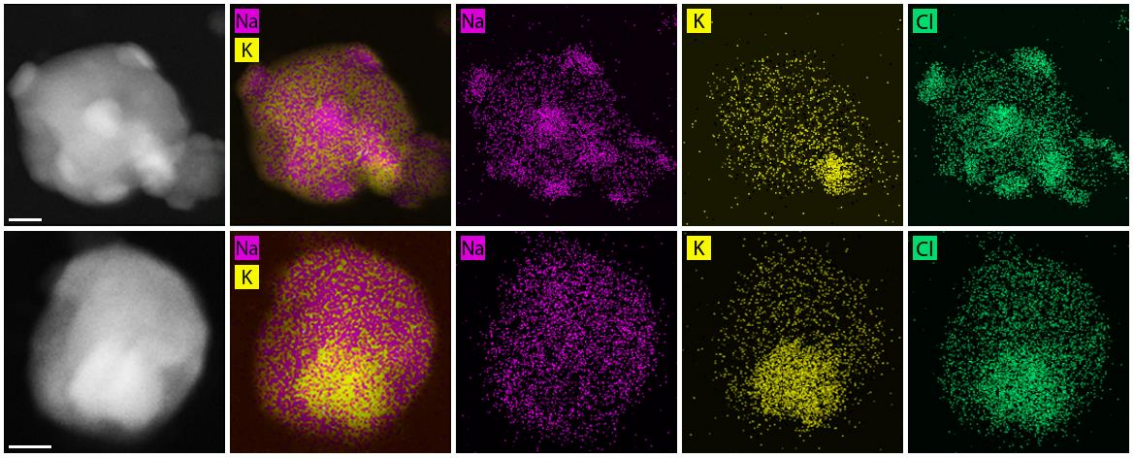

Figure 2

CONCLUSIONS

Numerous physical and chemical properties of bulk and aerosol phase PRF were measured and compared to DMEM. PRF and DMEM were not similar in any measured metric, indicating that cell culture media are likely not representative of respiratory fluid, and therefore it is uncertain if they are suitable for use in aerovirology studies. PRF, however, appears similar to human respiratory fluid and therefore may be a candidate surrogate for future work. The crystal nucleation in lung and trachea aerosols differed and may be due to rheological properties in the fluid. It is unclear how the physical and chemical properties of the pathogen microenvironment may affect the viability of an embedded virus and further characterisation is needed.

ACKNOWLEDGEMENTS

This study was funded by the Australian Research Council discovery grant no. DP210103284. This work was enabled by the Central Analytical Research Facility (CARF) at the Queensland University of Technology (QUT).

REFERENCES

Cravigan, L. T., Mallet, M. D., Vaattovaara, P., Harvey, M. J., Law, C. S., Modini, R. L., Russell, L. M., Stelcer, E., Cohen, D. D., Olsen, G., Safi, K., Burrell, T. J., & Ristovski, Z. (2020). Sea spray aerosol organic enrichment, water uptake and surface tension effects. *Atmospheric Chemistry and Physics*, *20*(13), 7955–7977. https://doi.org/10.5194/acp-20-7955-2020

Duplissy, J., Gysel, M., Sjogren, S., Meyer, N., Good, N., Kammermann, L., Michaud, V., Weigel, R., Martins dos Santos, S., Gruening, C., Villani, P., Laj, P., Sellegri, K., Metzger, A., McFiggans, G. B., Wehrle, G., Richter, R., Dommen, J., Ristovski, Z., … Weingartner, E. (2009). Intercomparison study of six HTDMAs: Results and recommendations. *Atmospheric Measurement Techniques*, *2*(2), 363–378. https://doi.org/10.5194/amt-2-363-2009

Facchini, M. C., Rinaldi, M., Decesari, S., Carbone, C., Finessi, E., Mircea, M., Fuzzi, S., Ceburnis, D., Flanagan, R., Nilsson, E. D., de Leeuw, G., Martino, M., Woeltjen, J., & O'Dowd, C. D. (2008). Primary submicron marine aerosol dominated by insoluble organic colloids and aggregates. *Geophysical Research Letters*, *35*(17), L17814. https://doi.org/10.1029/2008GL034210

Groth, R., Cravigan, L. T., Niazi, S., Ristovski, Z., & Johnson, G. R. (2021). *In situ* measurements of human cough aerosol hygroscopicity. *Journal of The Royal Society Interface*, *18*(178), 20210209. https://doi.org/10.1098/rsif.2021.0209

Groth, R., Niazi, S., Johnson, G. R., & Ristovski, Z. (2022). Nanomechanics and Morphology of Simulated Respiratory Particles. *Environmental Science & Technology*, *56*(15), 10879–10890. https://doi.org/10.1021/acs.est.2c01829

Gysel, M., McFiggans, G. B., & Coe, H. (2009). Inversion of tandem differential mobility analyser (TDMA) measurements. *Journal of Aerosol Science*, *40*(2), 134–151. https://doi.org/10.1016/j.jaerosci.2008.07.013

Johnson, G. R., Fletcher, C., Meyer, N., Modini, R., & Ristovski, Z. D. (2008). A robust, portable H-TDMA for field use. *Journal of Aerosol Science*, *39*(10), 850–861. https://doi.org/10.1016/j.jaerosci.2008.05.005

Quinn, P. K., Bates, T. S., Schulz, K. S., Coffman, D. J., Frossard, A. A., Russell, L. M., Keene, W. C., & Kieber, D. J. (2014). Contribution of sea surface carbon pool to organic matter enrichment in sea spray aerosol. *Nature Geoscience*, *7*(3), 228–232. https://doi.org/10.1038/ngeo2092

Formation mechanisms of high-level hydroxyl dicarboxylic acids in China's outflows

Hai Guo*, Yunxi Huo, Xiaopu Lyu
Department of Civil and Environmental Engineering, The Hong Kong Polytechnic University, Hong Kong, China

Abstract

As a major constituent of secondary organic aerosol (SOA), low molecular weight dicarboxylic acids and their oxygenated analogues are ubiquitous in the atmosphere and have a non-negligible impact on climate. High levels of hydroxyl dicarboxylic acids (OHDCA) were observed in Hong Kong aerosol samples, yet the formation mechanisms remain unclear. At an urban background site in South China, the mean concentration of malic acid (a representative of OHDCA) was as high as 332.7 ng m-3, exceeding the levels reported in the literature around the world. The formation mechanism of OHDCA varied with atmospheric conditions. In coastal air, especially when the relative humidity was high, good correlation between OHDCA and sulfate was found. The correlation and OHDCA concentration were enhanced when sulfate distribution shifted from a condensation mode (μ = 360 nm) to a droplet mode (μ = 620 nm). In continental air, a significant rise in OHDCA was observed from morning through early afternoon, which was more pronounced under higher daytime increment of odd oxygen (Ox) and better correlation between OHDCA and Ox, indicative of photochemical origin. Therefore, aqueous and photochemical processes played critical role in OHDCA formation in coastal and continental air, respectively. While biogenic emissions could be the main precursors of OHDCA, the contribution of anthropogenic precursors was also evident in continental air. The OHDCA formation mechanisms probed through observational evidence will be an important reference for modelling the air quality and climate impacts of organic aerosols.

Keywords: Hydroxyl dicarboxylic acids, Malic acid, Aqueous processes, Photochemical oxidation, Formation mechanisms

SEASONAL VARIATION OF OXYGENATED ORGANIC MOLECULES IN URBAN BEIJING

YISHUO GUO[1], CHAO YAN[1,2,3], YULIANG LIU[3], XIAOHUI QIAO[4], WEI NIE[3], JINGKUN JIANG[4], YONGCHUN LIU[1], VELI-MATTI KERMINEN[2], MARKKU KULMALA[1,2]

[1]Beijing Advanced Innovation Center for Soft Matter Science and Engineering, Beijing University of Chemical Technology, Beijing, China.
[2]Institute for Atmospheric and Earth System Research / Physics, University of Helsinki, Helsinki, Finland.
[3]School of Atmospheric Sciences, Nanjing University, Nanjing, China.
[4]School of Environment, Tsinghua University, Beijing, China.

Keywords: OXYGENATED ORGANIC MOLECULES, CONCENTRATION, CHEMICAL COMPOSITION, SECONDARY ORGANIC AEROSOL.

INTRODUCTION

Atmospheric aerosols affect global climate both directly and indirectly (Stocker, 2014) and are known to have a detrimental influence on human health (Lelieveld *et al.*, 2015). Modeling studies have suggested that new particle formation (NPF) dominates the number concentration of particles and is an important contributor to cloud condensation nuclei (CCN) in the global atmosphere (Merikanto *et al.*, 2009; Gordon *et al.*, 2017). In terms of aerosol mass, it has been shown that a significant fraction is composed of secondary organic aerosol (SOA; Zhang *et al.*, 2007; Jimenez *et al*., 2009; Hallquist *et al.*, 2009). In both NPF and SOA formation processes, oxygenated organic molecules (OOMs) have been acknowledged as an important contributor, and thus, advanced understanding of OOMs is crucial.

Up until now, the majority of reported sites in the lower troposphere with OOM measurement are non-urban areas, such as forest, agricultural pasture, and countryside, where the most abundant OOM species are oxidized products from monoterpenes and isoprene. In the boreal forest of southern Finland, the reported OOM concentration was the highest in summer (4.6×10^8 cm^{-3}; Huang *et al.*, 2021), followed by autumn (8.0×10^7 cm^{-3}; Zha *et al.*, 2018) and spring ($\sim 4.0 \times 10^7$ cm^{-3}; Yan *et al.*, 2016; Roldin *et al.*, 2019; Bianchi *et al.*, 2017). The level of OOMs also varied significantly at different sites. In Melpitz agricultural forest of central Europe, the OOM concentration (2.5×10^8 cm^{-3} in summer; Mutzel *et al.*, 2015) was comparable with that in Hyytiälä, while in the Alabama forest of the United States, the OOM concentration was much higher (4.8×10^9 cm^{-3} in summer; Massoli *et al.*, 2018; Krechmer *et al.*, 2015), possibly due to higher UVB and temperature. Besides, monoterpene OOMs at agricultural–rural mixed Vielbrunn were also detected (3.6×10^6 cm^{-3} in spring), and results showed that many other unidentified species also took a large fraction, especially at night (Kürten *et al.*, 2016). All of these studies highlight the importance of OOM measurement worldwide. Several urban observations were also reported (Brean *et al.*, 2019; Ye *et al.*, 2021). Although they showed that OOMs in Chinese urban cities contain a significant fraction of compounds with six to nine carbons, and that many contain nitrogen, they either reported concentrations of a few chosen species or just spectral signals. Moreover, due to the limitation of short measurement periods, they were incapable of exploring the seasonal behavior of OOM concentration and detailed composition, which are crucial for fully evaluating their potential contribution to the growth of SOA.

Here, we studied the OOMs measured by a CI-APi-TOF mass spectrometer using nitrate (NO_3^-) as reagent ions. The dataset covers four seasons of Year 2019. The seasonal variations of OOM concentration, molecular composition, volatility distribution, and potential SOA contribution were systematically investigated. With a newly developed workflow, we traced their potential sources, including aromatics, aliphatics, monoterpenes, and isoprene. Finally, the relative contribution of anthropogenic and biogenic OOMs in different seasons were also evaluated.

METHODS

A recently developed workflow, based on the molecular composition as well as the up-to-date knowledge of atmospheric OOM formation chemistry, was used for retrieving their possible sources (Xu *et al.*, 2021; Nie *et al.*, 2022). In this approach, mass spectral binning combined with positive matrix factorization (binPMF) (Zhang *et al.*, 2019) needs to be performed first to extract the factor of monoterpene OOMs. However, as performing binPMF is time-consuming and not suitable for large data sets as used in this study, we replaced the binPMF step by the criteria of nC=10, $nO_{eff} \geqslant 4$, and $2 \leqslant DBE \leqslant 4$ (**Fig. 1**) for the selection of MT OOMs. Such standards were set based on their reported composition (Ehn *et al.*, 2012; Yan *et al.*, 2016; Jokinen *et al.*, 2014; Boyd *et al.*, 2015; Berndt *et al.*, 2016; Berndt *et al.*, 2018). Here, nC is the carbon number. nO_{eff} (= nO–2×nN) is the effective oxygen number, which subtracts the number of oxygen bonded to nitrogen by assuming that all nitrogen atoms are in the form of nitrate groups ($-ONO_2$) or peroxynitrate nitrate group ($-OONO_2$). To our best knowledge, this is the common case for all nitrogen-containing compounds formed through the reaction between RO_2 and NO_x (Orlando and Tyndall, 2012; Seinfeld and Pandis, 2016).

DBE denotes the double bond equivalence and is calculated as (2nC+2–nH–nN)/2, which is the same as the term degree of unsaturation. The DBE of OOM molecule is influenced by both precursor and oxidation processes. For example, aromatic VOCs have DBE values no smaller than 4. For their oxidation products, a previous study has shown that under OH exposures equivalent to approximately 10-15 days in typical atmospheric conditions, they possess DBE values no smaller than 2 (Garmash *et al.*, 2020). The reported MT OOMs also have DBE values the same as those of aromatic OOMs, making them difficult to distinguish. According to laboratory studies, the majority of monomer products from monoterpene oxidation are C_{10} compounds (Yan *et al.*, 2020). Measurement results also showed that the concentration of C_{10} aromatic VOCs is very low (Zhang *et al.*, 2017) compared with other C_6-C_9 ones. Therefore, those C_{10} OOMs with DBE values from 2 to 4 are most likely MT OOMs. For OOMs with DBE values smaller than 2, neither aromatics nor monoterpenes oxidation could explain their formation. Hence, the precursors of those OOMs should be the ones without aromatic rings and have smaller DBE values, such as alkanes, alkenes, and some unsaturated oxygen-containing VOCs (OVOCs). OOMs with DBE values of 2 are rather complex. Their precursors could be aromatics, aliphatics, or other unknown sources, and a detailed discussion of the classification criteria could be found in Nie et al. (Nie *et al.*, 2022). By performing this revised workflow, OOMs were finally divided into five groups: isoprene (IP) OOMs, monoterpene (MT) OOMs, aromatic OOMs, aliphatic OOMs, and a small amount of undistinguished OOMs (6-9 %) that cannot be classified into those four types.

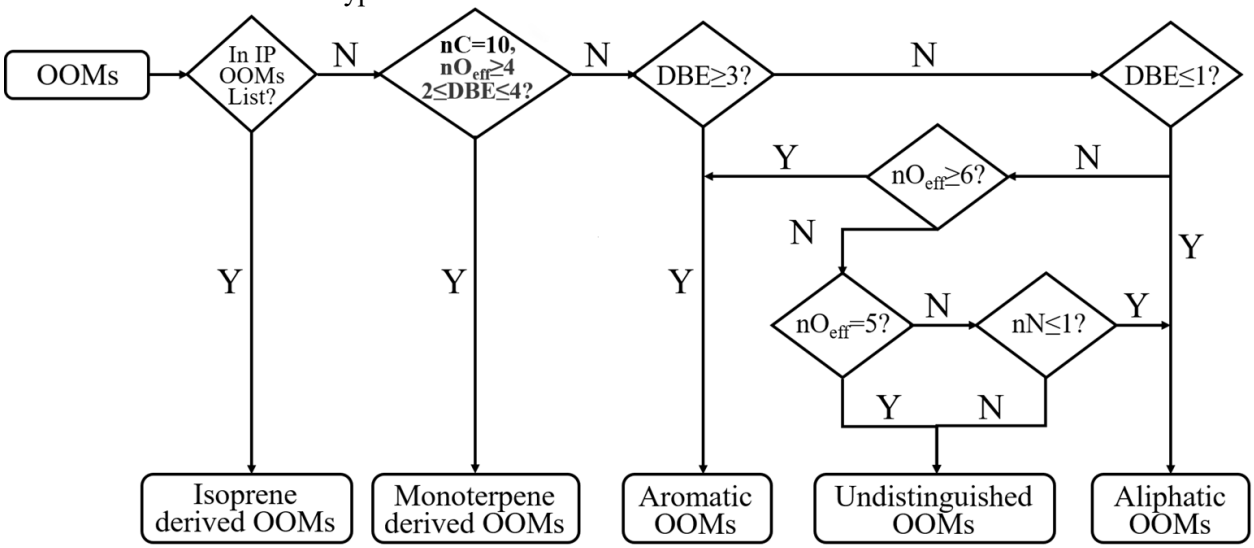

Figure 1. Workflow for retrieving OOM sources. "IP OOMs" represents isoprene-derived OOMs. nO_{eff} and nN are the numbers of effective oxygen and nitrogen in each OOM molecule, respectively. "Y" and "N" denote "Yes" and "No", respectively.

RESULTS AND CONCLUSIONS

The OOM concentration in urban Beijing was found to be the highest in summer (1.6×10^8 cm^{-3}), followed by autumn (7.9×10^7 cm^{-3}), spring (5.7×10^7 cm^{-3}) and winter (2.3×10^7 cm^{-3}), suggesting that enhanced photo-oxidation together with the rise of temperature promote the formation of OOMs. By performing the workflow, OOMs were classified into four types: aromatic OOMs, aliphatic OOMs, isoprene OOMs, and monoterpene OOMs. Among them, aromatic OOMs (29-41 %) and aliphatic OOMs (26-41 %) were the main contributors in all seasons. The aerosol dynamic model also showed that aromatic (46-62 %) and aliphatic (14-32 %) OOMs were found to be dominant contributors to SOA regardless of seasons. In comparison, the two biogenic ones, MT OOMs (8-12 %) and IP OOMs (3-5 %), have smaller contribution in all four seasons. This indicates that the formation of SOA through condensation in urban Beijing is dominated by anthropogenic sources, which is in line with the previously reported SOA composition (Le Breton *et al.*, 2018; Mehra *et al.*, 2021). Our results suggest that in order to control the formation of SOA, the emission of anthropogenic VOCs, especially aromatics, should be restricted with a high priority.

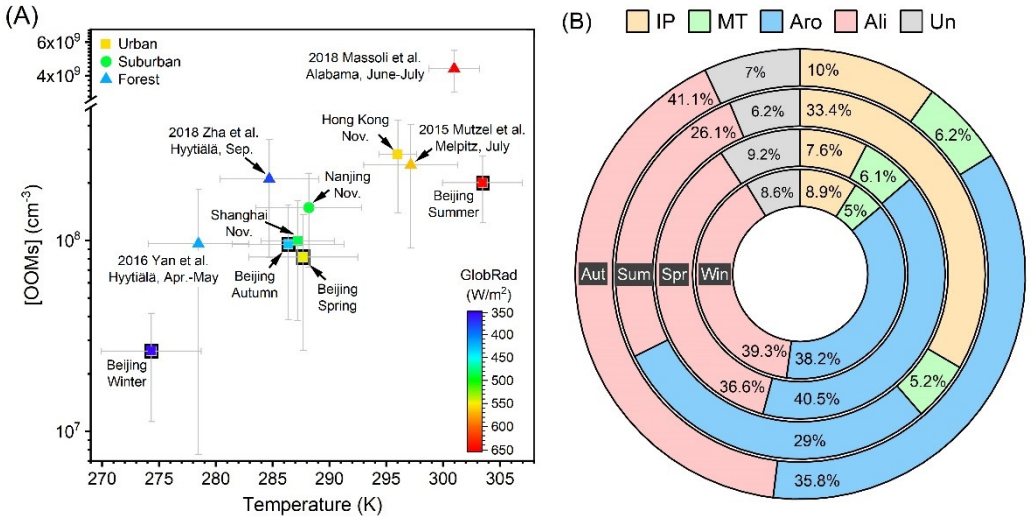

Figure 2. (A) OOM concentration vs. temperature at various lower tropospheric sites during daytime (07:00 – 17:00). Data points are colored by theoretical global radiation (GlobRad). Square, circle, and triangle markers represent urban, suburban, and forest areas, respectively. The gray error bars show standard deviations (1σ). (B) Fraction of source-classified OOMs in four seasons. The abbreviations "IP" "MT" "Aro" "Ali" and "Un" stand for IP OOMs, MT OOMs, aromatic OOMs, aliphatic OOMs and undistinguished OOMs respectively. "Win" "Spr" "Sum" and "Aut" represent winter, spring, summer and autumn separately.

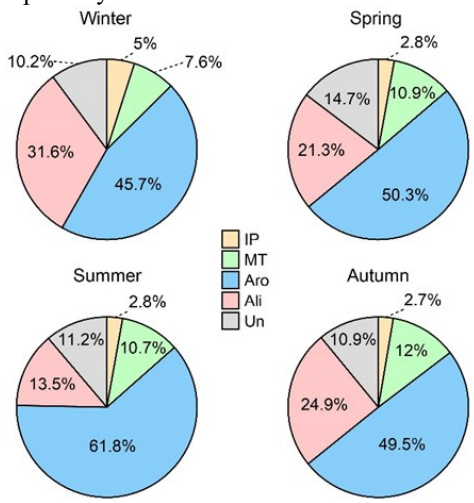

Figure 3. Estimated condensation flux contribution of four source-classified OOMs in four seasons. The abbreviations "IP" "MT" "Aro" "Ali" and "Un" stand for IP OOMs, MT OOMs, aromatic OOMs, aliphatic OOMs and undistinguished OOMs respectively.

ACKNOWLEDGEMENTS

Heikki Junninen is acknowledged, for providing the tofTool package used for processing LTOF-CIMS data. This work was supported by the National Natural Science Foundation of China (NSFC) project (grant nos. 41875175, 42075101, and 22188102) and Samsung $PM_{2.5}$ SRP.

REFERENCES

Berndt, T., Richters, S., et al. (2016). Hydroxyl radical-induced formation of highly oxidized organic compounds, *J. Nature Communications* **7**, 13677.

Berndt, T., Mentler, B., et al. (2018). Accretion Product Formation from Ozonolysis and OH Radical Reaction of α-Pinene: Mechanistic Insight and the Influence of Isoprene and Ethylene, *J. Environmental science & technology* **52**, 11069.

Bianchi, F., Garmash, O., et al. (2017). The role of highly oxygenated molecules (HOMs) in determining the composition of ambient ions in the boreal forest, *J. Atmospheric Chemistry and Physics* **17**, 13819.

Boyd, C. M., Sanchez, J., et al. (2015). Secondary organic aerosol formation from the β-pinene + NO_3 system: effect of humidity and peroxy radical fate, *J. Atmospheric Chemistry and Physics* **15**, 7497.

Brean, J., Harrison, R. M., et al. (2019), Observations of highly oxidized molecules and particle nucleation in the atmosphere of Beijing, *J. Atmospheric Chemistry and Physics* **19**, 14933.

Ehn, M., Kleist, E., Junninen, H., et al. (2012). Gas phase formation of extremely oxidized pinene reaction products in chamber and ambient air, *J. Atmospheric Chemistry and Physics* **12**, 5113.

Garmash, O., Rissanen, M. P., et al. (2020). Multi-generation OH oxidation as a source for highly oxygenated organic molecules from aromatics, *J. Atmospheric Chemistry and Physics* **20**, 515.

Gordon, H., Kirkby, J., et al. (2017). Causes and importance of new particle formation in the present-day and preindustrial atmospheres, *J. Journal of Geophysical Research-Atmospheres* **122**, 8739.

Hallquist, M., Wenger, J. C., et al. (2009). The formation, properties and impact of secondary organic aerosol: current and emerging issues, *J. Atmospheric Chemistry and Physics* **9**, 5155.

Huang, W., Li, H., et al. (2021). Measurement report: Molecular composition and volatility of gaseous organic compounds in a boreal forest – from volatile organic compounds to highly oxygenated organic molecules, *J. Atmospheric Chemistry and Physics* **21**, 8961.

Jimenez, J. L., Canagaratna, M. R., et al. (2009). Evolution of Organic Aerosols in the Atmosphere, *J. Science* **326**, 1525.

Jokinen, T., Sipilä, M., et al. (2014). Rapid Autoxidation Forms Highly Oxidized RO_2 Radicals in the Atmosphere, *J. Angewandte Chemie International Edition* **53**, 14596.

Krechmer, J. E., Coggon, M. M., et al. (2015). Formation of Low Volatility Organic Compounds and Secondary Organic Aerosol from Isoprene Hydroxyhydroperoxide Low-NO Oxidation, *J. Environmental science & technology* **49**, 10330.

Kürten, A., Bergen, A., et al. (2016). Observation of new particle formation and measurement of sulfuric acid, ammonia, amines and highly oxidized organic molecules at a rural site in central Germany, *J. Atmospheric Chemistry and Physics* **16**, 12793.

Lelieveld, J., Evans, J. S., et al. (2015). The contribution of outdoor air pollution sources to premature mortality on a global scale, *J. Nature* **525**, 367.

Massoli, P., Stark, H., et al. (2018). Ambient Measurements of Highly Oxidized Gas-Phase Molecules during the Southern Oxidant and Aerosol Study (SOAS) 2013, *J. ACS Earth and Space Chemistry* **2**, 653.

Merikanto, J., Spracklen, D. V., et al. (2009). Impact of nucleation on global CCN, *J. Atmospheric Chemistry and Physics* **9**, 8601.

Mutzel, A., Poulain, L., et al. (2015). Highly Oxidized Multifunctional Organic Compounds Observed in Tropospheric Particles: A Field and Laboratory Study, *J. Environmental science & technology* **49**, 7754.

Nie, W., Yan, C., et al. (2022). Secondary organic aerosol formed by condensing anthropogenic vapours over China's megacities, *J. Nature Geoscience* **15**, 255.

Orlando, J. J. and Tyndall, G. S. (2012). Laboratory studies of organic peroxy radical chemistry: an overview with emphasis on recent issues of atmospheric significance, *J. Chemical Society Reviews* **41**, 6294.

Roldin, P., Ehn, M., et al. (2019). The role of highly oxygenated organic molecules in the Boreal aerosol-cloud-climate system, *J. Naure Communications* **10**, 4370.
Seinfeld, J. H. and Pandis, S. N. (2016). *Atmospheric chemistry and physics: from air pollution to climate change* (John Wiley & Sons, Inc., New Jersey, U.S.A.).
Stocker, T. (2014). *Climate change 2013: the physical science basis: Working Group I contribution to the Fifth assessment report of the Intergovernmental Panel on Climate Change* (Cambridge University Press, Cambridge, New York, U.S.A.).
Xu, Z. N., Nie, W., et a. (2021). Multifunctional Products of Isoprene Oxidation in Polluted Atmosphere and Their Contribution to SOA, *J. Geophysical Research Letters* **48**, e2020GL089276.
Yan, C., Nie, W., et al. (2016). Source characterization of highly oxidized multifunctional compounds in a boreal forest environment using positive matrix factorization, *J. Atmospheric Chemistry and Physics* **16**, 12715.
Yan, C., Nie, W., et al. (2020). Size-dependent influence of NO_x on the growth rates of organic aerosol particles, *J. Science Advances* **6**, eaay4945.
Ye, C., Yuan, B., et al., (2021) Chemical characterization of oxygenated organic compounds in the gas phase and particle phase using iodide CIMS with FIGAERO in urban air, *J. Atmospheric Chemistry and Physics* **21**, 8455.
Zha, Q., Yan, C., et al. (2018). Vertical characterization of highly oxygenated molecules (HOMs) below and above a boreal forest canopy, *J. Atmospheric Chemistry and Physics* **18**, 17437.
Zhang, H., Li, H., et al. (2017). Atmospheric Volatile Organic Compounds in a Typical Urban Area of Beijing: Pollution Characterization, Health Risk Assessment and Source Apportionment, *J. Atmosphere* **8**, 61.
Zhang, Q., Jimenez, J. L., et al. (2007). Ubiquity and dominance of oxygenated species in organic aerosols in anthropogenically-influenced Northern Hemisphere midlatitudes, *J. Geophysical Research Letters* **34**, L13801.
Zhang, Y., Peräkylä, O., et al. (2019). A novel approach for simple statistical analysis of high-resolution mass spectra, *J. Atmospheric Measurement Techniques* **12**, 3761.

FORMATION AND GROWTH RATES OF SECONDARY AEROSOLS IN SOUTH KOREA

Y. HA[1], J. KIM[1], S. LEE[1], K. CHO[1], M. SONG[2,3], J. LEE[4], K. JANG[5], K. LEE[6], J. AHN[6] and C. KIM[1]

[1]School of Civil and Environmental Engineering, Pusan National University, Busan, 46241, Republic of Korea
[2]Department of Earth and Environmental Sciences, Jeonbuk National University, Jeonju, 54896, Republic of Korea
[3]Department of Environment and Energy, Jeonbuk National University, Jeonju, 54896, Republic of Korea
[4]Department of Environmental Science and Engineering, Ewha Womans University, Seoul, 03760, Republic of Korea
[5]Bio-Chemical Analysis Team, Korea Basic Science Institute, Cheongju, 28119, Republic of Korea
[6]Division of Climate and Air Quality Research, National Institute of Environmental Research, Incheon, 22689, Republic of Korea

Keywords: NEW PARTICLE FORMATION, FORMATION RATE, GROWTH RATE, SECONDARY AEROSOL, $PM_{2.5}$

INTRODUCTION

Atmospheric aerosols at high concentrations have caused severe environmental problems in many Northeast Asia countries. Inhaling high concentration aerosols such as $PM_{2.5}$ (particulate matters smaller than 2.5 μm in the aerodynamic particle size) can increase the mortality rate and cause cancers. It is well known that secondary aerosols synthesized in the atmosphere through photochemical reactions occupy more than 75% of $PM_{2.5}$. Therefore, understanding the secondary aerosols formation mechanism in the atmosphere is important to mitigate the environmental issues related to $PM_{2.5}$ in Northeast Asia. The new particle formation (NPF) in the atmosphere is generally depending on the seasonal and regional conditions. In this study, we measured the particle number size distributions (PNSDs) in real-time in Seosan (SS, rural) and Seoul (SE, urban) in South Korea for winter and summer and calculated formation and growth rates based on the PNSDs to understand NPF processes in the two different kinds of cities in South Korea.

METHODS

As a part of the Fine particle Research Initiative in East Asia Considering National Differences (FRIEND) Project, the real-time aerosol measurement campaigns were conducted at SS and SE sites during 2020/12/15 - 2021/01/15 (winter) and 2021/06/01 - 2021/06/30 (summer) by deploying nano- and regular-scanning mobility particle sizers (NSMPS and RSMPS, respectively) and aerodynamic particle sizer (APS). A beta attenuation monitor (BAM) was also used to monitor the real-time $PM_{2.5}$ mass concentration ($C_{PM2.5}$). The wide-range PNSDs of $PM_{2.5}$ were obtained by merging the PNSDs measured by NSMPS, RSMPS and APS (Ha *et al.*, 2023).

Based on the wide-range PNSDs, formation and growth rates (FR and GR, respectively), condensation and coagulation sinks (CS and CoagS, respectively) were calculated for investigating the NPF processes at the two sites in South Korea. FRs were calculated at the 3 nm particles (the smallest particle size measured by NSMPS) through the following equation (Kulmala *et al.*, 2012),

$$FR = J_3 = \left(\frac{dN_3}{dt} + CoagS_3 \cdot N_3 + \frac{GR_3}{\Delta d_p} \cdot N_3 + S_{losses}\right) \times 10^{-6},$$

where dN_3/dt is the change in the total number of particles in the 3 nm particle size bin per unit time (dt is 300s in this study) (particles·m^{-3}·s^{-1}), N_3 is the total number of 3 nm particles, $CoagS_3$ is the scavenging rate through coagulation of 3 nm particles (particles·s^{-1}). GR_3 is the growth rate (m·s^{-1}) of the particle in the 3 nm size bin, Δd_p is the length of the particle size bin (m), S_{losses} is the total loss of particles (assumed as zero in this study), and 10^{-6} used for unit correction from international system units (SI) to cm-g-s unit system (CGS). When calculating FR, GR_3 was assumed to be same as GR_{3-7} (GR between 3 and 7 nm), thus using GR_{3-7} for GR_3. The 50% appearance time method was used for calculating GRs (Kulmala *et al.*, 2012). CSs and CoagSs were calculated through the equations as (Deng *et al.*, 2020; Kulmala *et al.*, 2012),

$$CS_3 = 2\pi \cdot D_{H_2SO_4} \cdot \sum_{d_p=3\ nm}^{d_{p,max}} \beta_{m,d_p} \cdot d_p \cdot N_{d_p},$$

$$CoagS_3 \cong \sum_{d_p'=d_p=3\ nm}^{d_p'=d_{p,max}} K(d_p, d_p') \cdot N_{d_p'},$$

where D_{H2SO4} is the diffusion coefficient of sulfuric acid (H_2SO_4) molecules ($m^2 \cdot s^{-1}$), $\beta_{m,dp}$ is the transition-regime correction factor at size bin has particle size (d_p) as the midpoint, N_{dp} is the number concentration of particles in the size bin, which has d_p as the midpoint (particles$\cdot m^{-3}$), and $K(d_p, d_p')$ is the coagulation coefficient of particle sizes with d_p and d_p'.

RESULTS AND DISCUSSION

Both SS and SE sites showed 1.2~1.4 times more frequent NPF occurrences in winter than summer (Figure 1). In addition, NPF was more frequently observed at SE site than SS, where gaseous precursors for secondary aerosol formation were more abundant as an urban site. However, NPF did not occur at $PM_{2.5}$ mass concentrations higher than 35μg$\cdot m^{-3}$, due to the suppression effects of pre-existing $PM_{2.5}$ particles. The high concentration pre-existing particles prohibited NPF by intercepting condensable gas molecules and scavenging the freshly formed tiny nuclei. This can be clearly seen through the relationship between CS, CoagS, and $C_{PM2.5}$.

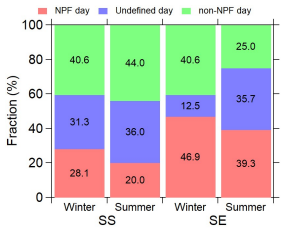

Figure 1. New particle formation (NPF) frequencies at Seosan (SS) and Seoul (SE) sites, South Korea during winter and summer measurements.

CS and CoagS generally followed the temporal changes of $C_{PM2.5}$ during the winter and summer campaigns as shown in Figure 2. Both CS and CoagS were higher in winter than in summer. Even though CS shows the similar trend with CoagS, CoagS values were 10 times lower than CS ones. Once NPF occurred, CS and CoagS increased with $C_{PM2.5}$. Then, NPF disappeared as $C_{PM2.5}$ was higher than 35 μg$\cdot m^{-3}$ due to the high concentration of pre-existing particles.

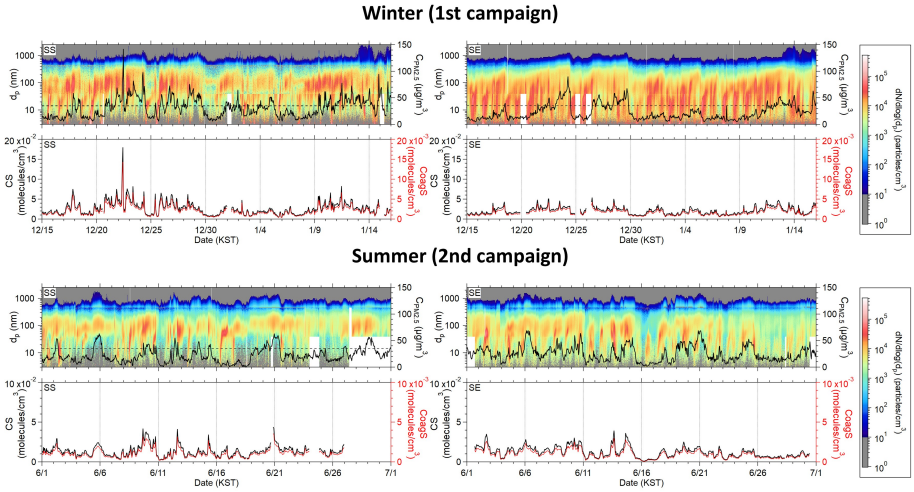

Figure 2. Merged number size distributions of the atmospheric particles (PNSDs) from 3 nm to 2.5 μm with the $PM_{2.5}$ mass concentrations ($C_{PM2.5}$) measured at Seosan (SS) and Seoul (SE) sites, South Korea as well as corresponding condensation and coagulation sinks (CS and CoagS) for the sites during the winter and summer campaigns. The black solid lines in PNSDs represent $C_{PM2.5}$, and the black dashed lines in PNSDs indicate $C_{PM2.5}$ = 35 μg$\cdot m^{-3}$.

CS and CoagS showed larger values at SS site than SE site in winter as shown in Figure 3, because the average $C_{PM2.5}$ at SS (31.4 μg·m^{-3}) was higher than that at SE (23 μg·m^{-3}) in winter. Whereas, SS and SE had similar $C_{PM2.5}$ values (SS: 21.7 μg·m^{-3}, SE: 25.5 μg·m^{-3}) in summer. Then, the two sites had similar CS and CoagS values in summer. Interestingly, the average $C_{PM2.5}$ at SE site was higher in summer (25.5 μg·m^{-3}) than in winter (23 μg·m^{-3}). Even though similar level $C_{PM2.5}$ values were observed at SE in both seasons, CS and CoagS were higher in winter than in summer. This might be related to the total number concentration of $PM_{2.5}$ particles (N_{tot}, 3 nm ~ 2.5 μm). The mean N_{tot} in winter (29.4 × 10^3 particles·cm^{-3}) was about three times higher than that in summer (9.4 × 10^3 particles·cm^{-3}) at SE site. Because CS and CoagS are strongly affected by the number of pre-existing particles, the higher N_{tot} in winter might scavenge more fresh nuclei and gaseous precursors, thus suppressing NPF and increasing CS and CoagS. When CS and CoagS are compared in terms of the occurrence of NPF (NPF vs non-NPF days), both CS and CoagS were higher during non-NPF days than NPF days in winter. However, the differences between NPF and non-NPF days were not significant in summer at both sites.

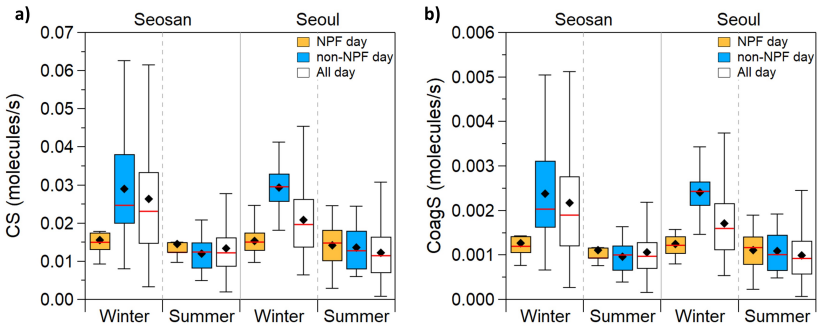

Figure 3. Seasonal variations of condensation and coagulation sink (CS and CoagS) for NPF, non-NPF and all days at Seosan (SS) and Seoul (SE) sites during the winter and summer campaigns. The whiskers are adjacent data points, and box edges are 1st and 3rd quartiles. Red lines and diamond markers represent median and mean values, respectively.

GRs were generally higher in summer than winter in both sites. When GRs for the two sites were compared to each other, SE showed higher values than SS in winter, but lower in summer. For SE site, the GRs in summer were slightly higher than in winter for all formation stages. Meanwhile, the GRs for SS site drastically increased compared to those in winter (Figure 4a). FRs at SS and SE sites were higher in summer and winter, respectively (Figure 4b). Compared to other Chinese megacities (Beijing, Shanghai, and Nanjing) reported in the literature, GRs were similar levels among those observed in the Chinese cities. In addition, FRs (J_3) were similar to Shanghai's J_3 values (Deng *et al.*, 2020; Yao *et al.*, 2018; Yu *et al.*, 2016).

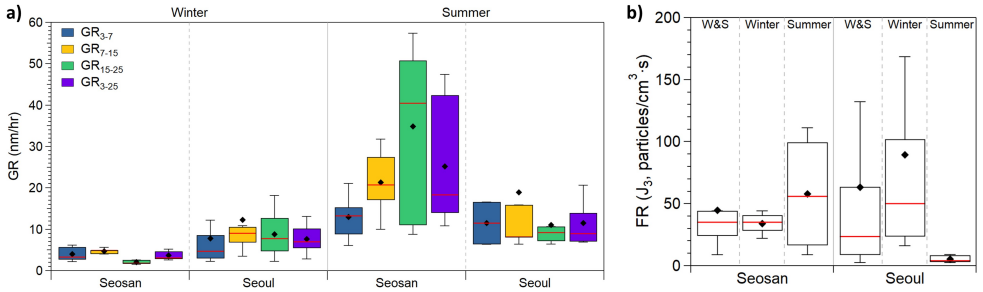

Figure 4. a) Growth rates (GR) calculated from the merged number size distributions at Seosan (SS) and Seoul (SE) sites during the winter and summer campaigns, in the three stages of the nucleation mode (3–7, 7–15, and 15–25 nm; $GR_{3–7}$, $GR_{7–15}$, and $GR_{15–25}$). b) Seasonal variations of daily maximum formation rates (FRs, or J_3) for SS and SE sites. The whiskers are adjacent data points and box edges are 1st and 3rd quartiles. Red lines and diamond markers represent median and mean values, respectively.

CONCLUSIONS

In this study, real-time measurement campaigns were conducted in winter and summer seasons at two Korean sites Seosan and Seoul (SS and SE). Both regions showed higher NPF frequency, CS and CoagS

values in winter than in summer. Furthermore, CS and CoagS values were higher during non-NPF days than NPF days in winter, which were strongly influenced by pre-existing particles and suppressed NPF simultaneously. However, CS and CoagS were similar between two sites, regardless of NPF occurrence. Other factors related to gaseous precursors, atmospheric temperature, relative humidity, solar radiation, wind speed and direction also should be considered together for understanding NPF in South Korea. FR and GR also showed spatiotemporal differences at the two sites. SS showed dramatic increase of FR and GR in summer, compared to winter. However, SE showed different trend of FR and GR with SS. Further study is needed to figure out the reasons for the spatiotemporal differences on the physical properties related to NPF in South Korea, by considering meteorological data together.

ACKNOWLEDGEMENTS

This research was supported in part by the Fine particle Research Initiative in East Asia Considering National Differences (FRIEND) Project through the National Research Foundation of Korea (NRF) (NRF-2020M3G1A1114548) and in part by the Basic Science Research Program through NRF (NRF-2022R1C1C1008367), both funded by the Ministry of Science and ICT.

REFERENCES

Deng, C., Fu, Y., Dada, L., Yan, C., Cai, R., Yang, D., Zhou, Y., Yin, R., Lu, Y., Li, X., Qiao, X., Fan, X., Nie, W., Kontkanen, J., Kangasluoma, J., Chu, B., Ding, A., Kerminen, V.M., Paasonen, P., Worsnop, D.R., Bianchi, F., Liu, Y., Zheng, J., Wang, L., Kulmala, M. and Jiang, J. (2020). Seasonal characteristics of new particle formation and growth in urban Beijing. *Environ Sci Technol* **54**, 8547–8557

Ha, Y., Kim, J., Lee, S., Cho, K., Shin, J., Kang, G., Song, M., Lee, J.Y., Jang, K.S., Lee, K., Ahn, J., Wu, Z., Matsuki, A., Tang, N., Sadanaga, Y., Natsagdorj, A. and Kim, C. (2023). Spatiotemporal differences on the real-time physicochemical characteristics of $PM_{2.5}$ particles in four Northeast Asian countries during Winter and Summer 2020–2021. *Atmos Res* **283**.

Kulmala, M., Petäjä, T., Nieminen, T., Sipilä, M., Manninen, H.E., Lehtipalo, K., Dal Maso, M., Aalto, P.P., Junninen, H., Paasonen, P., Riipinen, I., Lehtinen, K.E.J., Laaksonen, A. and Kerminen, V.M. (2012). Measurement of the nucleation of atmospheric aerosol particles. *Nat Protoc* **7**, 1651–1667.

Yao, L., Garmash, O., Bianchi, F., Zheng, J., Yan, C., Kontkanen, J., Junninen, H., Mazon, S.B., Ehn, M., Paasonen, P., Sipilä, M., Wang, M., Wang, X., Xiao, S., Chen, H., Lu, Y., Zhang, B., Wang, D., Fu, Q., Geng, F., Li, L., Wang, H., Qiao, L., Yang, X., Chen, J., Kerminen, V.-M., Petäjä, T., Worsnop, D.R., Kulmala, M. and Wang, L. (2018). Atmospheric new particle formation from sulfuric acid and amines in a Chinese megacity. *Science* (1979) **361**, 278–281.

Yu, H., Zhou, L., Dai, L., Shen, W., Dai, W., Zheng, J., Ma, Y. and Chen, M. (2016). Nucleation and growth of sub-3 nm particles in the polluted urban atmosphere of a megacity in China. *Atmos Chem Phys* **16**, 2641–2657

EXTENDED CORRESPONDING-STATES ANALYSIS OF HOMOGENEOUS NUCLEATION: UNIVERSAL BEHAVIOR AND CHARACTERISTIC PATTERNS

R. HALONEN

Center for Joint Quantum Studies and Department of Physics, School of Science, Tianjin University, 92 Weijin Road, Tianjin 300072, China.

Keywords: NUCLEATION THEORY, HOMOGENEOUS NUCLEATION

INTRODUCTION

The past decades of experimental research on homogeneous gas-phase nucleation have led to an accumulation of information regarding the specific onset conditions (pressure P and temperature T) of different condensing vapors (from monatomic argon to large n-alkanes) nucleating at various rates. The recent measurements probing the most extreme conditions (low T and high nucleation rates) crucially complement the existing data sets, and this enables us to extensively reanalyze the observed nucleation events and revisit the nucleation models based on scaling laws.

In classical nucleation theory (CNT), the nucleation rate J depends on the work required to form a critical cluster consisting n_c monomers, $W(n_\mathrm{c})$:

$$J = CP^2 \exp\left(-\frac{W(n_\mathrm{c})}{RT}\right), \tag{1}$$

where C is a kinetic factor and R is the gas constant. Previous scaling theories based on Eq. (1) (McGraw, 1981; Hale, 1986, 1992) are derived from the principle of corresponding states: properties of different systems are similar when the variables are normalized against their critical values, *e.g.*, $T^* = {}^{T}\!/_{T_\mathrm{c}}$, $P^* = {}^{P}\!/_{P_\mathrm{c}}$. Fundamentally, this idea of universality helps us to locate the coexistence curve of two equilibrium phases by constructing a general equation of state, $f_\mathrm{eq}(T^*, P^*) = 0$. Similarly, one can try to locate metastable states by formulating a *nonequilibrium* equation of state by introducing an extra variable (as required by Gibbs' phase rule). A convenient choice to describe a nucleating nonequilibrium system is its nucleation rate J (reduced to $J_\mathrm{c} \equiv CP_\mathrm{c}^2$):

$$f_\mathrm{noneq}(T^*, P^*, J^*) = 0. \tag{2}$$

Yet, even in equilibrium, only a rather limited group of compounds and their properties can be accurately described solely with parameters T^* and P^*. An often-used parameter to improve the capture of the similarities between systems is Pitzer's acentric factor, which assesses the differences in molecular geometries. More recently, Noro and Frenkel (2000) showed that the generality of phase-coexistence predictions is enhanced by extending the corresponding-states analysis with the system's characteristic range of attraction $\mathcal{R}$. In this work, we show, by analyzing over 30 sets of data covering 12 different nonpolar compounds,* that the onset of unary nucleation can be conveniently generalized with an extended corresponding-states scaling model.

CLASSICAL LIQUID DROP MODEL AND EMPIRICAL RELATIONS

Classically, the work required for the formation of a spherical n-cluster is partitioned between volume ($\propto n$) and surface ($\propto n^{2/3}$) contributions as follows

$$\frac{W(n)}{RT} = -(n-\iota)\ln\frac{P}{P_\mathrm{eq}} + (n^{2/3}-\iota)\frac{A_1\sigma}{RT}. \tag{3}$$

In CNT $\iota = 0$, whereas in the self-consistent theory $\iota = 1$ (Girshick and Chiu, 1990). Here, instead of using measured values for the equilibrium vapor pressure P_{eq} or the surface energy $A_1\sigma$, $W(n)$, and its temperature dependence in particular, is analyzed with well-known empirical relations: The Clausius-Clapeyron equation for P_{eq} can be given in terms of boiling point entropy of vaporization ($\Delta s_{\mathrm{v}} = {}^{\Delta H}/_{RT_{\mathrm{b}}}$) and the Guldberg factor ($f_{\mathrm{G}} = {}^{T_{\mathrm{b}}}/_{T_{\mathrm{c}}}$, for most liquids about ⅔):

$$\ln \frac{P_{\mathrm{eq}}}{P_{\mathrm{c}}} = -\frac{\Delta H}{R}\left(\frac{1}{T} - \frac{1}{T_{\mathrm{c}}}\right) = -\frac{\Delta s_{\mathrm{s}}}{R} f_{\mathrm{G}}\left(\frac{1}{T^*} - 1\right) = -\mathcal{A}X. \tag{4}$$

Whereas, the Eötvös rule states the surface term in Eq. (3) is a function of surface entropy (Δs_{s}):

$$\frac{A_1\sigma}{RT} = \frac{\Delta s_{\mathrm{s}}}{R}\left(\frac{1}{T^*} - 1\right) = \mathcal{B}X, \tag{5}$$

where $X = {}^{1}/_{T^*} - 1$. The corresponding-state laws given by Eqs. (4) and (5) suggests that the basic thermodynamics of a liquid cluster can be generally characterized *via* constant quantities $\mathcal{A}$ and $\mathcal{B}$. The relevant parameters for the studied compounds are given in Table 1.

ONSET PRESSURE AND CORRESPONDING-STATES CORRELATION

Against the convention, here we concentrate on studying the onset pressures in particular instead of the nucleation rates. According to Eqs. (1) and (3)–(5), the onset pressure for some n_{c} is

$$\ln \frac{P(n_{\mathrm{c}})}{P_{\mathrm{c}}} = \frac{\ln J^* - (n_{\mathrm{c}} - \iota)\mathcal{A}X + (n_{\mathrm{c}}^{2/3} - \iota)\mathcal{B}X}{n_{\mathrm{c}} + 2 - \iota}. \tag{6}$$

Due to the algebraic effort and general convenience of limiting n_{c} to natural numbers, the actual pressure inducing nucleation at some rate J^* at T^* is solved numerically:

$$\ln P^* = \max\left[\ln \frac{P(n_{\mathrm{c}})}{P_{\mathrm{c}}}\right]. \tag{7}$$

Thus, if the critical cluster is very large and J is considered to be relatively constant, $\ln P^* \propto -\mathcal{A}X$. This linear behavior is indeed often seen in the so-called Volmer plots where $\ln P$ is presented against T^{-1}. When approaching rather small n_{c}, such linearity breaks down as demonstrated recently by Dingilian et al. (2021) in their analysis of CO_2 nucleation.

	T_{b}	T_{c}	f_{G}	$\Delta s_{\mathrm{v}}/R$	$\mathcal{A}$	$\mathcal{B}$	$\mathcal{B}/\mathcal{A}$	$\mathcal{R}$
Argon	87.3	150.7	0.58	8.9	5.1	7.7	**1.49**	0.48
Nitrogen	77.4	126.2	0.61	8.7	5.3	8.2	**1.54**	0.55
CO_2	194.7	304.1	0.64	10.4	6.7	10.2	**1.52**	0.38
SF_6	209.4	318.7	0.66	10.2	6.7	9.7	**1.44**	0.28
Toluene	383.8	591.9	0.65	10.4	6.7	10.5	**1.55**	0.37
Propane	231.0	369.9	0.63	9.9	6.2	9.6	**1.55**	0.48
n-alkanes:								
Pentane	309.2	469.7	0.66	10.0	6.6	10.5	**1.59**	0.40
Hexane	341.9	507.5	0.67	10.2	6.8	10.8	**1.58**	0.42
Heptane	371.5	540.1	0.69	10.3	7.1	11.1	**1.57**	0.38
Octane	398.8	568.7	0.70	10.4	7.3	11.5	**1.57**	0.37
Nonane	424.0	594.2	0.71	10.5	7.5	11.8	**1.57**	0.37
Decane	447.3	618.1	0.72	10.6	7.7	12.1	**1.57**	0.38

Table 1: Thermodynamic properties of studied compounds: boiling (T_{b}) and critical temperature (T_{c}), the Guldberg factor (f_{G}), entropy of vaporization ($\Delta s_{\mathrm{v}}/R$), the apparent entropy of vaporization ($\mathcal{A} = \Delta s_{\mathrm{v}} f_{\mathrm{G}}/R$), and surface entropy ($\mathcal{B} = \Delta s_{\mathrm{s}}/R$). The dimensionless hard-sphere equivalent ranges of attraction $\mathcal{R}$ are estimated for the Mie-models by Dufal et al. (2015) using the method by Noro and Frenkel (2000).

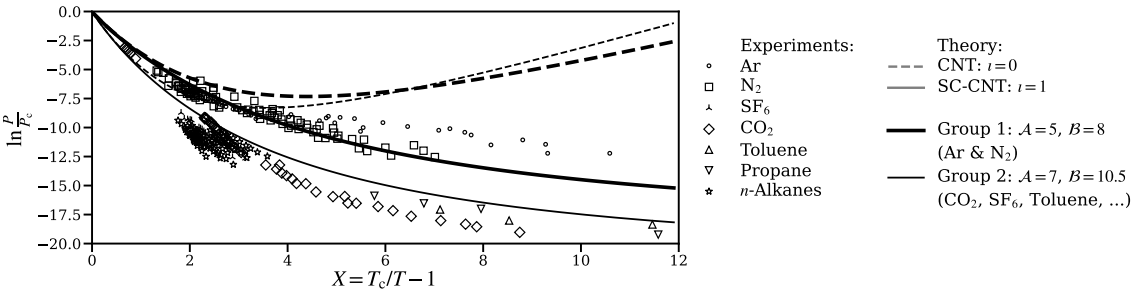

Figure 1: Corresponding-states presentation of the nucleation onset pressures of nonpolar vapors nucleating at the rate of $J \approx 10^{17\pm2}$ cm^{-3}s^{-1}. The solid and dashed lines correspond to the theoretical predictions given by Eqs. (6) and (7).

In Figure 1, the onset data from various experiments for nonpolar compounds (listed in Table 1), corresponding to $J \approx 10^{17\pm2}$ cm^{-3}s^{-1}, are presented with the theoretical predictions given by Eqs. (6) and (7). For all systems, the reference rate $J_c \approx 10^{34}$ cm^{-3}s^{-1}. Firstly, the different systems are roughly grouped into two distinct groups based on their respective thermodynamic features: $\mathcal{A} \approx 5$ and $\mathcal{B} \approx 8$ (Ar and N_2), and $\mathcal{A} \approx 7$ and $\mathcal{B} \approx 10.5$ (others). Secondly, with these parameters, the predicted $\ln P^*$ agree very well with the experimental values, but only when the limiting self-consistency is guaranteed, *i.e.*, $\iota = 1$. Already at moderate supercooling, $X \approx 2$, the values obtained for $\iota = 0$ diverge from the experimental data indicating that the CNT formalism for $W(n)$ inadequately describes the thermodynamics of the clusters.

RANGE OF ATTRACTION AND KINETIC LIMIT OF NUCLEATION

According to Figure 1, the given prediction holds even at the very low T (high X), and the observed grouping is due to similar $\mathcal{A}$, $\mathcal{B}$, and J. Furthermore, for all systems $\mathcal{B}/\mathcal{A} \approx 1.5$ (Table 1). So, at the kinetic limit, where $W(n = 2) \to 0$ and $n_c \to 1$, the following holds (assuming $\iota = 1$)

$$\ln P^*_{\text{kin}} = \frac{\ln J^*}{2} = \mathcal{A} X_{\text{kin}} \left[\left(2^{2/3} - 1 \right) \frac{\mathcal{B}}{\mathcal{A}} - 1 \right]. \tag{8}$$

Thus, the extremum of Eq. (6) can thus be expressed as a function of $\mathcal{B}/\mathcal{A}$ and $X_{\text{kin}} = T_c/T_{\text{kin}} - 1$,

$$\frac{\ln P^*}{\ln P^*_{\text{kin}}} = \frac{\ln P^*}{1/2 \ln J^*} = \min \left\{ \frac{1}{n_c + 1} \left[2 + \frac{X}{X_{\text{kin}}} \frac{\left(n_c^{2/3} - 1 \right) \frac{\mathcal{B}}{\mathcal{A}} + 1 - n_c}{\left(2^{2/3} - 1 \right) \frac{\mathcal{B}}{\mathcal{A}} - 1} \right] \right\}. \tag{9}$$

Since the second virial coefficient B_2^* (reduced to $|B_2(T_c)| \equiv RT_c/P_c$) describes the abundance of dimers in equilibrium, the temperature parameter X_{kin} can be determined for J^*:

$$-\frac{B_2(T_{\text{kin}})}{RT_{\text{kin}}} = \frac{\exp\left(-W(2)/RT_{\text{kin}}\right)}{P_{\text{kin}}} \Rightarrow B_2^*(T_{\text{kin}}) \frac{T_c}{T_{\text{kin}}} = J^{*-1/2}. \tag{10}$$

As demonstrated by Noro and Frenkel (2000), for simple systems B_2^* is a function of compound-specific $\mathcal{R}$. The monomer–monomer interactions, used to determine B_2^*, are conveniently computable in a conformal manner for the studied compound using the Mie potential (Dufal et al., 2015) (listed in Table 1). And a numerical analysis of Eq. (10) further reveals that $X_{\text{kin}}^{\text{Mie}} \approx -(1.1\mathcal{R} + 0.1) \ln J^*$. As shown in Figure 2, the experimental values of $\ln P^* / 1/2 \ln J^*$ over a range of different systems and various J (from 10^3 to 10^{22} cm^{-3}s^{-1}) scale universally with respect to $X/X_{\text{kin}}^{\text{Mie}}$ and agree extremely well with the extended corresponding-states formulation given by Eq. (9).

If the analysis is performed in terms of B_2 instead of more intuitive $\mathcal{R}$, Eq. (9) is equally applicable for strongly associated polar systems, with highly orientation-dependent interactions. For each compound, however, the accuracy of B_2 should be assured by quantum mechanical calculations as phenomenological parametrizations of B_2 are not valid at temperatures relevant for nucleation.

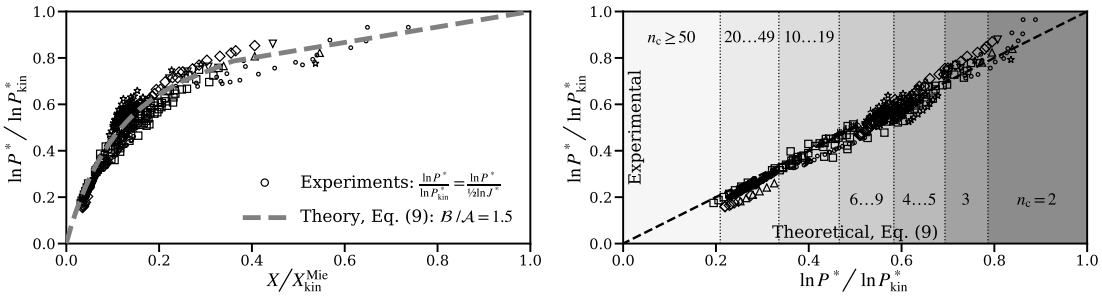

Figure 2: Experimental (symbols same as in Figure 1) and theoretical values for $\ln P^* / \ln P^*_{\rm kin}$ as a function of the "Mie" temperature parameter $X/X^{\rm Mie}_{\rm kin}$ (left) and with respect to each other (right). The shaded areas on the right-hand side panel indicate the corresponding range of critical cluster sizes minimizing Eq. (9).

CONCLUSIONS

A general nonequilibrium equation of state for homogeneous nucleation can be formulated for non-polar compounds with variable range attraction using the classical nucleation framework, Eq. (1), with some thermodynamic empiricism, Eqs. (4) and (5). However, as a degree of atomistic realism is introduced *via* $\mathcal{R}$, the presented approach is fundamentally different from CNT (*e.g.*, the obtained $n_{\rm c}$ are not equivalent with the Gibbs–Thomson equation). While different finite-size corrections on Eq. (3) affect significantly the predicted J, by focusing on the most rudimentary experimental data (onset P and T) the key thermophysical relationships and factors involved in gas-phase nucleation can be identified. Ultimately, our analysis reveals the most profound similarities among a diverse set of nucleating systems. In addition, the results help us, *e.g.*, to elucidate the (previously unknown) reasons for the apparent predictive power of Hale's scaling formalism (Hale, 1986, 1992).

REFERENCES

Dingilian, K. K., Lippe, M., Kubečka, J., Krohn, J., Li, C., Halonen, R., Keshavarz, F., Reischl, B., Kurtén, T., et al. (2021). New particle formation from the vapor phase: From barrier-controlled nucleation to the collisional limit. *J. Phys. Chem. Lett.*, 12(19):4593–4599.

Dufal, S., Lafitte, T., Galindo, A., Jackson, G., and Haslam, A. J. (2015). Developing intermolecular-potential models for use with the SAFT-VR Mie equation of state. *AIChE Journal*, 61(9):2891–2912.

Girshick, S. L. and Chiu, C.-P. (1990). Kinetic nucleation theory: A new expression for the rate of homogeneous nucleation from an ideal supersaturated vapor. *J. Chem. Phys.*, 93(2):1273–1277.

Hale, B. N. (1986). Application of a scaled homogeneous nucleation-rate formalism to experimental data at $T \ll T_{\rm c}$. *Phys. Rev. A*, 33(6):4156.

Hale, B. N. (1992). The scaling of nucleation rates. *Metall. Trans. A*, 23(7):1863–1868.

McGraw, R. (1981). A corresponding states correlation of the homogeneous nucleation thresholds of supercooled vapors. *J. Chem. Phys.*, 75(11):5514–5521.

Noro, M. G. and Frenkel, D. (2000). Extended corresponding-states behavior for particles with variable range attractions. *J. Chem. Phys.*, 113(8):2941–2944.

***Experimental data is from the following publications:** S. Sinha, A. Bhabhe, H. Laksmono, J. Wölk, R. Strey, and B. Wyslouzil, J. Chem. Phys. **132**, 064304 (2010). K. Iland, J. Wölk, R. Strey, and D. Kashchiev, J. Chem. Phys. **127**, 154506 (2007). A. Fladerer and R. Strey, J. Chem. Phys. **124**, 164710 (2006). G. Koppenwallner and C. Dankert, J. Phys. Chem. **91**, 2482 (1987). A. Bhabhe and B. Wyslouzil, J. Chem. Phys. **135**, 244311 (2011). K. Iland, J. Wedekind, J. Wölk, and R. Strey, J. Chem. Phys. **130**, 114508 (2009). K. K. Dingilian, R. Halonen, V. Tikkanen, B. Reischl, H. Vehkamäki, and B. E. Wyslouzil, Phys. Chem. Chem. Phys. **22**, 19282 (2020). K. K. Dingilian, M. Lippe, J. Kubečka, J. Krohn, C. Li, R. Halonen, F. Keshavarz, B. Reischl, T. Kurtén, *et al.*, J. Phys. Chem. Lett. **12**, 4593 (2021). K. M. Duff, *Ph.D. thesis* (MIT, 1966). B. J. Wu, P. P. Wegener, and G. D. Stein, J. Chem. Phys. **68**, 308 (1978). S. Chakrabarty, J. J. Ferreiro, M. Lippe, and R. Signorell, J. Phys. Chem. A **121**, 3991 (2017). J. Schmitt, R. Zalabsky, and G. Adams, J. Chem. Phys. **79**, 4496 (1983). J. J. Ferreiro, S. Chakrabarty, B. Schläppi, and R. Signorell, J. Chem. Phys. **145**, 211907 (2016). M. Lippe, S. Chakrabarty, J. J. Ferreiro, K. K. Tanaka, and R. Signorell, J. Chem. Phys. **149**, 244303 (2018). K. E. Ogunronbi, A. Sepehri, B. Chen, and B. E. Wyslouzil, J. Chem. Phys. **148**, 144312 (2018). K. E. Ogunronbi and B. E. Wyslouzil, J. Chem. Phys. **151**, 154307 (2019). D. Ghosh, D. Bergmann, R. Schwering, J. Wölk, R. Strey, S. Tanimura, and B. E. Wyslouzil, J. Chem. Phys. **132**, 024307 (2010). S. Feusi, J. Krohn, C. Li, and R. Signorell, J. Chem. Phys. **158**, 074301 (2023).

OVERVIEW OF THE AUSTRALIAN MARINE CLOUD BRIGHTENING PROGRAM

D. P. HARRISON[1,2], I. JONES[2], M. LAWRENCE[3], R. WHEEN[3], W. DAVIES[3], P. BAKER[3], Z. RISTOVSKI[4], B. KELAHER[1], L. HARRISON[2], D. HERNANDEZ[1], L. CRAVIGAN[4], R. ROSENFELD[5], R. SCHOFIELD[6], R. BRAGA[1], C. MEDCRAFT[1], P. BUTCHERINE[1], S. ELLIS[1], C. HALLOWAY[1]

[1] National Marine Science Centre, Southern Cross University (SCU),
[2]School of Geosciences, University of Sydney
[3]Sydney Institute of Marine Science
[4] Queensland University of Technology (QUT), Brisbane, QLD, Australia
[5] Hebrew University of Jerusalem
[6] University of Melbourne

Keywords: MARINE CLOUD BRIGHTENING, CLOUD AEROSOL INTERACTIONS, AEROSOL CLOUD RADIATION, CORAL REEFS, BLEACHING

INTRODUCTION

Marine cloud brightening (MCB) is a potential regional atmospheric-engineering strategy to reduce environmental stress on the Great Barrier Reef during marine heatwaves. Atmospheric, biogeochemical, and ecological modelling have been undertaken and suggest that the potential exists to reduce light and thermal stress that cause coral bleaching. Despite three decades of theoretical research into MCB as a solar radiation management technology, until now there have been no outdoor field experiments directly evaluating the concept. In this talk I will give an overview of the Australian research program with a focus on the field measurements of characteristics of the sea salt aerosol spray produced and preliminary results of its impact on cloud microphysical properties.

METHODS

We have now progressed development of seawater atomisation technology to a scale which allows us to empirically examine foundational assumptions of MCB. These include the ability to generate sufficient sea salt aerosols within a suitable size range and reliance on natural mixing processes to transport them to cloud base height. A major focus of the research program us under what conditions the cloud microphysical response is favorable in terms of increased droplet number concentration, reduced droplet radius, any impacts on cloud liquid water and ultimately enhancement to cloud albedo. We have conducted 3 experimental campaigns within the Great Barrier Reef Marine Park with a 4th to take place during February and March 2023. The campaign in 2023 will involve 2 research vessels, 2 GBR island research stations, and will be the first to make use of a Cloud Microphysical Aircraft to sample within perturbed and unperturbed clouds and compare with satellite observations.

CONCLUSIONS

This talk will provide an overview of the results of the Australian Marine Cloud Brightening program focusing on the results of the most recent field campaigns in 2022 and early 2023. In the 2022 campaign we demonstrated for the first time the ability to generate sufficient quantities of sea salt aerosols and observed their dispersion and transport to cloud base height. Using ship-based LiDAR we clearly tracked the vertical mixing of the plume and with aircraft we observed just below cloud base a region of around 10 km^2 of elevated aerosol concentrations ~1000 cm^{-3} over background. The cloud microphysical response to the perturbation is expected to be elucidated during the 2023 campaign with the expectation of some very preliminary results available for this talk.

From its inception our research program has involved consultation, participation, and the consent of indigenous traditional custodians of the reef and has proceeded within the regulatory oversight of one of the world's most actively managed marine estates.

FUNDING ACKNOWLEDGEMENT

The Reef Restoration and Adaptation Program is funded by the partnership between the Australian Governments Reef Trust and the Great Barrier Reef Foundation.

TRADITIONAL OWNER ACKNOWLEDGEMENT

The authors would like to thank the Traditional Owners of the Great Barrier Reef for their involvement and support of the project.

AN AUSTRALIAN AIRBORNE PLATFORM FOR ATMOSPHERIC SCIENCE

D. P. HARRISON[1], D. HERNANDEZ[1], Z. RISTOVSKI[2], C. MEDCRAFT[1], P. BUTCHERINE[1]

[1] National Marine Science Centre, Southern Cross University (SCU),
[2] Queensland University of Technology (QUT), Brisbane, QLD, Australia

Keywords: MARINE CLOUD BRIGHTENING, CLOUD AEROSOL INTERACTIONS, AEROSOL CLOUD RADIATION, CORAL REEFS, BLEACHING

ABSTRACT

Our work on aerosol-cloud-radiation interactions over the Great Barrier Reef as part of the Reef Restoration and Adaptation Program became hamstrung by the lack of a suitable aerosol and cloud microphysics equipped aircraft platform in Australia. The use of unmanned aerial vehicles and small manned motorized gliders fitted with aerosol counting and sizing equipment fulfilled some initial project objectives but were not capable of collecting the comprehensive datasets required to examine key hypothesis. To address this critical infrastructure gap, Southern Cross University has purchased a Cessna 337 aircraft and outfitted it with a comprehensive suite of meteorological, aerosol, and cloud microphysics instrumentation. Both the choice of aircraft platform itself and the implementation of the instrumentation, navigation, and computer infrastructure fit out were designed from the outset to be as flexible as possible, to potentially serve other airborne scientific roles in the future. We hope that this new piece of research infrastructure can be of benefit to the Australian aerosol and cloud microphysics research communities in addition to filling the immediate need for our own project.

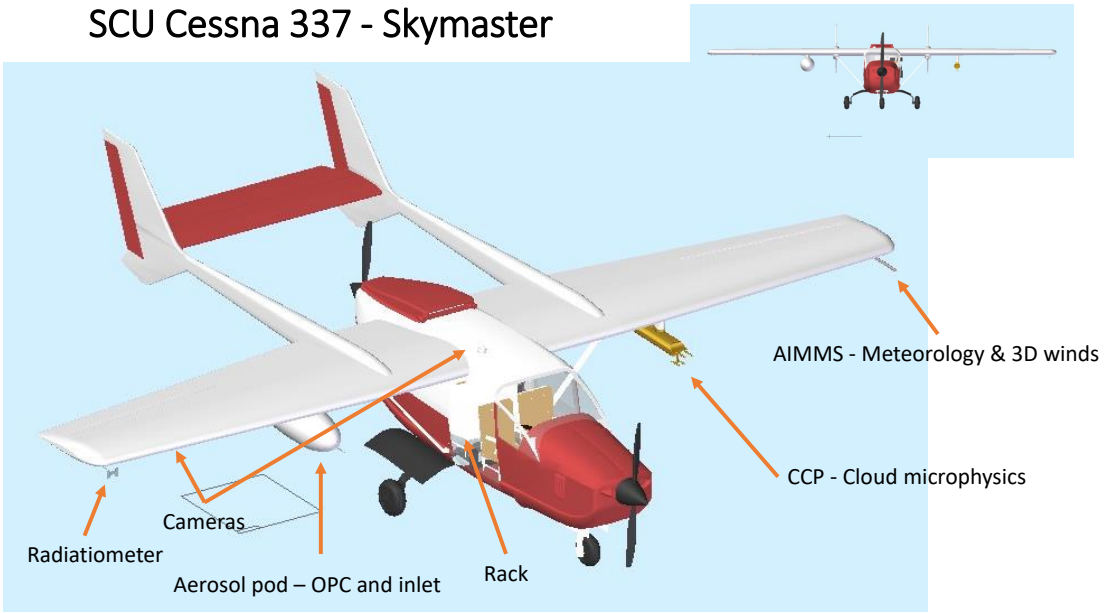

Figure 1: Aircraft sampling platform showing major external instrumentation

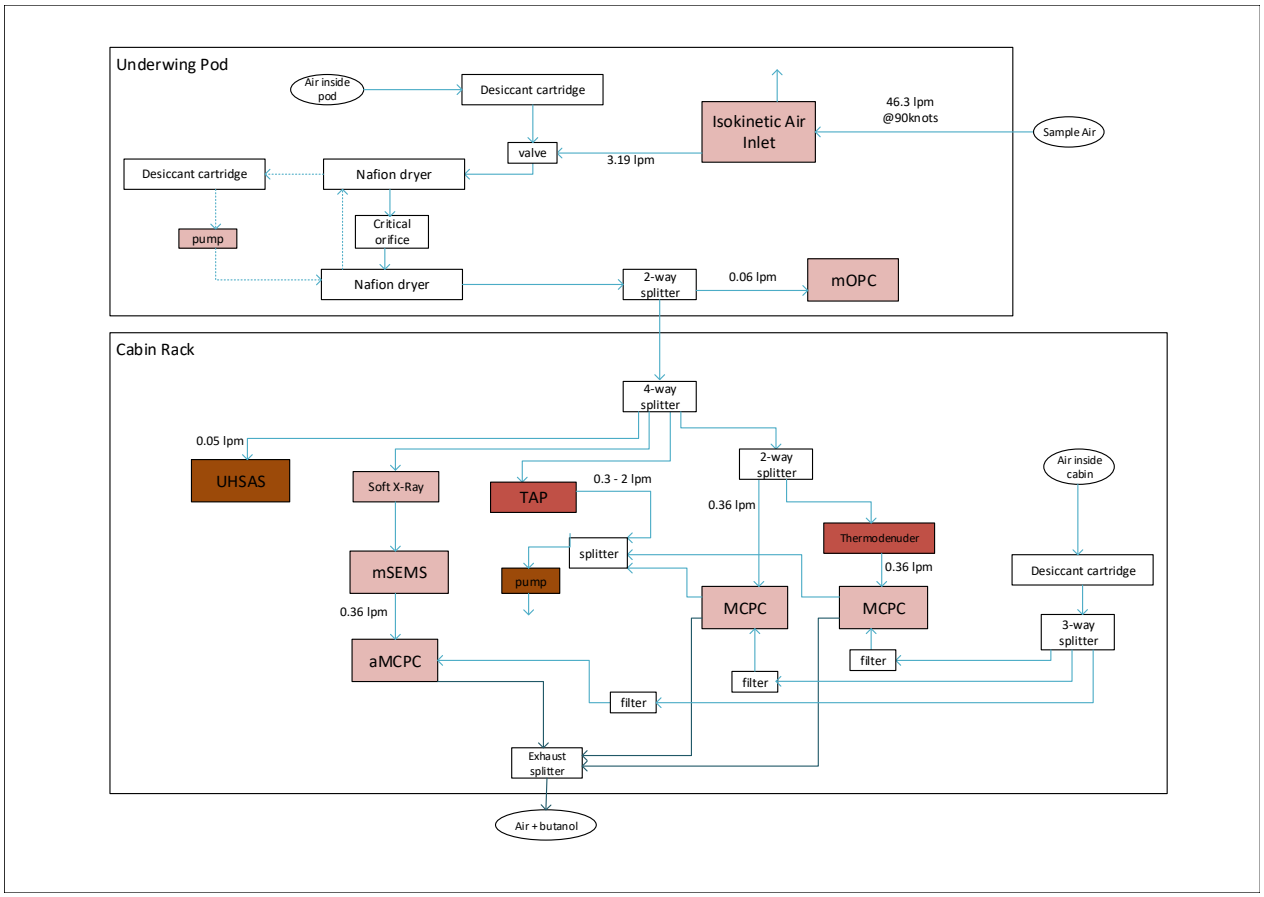

Figure 2: Flow diagram of the aerosol instrumentation accessing sample air from the isokinetic inlet in the underwing pod, and cabin

THE CHALLENGES OF PRODUCING 10^{16} PARTICLES/SEC, FOR MARINE CLOUD BRIGHTENING

L. HARRISON[1], D. HARRISON[2,4], R. ALLUM[3], I.S.F. JONES[4]

[1]School of Aerospace, Mechanical and Mechatronic Engineering, Faculty of Engineering, University of Sydney, Camperdown NSW, Australia.

[2]National Marine Science Centre, Southern Cross University, Coffs Harbour NSW, Australia.

[3]Ron Allum Deepsea Services pty ltd., Taren Point NSW, Australia.

[4]School of Geosciences, Faculty of Science, University of Sydney, Camperdown NSW, Australia.

Keywords: MARINE CLOUD BRIGHTENING, AEROSOLS, EFFERVESCENT NOZZLE, CLIMATE INTERVENTION.

INTRODUCTION

Marine Cloud Brightening (MCB) is a proposed climate intervention with the goal of maintaining current world temperatures in the face of climate change. More specifically MCB is a solar radiation management technique aimed at enhancing cloud albedo of low-level marine clouds (Latham et al. 2012). By increasing the available cloud condensation nuclei (CCN) available as the clouds form, the effective cloud droplet radius is decreased whilst the cloud droplet number increases (Hoffmann et al. 2021). The greater number of cloud droplets would reduce the solar radiation reaching the surface of the ocean, decreasing the heat forcing in the sea surface and reducing temperature (Stjern et al. 2018).

More recently Marine Cloud Brightening has been proposed as a method to reduce the impact of marine heatwave conditions on coral reefs such as the Great Barrier Reef (Latham et al. 2013). Coral reefs throughout the world have faced repeated mass bleaching events from marine heatwaves, exacerbated by climate change and rising sea temperatures (Hughes et al. 2017). The Australian Great Barrier Reef has recorded recurrent mass bleaching events in recent years.

The most technologically feasible method of increasing the available CCN within marine clouds over large regions is spraying sub micrometer sized seawater droplets at sea surface and relying on turbulent mixing for transport through the marine boundary layer (Salter et al. 2008). However, this method would require the production of an extremely large number of particles in order to increase the total amount of aerosols within the boundary layer by a sufficient quantity. There remains some discussion on how much of an increase over background particles would be required and thus what a single MCB 'station' should be capable of producing, with estimates ranging from 10^{15}-10^{16} (Latham et al. 2012) to 10^{17} (Cooper et al. 2013) particles per second.

Additionally, produced particles must be within a narrow size range which is both optimized for energy efficiency and for effectiveness to act as CCN. Connolly et al. (2014) carried out a study into the most effective sized particle for a range of spraying methods with regard to energy consumption and concluded that particles with diameters from 30-100nm were optimal. This is in approximate agreement with several other papers which range in ideal particles diameters from 35nm (Cooper et al. 2013) to 200nm (Salter et al. 2008) dry particle diameter. Similarly, Latham et al. (2012) suggests that salt particles with a mass greater than 5-7 x 10^{-20}kg (35-40nm dry sphere diameter) are large enough to be activated into CCN.

METHODS

NOZZLE TESTING

Nozzles were evaluated for their efficacy in terms of Marine Cloud Brightening within a small, 0.6m diameter, flow through wind tunnel with a range of aerosol sizing instrumentation. A Brechtel Scanning Electrical Mobility Sizer (SEMS) and a TSI Aerodynamic Particle Sizer (APS) were used in parallel to produce a complete size distribution of the aerosol plume from 10-5000nm dry aerosol diameter. And a Brechtel Mixing Condensation Particle Counter (MCPC) measured the total aerosol concentration. Two nafion dryers were used to ensure that the sample was fully dried prior to measurement. The size dependent inlet efficiency was calculated using the *particle loss calculator* and used to correct the size distribution measurement.

CONSTRUCTION OF THE SPRAYER

To enable field testing of our selected nozzle, a 100 and subsequently a 320 nozzle sprayer prototype was constructed. A modified dust suppression machine (V22 CLOUD, EmiControls, Italy) was purchased which acted as the base of the sprayer and was fitted with the effervescent nozzles. The V22 CLOUD included a large fan which was used to spread the particles forward and away from the vessel. This sprayer required one and subsequently 3 Denair DG3/200 air compressors to provide the compressed air required in our nozzles. Each Denair compressor produces $3m^3\ s^{-1}$ air compressed to a maximum of 20MPa and requires ~55 kW. The water, filtered seawater, is provided by a 20MPa Stainless Steel pump.

FIELDWORK METHODS

Field measurements of the prototype sprayer took place in a variety of locations and under variable conditions. The prototype was deployed on the Great Barrier Reef on three separate occasions, once per year from 2020 to 2022 inclusive, with some modifications/improvements conducted between each deployment. Sampling strategies utilized two vessels, one spraying vessel and another for downwind sampling to characterize the produced aerosols and the spread/evolution of the plume. Transects perpendicular to the wind direction were carried out at a range of distances downwind from the spraying vessel, to examine the spread of the plume. Additionally, the sampling vessel was positioned directly downwind of the spraying vessel, within the plume, in order to measure the size distribution of the produced aerosol plume.

CONCLUSIONS

A nozzle was developed capable of producing 4×10^{11} particles within 30-1000nm dry salt diameter, a size range that is thought to be useful for Marine Cloud Brightening. From this technology a prototype Marine Cloud Brightening station was designed and costructed using first 100 and then 320 nozzles. This protoype station was deployed on the Great Barrier Reef on three separate occasions over three years for field trials. In the most recent experiment the production rate was an estimated 1×10^{14} particles s^{-1} within the 30-1000nm range. However, in order to achieve this, the power requirement was aproximately 54kW. This represents a significant challenge moving forward with this technology considering a single station would theoretically be at least one order of magnitude bigger, 540kW, a non trivial amount of power.

ACKNOWLEDGEMENTS

SBIR acknowledgements?

The Reef Restoration and Adaptation Program is funded by the partnership between the Australian Governments Reef Trust and the Great Barrier Reef Foundation.

Traditional Owner acknowledgements?

REFERENCES

Connolly PJ, McFiggans GB, Wood R, Tsiamis A. 2014 Factors determining the most efficient spray distribution for marine cloud brightening. *Phil. Trans. R. Soc. A* 372:20140056.

Gary Cooper, David Johnston, Jack Foster, Lee Galbraith, Armand Neukermans, Robert Ormond, John Rush, Qin Wang. 2013 A Review of Some Experimental Spray Methods for Marine Cloud Brightening. *International Journal of Geosciences*, 2013, 4, 78-97

Hoffmann, F. and Feingold, G., 2021. Cloud microphysical implications for marine cloud brightening: The importance of the seeded particle size distribution. *Journal of the Atmospheric Sciences*, *78*(10), pp.3247-3262.

Hughes, T.P., Kerry, J.T., Álvarez-Noriega, M., Álvarez-Romero, J.G., Anderson, K.D., Baird, A.H., Babcock, R.C., Beger, M., Bellwood, D.R., Berkelmans, R. and Bridge, T.C., 2017. Global warming and recurrent mass bleaching of corals. *Nature*, *543*(7645), pp.373-377.

Latham, J., Bower, K., Choularton, T., Coe, H., Connolly, P., Cooper, G., Craft, T., Foster, J., Gadian, A., Galbraith, L. and Iacovides, H., 2012. Marine cloud brightening. *Philosophical Transactions of the Royal Society A: Mathematical, Physical and Engineering Sciences*, 370(1974), pp.4217-4262.

Latham, J., Kleypas, J., Hauser, R., Parkes, B. and Gadian, A., 2013. Can marine cloud brightening reduce coral bleaching?. *Atmospheric Science Letters*, *14*(4), pp.214-219.

Salter, S., Sortino, G. and Latham, J., 2008. Sea-going hardware for the cloud albedo method of reversing global warming. *Philosophical Transactions of the Royal Society A: Mathematical, Physical and Engineering Sciences*, 366(1882), pp.3989-4006.

Stjern, C.W., Muri, H., Ahlm, L., Boucher, O., Cole, J.N., Ji, D., Jones, A., Haywood, J., Kravitz, B., Lenton, A. and Moore, J.C., 2018. Response to marine cloud brightening in a multi-model ensemble. *Atmospheric Chemistry and Physics*, *18*, pp.621-634.

GLOBAL RELEVANCE OF IODINE OXOACID NUCLEATION

X.-C. HE[1], H.-B. XIE[2], D.R. WORSNOP[1,3], N.M. DONAHUE[4], R. VOLKAMER[5], J. KIRKBY[6], M. SIPILÄ[1], M. KULMALA[1], and the CLOUD CONSORTIUM[6]

[1]INAR/PHYSICS, UNIVERSITY OF HELSINKI, HELSINKI, FINLAND
[2]KEY LABORATORY OF INDUSTRIAL ECOLOGY AND ENVIRONMENTAL ENGINEERING, DALIAN UNIVERSITY OF TECHNOLOGY, DALIAN, CHINA
[3]AERODYNE RESEARCH, INC., MA, USA
[4]CENTER FOR ATMOSPHERIC PARTICLE STUDIES, CARNEGIE MELLON UNIVERSITY, PA, USA
[5]DEPARTMENT OF CHEMISTRY AND CIRES, UNIVERSITY OF COLORADO, CO, USA
[6]CERN, GENEVA, SWITZERLAND

Keywords: IODINE OXOACID, IODIC ACID, MARINE NUCLEATION.

INTRODUCTION

The formation of new particles has a substantial impact on the global cloud condensation nuclei (CCN) population. While the role of sulfuric acid (combined with base species) and oxidized organic molecules in NPF has been extensively studied, the mechanism behind iodine particle formation and its worldwide significance remains unresolved.

Traditionally, iodine particle formation was thought to start from the nucleation of iodine oxides and it was only considered important in coastal regions (Saiz-Lopez *et al*., 2012). However, a previous study by Sipilä *et al*. (2016) challenged this view and instead suggested that the critical step in forming new particles is the sequential addition of iodic acid (HIO_3). Additionally, recent field observations in the Arctic demonstrated the crucial role of iodine species in the formation of particles and CCN (Baccarini *et al.*, 2020; Beck *et al.*, 2021), thus indicating that iodine species may play larger roles in atmospheric aerosol nucleation than previously thought.

In this study, we present the latest findings on the iodine particle formation mechanisms through a combination of quantum chemical calculations and smog chamber experiments. We also provide and discuss field observations that demonstrate the global relevance of iodine oxoacid nucleation.

METHODS

Iodine particle formation experiments were carried out in the CLOUD (Cosmics Leaving Outdoor Droplets) chamber at CERN. The experiments were initiated by illuminating a mixture of molecular iodine, ozone and water vapour in the chamber. Photo-oxidation of the molecular iodine produces iodine oxoacids which in turn initiate aerosol nucleation (Finkenzeller *et al.*, 2022).

Additionally, these laboratory experiments are accompanied by quantum chemical calculations. The geometries of the nucleating iodine oxoacids clusters are optimised using configurational sampling. The thermodynamic parameters are further calculated from the global minimum structures which are further fed into the Atmospheric Cluster Dynamics Code to predict the aerosol nucleation rates.

RESULTS AND CONCLUSIONS

Interestingly, we find that the sequential addition of HIO_3 is only important in the ion-induced nucleation channel (He *et al.*, 2021b). In the neutral nucleation channel, ACDC simulation suggests that the nucleation

rates from iodic acid alone are many orders of magnitude lower than the CLOUD results (Zhang *et al.*, 2022).

Chemical ionisation mass spectrometry revealed another important species in neutral clusters – iodous acid (HIO_2). The critical role of iodous acid (HIO_2) was explored using a combination of chemical ionization mass spectrometry, high-level quantum chemical calculations, and the Atmospheric Cluster Dynamic Code (ACDC). The results show that neither pure HIO_3 nucleation nor pure HIO_2 nucleation alone could account for the rapid nucleation rates observed at the CLOUD chamber. However, the rates of synergistic HIO_3-HIO_2 nucleation reached a level of agreement with the CLOUD measurements. Therefore, HIO_3 plays a role in the formation of charged clusters and particle growth, while the nucleation of uncharged clusters also requires the presence of HIO_2 (He *et al*., 2021a,b).

The nucleation and growth rates of iodine particles are extremely fast, sometimes even outpacing those of sulfuric acid - ammonia (100 pptv) particle formation. Importantly, ambient observations show that HIO_3 is a widespread presence in the boundary layer atmosphere, from pristine environments to heavily polluted cities (Figure 1; He *et al*., 2021a). The daily maximum concentrations frequently reach a level that would initiate aerosol nucleation pointing to its potential for a global impact.

Despite its significance, iodine oxoacid nucleation has never been considered in global simulations to assess its impact on a global scale. This study provides a detailed mechanism and the necessary parameterization for neutral iodine oxoacid nucleation, which will facilitate the integration of iodine particle formation into global simulations.

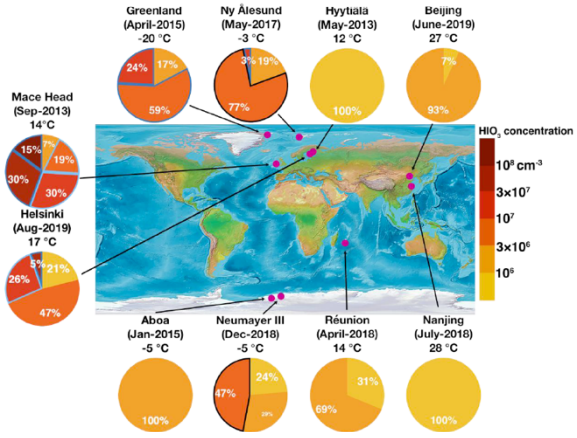

Figure 1. Frequency of daily maxima of iodic acid at diverse sites. Pie charts showing the percentage of days where the daily HIO_3 maxima fall into the indicated range (evaluated for one-hour-averaged data). Adopted from He *et al.* (2021a).

ACKNOWLEDGEMENTS

We thank the European Organization for Nuclear Research (CERN) for supporting CLOUD with important technical and financial resources and for providing a particle beam from the CERN Proton Synchrotron. This research has received support from the Academy of Finland (projects 316114, 307331, 310682, 266388, 3282290, 306853, 296628, 229574, 333397, 326948, and 1325656); the European Research Council (projects 692891, 616075, 764991, 316662, 742206, and 714621.

REFERENCES

A. Baccarini, L. Karlsson, …, P. Zieger, J. Schmale, Frequent new particle formation over the high Arctic pack ice by enhanced iodine emissions. *Nature Communications*. **11**, 4924 (2020).

L. J. Beck, N. Sarnela, …, V.-M. Kerminen, M. Sipilä, Differing mechanisms of new particle formation at two Arctic sites. *Geophysical Research Letters*. **48**, e2020GL091334 (2021)

X.-C. He, Y. J. Tham, …, D. R. Worsnop, M. Sipilä, Role of iodine oxoacids in atmospheric aerosol nucleation. *Science*. **371**, 589–595 (2021a).

X.-C. He, S. Iyer, ..., T. Kurtén, M. Kulmala, Determination of the collision rate coefficient between charged iodic acid clusters and iodic acid using the appearance time method. *Aerosol Science & Technology*. **55**(2), 231-242 (2021b).

A. Saiz-Lopez, J. M. C. Plane, …, G. McFiggans, R. W. Saunders, Atmospheric Chemistry of Iodine. *Chem. Rev.* **112**, 1773–1804 (2012).

M. Sipilä, N. Sarnela, …, M. Kulmala, C. O'Dowd, Molecular-scale evidence of aerosol particle formation via sequential addition of HIO_3. *Nature*. **537**, 532–534 (2016).

R. Zhang, H.-B. Xie, …, M. Kulmala, X.-C. He, Critical Role of Iodous Acid in Neutral Iodine Oxoacid Nucleation. *Environ. Sci. Technol.* **56**, 14166–14177 (2022).

AIRBORNE MEASUREMENTS OF MARINE CLOUD BRIGHTENING SEA-SALT CONCENTRATIONS

D.C. HERNANDEZ-JARAMILLO[1], W. JUNKERMANN[2], J. HACKER[2], A. MCGRAW[2], G. GUNNER[2], W. LEIFF[2], D. HARRISON[1]

[1]Southern Cross University, National Marine Science Centre, Coffs Harbour, NSW., Australia

[2]Airborne Research Australia, Parafield, SA, Australia

Keywords: MARINE CLOUD BRIGHTENING, PLUME DISPERSION, AIRBORNE MEASUREMENTS, CORAL BLEACHING, SEA-SALT AEROSOLS

ABSTRACT

Localised Marine Cloud Brightening (MCB) emissions could have important impact on the long-term survival of the Great Barrier Reef (GBR). The sea-salt particles emitted are expected to reach low level maritime clouds increasing albedo and creating a cooling effect on ocean surface. Here we used the motor glider Diamond HK36TTC ECO-Dimona to sample particle number concentration of sea-salt aerosols within the MCB plume at multiple distances downwind and heights to resolve its far-field (1 to 10 km downwind) and vertical dispersion. This work was undertaken as part of the Reef Restoration and Adaptation Program, funded by the partnership between the Australian Governments Reef Trust and the Great Barrier Reef Foundation.

INTRODUCTION

As the frequency and severity of extreme marine heatwaves continues to threat the long-term survival of the Great Barrier Reef (GBR) by triggering mass bleaching events (Heron et al., 2016; Terry P Hughes et al., 2018; Terry P. Hughes et al., 2018), interventions such as marine cloud brightening (MCB) become critical to mitigate the effects of climate change. MCB proposes to enhance cloud droplet number concentration by adding sub-micrometre sea water particles to marine stratocumulus clouds (Latham, 1990; Latham, 2002; Latham et al., 2012), this could, theoretically increase cloud albedo and create a cooling effect on the ocean surface. A localised implementation of cloud brightening targeting specific areas of the GBR (Harrison et al., 2020), could alleviate heat stressors on coral reefs and help maintain coral cover over the next two decades (Condie et al., 2021).

This study outlines the approach used to resolve the vertical mixing and far-field dispersion (1 – 10 km) of the MCB plume using in situ measurements of particle number concentrations. A crewed aircraft was used to characterise the dispersion of the sea-salt particles emitted from a spraying source during the at-sea MCB trial over the Great Barrier Reef in February 2022. The characterisation is focused on the vertical dispersion of the plume in order to determine the height reached by the particles with the current MCB spraying technology.

METHODS

The MCB sprayer was tested during the Australian Reef Restoration and Adaptation Program (RRAP) Cooling and Shading campaign to Big Broadhurst Reef (18°53'59"S, 147°45'19"E, Great Barrier Reef, Australia) in February 2022 with regulatory approval from the Great Barrier Reef Marine Park Authority. The sea sprayer was operated from a main vessel emitting seawater droplets over the reef, which evaporated and produced a dispersed plume of sea-salt aerosols (SSA) particles. The motor glider Diamond Aircraft HK36TTC ECO-Dimona, owned and operated by ARA (Airborne Research Australia) flew across the plume collecting data of the particle number concentration of SSA. These measurements give relevant information about the vertical mixing and dispersion of the particles. The Dimona aircraft has been chosen due to its ability of flying safely at low altitudes and low speeds and also because its low environmental footprint compared with other airborne platforms (Hacker et al., 2106).

The flight strategy consisted on following horizontal transects, perpendicular to the plume, at several altitudes above sea level and at different distances from the stationary sprayer. A second scenario consisted on moving the spraying boat with the wind so that there is zero relative velocity. This allowed the plume to develop on top of the boat and enhanced its effect. During this manoeuvre, the aircraft performed transects on top of the boat in different directions and at different heights up to cloud base (2000 – 3000 ft AMSL), creating what we called star pattern. Data collected on this field test, was processed to characterise the dispersion, mixing and advection of the plume and to determine the height reached by SSA particles at far-field distances from the sprayer source. The sprayer was operated in different modes, mode 1, 2 and 3, which are related to the number of compressors running.

RESULTS

Scenario 1: spraying from an anchored boat. During this day (08/02/2022), typical background concentrations from sea surface up to cloud base (0.780 km) were approximately 550 cm^{-3}. Despite obtaining an incomplete set of transects with the boat anchored and the sprayer operating on mode 1, the highest concentration detected at 2 km downwind was 1460 cm^{-3} at an altitude of 0.300 km AMSL. The upper limit of the plume at the same distance was detected at an altitude of 0.540 km AMSL with peak concentrations of 630 cm^{-3}. From a transect at cloud base (0.780 km) at 10 km downwind, measured peak concentration was 670 cm^{-3}, while the highest concentration detected at 5 km downwind and 0.700 km altitude AMSL was 655 cm^{-3}.

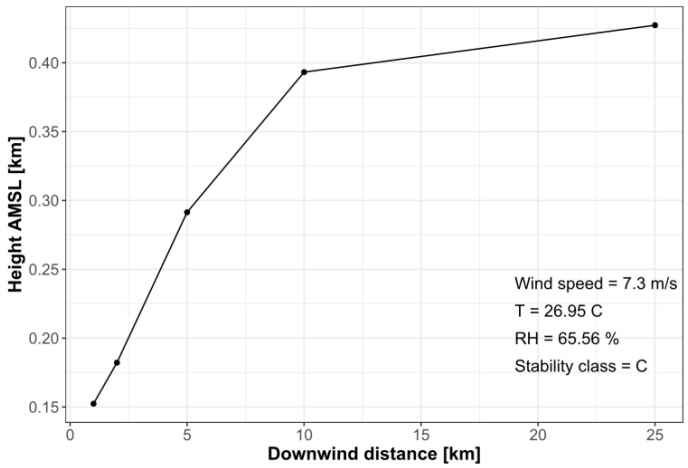

Figure 1. Rise of the centre of the plume calculated from the planar transect centroids from data collected with the sprayer operating on mode 3 while the boat was anchored.

Figure 1. shows the rising of the centre of the plume up to 0.400 km of altitude at 10km downwind and up to 0.450 km altitude at 25 km downwind for measurements of the sprayer operating on mode 3. The upper limit of the plume was detected at cloud base at 10 km downwind with aerosol concentrations of approximately 650 cm 3 (Fig. 4b). Peak concentration decreased with distance downwind and altitude. The highest concentrations were detected between 2 and 5 km downwind with peak concentrations of 1800 cm 3 between 0.140 and 0.190 km AMSL.

Scenario 2: spraying from a moving boat. During these days (09/02/2022 – mode 2 and 12/02/2022 – mode 3), typical background concentrations from sea surface up to cloud base were approximately 650 cm^{-3}. The highest concentrations were detected during the lowest transects completed on top of the boat (0.150 km AMSL) with peak concentrations of approximately 13,800 cm^{-3} with the sprayer operating on mode 3. Observations show how peak concentration decreased with altitude reaching up to 970 – 1200 cm^{-3} at approximately 1km AMSL.

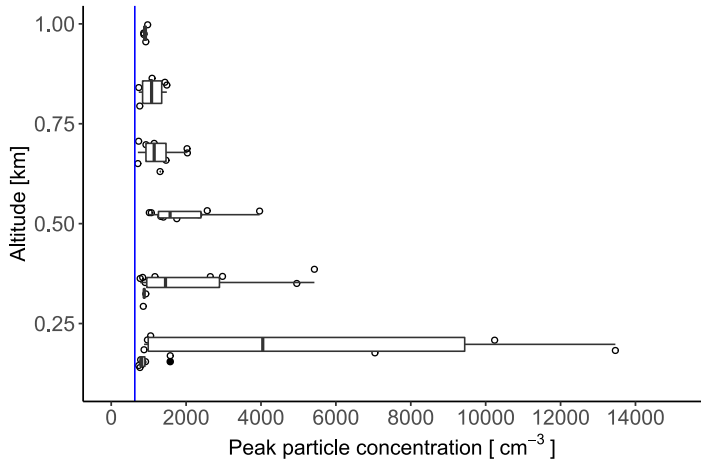

Figure 2. Summary of peak concentration at different altitudes above mean sea level (AMSL) with the sprayer operating on mode 3 and the aircraft performing star pattern transects.

FUNDING ACKNOWLEDGEMENT

The Reef Restoration and Adaptation Program is funded by the partnership between the Australian Governments Reef Trust and the Great Barrier Reef Foundation.

TRADITIONAL OWNER ACKNOWLEDGEMENT

The authors would like to acknowledge the Traditional Owners of the Great Barrier Reef for permission to conduct seawater fogging experiments on their land and sea Country.

REFERENCES

Condie, S. A., Anthony, K. R. N., Babcock, R. C., Baird1, M. E., Beeden, R., Fletcher, C. S., Gorton, R., Harrison, D., Hobday, A. J., Plagányi, É. E., & Westcott, D. A. (2021). Large-scale interventions may delay decline of the Great Barrier Reef. *Royal Society Open Science, 8*(201296). https://doi.org/10.1098/rsos.201296

Harrison, D. P., Harrison, L. P., Cravigan, L., & Kelaher, B. (2020). *Final Report - Marine cloud brightening proof of concept study* (Boosting Coral abundance on the Great Barrier Reef Challenge, Issue.

Heron, S. F., Maynard, J. A., Hooidonk, R. v., & Eakin, C. M. (2016). Warming Trends and Bleaching Stress of the World's Coral Reefs *Scientific Reports, 6*(38402). https://doi.org/10.1038/srep38402

Hughes, T. P., Anderson, K. D., Connolly, S. R., Heron, S. F., Kerry, J. T., Lough, J. M., Baird, A. H., Baum, J. K., Berumen, M. L., Bridge, T. C., Claar, D. C., Eakin, C. M., Gilmour, J. P., Graham, N. A. J., Harrison, H., Hobbs, J.-P. A., Hoey, A. S., Hoogenboom, M., Lowe, R. J., McCulloch, M. T., Pandolfi, J. M., Pratchett, M., Schoepf, V., Torda, G., & Wilson, S. K. (2018). Spatial and temporal patterns of mass bleaching of corals in the Anthropocene. *Science, 5*(6371), 80-83. https://doi.org/10.1126/science.aan8048

Hughes, T. P., Kerry, J. T., Baird, A. H., Connolly, S. R., Dietzel, A., Eakin, C. M., Heron, S. F., Hoey, A. S., Hoogenboom, M. O., Liu, G., McWilliam, M. J., Pears, R. J., Pratchett, M. S., Skirving, W. J., Stella, J. S., & Torda, G. (2018). Global warming transforms coral reef assemblages. *Nature 556*, 492 - 495. https://doi.org/10.1038/s41586-018-0041-2

Latham, J. (1990). Control of global warming? *Nature, 347*, 339-340.

Latham, J. (2002). Amelioration of global warming by controlled enhancement of the albedo and longevity of low-level maritime clouds. *Atmospheric Science Letters* https://doi.org/10.1006/asle.2002.0048

Latham, J., Bower, K., Choularton, T., Coe, H., Connolly, P., Cooper, G., Craft, T., Foster, J., Gadian, A., Galbraith, L., Iacovides, H., Johnston, D., Launder, B., Leslie, B., Meyer, J., Neukermans, A., Ormond, B., Parkes, B., Rasch, P., Rush, J., Salter, S., Stevenson, T., Wang, H., Wang, Q., & Wood, R. (2012). Marine cloud brightening. *Philosophical transactions of the royal society, 370*, 4217–4262. https://doi.org/10.1098/rsta.2012.0086

IMPACT OF TRAFFIC EMISSIONS ON LUNG-DEPOSITED SURFACE AREA IN URBAN

P. K. CHANG[1] and T. C. HSIAO[1]

[1]Graduate Institute of Environmental Engineering, National Taiwan University, Taipei, Taiwan.

Keywords: Ultrafine particle, Lung deposited surface area, Traffic, Urban

INTRODUCTION

In urban environments, airborne particulate matter (PM) is primarily anthropogenic and majorly derived from local traffic emissions. Studies have shown that exposure to traffic-related PM is associated with various cardiovascular diseases, partly due to these emissions' size distribution and composition. In addition, because of the poor ventilation caused by high building density and complex structures, traffic-related PM is easily accumulated in urban areas, affecting urban air quality and public health. $PM_{2.5}$, especially ultrafine particles (UFPs), have the potential to go across different biological barriers and translocate into different human organs (Wang et al., 2022). However, the mass-based concentrations are not sufficiently sensitive for UFPs, which may not be a good indicator for the health risks of UFPs.

Lung deposited surface area (LDSA), the total surface area of particles deposited in the lung, has been proposed as the critical predictor for health effects from aerosol exposure in recent years (Hammer et al., 2020; Kuula et al., 2020; Kuuluvainen et al., 2016). Furthermore, toxicological studies have shown that the correlation between LDSA and health effects is especially significant for UFPs (Brown et al., 2001). Although the studies had investigated LDSA levels in different cities (Cheristanidis et al., 2020), most of these studies measured "total" LDSA concentrations, which is the sum of the various sources' contributions. However, it is necessary to accurately quantify LDSA from the pollution source when assessing the specific source's exposure risk. Therefore, the objectives of this study are: (1) to investigate the LDSA and PM characteristics in the urban microenvironment and (2) to quantify the LDSA concentration from source apportionment analysis.

METHODS

The study and data analysis was conducted in the following manners. Firstly, the particle number size distribution (PNSD), PM_1 and black carbon in a roadside environment were investigated (Figure 1). Secondly, PNSD had been used to identify different pollution sources by

assuming each source had a characteristic PNSD profile. The hourly PNSD datasets, each with 112 different size channels covering the size range of 18 to 1,000 nm, were applied in the positive matrix factorization (PMF) analysis. After conducting the source apportionment, the LDSA was estimated according to the apportioned PSD and the lung deposition curve for the alveolar region proposed by International Commission on Radiological Protection.

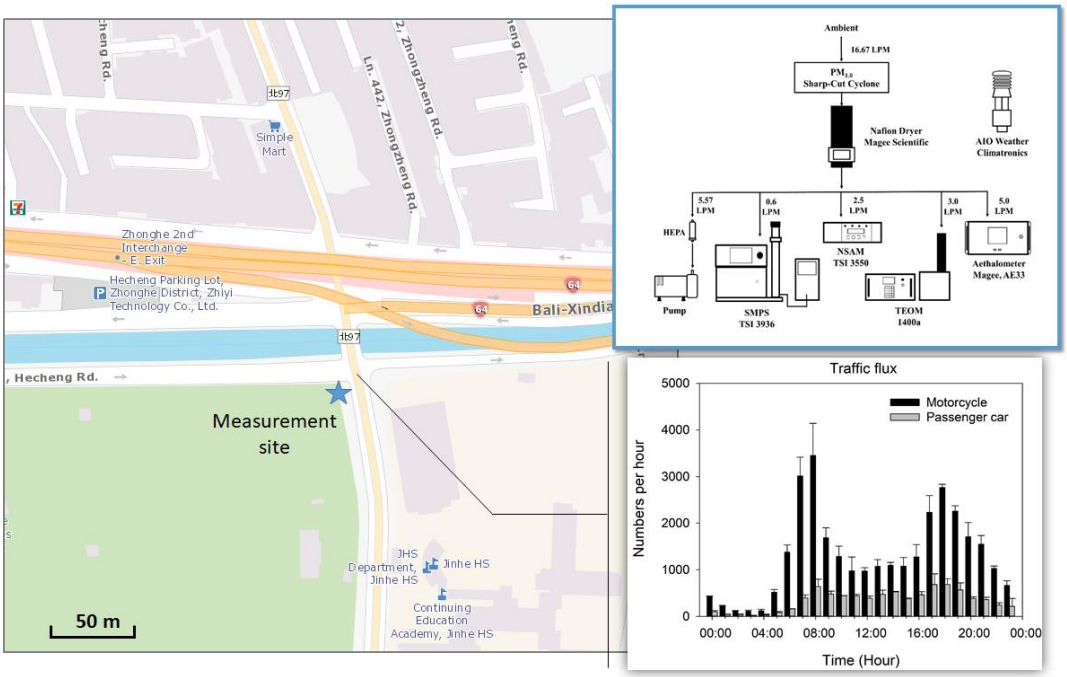

Figure 1. Measurement site and system

Furthermore, we analyzed the wind field and particle transmission in the microenvironment using computational fluid dynamics (CFD) to assess the impact of traffic-related pollution on the surrounding area. Finally, the traffic-related LDSA in the urban microenvironment can be obtained by combining the CFD and measuring results.

RESULTS AND DISCUSSION

A measurement station was established at an intersection in New Taipei City for six months of investigation. More than 80% of the wind speed was lower than 2.0 m/s, and the prevailing wind direction was easterly and southwesterly. Figure 2 shows the PSD and number-concentration variations during the entire day. The number-concentrations of small particles increased in the daytime, especially during traffic rush hours. The mode of PNSD during rush hours was about 30 nm. In contrast, the mode of PNSD was 60 nm in the early morning due to the low anthropogenic emission.

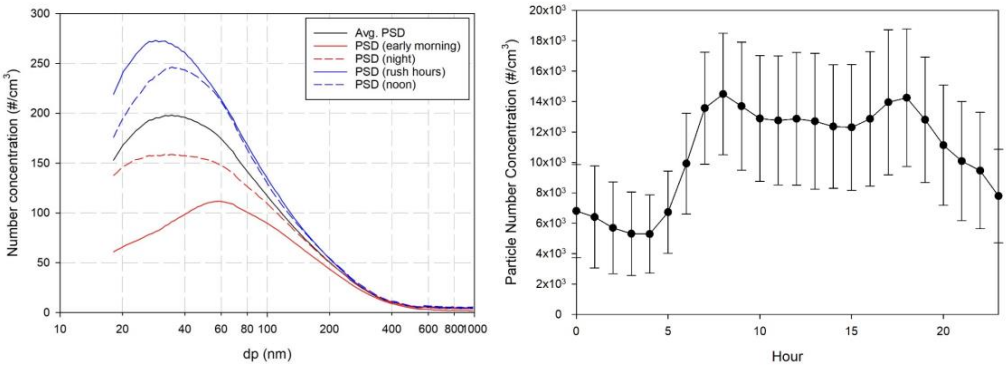

Figure 2. The PNSD and number concentration variations during entire day.

Table 1 summarizes the characteristics of each factor. Factor 1 was attributed to the fresh traffic source, which was likely located just east of the measurement station at the four-way intersection, according to the wind-based conditional probability function results. Factor 2 might be affected by the aged traffic source in the southwest of the measurement station, national highways and a sports park. Thus traffic-related air pollutants could be transported, potentially even mixed with additional VOC emissions from biogenic sources, delivering a partially aged air mass to the study site. Factor 3 and 4 were considered non-traffic sources because of the low correlation with traffic flux.

Table 1. The summary of factor's characteristics.

Factor	Mode of PNSD (nm)	R^2 with traffic flux	Wind direction	Source classification
1	20	0.78	70°~90°	Fresh traffic
2	40	0.77	210°~260°	Aged traffic
3	175	0.06	170°~210°	Non-traffic
4	74 & 359	0.22	190°~210°	Non-traffic

Based on the PNSD source apportionment results, the average total LDSA was 38.9 $\mu m^2/cm^3$, including 36% of fresh traffic emission, 33% of aged traffic emission, and 31% of non-traffic sources (Figure 3). The diurnal patterns of LDSA correlated well with traffic flux, which implied that the LDSA variations were strongly affected by traffic emission. Moreover, although the measurement site is located at the roadside, the LDSA contributed from non-traffic sources should not be ignored

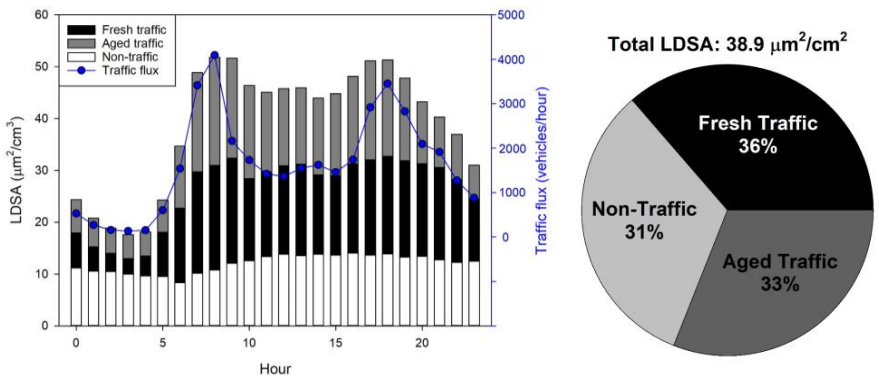

Figure 3. The diurnal patterns of LDSA concentrations and the percentage of LDSA from different sources.

REFERENCES

Wang, W., Lin, Y., Yang, H., Ling, W., Liu, L., Zhang, W., Lu, D., Liu, Q., Jiang, G., (2022) Internal Exposure and Distribution of Airborne Fine Particles in the Human Body: Methodology, Current Understandings, and Research Needs. *Environmental Science & Technology* 56.11: 6857-6869.

Hammer, T., Gao, H., Pan, Z., Wang, J., (2020) Relationship between Aerosols Exposure and Lung Deposition Dose. *Aerosol and Air Quality Research* 20, 1083-1093.

Kuula, J., Kuuluvainen, H., Niemi, J. V., Saukko, E., Portin, H., Kousa, A., Aurela, M., Rönkkö, T., Timonen, H., 2020. Long-term sensor measurements of lung deposited surface area of particulate matter emitted from local vehicular and residential wood combustion sources. *Aerosol Science and Technology* 54, 190-202.

Kuuluvainen, H., Rönkkö, T., Järvinen, A., Saari, S., Karjalainen, P., Lähde, T., Pirjola, L., Niemi, J. V., Hillamo, R., Keskinen, J., 2016. Lung deposited surface area size distributions of particulate matter in different urban areas. *Atmospheric Environment* 136, 105-113.

Brown, D. M., Wilson, M. R., MacNee, W., Stone, V., Donaldson, K., (2001) Size-Dependent Proinflammatory Effects of Ultrafine Polystyrene Particles: A Role for Surface Area and Oxidative Stress in the Enhanced Activity of Ultrafines. *Toxicology and applied pharmacology* 175, 191-199.

Cheristanidis, S., Grivas, G., Chaloulakou, A., (2020) Determination of total and lung deposited particle surface area concentrations, in central Athens, Greece. *Environmental Monitoring and Assessment* 192, 627.

POTENTIAL PRE-INDUSTRIAL NEW PARTICLE FORMATION HIDDEN IN THE AIR POCKET OF FINNISH PEATLAND

W. HUANG[1], H. JUNNINEN[2], O. GARMASH[3], K. LEHTIPALO[1,4], D. STOLZENBURG[1], J. L. P. LAMPILAHTI[1], E. EZHOVA[1], S. SCHALLHART[4], P. RANTALA[1], D. ALIAGA[1], L. AHONEN[1], J. SULO[1], L. L. J. QUELEVER[1], R. CAI[1], P. ALEKSEYCHIK[1,5], S. B. MAZON[1], L. YAO[6], S. M. BLICHNER[7], Q, ZHA[1], I. MAMMARELLA[1], J. KIRKBY[8,9], V.-M. KERMINEN[1], D. R. WORSNOP[1,10], M. KULMALA[1], and F. BIANCHI[1]

[1]*Institute for Atmospheric and Earth System Research / Physics, Faculty of Science, University of Helsinki, 00014, Helsinki, Finland*

[2]*Institute of Physics, University of Tartu, 50411, Tartu, Estonia*

[3]*Aerosol Physics Laboratory, Physics Unit, Tampere University, 33720, Tampere, Finland*

[4]*Atmospheric Composition Unit, Finnish Meteorological Institute, 00101, Helsinki, Finland*

[5]*Bioeconomy and Environment, Natural Resources Institute Finland, 00790, Helsinki, Finland*

[6]*Shanghai Key Laboratory of Atmospheric Particle Pollution and Prevention (LAP3), Department of Environmental Science & Engineering, Fudan University, 200438, Shanghai, China*

[7]*Department of Environmental Science, Stockholm University, 11418, Stockholm, Sweden*

[8]*Institute for Atmospheric and Environmental Sciences, Goethe University Frankfurt, 60438, Frankfurt am Main, Germany*

[9]*CERN, the European Organization for Nuclear Research, CH-1211 Geneve 23, Switzerland*

[10]*Aerodyne Research Inc., Billerica, Massachusetts 01821, USA*

Keywords: pre-industrial atmosphere, new particle formation, biogenics

INTRODUCTION

Aerosol particles cool the atmosphere by scattering incoming radiation and acting as cloud condensation nuclei (IPCC, 2013), over half of which are estimated to be formed from nucleation of chemically oxidized precursors (Merikanto et al., 2009). Ion induced nucleation of pure biogenic particles at very low sulphuric acid concentrations (Kirkby et al., 2016) could be an important mechanism for pre-industrial aerosol formation. However, no pure biogenic new particle formation (NPF) has been unambiguously confirmed in the ambient till now, due to the scarcity of truly pristine continental locations in the present-day atmosphere (Andreae, 2007) or the lack of chemical characterization of NPF precursors.

METHODS

We performed trace gas and particle measurements between March 10 and June 20, 2016 in a pristine peatland, Siikaneva, southern Finland (61° 49’ 59.4”N, 24°92 11’ 32.4”E). The site is located at a class II ecosystem Integrated Carbon Observation System (ICOS) station which is about 5 km west from the Station for Measuring Ecosystem – Atmosphere Relations (SMEAR) II station, Hyytiälä and about 60 km north east from the nearest big city, Tampere, with more than 200000 inhabitants. An atmospheric pressure interface time-of-flight mass spectrometer (APi-ToF, Aerodyne Research Inc.) was used to analyze the molecular composition of ambient positively charged clusters and negatively charged clusters. An APi-ToF equipped with NO3- chemical ionization inlet (CI-APi-ToF, Aerodyne Research Inc.) was deployed

to measure the molecular composition of neutral vapours including sulphuric acid and highly oxygenated organic molecules (HOM).

CONCLUSIONS

During the measurement period, nighttime NPF events were frequently observed, starting after sunset and lasting for a few hours. The strong inversions on these nights hinder turbulent mixing, causing the lowest surface layer above the peatland (up to few meters high) to be decoupled from the rest of the nocturnal boundary layer (Junninen et al., 2022). During this process, initial vapours (e.g., O_3) or anthropogenic pollutants (e.g., NO_x) were largely depleted by dry deposition to the wet peatland surface inside the shallow decoupled layer (i.e., "air pocket") (Lelieveld and Dentener, 2000;Huff et al., 2011;Zhou et al., 2017). In contrast, peatland emissions such as terpenes were trapped and concentrated within the layer (Junninen et al., 2022).

The formed particles were found to grow further, at least to several tens of nanometers, during some of the events (e.g., Figure 1), while during some other event nights, particles did not grow above ~10 nm after the clustering process. The latter events were also observed in the nearby forest in Hyytiälä, which were found to be connected to HOM produced by monoterpene ozonolysis. On nights when no cluster formation was observed at all, the surface layer was in a coupled condition.

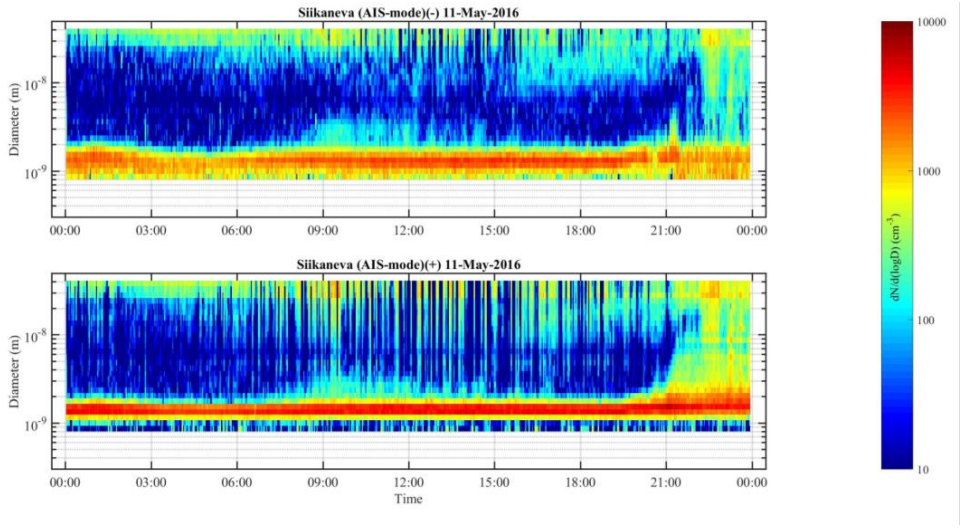

Figure 1. Nighttime clustering and growth events observed in Siikaneva.

By comparing the concentrations of NPF precursors and molecular composition of charged and neutral clusters from the three types of situations (i.e., clustering with growth events, clustering without growth events, and nonevents), we found the sulphuric acid-related nucleation process seems not to play a role alone or synergistically with other precursors in the Siikaneva nighttime events. Instead, HOM dimers from monoterpene ozonolysis (i.e., CHO HOM dimers) as opposed to the total HOM are important in the early growth of small clusters, consistent with laboratory observations (Lehtipalo et al., 2018).

In addition, formation rates (J) were found to be comparable to the J of pure biogenic nucleation experiments from the CLOUD at similar HOM concentrations (Kirkby et al., 2016), and therefore it is plausible that pure biogenic HOM initiated the observed nucleation in Siikaneva. Comparison of measured growth rate and calculated growth rate suggests that HOM of biogenic origin are the dominant contributor to the particle growth at this measurement site.

For the first time we provide direct evidence of pure biogenic HOM induced NPF, i.e., nucleation followed by growth to larger sizes (e.g., Aitken mode), during the nighttime in the Siikaneva peatland. Meteorological decoupling processes formed an "air pocket" (i.e., a very shallow surface layer) at night and favoured NPF initiated entirely by highly oxygenated organic molecules (HOM) formed from biogenic emissions of this peatland. This biogenically induced NPF observed in Siikaneva mimics the pre-industrial atmosphere, where no anthropogenic influence is apparent. Our study sheds light on pre-industrial aerosol formation, which represents the baseline for estimating the impact of present and future aerosol on climate, as well as on future NPF, the features of which may revert towards pre-industrial conditions as a result of air pollution mitigation.

ACKNOWLEDGEMENTS

This work was supported by the staff at INAR. We thank the tofTools team for providing tools for mass spectrometry data analysis. We thank the financial support by the H2020 European Research Council (CHAPAs (grant no. 850614), COALA (grant no. 638703), and ATM-GTP (grant no. 742206)), the Academy of Finland (grant no. 323255), European Union's Horizon 2020 research and innovation programme (FORCeS (grant no. 821205)), European Research Council (Consolidator grant INTEGRATE (grant no. 865799)), Knut and Alice Wallenberg foundation (Wallenberg Academy Fellowship projects AtmoRemove No. 2015.0162), Academy of Finland Flagship Program for financial support of "Atmosphere and Climate Competence Center (ACCC)" (grant no.: 337549 (University of Helsinki), 337552 (Finnish Meteorological Institute), and 337551 (Tampere University)), Academy of Finland Flagship Program for financial support of 'Forest-Human-Machine Interplay - Building Resilience, Redefining Value Networks and Enabling Meaningful Experiences (UNITE)' flagship (decision no. 337655), postdoctoral project DRONESTRESS funded by the Finnish Academy (decision no. 351129), and the European Union's Horizon 2020 research and innovation program under the Marie Sklodowska-Curie grant agreement no. 895875 ("NPF-PANDA").

REFERENCES

Andreae, M. O.: Aerosols before pollution, Science, 315, 50–51, 2007.

Huff, D. M., et al: Deposition of dinitrogen pentoxide, N2O5, to the snowpack at high latitudes, Atmos Chem Phys, 11, 4929–4938, 2011.

IPCC: Climate change 2013: the physical scientific basis, in, Cambridge University Press, Cambridge, England, 622−623, 2013.

Junninen, H., et al: Terpene emissions from boreal wetlands can initiate stronger atmospheric new particle formation than boreal forests, Commun Earth Environ, 3, 93, 2022.

Kirkby, J., et al: Ion-induced nucleation of pure biogenic particles, Nature, 533, 521–526, 2016.

Lehtipalo, K., Yan, C., Dada, L., Bianchi, F., Xiao, M., Wagner, R., Stolzenburg, D., Ahonen, L. R., Amorim, A., et al: Multicomponent new particle formation from sulfuric acid, ammonia, and biogenic vapors, Science Advances, 4, eaau5363, 2018.

Lelieveld, J., and Dentener, F. J.: What controls tropospheric ozone?, J Geophys Res-Atmos, 105, 3531–3551, 2000.

Merikanto, J., et al: Impact of nucleation on global CCN, Atmos Chem Phys, 9, 8601–8616, 2009.

Zhou, P. T., et al: Simulating ozone dry deposition at a boreal forest with a multi-layer canopy deposition model, Atmos Chem Phys, 17, 1361–1379, 2017.

UNDERSTANDING THE SEASONAL CYCLE OF SOUTHERN OCEAN AEROSOLS

R.S. HUMPHRIES[1,2], M.D. KEYWOOD[1,2], J.P. WARD[1], J. HARNWELL[1], S.P. ALEXANDER[3,2], A.R. KLEKOCIUK[3,2], K. HARA[4], I.M. MCROBERT[5], A. PROTAT[6,2], J. ALROE[7], L.T. CRAVIGAN[7], B. MILJEVIC[7], Z.D. RISTOVSKI[7], R. SCHOFIELD[8], S.R. WILSON[9], C.J. FLYNN[10], G.R. KULKARNI[11], G.G. MACE[12], G.M. MCFARQUHAR[13], S.D. CHAMBERS[14], A.G. WILLIAMS[14], and A.D. GRIFFITHS[14]

1. *Climate Science Centre, CSIRO Oceans and Atmosphere, Melbourne, Australia*
2. *Australian Antarctic Program Partnership, Institute for Marine and Antarctic Studies, University of Tasmania, Hobart, Tasmania, Australia*
3. *Australian Antarctic Division, Channel Highway, Kingston, Tasmania, Australia*
4. *Department of Earth Science System, Faculty of Science, Fukuoka University, Jyonan, Fukuoka, Japan*
5. *Engineering and Technology Program, CSIRO National Collections and Marine Infrastructure, Hobart, Australia*
6. *Australian Bureau of Meteorology, Melbourne, Australia*
7. *School of Earth and Atmospheric Sciences, Queensland University of Technology, Brisbane, Australia*
8. *School of Geography, Earth and Atmospheric Sciences, University of Melbourne, Parkville, Victoria, Australia*
9. *Centre for Atmospheric Chemistry, School of Earth, Atmospheric and Life Sciences, University of Wollongong, Wollongong, New South Wales, Australia*
10. *School of Meteorology, University of Oklahoma, Norman, United States of America*
11. *Atmospheric Sciences and Global Change Division, Pacific Northwest National Laboratory, Richland, United States of America*
12. *Department of Atmospheric Science, University of Utah, Salt Lake City, United States of America*
13. *Cooperative Institute for Mesoscale Meteorological Studies, University of Oklahoma, Norman, United States of America*
14. *Environmental Research, ANSTO, Lucas Heights, New South Wales, Australia*

Keywords: Aerosols, Cloud Condensation Nuclei, Condensation Nuclei, Southern Ocean, Antarctica

ABSTRACT

The remoteness and extreme conditions of the Southern Ocean and Antarctic region have meant that observations in this region are rare, and typically restricted to summertime during research or resupply voyages. Observations of aerosols outside of the summer season are typically limited to long-term stations, such as Kennaook/Cape Grim (KCG, 40.7°S, 144.7°E) which is situated in the northern latitudes of the Southern Ocean, and Antarctic research stations, such as the Japanese operated 5 Syowa (SYO, 69.0°S, 39.6°E). Measurements in the mid-latitudes of the Southern Ocean are important, particularly in light of recent observations that highlighted the latitudinal gradient that exists across the region in summertime. Here we present two years (March 2016 - March 2018) of observations from Macquarie Island (MQI, 54.5°S, 159.0°E) of aerosol (condensation nuclei larger than 10 nm, CN10) and cloud condensation nuclei (CCN at various supersaturations) concentrations. This important multi-year data set is characterised, and its features are compared with the long-term data sets from KCG and SYO 10 together with those from recent, regionally relevant voyages. CN10 concentrations were the highest at KCG by a factor of ~50% across all non-winter seasons compared to the other two stations which were similar (summer medians of 530 cm^{-3},426 cm^{-3} and 468 cm^{-3} at KCG, MQI and SYO, respectively). In wintertime, seasonal minima at KCG and MQI were similar (142 cm^{-3} and 152 cm^{-3}, respectively), with SYO being distinctly lower (87 cm^{-3}), likely the result of the reduction in sea spray aerosol generation due to the sea-ice ocean cover around the site. CN10 seasonal maxima were observed at the stations at different times 15 of year, with KCG and MQI exhibiting January maxima and SYO having a distinct February high. Comparison of CCN0:5 data between KCG and MQI showed similar overall trends with

summertime maxima and wintertime minima, however KCG exhibited slightly (~10%) higher concentrations in summer (medians of 158 cm^{-3} and 145 cm^{-3}, respectively), whereas KCG showed ~40% lower concentrations than MQI in winter (medians of 57 cm^{-3} and 92 cm^{-3}, respectively). Spatial and temporal trends in the data were analysed further by contrasting data to coincident observations that occurred aboard several voyages of the RSV Aurora Australis and the RV Investigator. Results from this study are important for validating and improving our models, highlight the heterogeneity of this pristine region, and the need for further long-term observations that capture the seasonal cycles.

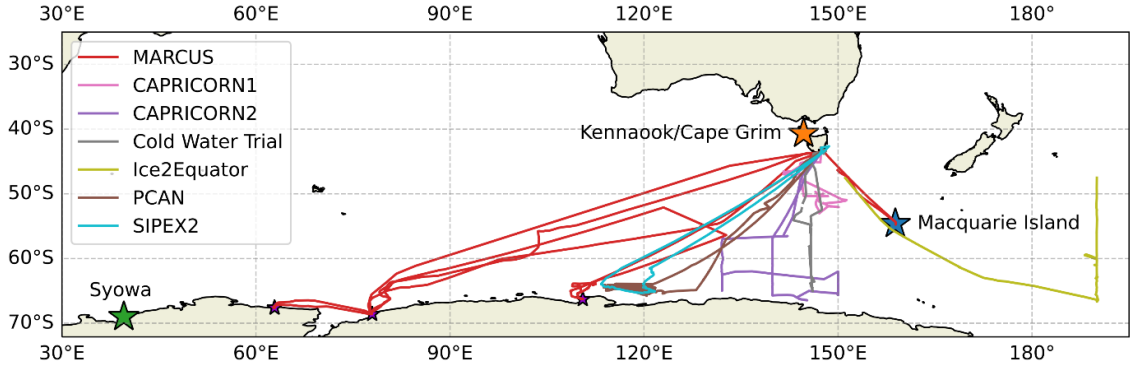

Figure 1: Map showing the relative locations of the three long term stations utilised in this study: Kennaook/Cape Grim (40.7ºS, 144.7ºE), Macquarie Island (54.5ºS, 159.0ºE) and Syowa (69.0ºS, 39.6ºE). Voyage tracks of those voyages utilised in this study are also shown.

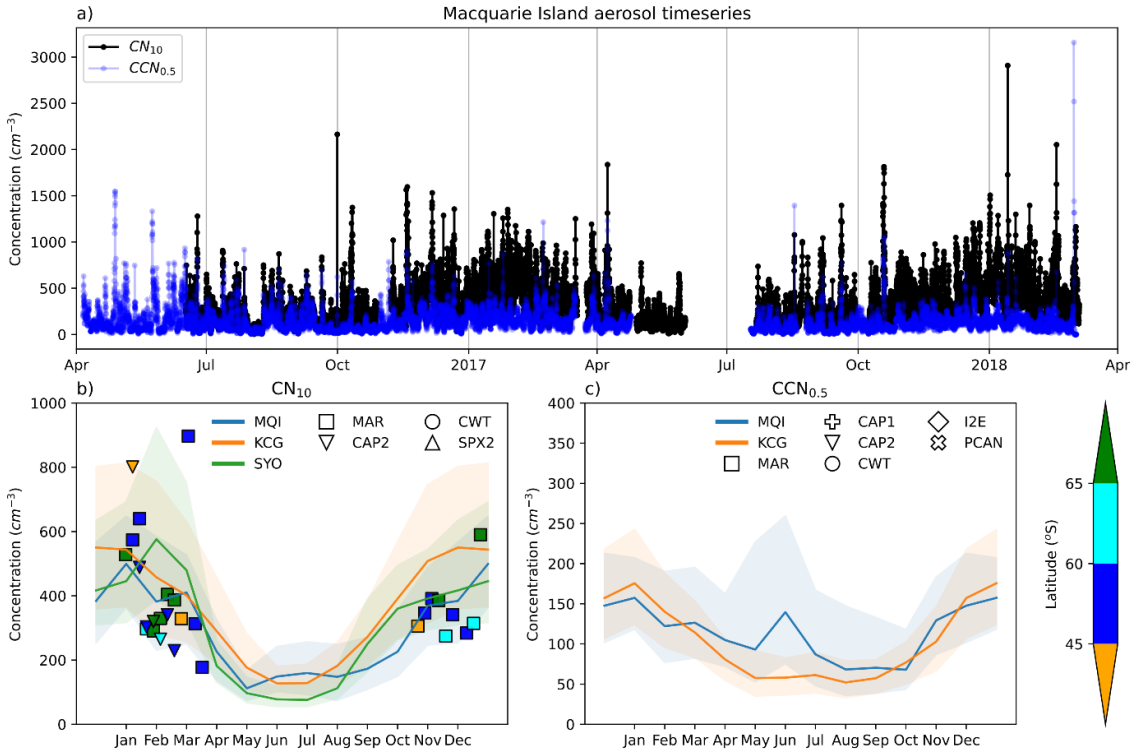

Figure 2: The full time series (a) of hourly median aerosol observations (only showing CN_{10} and $CCN_{0.5}$) from Macquarie Island between April 2016 to March 2018. Seasonal cycles of CN_{10} (b) and $CCN_{0.5}$ (c) from Macquarie Island (MQI, 2016-2018), Kennaook/Cape Grim (KCG, 2011 - 2020) and Syowa (SYO, 2004 - 2016) are shown, with monthly medians (solid line) and interquartile range (shaded regions) shown. Overlaid on the seasonal cycles are the weekly medians from ship-based campaigns coloured by latitudinal bins.

ACKNOWLEDGEMENTS

Technical and logistical support for the deployment to Macquarie Island were provided by the Australian Antarctic Division through Australian Antarctic Science Project 4292, and we thank John French, Peter de Vries, Terry Egan, Nick Cartwright, Ken Barrett, George Brettingham-Moore and Emry William Crocker for their assistance.

Funding for the ACRE and MICRE projects was provided by Australian Antarctic Science projects 4292 and 4431, and the United States Department of Energy through Grant DE-SC0018626. Funding for voyages was provided by the Australian Government and the U.S.Department of Energy.

MARCUS data were obtained from the Atmospheric Radiation Measurement (ARM) Program sponsored by the U.S. Department of Energy, Office of Science, Office of Biological and Environmental Research, and Climate and Environmental Sciences Division. We thank all the ARM technicians who collected the radiosonde and other data onboard R/V Aurora Australis. Technical, logistical, and ship support for MARCUS were provided by the Australian Antarctic Division through Australia Antarctic Science projects 4292 and 4387 and we thank Steven Whiteside, Lloyd Symonds, Rick van den Enden, Peter de Vries, Chris Young and Chris Richards for assistance.

The SIPEXII project was funded by the Australian Antarctic Science Grant Program (AAS Project 4032) and several RV Investigator voyages were supported by Australia Research Council Linkage Infrastructure, Equipment and Facilities grant LE150100048.

The Authors wish to thank the CSIRO Marine National Facility (MNF) for their support in the form of sea time on RV Investigator and associated support personnel, scientific equipment and data management. In particular we thank the Seagoing Instrumentation Team, the Data Acquisition and Processing Team, the Data Centre and the MNF Operations Team for their technical, IT and logistical support.

The authors would also like to acknowledge the Australian Bureau of Meteorology for their long term and continued support of the Kennaook/Cape Grim Baseline Air Pollution Monitoring Station, and all the staff from the Bureau of Meteorology and CSIRO.

This research was supported in part by BER Award DE-SC0018995 (GM and RH) and NASA grants 80NSSC19K1251 (GM). The work of GMM was funded by the United States Department of Energy Awards DE-SC0018626 and DE-SC0021159. GK acknowledges support from the Office of Science of the U.S. Department of Energy (DOE) as part of the Atmospheric System Research Program. The work of AP was partly funded by the National Environmental Science Program (NESP), Australia.

This project received grant funding from the Australian Government as part of the Antarctic Science Collaboration Initiative program (RH, MK, AP, SA, AK).

CCN SPECTRAL RELATIONSHIP VARIATIONS WITH DRIZZLE IN STRATUS AND CUMULI

J.G. HUDSON[1] and S. Noble[2]

[1]Desert Research Institute, Division of Atmospheric Science, Reno, Nevada, USA

[2]Savannah River National Laboratory, Aiken, South Carolina, USA

Key words: CCN, DRIZZLE, AEROSOL INDIRECT EFFECT, CUMULUS, STRATUS

The second aerosol indirect effect (AIE, cloud lifetime) is due to drizzle suppression by greater CCN concentrations, N_{CCN}. However, observations in the Rain in Cumulus over the Ocean (RICO) project and the Physics of Stratocumulus Tops (POST) experiment demonstrate opposite positive relationships with drizzle drop concentrations (N_d) for CCN active at many supersaturations (S). In RICO positive relationships were found for CCN active at low S, such as 0.06% ($N_{0.06\%S}$) shown in Figs 1A & B where drizzle drop spectra are sorted into 6 groups according to the CCN spectra associated with each of the clouds that contained the drizzle. Red octagons represent the highest N_{CCN} octile, orange diamonds correspond to the highest N_{CCN} quartile, pink inverted triangles

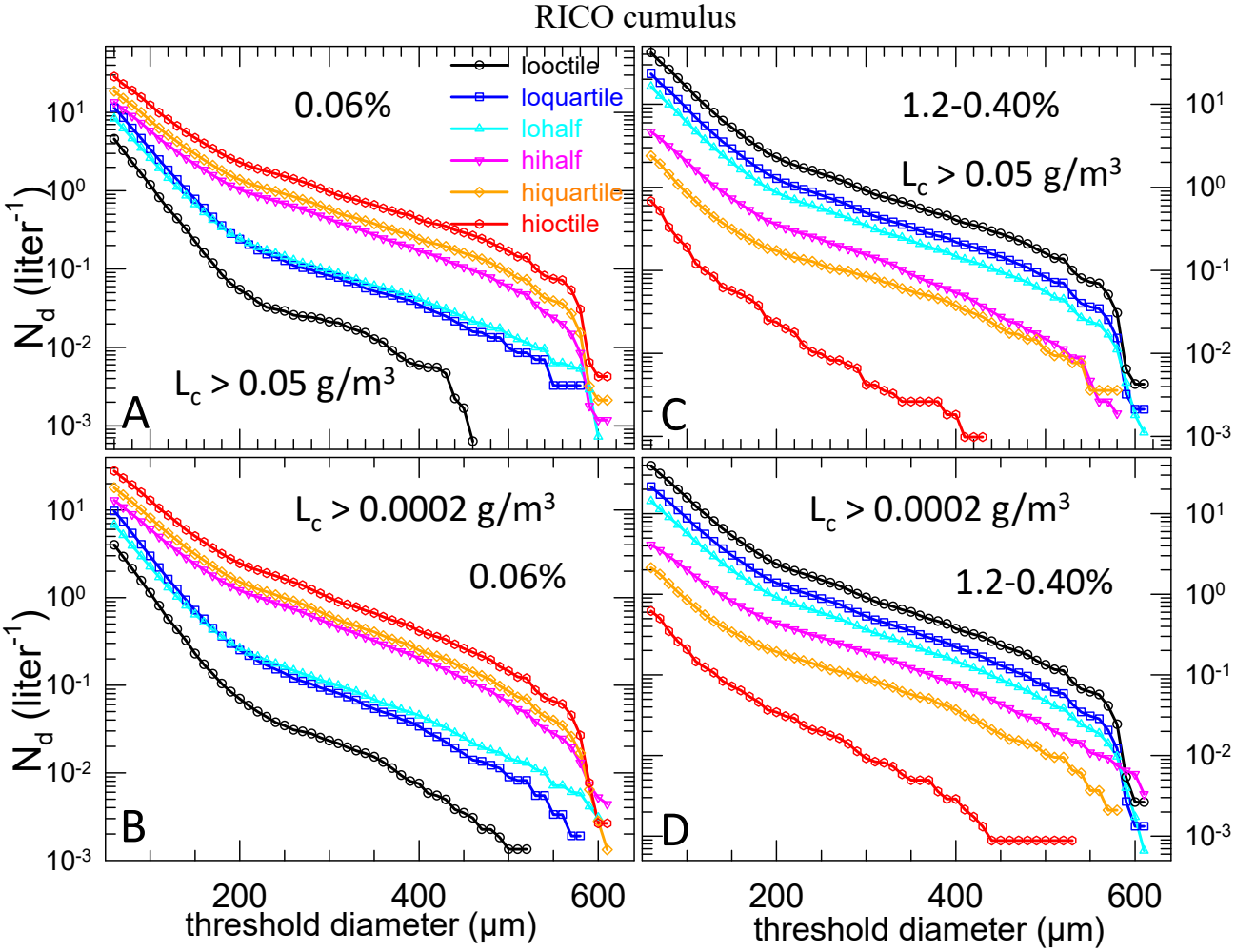

Figure 1. Cumulative drizzle drop concentrations, N_d, larger than the abscissa diameters and within cloud parcels with cloud droplet liquid water contents, L_c, greater than denoted for clouds associated with six divisions of $N_{0.06\%S}$ and $N_{1.2\text{-}0.4\%S}$ in RICO cumuli. This is for all 17 flights with 147 clouds and 31 CCN measurements. Legend in A applies to all panels.

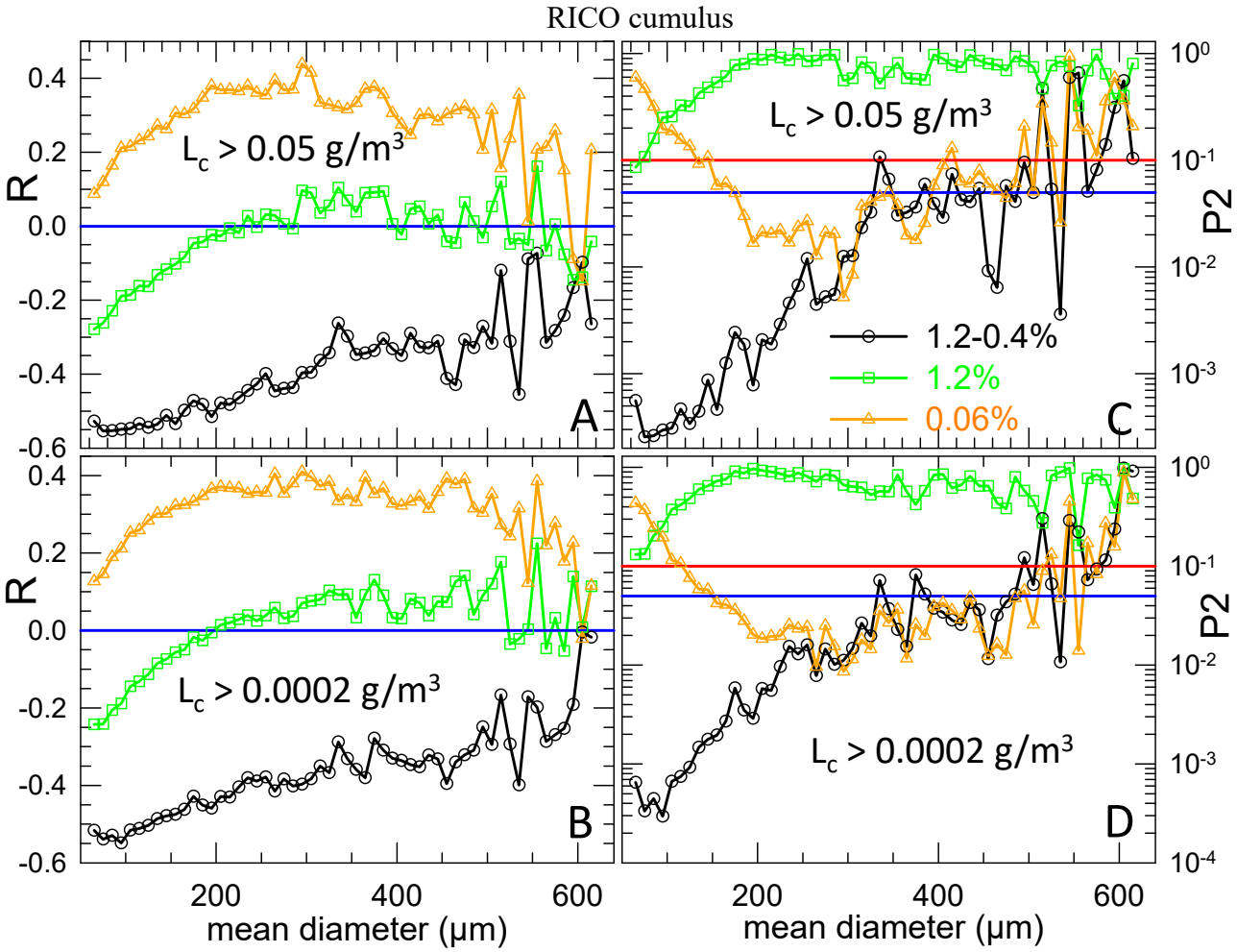

Figure 2. A-C. Correlation coefficients of drizzle drop concentrations, N_d, within abscissa diameters and within cloud parcels with L_c greater than denoted with $N_{1.2\text{-}0.4\%}$, $N_{1.2\%}$ and $N_{0.06\%}$. This is for 17 RICO flights with 147 clouds and 31 CCN measurements. **C & D.** Corresponding two-tailed probabilities, where red lines are at P2 = 0.1 and blue lines are at P2 = 0.05.

represent the higher half of N_{CCN}, cyan triangles the lower half, blue squares the lowest quartile and black circles the lowest N_{CCN} octile. Therefore, Fig. 1A & B shows greater drizzle associated with higher $N_{0.06\%S}$. In both of these panels N_d is exactly in the order of $N_{0.06\%S}$ from red to orange to pink to cyan, then blue and finally black. When only CCN active at very high S are considered by subtracting N_{CCN} at lower S from N_{CCN} at higher S, the relationship signs reverse as in Fig. 1C & D. Here greater drizzle is associated with lower $N_{1.2\text{-}0.40\%S}$ as the drizzle spectra are in exact inverse order compared to $N_{0.06\%S}$ of Fig. 1A & B. Here black shows the most drizzle and red by far the least drizzle. Figure 2A & B quantifies these contrasting relationships for these two components of CCN spectra with positive R for $N_{0.06\%S}$ (orange triangles) and negative R for $N_{1.2\text{-}0.40\%S}$ (black circles). The green squares for $N_{1.2S\%}$ (all CCN) then demonstrate the apparent result of the CCN components. Figure 2C & D then demonstrate the significance of these R. The two CCN components show good significance with P2 < 0.1 or even < 0.05 over most of the drizzle size range, but $N_{1.2S\%}$ (green squares) shows nearly complete insignificance with P2 > 0.1 over nearly the entire size range for the low magnitude Rs of Fig. 2A & B. These results indicate that AIE in RICO was often reduced by greater N_{CCN} at low S where they seemed to function as giant nuclei, GN. However, these low S CCN are much smaller and in much higher concentrations than GN. Moreover, unlike GN they were unrelated to horizontal wind speed. These RICO drizzle-CCN

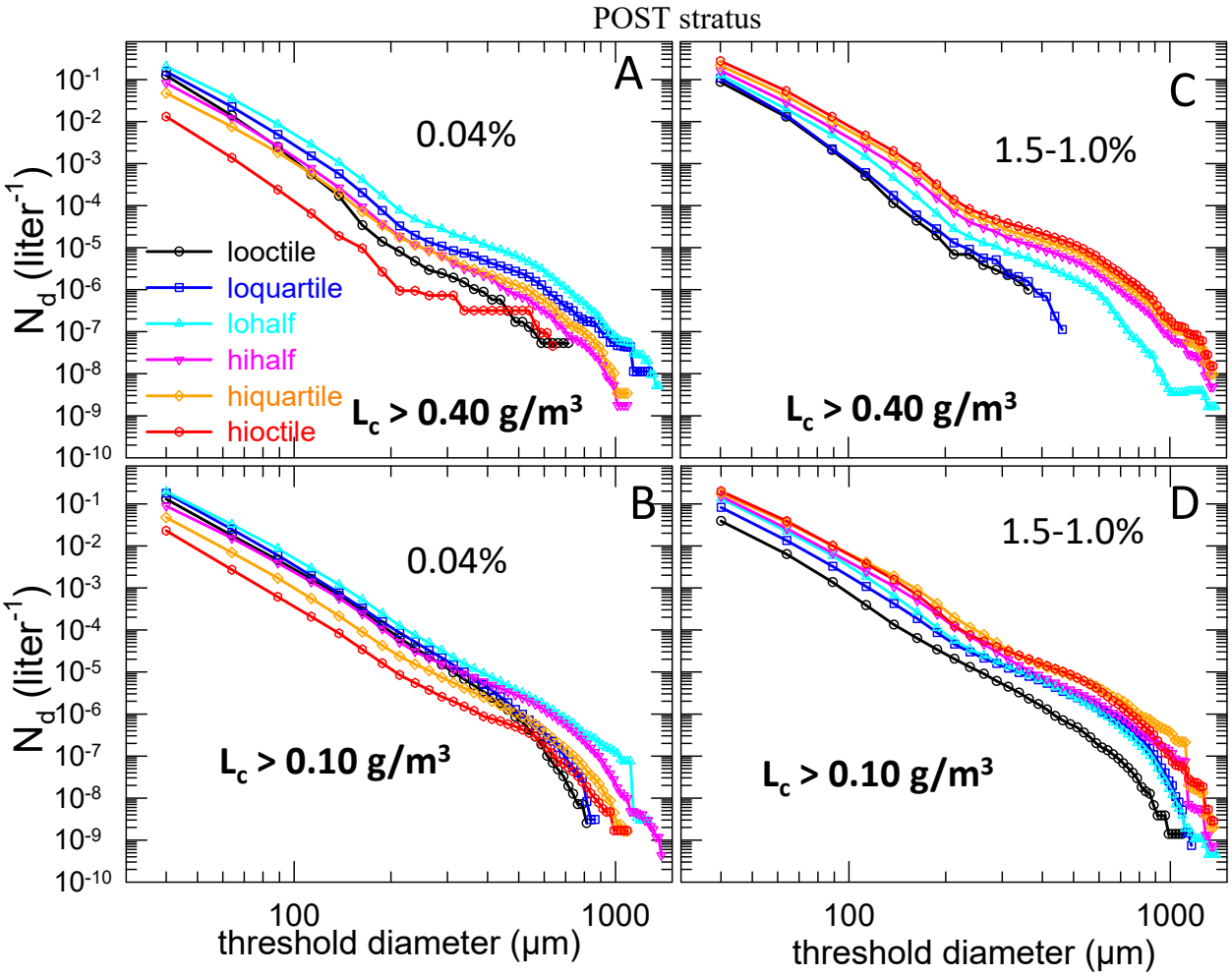

Figure 3. As Fig. 1 but for POST $N_{0.04\%}$ and $N_{1.5\text{-}1.0\%}$. This is for all 14 flights with 141 clouds and 54 CCN measurements.

results are consistent with CCN bimodality positive relationships to drizzle (Hudson & Noble 2022) in RICO. Greater bimodality means relatively greater concentrations of low S CCN compared to higher S CCN. Low S CCN are mostly within the accumulation mode, which is predominantly caused by cloud processing (Hoppel et al. 1986; Noble & Hudson 2019). This occurs through gas-to-particle chemical reactions within droplets, Brownian capture of interstitial material and droplet coalescence. High S CCN are mostly within the Aitken mode. Unimodality indicates a smaller accumulation mode and a greater Aitken mode.

Figure 3A & B for POST stratus demonstrate less drizzle when $N_{0.04S\%}$ is higher (red, orange and pink mostly below cyan, blue and black). Fig. 3C & D is also opposite of Fig. 1 with more drizzle when concentrations of only high S CCN (here $N_{1.5\text{-}1.0\%S}$) are greater. These results are consistent with the Marine Stratus/Stratocumulus Experiment (Hudson et al. 2018) where there was more drizzle when CCN spectra were more unimodal. Low vertical wind, W, of stratus would restrict droplet activation to the accumulation mode, especially when spectra are more bimodal (accumulation mode dominant). Spectra that are more unimodal (Aitken dominant) have fewer accumulation mode particles (less cloud processing), which would then make fewer droplets that could thus attain larger sizes and therefore foster drizzle. On the other hand, the greater W of cumuli such as RICO would allow activation of the Aitken and accumulation modes, which could provide greater droplet size diversity that would promote autoconversion to drizzle.

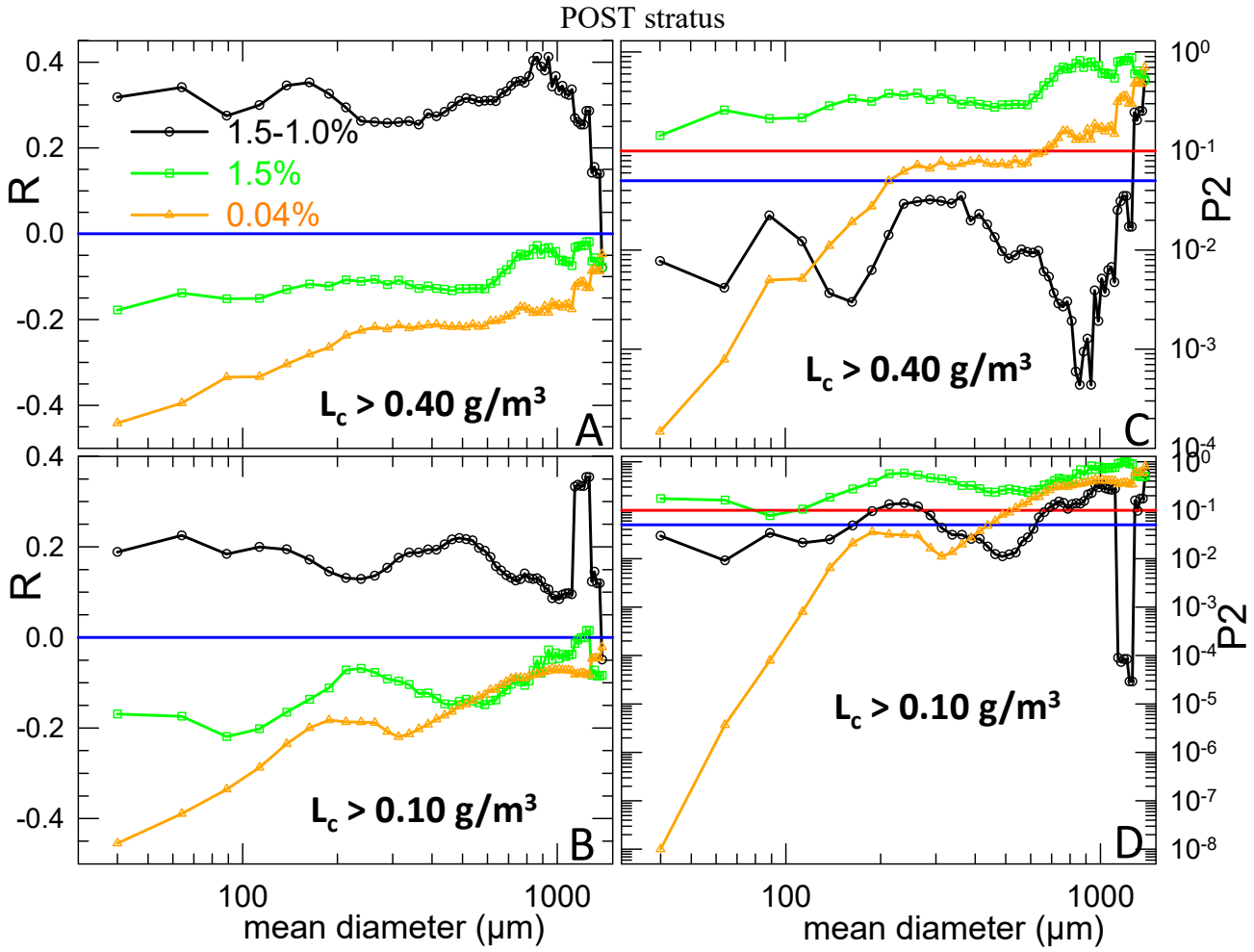

Figure 4. As Fig. 2 but for POST $N_{1.5\text{-}1.0\%}$ and $N_{0.04\%}$. This is for all 14 flights with 141 clouds and 54 CCN measurements.

IMPLICATIONS

These results indicate that 2nd AIE is under conflicting influences by different components of CCN spectra. This would seem to reduce 2nd AIE and should be considered in attempts to alter cloud microphysics to change brightness, thickness, coverage or to suppress or induce drizzle.

REFERENCES

Hoppel, W.A., Frick, G.M. & Larson, R.E. (1986). Effect of nonprecipitating clouds on the aerosol size distribution in the marine boundary layer. *Geophys. Res. Lets.,* **13**(2), 125-128.

Hudson, J. G., & Noble, S. (2022). CCN spectral modality compared to droplet spectra and drizzle in RICO cumuli. *J. Geophys. Res.*, **127**, e2022JD037189. https://doi.org/10.1029/2022JD037189

Noble, S.R., and Hudson, J.G. (2019). Effects of continental clouds on surface Aitken and accumulation modes. *J. Geophys. Res.,* **124**, 5479-5502.

Hudson, J.G., S. Noble, and S. Tabor (2018). CCN spectral shape and stratus cloud and drizzle microphysics. *J. Geophys. Res.,* **123**, 9635-9651.

APPARENT PARTICLE SHRINKAGE EVENTS IN SAUDI ARABIA EXPLAINED WITHOUT EVAPORATION

S. HAKALA[1], V. VAKKARI[2,3], H. LIHAVAINEN[2,4], A. HYVÄRINEN[2], K. NEITOLA[1,5], J. KONTKANEN[1,6], V-M KERMINEN[1], M. KULMALA[1], T. PETÄJÄ[1], T. HUSSEIN[1,7], M. I. KHODER[8] M. A. ALGHAMDI[9], P. PAASONEN[1]

[1]Institute for Atmospheric and Earth System Research (INAR) /Physics, Faculty of Science, University of Helsinki, Helsinki, Finland
[2]Finnish Meteorological Institute, Helsinki, Finland
[3]Atmospheric Chemistry Research Group, Chemical Resource Beneficiation, North-West University, Potchefstroom, South Africa
[4]Svalbard Integrated Arctic Earth Observing System (SIOS), Longyearbyen, Norway
[5]Vaisala Oyj, Vantaa, Finland
[6]CSC – IT Center for Science, Espoo, Finland
[7]Environmental and Atmospheric Research Laboratory (EARL), Department of Physics, School of Science, the University of Jordan, Amman 11942, Jordan
[8]Air Pollution Research Department, Environment and Climate Change Research Institute, National Research Centre, El Behooth Str., Dokki, Giza 12622, Egypt.
[9]Department of Environmental Sciences, Faculty of Meteorology, Environment and Arid Land Agriculture, King Abdulaziz University, Jeddah, Saudi Arabia

Keywords: aerosol particles, new particle formation, size distribution, aerosol shrinkage

INTRODUCTION

Several studies on new particle formation (NPF) events have pointed out an interesting phenomenon, where the average diameter of a particle mode formed in an NPF event begins to decrease after the growth phase. This is often referred to as aerosol shrinkage, but we will use the term DMD (decreasing mode diameter) event, since aerosol shrinkage quite directly implies a reduction in the size of individual particles, which is not necessarily the case. Typically, these DMD events are speculated to be caused by the evaporation of semivolatile compounds, due to changes in environmental conditions (Alonso-Blanco et al., 2017). However, the reduction in the mean diameter of the particle mode may also occur without evaporation, if less grown particles are transported to the measurement site after more grown ones (Kivekäs et al., 2016). Concrete evidence for explaining the DMD events is still lacking, highlighting a rather fundamental gap in our knowledge regarding aerosol processes. Here, we apply a Lagrangian single-particle growth model to evaluate factors affecting the appearance of NPF events at Hada Al Sham, Saudi Arabia, where DMD events were found to occur very frequently (Hakala et al., 2019)

METHODS

Our Lagrangian-single particle growth model considers the condensation/evaporation of two compounds, out of which one is completely non-volatile and the other is potentially volatile. We assume that the spatially varying precursor vapor concentrations of both compounds are represented by satellite-derived SO_2 concentration and that the production of the condensable compounds from the precursor occurs via photochemistry. Particles observed at each hour of the day are modelled individually, accounting for their transport history via air mass back trajectories. Therefore, the model is able to produce true diameter changes of individual particles by condensation and evaporation, as well as apparent diameter changes caused by differing conditions during transport. The model is run with varying configurations in order to find a description that would best match the observations.

CONCLUSIONS

We find the best match with the observed and modelled particle diameter development when practically only the non-volatile compound affects the particle diameter changes. In this case, the DMD events are solely caused by the transport of smaller particles (Fig. 1) that have spent an increasing fraction of their lifetime in a lower growth environment. This is mainly enabled by a nearby spatial gradient in the precursor vapor concentrations, with the concentrations being lower further away from the measurement site, and the decreasing photochemical production of condensable vapors in the afternoon.

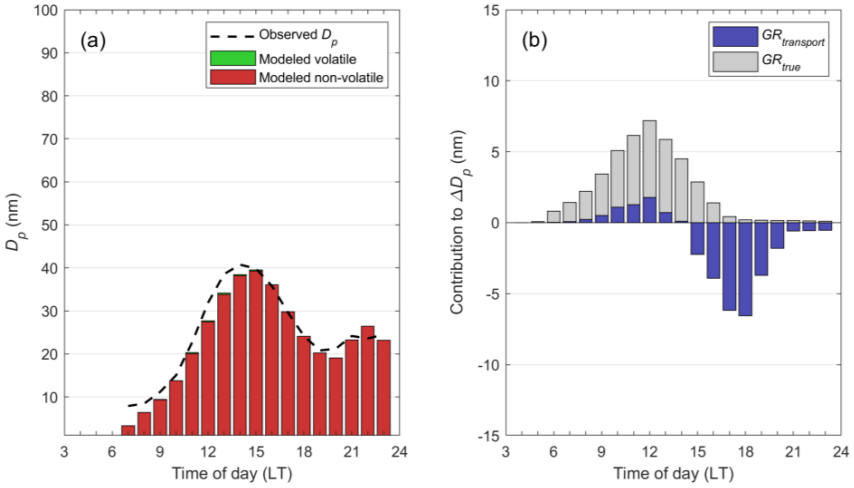

Figure 1. (a) Observed and modeled mean particle diameter during 138 NPF events. (b) Mean contributions to modeled diameter changes from true diameter changes (GR_{true}; condensation, evaporation) and transport ($GR_{transport}$).

Our findings demonstrate that evaporation of semivolatile species is not needed for explaining the observations of decreasing particle sizes in Hada al Sham, and that care should also be taken when interpreting the cause of similar events elsewhere. The correct identification of the cause of the decreasing particle sizes is important e.g. for estimating the production of cloud condensation nuclei, since in the case of particle evaporation, the net flux of particles above a certain diameter would be reduced.

ACKNOWLEDGEMENTS

This study was funded by the Deanship of Scientific Research (DSR, grant no I-122-430) at King Abdulaziz University (KAU), the Academy of Finland (ACCC Flagship, project 337549; Centre of Excellence program, projects 272041 and 307331; Profi 3 program, project 311932; Academy professorship, project 302958; and projects 325656 and 325647), the European Research Council (ERC) under the European Union's Horizon 2020 research and innovation program (ATM-GTP, grant agreement 742206; FORCeS, grant agreement 821205), the European Commission Horizon Europe project FOCI, "Non-CO2 Forcers and Their Climate, Weather, Air Quality and Health Impacts (project 101056783) and the Doctoral Programme in Atmospheric Sciences at the University of Helsinki (ATM-DP). TH acknowledges The Eastern Mediterranean and Middle East Climate and Atmosphere Research (EMME-CARE) project, which received funding from the European Union's Horizon 2020 Research and Innovation Programme (Grant Agreement Number 856612) and the Government of Cyprus. The sole responsibility of this publication lies with the authors.

REFERENCES

Alonso-Blanco, E., Gómez-Moreno, F. J., Núñez, L., Pujadas, M., Cusack, M., & Artíñano, B. (2017). Aerosol particle shrinkage event phenomenology in a South European suburban area during 2009–2015. *Atmospheric Environment, 160*, 154-164. doi:10.1016/j.atmosenv.2017.04.013

Hakala, S., Alghamdi, M. A., Paasonen, P., Vakkari, V., Khoder, M. I., Neitola, K., . . . Hyvärinen, A. P. (2019). New particle formation, growth and apparent shrinkage at a rural background site in western Saudi Arabia. *Atmos. Chem. Phys., 19*(16), 10537-10555. doi:10.5194/acp-19-10537-2019

Kivekäs, N., Carpman, J., Roldin, P., Leppa, J., O'Connor, E., Kristensson, A., & Asmi, E. (2016). Coupling an aerosol box model with one-dimensional flow: a tool for understanding observations of new particle formation events. *Tellus Series B-Chemical and Physical Meteorology, 68*. doi:ARTN 29706 10.3402/tellusb.v68.29706

INVESTIGATION OF NEW PARTICLE FORMATION AND SIZE DISTRIBUTION OF AEROSOLS IN THE SOUTHERN OCEAN AND ANTARCTIC OCEAN

Y. INOMATA[1], M. TSUSUMI[2], M. HAYASHI[3], K. HARA[3], N. HIRASAWA[4], T. SETO[5]

[1]Institute for Nature and Environmental Technology, Kanazawa University, Ishikawa, 920-1192, Japan.

[2]Faculty of Engineering, Kyushu University, Fukuoka, Japan.

[3] Department of Earth System Science, Faculty of Science, Fukuoka University, Fukuoka, Japan.

[4]National Institute of Polar Research, Tokyo, Japan.

[5.] Institute of Science and Engineering, Kanazawa University, Kanazawa, Ishikawa, Japan.

Keywords: Aerosols, New Particle Formation, $nssSO_4^{2-}$, MSA, Southern Ocean, Antarctic Ocean

INTRODUCTION

Understanding chemical and physical processes to formation of atmospheric aerosols are very important effect to climate via radiation associated with influencing cloud optical properties, cloud life time (e.g., Charlson et al., 1987; IPCC, 2021). In the ocean remote area such as Antarctic Ocean in the southern hemisphere, oxidation of dimethyl sulfide (DMS) produced by phytoplankton is an important source of aerosols. In the atmosphere, DMS is oxidized into sulfate ($nssSO_4^{2-}$) and methane sulfonate (MSA) aerosols, which is influence to the solar radiation by scattering of solar energy, acting as condensation nuclei for cloud formation. The purpose of this study is to investigate the formation of atmospheric aerosols and these chemical constituents in the western Pacific Ocean, Southern Ocean, and Antarctic Ocean during the Japan Antarctic Research Expedition (JARE). In this study, we present the spatial and temporal variations of number-size distribution of atmospheric aerosols concentrations and chemical composition of aerosols such as $nssSO_4^{2-}$ and MSA.

METHODS

Observation of atmospheric aerosols was performed from 10th November to 11th December 2021 (Reg 1) and 7th February-26th March 2022 (Reg 2) over the western Pacific Ocean, Southern Ocean, and Antarctic Ocean during the Japanese Antarctic Research Expedition 63 (JARE63). Observation did not conduct during the Exclusive Economic Zone (EEZ). During JARE63, we observed concentrations of number-size distribution of atmospheric aerosols particles (6~224 nm) by Scanning Mobility Particle Sizer (SMPS Model 3936, TSI) and Condensation Particle Counter (Model 3788, TSI). The measurement was conducted in the 5 min interval. In order to investigate the chemical composition, size segregated atmospheric aerosols were collected in the Teflon and sus filter with 6 stage, $PM_{>10}$, $PM_{2.5\text{-}10}$, $PM_{1\text{-}2.5}$, $PM_{0.5\text{-}1}$, $PM_{0.1\text{-}0.5}$, $PM_{<0.1}$μm) by using Nano-sampler. Sampling interval was 2-3 days. The sampled filters were immersed in ultrapure water, and shaking, and filtered through a disk filter. The water soluble ion species were analyzed by ion chromatography (Thermo Co. Ltd.). In order to prevent sampling exhaust by ship, aerosol sampling was only conducted with relative wind direction from -90° to 90° against the ships bow.

RESULTS AND DISCUSSION

Figure 1 shows the five-days air mass backward trajectories by NOAA HYSPLIT Trajectory Model. In the western North Pacific Ocean near Japan, the air mass transported from the Asian continent with westerly wind. The air mass in the subtropical North Pacific Ocean were transported from the Pacific Ocean. In the Southern Ocean and Antarctic Ocean, the air mass transported from the Southern Ocean or Antarctica.

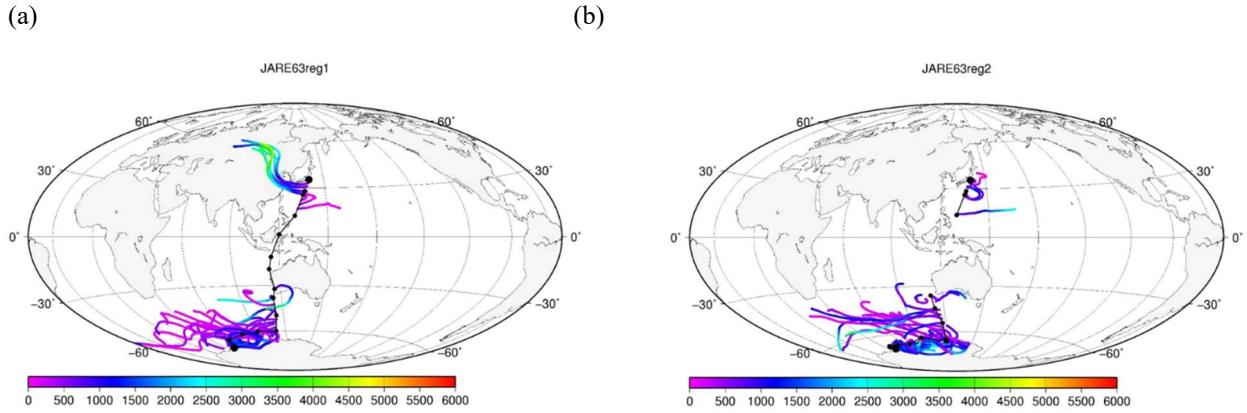

Figure 1. The five days air mass back trajectory analysis during the JARE63 observations. Black circles mean sampling start location. (a) Leg1; 10th November-11th December 2021, (b) Leg2; 7th February-26thMarch 2022.

Figure 2 shows latitudinal and longitudinal variations of size distributions of $nssSO_4^{2-}$ concentrations observed from 10th November 2021 to 11th December 2021 and 7th February to 26th March 2022 during the JARE63. Higher concentrations of $nssSO_4^{2-}$ were observed in the region near Japan due to the transboundary transport of anthropogenic sources. Except for these higher concentrations, concentrations of $nssSO_4^{2-}$ varied from 1.8-2.9 $nmolm^{-3}$ during Leg 1 and 1.7-4.3 $nmolm^{-3}$. $nssSO_4^{2-}$ were observed in all size particles. Particularly, existence of $nssSO_4^{2-}$ in $PM_{<0.1}$, $PM_{0.1\text{-}0.5}$, $PM_{0.5\text{-}1}$, $PM_{1\text{-}2.5}$, $PM_{2.5\text{-}10}$, and $PM_{>10}$ were 3.5%, 24.8%, 25.1%, 10.0%, 9.9%, and 26.7%, respectively (Figure 4).

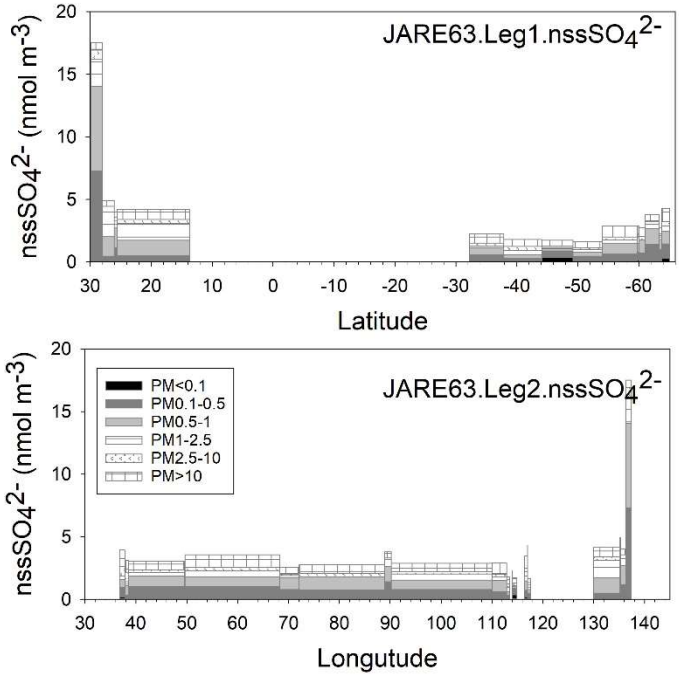

Figure 2. Latitudinal and longitudinal variations of size segregated $nssSO_4^{2-}$ concentrations.

Latitudinal and longitudinal distributions of MSA concentrations were larger fluctuations compared with those in the $nssSO_4^{2-}$ concentrations. During Leg 1, MSA concentrations varied with 0.29-0.98 $nmolm^{-3}$. These tend to increase toward south, and higher concentrations were observed around 60°S. During Leg 2, MSA concentrations were fluctuated with 0.25-1.23 $nmolm^{-3}$. The observed region with 35-115°E were costa of the Antarctica (66-69°S), which mean close to sea ice. Existence of MSA in $PM_{<0.1}$, $PM_{0.1-0.5}$, $PM_{0.5-1}$, $PM_{1-2.5}$, $PM_{2.5-10}$, and $PM_{>10}$ were 0.7%, 40.4%, 32.2%, 23.6%, 2.7%, and 0.4%, respectively. Most of MSA were distributed in the $PM_{0.1-0.5}$, $PM_{0.5-1}$, $PM_{1-2.5}$ (Figure 4).

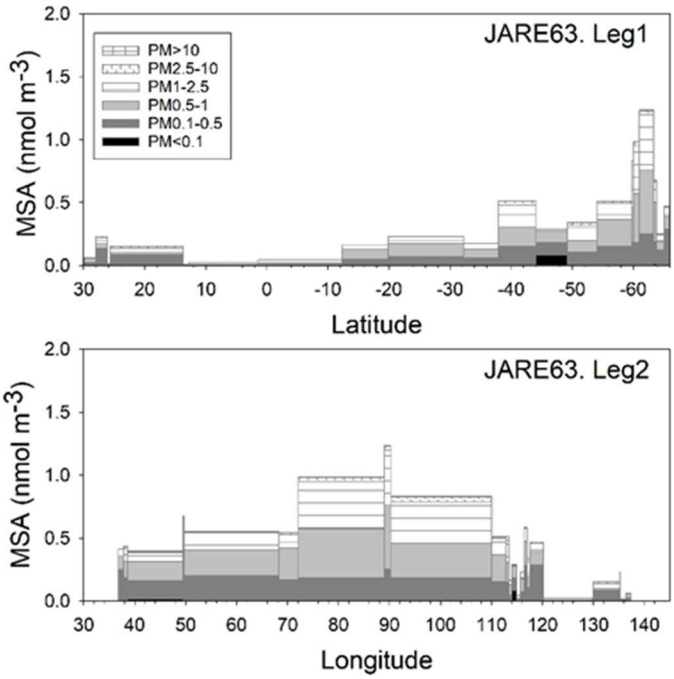

Figure 3. Latitudinal and longitudinal variations of size segregated MSA concentrations. In the region 115-135°E, the observations were conducted during northward transport.

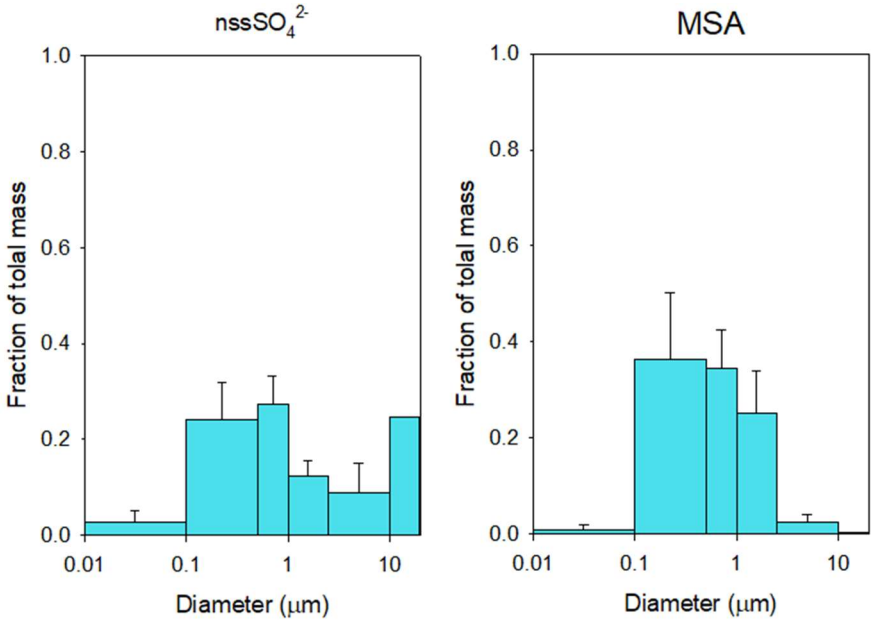

Figure 4. Average size distributed mass composition of $nssSO_4^{2-}$ and MSA during JARE63.

Although MSA were mainly distributed in the $PM_{0.1\text{-}0.5}$, $PM_{0.5\text{-}1}$, $PM_{1\text{-}2.5}$, MSA was also detected in the $PM_{<0.1}$ and these were contained to 30% those in total MSA concentrations in 29th November-1th December, 2021. During this period, strong new particle formation occurred. It is possible to consider that MSA exists in nanoparticles ($PM_{<0.1}$) under the new particle formation.

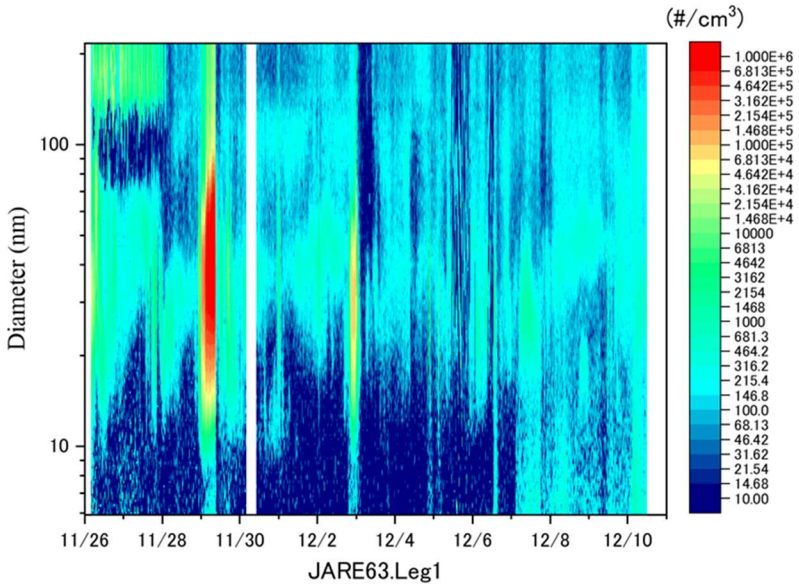

Figure 5. Number size distributions of aerosols from 28th November to 11th December 2021 during JARE63 (Leg 1). Strong new particle formation occurred in 29th November, 2021.

CONCLUSIONS

In this study, size segregated sulfur derived aerosol ($nssSO_4^{2-}$, MSA) concentrations observed in the Southern Ocean and Antarctic Ocean were documented. Prominent feature in size distribution of $nssSO_4^{2-}$ and MSA were found. The $nssSO_4^{2-}$ were distributed to all size range, whereas MSA were manly distributed in the $PM_{0.1\text{-}0.5}$, $PM_{0.5\text{-}1}$, $PM_{1\text{-}2.5}$. MSA detected in $PM_{<0.1}$ were measured during the strong new particle formation.

ACKNOWLEDGEMENTS

This study is a part of the Science Program of Japanese Antarctic Research Expedition 63 (JARE63). We thank crew and staff of the Antarctic research vessels (Shirase) for their help during observations. It was supported by Researchers exchange promotion program in National Institute of Polar Research and Research Organization of Information and Systems.

REFERENCES

Charlson, R.J., Lovelock, J.E., Andreae, M. O., and Warren, S.G. (1987). Oceanic Phytoplankton, tropospheric sulfur, cloud albedo and climate, *Nature* **326**, 655-661.

IPCC (2021) Climate Change 2021: The Physical Science Basis, : Contribution of Working Group I to the Sixth Assessment Report of the Intergovernmental Panel on Climate Change [Masson-Delmotte, V., P. Zhai, A. Pirani, S.L. Connors, C. Péan, S. Berger, N. Caud, Y. Chen, L. Goldfarb, M.I. Gomis, M. Huang, K. Leitzell, E. Lonnoy, J.B.R., Matthews, T.K. Maycock, T. Waterfield, O. Yelekçi, R. Yu, and B. Zhou (eds.)]. Cambridge University Press, Cambridge, United Kingdom and New York, NY, USA, 2391 pp. doi:10.1017/9781009157896

DISCRETE PHASE-EULERIAN WALL FILM MODEL IN PREDICTING COUGHING RESPIRATORY DROPLET

ND. KHOA[1], K. KUGA[2], and K. ITO[2]

[1]Interdisciplinary Graduate School of Engineering Sciences, Kyushu University, Kasuga, Japan
[2]Faculty of Engineering Sciences, Kyushu University, Kasuga, Japan

Keywords: COMPUTATIONAL FLUID DYNAMICS-CFD, COUGHING, EULERIAN WALL FILM, DISCRETE PHASE MODEL, RESPIRATORY DROPLET GENERATION

INTRODUCTION

Respiratory diseases have caused the most public concern throughout human history. In addition to diseases such as measles and tuberculosis, the most recent infectious disease outbreak has been coronavirus disease 2019. Pathogenic transmission is primarily through expelled droplets that contain germs (i.e., viruses, bacteria, or microbes) from infected hosts (Jayaweera et al. 2020). One of the droplet formation mechanism is the stripping and rupturing of mucus or saliva layers owing to excessive shear stress imposed by high expiratory flow during coughing (Dhand and Li 2020). Experimental studies have long been conducted to describe droplet size and dispersion due to coughing (Chao et al. 2009; Wang et al. 2022). Nonetheless, the cost of experimentation is an existential barrier; meanwhile, the computational fluid dynamics (CFD) method is a promising alternative for analyzing droplet spreading phenomena. Thus, this study aimed to apply the discrete phase-coupled Eulerian wall film (DP-EWF) model to characterize droplet properties during coughing.

METHODS

A computational oral-airway model was generated using computed tomography (CT) images of a male adult (Fig. 1A). Detailed oral cavity morphometry including teeth created using DAZ studio, software for obtaining human geometry, was seamlessly integrated into our airway model. The mesh design was constructed using polyhedral elements with 10 prism layers adjacent to the boundary walls (Fig. 1B). In this study, assuming unsteady, incompressible, and isothermal flow, we used the coughing flow rate proposed by Gupta et al. (Gupta, Lin, and Chen 2009). Simultaneously, the EWF model was used to predict the stripped droplets from the mucus or saliva layers, and the discrete phase model was used to account for their transportation and absorption. The expelled droplets were sampled at the mouth opening, as shown in Fig. 1A. The thickness of the mucus or saliva layers was assigned as 85 μm for the oral cavity (Collins and Dawes 1987) and 30 μm for the airway region (Matsui et al. 1998), as depicted in Fig. 1C. For the EWF model, surface tension of 0.072 N/m and critical shear stress (CSS) of 1 Pa were assumed. The time step size of the fluid flow and EWF were set at 10^{-3} and 10^{-4} s, respectively. The numerical boundary conditions and mucus or saliva properties are summarized in Table 1.

Parameter	**Information**
Turbulent model	SST k-ω
Turbulent intensity	5%
Viscosity	Air: 1.81×10^{-5} Pa s Mucus/saliva: 1×10^{-3} Pa s
Density	Air: 1.185 kg/m^3 Mucus/saliva: 998.2 kg/m^3

Table 1. Numerical boundary conditions and mucus or saliva properties

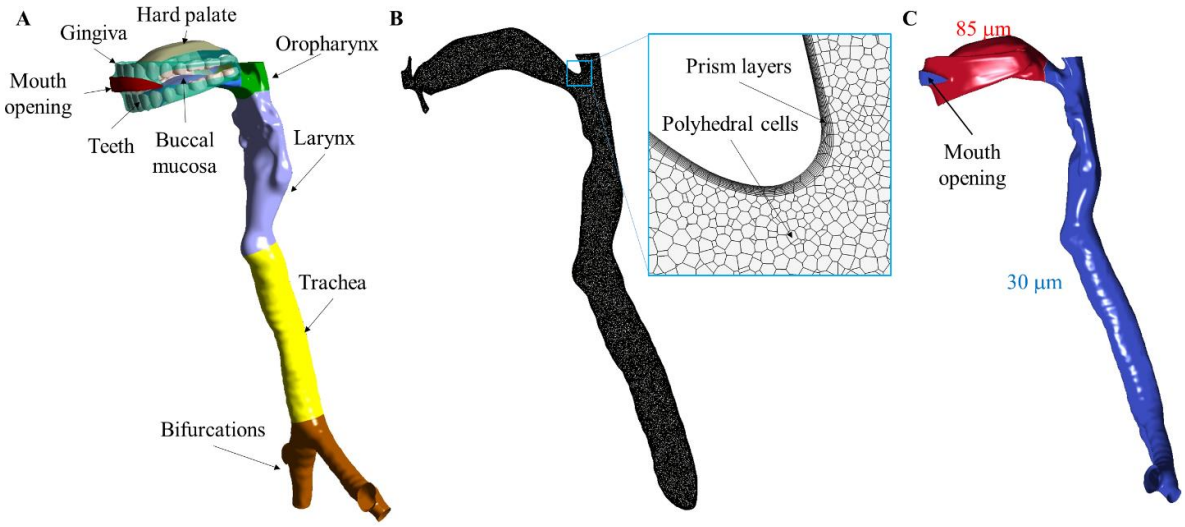

Fig. 1. Outline of the interested domain. (A) Constituting components of the oral-airway model. (B) Mesh design for the computational domain. (C) Mucus thickness distribution on the oral-airway model.

RESULTS AND DISCUSSION

The coughing flow pattern in the oral-airway model is displayed in Fig. 2 at the specific times of 0.025, 0.1, and 0.3 s. Notably, the flow features at t=0.1 s were associated with the cough peak flow rate (CPFR). A high velocity was observed at the bifurcation, trachea, glottis, and oropharynx regions from the beginning of coughing (t=0.025 s) to the CPFR; the flow rate then gradually reduced until the end of coughing. Apart from the above-mentioned regions, the remaining regions of the oral-airway model also experienced a high velocity, especially at the CPFR (approximately 18 m/s). Therefore, the complex nature of the oral-airway model was responsible for local airflow acceleration, which was closely related to excessive shear stress development in the corresponding regions.

Fig. 3 presents the distribution of wall shear stress (WSS), mucus or saliva thickness, and stripped droplets at t=0.025 and 1 s. As expected, a high WSS of 1.5 Pa was imposed, coinciding with the high-airflow velocity regions (Fig. 3A). Consequently, the mucus or saliva layers in the region of WSS larger than the CSS (assumed to be 1 Pa) started to exuviate and form ruptured droplets at the corresponding position (Fig. 3A). At the CPFR (Fig. 3B), the high WSS of 5 Pa almost covered the entire oral-airway surface, and the mucus or saliva thickness was substantially worn down to almost 0 μm, resulting in the droplets occupying the entire model. The results showed that coughing could produce considerable droplets from the beginning of coughing until CPFR.

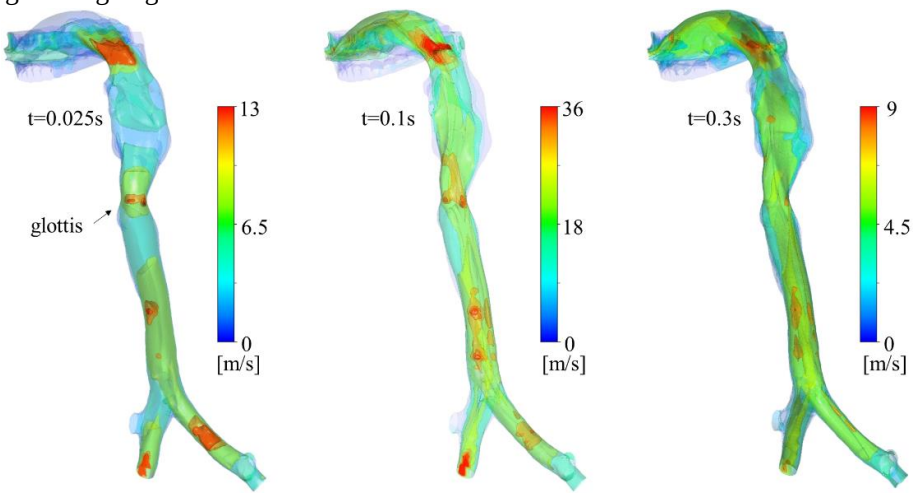

Fig. 2. Iso-surface distribution of the fluid flow characteristic following the time series of coughing

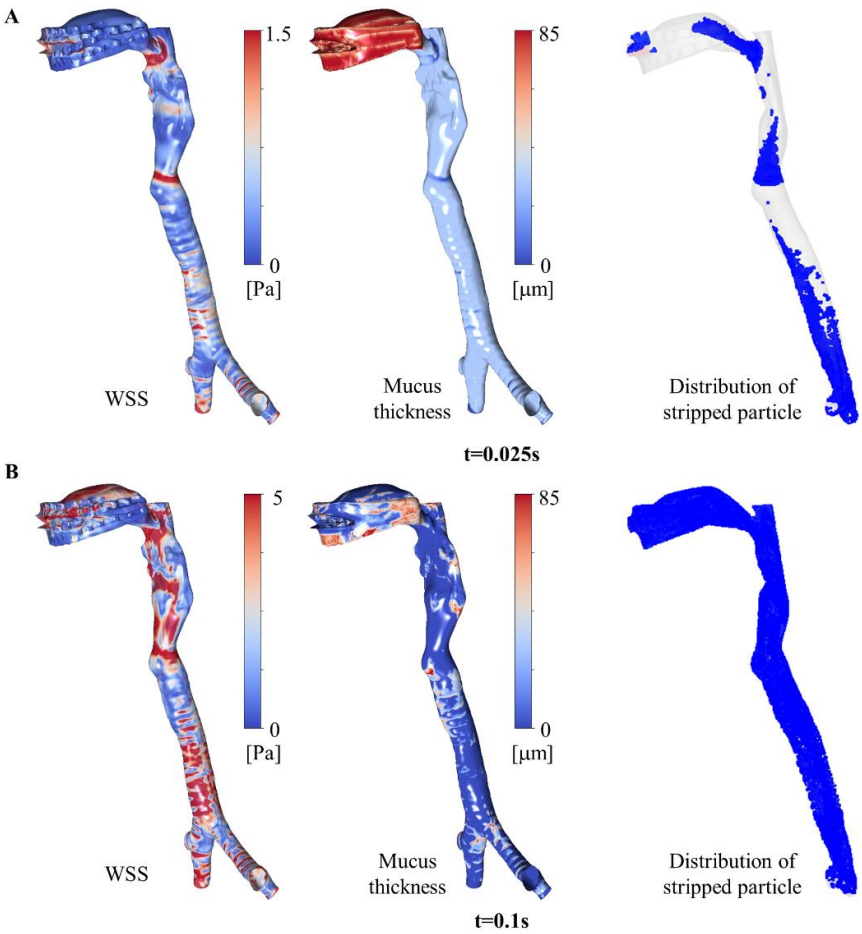

Fig. 3. Characteristics of wall shear stress (WSS), mucus thickness, and stripped droplets at (A) t = 0.025 s and (B) t = 0.1 s

The performance of the DP-EWF model was validated using field measurements conducted on volunteers (Chao et al. 2009). Fig. 4(A) compares the two datasets against the droplet diameter bin. In this case, the expelled droplet number fraction is defined as the ratio between the number of droplets in a specific diameter bin and the total droplet number in all diameter bins. As a result, our simulation data were comparable with those of the experiment in terms of the droplet size distribution; specifically, the highest fraction of generated droplets was recorded in the diameter bin of 4-8 μm for both datasets. For the larger diameter bin (75-100 μm), the collected droplet number rapidly decreased to almost 0%.
Additionally, not all the stripped droplets were expelled into the environment during the coughing; therefore, reabsorption into the mucus or saliva layers is possible. Fig. 4(B) shows the absorption efficiency of droplets following the oral-airway model regions. The results show the peak absorption efficiency in the laryngeal region (approximately 20%), followed by the trachea, teeth, bifurcation, and gingiva. This is attributed to the acceleration of fluid flow, and the complex structure in these regions enhanced the absorption prospect owing to the high inertia impaction. Interestingly, the integration of the teeth, which has been neglected in other studies, contributed to the considerable absorption efficiency of the stripped droplets. Based on the findings, the morphometric features of the oral-airway model play a critical role in minimizing expelled droplets, which may reduce transmission risks in the environment.

CONCLUSIONS

This study successfully applied the DP-EWF model to predict droplet formation induced by coughing, paving the way for further studies on the prognostication of expelled droplets during speaking or sneezing.

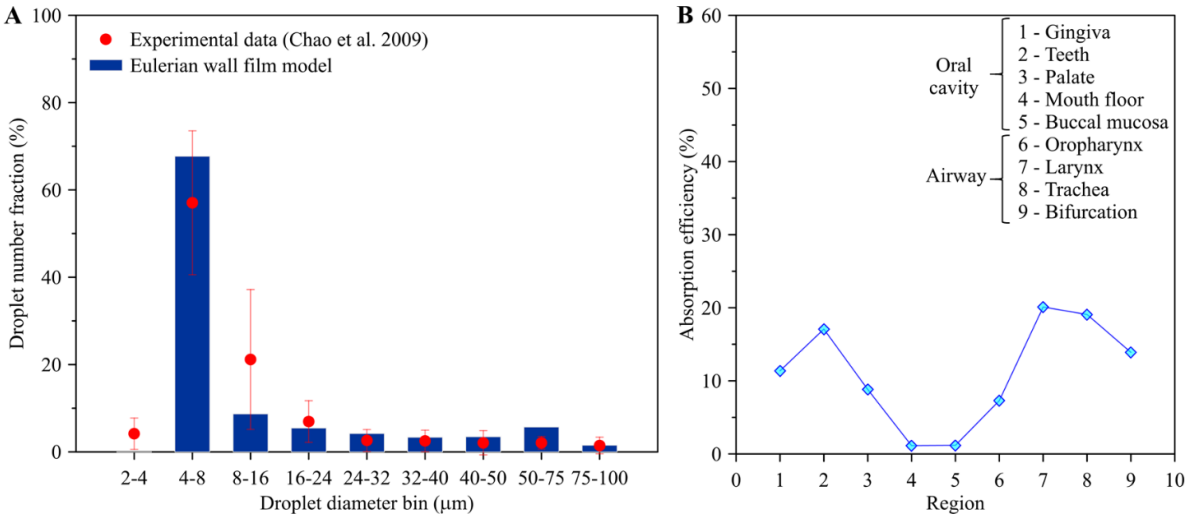

Fig. 4. (A) Size distribution of stripped droplets at the mouth opening validated with experimental data. (B) Absorption efficiency of the droplets per region in the oral-airway model.

We confirmed that germs are primarily transmitted in the environment by droplets sized 4-8 μm. Additionally, proper mimicking of the realistic geometry of the oral airway should be considered in research concerning quantitative droplet generation from humans. The limitations of this study include the unoptimized CSS for balancing the computational cost and accuracy.

ACKNOWLEDGEMENTS

This study was partially funded by Japan Science and Technology (JST), CREST Japan (JP 20356547), and JSPS KAKENHI (JP 22H00237, JP 22K18300, JP 20KK0099, JP 22K14371), Health Labour Sciences Research Grant (JP 21KD2002), and MEXT as "Program for Promoting Researches on the Supercomputer Fugaku" (JPMXP1020210316).

REFERENCES

Chao, C.Y.H. et al. 2009. "Characterization of Expiration Air Jets and Droplet Size Distributions Immediately at the Mouth Opening." *Journal of Aerosol Science* 40(2): 122–33.

Collins, L.M.C., and C. Dawes. 1987. "The Surface Area of the Adult Human Mouth and Thickness of the Salivary Film Covering the Teeth and Oral Mucosa." *Journal of Dental Research* 66(8): 1300–1302.

Dhand, Rajiv, and Jie Li. 2020. "Coughs and Sneezes: Their Role in Transmission of Respiratory Viral Infections, Including SARS-CoV-2." *American Journal of Respiratory and Critical Care Medicine* 202(5): 651–59.

Gupta, J. K., C.-H. Lin, and Q. Chen. 2009. "Flow Dynamics and Characterization of a Cough: Flow Dynamics and Characterization of a Cough." *Indoor Air* 19(6): 517–25.

Jayaweera, Mahesh, Hasini Perera, Buddhika Gunawardana, and Jagath Manatunge. 2020. "Transmission of COVID-19 Virus by Droplets and Aerosols: A Critical Review on the Unresolved Dichotomy." *Environmental Research* 188: 109819.

Matsui, Hirotoshi et al. 1998. "Evidence for Periciliary Liquid Layer Depletion, Not Abnormal Ion Composition, in the Pathogenesis of Cystic Fibrosis Airways Disease." *Cell* 95(7): 1005–15.

Wang, Hongping et al. 2022. "Experimental Study of the Dispersion of Cough-Generated Droplets from a Person Going up- or Downstairs." *AIP Advances* 12(1): 015002.

EFFECT OF WIND SPEED ON PHYSICO-CHEMICAL PROPERTIES OF SEA-SPRAY AEROSOLS

K.A. KIMBLE[1], R.J. LEIBENSPERGER III[2], C. LEE[2], G.B. DEANE[2], M.D. STOKES[2], and K.A. PRATHER[1,2]

[1]Department of Chemistry and Biochemistry, University of California, San Diego. La Jolla, CA, United States of America.

[2]Scripps Institute of Oceanography, University of California, San Diego; La Jolla, CA, United States of America.

Keywords: SEA-SPRAY AEROSOLS, WIND SPEED, MASS SPECTROMETRY

INTRODUCTION

Water covers mostly two-thirds of the earth's surface, and over 96% of it exists in oceans. When ocean surface waves break, particles and gases are ejected into the earth's atmosphere via bursting bubbles. These particles, sea spray aerosols (SSA), can undergo oxidation and photochemical reactions, or participate in heterogenous reactions with other constituents in the atmosphere. Sea spray aerosols can also act as nuclei for ice formation and cloud condensation. The exact role of SSA in climate processes is still poorly understood and necessitates studies in isolated environments under various conditions. In a controlled wind and wave ocean atmosphere simulator, we studied the effect of wind speed on primary sea spray aerosol production. Using an aerosol time-of-flight mass spectrometer (ATOFMS), the size (between 0.1-1.0 μm) and chemical composition of particles were analyzed at the individual level.

METHODS

The Scripps Ocean Atmosphere Research Simulator (SOARS) is a 36-meter-long wind and wave channel with the ability to control wave breaking patterns, wind speed, water temperature, and mesocosm experiments (Figure I). For these studies, multiple wind speeds were varied with different wave breaking patterns to observe the trends in size and composition produced from sea spray in a controlled environment. The vacuum aerodynamic diameter and chemical composition of particles produced in SOARS were measured using an aerosol time-of-flight mass spectrometer (ATOFMS) (Gard et al., 1997; Pratt et al., 2009). To summarize, single particles pass through a Po-210 neutralizer prior to entering an aerodynamic lens that collimates the particle stream (Liu et al., 1995b, 1995a; Zhang et al., 2002, 2004). Particles are then optically detected upon scattering light from two, 532 nm continuous-wave lasers (JDSU, Model 21011871-200). The velocity of each particle is determined based on the time passed between the scattering signals of both lasers. The vacuum aerodynamic diameter is calculated using a calibration with polystyrene latex spheres of known diameters. The ATOFMS used in this study detects particles with diameters between 100–1000 nm with the peak detection efficiency between ~250–500 nm (Pratt et al., 2009). The scattering information is also used to trigger a Q-switched pulsed 266 nm, Nd:YAG laser (CFR200, Lumibird), with laser energy around 1 mJ, a ~0.45 mm spot size, and 8 ns pulse width, that desorbs and ionizes refractory and nonrefractory components of incoming particles. Once ablated and ionized, positive and negative ion mass spectra for each particle are collected using a dual polarity reflectron time-of-flight mass spectrometer. A scanning mobility particle sizer (SMPS) was also used to simultaneously measure the particle size and aerosol mass distributions. The SMPS utilizes an electrostatic classifier and differential mobility analyzer (DMA) (TSI, Model 3082), for particle size selection based on electrical mobility diameter and is followed by a condensation particle counter (CPC, TSI, Model 3787) for particle detection.

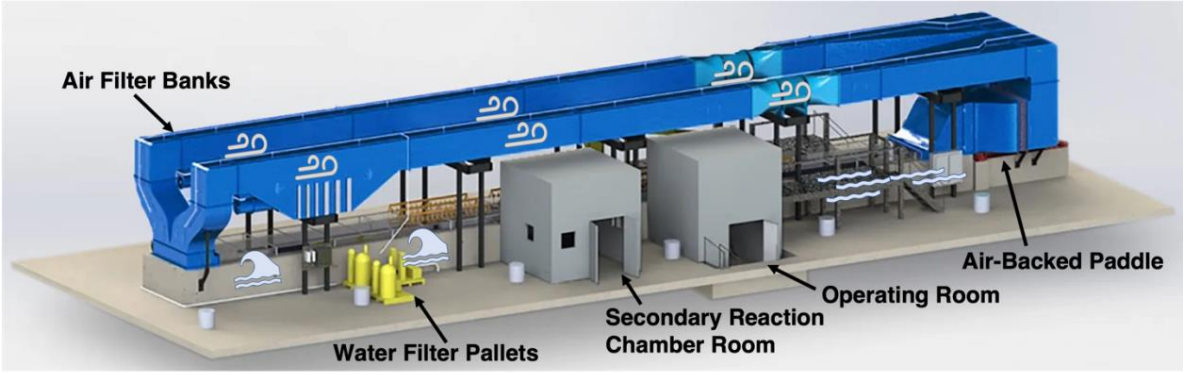

Figure 1. Illustration of the Scripps Ocean Atmosphere Research Simulator (SOARS).

CONCLUSION

We found that at higher wind speeds, there is a greater ejection of salt-dominant particles with compositions like that of the bulk seawater. On the contrast, at lower wind speeds, there is a higher contribution of salt particles with an organic coating, indicating a higher transfer of the sea surface microlayer under this condition. Similar to other field and experimental measurements with the ATOFMS, the fraction of sea-salt dominant particles increased with size while sea-salt particles with an organic coating present remained dominant in the lower sizes. Confirming previous results is the first step in building the chemical complexity of seawater in laboratory-scale simulators, which opens the door for elucidating the specific effects of SSA on climate under various conditions such as wind speed, water temperature, and biological activity.

ACKNOWLEDGEMENTS

This work was supported by NSF through the NSF Center for Aerosol Impacts on Chemistry of the Environment (CAICE), an NSF Funded Center for Chemical Innovation (CHE-1801971). Any opinions, findings, and conclusions or recommendations expressed in this material are those of the author(s) and do not necessarily reflect the views of the National Science Foundation (NSF).

REFERENCES

Gard, E., Mayer, J. E., Morrical, B. D., Dienes, T., Fergenson, D. P., & Prather, K. A. (1997). Real-time analysis of individual atmospheric aerosol particles: Design and performance of a portable ATOFMS. *Analytical Chemistry*, *69*(20), 4083–4091.

Liu, P., Ziemann, P. J., Kittelson, D. B., & McMurry, P. H. (1995a). Generating particle beams of controlled dimensions and divergence: I. Theory of particle motion in aerodynamic lenses and nozzle expansions. *Aerosol Science and Technology*, *22*(3), 293–313.

Liu, P., Ziemann, P. J., Kittelson, D. B., & McMurry, P. H. (1995b). Generating particle beams of controlled dimensions and divergence: II. Experimental evaluation of particle motion in aerodynamic lenses and nozzle expansions. *Aerosol Science and Technology*, *22*(3), 314–324.

Pratt, K. A., Mayer, J. E., Holecek, J. C., Moffet, R. C., Sanchez, R. O., Rebotier, T. P., Furutani, H., Gonin, M., Fuhrer, K., Su, Y., Guazzotti, S., & Prather, K. A. (2009). Development and characterization of an aircraft aerosol time-of-tlight mass spectrometer. *Analytical Chemistry*, *81*(5), 1792–1800.

Zhang, X., Smith, K. A., Worsnop, D. R., Jimenez, J., Jayne, J. T., & Kolb, C. E. (2002). A numerical characterization of particle beam collimation by an aerodynamic lens-nozzle system: Part I. An individual lens or nozzle. *Aerosol Science and Technology*, *36*(5), 617–631.

Zhang, X., Smith, K. A., Worsnop, D. R., Jimenez, J. L., Jayne, J. T., Kolb, C. E., Morris, J., & Davidovits, P. (2004). Numerical characterization of particle beam collimation: Part II integrated aerodynamic-lens-nozzle system. *Aerosol Science and Technology*, *38*(6), 619–638.

WHY ATMOSPHERIC ICE NUCLEATION PARAMETERIZATIONS MATTER: LABORATORY, FIELD, AND MODEL

D. A. KNOPF[1]

[1]*School of Marine and Atmospheric Sciences, Stony Brook University, Stony Brook, NY, USA*

Keywords: ICE-NUCLEATING PARTICLE,

AEROSOL, CLOSURE, MICROPHYSICS

INTRODUCTION

Atmospheric ice crystal formation is recognized as an important cloud microphysical process affecting precipitation and climate by altering cloud structure, albedo and lifetime (Mülmenstädt et al., 2015; Murray and Liu, 2022; Boucher et al., 2013). For example, the greatest variations in climate model predicted equilibrium climate sensitivity can be attributed to the partitioning between supercooled water droplets and ice crystals in extratropical mixed-phase clouds (McCoy et al., 2022). Predicting atmospheric ice nucleation, in general, is one of the grand challenges in the atmospheric sciences for manifold reasons. In particular, ice-nucleating particles (INPs) are physicochemically complex, only a few particles activate as INPs, several different primary ice nucleation pathways exist, ice nucleation proceeds on a microscale and timescales not typically covered by large scale atmospheric models, and finally measurements of INPs and ice crystals in the laboratory and in the field are challenging to make (Demott et al., 2010; Kanji et al., 2017; Knopf et al., 2018; Burrows et al., 2022). Ice nucleation parameterizations are crucial for interpretation and analysis of laboratory and field data and to evaluate our predictive understanding of ice crystal formation in process and large-scale models.

METHODS

Different approaches to best represent ice nucleation measurements exist and can be divided into three general types: i) singular or deterministic descriptions in which specific particles serve as INPs, each possessing a characteristic activation temperature (Vali, 1971); ii) a stochastic description following classical nucleation theory (CNT) which treats nucleation as a random process and, thus, is time dependent (Knopf et al., 2020); iii) hybrid cases, where specific particles are selected in a deterministic manner and then are assigned a time dependence of nucleation (Vali and Snider, 2015). Each of these approaches will yield different interpretations of measured ice nucleation data and result in different predictions of INP number concentrations and, ultimately, ice crystal number concentrations.

DISCUSSION

In this paper, the focus is on immersion freezing, where ice forms on an INP from the supercooled aqueous phase, and deposition ice nucleation, where ice forms on the INP from the supersaturated vapor phase. Homogeneous ice nucleation and pore condensation freezing are also included.

In the first part, the impact of the various parameterizations on interpretation and analysis of laboratory immersion freezing data is discussed (Knopf et al., 2020; Alpert and Knopf, 2016). The importance of considering the stochasticity of nucleation and time dependence is highlighted. Accuracy of determining the INP surface area is shown to be the most limiting factor in unambiguous interpretation of heterogeneous ice nucleation data. Accounting directly for particle surface area measurement uncertainty and variability in specific experiments can explain typically observed variances in freezing temperatures, including cold stage, continuous flow, and chamber instrumentation. It is demonstrated that the water activity criterion can be universally employed to described immersion freezing, deposition

ice nucleation, and homogeneous ice nucleation well into the no man's land region.

In the second part, the results of an aerosol – ice formation closure study are discussed (Knopf et al., 2021). Different immersion freezing parameterizations, derived from the same laboratory experiments, are evaluated for their capability to predict INP number concentrations from ambient aerosol in comparison to measured INP number concentrations. Agreement between predicted and measured INP number concentrations, accounting for measurement and modeling uncertainties, yields "closure". Although, singular and CNT formulations describe equally well the underpinning laboratory measurements, differences in scaling behavior yield drastically different INP number concentrations when applied to the ambient particles.

In the last part, the application of a simplistic 1D aerosol-cloud LES modeling study is discussed to infer the continuing ice crystal formation in long-lived Arctic mixed phase clouds. This simplistic model is based on a well-studied field-observational and LES model case study (Curry et al., 2000; Fridlind et al., 2012). Ice nucleation is initiated by a given aerosol type, e.g., mineral dust, and its size distribution using singular and CNT-based immersion freezing descriptions. Due to its simplicity this model can treat INPs both *i*) diagnostically, i.e., INP number concentrations are derived at each modeling time step according to environmental conditions and *ii*) prognostically, i.e., INPs are coupled to the aerosol population and sources and sinks of INPs are accounted for. The latter implies that aerosol particles and INPs need to be continuously tracked during the simulation. A specific focus is placed on the INP reservoir dynamics, which reflects the INPs that are available to activate as ice crystals. Application of singular- or CNT-based immersion freezing descriptions yield extremely different number concentrations of INPs capable of being activated. This can lead either to a very brief burst of ice crystal formation or to continuous ice crystal formation to be observed over the course of hours.

CONCLUSIONS

The ability to predict ice nucleation depends on the physicochemical characterization of INPs including the particle types, sizes, sources and abundance in the atmosphere. However, the choice of parameterization to represent laboratory and field data crucially influences predictive capability. Considering that typical INP measurements in the laboratory and field do not reflect cloud conditions with regard to updraft velocities, ice nucleation activation times, supersaturation and particle size distributions, translating ice nucleation parameterizations to atmospheric conditions, especially when using conceptual or empirical descriptions not based in theory, has to be evaluated. Closure studies that apply laboratory derived theoretical understanding of ice nucleation to field measurements of INPs are a possible path forward to assess such parameterizations (Knopf et al., 2021; Burrows et al., 2022).

When modeling cloud structure and evolution, the INP reservoir should be treated prognostically, coupled to the underlying aerosol population considering sources and sinks of INPs. This necessitates the tracking of INPs in models posing a computational challenge, especially in large scale models. By definition, singular and deterministic freezing descriptions are non-stochastic and as such the specific particles in the aerosol population acting as INPs have to be individually tracked, increasing memory and computational demand. In contrast, CNT-based descriptions invoking a rate-based, stochastic formulation are less computationally demanding since they do not need to store the individual particles acting as INPs.

Recent years have seen numerous laboratory and field studies identifying and characterizing INPs that also suggest various ways to parameterize the ice nucleation data for model application. However, fewer efforts have been initiated to carefully assess how these parameterizations impact prediction of INPs under different cloud conditions. The effect of ice nucleation parameterizations on interpretation and prediction of INPs in laboratory settings, field measurements, and modeling studies highlighted in this paper will yield greater accuracy and understanding of formation and evolution of ice in the atmosphere.

ACKNOWLEDGEMENTS

This work was supported by the U.S. Department of Energy (DOE), Office of Science, Office of Biological and Environmental Research (OBER), Climate and Environmental Sciences Division (CESD), Awards DE-SC0020006 and DE-SC0021034.

REFERENCES

Alpert, P. A. and Knopf, D. A.: Analysis of isothermal and cooling-rate-dependent immersion freezing by a unifying stochastic ice nucleation model, *Atmos. Chem. Phys.*, 16, 2083-2107, 10.5194/acp-16-2083-2016, 2016.

Boucher, O., Randall, D., Artaxo, P., Bretherton, C., Feingold, G., Forster, P., Kerminen, V.-M., Kondo, Y., Liao, H., Lohmann, U., Rasch, P., Satheesh, S. K., Sherwood, S., Stevens, B., and Zhang, X. Y.: Clouds and Aerosols, in: *Climate Change 2013: The Physical Science Basis. Contribution of Working Group I to the Fifth Assessment Report of the Intergovernmental Panel on Climate Change*, edited by: Stocker, T. F., Qin, D., Plattner, G.-K., Tignor, M., Allen, S. K., Boschung, J., Nauels, A., Xia, Y., Bex, V., and Midgley, P. M., Cambridge University Press, Cambridge, United Kingdom and New York, NY, USA, 2013.

Burrows, S. M., McCluskey, C. S., Cornwell, G., Steinke, I., Zhang, K., Zhao, B., Zawadowicz, M., Raman, A., Kulkarni, G., China, S., Zelenyuk, A., and DeMott, P. J.: Ice-Nucleating Particles That Impact Clouds and Climate: Observational and Modeling Research Needs, *Rev. Geophys.*, 60, 45, 10.1029/2021rg000745, 2022.

Curry, J. A., Hobbs, P. V., King, M. D., Randall, D. A., and Minnis, P.: FIRE arctic clouds experiment, *Bull. Amer. Meteorol. Soc.*, 81, 5-29, 2000.

DeMott, P. J., Prenni, A. J., Liu, X., Kreidenweis, S. M., Petters, M. D., Twohy, C. H., Richardson, M. S., Eidhammer, T., and Rogers, D. C.: Predicting global atmospheric ice nuclei distributions and their impacts on climate, *Proc. Natl. Acad. Sci. U. S. A.*, 107, 11217-11222, 10.1073/pnas.0910818107, 2010.

Fridlind, A. M., van Diedenhoven, B., Ackerman, A. S., Avramov, A., Mrowiec, A., Morrison, H., Zuidema, P., and Shupe, M. D.: A FIRE-ACE/SHEBA Case Study of Mixed-Phase Arctic Boundary Layer Clouds: Entrainment Rate Limitations on Rapid Primary Ice Nucleation Processes, *J. Atmos. Sci.*, 69, 365-389, 10.1175/jas-d-11-052.1, 2012.

Kanji, Z. A., Ladino, L. A., Wex, H., Boose, Y., Burkert-Kohn, M., Cziczo, D. J., and Krämer, M.: Overview of Ice Nucleating Particles, in: *Ice Formation and Evolution in Clouds and Precipitation: Measurement and Modeling Challenges*, Meteorological Monographs, American Meteorological Society, 1.1-1.33, DOI: 10.1175/AMSMONOGRAPHS-D-16-0006.1, 2017.

Knopf, D. A., Alpert, P. A., and Wang, B.: The Role of Organic Aerosol in Atmospheric Ice Nucleation: A Review, *ACS Earth Space Chem.*, 2, 168–202, 10.1021/acsearthspacechem.7b00120, 2018.

Knopf, D. A., Alpert, P. A., Zipori, A., Reicher, N., and Rudich, Y.: Stochastic nucleation processes and substrate abundance explain time-dependent freezing in supercooled droplets, *npj Clim. Atmos. Sci.*, 3, 1-9, 10.1038/s41612-020-0106-4, 2020.

Knopf, D. A., Barry, K. R., Brubaker, T. A., Jahl, L. G., Jankowski, K. A., Li, J., Lu, Y., Monroe, L. W., Moore, K. A., Rivera-Adorno, F. A., Sauceda, K. A., Shi, Y., Tomlin, J. M., Vepuri, H. S. K., Wang, P., Lata, N. N., Levin, E. J. T., Creamean, J. M., Hill, T. C. J., China, S., Alpert, P. A., Moffet, R. C., Hiranuma, N., Sullivan, R. C., Fridlind, A. M., West, M., Laskin, A., DeMott, P. J., and Liu, X.: Aerosol–Ice Formation Closure: A Southern Great Plains Field Campaign, *B. Am. Meteorol. Soc.*, 102, E1952–E1971 10.1175/BAMS-D-20-0151.1, 2021.

McCoy, D. T., Field, P., Frazer, M. E., Zelinka, M. D., Elsaesser, G. S., Mulmenstadt, J., Tan, I., Myers, T. A., and Lebo, Z. J.: Extratropical Shortwave Cloud Feedbacks in the Context of the Global Circulation and Hydrological Cycle, *Geophys. Res. Lett.*, 49, 11, 10.1029/2021gl097154, 2022.

Mülmenstädt, J., Sourdeval, O., Delanoe, J., and Quaas, J.: Frequency of occurrence of rain from liquid-, mixed-, and ice-phase clouds derived from A-Train satellite retrievals, *Geophys. Res. Lett.*, 42, 6502-6509, 10.1002/2015gl064604, 2015.

Murray, B. J. and Liu, X.: Ice-nucleating particles and their effects on clouds and radiation, in: *Aerosols and Climate*, edited by: Carslaw, K. S., Elsevier, Amsterdam, NEtherlands, 619-649, 10.1016/B978-0-12-819766-0.00014-6, 2022.

Vali, G.: Quantitative evaluation of experimental results on heterogeneous freezing nucleation of supercooled liquids, *J. Atmos. Sci.*, 28, 402-409, 1971.

Vali, G. and Snider, J. R.: Time-dependent freezing rate parcel model, *Atmos. Chem. Phys.*, 15, 2071-2079, 10.5194/acp-15-2071-2015, 2015.

INTRODUCTION TO NPF RESEARCH IN CHINA BY UNIVERSITY OF HELSINKI

J. KUJANSUU[1,2] C. YAN[1,2,3], T. PETÄJÄ[1], A. DING[3],V.-M. KERMINEN[1] and M. KULMALA[1,2,3]

[1]*Institute for Atmospheric and Earth System Research (INAR), University of Helsinki, Helsinki, 00560, Finland*

[2]*Aerosol and Haze Laboratory, Beijing Advanced Innovation Center for Soft Matter Science and Engineering, Beijing University of Chemical Technology, Beijing, 100029, China*

[3] *Joint International research Laboratory of Atmospheric and Earth System Research, School of Atmospheric Sciences, Nanjing University, Nanjing, China.*

Keywords: NEW PARTICLE FORMATION, CHINA, BEIJING, NANJING

INTRODUCTION

New particle formation (NPF) has been observed in China since the 1990s and continues to be a major concern due to its potential effects on human health. Additionally, the presence of aerosol particles can also play a role in the formation of new particles. Studies have indicated that the formation of new particles in China is largely driven by photochemical processes, which are associated with increased levels of nitrogen oxides and volatile organic compounds (VOCs). These particles are formed through the condensation and coagulation of VOCs, nitrogen oxides (NOx), and sulfur dioxide (SO_2). Once formed, these particles can become a major source of air pollution in China.

The Chinese government has taken a number of steps to address NPF. These include the adoption of stricter emissions standards, the promotion of cleaner energy sources such as natural gas, and the introduction of air pollution control measures such as the "10+10" plan. This plan requires 10 of the most polluted cities to reduce their emissions by 10 percent in the next five years. To achieve these goals, more research is needed to better understand the processes involved in new particle formation in China, and to develop more effective strategies for mitigating its impacts.

NPF is a process by which atmospheric aerosols form from precursor gases in the atmosphere. In recent years, new particle formation has been a major focus of atmospheric research in China. Studies have found that NPF events occur frequently in China, especially in the northern parts of the country. The sources of precursor gases for NPF in China include both anthropogenic sources, such as combustion-related emissions, and natural sources, such as biogenic volatile organic compounds. Research has found that NPF events are closely related to air pollution, leading to increases in concentrations of aerosols and secondary pollutants that are closely linked to the occurrence of haze and smog, as both are caused by the formation of aerosols. Furthermore, NPF events can affect the regional climate, influencing temperature, precipitation, and visibility.

NPF in cities such as Beijing, where tiny particles of aerosols, such as sulfate, nitrate, and ammonium, form from the condensation of gas-phase precursors, such as sulfur dioxide and nitrogen oxides. These particles then grow in size via a process known as coagulation, forming aerosols that can affect air quality. The particles can also act as condensation nuclei for clouds, impacting atmospheric chemistry and sunlight.

In Beijing, NPF occurs when precursor gases such as sulfur dioxide (SO_2), nitrogen oxides (NOx), ozone (O_3), and volatile organic compounds (VOCs) react in the atmosphere and form aerosol particles. This is often a result of anthropogenic activities such as the burning of fossil fuels, industrial activities, and vehicle exhaust. These reactions can create a variety of new particles, including sulfates, nitrates, and ammonium. These particles can be transported long distances and can cause a variety of health problems. Long-term exposure to these particles can lead to respiratory and cardiovascular problems, as well as other health issues. NPF is especially problematic in Beijing due to its large population, high levels of air pollution, and the

prevalence of coal burning. As NPF continues to be studied, efforts are being made to reduce its prevalence in Beijing and other areas. These efforts include reducing emissions from coal burning, promoting clean transportation solutions, and increasing the use of renewable energy sources.

RESULTS AND CONCLUSIONS

In Nanjing, NPF has been studied extensively in The Joint International Research Laboratory of Atmospheric and Earth System Sciences between Nanjing University and University of Helsinki (JirLATEST). Studies have found that NPF is enhanced in Nanjing due to the high levels of sulfur dioxide, nitrogen oxides, and volatile organic compounds from these sources (Nie *et al*., 2022). Finally, NPF can be influenced by meteorological conditions such as wind speed and air temperature, which can vary depending on the season.

To resolve air quality issues in China, INAR have conducted intensive and comprehensive measurements in Beijing University of Chemical Technology West Campus in close collaboration with Tsinghua University, Fudan University, and Nanjing University of Information Science and Technology. Based on our comprehensive observations, we have been able to demonstrate the crucial role of NPF in haze formation. We have also shown that 80–90 % of the aerosol mass (PM2.5) was formed via atmospheric reactions during the haze days and over 65 % of the number concentration of haze particles resulted from NPF. Our findings suggest that in practice almost all present-day haze episodes in Beijing originate from NPF, mainly since the direct emissions of primary particles in Beijing have considerably decreased during the recent years.

It has been shown that the acid-base clustering involving sulfuric acid, amines and ammonia synergistically drives NPF in Beijing (Yan *et al*., 2021), especially when the amine concentration is not high enough and NH3 is abundant. On the other hand, in Shanghai the main compounds initiating NPF are sulfuric acid and amines (Yao *et al*., 2018). This means that the detailed clustering mechanisms in the two corners of the gigacity, Beijing and Shanghai, seem not identical, mainly because amine and ammonia concentrations have a spatial variation inside the gigacity. On one hand, based on ambient measurements in Beijing and a roadside test in Nanjing, traffic exhaust was identified as a source of amines and ammonia in urban environments. On the other hand, when the COVID-19 lockdown policy was imposed, we did not observe significant changes in a NPF mechanism in Beijing, suggesting that atmospheric abundances of amines and ammonia are not solely associated with traffic exhaust (Yan *et al*., 2022).

REFERENCES

Nie, Wei & Yan, Chao & Huang, Dan & Wang, Zhe & Liu, Yuliang & Qiao, Xiaohui & Guo, Yishuo & Tian, Linhui & Zheng, Penggang & Xu, Zhengning & Li, Yuanyuan & Xu, Zheng & Qi, Ximeng & Sun, Peng & Wang, Jiaping & Zheng, Feixue & Li, Xiaoxiao & Yin, Rujing & Dallenbach, Kaspar & Ding, Aijun. (2022). Secondary organic aerosol formed by condensing anthropogenic vapours over China's megacities. Nature Geoscience. 15. 1-7. 10.1038/s41561-022-00922-5.

Yan, C., Yin, R., Lu, Y., Dada, L., Yang, D., Fu, Y., et al. (2021). The synergistic role of sulfuric acid, bases, and oxidized organics governing new-particle formation in Beijing. Geophysical Research Letters, 48, e2020GL091944. https://doi.org/10.1029/2020GL091944.

Yan, C., Shen, Y., Stolzenburg, D., Dada, L., Qi, X., Hakala, S., Sundström, A.-M., Guo, Y., Lipponen, A., Kokkonen, T. V., Kontkanen, J., Cai, R., Cai, J., Chan, T., Chen, L., Chu, B., Deng, C., Du, W., Fan, X., He, X.-C., Kangasluoma, J., Kujansuu, J., Kurppa, M., Li, C., Li, Y., Lin, Z., Liu, Y., Liu, Y., Lu, Y., Nie, W., Pulliainen, J., Qiao, X., Wang, Y., Wen, Y., Wu, Y., Yang, G., Yao, L., Yin, R., Zhang, G., Zhang, S., Zheng, F., Zhou, Y., Arola, A., Tamminen, J., Paasonen, P., Sun, Y., Wang, L., Donahue, N. M., Liu, Y., Bianchi, F., Daellenbach, K. R., Worsnop, D. R., Kerminen, V.-M., Petäjä, T., Ding, A., Jiang, J., and Kulmala, M. (2022) The effect of COVID-19 restrictions on atmospheric new particle formation in Beijing, Atmos. Chem. Phys., 22, 12207–12220, https://doi.org/10.5194/acp-22-12207-2022.

Yao , L , Garmash , O , Bianchi , F , Zheng , J , Yan , C , Kontkanen , J , Junninen , H , Mazon , S B , Ehn , M , Paasonen , P , Sipilä , M , Wang , M , Wang , X , Xiao , S , Chen , H, Lu , Y , Zhang , B , Wang , D , Fu , Q , Geng , F , Li , L , Wang , H , Qiao , L , Yang , X , Chen , J , Kerminen , V-M , Petäjä , T , Worsnop , D R , Kulmala , M & Wang , L. (2018). Atmospheric new particle formation from sulfuric acid and amines in a Chinese megacity ' Science , vol. 361 , no. 6399 , pp. 278-281 . https://doi.org/10.1126/science.aao4839.

ON THE RECENT PROGRESS OF UNDERSTANDING OF ATMOSPHERIC NEW PARTICLE FORMATION

M. KULMALA[1,2,3], R. CAI[1], C. YAN[1,2,3], D. STOLZENBURG[1,4], L. DADA[1,5.], T. KOKKONEN[1], W. NIE[3], E. EZHOVA[1], J. KANGASLUOMA[1], K. LEHTIPALO[1], F. BIANCHI[1], A.-M. SUNDSTRÖM[6], T. PETÄJÄ[1], D. WORSNOP[1], U. PÖSCHL[7], H. SU[7], J. TAMMINEN[6], I. SALMA[8], H. JUNNINEN[9], A. DING[3], Y. CHENG[7] and V.-M. KERMINEN[1]

[1] Institute for Atmospheric and Earth System Research/Physics, Faculty of Science, University of Helsinki, 00014 Helsinki, Finland
[2] Aerosol and Haze Laboratory, Beijing Advanced Innovation Center for Soft Matter Science and Engineering, Beijing University of Chemical Technology, Beijing, China
[3] Joint International research Laboratory of Atmospheric and Earth System Research, School of Atmospheric Sciences, Nanjing University, Nanjing, China.
[4] Institut für Materialchemie, Technische Universität Wien, 1060 Vienna, Austria
[5] Laboratory of Atmospheric Chemistry, Paul Scherrer Institute, 5232 Villigen, Switzerland
[6] Finnish Meteorological Institute, Helsinki, Finland
[7] Max Planck Institute for Chemistry, Mainz, Germany
[8] Institute of Chemistry, Eötvös Loránd University, Budapest, Hungary
[9] Institute of Physics, University of Tartu, Estonia

Keywords: ATMOSPHERIC CLUSTERING, NEW PARTICLE FORMATION, FORMATION AND GROWTH RATES

INTRODUCTION

Besides directly emitted primary aerosol particles, large fractions of atmospheric aerosols relevant to both air quality and climate are produced via new particle formation (NPF; Kerminen et al., 2018; Chu et al., 2019; Kulmala et al., 2021b). Atmospheric NPF, together with secondary formation of particulate matter (secondary aerosol formation), modify the number concentration, size distribution, chemical composition and mass loading of atmospheric aerosol populations. Kulmala et al. (2021b) showed that NPF and secondary aerosol formation contribute to over 2/3 of the haze particle number load and over 80% of the corresponding mass load in Beijing. Physically, the influences of atmospheric NPF and secondary aerosol formation depend on particle formation rates and on rates at which newly formed particles grow to larger sizes (Kulmala et al., 2017).

Multiphase chemistry associated with particle growth is thus expected to provide explanation for the limited variability in the growth rates. Recently, Zheng et al. (2020) found that aerosol acidity, which regulates multiphase chemistry of atmospheric particles in many ways, is strongly buffered through gas-particle partitioning of ammonia. Moreover, different multiphase processes that lead to aerosol formation and growth at high ionic strengths and in complex solutions were found to proceed either much faster or slower than previously expected from the lab studies, and the role of nano-size effect and phase state in the initial particle growth is also still unknown (Cheng et al., 2016).

METHODS

We are combining the following tools to be able to find out physical and chemical mechanisms of atmospheric NPF: i) targeted laboratory experiments, ii) comprehensive *in situ* observations including supersites in the Chinese gigacity (see Kulmala et al., 2021a), iii) comprehensive vertical observations using aircrafts, tall towers, tethered-airships and ground-based remote sensing, iv) satellite remote sensing and v) multi-scale modelling and model development.

Understanding chemistry and physics at the 2–25 nm size range for atmospheric aerosol particles and sub 2 nm atmospheric clusters are grand challenges for both fundamental and applied sciences. Thus, we have developed and will further develop novel methodologies aiming at overcoming these grand challenges, including:

- direct measurements of the evolution of aerosol compositions at the 2–25 nm size range,
- direct measurements of kinetics and thermodynamic constants for atmospheric relevant aerosols systems, especially the systems of extremely high ionic strength,
- direct measurements of surface reactions/processes, and
- molecular-dynamic model simulations of atmospheric relevant clusters and nanoparticles.

We are in process developing several other tools

- establishment of continuous, comprehensive measurements networks for gigacity observations, including ACTRIS (Aerosols, Clouds, and TRace Gases Infrastructure) instrumentation,
- development and integration of multiscale modelling from process models (NPF, multiphase chemistry) to boundary layer and regional models of air quality, and
- integration of *in-situ* observations and remote sensing (tailored and novel satellite data products) to derive parameterizations for proxies based on process understanding, and to obtain a regional and potentially global coverage of favorable conditions for NPF, secondary aerosol, and haze formation.

RESULTS AND CONCLUSIONS

Here, we summarize our latest findings on atmospheric new particle formation (NPF) based on atmospheric observations and model simulations. Our first investigation was a closure study on sub-6 nm atmospheric aerosol particles and clusters, which showed that present observations are able to detect a major fraction of existing atmospheric clusters (Kulmala et al. 2022a). Our second finding, based on long-term measurements in four very different environments, was that atmospheric NPF tends to occur also on days characterized traditionally as non-event days (days with no observed NPF), with typical particle formation rates ranging between about 2 and 20 % of those on traditional NPF event days (Kulmala et al. 2022b). We termed this phenomenon “quiet NPF” and showed that it may have a significant contribution to the production of secondary particles in the atmosphere. Thirdly, we investigated the growth of newly-formed particles into sizes relevant to climate and air quality using box model simulations that were constrained with atmospheric observations in two very different environments: 1) Beijing, a polluted megacity in China, and 2) SMEAR II station, a boreal forest site in Finland. Our simulations for Beijing showed that NPF is capable of giving large contributions of haze particle mass and number concentrations (Kulmala et al. 2022c). The results indicate that reducing primary particle emissions may not decrease PM pollution effectively in heavily polluted environments without simultaneous emission reductions for precursor gases responsible for NPF and subsequent particle growth. At SMEAR II, we used simulations to investigate the role of NPF in the Continental Biosphere-Atmosphere-Cloud-Climate (COBACC) feedback mechanism (Kulmala et al. 2023). We found that outside the late autumn and winter periods when NPF events tend to be rare at SMEAR II, NPF gives a dominant contribution to both condensation sink and cloud condensation nuclei concentration – the two most relevant quantities in the COBACC feedback mechanism. We estimated that the same conclusion is likely to hold over large regions in the boreal forest zone, as it has been demonstrated that the oxidized products of biological volatile organics (VOCs) sustain the strong particle formation and condensational growth that contributes about 90% of the cloud condensational nucleus (CCN) at high altitude over Amazon basin (Liu et al., 2023).. As a side product of our observations, we found surprisingly low variability in growth rates of newly formed particles in both Beijing and SMEAR II. This points toward a potentially important role of multiphase reactions causing the bulk growth of newly formed atmospheric particles – a phenomenon that needs to be investigated in more detail in the future.

ACKNOWLEDGEMENTS

This work was supported by the Wihuri Foundation, ACCC Flagship funded by the Academy of Finland grant numbers 337549 and 337552 and the EMME-CARE project, which received funding from the

European Union's Horizon 2020 Research and Innovation Programme, under Grant Agreement No. 856612 and the Cyprus Government. European Regional Development Fund (project MOBTT42), Estonian Research Council (project PRG714)

REFERENCES

Chu, B., Kerminen, V.-M., Bianchi, F., Yan, C., Petäjä, T., and Kulmala, M.: Atmospheric new particle formation in China, Atmos. Chem. Phys., 19, 115–138, 2019.

Cheng, Y., Zheng, G., Wei, C., Mu, Q., Zheng, B., Wang, Z., Gao, M., Zhang, Q., He, K., Carmichael, G., Pöschl, U., and Su, H.: Reactive nitrogen chemistry in aerosol water as a source of sulfate during haze events in China, Sci. Adv., 2, https://doi.org/10.1126/sciadv.1601530, 2016.

Kerminen, V.-M., Chen, X., Vakkari, V., Petäjä, T., Kulmala, M., and Bianchi, F.: Atmospheric new particle formation and growth: review of field observations, Environ. Res. Lett., 13, 103003, https://doi.org/10.1088/1748-9326/aadf3c, 2018.

Kulmala, M., Kerminen, V.-M., Petäjä, T., Ding, A., and Wang, L.: Atmospheric gas-to-particle conversion: why NPF events are observed in megacities?, Faraday Discuss., 200, 271–288, https://doi.org/10.1039/C6FD00257A, 2017.

Kulmala, M., Kokkonen, T. V., Pekkanen, J., Paatero, S., Petäjä, T., Kerminen, V.-M., and Ding, A.: Opinion: Gigacity – a source of problems or the new way to sustainable development, Atmos. Chem. Phys., 21, 8313–8322, https://doi.org/10.5194/acp-21-8313-2021, 2021a.

Kulmala, M., Dada, L., Daellenbach, K. R., Yan, C., Stolzenburg, D., Kontkanen, J., Ezhova, E., Hakala, S., Tuovinen, S., Kokkonen, T. V., Kurppa, M., Cai, R., Zhou, Y., Yin, R., Baalbaki, R., Chan, T., Chu, B., Deng, C., Fu, Y., Ge, M., He, H., Heikkinen, L., Junninen, H., Liu, Y., Lu, Y., Nie, W., Rusanen, A., Vakkari, V., Wang, Y., Yang, G., Yao, L., Zheng, J., Kujansuu, J., Kangasluoma, J., Petäjä, T., Paasonen, P., Järvi, L., Worsnop, D., Ding, A., Liu, Y., Wang, L., Jiang, J., Bianchi, F., and Kerminen, V.-M.: Is reducing new particle formation a plausible solution to mitigate particulate air pollution in Beijing and other Chinese megacities?, Faraday Discuss., 226, 334–347, https://doi.org/10.1039/D0FD00078G, 2021b.

Kulmala M., Stolzenburg D., Dada L., Cai R., Kontkanen J., Yan C., Kangasluoma J., Ahonen L. R., Gonzalez-Carracedo L., Sulo J., Tuovinen S., Deng C., Li Y., Lehtipalo K., Lehtinen K. E. J., Petäjä T., Winkler P. M., Jiang J. and Kerminen V.-M. (2022a) Towards a concentration closure of sub-6 nm aerosol particles and sub-3 nm atmospheric clusters. J. Aerosol Sci., 159, 105878,

Kulmala M., Junninen H., Dada L., Salma I., Weidinger T., Thén W., Vörösmarty M., Komsaare K., Stolzenburg D., Cai R., Yan C., Li X., Deng C., Jiang J., Petäjä T., Nieminen T. and Kerminen V.-M. (2022b) Quiet New Particle Formation in the Atmosphere. Front. Environ. Sci., 10, 912385, doi: 10.3389/fenvs.2022.912385.

Kulmala M., Cai R., Stolzenburg D., Zhou Y., Dada L., Guo Y., Yan C., Petäjä T., Jiang J. and Kerminen V.-M. (2022c) The contribution of new particle formation and subsequent growth to haze formation. Environ. Sci.: Atmos., 2, 352-361.

Kulmala M., Cai R., Ezhova E., Deng C., Stolzenburg D., Dada L., Guo Y., Yan C., Peräkylä O., Lintunen A., Nieminen T., Kokkonen T. V., Sarnela N., Petäjä T. and Kerminne V.-M. (2023) Direct link between the characteristics of atmospheric new particle formation and Continental Biosphere-Atmosphere-Cloud-Climate (COBACC) feedback loop. Boreal. Env. Res., 28, 1-13.

Liu, Y., Su, H., Wang, S., Wei, C., Tao, W., Pöhlker, M. L., Pöhlker, C., Holanda, B. A., Krüger, O. O., Hoffmann, T., Wendisch, M., Artaxo, P., Pöschl, U., Andreae, M. O., and Cheng, Y.: Strong particle production and condensational growth in the upper troposphere sustained by biogenic VOCs from the canopy of the Amazon Basin, Atmos. Chem. Phys., 23, 251–272, https://doi.org/10.5194/acp-23-251-2023, 2023.

Zheng, G., Su, H., Wang, S., Andreae, M. O., Pöschl, U., and Cheng, Y.: Multiphase buffer theory explains contrasts in atmospheric aerosol acidity, Science, 369, 1374–1377, https://doi.org/10.1126/science.aba3719, 2020.

Carbonaceous Aerosol Analysis Tool CAAT Software package for data analysis

Klemen Kunstelj[1], Matej Zemljak[1], Matic Ivančič[1], Asta Gregorič[1,2] and Martin Rigler[1]

[1]Aerosol d.o.o., SI-1000 Ljubljana, Slovenia
[2]School of Environmental Sciences, University of Nova Gorica, SI-5000 Nova Gorica, Slovenia
Keywords: Data analysis, Black Carbon, Brown Carbon, Carbonaceous aerosols
Presenting author email: klemen.kunstelj@aerosol.eu

Introduction

Carbonaceous aerosols are usually the most significant contributor to fine particulate matter (PM2.5). They are frequently separated into organic carbon (OC) and elemental carbon (EC) based on their volatility using thermal-optical methods.

The Aethalometer model AE33 collects aerosol particles continuously by drawing the aerosol-laden air stream through a spot on the filter tape. It analyzes the aerosol by measuring light transmission at seven wavelengths through one portion of the filter tape containing the sample versus the transmission through an unloaded part of the filter tape acting as a reference area. The Magee Scientific Total Carbon Analyzer, Model TCA08, is a newly developed scientific instrument that measures the Total Carbon Content ("TC") of suspended aerosol particles in near real-time using a simplified thermal method (Rigler et al., 2020).

The combination of Total Carbon Analyzer TCA08 and the Magee Scientific Aethalometer® model AE33 provides a novel approach for measuring TC, eBC, OC, EC, Brown Carbon content of suspended aerosol particles in near-real-time with high-time resolution.

Abstract Review

The CAAT abbreviation stands for Carbonaceous Aerosol Analysis Tool and is a software tool for analyzing data from the AE33 Aethalometer® and the TCA08 Total Carbon Analyzer.

Its main progression tasks are as follows: Import, Validation and Analysis procedures, such as diurnal profiles, Time averages, Absorption coefficient, Angstrom exponent, Attenuation, Source Apportionment, concentration determination of some most relevant carbonaceous aerosol species (Total Carbon, Elemental Carbon, Organic Carbon, Black and Brown Carbon).

With this work, we want to show the importance and capabilities of the newly developed Analytical software to indicate and forecast particular trends and seasonal variations of concentrations of the specific carbonaceous aerosols.

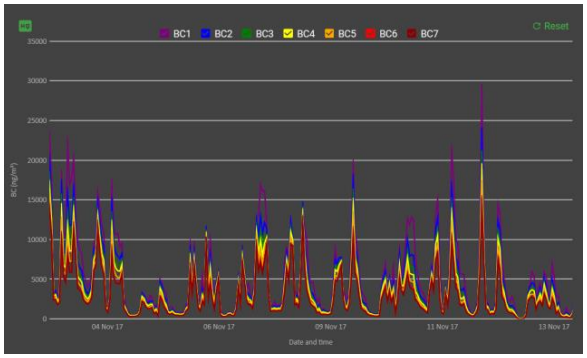

Figure 1 Example of the data analyzed with CAAT Software.

References

Sandradewi, J., Prévôt, A. S. H., Szidat, S., Perron, N., Alfarra, M. R., Lanz, V. A., Weingartner, E., and Baltensperger, U. Environ. Sci. Technol., 42, 3316-3323, 10.1021/es702253m, 2008.

Drinovec L. et al. (2015), AMT, 8, 1965-1979.

Rigler, M., et al.: 13, 4333–4351, https://doi.org/10.5194/amt-13-4333-2020, 2020.

VOLATILITY MEASUREMENTS OF INDIVIDUAL COMPONENTS IN ORGANIC AEROSOL MIXTURES

C. WEST, Y. HSU, K. MACFEELY, S. HUSTON, B. ARIDJIS-OLIVOS, A. MORALES, A. LASKIN

Department of Chemistry, Purdue University, West Lafayette, IN, USA.

Keywords: organic aerosol, volatility, high-resolution mass spectrometry, direct analysis in real time ionization.

INTRODUCTION

Primary and secondary organic aerosols (POA and SOA) comprise anywhere from 20% to 90% of atmospheric particulate matter (Hallquist *et al,* 2009). As they age in the atmosphere, POA and SOA undergo transformations through atmospheric multi-phase reaction chemistry such as oxidation, fragmentation, oligomerization, gas-to-particle partitioning, and cloud processing, which modify their composition and eventually blur original identity of aged organic aerosol (OA). Quantitative assessment of gas-particle equilibrium of OA components is critical to understand formation, growth, distribution, and evolution of the OA composition in the atmosphere. In this work, we present a novel ambient pressure measurement platform developed and tested for untargeted screening of components of complex OA mixtures, followed by targeted chemical speciation of components with identified chemical composition, and assessment of their physicochemical properties such as vapor pressure and heats of sublimation.

METHODS

Presented approach of untargeted OA characterization employes temperature programmed desorption (TPD) experiments coupled to 'direct analysis in real time' (DART) ionization technique (Cody *et al*, 2005, 2020) and high-resolution mass spectrometry (HRMS). In these experiments, OA laden samples are placed on a heating stage subjected to the TPD linear ramp from room temperature to 600 °C. Fumes of the evaporated sample components are directed into a T-shaped glass junction where they are ionized by the flow of metastable He ions from the DART source, followed by detection using the Q-ExactiveTM Orbitrap HRMS (Nizkorodov *et al*, 2011). Progression of the TPD-DART-HRMS spectra is acquired and extracted ion thermogram EIT records are used to infer composition and quantify volatility properties of untargeted individual species detected within complex OA sample.

CONCLUSIONS

We demonstrated successful applications of the TPD-DART-HRMS platform for analysis of selected standards, i.e. organic compounds with known ambient vapor pressure (p_0, atm; or C* μg m^{-3}) and apparent heat of sublimation (ΔH_{sub}). Figure 1 illustrates excellent agreement of our experimentally derived results with the literature tabulated values for the tested standards.

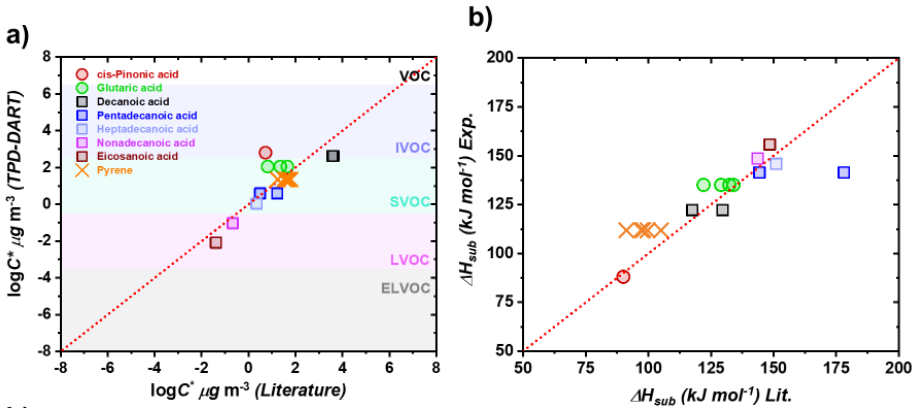

Figure 1. Correlation plot of our experimental TPD-DART-HRMS data vs. literature reported values of a) *logC** and b) ΔH_{sub} for selected organic standards tested in our study. Red dashed line indicates 1:1 correlation.

We extended these experiments to interrogate individual organic components in complex samples of SOA generated in the laboratory-controlled ozonolysis of α-pinene, limonene and ocimene (PSOA, LSOA and OSOA). The prominent species of interest within SOA mixtures were distinguished based on their accurate mass measurements, and their TPD profiles were used to experimentally determine their apparent flash temperatures (T_{flash}) and ΔH_{sub} values. Then, based on the experimental values of T_{flash} and ΔH_{sub}, and applying Clausius-Clapeyron equation, we were able to calculate gas-phase partial pressures (p_T) of the identified species for the range of experimental temperatures T. Figure 2 illustrates correlation plot between p_{298K} values of OA components determined from the presented untargeted TPD-DART-HRMS measurements versus the 'Molecular Corridors (MC)' model (Li *et al*, 2016) calculations of p_{298K}, which showed overall good consistency between our experimental results and the MC modeled values. However, the observed deviation 1:1 correlation line suggested overprediction of the equilibrium vapor pressures by modeling results, which is more pronounced for species with larger molecular weight.

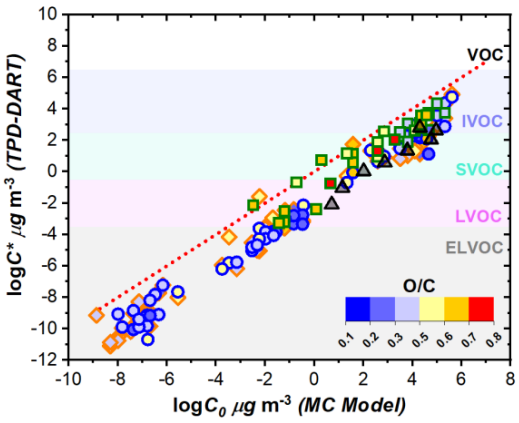

Figure 2. Correlation plot of *logC** measured in our experiments versus values predicted by MC model for constituents in PSOA (orange diamonds), LSOA (blue circles), OSOA (olive squares). Areas inside the symbols are color-coded with respect to O/C ratio. Grey triangles correspond to the organic standards used in this work. Red dashed line indicates 1:1 correlation.

Presented results indicate very promising applicability of the reported TPD-DART-HRMS method for untargeted analysis of organic molecules in OA and other environmental mixtures, enabling rapid detection and quantification of organic pollutants in the real-world condensed-phase samples with no sample preparation.

ACKNOWLEDGEMENTS

The work was partially supported by the U.S. National Science Foundation (grant AGS-2039985) and the U.S. National Oceanic and Atmospheric Administration (grant NA22OAR4310195).

REFERENCES

Cody, R. B.; Fouquet, T. N. J.; Takei, C. Thermal Desorp-tion and Pyrolysis Direct Analysis in Real Time Mass Spec-trometry for Qualitative Characterization of Polymers and Polymer Additives. *Rapid Commun. Mass Spectrom*. 2020, 34 (S2), e8687.

Cody, R. B.; Laramée, J. A.; Durst, H. D. Versatile New Ion Source for the Analysis of Materials in Open Air under Ambient Conditions. *Anal. Chem.* 2005, 77 (8), 2297–2302.

Hallquist, M.; Wenger, J. C.; Baltensperger, U.; Rudich, Y.; Simpson, D.; Claeys, M.; Dommen, J.; Donahue, N. M.; George, C.; Goldstein, A. H.; et al. The Formation, Proper-ties and Impact of Secondary Organic Aerosol: Current and Emerging Issues. *Atmospheric Chem. Phys.* 2009, 9 (14), 5155–5236.

Li, Y.; Pöschl, U.; Shiraiwa, M. Molecular Corridors and Parameterizations of Volatility in the Chemical Evolution of Organic Aerosols. *Atmospheric Chem. Phys*. 2016, 16 (5), 3327–3344.

Nizkorodov, S.A.; Laskin, J.; Laskin, A. Molecular Chemistry of Organic Aerosols Through Applications of the High Resolution Mass Spectrometry" *Phys. Chem. Chem. Phys.*, 2011, 13, 3612–3629.

IMPACT OF REGIONAL POLLUTION OUTFLOW ON PARTICLE NUMBER AND FORMATION

C.S.L. LEE [1], H. WANG [2] and H.C. CHEUNG [3]

[1] *Department of Civil Engineering, Hong Kong Chu Hai College, Hong Kong SAR, China*

[2] *Institute for Environmental and Climate Research, Jinan University, Guangdong, China*

[3] *School of Atmospheric Sciences and Guangdong Province Key Laboratory for Climate Change and Natural Disaster Studies, Sun Yat-sen University, Guangzhou, China*

Keywords: Megacity, New particle formation, Particle number, Regional pollution, Winter monsoon

INTRODUCTION

A measurement campaign of particle number concentration and size distribution was conducted at urban (SYSU) and suburban (Panyu) areas of Guangzhou, South China, during 16 January to 3 February 2020 before and during the Chinese New Year (CNY) holiday. Average particle number concentration (PNC) was 6.3×10^3 cm^{-3} and 9.7×10^3 cm^{-3}, respectively, at urban and suburban sites, indicating the severe particulate matter (PM) pollution. The PNC in the region was influenced by monsoon and the land–sea breeze systems. During monsoon seasons, PM pollution occurred at a regional scale affecting the urban and suburban areas as indicated by the high PNC correlation (r value = 0.70), but the PNCs were lower than that during land-sea breeze period (with lower PNC_{M1}/PNC_{LSB1} and PNC_{M2}/PNC_{LSB2} ratios) due to the higher atmospheric dispersion. There is a strong local emission (mainly vehicular emissions) in both urban and suburban areas which was significantly lowered during the CNY period due to reduced human activities. The PM pollution was found to be significantly influenced by local emissions (dominated by Aitken mode particles) and new particle formation (NPF) process (dominated by nucleation mode particles). NPF event was found to be associated with a higher $N_{10\text{-}25}/H_2SO_4$ proxy ratio during the low wind speed condition.

METHODS

Field measurements of particles and gaseous pollutants were conducted at two locations in the mega city of Guangzhou (with a population of 18.8 million) during 16 January to 3 February 2020, to represent the urban and semi-urban environments. Figure 1 illustrates the sampling location of urban site at rooftop of the eight-floor campus building at Sun Yat-sen University located in Haizhu District of Guangzhou (SYSU, 23.10°N, 113.30°E), and semi-urban site at rooftop of the building of Bureau of Ecology and Environmental Protection at Panyu, approximately 25 km southeast from the central city area of Guangzhou (PY, 22.94°N, 113.37°E). The SYSU site is situated in the center of Guangzhou which is primarily affected by vehicle emissions as Guangzhou was known to have one of the highest traffic in China (16.5 million daily traffic) (Zhao and Moh, 2005), and the PY site is situated in the suburban areas of Panyu, dominated by local light industrial and domestic emissions. Panyu is one of urban districts of the prefecture-level city of Guangzhou. It was a separate county-level city before its incorporation into modern Guangzhou in 2000.

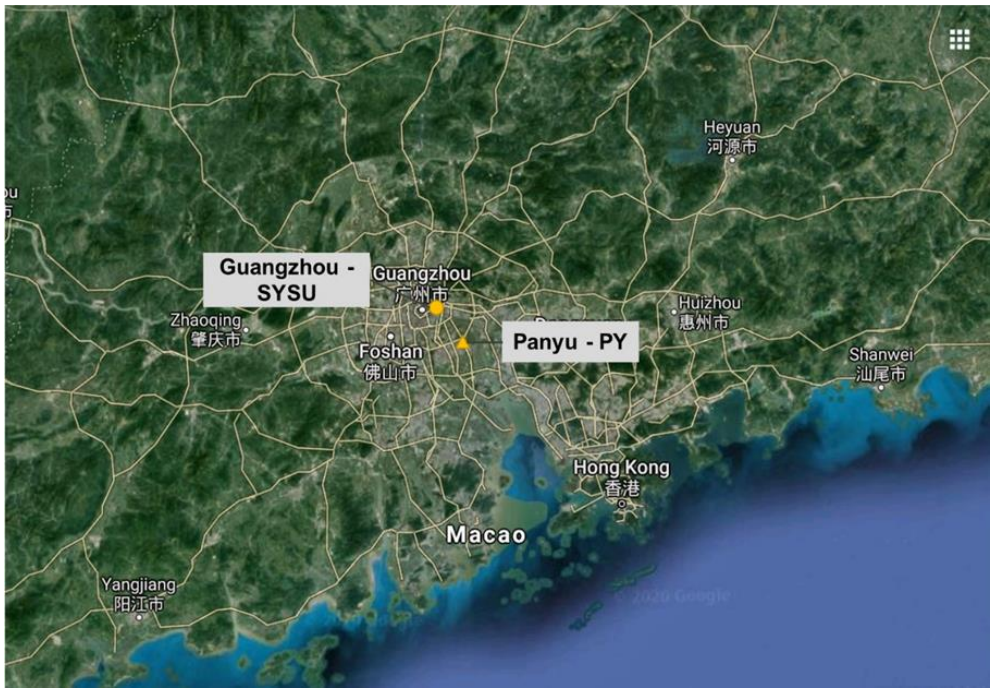

Figure 1. Locations of sampling sites: urban monitoring site at Sun Yat-sen University (SYSU), Guangzhou (circle); suburban monitoring site at Panyu (PY), Panyu (triangle).

CONCLUSIONS

This result showed the stronger influence of winter monsoon at the upwind urban site (SYSU) compared with that at downwind suburban site (PY). We further investigate the PNC under different wind direction for two sites. Highest PNC (i.e., 12.6×10^3 cm^{-3}) was obtained under the wind direction (225–270 degree) in urban site, while highest PNC (i.e., 10.0×10^3 cm^{-3}) was obtained under the wind direction (0–45 degree) in suburban site. Similar observations for NO_x were obtained where higher NO_x observed under southerly wind in urban, and higher NO_x observed under northerly wind in suburban, respectively. These finding showed that the different variation patterns of PNC at the urban (SYSU) and suburban (PY) sites were obtained under the influence of the winter monsoon.

	SYSU									PY								
	PNC (10^3 cm^{-3})			NO_x (μg m^{-3})			WS (m s^{-1})			PNC (10^3 cm^{-3})			NO_x (μg m^{-3})			WS (m s^{-1})		
WD	Avg.	S.D.	n	Avg.	S.D.	n	Avg.	S.D.	n	Avg.	S.D.	n	Avg.	S.D.	n	Avg.	S.D.	n
0 ≤ WD < 45	3.9	3.8	109	14.9	10.7	107	2.2	0.7	109	10.3	5.3	32	24.7	10.1	33	0.2	0.3	33
45 ≤ WD < 90	6.9	2.4	60	32.0	15.3	63	1.5	0.8	67	8.4	2.7	34	27.2	10.4	41	0.2	0.3	41
90 ≤WD< 135	8.0	3.4	63	36.4	25.9	75	1.2	0.7	75	7.8	3.0	108	22.2	11.3	112	0.3	0.5	112
135≤WD< 180	8.9	3.3	28	48.4	41.9	30	0.7	0.5	30	7.0	5.9	22	13.6	9.1	22	1.1	0.8	22
180≤WD < 225	8.0	3.9	26	67.6	41.0	25	0.3	0.1	27	8.1	4.2	32	19.5	12.8	32	1.0	1.2	32
225≤WD < 270	12.6	4.6	8	51.8	23.8	8	0.4	0.2	9	5.1	4.8	32	8.4	4.5	33	2.2	0.8	33
270 ≤WD< 315	8.7	4.8	14	35.3	26.2	12	3.1	5.2	14	6.0	2.9	113	14.8	10.1	113	2.7	1.1	113
315≤WD < 360	5.5	3.7	123	23.3	16.7	121	1.7	0.6	124	9.1	3.6	59	32.6	23.8	67	1.0	0.9	67

Table 1. Averaged PNC observed at SYSU and PY associated with different wind direction. The NO_x and wind speed data for SYSY and PY were measured at HZP and DS stations.

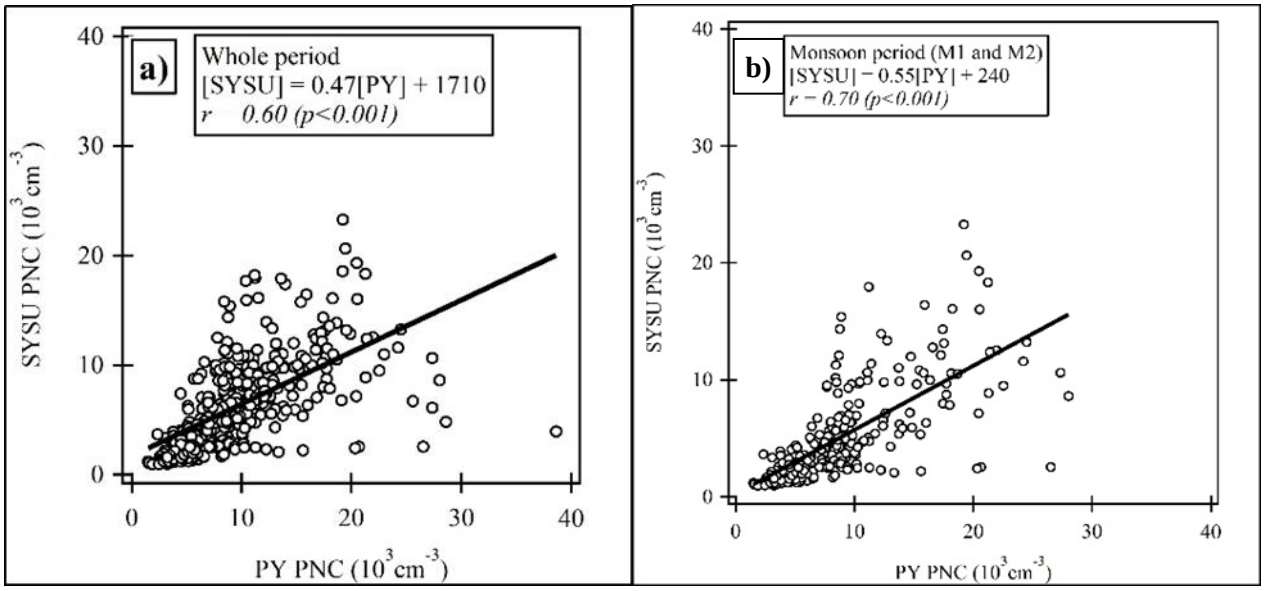

Figure 2. Scatterplots between the PNCs of SYSU and PY for (a) whole measurement period and (b) monsoon period.

For monsoon periods, the r value is 0.70 ($p < 0.001$) a slightly higher than that for whole period ($r = 0.60$) (Figures. 2(a) and 2(b)) which implied the stronger influence of particle emission sources from upwind urban site (i.e., SYSU) to downwind suburban site (i.e., Panyu) under the northerly winds during the monsoon periods. In contrast, the r value is weaker (0.30, $p < 0.001$) during land–sea breeze periods which implied that the PNCs at both sites were primarily attributed to local emissions.

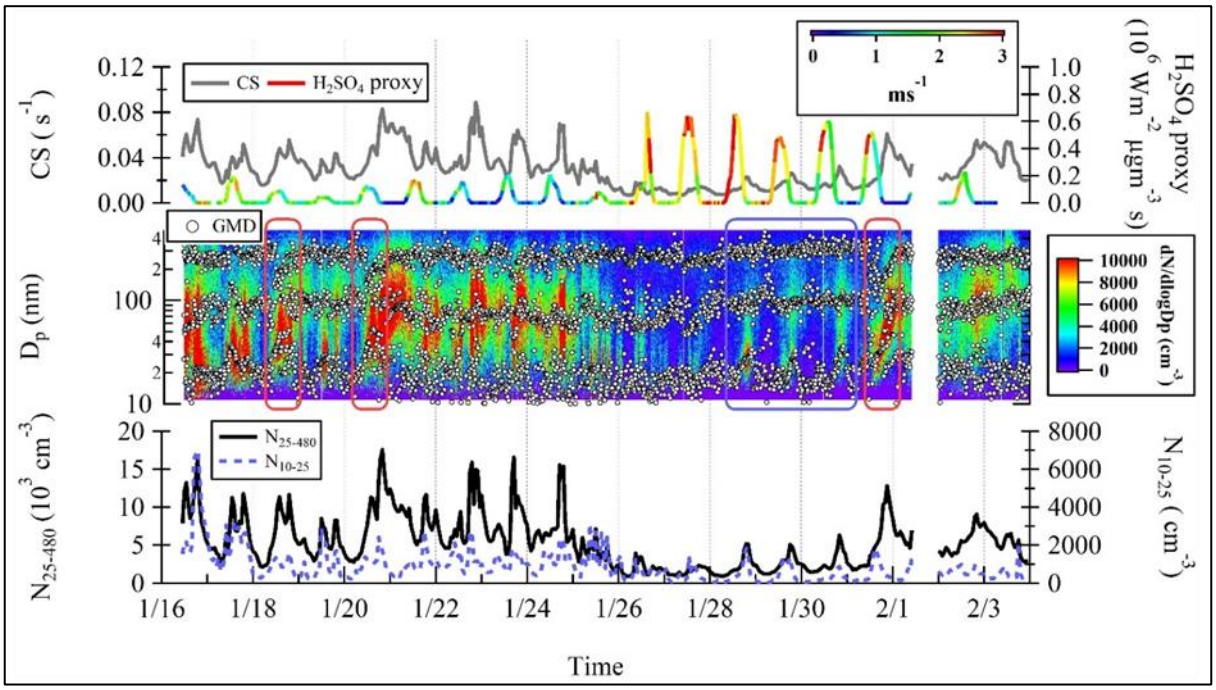

Figure 3. From bottom to top panel. Temporal profiles of (a) Number concentrations of particles ranging from 10–25 nm diameter ($N_{10\text{-}25}$), and 25–480 nm diameter ($N_{25\text{-}480}$); (b) particle size distribution, geometric mean diameter (GMD); (c) particle condensation sink and H_2SO_4 proxy with wind speed on color scale. NPF events were highlighted by red rectangular, and weak NPF events were highlighted by blue rectangular.

The averaged H_2SO_4 proxies during LSB1 and LSB2 (land-see breeze periods) were 11.3×10^3 Wm^{-2} ppb s and 39.0×10^3 Wm^{-2} ppb s, respectively, while average $N_{10\text{-}25}$ for these periods were 1390 cm^{-3} and 490 cm^{-3}, respectively. Relatively high H_2SO_4 proxies observed in the M2 period (monsoon period during the CNY holiday) in which only three weak NPF events occurred (i.e., 28 January, 29 January, 30 January), demonstrating that occurrence of NPF in urban Guangzhou is not solely governed by precursors such as sulfuric acid. In addition, we observed that a relatively stronger wind speed was found during the weak NPF event days (i.e., 28 January, 29 January, 30 January, averaged wind speed: 2.2 ± 0.7 m s^{-1}) compared to that for strong NPF event days (i.e., 18 January, 20 January and 31 January, averaged wind speed: 1.3 ± 0.7 m s^{-1}) (see Figure 3). In this study, the condensation sink (CS) for different periods were 0.0363 s^{-1} and 0.0143 s^{-1} for M1 and M2, and 0.0416 s^{-1} and 0.0357 s^{-1} for LSB1 and LSB2, respectively. In general, higher condensation sink (CS) was observed during the period before the CNY holiday (i.e., M1 and LSB1) and also higher for land-sea breeze periods than that of monsoon periods, as more pre-existing particle existed due to more local emissions, which impede the NPF processes. Bousiotis *et al.* (2021) showed that the wind speed has positive and negative effects on the occurrence of NPF event which varied depending on the air masses and local conditions. High wind speed could enhance the occurrence of NPF event by increased mixing of condensable compounds which eventually lower the condensation sink. On the other hand, the high wind speed may impede NPF due to increased atmospheric dilution (Bousiotis *et al.*, 2021). Our results therefore provide evidence that mix of conditions were affecting the NPF process, where NPF events occurred when the CS level and wind speed are low. This indicated that local conditions need to assess to better understand the NPF process.

ACKNOWLEDGEMENTS

This research was supported by the research startup fund of Sun Yat-sen University (Project number: 74110-18841227) and the Ministry of Science and Technology, Guangdong Province (Project number: 2020A1515011138).

REFERENCES

Bousiotis, D., J. Brean, F.D. Pope, M. Dall'Osto, X Querol, A. Alastuey, N. Perez, T. Petäjä, A. Massling, J.K. Nøjgaard, C. Nordstrøm, G. Kouvarakis, S. Vratolis, K. Eleftheriadis, J.V. Niemi, H. Portin, A. Wiedensohler, K. Weinhold, M. Merkel, T. Tuch, R.M. Harrison (2021). The effect of meteorological conditions and atmospheric composition in the occurrence and development of new particle formation (NPF) events in Europe. *Atmos. Chem. Phys.* **21**, 3345–3370. https://doi.org/10.5194/acp-21-3345-2021

Zhao, R.-J. and W.H. Moh (2015). Development of New Modality Municipal Public Transportation for Guangzhou – Group Rapid Transit System as Supplementary Linkage from Guangzhou City Centre to its Eastern Tourism Zone. *Front. Eng. Manag.* **2**, 378-390.

IMPROVED CLASSIFICATION SCHEME OF ATMOSPHERIC NEW PARTICLE FORMATION EVENTS

K. LEHTIPALO[1,2], T. NIEMINEN[1], A. LAMPILAHTI[1], J. SULO[1], S. TUOVINEN[1], M. KULMALA[1] and P. PAASONEN[1]

[1]Institute for Atmospheric and Earth System Research/ Physics, Faculty of Science, University of Helsinki, Finland.
[2]Finnish Meterological Institute, Helsinki, Finland.

Keywords: new particle formation, nucleation, clustering, aerosol growth

INTRODUCTION

New particle formation (NPF) is a process, in which vapor molecules form molecular clusters, which can grow further to aerosol particles via condensation of the same or other vapor molecules. NPF is typically observed in the atmosphere as sudden bursts of recently formed particles. Such *NPF events (NPFE)* happen frequently around the world in many different kinds of environments (Kulmala et al. 2004; Nieminen et al. 2018). Dal Maso et al. (2005) presented a scheme to classify days into *event days* and *non-event days* depending on if a new, growing mode of particles was appearing or not. All unclear days in this regard were lumped into a class called *undefined*. Later on, it has been recognized NPF happens also on days that are classified as undefined or non-event (Buenrostro Mazon et al. 2009; Kulmala et al. 2022), even though the size distribution would not show a typical "banana-shape" resulting from a regional-scale NPFE. Also, there is now instrumentation available that can detect the particle size distribution down to <3 nm in particle diameter, where the first steps of particle formation happen, making it possible to differentiate between NPFE taking place at or very near the measurement site and NPFE where particles are forming somewhere else and are transported to the measurement site.

As the knowledge of new particle formation process has vastly increased in the past decades, it is crucial to agree on a new NPFE classification scheme. Our aims for the improved classification scheme are: **1)** it should be universal, so that it can be applied in different kinds of environments from clean to very polluted, **2)** instead of a time resolution of a day, it should give the exact time windows when a NPFE is observed and be able to identify several NPFEs on one day if needed, **3)** it should be able to distinguish if the NPFE happens at the measurement site or further away and **4)** it should be able to classify NPFEs that happen in a spatially limited area (e.g. in the vicinity of a point or line source) rather than only classical "banana-type" NPFEs happening on a regional scale. The classification was built assuming that there is an instrument available that can measure the size distribution at least down to 3 nm, preferable lower.

METHODS

The decision tree for manual classification, based solely on visual inspection of the aerosol particle size distribution data, is presented as Figure 1, and the resulting classes are summarized in Table 1.

The new classification scheme differentiates between NPFEs happening at or very near the observation site (1a and 1b), evidenced by the presence of recently formed particles (new particle mode mainly in the size range smaller than 5 nm), and transported NPFEs, where the main mode has grown beyond 5 nm at the time when the particles are first observed (1c and 2c). If the size distribution shows a clear growth pattern, typical for regional NPFEs, it always classified as NPFE (1a or 1c), while cases which do not show a clear growth pattern are classified either as NPFE at/near the site but in a limited area (1b; also sometimes called "clustering" due to the presence of small clusters which do not grow), or *uncertain, potential NPFE in limited area* (2c). The latter could result from a NPF precursor source over a limited area at a distance from the observation site, e.g. coastline resulting in "apple-type events", however one

needs site-specific information to distinguish these from other emission related sources of nucleation mode particles.

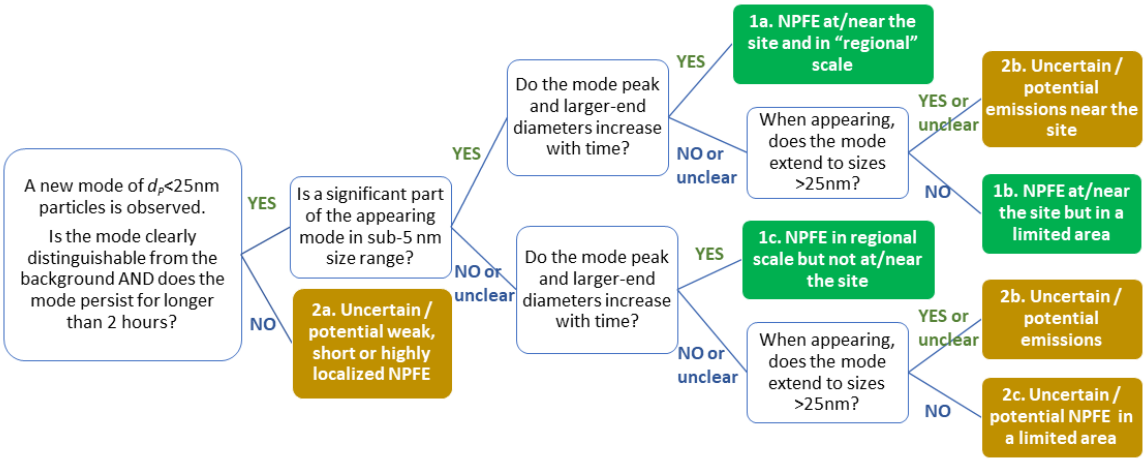

Figure 1. New decision tree for classifying new particle formation events.

Table 1. Classes used in the new classification scheme and their typical interpretation.

Class	**Smallest size of appearing mode**	**Subsequent growth observed**	**Additional remarks**	**Typical interpretation and earlier names**
1a: NPFE at/near the site and in regional scale	< 5 nm	YES	-	Regional NPFE taking place also at or very near the observation site. Also called *"Banana-type event".*
1b: NPFE at/near the site but in a limited area	< 5 nm	NO or not clear	-	NPFE taking place in a limited area at or very near the observation site. Also called *"Clustering" or "local event"*
1c: NPFE in regional scale but not at/near the site	5-25 nm	YES	-	Regional NPFE, which does not take place at the observation site. Also called *"Transported event".*
2a: Uncertain, potential weak, short or highly localized NPFE	<25 nm*	NO or not clear	Mode not clear or NPFE lasts <2h	Weak or fluctuating NPFE that cannot be clearly distinguished from the background or a temporally short particle burst, which could be also related to emissions.
2b: Uncertain, potential emissions	<25nm*	NO or not clear	Very wide mode extending to >25 nm at appearance	Likely related to anthropogenic emissions (e.g. traffic rush hour), but NPFE cannot be ruled out
2c: Uncertain, potential NPFE in a limited area	5-25 nm	NO or not clear		Potential NPFE taking place in a limited area further away from the observation site, but emissions cannot be ruled out without more information. Also called *"Apple-type event".*

* Times with <5 nm particles present should be included in the time series of potential NPFE at/near the site

Note, that here we aim to classify atmospheric NPFEs, i.e. NPFE happening in a mixed atmospheric layer. Therefore, the decision tree is formulated in such a manner that direct emissions of nucleation-mode

particles from traffic or some other combustion sources (even though they might have resulted from new particle formation in the tailpipe, or directly after it) would end up in class *Uncertain, potential emissions* (2b), as they typically lead to a very wide particle mode, extending to >25 nm. However, based on measured particle size distribution only, it is not always possible to distinguish atmospheric NPFEs, especially those occurring at a distance from the observation site, from primary sources of nucleation mode particles.

Therefore, we define three different *uncertain* classes for cases, where it is not possible to say, whether the observed nucleation-mode is related to a NPFE. Unlike the earlier *undefined* class (Dal Maso et al. 2005), the *uncertain* cases should be regarded as potential NPFEs, which can be further analyzed with the help of other data, if that is of interest. Site-specific information, e.g. gas concentrations, traffic flow rates or wind directions, can help to interpret these cases, but we suggest that the main classification is first done solely based on the particle size distribution so that different sites are comparable, and that additional site-specific sub-classes or flagging can be done as second step. Sites that have size distribution data starting only at 5 nm/ 10 nm may use the main classes 1 and 2, but cannot fully distinguish between NPFEs happening on-site and further away.

CONCLUSIONS

The finalized classification scheme will be tested by several people classifying size distribution data from several different measurement sites both individually and in pairs. We will present the agreement between different classifiers and compare the results with the original Dal Maso scheme. We will also show examples of cases in which distinguishing NPFE from anthropogenic sources is difficult and how using additional data helps to confirm the classification.

We believe that the new classification scheme can help to unify the method and terminology for classifying new particle formation events. The classification should not be taken as an absolute measure on whether NPF process happens or not, but it can serve as a tool to separate intense NPF times (i.e. times when a NPFE is taking place) from conditions that are not favorable for NPF. When combined to information on the precursor concentrations or cluster composition, it can be used to identify the NPF mechanisms or necessary preconditions leading to a NPFE. It is likely that in future different artificial intelligence or machine learning methods will help in or even replace the manual classification step, but it is still highly important that we agree on the terminology and relevant classes based on our physical understanding of the NPF process.

ACKNOWLEDGEMENTS

We acknowledge ACCC Flagship funded by the Academy of Finland grant number 337549, ACTRIS-Finland and all the colleagues involved in the discussions of the new classification.

REFERENCES

Buenrostro Mazon, S. et al. (2009). Classifying Previously Undefined Days from Eleven Years of Aerosol-Particle-Size Distribution Data from the SMEAR II Station, Hyytiälä, Finland. Atmos. Chem. Phys. 9, 667–676. doi:10.5194/ acp-9-667-2009.

Dal Maso et al. (2005). Formation and growth of fresh atmospheric aerosol: eight years of aerosol size distribution data from SMEAR II, Hyytiälä, Finland. *Boreal Env. Res*. 10: 323-336.
Kulmala, M. et al (2004). Formation and growth rates of ultrafine atmospheric particles: A review of observations. *J. Aerosol Sci.* 35: 143-176.

Kulmala, M. et al. (2022). Quiet New Particle Formation in the Atmosphere. Front. Environ. Sci. 10:912385. doi: 10.3389/fenvs.2022.912385.

Nieminen, T. et al (2018). Global analysis of continental boundary layer new particle formation based on long-term measurements. *Atmos. Chem. Phys.* 18, 14737-14756.

MULTI-YEAR VARIATIONS OF SUBMICRON AEROSOL COMPOSITION AND SOURCES IN IRELAND

L. LEI[1], K.N. FOSSUM[1], T. SPOHN[1], C. LIN[1,2], C. O'DOWD[1] and J. OVADNEVAITE[1]

[1]The Ryan Institute's Centre for Climate & Air Pollution Studies (C-CAPS), University of Galway, Galway, H91 CF50, Ireland
[2]CAS Center for Excellence in Quaternary Science and Global Change & State Key Laboratory of Loess and
Quaternary Geology, Chinese Academy of Sciences, Xi'an 710061, China

Keywords: SUBMICRON AEROSOL, SOURCE APPORTIONMENT, AIR QUALITY, DUBLIN.

INTRODUCTION

The particulate matter (PM) in the atmosphere has been well confirmed to have adverse impacts on human health and complicated effects on climate. The air quality in Ireland was once significantly deteriorated by air pollutants emitted from domestic coal combustion activities in the 1980s (Clancy et al., 2002). The Irish government introduced the smokey coal ban in 1990, which resulted in immediate and sustained reductions in PM levels, e.g., the field observation results showed that the black smoke concentrations in Dublin, the capital city of Ireland, was reduced by ~70% after the ban was put into force (Goodman et al., 2009). The air quality in Ireland has been improving gradually and surely with natural gas and electricity becoming more and more dominate residential energy and heating sources. However, extreme air pollutions with the mass concentration of submicron aerosols exceeding 300 μg m^{-3} were still observed occasionally during cold months, which were mainly related to domestic solid fuel combustion, and the disproportionate impacts from so-called "low-carbon" and "carbon-neutral" solid fuels (e.g., peat and wood) (Lin et al., 2018). Moreover, due to the increasing wood stove advertisements and significant fuel price increase caused by Ukrainian-Russian war, the emissions from local solid fuel combustion activities are supposed to impair the air quality in Ireland greatly and continuously. In the past decade, extensive studies have been conducted to characterize the air pollution in Ireland (Lin et al., 2020; Lin et al., 2022), while the long-term trends of air pollution and corresponding influencing factors are still understudied. Since the situation is changing year to year, it's very critical to conduct continuous field aerosol measurements and have a deeper insight into the long-term variations for more targeted and effective regulations in the future. In this study, based on the parallel real-time measurements of submicron aerosol species at three representative sites over Ireland, the multi-year variations of aerosol chemical composition and source emissions have been analyzed.

METHODS

AEROSOURCE is a next-generation in-situ Air Quality network measuring speciated aerosol concentrations in real-time at high temporal resolution over Ireland at three strategic sampling sites in parallel, i.e., Mace Head (MHD, 53.33 °N, 9.54 °W), University College Dublin (UCD, 53.31 °N, 6.22 °W), and Carnsore Point (CRP, 52.18 °N, 6.37 °W). The location of the three sites were shown in Figure 1. An Aerodyne High-Resolution Time-of-Flight Aerosol Mass Spectrometer (HR-ToF-AMS) was deployed at MHD, and two Quadrupole Aerosol Chemical Speciation Monitors (Q-ACSM) (Ng et al., 2011) were deployed at UCD and CRP respectively to measure the real-time mass concentrations of non-refractory chemical species in submicron aerosols (NR-PM_1). The measured chemical species of NR-PM_1 included organics (Org), sulfate (SO_4), nitrate (NO_3), ammonium (NH_4) and chloride (Chl). Optical absorption of black carbon was measured by collocated Aethalometers (model AE33) and the mass concentration of equivalent black carbon (eBC) was retrieved from the standard 880 nm wavelength channel. The duration of the NR-PM_1 and eBC field sampling and the coverage of hourly data throughout every year at UCD were summarized in Table 1. Positive Matrix Factorization (PMF) combined with

multilinear engine (ME-2) were used for the source apportionment of organic aerosols (OA) (Ulbrich et al., 2009).

Year	Duration		Data coverage	
	Q-ACSM	AE33	Q-ACSM	AE33
2016	Aug-Dec.	Aug-Dec.	39.6%	39.7%
2017	Jan.-Dec.	Jan.-Dec.	96.2%	96.2%
2018	Jan.-May, Sep.-Dec.	Jan.-May	68.1%	35.8%
2019	Jan.-Mar., Sep.-Dec.	-	44.6%	0
2020	Jan.-Dec.	-	92.2%	0
2021	Jan.-Dec.	Jan.-Dec.	97.8%	97.8%
2022	Jan.-Dec.	Jan.-Dec.	92.3%	92.3%

Table 1. Summary of the PM_1 sampling duration and hourly data coverage from 2016 to 2022 at UCD.

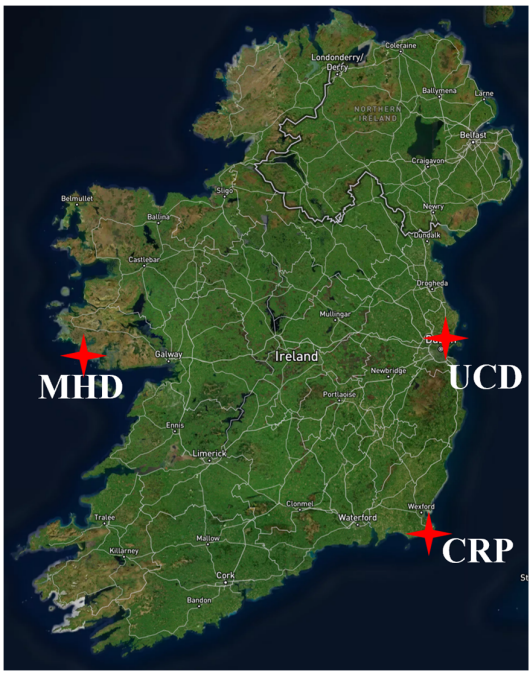

Figure 1. Location of the three sampling sites, i.e., MHD, UCD and CRP.

CONCLUSIONS

The air quality in Dublin has been improving gradually and furtherly since 2016, with the annual average mass concentration of PM_1 decreased from 8.0 μg m^{-3} in 2016 to 4.1 μg m^{-3} in 2022, and the total number of days when PM_1 concentration exceeds the WHO recommendation value (15 μg m^{-3}) has decreased to 11 days in 2022. Specifically, the extreme air pollutions have been reduced significantly, e.g., the maximum hourly PM_1 concentration has decreased to 77 μg m^{-3} in 2022 compared to 317 μg m^{-3} in 2016. The high PM_1 concentrations in Dublin was more related to local emissions, especially domestic solid fuel burning, characterizing by large contributions from primary organic aerosols. While the long-range transport also plays an important role with high fractions of inorganics especially NO_3. The chemical composition of PM_1 in Dublin was similar over the years, i.e., dominated by Org and then followed by NO_3 or SO_4. However, it's quite worrisome to see that the mass concentration of SO_4 has been increasing since 2021 and showed higher contribution to PM_1 especially during cold months, indicating that the sharply

increasing fuel prices recently may have led to a change in fuel usage, possibly with more coal and solid fuel combustion in households. This could indicate severe air pollution episodes that may need further and more effective regulations in the near future to ensure good enough air quality.

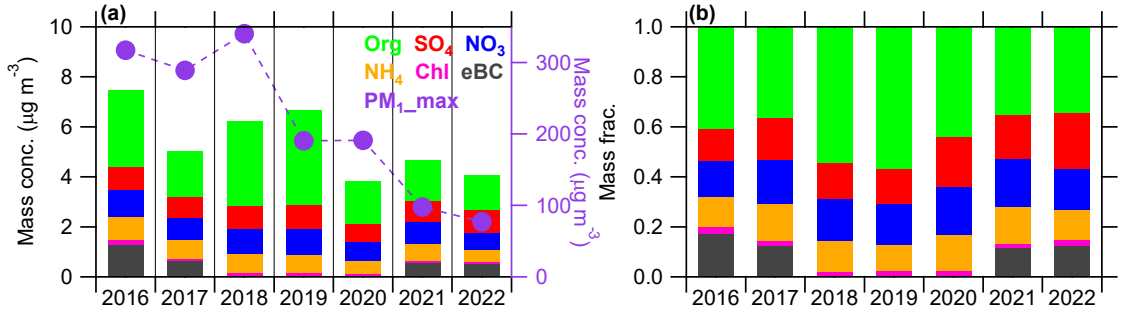

Figure 1. Changes of average (a) mass concentrations and (b) mass fractions of PM_1 species from 2016 to 2022, the variations of maximum hourly PM_1 mass concentration were also shown. Note that the eBC data were not available in 2018, 2019 and 2020.

ACKNOWLEDGEMENTS

This work was funded by the Irish EPA (AEROSOURCE,502 2016-CCRP-MS-31).

REFERENCES

Clancy, L., Goodman, P., Sinclair, H., and Dockery, D. W.: Effect of air-pollution control on death rates in Dublin, Ireland: an intervention study, Lancet, 360, 1210-1214, 10.1016/S0140-6736(02)11281-5, 2002.

Goodman, P. G., Rich, D. Q., Zeka, A., Clancy, L., and Dockery, D. W.: Effect of Air Pollution Controls on Black Smoke and Sulfur Dioxide Concentrations across Ireland, J Air Waste Manag Assoc, 59, 207-213, 10.3155/1047-3289.59.2.207, 2009.

Lin, C., Ceburnis, D., O'Dowd, C., and Ovadnevaite, J.: Seasonality of Aerosol Sources Calls for Distinct Air Quality Mitigation Strategies, Toxics, 10, 10.3390/toxics10030121, 2022.

Lin, C., Ceburnis, D., Xu, W., Heffernan, E., Hellebust, S., Gallagher, J., Huang, R.-J., O'Dowd, C., and Ovadnevaite, J.: The impact of traffic on air quality in Ireland: insights from the simultaneous kerbside and suburban monitoring of submicron aerosols, Atmospheric Chemistry and Physics, 20, 10513-10529, 10.5194/acp-20-10513-2020, 2020.

Lin, C., Huang, R.-J., Ceburnis, D., Buckley, P., Preissler, J., Wenger, J., Rinaldi, M., Facchini, M. C., O'Dowd, C., and Ovadnevaite, J.: Extreme air pollution from residential solid fuel burning, Nature Sustainability, 1, 512-517, 10.1038/s41893-018-0125-x, 2018.

Ng, N. L., Herndon, S. C., Trimborn, A., Canagaratna, M. R., Croteau, P. L., Onasch, T. B., Sueper, D., Worsnop, D. R., Zhang, Q., Sun, Y. L., and Jayne, J. T.: An aerosol chemical speciation monitor (ACSM) for routine monitoring of the composition and mass concentrations of ambient aerosol, Aerosol Science and Technology, 45, 780-794, 10.1080/02786826.2011.560211, 2011.

Ulbrich, I. M., Canagaratna, M. R., Zhang, Q., Worsnop, D. R., and and Jimenez, J. L.: Atmospheric Chemistry and Physics Interpretation of organic components from Positive Matrix Factorization of aerosol mass spectrometric data Atmos. Chem. Phys., 9, 2891–2918, org/10.5194/acp-9-2891-2009, 2009.

Nucleation and cluster growth in multicomponent vapors at low temperatures

CHENXI LI, [1] JAN KROHN[2], STEFAN FEUSI[2], and RUTH SIGNORELL[2]

[1] *School of Environmental Science and Engineering, Shanghai Jiao Tong University, Shanghai 200240, China*
[2]*Department of Chemistry and Applied Biosciences, Laboratory of Physical Chemistry, ETH Zürich, Vladimir-Prelog-Weg 2, CH-8093 Zürich, Switzerland*

Key words: nucleation, cluster growth, controlled Laval expansion, Chaperon mechanism

INTRODUCTION

Nucleation is the first step of the transition from the gas to the condensed phases. Despite being a ubiquitous phenomenon in the atmosphere and various industrial processes, the underlying mechanisms of nucleation as well as the subsequent cluster growth are in many cases not well understood, especially in multicomponent vapors where different species could interact to collectively determine the cluster formation pathway. Here we investigate phase transition on the molecular level in mixtures at temperatures lower than 100 K, using an experimental setup that combines the uniform postnozzle flow of pulsed Laval expansions, soft single-photon ionization, and time-of-flight mass spectrometry. We study nucleaiton and cluster growth in two types of systems. The first type of system (e.g. toluene-CO_2 mixture) consists of both high and low volatility vapors, while the second type of system (i.e., nonane-water mixture) consists of vapor components whose inter-species interactions are weak compared to the intra-species interactions.

METHODS

Detailed descriptions of the experimental setup can be found in our previous publications (Schläppi et al., 2015; Li et al., 2021) and a brief summary is given here. In our experiments nucleation occurs in a uniform postnozzle flow of a Laval nozzle expansion. The temperature of the flow is controlled by using nozzles of different dimensions and modifying carrier gas compositions. By changing the distance between the nozzle exit and a sampling skimmer (which is connected to a time-of-flight mass spectrometer equipped with single-photon ionization), the nucleation time can be adjusted. We retrieve the time-resolved cluster mass spectra with this setup, from which the cluster number concentrations are calculated with by comparing cluster signals to signals of a reference gas (i.e., methane). The nucleation rate is obtained by derivatizing the total cluster concentration with respect to

time. The cluster growth rate is calculated with an equation we developed in a previous work (Li et al., 2019). The nucleation rates and cluster growth rates are compared between single component and multicomponent systems. The differences revealed in this comparison shows the role of inter-species interactions in gas-to-particle phase transitions.

CONCLUSIONS

In systems of the first type (e.g., toluene-CO_2 mixture), we show that the phase transition in the gas mixtures starts with the formation of stable clusters made of the low volatility species, but both the nucleation rate and the initial cluster growth rate are enhanced by the presence of the high volatility vapor component (Li et al., 2021). The enhancements are explained by the formation of transient, heteromolecular clusters containing the high volatility vapor molecules, which help dissipate the excessive kinetic energies upon molecuar collisions (similar to the Chaperon mechanism). Once the clusters of the low volatility speices grow to certain sizes and become sufficiently cooled, they can serve as seeds for the heterogeneous condensation of the high volatility component. In the second type system with weak inter-species interactions, i.e., nonane-water mixture, it is shown that unlike the first system, the nucleation of both vapors proceeds independently, although there are indications that water cluster growth is slowed by surface sorption of nonane (Feusi et al., 2023). Our work demonstrates how different species interact to influence gas-to-particle conversion on the molecular level and opens up new avenues for the quantitative assessment of phase transition kinetics.

AKNOWLEDGEMENTS

This work was supported by the Swiss National Science Foundation (SNSF project number 200020_200306), ETH Zürich and the Natural Science Foundation of Shanghai (grant no. 21ZR1430100).

REFERENCES

Feusi, S., Krohn, J., Li, C., and Signorell, R.: Mutual independence of water and n-nonane nucleation at low temperatures, J. Chem. Phys., 10.1063/5.0138628, 2023.
Li, C., Krohn, J., Lippe, M., and Signorell, R.: How volatile components catalyze vapor nucleation, Sci. Adv., 7, eabd9954, 10.1126/sciadv.abd9954, 2021.
Li, C., Lippe, M., Krohn, J., and Signorell, R.: Extraction of monomer-cluster association rate constants from water nucleation data measured at extreme supersaturations, J. Chem. Phys., 151, 094305, 10.1063/1.5118350, 2019.
Schläppi, B., Litman, J. H., Ferreiro, J. J., Stapfer, D., and Signorell, R.: A pulsed uniform Laval expansion coupled with single photon ionization and mass spectrometric detection for the study of large molecular aggregates, Phys. Chem. Chem. Phys., 17, 25761-25771, 10.1039/C5CP00061K, 2015.

Comprehensive simulations of new particle formation events in Beijing

CHENXI LI[1], YUYANG LI[2], XIAOXIAO LI[2], JINGKUN JIANG[2]

[1]*School of Environmental Science and Engineering, Shanghai Jiao Tong University, 200240, Shanghai, China*

[2]*State Key Joint Laboratory of Environment Simulation and Pollution Control, School of Environment, Tsinghua University, 100084 Beijing, China*

INTRODUCTION

New particle formation (NPF) and growth is a major source of atmospheric fine particles. In the polluted urban environments of Beijing, NPF events occur frequently with characteristics distinct from those in clean environments. We have previously investigated the particle formation and growth mechanisms in Beijing (Cai et al., 2021; Qiao et al., 2021) but have not shown if the NPF events can be 'reproduced' by simulations which adopts the proposed mechanisms. Here we simulate several NPF events in urban Beijing with a discrete-sectional model that couples cluster dynamics and multicomponent particle growth. In the model, new particles are formed by sulfuric acid-dimethylamine nucleation, while particle growth is driven by particle coagulation and the condensation of sulfuric acid, its clusters, and oxygenated organic molecules (OOMs). We compare the simulation with field observations and trace the possible causes for simulation-observation differences with sensitivity analysis.

METHODS

The structure of the model used in this study is shown in Fig. 1 (Li et al., 2023). The model considers the formation, growth, and coagulation of both molecular clusters and particles, as well as their loss to pre-existing particles. Input to the model includes the ambient temperature, the cluster free energies, the time-resolved concentrations of gaseous precursors, and the particle size distribution outside the simulation domain. The simulation yields a rich set of information including the time dependent NPF rates, the cluster concentrations, the particle size distributions, and the time- and size-specific particle chemical compositions. These can be compared with the field observations to comprehensively assess the simulation-observation agreement. Sensitivity analysis with the model further quantifies how metrics of NPF events

(e.g., particle survival probability) respond to model input variations and serves as a diagnostic tool to pinpoint the key parameter that leads to simulation-observation discrepancies.

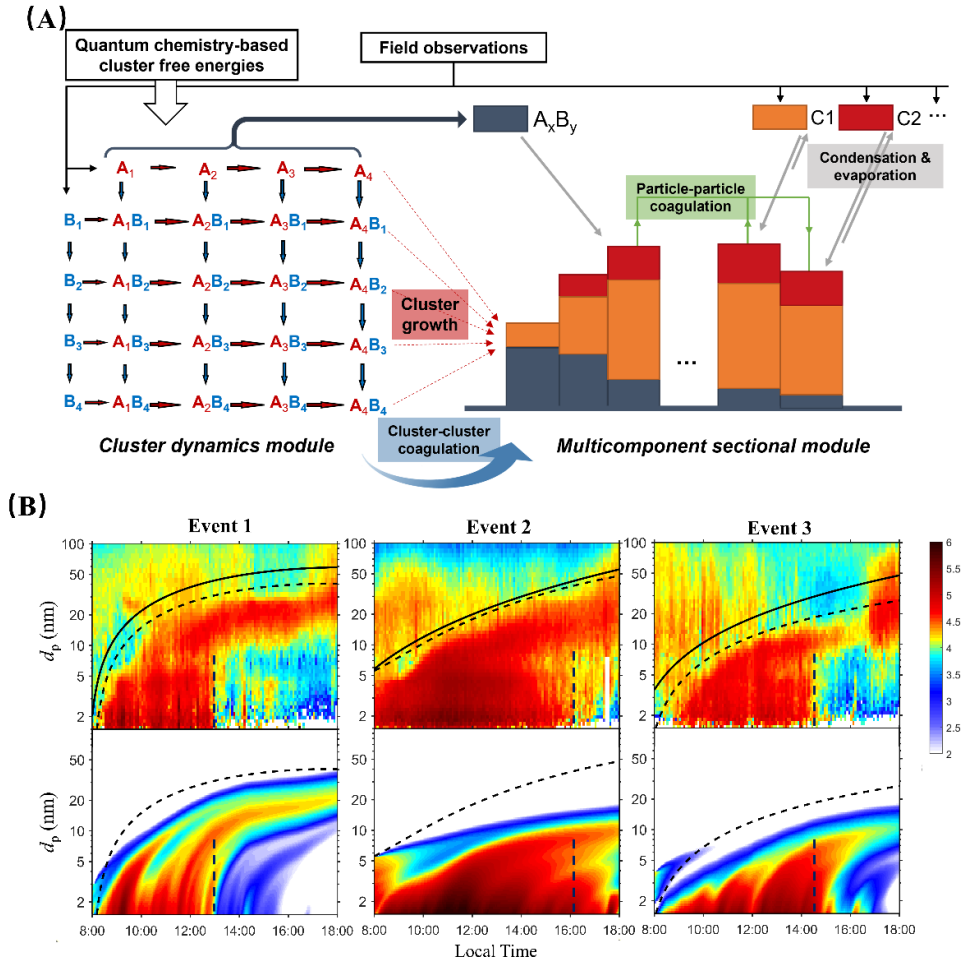

Figure 1. (A) A schematic of the simulation model used in this work. A and B represent acid and base molecules, respectively; C1 and C2 represent two condensing organic vapors of different volatilities. Cluster formation by cluster-cluster association is not shown in this figure but is included in the simulations. (B) Particle size distribution observed in the field observation (first row) and produced by the simulation (second row). The figure is a combination of Figs. 1&2 in Li et al. (2023)

The measurement data used in this work were obtained from the ambient observation between Oct. 1st, 2018 to Dec. 31st, 2018 at the AHL/BUCT station in Beijing. State-of-the-art instruments were deployed to measure the key parameters for new particle formation and growth including the gaseous concentration of sulfuric acid, dimethylamine and oxygenated molecules. We selected seven NPF events for analysis based on the availability of measurement

data, i.e., the availability of meteorological conditions, the PSD, and the concentrations of SA, DMA, and OOMs.

CONCLUSIONS

Several typical NPF events in urban Beijing were analyzed. We found that with the observed gaseous precursor concentrations and coagulation sink as model inputs, the simulations roughly captured the evolution of the observed particle size distributions, as shown in Fig. 1B. However, more detailed analysis show that the simulated particle growth rate was insufficient to yield the observed particle number concentrations, survival probability, and mode diameter. With the aid of sensitivity analysis, we identified underdetected OOMs as a likely cause for the discrepancy, and the agreement between the simulation and the observation was improved after we modulated particle growth rates in the simulation by adjusting the abundance of OOMs.

AKNOWLEDGEMENTS

This research has been supported by Natural Science Foundation of Shanghai (grant no. 21ZR1430100), the special fund of State Key Joint Laboratory of Environment Simulation and Pollution, National Natural Science Foundation of China (grant no. 22188102 and 92044301), Samsung $PM_{2.5}$ SRP, and the Academy of Finland (332547).

REFERENCES

Cai, R., Yan, C., Yang, D., Yin, R., Lu, Y., Deng, C., Fu, Y., Ruan, J., Li, X., Kontkanen, J., Zhang, Q., Kangasluoma, J., Ma, Y., Hao, J., Worsnop, D. R., Bianchi, F., Paasonen, P., Kerminen, V. M., Liu, Y., Wang, L., Zheng, J., Kulmala, M., and Jiang, J.: Sulfuric acid-amine nucleation in urban Beijing, Atmos. Chem. Phys., 21, 2457-2468, 10.5194/acp-21-2457-2021, 2021.

Li, C., Li, Y., Li, X., Cai, R., Fan, Y., Qiao, X., Yin, R., Yan, C., Guo, Y., Liu, Y., Zheng, J., Kerminen, V.-M., Kulmala, M., Xiao, H., and Jiang, J.: Comprehensive simulations of new particle formation events in Beijing with a cluster dynamics-multicomponent sectional model, Atmos. Chem. Phys. Discuss. [preprint], https://doi.org/10.5194/acp-2022-748, in review, 2023.

Qiao, X., Yan, C., Li, X., Guo, Y., Yin, R., Deng, C., Li, C., Nie, W., Wang, M., Cai, R., Huang, D., Wang, Z., Yao, L., Worsnop, D. R., Bianchi, F., Liu, Y., Donahue, N. M., Kulmala, M., and Jiang, J.: Contribution of Atmospheric Oxygenated Organic Compounds to Particle Growth in an Urban Environment, Environ. Sci. Technol, 55, 13646-13656, 10.1021/acs.est.1c02095, 2021.

PARAMETERIZATION OF ULTRAFINE PARTICLE FORMATION RATES IN DISTINCT ATMOSPHERIC ENVIRONMENTS

Xinyang Li[1], L. Dada[1,2], M. A. Zaidan[1,3], P. Paasonen[1,6], R. Makkonen[6], P. Zhou[1], N. Sarnela[1], R. Baalbaki[1], C. Yan[4,9], L. L. J. Quéléver[1], T. Jokinen[1,7], I. Salma[5], T. Petäjä[1], V-M. Kerminen[1], M. Kulmala[1,4], T. Nieminen[1,8]

[1]Institute for Atmospheric and Earth System Research (INAR), University of Helsinki, Helsinki, 00560, Finland
[2]Laboratory of Atmospheric Chemistry, Paul Scherrer Institute, 5232 Villigen, Switzerland
[3]Department of Computer Science, University of Helsinki, Helsinki, 00560, Finland
[4]Aerosol and Haze Laboratory, Beijing Advanced Innovation Center for Soft Matter Science and Engineering, Beijing University of Chemical Technology, Beijing, 100029, China
[5]Institute of Chemistry, Eötvös Loránt University, Budapest, Hungary
[6]Climate System Research, Finnish Meteorological Institute, P.O. Box 503, 00101 Helsinki, Finland
[7]Climate & Atmosphere Research Centre (CARE-C), Cyprus Institute, P.O. Box 27456, Nicosia, 1645, Cyprus
[8]Department of Physics, University of Helsinki. Helsinki, Finland
[9]Joint International research Laboratory of Atmospheric and Earth System Research (JirLATEST), School of Atmospheric Sciences, Nanjing University, Nanjing, China.

Keywords: New particle formation, global simulation, meteorology

INTRODUCTION

New particle formation (NPF) is a major source of atmospheric aerosols (Gordon et al., 2017; Kerminen et al., 2018; Nieminen et al., 2018). As particles form and grow, they can reach large enough sizes that can act as cloud condensation nuclei (CCN), affecting cloud properties (Spracklen et al., 2008; Roldin et al., 2011; Sanchez et al., 2016) and ultimately the global climate depending on the particle size and their chemical composition (Calvo et al. 2013; Bellouin et al. 2020). Particle formation rate (J), an essential parameter describing NPF, can provide information on the particle survivability, allowing us to represent NPF in global models to better understand the effect of NPF on cloud properties and radiative forcing. To understand the climatic effects of NPF, we require not only atmospheric measurement data of aerosol size-distributions for determining J, but also a universal parameterization of J which is representative for multiple environments. In this work, we develop a parameterization of J based on observations from field measurements to characterize important parameters for ultrafine aerosol formation, which can be subsequently incorporated into global models (e.g. the European community Earth-System Model, EC-Earth, chemistry transport model TM5: Tracer Model 5, version TM5-chem-v3.0) to represent new particle formation in global scale.

The parameterization focuses on particle formation rates at 5 nm particles (J_5) using data from seven distinct environments: Hyytiälä (boreal forest, Finland), Beijing (megacity, China), Värriö (sub-arctic remote boreal forest, Finland), Budapest (urban, Hungary), Agia Marina Xyliatos (rural, Cyprus), Marambio (polar-marine island, Antarctic Peninsula) and Manacapuru (Amazon basin, Brazil). By incorporating information from various types of environments, we will be able to demonstrate descriptive power of our models on J_5 in global scale. The aim of this work is to provide an effective tool for global particle formation rate estimations. Our parameterizations have three main features: (1) the number of inputs is limited to be the most essential parameters involved in NPF process, (2) they do not involve complex microphysics at particles smaller than 5 nm, and (3) they cover a wide range of environment types for an improved global simulation accuracy. These features will enhance the applicability of the parameterizations for the purpose of global model application.

METHODS

The parameterizations used the combined dataset from 7 measurement sites in hourly time resolution. Data points were selected considering the detection limit of the instruments and the validity of the values, such as $J_5 > 1\times10^{-5}$ ($cm^{-3}\ s^{-1}$), H_2SO_4 concentrations > 0 (cm^{-3}), RH ∈ [0,100]%. After that, the complete dataset was randomly resampled into a training set (75% from the complete dataset) and a testing set (25% the rest of the complete dataset). For an additional test on the trained model, we included H_2SO_4 proxy concentration developed by Dada et al. (2020) specifically, for Hyytiälä and Beijing as input variables. This is to test the feasibility and accuracy of our models when inputting values from other proxies.

Several functional forms were considered among the parameters (H_2SO_4, RH, CS) relating to *J*. All models regarded H_2SO_4 as the main precursor vapor, and the complexity of models increased on top of the previous model.

Model 1: $J_5 = k_0 * [H_2SO_4]$

Model 2: $J_5 = k_0 * [H_2SO_4] * RH^{kRH}$

Model 3: $J_5 = k_0 * [H_2SO_4] * RH^{kRH} * CS^{kCS}$

Model 4: $J_5 = k_0 * [H_2SO_4]^{kSA} * RH^{kRH} * CS^{kCS}$

First, the training dataset went through the optimization algorithm called "*fmincon*" in the programming software MATLAB to retrieve the values of each coefficient (k_0, k_{SA}, k_{RH} and k_{CS}). Second, we computed the modelled J_5 utilizing these coefficients and the input parameters from the testing dataset. Finally, we evaluate the model performance through comparison between the modelled and measured J_5 values.

RESULTS AND CONCLUSIONS

In Figure 1, we show the comparison between the measured and parametrized formation rates. Compared to model 1, all of models 2, 3, 4, show improved closure, demonstrating the significance of including meteorology and vapor loss impacts into the models. The modelled J_5 for individual sites reflected seemingly diverse particle formation pathways upon environment types. For boreal forests, the sulfuric acid-based models can predict J_5 on a satisfactory level. For urban environments, the predictions are typically underestimated. The results for Beijing were considerably improved when RH and CS were included, but it was not the same for Budapest. The J_5 predictions for Budapest can still benefit marginally from the parameters considered in our formulas; Underestimations in Cyprus and Amazon basin (rural) have not been resolved with the incorporation of meteorology and vapor loss consequences, allowing room for further NPF-related parameters to be included (Baalbaki et al., 2021). For Antarctica Peninsula (marine), our models underestimated the observations since the simplified formulas do not cover iodine-based formation pathway, which is presumably the dominating pathway in this environment (Quéléver et al., 2022). All models confirmed that using H_2SO_4 concentrations from proxies as the input parameter was feasible.

Overall, the model performances were significantly improved when including the meteorological and vapor loss impacts. Such improvements were in line with the facts that lower RH favoring NPF (Hellmuth, 2006; Dada et al., 2017, 2018; Ding et al., 2021), as well as the survivability of the H_2SO_4 concentrations indicated by CS during particle formation processes (Hellmuth, 2006; Kulmala et al., 2012). Based on these parameterization results, we meet our research objectives of (1) filling the knowledge gap on the particle formation rate at 5 nm, (2) describing global particle formation pathway across a wide range of environment types, and (3) developing the models with primarily the essential input parameters related to NPF processes. The models developed in this research can be included in global simulations.

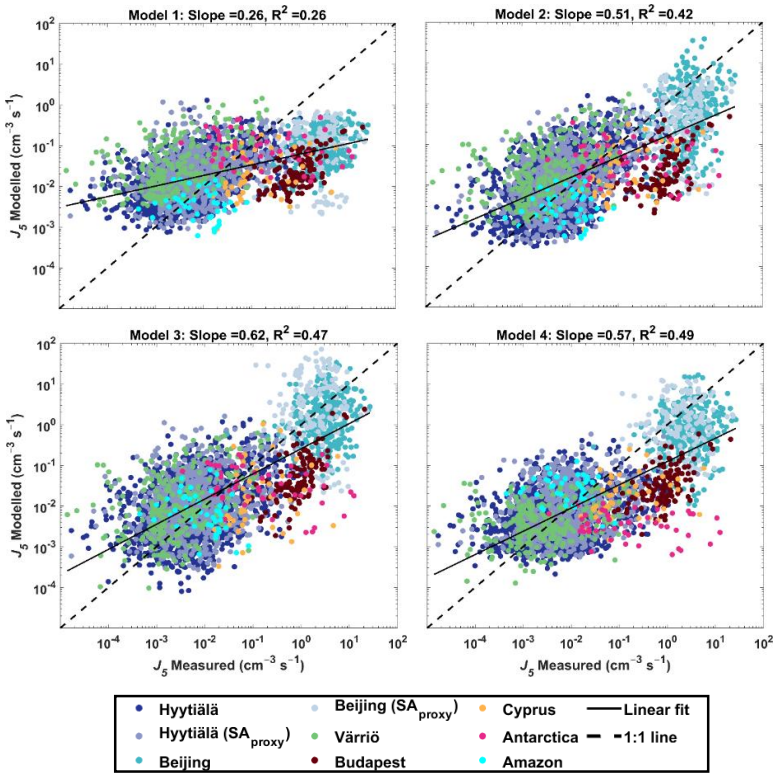

Figure 1. Comparison of the measured J_5 values to modelled values from the four models using testing dataset containing data from all sites in hourly time resolution. Each color represents the data from one measurement site, including datasets with H_2SO_4 proxy data from Hyytiälä and Beijing. The straight line shows the linear fit between the logarithmic values of the modelled and the measured J_5, and the dashed line represents the 1:1 line.

ACKNOWLEDGEMENTS

This work was supported by the European Research Council, H2020 European Research Council (GASPARCON (grant no. 714621), by the EMME-CARE project, which received funding from the European Union's Horizon 2020 Research and Innovation Programme, under Grant Agreement No. 856612 and the Cyprus Government and by ACCC Flagship funded by the Academy of Finland grant number 337549. It is also partially supported by the European Commission Horizon Europe project FOCI, "Non-CO2 Forcers and Their Climate, Weather, Air Quality and Health Impacts, project number 101056783. The authors thank the group of Professor Jim Smith (University of California Irvine) for providing the Amazon data.

REFERENCES

Baalbaki, R., Pikridas, M., Jokinen, T., Laurila, T., Dada, L., Bezantakos, S., Ahonen, L., Neitola, K., Maisser, A., Bimenyimana, E., Christodoulou, A., Unga, F., Savvides, C., Lehtipalo, K., Kangasluoma, J., Biskos, G., Petäjä, T., Kerminen, V.-M., Sciare, J., and Kulmala, M.: Towards understanding the characteristics of new particle formation in the Eastern Mediterranean, Atmospheric Chem. Phys., 21, 9223–9251, 2021.

Bellouin, N., Quaas, J., Gryspeerdt, E., Kinne, S., Stier, P., Watson-Parris, D., Boucher, O., Carslaw, K. S., Christensen, M., Daniau, A.-L., Dufresne, J.-L., Feingold, G., Fiedler, S., Forster, P., Gettelman, A., Haywood, J. M., Lohmann, U., Malavelle, F., Mauritsen, T., McCoy, D. T., Myhre, G., Mülmenstädt, J., Neubauer, D.,

Possner, A., Rugenstein, M., Sato, Y., Schulz, M., Schwartz, S. E., Sourdeval, O., Storelvmo, T., Toll, V., Winker, D., and Stevens, B.: Bounding Global Aerosol Radiative Forcing of Climate Change, Rev. Geophys., 58, e2019RG000660, 2020.

Calvo, A. I., Alves, C., Castro, A., Pont, V., Vicente, A. M., and Fraile, R.: Research on aerosol sources and chemical composition: Past, current and emerging issues, Atmospheric Res., 120–121, 1–28, 2013.

Dada, L., Paasonen, P., Nieminen, T., Buenrostro Mazon, S., Kontkanen, J., Peräkylä, O., Lehtipalo, K., Hussein, T., Petäjä, T., Kerminen, V.-M., Bäck, J., and Kulmala, M.: Long-term analysis of clear-sky new particle formation events and nonevents in Hyytiälä, Atmospheric Chem. Phys., 17, 6227–6241, 2017.

Dada, L., Chellapermal, R., Buenrostro Mazon, S., Paasonen, P., Lampilahti, J., Manninen, H. E., Junninen, H., Petäjä, T., Kerminen, V.-M., and Kulmala, M.: Refined classification and characterization of atmospheric new-particle formation events using air ions, Atmospheric Chem. Phys., 18, 17883–17893, 2018.

Dada, L., Ylivinkka, I., Baalbaki, R., Li, C., Guo, Y., Yan, C., Yao, L., Sarnela, N., Jokinen, T., Daellenbach, K. R., Yin, R., Deng, C., Chu, B., Nieminen, T., Wang, Y., Lin, Z., Thakur, R. C., Kontkanen, J., Stolzenburg, D., Sipilä, M., Hussein, T., Paasonen, P., Bianchi, F., Salma, I., Weidinger, T., Pikridas, M., Sciare, J., Jiang, J., Liu, Y., Petäjä, T., Kerminen, V.-M., and Kulmala, M.: Sources and sinks driving sulfuric acid concentrations in contrasting environments: implications on proxy calculations, Atmospheric Chem. Phys., 20, 11747–11766, 2020.

Ding, J., Dai, Q., Zhang, Y., Xu, J., Huangfu, Y., and Feng, Y.: Air humidity affects secondary aerosol formation in different pathways, Sci. Total Environ., 759, 143540, 2021.

Gordon, H., Kirkby, J., Baltensperger, U., Bianchi, F., Breitenlechner, M., Curtius, J., Dias, A., Dommen, J., Donahue, N. M., Dunne, E. M., Duplissy, J., Ehrhart, S., Flagan, R. C., Frege, C., Fuchs, C., Hansel, A., Hoyle, C. R., Kulmala, M., Kürten, A., Lehtipalo, K., Makhmutov, V., Molteni, U., Rissanen, M. P., Stozkhov, Y., Tröstl, J., Tsagkogeorgas, G., Wagner, R., Williamson, C., Wimmer, D., Winkler, P. M., Yan, C., and Carslaw, K. S.: Causes and importance of new particle formation in the present-day and preindustrial atmospheres, J. Geophys. Res. Atmospheres, 122, 8739–8760, 2017.

Hellmuth, O.: Columnar modelling of nucleation burst evolution in the convective boundary layer – first results from a feasibility study Part I: Modelling approach, Atmospheric Chem. Phys., 6, 4175–4214, 2006.

Kerminen, V.-M., Chen, X., Vakkari, V., Petäjä, T., Kulmala, M., and Bianchi, F.: Atmospheric new particle formation and growth: review of field observations, Environ. Res. Lett., 13, 103003, 2018.

Kulmala, M., Petäjä, T., Nieminen, T., Sipilä, M., Manninen, H. E., Lehtipalo, K., Dal Maso, M., Aalto, P. P., Junninen, H., Paasonen, P., Riipinen, I., Lehtinen, K. E. J., Laaksonen, A., and Kerminen, V.-M.: Measurement of the nucleation of atmospheric aerosol particles, Nat. Protoc., 7, 1651–1667, 2012.

Nieminen, T., Kerminen, V.-M., Petäjä, T., Aalto, P. P., Arshinov, M., Asmi, E., Baltensperger, U., Beddows, D. C. S., Beukes, J. P., Collins, D., Ding, A., Harrison, R. M., Henzing, B., Hooda, R., Hu, M., Hõrrak, U., Kivekäs, N., Komsaare, K., Krejci, R., Kristensson, A., Laakso, L., Laaksonen, A., Leaitch, W. R., Lihavainen, H., Mihalopoulos, N., Németh, Z., Nie, W., O'Dowd, C., Salma, I., Sellegri, K., Svenningsson, B., Swietlicki, E., Tunved, P., Ulevicius, V., Vakkari, V., Vana, M., Wiedensohler, A., Wu, Z., Virtanen, A., and Kulmala, M.: Global analysis of continental boundary layer new particle formation based on long-term measurements, Atmospheric Chem. Phys., 18, 14737–14756, 2018.

Quéléver, L. L. J., Dada, L., Asmi, E., Lampilahti, J., Chan, T., Ferrara, J. E., Copes, G. E., Pérez-Fogwill, G., Barreira, L., Aurela, M., Worsnop, D. R., Jokinen, T., and Sipilä, M.: Investigation of new particle formation mechanisms and aerosol processes at Marambio Station, Antarctic Peninsula, Atmospheric Chem. Phys., 22, 8417–8437, 2022.

Roldin, P., Swietlicki, E., Massling, A., Kristensson, A., Löndahl, J., Eriksson, A., Pagels, J., and Gustafsson, S.: Aerosol ageing in an urban plume – implication for climate, Atmospheric Chem. Phys., 11, 5897–5915, 2011.

Sanchez, K. J., Russell, L. M., Modini, R. L., Frossard, A. A., Ahlm, L., Corrigan, C. E., Roberts, G. C., Hawkins, L. N., Schroder, J. C., Bertram, A. K., Zhao, R., Lee, A. K. Y., Lin, J. J., Nenes, A., Wang, Z., Wonaschütz, A., Sorooshian, A., Noone, K. J., Jonsson, H., Toom, D., Macdonald, A. M., Leaitch, W. R., and Seinfeld, J. H.: Meteorological and aerosol effects on marine cloud microphysical properties, J. Geophys. Res. Atmospheres, 121, 4142–4161, 2016.

Spracklen, D. V., Bonn, B., and Carslaw, K. S.: Boreal forests, aerosols and the impacts on clouds and climate, Philos. Trans. R. Soc. Math. Phys. Eng. Sci., 366, 4613–4626, 2008.

Uno, I., Wang, Z., Itahashi, S., Yumimoto, K., Yamamura, Y., Yoshino, A., Takami, A., Hayasaki, M., and Kim, B.-G.: Paradigm shift in aerosol chemical composition over regions downwind of China, Sci. Rep., 10, 6450, 2020.

A NEW PARAMETERIZATION OF ATMOSPHERIC SULFURIC ACID-AMINE NUCLEATION

Y. Li[1], J. Shen[1, 2], B. Zhao[1, 2], R. Cai[3], S. Wang[1, 2], J. Zheng[4], Markku Kulmala[2, 5, 6], J. Jiang[1]

[1]State Key Joint Laboratory of Environment Simulation and Pollution Control, School of Environment, Tsinghua University, 100084 Beijing, China
[2]State Environmental Protection Key Laboratory of Sources and Control of Air Pollution Complex, Beijing, 100084, China
[3]Institute for Atmospheric and Earth System Research/Physics, Faculty of Science, University of Helsinki, 00014 Helsinki, Finland
[4]School of Environmental Science and Engineering, Nanjing University of Information Science & Technology, Nanjing 210044, China
[5]Aerosol and Haze Laboratory, Beijing Advanced Innovation Center for Soft Matter Science and Engineering, Beijing University of Chemical Technology, 100029 Beijing, China
[6]Joint International Research Laboratory of Atmospheric and Earth System Sciences, School of Atmospheric Sciences, Nanjing University, Nanjing, China

Keywords: SULFURIC ACID-AMINE, NUCLEATION RATES, PARAMETERIZATION.

INTRODUCTION

New particle formation (NPF) events, a major source of particle number concentrations all over the world, could be initiated by different nucleation mechanisms in diverse environments. Specifically, in polluted urban atmospheres, sulfuric acid (SA)-amine nucleation, such as SA-dimethylamine (DMA) nucleation usually initializes intense NPF events (Yao *et al.*, 2018; Cai *et al.*, 2021). This is mainly due to the relatively high stabilities of SA-DMA clusters and correspondingly high formation rates of larger clusters under high coagulation scavenging effects. However, the present parameterizations of SA-DMA nucleation applied in the chemical transport models have not quantitatively included the effects of coagulation scavenging and cluster stabilities. We herein report a parameterization of 1.4 nm particle formation rates ($J_{1.4}$) through SA-DMA nucleation based on cluster dynamic simulations and quantum chemistry calculations. We demonstrate the significant improvements in simulating the temporal characteristics of NPF using this parameterization through comparisons between simulated and measured $J_{1.4}$. Furthermore, we explored the availability of this methodology in parameterizing the formation rate through other SA-amine nucleation mechanisms.

METHODS

The parameterization of $J_{1.4}$ through SA-DMA nucleation was set up based on the key pathway of SA-DMA cluster formation presented in a previous cluster kinetic model (Cai *et al.*, 2021). The values of Gibbs free energy and enthalpies of SA-DMA clusters are achieved from quantum chemistry calculations (Myllys *et al.*, 2019). Finally, for SA-DMA nucleation, the parameterized $J_{1.4}$ could be derived through four different input variables (temperatures T, condensation sinks CS, [SA], and [DMA]).

Certain assumptions of quasi-steady-state have been made in this study to achieve an explicit expression of $J_{1.4}$ and reduce computational costs. The availability of these assumptions was evaluated by calculating the e-folding time of certain cluster formation processes under typical conditions. Comparisons have also been made between the parameterized $J_{1.4}$ and the simulated $J_{1.4}$ from the kinetic model and a cluster dynamic simulation.

The improvements of this parameterization to the temporal characteristics of NPF were further demonstrated through comparisons between this parameterization, previous parameterizations and the measured formation rates. The measured precursor concentrations and particle number size distributions were achieved from ambient observations at an urban site in Beijing. The concentrations of SA are measured using a chemical ionization high resolution time of flight mass spectrometer and a chemical ionization time of flight mass spectrometer with a long mass analyzer (Bertram *et al.*, 2011; Jokinen *et al.*, 2012). Amine concentrations are measured using a modified time of flight mass spectrometer (TOF-MS) (Zheng *et al.*, 2015). The PNSDs of particles from 1 nm to 10 μm were measured using a particle size distribution (PSD) and a diethyl glycol-scanning mobility particle sizer (DEG-SMPS) (Jiang *et al.*, 2011; Liu *et al.*, 2016; Cai *et al.*, 2017a). CS is calculated from the measured PNSDs and $J_{1.4}$ is calculated using an improved aerosol population balance formula (Cai *et al.*, 2017b).
Furthermore, we explore the potential of applying this methodology in parameterizing other SA-amine nucleation rates. With different values of Gibbs free energy and collision coefficients applied in the parameterization, it could be extended to simulate other SA-amine (such as SA-MA and SA-TMA) nucleation rates. The availability of the quasi-steady-state assumptions in different SA-amine mechanisms was also evaluated by calculating e-folding time.

CONCLUSIONS

As a parameterization based on cluster dynamic simulations and quantum chemistry calculations, this parameterization of $J_{1.4}$ in SA-DMA nucleation has included the effects of coagulation scavenging and cluster stabilities. Compared with previous parameterizations, this parameterization could reproduce the dependencies of $J_{1.4}$ on CS and T. Thus with this new parameterization, significant improvements have been achieved in simulating the different levels of $J_{1.4}$ on NPF and non-NPF events in urban atmospheres. Furthermore, with higher evaporation rates than those of DMA, the nucleation rates through clusters of SA and other amines, such as methylamine and trimethylamine, would also be available for quasi-steady-state assumptions. These results also indicate that in polluted urban atmospheres, consideration of high coagulation sinks and cluster stabilities into nucleation parameterizations could be essential. The methodology of applying quasi-steady-state assumptions into cluster dynamic models might be plausible in addressing these effects in the parameterizations of binary SA-amine nucleation or even other nucleation mechanisms.

ACKNOWLEDGEMENTS

This work was supported by financial support from the National Natural Science Foundation of China (22188102, 92044301 and 42275110), Tencent Foundation through the XPLORER PRIZE and Samsung PM2.5 SRP are acknowledged.

REFERENCES

Bertram, T.H., Kimmel, J.R., Crisp, T.A., Ryder, O.S., Yatavelli, R.L.N., Thornton, J.A., Cubison, M.J., Gonin, M. & Worsnop, D.R. (2011) A field-deployable, chemical ionization time-of-flight mass spectrometer. *Atmos. Meas. Tech.*, **4**, 1471-1479.

Cai, R., Chen, D.-R., Hao, J. & Jiang, J. (2017a) A miniature cylindrical differential mobility analyzer for sub-3 nm particle sizing. *Journal of Aerosol Science*, **106**, 111-119.

Cai, R.L., Yan, C., Yang, D.S., Yin, R.J., Lu, Y.Q., Deng, C.J., Fu, Y.Y., Ruan, J.X., Li, X.X., Kontkanen, J., Zhang, Q., Kangasluoma, J., Ma, Y., Hao, J.M., Worsnop, D.R., Bianchi, F., Paasonen, P., Kerminen, V.M., Liu, Y.C., Wang, L., Zheng, J., Kulmala, M. & Jiang, J.K. (2021) Sulfuric acid-amine nucleation in urban Beijing. *Atmos Chem Phys*, **21**, 2457-2468.

Cai, R.L., Yang, D.S., Fu, Y.Y., Wang, X., Li, X.X., Ma, Y., Hao, J.M., Zheng, J. & Jiang, J.K. (2017b) Aerosol surface area concentration: a governing factor in new particle formation in Beijing. *Atmos Chem Phys*, **17**, 12327-12340.

Jiang, J., Chen, M., Kuang, C., Attoui, M. & McMurry, P.H. (2011) Electrical Mobility Spectrometer Using a Diethylene Glycol Condensation Particle Counter for Measurement of Aerosol Size Distributions Down to 1 nm. *Aerosol Science and Technology*, **45**, 510-521.

Jokinen, T., Sipilä, M., Junninen, H., Ehn, M., Lönn, G., Hakala, J., Petäjä, T., Mauldin Iii, R.L., Kulmala, M. & Worsnop, D.R. (2012) Atmospheric sulphuric acid and neutral cluster measurements using CI-APi-TOF. *Atmos. Chem. Phys.*, **12**, 4117-4125.

Liu, J., Jiang, J., Zhang, Q., Deng, J. & Hao, J. (2016) A spectrometer for measuring particle size distributions in the range of 3 nm to 10 μm. *Frontiers of Environmental Science & Engineering*, **10**, 63-72.

Myllys, N., Kubecka, J., Besel, V., Alfaouri, D., Olenius, T., Smith, J.N. & Passananti, M. (2019) Role of base strength, cluster structure and charge in sulfuric-acid-driven particle formation. *Atmos Chem Phys*, **19**, 9753-9768.

Yao, L., Garmash, O., Bianchi, F., Zheng, J., Yan, C., Kontkanen, J., Junninen, H., Mazon, S.B., Ehn, M., Paasonen, P., Sipila, M., Wang, M.Y., Wang, X.K., Xiao, S., Chen, H.F., Lu, Y.Q., Zhang, B.W., Wang, D.F., Fu, Q.Y., Geng, F.H., Li, L., Wang, H.L., Qiao, L.P., Yang, X., Chen, J.M., Kerminen, V.M., Petaja, T., Worsnop, D.R., Kulmala, M. & Wang, L. (2018) Atmospheric new particle formation from sulfuric acid and amines in a Chinese megacity. *Science*, **361**, 278-281.

Zheng, J., Ma, Y., Chen, M.D., Zhang, Q., Wang, L., Khalizov, A.F., Yao, L., Wang, Z., Wang, X. & Chen, L.X. (2015) Measurement of atmospheric amines and ammonia using the high resolution time-of-flight chemical ionization mass spectrometry. *Atmos Environ*, **102**, 249-259.

DETERMINING SATURATION VAPOR PRESSURE OF LOW VOLATILITY ORGANIC COMPOUNDS

ZIJUN LI[1], NOORA HYTTINEN[2], MIIKA VAINIKKA[1], OLLI-PEKKA TIKKASALO[3], SIEGFRIED SCHOBESBERGER[1] and TAINA YLI-JUUTI[1]

[1]Department of Technical Physics, University of Eastern Finland, Kuopio, Finland

[2]Department of Chemistry, Nanoscience Center, University of Jyväskylä, Jyväskylä, Finland

[3]Natural Resources Institute Finland (LUKE), Helsinki, Finland

Keywords: saturation vapor pressure, low-volatility organic compounds

INTRODUCTION

Organic compounds with sufficiently low volatility can partition onto existing aerosol particles or form new particles. Low-volatility organic compounds (LVOCs) play a significant role in atmospheric aerosol formation. Under gas-particle equilibrium, LVOCs primarily partition into the particle phase and contribute significantly to aerosol mass. Saturation vapor pressure (p_{sat}) is the key thermodynamic property governing the equilibrium between gas and particle phases. Knowledge about p_{sat} of LVOCs is crucial to the understanding of the ambient aerosol budget.

Experimentally determining p_{sat} of LVOCs is challenging (Bilde *et al.* 2015). Although numerous techniques have been used for volatility measurements, very few are conducted at a temperature setting relevant to atmospheric aerosol formation. Here we experimentally determined the p_{sat} values of the selected LVOCs at 295 K by following the particle evaporation in a residence time chamber (RTC). Additionally, we applied quantum-chemistry-based COSMO*therm* calculations to estimate the p_{sat} values of the studied compounds. By coupling isothermal evaporation measurement and state-of-the-art computational simulation, we provide a comprehensive analysis of the volatilities of the selected LVOCs (Li *et al.* 2023), which is still rare in aerosol research.

METHODS

We selected 11 LVOCs for p_{sat} measurement (Table 1). Particle samples were generated by nebulising stock solutions with an atomizer. Either a silica gel diffusion dryer or a large dilution flow of dry purified air was used to remove the used solvent (water or acetonitrile). Monodisperse particles with 80 nm electrical mobility diameter were selected by nanometre aerosol mobility analysers (NanoDMA, model 3085, TSI). After the size selection, the resultant aerosol particles were fed into either bypass lines of varying lengths or a stainless steel RTC (25 L or 100 L in volume) for prolonged isothermal evaporation. Vapour wall losses in the bypass line and RTCs were fast enough to ensure negligible amounts of vapours in the gas phase. The measurement setup was maintained under dry conditions (< 5% RH) at 295 K.

Polyethylene Glycol (PEG)	Carboxylic Acid	Alcohol	Ester
PEG 6	palmitic acid		
PEG 7	stearic acid	meso-erythritol	di-ethylhexyl sebacate
PEG 8	azelaic acid	xylitol	(DEHS)
PEG 9	sebacic acid		

Table 1. List of the LVOCs measured in this study.

For each compound, we determined the optimized p_{sat} value from the time series of particle size change (Salo *et al.* 2010), with the use of the Approximate Bayesian Computation with Sequential Monte Carlo (ABC-SMC) algorithm (Sisson *et al.* 2007). Additionally, we used COSMO*therm* 2021 program (BIOVIA COSMO*therm* 2021) to compute the p_{sat} values for the studied compounds.

CONCLUSIONS

Our "RTC" method can characterize LVOCs with p_{sat} values between 10^{-8} and 10^{-4} Pa at an atmospherically relevant temperature of 295 K. The experimentally determined p_{sat} values are in the range of literature data, mostly within one order of magnitude. In addition, COSMO*therm* is able to predict p_{sat} values for the studied compounds within an order of magnitude, except for PEGs. The large difference between the measured and computed p_{sat} values for PEGs highlights the importance of conformer selection in COSMO*therm* calculations for new types of compounds that have not been implemented in the model parametrization. Applications of our "RTC" method can be further used to perform isothermal evaporation experiments at different temperatures and/or RH settings. This will help probe two other important thermodynamic properties – enthalpy of vaporization and organic activity coefficient.

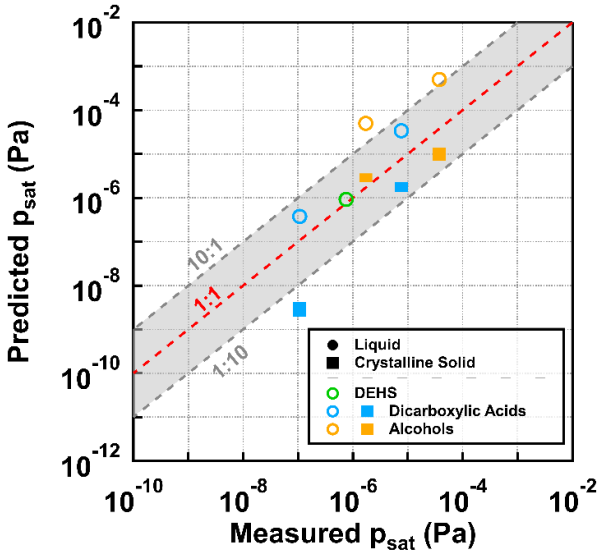

Figure 1. Comparison of p_{sat} values between the measurement in this study (x-axis) and different COSMO*therm* estimations (y-axis) at 295 K. The two different markers represent the comparisons of the computed p_{sat} values of liquid (filled circle) and crystalline solid (filled bars) phase states, respectively. The dashed red line is the 1:1 line, with grey shaded areas showing a deviation of one log unit.

ACKNOWLEDGEMENTS

This research has been supported by the Academy of Finland Flagship program (grant no. 337550), the Academy of Finland (grant nos. 317373, 338171, 346371), and the University of Eastern Finland Doctoral Program in Environmental Physics, Health, and Biology. We also thank CSC - IT Centre for Science, Finland, for computational resources.

REFERENCES

Bilde M., et al. 2015. Saturation vapor pressures and transition enthalpies of low-volatility organic molecules of atmospheric relevance: From dicarboxylic acids to complex mixtures. *Chemical Reviews* 115: 4115-4156.

BIOVIA COSMO*therm*. 2021. *Release 2021; dassault systèmes*.

Li Z., et al. 2023. Saturation vapor pressure characterization of selected low-volatility organic compounds using a residence time chamber. *Atmos. Chem. Phys. Discuss.* 2023: 1-21.

Salo K., et al. 2010. Aerosol volatility and enthalpy of sublimation of carboxylic acids. *Journal of Physical Chemistry A* 114: 4586-4594.

Sisson S.A., et al. 2007. Sequential monte carlo without likelihoods. *Proceedings of the National Academy of Sciences* 104: 1760-1765.

OVERLOOKED AEROSOL SOURCE FROM FIRELIGHTERS AND SOLID BIOMASS FUELS

C. LIN[1,2,3], D. CEBURNIS[1], C. O'DOWD[1], and J. OVADNEVAITE[1]

[1] School of Physics, Ryan Institute's Centre for Climate and Air Pollution Studies, National University of Ireland Galway. University Road, Galway. H91 CF50, Ireland
[2] State Key Laboratory of Loess and Quaternary Geology (SKLLQG), Center for Excellence in Quaternary Science and Global Change, Institute of Earth Environment, Chinese Academy of Sciences, Xi'an 710061, China
[3]Department of Civil and Environmental Engineering, The Hong Kong Polytechnic University, Hong Kong SAR 999077, China

Keywords: Biomass burning, Submicron aerosol, Source apportionment, Aerosol Mass Spectrometry

INTRODUCTION

Biomass burning is a major emission source of the atmospheric OA (Lin et al., 2018), partly due to its higher emission factor than conventional pollution sources e.g., traffic and industrial activities. The residential burning of wood and peat, an accumulation of partially decayed vegetation, is recently found to cause extreme air pollution events that rivalled the pollution levels in some of the most polluted cities e.g., Beijing, China (Lin et al., 2018). Along with OA, BC can also be emitted at a lesser extent as a result of incomplete combustion of biomass with its relative emissions depending on the types of biomass and combustion conditions, and typical BC to OA ratio is <0.1 (Bond et al., 2004).

METHODS

The aerosol samples generated from the combustion of test fuels were collected using a sampling line connected to the chimney flue. The sampling line was made of ordinary ½ inch copper pipe which extended approximately 5 cm inside the chimney flue, parallel to air flow. $PM_{2.5}$ cyclone was deployed to remove coarse particles and a water trap was fitted downstream of the sampling line. This was followed by a Dekati diluter (Dekati Ltd.) that allowed a dilution rate in the range of 70-250:1. An ACSM (Aerodyne Research Inc.) and an Aethalometer (AE-33; Magee Scientific) were used to measure the chemical composition of submicron aerosol samples. A Nafion dryer was used to dry the aerosol particles before they entered the ACSM and AE-33. The time resolution of ACSM was set to 2 min while it was 1 min for AE-33.

CONCLUSIONS

Smokeless coal and biomass briquette burning particles were smaller in size but had a much higher number emission factor than wood, peat, and smoky coal (Fig. 1a). Specifically, the emission factor from burning smokeless coal and biomass briquettes was 3.1×10^9 and 2×10^9 particles kg^{-1}, respectively, 2-3 times higher than that from wood (0.9×10^9 particles kg^{-1}), peat (1.0×10^9 particles kg^{-1}), and smoky coal (1.2×10^9 particles kg^{-1}). In contrast, in terms of particle mass emission, the emission factor for smokeless coal and biomass briquettes was

smaller than wood, peat, and smoky coal (Fig. 1b). This is because small particles ($PM_{0.1}$ <100 nm) contributed less to the particle mass, although they were high in numbers. The emission factor was 0.4 g kg^{-1} for smokeless coal and 0.3 g kg^{-1} for biomass briquettes, 50% - 77% lower than that for wood (1.3 g kg^{-1}), smoky coal (1.1 g kg^{-1}), and peat (0.8 g kg^{-1}). Therefore, consistent with what was expected, replacing smoky fuels with smokeless fuels was supposed to reduce particle mass emission and, therefore, increase the chances of meeting the air quality guidelines. However, this is because particles were made to be smaller not necessarily less in numbers. Unexpectedly, particle numbers were made even more numerous as shown in Fig. 1a. Switching to Eco design stoves reduced particle emission by 35-50%, which, however, were still higher than burning smoky fuels. What's more striking is that firelighter had the highest emission factor both in terms of particle mass (6.5 g kg^{-1}) and particle number (3.7 x 10^9 particles kg^{-1}).

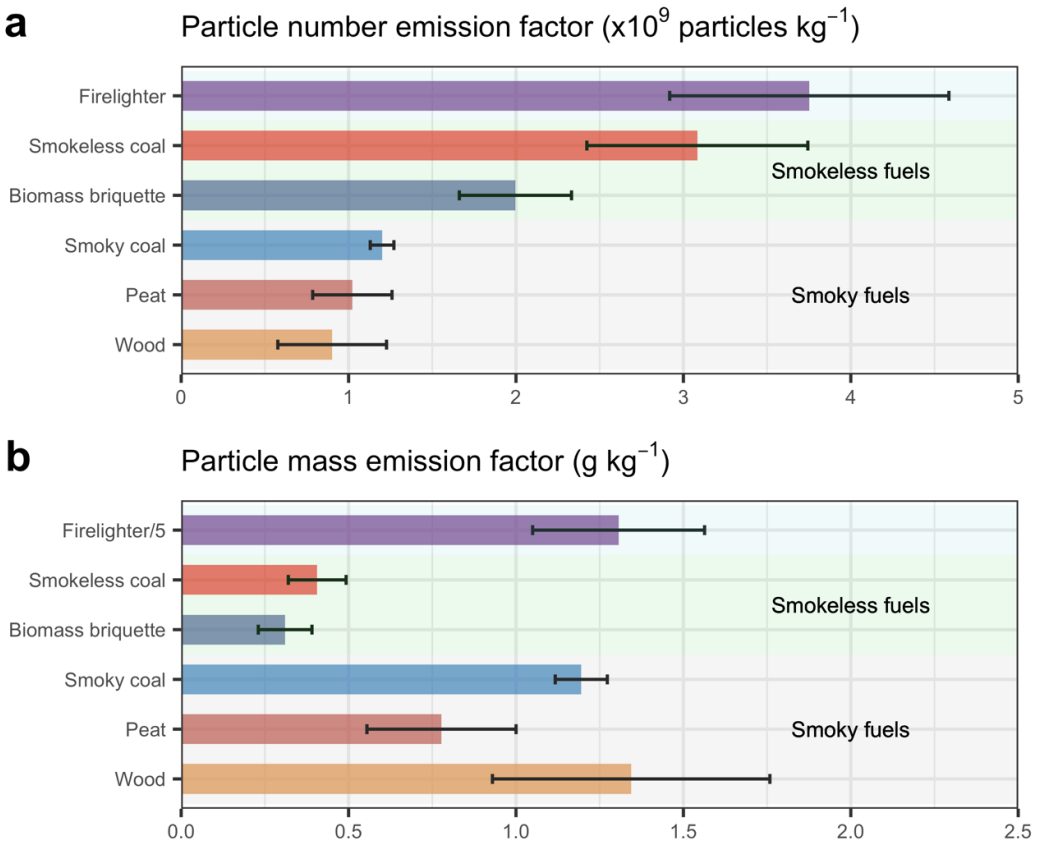

Figure 1. Submicron particle number and particle mass emission factor for smokeless and smoky solid fuels.

ACKNOWLEDGEMENTS

This work was supported by the EPA-Ireland (AEROSOURCE, 2016-CCRP-MS-31), the Department of the Environment, Climate and Communications. The authors would also like to acknowledge the contribution of the COST Action CA16109 (COLOSSAL) and MaREI, the SFI Research Centre for Energy, Climate and Marine.

REFERENCES

Bond, T. C. et al. A technology-based global inventory of black and organic carbon emissions from combustion. J. Geophys. Res. Atmos. **109**, doi:10.1029/2003jd003697 (2004).

Lin, C. *et al.* Extreme air pollution from residential solid fuel burning. *Nature Sustainability.* **1**, 512-517 (2018).

INCREASED SECONDARY POLLUTION IN FENWEI PLAIN IN CENTRAL CHINA

C. LIN[1,2], R.J. HUANG[2]

[1] Department of Civil and Environmental Engineering, The Hong Kong Polytechnic University, Hong Kong SAR 999077, China
[2] State Key Laboratory of Loess and Quaternary Geology (SKLLQG), Center for Excellence in Quaternary Science and Global Change, Institute of Earth Environment, Chinese Academy of Sciences, Xi'an 710061, China
Keywords: Secondary Organic Aerosol, Ozone, Source apportionment, Aerosol Mass Spectrometry

INTRODUCTION

The Fenwei Plain (about 760 km in length and 40–100 km in width) is the largest plain in the middle reaches of the Yellow River. It is home to over 50 million people in central China, surrounded by the Chinese Loess Plateau to the northwest and Qinling Mountains to the south. The rapid growth and urbanization of Fenwei Plain are accompanied by air pollution that is characterized by high concentrations of fine particulate matter ($PM_{2.5}$) in the heating season and high concentrations of ground-level ozone in the warm season (Cao and Cui, 2021; Li et al., 2021). Recently, air pollution in Fenwei Plain has been found to be more severe than in the Beijing-Tianjin-Heibei (BTH) region, Yangtze River Delta (YRD) region, and Pearl River Delta (PRD) region, making Fenwei Plain one of the most polluted regions in China (Li et al., 2022). In addition to being the emission hotspot of air pollutants, the unique topography of the Fenwei Plain is favorable for accumulating the air pollutants inside the basin, rapidly building up high levels of air pollutants e.g., under typical cold-haze conditions in calm weather with a wind speed of less than 2 m s^{-1}. In 2018, the Fenwei Plain was designated as one of the three key regions for the "Blue Sky Protection Campaign" (the other two are the BTH and YRD regions). To evaluate the effectiveness of the clean air policies and to further develop cost-effective mitigation policies in the Fenwei Plain, a better understanding of the trend in pollution patterns, sources, and formation mechanism of key pollutants i.e., $PM_{2.5}$ and ozone, is required.

METHODS

Hourly O_3, $PM_{2.5}$, NO_2, SO_2, and CO were continuously monitored at 13 sites within the city center of Xi'an from 2015 to 2021 (Fig. 1). Measurements of these pollutants were routinely managed by the China National Environmental Monitoring Centre. The distance between the sampling sites is up to 40 km. Despite the distance, the time series of $PM_{2.5}$ and O_3 monitored at different sites were well correlated with similar magnitude in concentrations. The consistency of the measurements between different sampling sites confirmed the data quality. The data from 13 sites were averaged to get the city-wide mean concentration of each pollutant and were used to perform the trend analysis.

VOC and OVOCs were measured using a Vocus-PTR which was equipped with a Long Time-of-Flight (LToF) mass analyzer. The chemical composition of non-refractory particulate matter (NR-$PM_{2.5}$) was measured using an AMS or an aerosol chemical speciation monitor (ACSM) at the old campus of the Institute of Earth Environment, Chinese Academy of Sciences in the winter of 2013 and 2014, and more recently in 2019, 2020, and 2021. OA factors were apportioned using the Positive Matrix Factorization (PMF) with the Multilinear Engine (ME-2)

Master Chemical Mechanism (MCM) v3.3.1 was incorporated in a chemical box model using the framework for 0-D Atmospheric Modeling (F0AM). Surface observational data were averaged for the overlapping period with OVOC measurements to get the diurnal profiles of each pollutant. The averaged air pollutants, including NO_2, O_3, CO, and the measured VOC/OVOCs, except for HCHO (which is the simulated target) were used to constrain the model at hourly resolution (Fig. 2).

CONCLUSIONS

Through the analysis of 7 years (2015-2021) of surface monitoring of the air pollutants in Xi'an, the largest city in the Fenwei Plain, we show that roughly 2/3 of the days exceeded either the $PM_{2.5}$ or the O_3 level-1 air quality standard, highlighting the severity of air pollution. Moreover, an increase in O_3 pollution

in the winter haze was also revealed, due to the constantly elevated reactive oxygenated volatile organic compounds (OVOCs), and in particular formaldehyde with ozone formation potential of over 50 μg m^{-3} in combination with the reduced NO_2. The abrupt decrease of NO_2, as observed during the lockdown in 2020, provided real-world evidence of the control measures, targeting only NO_x (70% decrease on average), were insufficient to reduce ozone pollution because reactive OVOCs remained constantly high in a VOC-limited regime. Model simulation results showed that with NO_2 reduction from 20-70%, the self-reaction rate between peroxy radicals, a pathway for SOA formation, was intensified by up to 75%, while the self-reaction rate was only reduced with a further reduction of VOCs of >50%. Therefore, a synergic reduction in $PM_{2.5}$ and O_3 pollution can only be achieved through a more aggressive reduction of their precursor gases. This study elucidates the status of ozone and $PM_{2.5}$ pollution in one of the most polluted regions in China, revealing a general trend of increasing secondary pollution i.e., ozone and SOA in winter haze. Controlling precursor gas emissions is anticipated to curb both ozone and SOA formation which will benefit not just the Fenwei Plain but also other regions in China.

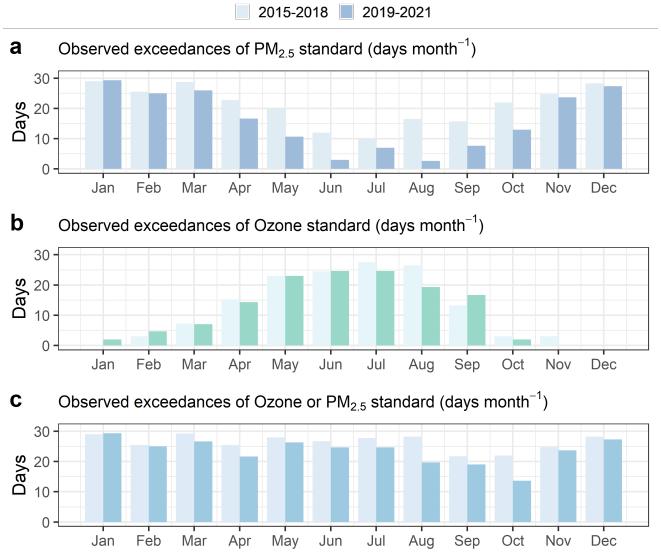

Figure 1. Observed exceedance frequency (in days $month^{-1}$) of Ozone or $PM_{2.5}$ standard in the biggest city (i.e., Xi'an) in Fenwei Plain, averaged over 2015-2018 and 2019-2021. Ozone and $PM_{2.5}$ were averaged from 13 monitoring sites in Xi'an.

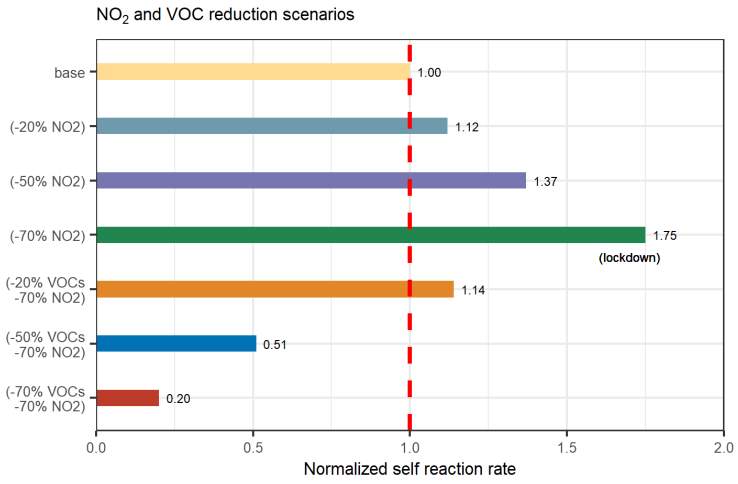

Figure 2. Changes in self-reaction rate between peroxy radicals with 20-70% reduction in NO_2 and a further 20-70% in VOC reduction. Covid-19 lockdown in 2020 correponded to a reduction of NO_2 of

70%. The reaction rate in different reduction scenarios was normalized to the value in the base run (guided by the red dash line).

ACKNOWLEDGEMENTS

This work was supported by National Natural Science Foundation of China (NSFC) under Grant No. 42277092, 42107126, 42207137, and 41925015, the Strategic Priority Research Program of Chinese Academy of Sciences (No. XDB40000000), the Chinese Academy of Sciences (no. ZDBS-LY-DQC001), Institute of Earth Environment (E051QB2837), and the Cross Innovative Team fund from the State Key Laboratory of Loess and Quaternary Geology (No. SKLLQGTD1801).

REFERENCES

Cao, J. J., and Cui, L.: Current Status, Characteristics and Causes of Particulate Air Pollution in the. Fenwei Plain, China: A Review, J. Geophys. Res. Atmos., 126, e2020JD034472, https://doi.org/10.1029/2020JD034472, 2021.

Li, K., Jacob, D. J., Liao, H., Qiu, Y., Shen, L., Zhai, S., Bates, K. H., Sulprizio, M. P., Song, S., Lu, X., Zhang, Q., Zheng, B., Zhang, Y., Zhang, J., Lee, H. C., and Kuk, S. K.: Ozone pollution in the North China Plain spreading into the late-winter haze season, Proc. Natl. Acad. Sci., 118, e2015797118, 10.1073/pnas.2015797118, 2021.

Li, C., Zhu, Q., Jin, X., and Cohen, R. C.: Elucidating Contributions of Anthropogenic Volatile Organic Compounds and Particulate Matter to Ozone Trends over China, Environ. Sci. Technol., 56, 12906-12916, 10.1021/acs.est.2c03315, 2022

SEASONAL VARIATION OF AEROSOL ACIDITY: IMPLICATIONS IN SECONDARY INORGANIC AEROSOL

Y. C. LIU[1], Y. S. ZHANG[1], B. Y. SONG[1], C. J. HUA[1], Y. Z. WANG[1], J. L. ZHAN[1], C. YAN[2], F. BIANCHI[3], T. PETÄJÄ[3], X. L. BAO[4] and M. KULMALA[1,3]

[1] Aerosol and Haze Laboratory, Advanced Innovation Center for Soft Matter Science and Engineering, Beijing University of Chemical Technology, Beijing, China
[2] Joint International Research Laboratory of Atmospheric and Earth System Sciences, School of Atmospheric Sciences, Nanjing University, Nanjing, China
[3] Institute for Atmospheric and Earth System Research, Faculty of Science, University of Helsinki, Helsinki, Finland
[4] Hebei Provincial Academy of Environmental Sciences, Shijiazhuang, China

Keywords: Aerosol acidity, Aerosol water content, Aqueous reactions, Inorganic salts.

INTRODUCTION

As an important property of aerosol particles, aerosol acidity can influence the secondary transformation of air pollutants, aerosol-cloud interactions, and toxicity of particles. It has been found that an increase in temperature enhances aerosol acidity by promoting the ionization of acids (Fountoukis and Nenes 2007, Pye et al. 2020). On the other hand, a high RH or aerosol water content (AWC) decreases aerosol acidity because of the dilution effect (Kakavas et al. 2021, Duan et al. 2019). In this work, an increase in aerosol acidity is observed as a function of RH or AWC in winter in the North China Plain. It is opposite to the expected one in summer. The possible mechanism related to aqueous reaction is discussed.

METHODS

Observations were carried out at Aerosol and Haze Laboratory, Beijing University of Chemical Technology (AHL/BUCT Station, Lat. 39º56′31″ and Lon. 116º17′52″) from August 2019 to November 2020 and Hebei Atmospheric Supersite (HAS/SJZ, Lat. 38.0281º and Lon. 114.6070º) from March 2018 to November 2020 (Liu et al. 2020). The concentrations of water-soluble ions (Cl^-, NO_3^-, SO_4^{2-}, Na^+, NH_4^+, K^+, Mg^{2+}, and Ca^{2+}) in $PM_{2.5}$ and gas pollutants (HCl, HONO, HNO_3, SO_2, and NH_3) were measured using analyzers for Monitoring AeRosols and Gases in ambient Air (MARGA, 2060R at the AHL/BUCT station and 2080 at the HAS/SJZ station, Metrohm Process Analytics) with 1 hour of time resolution. Trace gases including NO_x, SO_2, CO, and O_3 and meteorological parameters including temperature (*T*), RH, pressure, wind speed and direction were also measured at the same time. The details can be found elsewhere (Liu et al. 2022). Aerosol pH and AWC were estimated using the ISORROPIA II model using the measured particle and gas composition, *T*, and RH as the input and assuming that the aerosol system is in equilibrium (Shi et al. 2019, Ding et al. 2019). The γ_{H+} in concentrated electrolyte solutions was calculated according to the literature method (Glueckauf 1955, Glueckauf 1957).

RESULTS AND CONCLUSIONS

The aerosol pH varies from 3.15 to 8.83 with a mean value of 5.20±0.86 in Shijiazhuang. It is comparable with that in Beijing. Seasonal variation of aerosol acidity is observed in both Shijiazhuang and Beijing. The variation of aerosol pH can be described by a combination of a sine function and a linear function of time. The seasonal wave of aerosol pH is mainly driven by temperature variation, while the linear decline of aerosol pH is related to the emission reduction of dust (Liu et al. 2022). The aerosol pH increases with increasing RH or AWC in summer in both cities, while it exponentially decreases as a function of RH or AWC in winter (Figure 1). The aerosol acidity positively correlated with the ratio of SO_4^{2-}/NO_3^- regardless of the season. The ratio of SO_4^{2-}/NO_3^- increases with increasing RH or AWC in winter, while it decreases in summer. This well explains the observed opposite response of aerosol pH to RH or AWC in different

seasons. The calculated production rates of sulfate and nitrate via aqueous reactions further explain the different dependency of the SO_4^{2-}/NO_3^- on RH or AWC, i.e., the sulfate formation rate via aqueous reactions of SO_2 is more sensitive to RH or AWC in winter when compared with the nitrate formation via N_2O_5 hydrolysis and vice versa in summer. Our results imply the complex interactions between physiochemical properties and secondary aerosol formation.

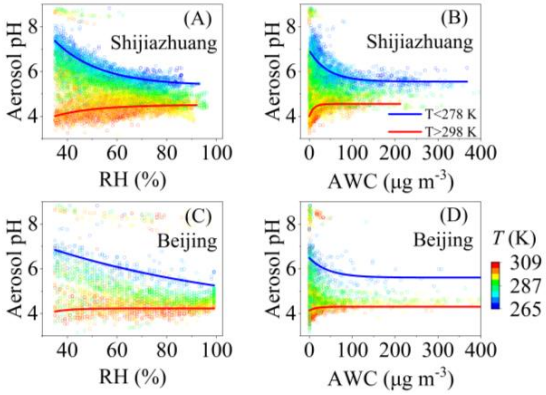

Figure 1. Dependence of aerosol pH on (A) RH and (B) AWC in Shijiazhuang and (C) and (D) in Beijing.

ACKNOWLEDGEMENTS

This work was supported by the National Natural Science Foundation of China (42275117).

REFERENCES

Ding, J., P. Zhao, J. Su, Q. Dong, X. Du & Y. Zhang (2019) Aerosol pH and its driving factors in Beijing. *Atmos. Chem. Phys.*, 19**,** 7939-7954.

Duan, J., R. Lyu, Y. Wang, X. Xie, Y. Wu, J. Tao, T. Cheng, Y. Liu, Y. Peng, R. Zhang, Q. He, W. Ga, X. Zhang & Q. Zhang (2019) Particle Liquid Water Content and Aerosol Acidity Acting as Indicators of Aerosol Activation Changes in Cloud Condensation Nuclei (CCN) during Pollution Eruption in Guangzhou of South China. *Aerosol Air Qual. Res.*, 9**,** 2662-2670.

Fountoukis, C. & A. Nenes (2007) ISORROPIA II: a computationally efficient thermodynamic equilibrium model for K^+–Ca^{2+}–Mg^{2+}–NH_4^+–Na^+–SO_4^{2-} –NO_3^- –Cl^- –H_2O aerosols. *Atmos. Chem. Phys.*, 7**,** 4639-4659.

Glueckauf, E. (1955) The influence of ionic hydration on activity coefficients in concentrated electrolyte solutions. *Trans. Faraday Soc.*, 51**,** 1235-1244.

Glueckauf, E. (1957) The influence of ionic hydration on activity coefficients in concentrated electrolyte solutions. *Trans. Faraday Soc.*, 53**,** 305-305.

Kakavas, S., D. Patoulias, M. Zakoura, A. Nenes & S. N. Pandis (2021) Size-resolved aerosol pH over Europe during summer. *Atmos. Chem. Phys.*, 21**,** 799-811.

Liu, Y., J. Zhan, F. Zheng, B. Song, Y. Zhang, W. Ma, C. Hua, J. Xie, X. Bao, C. Yan, F. Bianchi, T. Petäjä, A. Ding, Y. Song, H. He & M. Kulmala (2022) Dust emission reduction enhanced gas-to-particle conversion of ammonia in the North China Plain. *Nat. Commun.*, 13**,** 6887.

Liu, Y., Y. Zhang, C. Lian, C. Yan, Z. Feng, F. Zheng, X. Fan, Y. Chen, W. Wang, B. Chu, Y. Wang, J. Cai, W. Du, K. R. Daellenbach, J. Kangasluoma, F. Bianchi, J. Kujansuu, T. Petäjä, X. Wang, B. Hu, Y. Wang, M. Ge, H. He & M. Kulmala (2020) The promotion effect of nitrous acid on aerosol formation in winter in Beijing: possible contribution of traffic-related emissions. *Atmos. Chem. Phys.*, 20**,** 13023–13040.

Pye, H. O. T., A. Nenes, B. Alexander, A. P. Ault, M. C. Barth, S. L. Clegg, J. L. Collett Jr, K. M. Fahey, C. J. Hennigan, H. Herrmann, M. Kanakidou, J. T. Kelly, I. T. Ku, V. F. McNeill, N. Riemer, T. Schaefer, G. Shi, A. Tilgner, J. T. Walker, T. Wang, R. Weber, J. Xing, R. A. Zaveri & A. Zuend (2020) The acidity of atmospheric particles and clouds. *Atmos. Chem. Phys.*, 20**,** 4809-4888.

Shi, G., J. Xu, X. Shi, B. Liu, X. Bi, Z. Xiao, K. Chen, J. Wen, S. Dong, Y. Tian, Y. Feng, H. Yu, S. Song, Q. Zhao, J. Gao & A. G. Russell (2019) Aerosol pH Dynamics During Haze Periods in an Urban Environment in

China: Use of Detailed, Hourly, Speciated Observations to Study the Role of Ammonia Availability and Secondary Aerosol Formation and Urban Environment. *J. Geophys. Res.: Atmos.*, 124**,** 9730-9742.

WEAKENED GAS-TO-PARTICLE PARTITIOINING OF OVOCs IN LIQUIFIED AEROSOL PARTICLES

W. MA[1], F.X. ZHENG[1], Y.S. ZHANG[1], X. CHEN[1], J.L ZHAN[1], C.J. HUA[1], B.Y SONG[1], Z.C. WANG[1], J.L. XIE[1], C. YAN[3], M.T. KULMALA[1,2], Y.C. LIU[1*]

[1]Aerosol and Haze Laboratory, Advanced Innovation Center for Soft Matter Science and Engineering, Beijing University of Chemical Technology, Beijing, 100029, China
[2]Institute for Atmospheric and Earth System Research, Faculty of Science, University of Helsinki, Helsinki, 00014, Finland
[3]Joint International Research Laboratory of Atmospheric and Earth System Research, School of Atmospheric Sciences, Nanjing University, Nanjing, 210004, China

Keywords: GAS-TO-PARTICLE PARTITIOINING, SECONDARY ORGANIC AEROSOL, PHATE STATE OF AEROSOL, AEROSOL WATER CONTENT.

INTRODUCTION

In the past 10 years, the contribution of organic aerosol (OA), dominated by secondary OA (SOA), became more and more vital to $PM_{2.5}$ in the NCP.(Duan et al., 2020; Huang et al., 2019; Sun et al., 2020) Most SOA is produced by the oxidation of anthropogenic or biogenic volatile organic compounds (VOCs) in the atmosphere. Primary OA (POA) in the atmosphere could be oxidized to SOA in the heterogeneous interface of liquefied particles or fog/cloud droplets.(Ervens et al., 2011; Mcneill, 2015) Recently, extensive studies have already reported that the uptake of oxygenated VOCs (OVOCs) by liquefied aerosols and fog/clouds, subsequently, transformation to low volatile products, could also contribute to the SOA formation.(Sun et al., 2010; Ge et al., 2012; Kim et al., 2019; Chen et al., 2022; Wei Yuan, 2021) However, the mechanisms of SOA formation are poorly understood, which in turn hindered us from evaluating and simulating the responses of SOA mass loading to changes in VOC emissions and other factors.

The aqueous processes include reactions of condensed semi-volatile organic compounds (SVOCs) in aerosol liquid water to form organic acid, oligomers, organonitrogens, and organosulfates via various paths (e.g., photochemical reactions, acid-catalyzed condensation, and esterification with inorganic species, etc.).(Lim et al., 2010; Tolocka et al., 2004; Perri et al., 2010) It should be noted that those previously observational studies proposed the possible mechanisms mentioned above mainly based on mass spectrum analysis of OA and the correlation between OA factors from positive matrix factor (PMF) analysis and aerosol water content (AWC) or relative humidity (RH)**.** It has been well recognized that the partition of gas-phase oxidation intermediates of VOCs onto the preexisting aerosol particles is important for SOA formation according to the gas-to-particle partitioning theory.(Odum et al., 1996) However, little is known about how the partitioning of gaseous oxidation products or SVOCs involves in the aqueous processes due to the lack of simultaneous observations of the gas- and particle-phase markers in the atmosphere.

Here continuous measurements of gas- and particle-phases composition of organics were conducted by an iodine-adduct time-of-flight chemical ionization mass spectrometer (I^--TOF-CIMS) coupled with a filter inlet for gases and aerosols (FIGAERO) in Beijing.(Zheng et al., 2021) The gas-to-particle partitioning and equilibrium were explored. It has been found that the gas-to-particle partitioning of some oxygenated organic molecules tends to be weakened when particles transit from a solid or semi-solid to a liquid phase. The implication of this process on SOA formation has also been discussed. This work will help understand SOA formation via an aqueous process, especially the role of gas-to-particle partitioning and its equilibrium in SOA formation under conditions of higher AWC or RH during haze events.

METHODS

Continuous field observations were conducted at AHL/BUCT Site with a latitude of 39º56′31″ and longitude of 116º17′52″ from March 1 to 25, 2021. The detailed descriptions of this site have been discussed elsewhere.(Liu et al., 2020a) Briefly, the station, as a typical urban site surrounded by traffic and residential emissions, is on the rooftop of the main teaching building.

A I^--TOF-CIMS (TOF-CIMS, Aerodyne Research, Inc., USA) coupled with a FIGAERO inlet was used to measure both gas- and particle-phase organics. Iodide reagent ion provides a soft ionization technique with little fragmentation and high selectivity to multi-functional organic compounds. Thus, it is suitable for measuring thousands of complicated oxygenated compounds in the ambient.(Cai et al., 2022b) A Time-of-Flight Aerosol Chemical Speciation Monitor (ToF-ACSM, Aerodyne) was used to measure the bulk composition of non-refractory $PM_{2.5}$ (NR-$PM_{2.5}$), including chloride, nitrate, sulfate, ammonium, and organics. A Monitoring AeRrosol and Gases in ambient Air (MARGA, 2006R) was used to detect water-soluble ions (Cl^-, NO_3^-, SO_4^{2-}, Na^+, K^+, Mg^{2+}, and Ca^{2+}) in $PM_{2.5}$ and gas pollutants (e.g. NH_3) with a time resolution of 1 hour. Trace gases such as CO, SO_2, O_3, and NO*x* were measured with corresponding analyzers (Thermal Scientific, 42i, 43i, 48i, and 49i). Meteorological parameters including relative humidity (RH), pressure, temperature (T), wind speed, and direction were measured by a weather station (ASW310, Vaisala). The photolysis rate (J_{NO2}) was measured via continuous measurement of the actinic flux in the wavelength range of 285-375 nm using a J_{NO2} filter radiometer (J_{NO2} radiometer, Metcon). The details of the instrument calibration can be found in our previous work.(Liu et al., 2020a; Liu et al., 2021) The aerosol water content (AWC) was estimated by combining an aerosol thermodynamic model (ISORROPIA II)(Liu et al., 2020b) and the measured particle composition by the MARGA along with T and RH, assuming that the aerosol system was in equilibrium. The dataset was selected when RH>30% to reduce the uncertainty of AWC calculations.

PMF analysis was conducted on the organic mass spectra obtained from the TOF-ACSM by using the Igor PMF evaluation tool (PET, version 3.08).(Paatero and Tapper, 1994) (Ulbrich et al., 2009) The unit-mass-resolution (UMR) data between m/z 12 and 150 were used as input. The PMF analysis identified five OA factors for NR-$PM_{2.5}$ (Fig. 1a), including three factors related to primary OA (POA), that is, cooking-related OA (COA), biomass burning OA (BBOA), and fossil fuel OA (FFOA) from coal combustion and traffic emissions, and two oxygenated OA (OOA) factors, that is, aqueous-phase related OOA (aq-OOA) and MO-OOA.).

The glass transition temperature (T_g) of particles is calculated according to the Gordon-Taylor equation.(Koop et al., 2011) When $T/T_g>1$, SOA is solid, while $T/T_g<1$, SOA exists in semi-solid or liquid states. Here the threshold between the semi-solid and liquid states is $T/T_g=0.85$ (Fig 1b), slightly higher than the 0.8 (Koop et al., 2011).

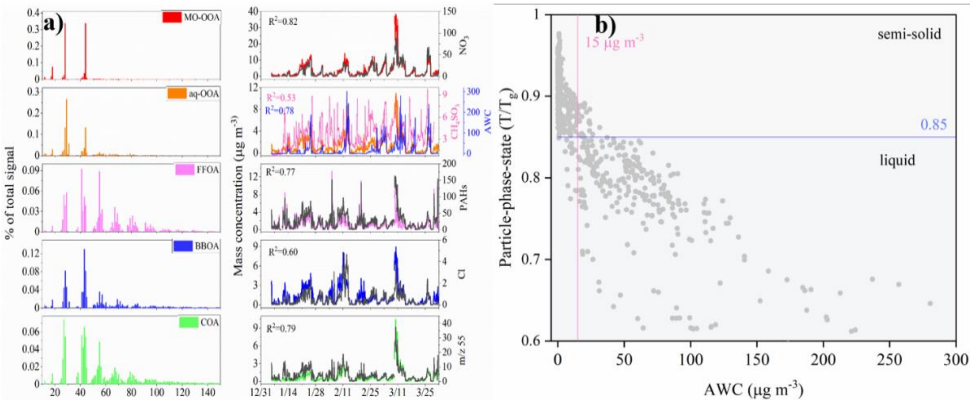

Fig 1. a) Mass spectra and time series of the five OA factors (MO-OOA, aq-OA, FFOA, BBOA, and COA) resolved from the PMF analysis; b) The particle-phase-state transition from semi-solid to liquid particles compared to AWC

RESULTS AND CONCLUSIONS

The average mass concentration for NR-$PM_{2.5}$ was 38.6±40.1 μg m^{-3}, lower than the annual values from 58.7 to 94.0 μg m^{-3} reported in Beijing from 2008 to 2016.(Duan et al., 2020). Unlike the previous studies, OA only contributed 26.0% to the mass concentration of NR-$PM_{2.5}$ on average and the mass ratio of sulfate to nitrate (0.2) was much lower than that in 2017 (1.6)(Zheng et al., 2021) and in 2018 (2.1)(Cai et al., 2022a) in Beijing, which implies a decreased aerosol acidity and an increased hygroscopicity, thus indirectly affecting SOA formation.

Aqueous-phase reactions can produce oligomers in the particle phase, such as oligomerization ($C_{4\text{-}7}H_{6\text{-}10}O_5$) from methylglyoxal ($C_3H_4O_2$) at high AWC values in Fig. 2a. Besides oligomerization, other processes such as the uptake of gas-phase oxygen-containing compounds might also contribute to the organic matter at high AWC. Here, the small carboxylic acids in both the gas- and particle- phases were selected to explore the gas-to-particle partitioning process, due to their large contributions to aq-OOA (21%-56%,). As shown in Fig. 2b, the particle-phase concentration of CH_2O_2 almost remained at constant values as a function of its gas-phase concentration and AWC. However, signals of CH_2O_2 in the gas phase decreased monotonously with AWC **(**>15 μg m^{-3}**)**. Unlike CH_2O_2, the signal intensities of $C_{2\text{-}6}H_{2\text{-}10}O_4$ in the particle phase increased as a function of their corresponding gas-phase concentrations. And the slopes are relatively higher when AWC is below 15 μg m^{-3} than the counterparts of AWC **(**>15 μg m^{-3}). This means gas-to-particle partitioning should be weakened for these molecules when AWC is > 15 μg m^{-3}, or it is hard to transform to other stable configurations or structures when compared with CH_2O_2. This should be related to the high nitrate-fraction in $PM_{2.5}$ at high AWC levels, which is in favor of the uptake of water due to its lower deliquescence RH than sulfate and chloride,(Liu et al., 2021) subsequently, particles being easily converted to liquid phase, then promotes the equilibrium of gas-to-particle partitioning. When AWC is <15 μg m^{-3}, these molecules tend to stay in the particle phase, thus, promoting OA accumulation. This is consistent with the previous conclusion that a higher OA fraction is usually observed under conditions at lower RH values than that at high RH values.(Zhao et al., 2019).

Interestingly, as shown in Fig. 2b, a good correlation between the gas- and particle-phase organic (except for CH_2O_2) can be observed when the particle-gas partition coefficient (K_p, using the Estimation Programs Interface model) of organic molecules ($C_xH_yO_z$) is larger than ~1.0×10^{-5} and AWC is over 15 μg m^{-3}. This is generally consistent with the observed decrease of the slope (Fig. 2b) when AWC is over 15 μg m^{-3}. In addition, the *K*p values of toluene-derived products and nitrophenols ($C_6H_5NO_3$ and $C_7H_7NO_3$) were larger than 10^{-5}, accompanied with a good positive correlation between their particle- and gas-phase concentrations, which indicating that *Kp* should be a good indicator for gas-to-particle partitioning for OVOCs, and the threshold value of *Kp* (10^{-5}) should be a necessary but not sufficient condition to understand the partition behavior of these compounds during the phase transition of ambient particles.

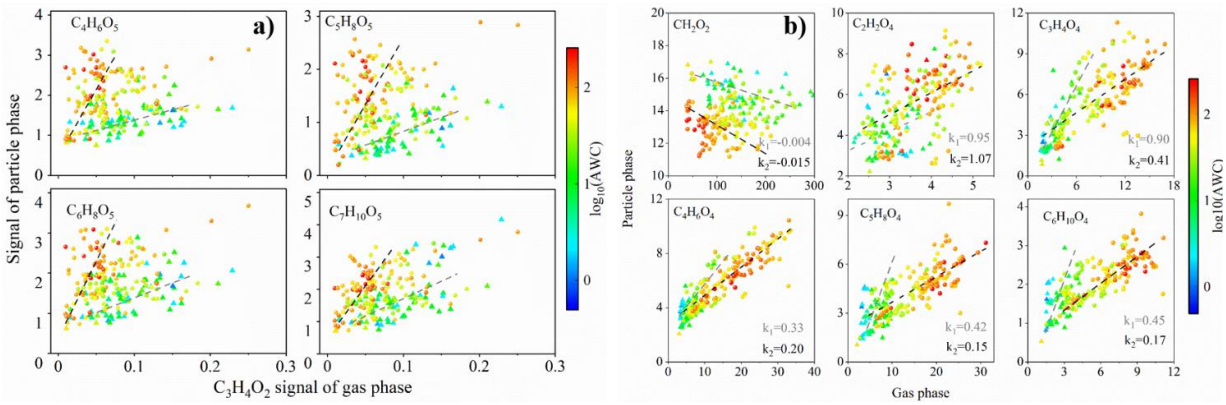

Fig. 2 a) Relationship between several particulate oligomers from the aqueous reaction and methylglyoxal colored with AWC. b) Correlations of CH_2O_2 and $C_{2\text{-}6}H_{2\text{-}10}O_4$ between gas-phase and particle-phase under the condition of different AWC. The filled triangle and circle represent the data with AWC less and larger than 15 μg m^{-3}, respectively.

ACKNOWLEDGEMENTS

This work was financially supported the National Natural Science Foundation of China (41877306, 42275117, 92044301), and the Ministry of Science and Technology of the People's Republic of China (2019YFC0214701).

REFERENCES

Cai, J., Wu, C., Wang, J., Du, W., and Daellenbach, K. R.: Influence of organic aerosol composition determined by offline FIGAERO-CIMS on particle absorptive properties in autumn Beijing, Atmos. Chem. Phys., **22**, 1251-1269, 2022a.

Cai, J., Wu, C., Wang, J., Du, W., Zheng, F., Hakala, S., Fan, X., Chu, B., Yao, L., Feng, Z., Liu, Y., Sun, Y., Zheng, J., Yan, C., Bianchi, F., Kulmala, M., Mohr, C., and Daellenbach, K. R.: Influence of organic aerosol molecular composition on particle absorptive properties in autumn Beijing, Atmos. Chem. Phys., **22**, 1251-1269, 2022b.

Chen, C., Qiu, Y., Xu, W., He, Y., Li, Z., Sun, J., Ma, N., Xu, W., Pan, X., Fu, P., Wang, Z., and Sun, Y.: Primary Emissions and Secondary Aerosol Processing During Wintertime in Rural Area of North China Plain, J. Geophys. Res.: Atmos., **127**, 2022.

Duan, J., Huang, R.-J., Li, Y., Chen, Q., Zheng, Y., Chen, Y., Lin, C., Ni, H., Wang, M., Ovadnevaite, J., Ceburnis, D., Chen, C., Worsnop, D. R., Hoffmann, T., O'Dowd, C., and Cao, J.: Summertime and wintertime atmospheric processes of secondary aerosol in Beijing, Atmos. Chem. Phys., **20**, 3793-3807, 2020.

Ervens, B., Turpin, B. J., and Weber, R. J.: Secondary organic aerosol formation in cloud droplets and aqueous particles (aqSOA): a review of laboratory, field and model studies, Atmos. Chem. Phys., **11**, 11069-11102, 2011.

Ge, X., Setyan, A., Sun, Y., and Zhang, Q.: Primary and secondary organic aerosols in Fresno, California during wintertime: Results from high resolution aerosol mass spectrometry, J. Geophys. Res.: Atmos., **117**, 2012.

Huang, R.-J., Wang, Y., Cao, J., Lin, C., Duan, J., Chen, Q., Li, Y., Gu, Y., Yan, J., Xu, W., Frohlich, R., Canonaco, F., Bozzetti, C., Ovadnevaite, J., Ceburnis, D., Canagaratna, M. R., Jayne, J., Worsnop, D. R., El-Haddad, I., Prevot, A. S. H., and O'Dowd, C. D.: Primary emissions versus secondary formation of fine particulate matter in the most polluted city (Shijiazhuang) in North China, Atmos. Chem. Phys., **19**, 2283-2298, 2019.

Kim, H., Collier, S., Ge, X., Xu, J., Sun, Y., Jiang, W., Wang, Y., Herckes, P., and Zhang, Q.: Chemical processing of water-soluble species and formation of secondary organic aerosol in fogs, Atmos. Environ., **200**, 158-166, 2019.

Koop, T., Bookhold, J., Shiraiwa, M., and Poeschl, U.: Glass transition and phase state of organic compounds: dependency on molecular properties and implications for secondary organic aerosols in the atmosphere, Phys. Chem. Chem. Phys., **13**, 19238-19255, 2011.

Lim, Y. B., Tan, Y., Perri, M. J., Seitzinger, S. P., and Turpin, B. J.: Aqueous chemistry and its role in secondary organic aerosol (SOA) formation, Atmos. Chem. Phys., **10**, 10521-10539, 2010.

Liu, Y., Yan, C., Feng, Z., Zheng, F., and Kulmala, M.: Continuous and comprehensive atmospheric observations in Beijing: a station to understand the complex urban atmospheric environment, Big Earth Data, **4**, 295-321, 2020a.

Liu, Y., Feng, Z., Zheng, F., Bao, X., Liu, P., Ge, Y., Zhao, Y., Jiang, T., Liao, Y., Zhang, Y., Fan, X., Yan, C., Chu, B., Wang, Y., Du, W., Cai, J., Bianchi, F., Petaja, T., Mu, Y., He, H., and Kulmala, M.: Ammonium nitrate promotes sulfate formation through uptake kinetic regime, Atmos. Chem. Phys., **21**, 13269-13286, 2021.

Liu, Y., Zhang, Y., Lian, C., Yan, C., Feng, Z., Zheng, F., Fan, X., Chen, Y., Wang, W., Chu, B., Wang, Y., Cai, J., Du, W., Daellenbach, K. R., Kangasluoma, J., Bianchi, F., Kujansuu, J., Petaja, T., Wang, X., Hu, B., Wang, Y., Ge, M., He, H., and Kulmala, M.: The promotion effect of nitrous acid on aerosol formation in wintertime in Beijing: the possible contribution of traffic-related emissions, Atmospheric Chemistry and Physics, **20**, 13023-13040, 2020b.

McNeill, V. F.: Aqueous Organic Chemistry in the Atmosphere: Sources and Chemical Processing of Organic Aerosols, Environ. Sci. Technol., **49**, 1237-1244, 2015.
Odum, J. R., Hoffmann, T., Bowman, F., Collins, D., Flagan, R. C., and Seinfeld, J. H.: Gas/Particle Partitioning and Secondary Organic Aerosol Yields, Environ. Sci. Technol., **30**, 2580-2585, 1996.
Paatero, P. and Tapper, U.: Positive matrix factorization: A non-negative factor model with optimal utilization of error estimates of data values, Environmetrics, **5**, 1994.
Perri, M. J., Lim, R. B., Seitzinger, R. P., and Turpin, R. J. J. A. E.: Organosulfates from glycolaldehyde in aqueous aerosols and clouds: Laboratory studies, **44**, 2658-2664, 2010.
Sun, Y., He, Y., Kuang, Y., Xu, W., Song, S., Ma, N., Tao, J., Cheng, P., Wu, C., Su, H., Cheng, Y., Xie, C., Chen, C., Lei, L., Qiu, Y., Fu, P., Croteau, P., and Worsnop, D. R.: Chemical Differences Between PM1 and PM2.5 in Highly Polluted Environment and Implications in Air Pollution Studies, Geophys. Res. Lett., **47**, 2020.
Sun, Y. L., Zhang, Q., Anastasio, C., and Sun, J.: Insights into secondary organic aerosol formed via aqueous-phase reactions of phenolic compounds based on high resolution mass spectrometry, Atmos. Chem. Phys., **10**, 4809-4822, 2010.
Tolocka, M. P., Jang, M., Ginter, J. M., Cox, F. J., Kamens, R. M., and Johnston, M. V.: Formation of oligomers in secondary organic aerosol, Environ. Sci. Technol., **38**, 1428-1434, 2004.
Ulbrich, I. M., Canagaratna, M. R., Zhang, Q., Worsnop, D. R., and Jimenez, J. L.: Interpretation of organic components from Positive Matrix Factorization of aerosol mass spectrometric data, Atmos. Chem. Phys., **9**, 2891-2918, 2009.
Wei Yuan, R.-J. H., Lu Yang, Ting Wang, Jing Duan, Jie Guo, Haiyan Ni, Yang Chen, Qi Chen, Yongjie Li, Ulrike Dusek, Colin O'Dowd, and Thorsten Hoffmann: Measurement report: PM2.5-bound nitrated aromatic compounds in Xi'an, Northwest China – seasonal variations and contributions to optical properties of brown carbon, Atmos. Chem. Phys., **21**, 3685-3697, 2021.
Zhao, J., Qiu, Y., Zhou, W., Xu, W., Wang, J., Zhang, Y., Li, L., Xie, C., Wang, Q., Du, W., Worsnop, D. R., Canagaratna, M. R., Zhou, L., Ge, X., Fu, P., Li, J., Wang, Z., Donahue, N. M., and Sun, Y.: Organic Aerosol Processing During Winter Severe Haze Episodes in Beijing, J. Geophys. Res.: Atmos., **124**, 10248-10263, 2019.
Zheng, Y., Chen, Q., Cheng, X., Mohr, C., Cai, J., Huang, W., Shrivastava, M., Ye, P., Fu, P., Shi, X., Ge, Y., Liao, K., Miao, R., Qiu, X., Koenig, T. K., and Chen, S.: Precursors and Pathways Leading to Enhanced Secondary Organic Aerosol Formation during Severe Haze Episodes, Environ. Sci. Technol., **55**, 15680-15693, 2021.

UNTANGLING THE INFLUENCE OF ANTARCTIC AND SOUTHERN OCEAN LIFE ON CLOUDS

MARC D. MALLET[1], RUHI S. HUMPHRIES[2,1], SONYA L. FIDDES[1], SIMON P. ALEXANDER[3,1], KATYE ALTIERI[4], HÉLÈNE ANGOT[5,10], N. ANILKUMAR[6], THORSTEN BARTELS-RAUSCH[7], JESSIE CREAMEAN[8], MANUEL DALL'OSTO[9], AURÉLIEN DOMMERGUE[10], MARKUS FREY[11], SILVIA HENNING[12], DELPHINE LANNUZEL[13,14], RÉMY LAPERE[10], GERALD G. MACE[15], ANOOP S. MAHAJAN[16], GREG M. MCFARQUHAR[17], KLAUS M. MEINERS[3,1,14], BRANKA MILJEVIC[18], ILKA PEEKEN[19], ALAIN PROTAT[20,1], JULIA SCHMALE[5], NADJA STEINER[21], KARINE SELLEGRI[22], RAFEL SIMÓ[9], JENNIE L. THOMAS[10], MEGAN D. WILLIS[23], V. HOLLY L. WINTON[24] AND MATTHEW T. WOODHOUSE[2,1]

1. Australian Antarctic Program Partnership, Institute for Marine and Antarctic Studies, University of Tasmania, Hobart, Australia
2. Climate Science Centre, Oceans and Atmosphere, Commonwealth Scientific and Industrial Research Organisation, Aspendale, Australia
3. Australian Antarctic Division, Channel Highway, Kingston, Tasmania, Australia
4. Department of Oceanography, University of Cape Town, Rondebosch 7700, South Africa
5. Extreme Environments Research Laboratory, École Polytechnique Fédérale de Lausanne (EPFL) Valais Wallis, Sion, Switzerland
6. National Centre for Polar and Ocean Research, Ministry of Earth Sciences, Government of India, Vasco da Gama, Goa, India
7. Laboratory of Environmental Chemistry, Paul Scherrer Institut, Villigen PSI, Switzerland
8. Department of Atmospheric Science, Colorado State University, Fort Collins, CO, United States
9. Institute of Marine Sciences, Consejo Superior de Investigaciones Científicas (CSIC), Barcelona, Spain
10. Univ. Grenoble Alpes, CNRS, INRAE, IRD, Grenoble INP, IGE, 38000 Grenoble, France
11. British Antarctic Survey – Natural Environment Research Council, Cambridge, UK
12. Leibniz Institute for Tropospheric Research, Permoserstraße 15, 04318 Leipzig, Germany
13. Institute for Marine and Antarctic Studies, University of Tasmania, Locked Bag 129, Hobart, Australia
14. ARC Australian Centre for Excellence in Antarctic Science, Institute for Marine and Antarctic Studies, University of Tasmania, Hobart, Tasmania, Australia
15. Department of Atmospheric Sciences, University of Utah, Salt Lake City
16. Indian Institute of Tropical Meteorology, Ministry of Earth Sciences, Pune, India
17. Cooperative Institute for Mesoscale Meteorological Studies, University of Oklahoma, Norman, United States of America
18. School of Earth and Atmospheric Sciences, Queensland University of Technology, Brisbane, Australia
19. Alfred-Wegener-Institut Helmholtz-Zentrum für Polar- und Meeresforschung, D-27570 Bremerhaven, Germany
20. Australian Bureau of Meteorology, Melbourne, Australia
21. Institute of Ocean Sciences, Fisheries and Oceans Canada, Sidney, BC, Canada
22. Université Clermont Auvergne, CNRS, LaMP, 63178 Aubière, France
23. Department of Chemistry, Colorado State University, Fort Collins, CO, United States
24. Antarctic Research Centre, Victoria University of Wellington, Wellington, New Zealand

Keywords: BIOGEOCHEMISTRY, AEROSOL, CLOUDS, SOUTHERN OCEAN, ANTARCTICA.

INTRODUCTION

Polar environments are among the fastest changing regions on the planet. It is a crucial time to make significant improvements in our understanding of how ocean and ice biogeochemical processes are linked with the atmosphere. This is especially true over Antarctica and the Southern Ocean where observations are severely limited, and the environment is far from anthropogenic influences. Here we give an overview of the large-scale measurement campaigns planned across Antarctica and the Southern Ocean in the next five years that will investigate interactions between biogeochemistry, aerosol, clouds, precipitation, and radiation. Until we do this, climate models will likely continue to exhibit biases in the simulated energy balance over this delicate region. Addressing these issues will require an international and interdisciplinary approach which we hope to foster and facilitate with ongoing community activities and collaborations.

MOTIVATION

The Southern Ocean and Antarctica are distant from human sources of atmospheric pollutants, instead being dominated by natural aerosol and vapours (Hamilton et al., 2014). These natural aerosol and vapours are mostly formed through an intricate process of emission by biological organisms modulated by biogeochemical processes, as well as sea spray production. Aerosol particles seed clouds that can produce rain and snowfall, and reflect energy back to space or trap it in the lower atmosphere.

Recent targeted field campaigns (e.g. Fossum et al., 2018; McFarquhar et al., 2021; Schmale et al., 2019; Sellegri et al., In Press) have measured aerosol, reactive gases, and cloud properties over the Southern Ocean. New datasets from these campaigns have been instrumental in tailoring our models of the Earth's systems to represent the Southern Ocean more realistically. Findings from these campaigns have highlighted that biological organisms in Southern Ocean surface waters and Antarctic sea-ice have a potentially large influence on our atmosphere (Dall'Osto et al., 2022; Landwehr et al., 2021; Mace et al., 2021; Rocco et al., 2021; Twohy et al., 2021). But these campaigns have also revealed major gaps in our understanding of complex processes influenced by these organisms. Despite the recent progress, our climate models still require improvements in their representation of aerosol and cloud processes operating in the Southern Ocean and Antarctica. Evidence of this is the persistent shortwave radiation bias that is still present in the latest generation of models prepared for the sixth Coupled-Model Intercomparison Project (Figure 1). New multidisciplinary observations are needed to build upon, evaluate, and challenge what we have already learned. Here, we outline more than 20 projects beginning in 2023 that will work towards collecting these new vital measurements.

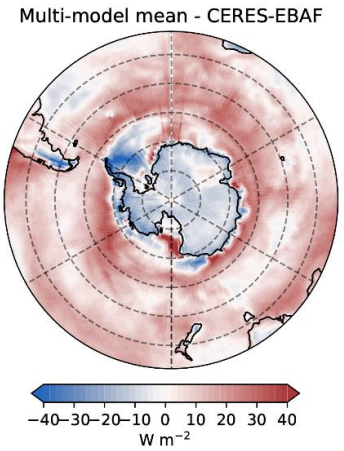

Figure 1. The mean austral summer time bias in the surface shortwave radiation in 22 of the Coupled Model Intercomparison Project phase 6 (CMIP6) models which fall into the 'likely' range of equilibrium climate sensitivity with respect to the CERES-EBAF satellite product (W m^{-2}).

UPCOMING FIELD WORK

Over the coming 4 years, we are aware of 22 fully funded or proposed campaigns (Figure 2) exploring the links between marine and terrestrial biogeochemistry and the atmosphere. This will include both in-situ and remote sensing observations on a range of platforms including land stations, ships, and aircraft. The campaigns will be complimented by remotely operated platforms such as gliders, floats, and moorings. We expect variability in biogeochemistry and atmospheric properties and their interactions in the different sectors around Antarctica.

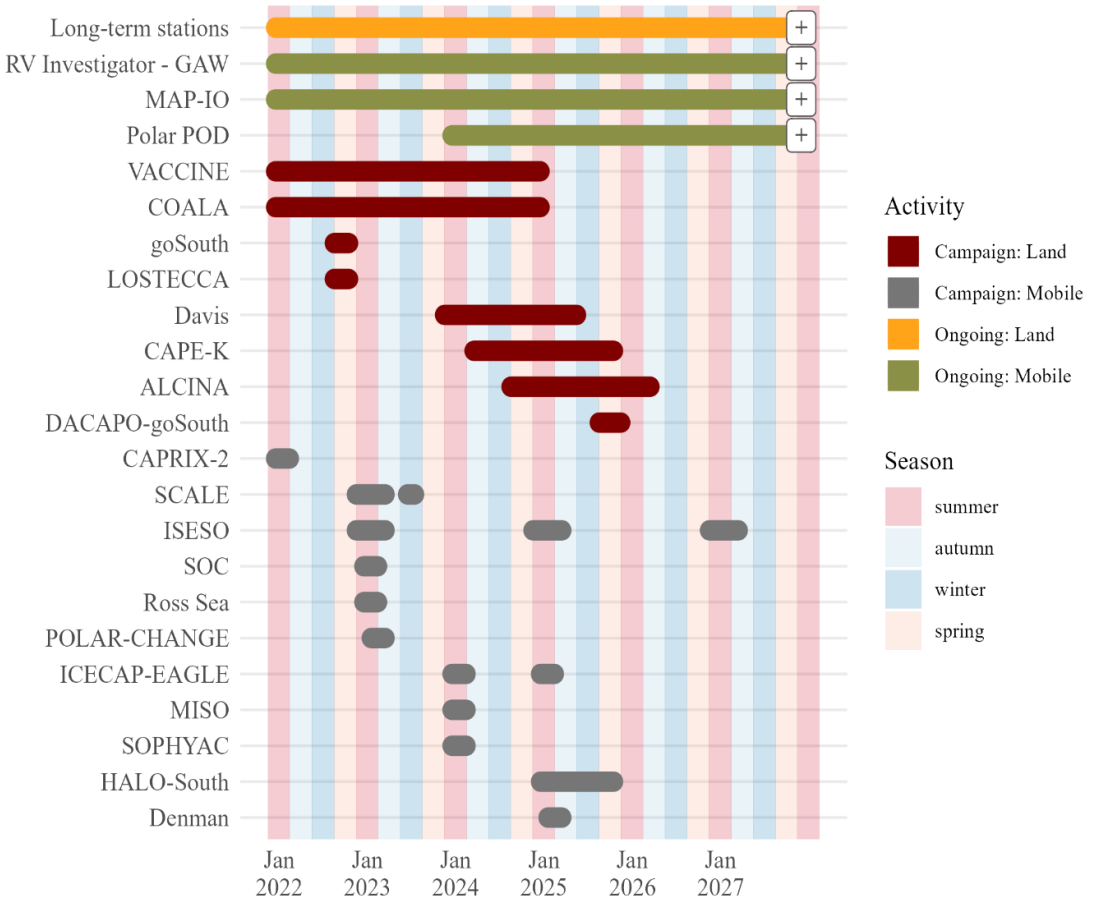

Figure 2. Upcoming measurement programs in the region targeting biogeochemistry-atmosphere measurements. Please note that this list might not be exhaustive and there could be changes to dates and positions prior to measurements.

While planning is well underway for the upcoming campaigns we have listed here, there is still scope to enhance interdisciplinarity and coordination to ensure we make the most of this unprecedented opportunity to understand the Southern Ocean and Antarctic region. It is likely that other research projects are currently being planned and so we encourage collaboration as much as possible. Furthermore, there is scope to augment the measurement campaigns already planned to maximise the scientific knowledge we can gain. We invite researchers and institutions in this space to join PICCAASO (Partnerships for Investigations of Clouds and the biogeoChemistry of the Atmosphere in Antarctica and the Southern Ocean), a recently launched initiative to improve coordination and collaboration of upcoming campaigns. The goal of PICCAASO is to augment and amplify the scientific discoveries from each independent project.

ACKNOWLEDGEMENTS

This project received grant funding from the Australian Government as part of the Antarctic Science Collaboration Initiative program, under the Australian Antarctic Program Partnership, ASCI000002. This research was undertaken with the assistance of resources and services from the National Computational Infrastructure (Project jk72). The authors would like to acknowledge the obs4MIPs activity, a project initiated by the National Aeronautical and Space Administration (NASA) and U.S. Department of Energy (DOE), with governance provided by the World Climate Research Program's (WCRP) Data Advisory Council (WDAC). We further acknowledge the WCRP, which, through its Working Group on Coupled Modelling, coordinated and promoted CMIP6. We thank the climate modelling groups for producing and making available their model output, the Earth System Grid Federation (ESGF) for archiving the data and providing access, and the multiple funding agencies who support CMIP6 and ESGF. We also acknowledge the teams at NASA CERES and NASA Earth Data for making the CERES-EBAF data available for use. H.A. received funding from the Swiss National Science Foundation (grant no. 200021_188478). J.S. holds the Ingvar Kamprad Chair for Extreme Environments Research funded by Ferring Pharmaceuticals. K.S. received funding from the European Research Council (ERC) under the European Union's Horizon 2020 research and innovation programme (Grant agreement No. 771369). V.H.L.W was supported by a Rutherford Foundation Postdoctoral Fellowship administered by the Royal Society Te Apārangi (contract: RFT-VUW1801-PD).

REFERENCES

Dall'Osto, M., et al., 2022. Leaching material from Antarctic seaweeds and penguin guano affects cloud-relevant aerosol production. Science of The Total Environment 831, 154772. https://doi.org/10.1016/j.scitotenv.2022.154772

Fossum, K.N., et al., 2018. Summertime Primary and Secondary Contributions to Southern Ocean Cloud Condensation Nuclei. Sci Rep 8, 13844. https://doi.org/10.1038/s41598-018-32047-4

Hamilton, D.S., et al., 2014. Occurrence of pristine aerosol environments on a polluted planet. Proc Natl Acad Sci USA 111, 18466–18471. https://doi.org/10.1073/pnas.1415440111

Landwehr, S., et al., 2021. Exploring the coupled ocean and atmosphere system with a data science approach applied to observations from the Antarctic Circumnavigation Expedition. Earth Syst. Dynam. 12, 1295–1369. https://doi.org/10.5194/esd-12-1295-2021

Mace, G.G., Protat, A., Humphries, R.S., Alexander, S.P., McRobert, I.M., Ward, J., Selleck, P., Keywood, M., McFarquhar, G.M., 2021b. Southern Ocean Cloud Properties Derived From CAPRICORN and MARCUS Data. Geophys Res Atmos 126. https://doi.org/10.1029/2020JD033368

McFarquhar, G.M., et al., 2021. Observations of Clouds, Aerosols, Precipitation, and Surface Radiation over the Southern Ocean: An Overview of CAPRICORN, MARCUS, MICRE, and SOCRATES. Bulletin of the American Meteorological Society 102, E894–E928. https://doi.org/10.1175/BAMS-D-20-0132.1

Rocco, M., et al., 2021. Oceanic phytoplankton are a potentially important source of benzenoids to the remote marine atmosphere. Commun Earth Environ 2, 175. https://doi.org/10.1038/s43247-021-00253-0

Schmale, J.,et al., 2019. Overview of the Antarctic circumnavigation expedition: Study of preindustrial-like aerosols and their climate effects (ACE-SPACE). Bulletin of the American Meteorological Society 100, 2260–2283.

Sellegri, K., et al., n.d. Sea2Cloud: from biogenic emission fluxes to cloud properties in the South Western Pacific. Bulletin for the American Meteorological Society.

Twohy, C.H., et al., 2021. Cloud-Nucleating Particles Over the Southern Ocean in a Changing Climate. Earth's Future 9. https://doi.org/10.1029/2020EF001673

FLUORESCENCE SUPPRESSION OF INDIVIDUAL CLAY MINERAL PARTICLES BY ES-SERS

R. KANAI[1], R. KUNIHISA[1], K. ONO[1], M. GEN[2], C.K. CHAN[3] and A. MATSUKI[4]

[1]Graduate School of Natural Science and Technology, Kanazawa University, Kanazawa, Japan.
[2]Institute of Multidisciplinary Research for Advanced Materials, Tohoku University, Sendai, Japan.
[3]School of Energy and Environment, City University of Hong Kong, Kowloon, Hong Kong, China.
[4]Insitute of Nature and Environmental Science, Kanazawa University, Kanazawa, Japan.

Keywords: Dust aerosol, Clay mineral, Raman spectroscopy, Fluorescence, SERS, PAHs.

INTRODUCTION

Although mineral dust makes up the majority of atmospheric aerosols by mass, our understanding of chemical reactions in the atmosphere involving the particle surface is limited. For example, polycyclic aromatic hydrocarbons (PAHs) and their derivatives, which are known to be harmful to human health even in trace amounts, have been detected in dust aerosols (Kameda et al., 2016). However, there is a lack of knowledge on the detailed reaction mechanisms and resulting particle mixing states. Micro Raman spectroscopy is considered applicable for identifying the mixture of dust and PAHs on single particle basis due to its microscopic spatial resolution and selectivity to both inorganic and organic compounds. However, interference from typical fluorescence background often found in the Raman spectra of clay minerals hampers its use on dust aerosols (Sobanska et al., 2012). Electrospray surface-enhanced Raman spectroscopy (ES-SERS) involves pre-treatment of sample surface with silver nano-particle coating, thereby, dramatically enhances Raman signals and enables highly sensitive detection of organic compounds on the particle surface. It is also suggested to potentially eliminate fluorescence background without major modification on the conventional micro-Raman spectroscopy setup (Gen and Chan, 2017; Gen et al., 2019). In this study, laboratory experiments were conducted to test the applicability of ES-SERS as a new fluorescence suppression technique for typical clay mineral particles. In addition, the selectivity of ES-SERS on the organic compounds adhered on clay mineral particles was demonstrated.

METHODS

In this study, saponite, montmorillonite and kaolinite were selected as representative pure-component clay minerals. Samples were aerosolized and collected on a silicon substrate by impaction. The individual particles were subjected to normal Raman (NR) spectroscopy (nanofinder HE, Tokyo Instruments, Japan) with a λ=532 nm laser at 13 mW. The exposure time was set to 1 s with 3 integrations. The same particles analyzed by NR were identified and analyzed again after silver nanoparticles (AgNPs) deposition on the sample surface by electrospray (ES-SERS). Mixture of Arizona test dust (ATD) and naphthalene was prepared by dropping and drying solution on the silicon substrate. Analyses by NR and ES-SERS were performed with the same procedure as for the pure clay samples.

RESULTS AND DISCUSSION

A total of 175 particles of saponite, montmorillonite and kaolinite were analyzed first by NR. However, regardless of the clay mineral type or particle size, all measured particles showed significant fluorescent background, and no peaks specific to the minerals could be detected. On the other hand, ES-SERS spectra showed almost complete elimination of fluorescence background depending on the density of AgNPs deposited on the surface. Figure 1 shows the comparison of NR and ES-SERS spectra of a representative montmorillonite particle. A broad background peak can be found in the NR spectrum which hampers the detection of sample specific peaks. ES-SERS spectra on the other hand, shows significant reduction in the background signal and sharp peaks specific to montmorillonite can be found. The prominent and reproducible peaks were found at 148~164 cm^{-1}, 294~304 cm^{-1}, 692~698 cm^{-1} and 1059~1064 cm^{-1}, which

can be assigned to σ(Al-O), σ(O-H-O), ν(Si-O-Si) and ν(Al, Mg)$O_4(OH)_2$, respectively. These peaks assignments are consistent with those found in the literature. As in the case of pure-component clay minerals, mixture of ATD and naphthalene also showed significant fluorescence background by NR. After deposition of AgNPs, the background was eliminated in the similar manner and peaks specific to naphthalene were detected.

By using ES-SERS, we successfully demonstrated the complete elimination of the fluorescence background from the four representative clay minerals even under significantly reduced laser exposure. Unique peaks from the clay and PAH mixture were also identified. Although some peak shifts were observed in the case of ES-SERS (as compared to reference NR spectra), it was found that it is intrinsic to molecular vibrations. In conclusion, ES-SERS can not only eliminate fluorescence instantaneously from clay minerals, but also sensitively detect organic compounds adsorbed on the particle surface. Expectations are high for ES-SERS for understanding the dynamics of dust aerosols and organics (e.g. PAHs) in the ambient atmosphere.

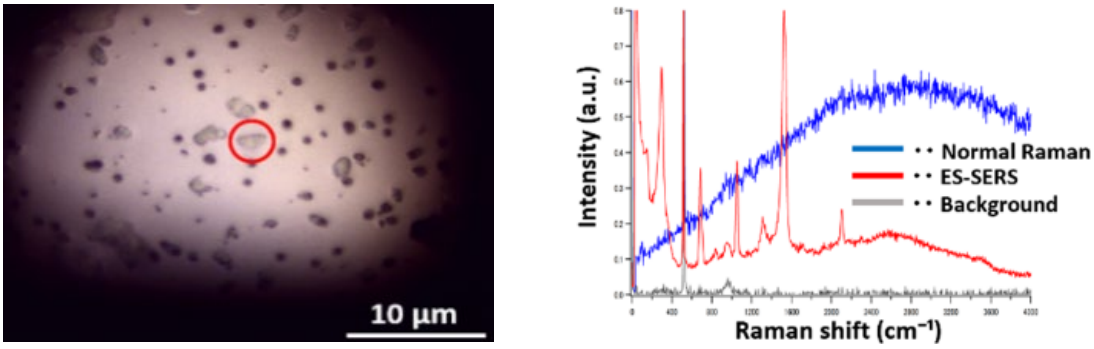

Figure 1. Optical microscope image of a montmorillonite particle (left panel), and corresponding Raman spectra (right panel). The same particle was analyzed first by normal Raman (NR) and by ES-SERS post AgNPs deposition. Background denotes spectrum taken from the silicon substrate.

ACKNOWLEDGEMENTS

This work was supported by the JSPS Funding Program for Next Generation World-Leading Researchers (GR045), KAKENHI Grant-in-Aid for Scientific Research B (JP18H03355), JST CREST (JPMJCR18H4), and the cooperative research program of Institute of National and Environmental Technology, Kanazawa University (No. 20011).

REFERENCES

Kameda, T., E. Azumi, A. Fukushima, N. Tang, A. Matsuki, Y. Kamiya, A. Toriba and K. Hayakawa (2016). Mineral dust aerosols promote the formation of toxic nitropolycyclic aromatic compounds. *Scientific Reports*, **6**:24427, 1-10.

Sobanska, S., H. Hwang, M. Cheol, H.J. Jung, H.J. Eom, H.K. Kim, J. Barbillat and C.U. Ro (2012). Investigation of the chemical mixing state of individual Asian dust particles by the combined use of electron probe X-ray microanalysis and Raman microspectrometry. *Analytical Chemistry*, **84**, 3145-3154.

Gen, M. and C.K. Chan (2017). Electrospray surface-enhanced Raman spectroscopy (ES-SERS) for probing surface chemical compositions of atmospherically relevant particles, *Atmospheric Chemistry and Physics*, **17**, 14025-14037.

Gen, M., R. Kunihisa, A. Matsuki and C.K. Chan (2019). Electrospray surface-enhanced Raman spectroscopy (ES-SERS) for studying organic coatings of atmospheric aerosol particles, *Aerosol Science and Technology*, **53** (7), 760-770.

IMPROVED SENSITIVITY OF SINGLE NANOPARTICLE CHEMICAL SPECIATION BY CG-SERS

T. Tsutsui[1], K. ONO[1], T. Fukuma[2], M. GEN[3], C.K. CHAN[4] and A. MATSUKI[5]

[1]Graduate School of Natural Science and Technology, Kanazawa University, Kanazawa, Japan.
[2]Nano Life Science Institute, Kanazawa University, Kanazawa, Japan
[3]Institute of Multidisciplinary Research for Advanced Materials, Tohoku University, Sendai, Japan.
[4]School of Energy and Environment, City University of Hong Kong, Kowloon, Hong Kong, China.
[5]Insitute of Nature and Environmental Science, Kanazawa University, Kanazawa, Japan.

Keywords: Nano particle, Condensational growth, SERS, New particle formation.

INTRODUCTION

Newly borne secondary particles in the atmosphere are often observed as nanoparticles with diameters of 100 nm or less, but their inherently small mass makes size resolved chemical speciation difficult. We previously proposed the Condensational Growth-Surface Enhanced Raman Spectroscopy (CG-SERS) as a simple method to collect and chemically speciate nanoparticles on individual basis (Kunihisa et al., 2020). The technique involves activation of nanoparticles into water droplets by condensational growth, followed by direct collection onto SERS substrate. However, due to the extreme sensitivity and reactivity of silver coating on the SERS substrate, oxidation of the surface rapidly reduces the analytical sensitivity, and trace contaminants cause interfering peaks in the background Raman spectra, together compromises the quantitative evaluation of CG-SERS spectra. Here, we present our efforts to improve the analytical sensitivity of the CG-SERS method by applying Argon plasma on the SERS substrate to clean and reactivate its surface.

METHODS

Ammonium sulfate, glucose solutions and their mixture in various mixing ratios were atomized and dried before being introduce into a nano DMA (Model 3085, TSI, USA). Mono-dispersed particles at 100 nm were then guided into Spot Sampler (Aerosol Device Inc., USA) and activated into super-micron droplets, thereby directly collected onto SERS substrate (Ag SERStrate, Silmeco, Denmark) by impaction. Each droplet leaves a characteristic trace on the SERS substrate, which can be located and analyzed by micro-Raman spectroscopy (Nanofinder HE, Tokyo Instruments, Japan). Raman spectra were obtained using 532 nm excitation laser at 0.08-0.018 mW. Exposure time was set as 1 s and 10 accumulations. Ar plasma cleaner (SC-701, Sanyu Electron, Japan) was used to process the substrate with different plasma intensities. The output current and exposure time were varied between 2-7 mA and 30 s to 3 min, respectively.

RESULTS AND DISCUSSION

Firstly, the sensitivity decay of the aged SERS substrate was evaluated. The SERS sensitivity, shown in terms of the peak intensity at 40 cm^{-1} (Wei et al., 2019), is shown in Figure 1. Even though the substrates are stored and sealed in inert gas, the signal drops by 73% in a matter of 6 months after delivery. In addition to the sensitivity reduction, traces of droplets, which are essential for the identification of individual particles, are no longer visible in the case of aged substrates. These optical and sensitivity losses become critical for the CG-SERS method. Then, we applied Ar plasma on the decayed SERS substrate to remove the oxidized film and contaminants on the surface. After testing several exposure settings, it was found that treating with a mild exposure at 3 mA for 0.5 min, is capable of significantly recovering the sensitivity of the 6 month old substrate (up to about 50% of the entirely fresh substrate). In addition, the droplet traces of individual particles became visible again. It was also possible to reduce the background $\nu(SO_4^{2-})$ peak found at 970 cm^{-1} after plasma cleaning. This is notable, since sulfate is considered to be one of the major components involved in the new particle formation. By comparing the normalized peak intensities of $\nu(SO_4^{2-})$ and C-H

stretching region (2900 cm^{-1}) obtained by measuring mixed ammonium sulfate and glucose particles with different degree of mixing ratios, corresponding change in the peak intensities were found from the new and argon plasma cleaned SERS substrates (Figure 2), suggesting the possibility of semi-quantitative evaluation. These results justify the application of plasma treatment for making the CG-SERS method more robust and applicable in more demanding field studies. In the future, this method is expected to contribute to the better understanding of the chemical dynamics of nanoparticles e.g. during new particle formation events.

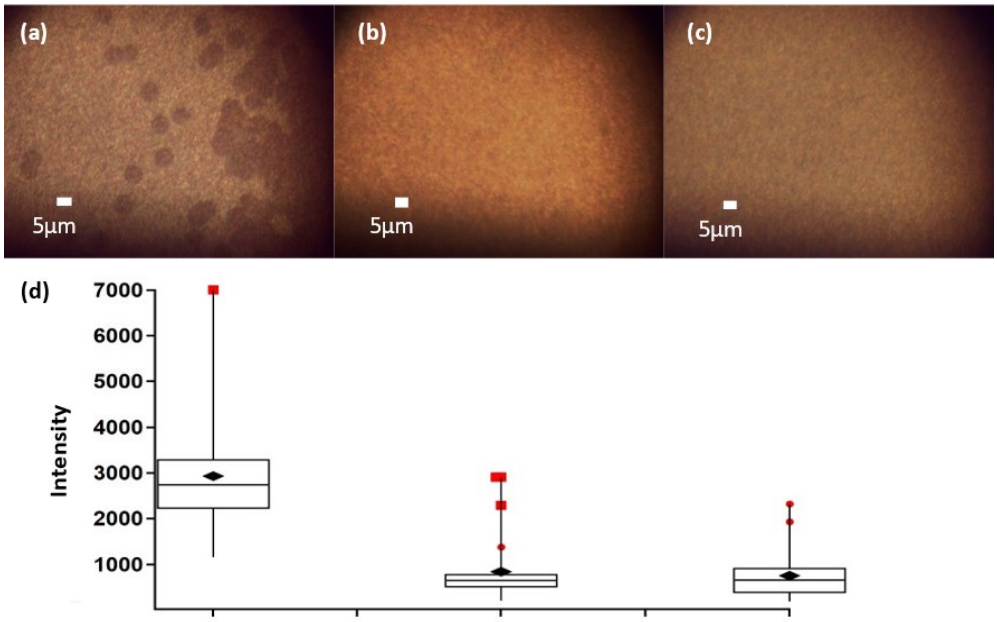

Figure 1. Comparison of optical images (upper panel) and sensitivity (lower panel) of new and aged SERS substrates. The results are shown in the order from left to right, 0, 6 and 9 months after delivery.

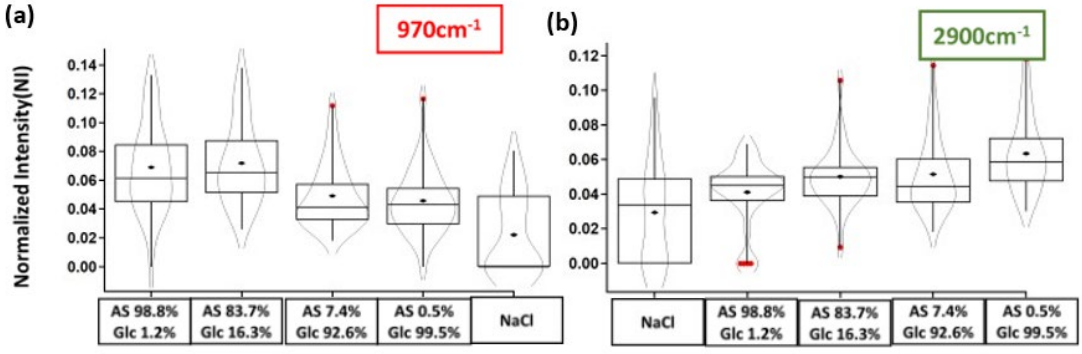

Figure 2. Comparison of the SERS peak intensities for sulfate (970 cm-1) and organics (2900 cm-1) obtained from 6 month old substrate treated with Ar plasma. Results based on ammonium sulfate and glucose particles with various mixing ratios. NaCl particles were also measured as background.

ACKNOWLEDGEMENTS

This work was supported by the JSPS Funding Program for Next Generation World-Leading Researchers (GR045), KAKENHI Grant-in-Aid for Scientific Research B (JP18H03355), JST CREST (JPMJCR18H4), and the cooperative research program of Institute of National and Environmental Technology, Kanazawa University (No. 20011).

REFERENCES

Kunihisa, R., A. Iwata, M. Gen, C.K. Chan and A. Matsuki (2020). Application of SERS on the chemical speciation of individual Aitken mode particles after condensational growth. *Aerosol Science and Technology*, **54** (7), 826-836.

Wei, H., W. Leng, J. Song, C. Liu, M.R. Willner, Q. Huang, W. Zhou and P.J. Vikesland (2019). Real-time monitoring of ligand exchange kinetics on gold nanoparticle surfaces enabled by hot spot-normalized Surface-Enhanced Raman Scattering. *Environmental Science and Technology*, **53** (2), pp. 575-585.

Size distributions of sea salt aerosols for marine cloud brightening over the Great Barrier Reef

C. MEDCRAFT[1], D.C. HERNANDEZ-JARAMILLO[1], L. HARRISON[2], R.C. BRAGA[1], P. BUTCHERINE[1] and D.P. HARRISON[1]

[1]National Marine Science Centre, Southern Cross University, Coffs Harbour, New South Wales, Australia

[2]School of Aerospace, Mechanical and Mechatronic Engineering, University of Sydney, New South Wales, Australia

Keywords: Marine Cloud Brightening, sea salt aerosol, YYYYY, ZZZZZ.

INTRODUCTION

Marine cloud brightening (MCB) aims to increase the albedo of low lying marine clouds by the introduction of additional sea salt aerosol particles (SSA) increasing the population of cloud condensation nuclei which activate to form cloud droplets. The outcomes of this intervention inherently depend on the size and hygroscopicity of the introduced aerosol particles among other factors such as updraft velocity and cloud supersaturation levels. SSA that are too small or too large are both speculated to reduce the magnitude of the desired net albedo increase, or even have the opposite effect of reducing albedo. The ideal SSA size distribution is subject to debate however literature suggests dry diameters in the range of 60-1000 nm may be effective. Current technologies produce a distribution of SSA particles sizes, rather than the monomodal size originally proposed for MCB.

METHODS

We have studied numerous nozzle technologies to continuously efficiently and effectively produce sufficient quantities of sea salt aerosols from sea water. Size distributions and production rates of these various nozzle technologies from laboratory data tests will be presented. Currently our best candidate technology type are effervescent nozzles where high pressure (ca.100 bar) air and seawater are mixed prior to being sprayed through a small (100-400 μm) orifice.
Laboratory experiments were performed in a wind tunnel where sampling took place 10 metres downwind of the nozzle. We use standard aerosol sampling apparatus with an array of detection and sizing instruments to record the dry particle size distributions. Total particle counts are measured from condensation particle counters (CPC). Particle size distributions are measured using aerodynamic particle sizers (APS) for larger particles and scanning mobility particle sizers (SMPS) for smaller particles.

CONCLUSIONS

Size distribution data from these nozzles used during previous field work have shown inconsistences between campaigns and when compared to laboratory studies. Laboratory data suggests these inconsistences are not from differences in the manufacturer of the mixing tee pieces (figure 1), nor the orientation of the nozzles with respect to the wind direction (figure 2).

These data will be compared to data measured during a recent field campaign (Feb – April 2023) on the southern Great Barrier Reef. Data from this campaign was measured from an aircraft, drones and on the surface from a research ship following another vessel containing the spraying apparatus. The implications for the effectivity of MCB due to changes in size distribution with distance and altitude from the spraying source will be discussed.

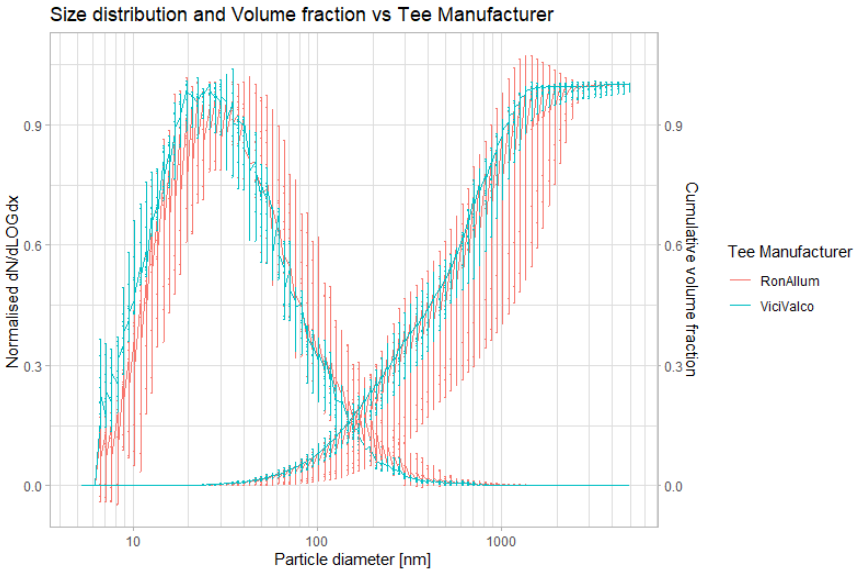

Figure 1. Normalised Size distribution and cumulative volume fraction for the MFG2010 nozzle using the ViciValco and the RADS tee pieces.

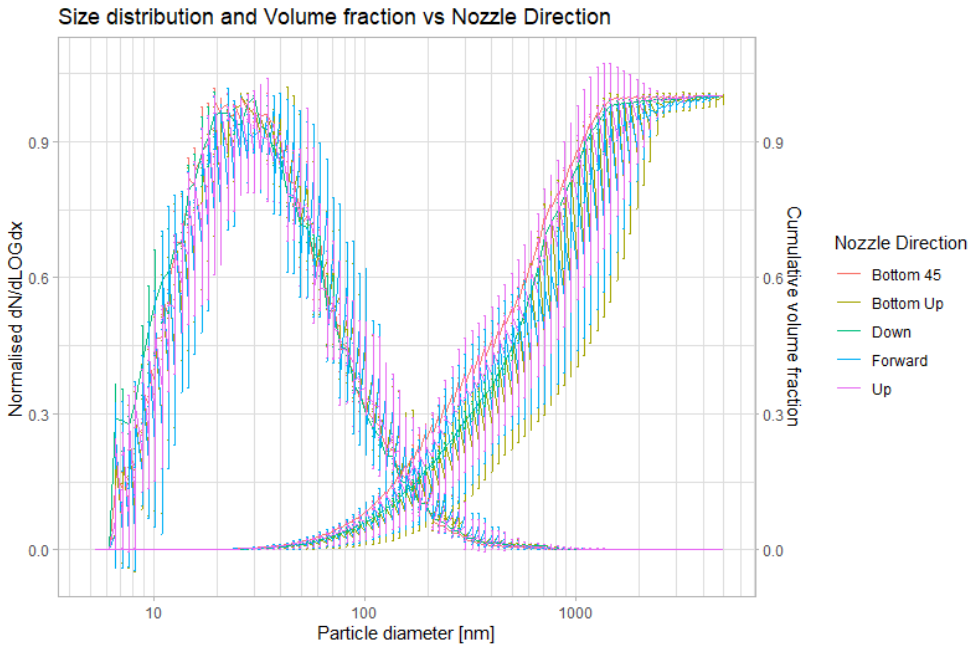

Figure 2: Normalised Size distribution and cumulative volume fraction for the MFG2010 nozzle with varying orientation with respect to the wind direction.

ACKNOWLEDGEMENTS

This work was undertaken as part of the Reef Restoration and Adaptation Program, funded by the partnership between the Australian Governments Reef Trust and the Great Barrier Reef Foundation.

"HIGH METHANESULFONIC ACID (MSA)" EVENT DURING CAPRICORN-2 SOUTHERN OCEAN VOYAGE

M.D. MALLET[2], C.G. OSUAGWU[1], R. HUMPHRIES[3], Z.D. RISTOVSKI[1] and B. MILJEVIC[1]

[1]International Laboratory for Air Quality and Health, School of Earth and Atmospheric Sciences, Queensland University of Technology, Brisbane, Australia

[2] Institute for Marine and Antarctic Studies (IMAS), University of Tasmania, Hobart, Australia

[3]Climate Science Centre, Oceans and Atmosphere, CSIRO, Melbourne, Victoria, Australia

Keywords: Southern Ocean, aerosol precursors, methanesulfonic acid, sulfuric, aerosol size distribution.

INTRODUCTION

The Southern Ocean (SO) is a region of the world where most climate models have a persistent positive bias in the amount of sunlight reaching the Earth's surface. This bias is caused, in part, because models consistently underpredict aerosol and cloud cover in this region, which, in turn, stems from insufficient understanding of aerosol-cloud interactions and aerosol production mechanisms in this pristine environment (Carslaw et al., 2013). This can be attributed to the scarcity of relevant, comprehensive in situ atmospheric observations in the SO region. Aerosol-cloud interactions represent the largest source of uncertainty in estimating the trajectory of human-induced global warming and future climate. The biggest gains in reducing this uncertainty have been found to come from a better understanding of pre-industrial aerosols, which can provide a more constrained baseline for estimating human-induced warming [2]. The Southern Ocean aerosols are our best proxy for those of pre-industrial time. This has motivated a number of recent and upcoming field campaigns in the Southern Ocean. Here we present findings from the summertime CAPRICORN-2 SO voyage (2018) with a focus on low volatility vapours relevant for marine new particle formation (sulfuric acid, methanesulfonic acid (MSA) and iodic acid) and aerosol size distribution.

METHODS

CAPRICORN-2 (Clouds, Aerosols, Precipitation, Radiation, and atmospheric Composition Over the southeRn oceaN) campaign aboard the *RV Investigator* during January–February of 2018 took place in the western Pacific sector of the Southern Ocean. Periods influenced by ship exhaust have been identified according to *Humphries et al, 2019* (Humphries et al., 2019) and removed from the dataset. It was found that less than 15% of the data was contaminated by the ship's exhaust.

Sulfuric acid, MSA and iodic acid were measured using a nitrate Chemical Ionisation Mass Spectrometer (NO_3-CIMS). The aerosol size distribution) was measured using two Scanning Mobility Particle Sizers (SMPS; Grimm and TSI)) covering together a size range from 4 nm to 660 nm.

Standard meteorological variables, such as air temperature, pressure, relative humidity, wind speed and direction were measured as a part of the ongoing underway systems and whose data are known as "underway data".

RESULTS

The main feature of the 2018 CAPRICORN-2 SO voyage was a week-long period of unusually high gaseous MSA levels after crossing the Polar Front heading south (Fig 1). This was correlated with increased levels of gaseous H_2SO_4 and HIO_3, however, their counts were substantially lower than for MSA. Previously published data on CAPRICORN-2 voyage shows that during that same period particulate SO_4^{2-} and MSA, as well as Cloud Condensation Nuclei (CCN) number concentration were

increased (Humphries et al., 2021; McFarquhar et al., 2021). However, SMPS data indicate that there were no nucleation events during the "high MSA" and the whole sampling period. HYSPLIT backtrajectories analysis shows that "high MSA" airmasses come from Antarctica and higher altitudes (~1500-3000 m) suggesting new particle formation had occurred in the free troposphere. Previously published satellite data for that time period and region shows an increased cloud droplet number (Mace et al., 2021), demonstrating a direct link between marine biogenic emissions and cloud properties. This study demonstrates that aerosol precursors availability is not the same at low and high latitudes of the Southern Ocean. It also brings into focus the importance of MSA for high latitude CCN concentrations and raises an important question: how frequent and important are these "high MSA" events in high latitude regions?

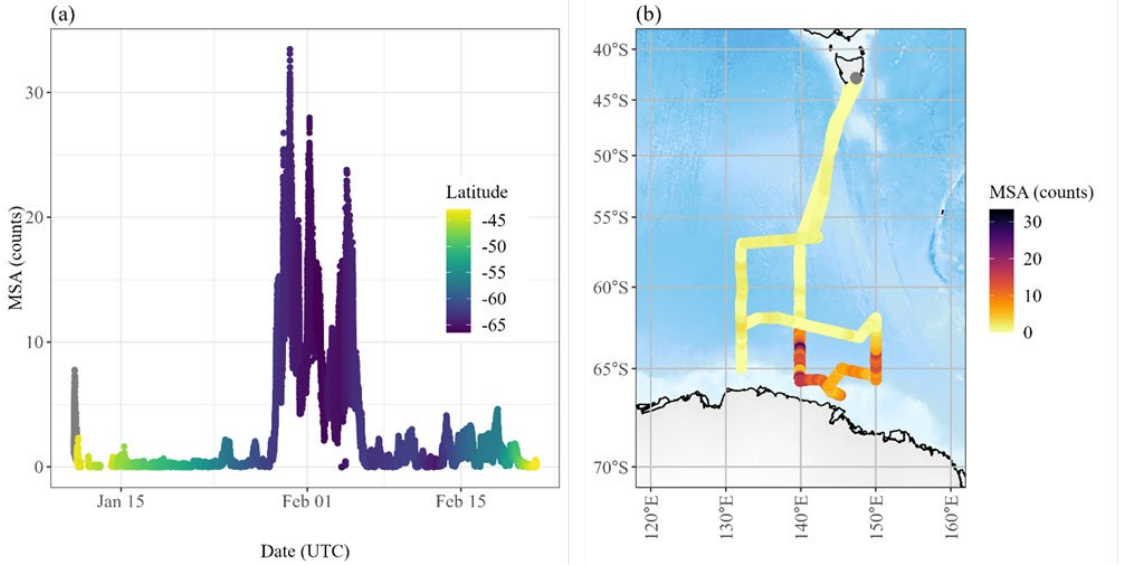

Figure 1. (a) Time series of MSA during CAPRICORN-2 SO voyage colour-coded by latitude and (b) voyage track of CAPRICORN-2 colour-coded by the MSA counts. Note high MSA counts south of the polar front.

ACKNOWLEDGEMENTS

The authors wish to thank the CSIRO Marine National Facility (MNF) for their support in the form of sea time on *RV Investigator* and associated support personnel, scientific equipment and data management during CAPRICORN-2.

REFERENCES

Carslaw, K. S., Lee, L. A., Reddington, C. L., Pringle, K. J., Rap, A., Forster, P. M., . . . Pierce, J. R. (2013). Large contribution of natural aerosols to uncertainty in indirect forcing. *Nature, 503*(7474), 67-71. doi:10.1038/nature12674

Humphries, R. S., Keywood, M. D., Gribben, S., McRobert, I. M., Ward, J. P., Selleck, P., . . . McFarquhar, G. (2021). Southern Ocean latitudinal gradients of cloud condensation nuclei. *Atmos. Chem. Phys., 21*(16), 12757-12782. doi:10.5194/acp-21-12757-2021

Humphries, R. S., McRobert, I. M., Ponsonby, W. A., Ward, J. P., Keywood, M. D., Loh, Z. M., . . . Harnwell, J. (2019). Identification of platform exhaust on the RV Investigator. *Atmos. Meas. Tech., 12*(6), 3019-3038. doi:10.5194/amt-12-3019-2019

Mace, G. G., Protat, A., Humphries, R. S., Alexander, S. P., McRobert, I. M., Ward, J., . . . McFarquhar, G. M. (2021). Southern Ocean Cloud Properties Derived From CAPRICORN and MARCUS Data. *Journal of Geophysical Research: Atmospheres, 126*(4), e2020JD033368. doi:https://doi.org/10.1029/2020JD033368

McFarquhar, G. M., Bretherton, C. S., Marchand, R., Protat, A., DeMott, P. J., Alexander, S. P., . . . McDonald, A. (2021). Observations of Clouds, Aerosols, Precipitation, and Surface Radiation over the Southern Ocean: An Overview of CAPRICORN, MARCUS, MICRE, and SOCRATES. *Bulletin of the American Meteorological Society, 102*(4), E894-E928. doi:10.1175/bams-d-20-0132.1

MAJOR SOURCES OF AEROSOL OXIDATIVE POTENITAL IN WINTERTIME BEIJING, CHINA

K.Y. CHEUNG[1], L. QI[1], J. V. PUTHUSSERY[2], T. CUI[1], T. WANG[1], M. MANOUSAKAS[1], Y. GE[3], G. WEI[3], Y. KUANG[3], M. SHENG[3], Z. CHENG[3], A. LI[3], Z. LI[4], W. RAN[4], W. XU[5], R. ZHANG[5], Y. HAN[4], Q. WANG[4], Z. WANG[5], Y. SUN[5], J. CAO[4, 5], K. DAELLENBACH[1], V. VERMA[2], M. GYSEL-BEER[1], X. QIU[3], Q. CHEN[3], J. SHANG[3], I. E. HADDAD[1], A. S. H. PREVOT[1], and R. L. MODINI[1]

[1]Laboratory of Atmospheric Chemistry, Paul Scherrer Institute, 5232 Villigen PSI, Switzerland.
[2]Department of Civil & Environmental Engineering, University of Illinois at Urbana-Champaign, Urbana, Illinois 61801, United States.
[3]State Key Joint Laboratory of Environmental Simulation and Pollution Control, College of Environmental Sciences and Engineering, Peking University, Beijing 100871, China.
[4]Key Laboratory of Aerosol Chemistry and Physics, Institute of Earth Environment, Chinese Academy of Sciences, Xi'an, 710061, China.
[5]Key Laboratory of Atmospheric Boundary Layer Physics and Atmospheric Chemistry, Institute of Atmospheric Physics, Chinese Academy of Sciences, Beijing, 100029, China.

Keywords: urban aerosols, oxidative potential, source apportionment, aerosol health effects.

INTRODUCTION

An increasing majority of the world's population resides in urban areas where they are exposed to a wide range of different atmospheric aerosol sources. It is challenging to quantify the various different health effects resulting from these exposures. One promising toxicity metric amongst many is aerosol oxidative potential measured with the dithiotreitol (DTT) chemical assay, or OP^{DTT} (Bates et al., 2019). OP^{DTT} aims to quantify the ability of aerosol to generate reactive oxygen species (ROS) in vivo, a process which contributes to oxidative stress and ultimately a range of adverse health effects.

Traditionally, OP^{DTT} measurements have been performed offline, i.e., on samples extracted from filters collected previously in the field. This process is labor intensive and the resulting datasets are usually limited to relatively small sample sizes that cover, e.g., seasonal time scales (e.g. Calas et al., 2018). The current state-of-the-art approach is to combine these measurements with chemical composition measurements, source apportionment, and regression modeling in order to identify the aerosol sources that contribute most strongly to the aerosol oxidative potential (Daellenbach et al., 2020). Recently, a number of new instruments have been developed for performing semi-continuous, online measurements of aerosol OP at hourly time resolution (e.g. Puthussery et al., 2018). These measurements are able to capture diurnal to weekly variations in aerosol OP, which could be an important advantage in OP source apportionment studies. However, only a very limited number of such studies have been performed so far (Puthussery et al., 2022).

In the present study, online measurements of OP^{DTT} and chemical composition in $PM_{2.5}$ were made during a three month period in Beijing, China (Jan – March 2021). The primary goal of the study was to identify the major sources of aerosol oxidative potential during winter in the polluted megacity Beijing, specifically focusing on the contributions of primary aerosol versus aged organic aerosol, as well as the impacts of specific, short-term pollution events. Secondly, the study also aimed to explore some of the benefits and limits of using hourly-resolved OP^{DTT} in a source apportionment and regression modeling analysis.

METHODS

Measurements were performed at three locations in and around Beijing over a three month period in 2021: Peking University (PKU; 15 Jan. to 4 Feb.), the Institute of Atmospheric Physics Iron Tower Branch (IAP-1; 10 to 20 Feb.), and Xianghe Observatory (IAP-2: 26 Feb. to 20 Mar.). The third site Xianghe is located nearby Beijing, in an area which is subject to less pollution control measures than central Beijing where the other two sites are located. $PM_{2.5}$ OP^{DTT} was measured with an online system operating at hourly time resolution (Puthussery et al., 2018). Co-located $PM_{2.5}$ chemical composition measurements were obtained with aerosol mass spectrometers (AMS) and/or aerosol chemical speciation monitors (ACSM), ambient trace metal analyzers (Xact 625), and aethalometers (AE33).

To identify major aerosol sources we applied positive matrix factorization (PMF) separately for the different measurement sites and instrument datasets using SoFi Pro version 8.2. Four factor solutions were obtained from the ACSM/AMS organic aerosol (OA) measurements (hydrocarbon-like, HOA; cooking, COA; solid fuel combustion, SFC-OA; and oxygenated, OOA). The OOA factor likely contained strong contributions from secondary organic aerosol, however additional contributions from aged and highly-oxidized primary organic aerosols cannot be ruled out. Six factor solutions were obtained from the Xact trace metals data: biomass burning, dust, industrial emissions, traffic non-exhaust, coal combustion, and fireworks. The aethalometer model was used to apportion the equivalent black carbon data into traffic exhaust and solid fuel combustion factors (Zotter et al., 2017).

To quantitatively link the aerosol sources to the measured OP^{DTT} we applied multilinear regression (MLR) using the Car package in the R programming language. Although it was possible to chemically distinguish a large number of factors corresponding to different aerosol sources, many of the factors exhibited high degrees of temporal collinearity with each other, a condition which is not suitable for a robust multilinear regression analysis. Therefore to obtain the MLR input, we further reduced the number of aerosol sources into four broad types using clustering methods and a priori knowledge. The four broad types were: primary aerosol (which contains contributions from the traffic exhaust, traffic non-exhaust, cooking, and solid fuel combustion factors), oxygenated organic aerosol (secondary or aged primary organic aerosol), dust (local or regional), and fireworks. Bootstrapping was also performed with 200 repeats to assess the robustness of the model estimation.

RESULTS AND DISCUSSION

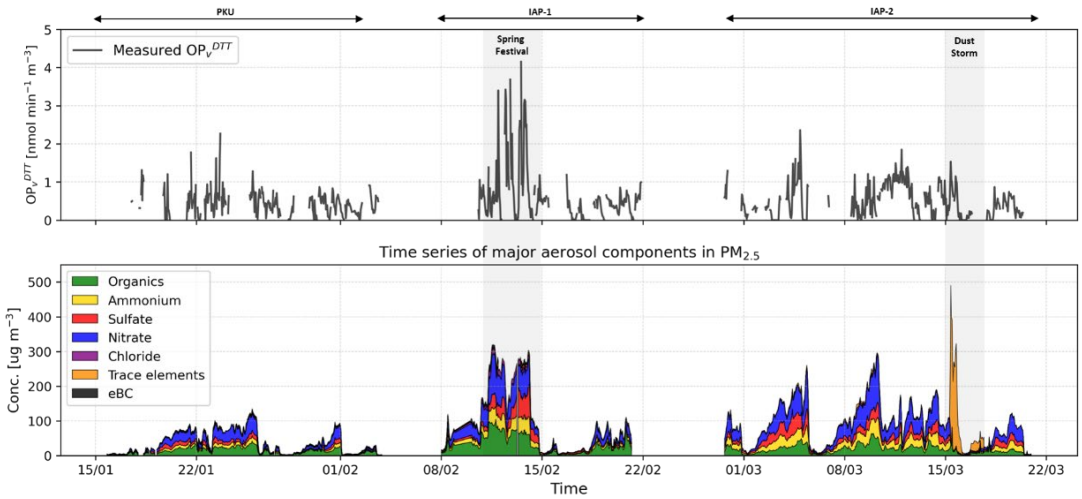

Figure 1. Times series of hourly $PM_{2.5}$ OP_V^{DTT} (top panel) and of the mass concentrations of the major aerosol components in $PM_{2.5}$ (bottom panel) from January 15 to March 20, 2021 at three locations in the Beijing area (PKU, IAP-1, and IAP-2; see main text for abbreviations). The grey shaded areas represent two distinct, short-term pollution events: the Spring Festival and a major regional dust storm.

Time series of OP_V^{DTT} (i.e., OP^{DTT} normalized by the sampled air volume, otherwise known as extrinsic OP^{DTT}; units nmol min^{-1} m^{-3}) and the mass concentrations of the major chemical components in $PM_{2.5}$ are displayed in Fig. 1. Elevated total $PM_{2.5}$ concentrations (i.e., > 100 µg m^{-3}) occurred during haze events, the Spring Festival (~11 – 15 Feb.), and the largest regional dust storm in northern China in a decade (~15 – 16 Mar.). In some cases, such as the Spring Festival period, OP_V^{DTT} increased dramatically in tandem with the peak in $PM_{2.5}$ mass. However in other periods, most notably during the regional dust storm, no proportionate increase in OP_V^{DTT} was observed as $PM_{2.5}$ mass spiked to hourly concentrations of almost 500 µg m^{-3}. This indicates that for the overall campaign period, $PM_{2.5}$ mass alone was a poor predictor of OP_V^{DTT}, and that chemically-resolved aerosol information is required to explain the observed variations in OP_V^{DTT}.

Figure 2 presents the results of the MLR analysis that aimed to introduce this chemically-resolved information and to quantify the contributions of four broad aerosol types to total OP_V^{DTT}. Panel a) displays the absolute contributions of primary aerosol, OOA, fireworks, and dust to OP_V^{DTT} for three different time periods: the Spring Festival and dust storm events (indicated by the grey shaded regions in Fig. 1), as well as all other periods. Panel b) compares total modeled and measured OP_V^{DTT} for the same three periods.

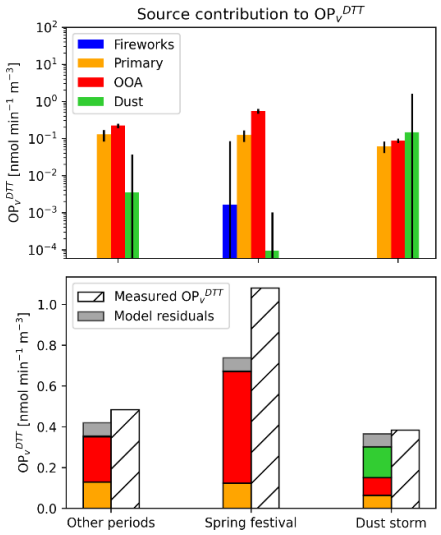

Figure 2. a) The absolute contributions of four broad aerosol types to OP_V^{DTT} as determined by MLR for three different time periods (the Spring Festival, the regional dust storm, and all other periods). Note the log y-axis. Error bars represent uncertainties in the modelled MLR coefficients as determined by bootstrapping. b) The total MLR modelled OP_V^{DTT} (including residuals) compared to total measured OP_V^{DTT} for the same periods.

Primary aerosols and OOAs both made substantial contributions to OP_V^{DTT} during all three periods. However, the contributions from the aged OOAs were always greater than those from the fresh primary aerosols. This was particularly clear during the Spring Festival period where OOA contributed ~70% of the total modelled OP_V^{DTT}.

The fireworks factor was derived from source apportionment of the Xact data and contained contributions from metal species such as K, Cu, and Ba. Cu is known to be redox-active and able to catalyze the generation of ROS. However, Fig. 2a) indicates that the fireworks factor contributed very little to modelled OP_V^{DTT}. We suggest that this physically inconsistent result was obtained because the fireworks event was too short for the MLR model to properly account for it. This is evidenced by the facts that the regression coefficients for this factor were dramatically more uncertain than those of the other factors (not shown here), and that overall, the MLR did a poorer job of reproducing measured OP_V^{DTT} during the Spring Festival period compared to the other two periods (Fig. 2b).

The dust factor only contributed substantially to OP_V^{DTT} during the large dust storm. The regression coefficient for this factor – which represents its intrinsic OP – was lower than for the primary and OOA factors (not shown here). However, during the dust storm this factor was present in very high concentrations, such that in absolute terms it still contributed substantially to OP_V^{DTT} during this event. During all other periods the contribution of dust to total OP_V^{DTT} was much smaller.

CONCLUSIONS

An online system for measuring $PM_{2.5}$ OP^{DTT} at hourly time resolution was successfully deployed over a three month period in wintertime Beijing along with comprehensive chemical composition measurements. A number of interesting pollution events were captured by the measurements (haze events, fireworks during the Spring Festival, a major dust storm). Total $PM_{2.5}$ mass was generally not well correlated with measured OP_V^{DTT}. To better explain the variations in OP_V^{DTT}, an MLR model was developed that took the concentrations of four major aerosol types as input: primary aerosol, OOA, fireworks, and dust. The model indicated that OOAs were a stronger source of oxidative potential than the fresh primary aerosols, although both fractions contributed substantially to total OP_V^{DTT}. The fireworks factor appeared to be associated with very little oxidative potential. However, this result is physically inconsistent and rather demonstrates the limitations of MLR modelling when dealing with short-term pollution events, even given the use of hourly OP_V^{DTT} measurements made with an online system. Dust was present in very high concentrations during a major dust storm, which resulted in substantial extrinsic oxidative potential despite the fact that the intrinsic oxidative potential of this factor was low. During all other periods dust contributed little to the aerosol oxidative potential.

ACKNOWLEDGEMENTS

This work was supported by the Swiss National Science Foundation under grant 189883 and the Sino-Swiss Cooperation on the Clean Air China program funded by Swiss DEZA under grant 7F-09802.01.03.

REFERENCES

Bates, J. T., Fang, T., Verma, V., Zeng, L., Weber, R. J., Tolbert, P. E., et al. (2019). Review of Acellular Assays of Ambient Particulate Matter Oxidative Potential: Methods and Relationships with Composition, Sources, and Health Effects. *Env. Sci. & Tech.*, *53*(8), 4003–4019.

Calas, A., Uzu, G., Kelly, F. J., Houdier, S., Martins, J. M. F., Thomas, F., et al. (2018). Comparison between five acellular oxidative potential measurement assays performed with detailed chemistry on PM_{10} samples from the city of Chamonix (France). *Atmos. Chem. Phys.*, *18*(11), 7863–7875.

Daellenbach, K. R., Uzu, G., Jiang, J., Cassagnes, L.-E., Leni, Z., Vlachou, A., et al. (2020). Sources of particulate-matter air pollution and its oxidative potential in Europe. *Nature*, *587*(7834), 414–419.

Puthussery, J. V., Zhang, C., & Verma, V. (2018). Development and field testing of an online instrument for measuring the real-time oxidative potential of ambient particulate matter based on dithiothreitol assay. *Atmos. Meas. Tech.*, *11*(10), 5767–5780.

Puthussery, J. V., Dave, J., Shukla, A., Gaddamidi, S., Singh, A., Vats, P., et al. (2022). Effect of Biomass Burning, Diwali Fireworks, and Polluted Fog Events on the Oxidative Potential of Fine Ambient Particulate Matter in Delhi, India. *Env. Sci. & Tech.*, *56*(20), 14605–14616.

Zotter, P., Herich, H., Gysel, M., El-Haddad, I., Zhang, Y., Močnik, G., et al. (2017). Evaluation of the absorption Ångström exponents for traffic and wood burning in the Aethalometer-based source apportionment using radiocarbon measurements of ambient aerosol. *Atmos. Chem. Phys.*, *17*(6), 4229–4249.

RESULTS FROM THE NEW DYNAMIC CLOUD SIMULATION CHAMBER AIDAd

O. MÖHLER[1], Z. DENG[1,2], N.S. Umo[1] and R. WAGNER[1]

[1]Institute of Meteorology and Climate Research, Karlsruhe Institute of Technology, Karlsruhe, 76021, Germany.

[2]Institute of Atmospheric Physics, Chinese Academy of Sciences, Beijing, 100029, China.

Keywords: Atmosphere, ice, nucleation, cloud, simulation.

INTRODUCTION

Enhancing the knowledge of microscale aerosol-cloud processes and improving their quantitative and aerosol-based formulations in cloud, weather and climate models is still among the major challenges in aerosol, cloud, and climate research. The AIDA (Aerosol Interaction and Dynamics in the Atmosphere) atmospheric simulation chamber (Möhler et al., 2003) at the Karlsruhe Institute of Technology (KIT) is in operation since more than 25 years for a wide range of trace gas, aerosol, cloud and climate research related experiment series. It is also used as an expansion-type cloud simulation chamber to investigate ice nucleation processes at simulated mixed-phase cloud (Niemand et al., 2012) and cirrus cloud (Möhler et al., 2006) conditions. During the expansion runs in AIDA, the temperature of the chamber walls remain almost constant. This results in an increasing temperature difference between the well mixed volume inside the chamber, which is cooled by the pressure decrease, and the chamber walls, and by that in an increasing heat flux from the walls into the volume of the cloud chamber. Therefore, the internal energy of the gas is increasing, and the temperature profile during expansion is deviating from the adiabatic cooling profile of an air parcel the experiences the same pressure reduction while ascending in the atmosphere at a certain updraft velocity occurring for instance in convective clouds. To reduce this deficiency for lab-based cloud simulation experiments in an expansion-type cloud simulation chamber, the new dynamic cloud simulation chamber AIDAd (Aerosol Interaction and Dynamics in the Atmosphere – dynamic version) was built at the Karlsruhe Institute of Technology and came into operation in 2022. In this cloud chamber, the walls can be cooled at the same rate as the gas inside, so that cloud simulation experiments can be performed at or at least close to adiabatic expansion conditions which air parcels also experience during their rise in the atmosphere.

METHODS

The new dynamic cloud simulation chamber AIDAd has a double-chamber design (Figure 1), which is similar to the design of the dynamic cloud chambers operated at the Colorado State University (Demott and Rogers, 1990) or still in use at the Meteorological Research Institute in Tsukuba, Japan (Tajiri et al., 2013). It has a new mechanical engineering and cooling design developed in collaboration with the Bilfinger Noell GmbH in Würzburg, Germany, and the Institut für Luft- und Kältetechnik gGmbH in Dresden, Germany. The walls of the cloud chamber located inside a vacuum chamber can actively be cooled at constant rates up to 10 °C min^{-1} (equivalent to an updraft velocity of about 15 m s^{-1} in the troposphere) within the temperature range of +30°C to -55°C. The volumes of the vacuum chamber and the cloud chamber are 15.8 m^3 and 3.8 m^3, respectively. The cloud chamber is made of five segments with independent temperature control. Therefore, the chamber can be operated at either isothermal or controlled temperature gradient conditions. The unique technical design of AIDAd enables the simulation and investigation of tropospheric cloud processes in a wide range of cooling rates and liquid condensation levels.

Figure 1. Construction of the AIDAd vacuum and cloud chambers.

The technical performance of AIDAd was demonstrated in series of test runs with cooling rates between 1 and 10 °C min^{-1}. Figure 2 shows an example of gas temperature measurements inside the cloud chamber during expansion runs from about +5°C to -45°C at constant cooling rates of 1 °C min-1 (blue lines), 4 °C min^{-1} (green lines), and 10 °C min^{-1} (red lines). The solid lines show the mean temperature from all sensors inside the cloud chamber, the thin lines the minimum and maximum value from all individual sensors at a given time. The lower panel shows the difference of the minimum and maximum value from the mean temperature. The gas temperature inhomogeneity is increasing towards the end of an expansion run and is also somewhat higher for the runs at higher cooling rate, but still remains within about ± 2 °C even at the highest cooling rates.

The performance and quality of AIDAd for cloud droplet activation and ice nucleation studies was investigated with a series of cloud droplet freezing experiments, which showed the homogeneous freezing of pure water droplets to occur, as expected, at temperatures between -35°C and -37°C. Furthermore, series of cloud activation experiments were performed with ambient air and with minerals dust aerosols to investigate and document the performance of AIDAd for investigating heterogeneous ice nucleation processes.

Figure 2: Mean gas temperatures (solid lines) and maximum/minimum temperatures (thin lines) from three AIDAd expansion runs with cooling from about +5°C to -45°C at constant rates of 1 °C min-1 (blue lines), 4 °C min^{-1} (green lines), and 10 °C min^{-1} (red lines). The lower panel shows the difference between the maximum/minimum temperatures and the mean gas temperature.

CONCLUSIONS

The dynamic cloud simulation chamber AIDAd came into operation in 2022 as a new research and user facility for investigating aerosol-cloud processes at simulated atmospheric cloud conditions with well controlled pressure, temperature, cooling rate, and moisture content. Test runs and proof-of-concept experiments demonstrated the performance of AIDAd for cloud activation and ice formation experiments. More recently, repeated experiments with mineral dust aerosols were performed to investigate the nature of immersion freezing and its formulation or parameterization as a more stochastic or active site related process. Results from both the test runs and first science-oriented experiment series will be discussed at the conference as part of this contribution.

ACKNOWLEDGEMENTS

This work was supported by the Helmholtz Association through the research field “Earth and Environment” and by the European Union through the Horizon 2020 project EUROCHAMP-2020 Infrastructure Activity (grant agreement No. 730997).

REFERENCES

DeMott, P. J., and D. C. Rogers (1990). Freezing Nucleation Rates of Dilute Solution Droplets Measured between −30° and −40°C in Laboratory Simulations of Natural Clouds, *J. Atmos. Sci.*, **47**, 1056–1064, https://doi.org/10.1175/1520-0469(1990)047<1056:FNRODS>2.0.CO;2.

Möhler, O., Stetzer, O., Schaefers, S., Linke, C., Schnaiter, M., Tiede, R., Saathoff, H., Krämer, M., Mangold, A., Budz, P., Zink, P., Schreiner, J., Mauersberger, K., Haag, W., Kärcher, B., and Schurath, U. (2003). Experimental investigation of homogeneous freezing of sulphuric acid particles in the aerosol chamber AIDA, Atmos. Chem. Phys., **3**, 211–223, https://doi.org/10.5194/acp-3-211-2003, 2003.

Möhler, O., Field, P. R., Connolly, P., Benz, S., Saathoff, H., Schnaiter, M., Wagner, R., Cotton, R., Krämer, M., Mangold, A., and Heymsfield, A. J. (2006). Efficiency of the deposition mode ice nucleation on mineral dust particles, Atmos. Chem. Phys., **6**, 3007-3021, 10.5194/acp-6-3007-2006.

Niemand, M., Möhler, O., Vogel, B., Vogel, H., Hoose, C., Connolly, P., Klein, H., Bingemer, H., DeMott, P., Skrotzki, J., and Leisner, T. (2012). A Particle-Surface-Area-Based Parameterization of Immersion Freezing on Desert Dust Particles, J. Atmos. Sci., **69**, 3077-3092, 10.1175/jas-d-11-0249.1, 2012.

Tajiri, T., K. Yamashita, M. Murakami, A. Saito, K. Kusunoki, N. Orikasa and L. Lilie (2013). A novel adiabatic-expansion-type cloud simulation chamber, *J. Meteorol. Soc. Jpn.*, **91**, 687-704.

FREQUENCY OF NEW PARTICLE FORMATION IN BRISBANE OVER THE YEARS

LIDIA MORAWSKA, ROHAN JAYARATNE, CONGRONG HE, ZORAN RISTOVSKI

International Laboratory for Air Quality and Health, School of Earth and Atmospheric Sciences, Queensland University of Technology, QLD 4000, Australia.

Keywords: Particle Formation, Particle Growth, Nucleation, Atmospheric Aerosols

INTRODUCTION

The International Laboratory for Air Quality and Health (ILAQH) has been monitoring new particle formation (NPF) in Brisbane for over 20 years. In this paper, we look at the results of six studies and investigate how the frequency of NPF has varied over the years. Five of these studies have been previously published in peer-reviewed journals, and the sixth is an on-going study at ILAQH, being reported here for the first time.

The occurrence of NPF depends on many factors, principally the prevalent precursor gas concentration and the pre-existing aerosol particle concentration (Kulmala et al, 2013; Kerminen et al, 2018). Aerosols in the air act as condensation sinks in mitigating the concentration of precursor gases. Thus, an NPF event is more likely to occur on a day when the air is cleaner than when it is polluted. Jayaratne et al. (2015) showed that the particle back-scatter coefficient (BSP) is a good indicator of NPF. The BSP is an indicator of the airborne particle concentration and, thus, inversely proportional to the atmospheric visibility. Jayaratne et al. (2015) showed that the BSP may be used as a reliable indicator of the possibility of observing NPF on a given day and reported that the probability of observing an NPF event was greater than 95% when the BSP was less than 6.8 Mm^{-1}.

A key source of precursor gases and particles in the urban airshed is motor vehicle emissions (Morawska et al., 2008). Over the years, motor vehicle emission rates have been falling as standards have been made increasingly stringent. For example, the PM emission standard for diesel vehicles in Australia, a major source of environmental particle pollution, has been reduced from 140 mg/km in 1993 (Euro 1) to 5 mg/km at present (Euro 6). This is a reduction of over 96% of particles emitted into the airshed. It has been achieved by the use of increasingly efficient after-treatment devices and particle filters in vehicle exhaust. However, at the same time, there has been a concerted move to reduce the sulphur content in fuel. The sulphur level in diesel has been reduced from 5000 ppm at the turn of the century, in three steps through 500 ppm and 50 ppm, to 10 ppm today. This is expected to result in a reduction of Sulphur Dioxide (SO_2) in the air. SO_2 is the main precursor gas largely responsible for NPF in the atmosphere (Kerminen et al., 2018). Thus, the improvement of vehicle emission standards over the years has introduced two competing factors that control NPF in the atmosphere. First, we expect a decrease in NPF due to the decreased precursor gas concentrations and second, we expect an increase in NPF due to the decrease in particulate matter content and its associated condensation sink. In this study, we investigate the frequency of NPF events observed in Brisbane over the last 17 years in order to ascertain its trend.

METHODS

Study	Year	Measurement Period	Instrument	%NPF Days
Guo et al (2008)	2006	22 days	SMPS	35
Cheung et al (2011)	2009	1 year	SMPS	26
Salimi et al (2012)	2012a	285 days	SMPS	67
Jayaratne et al (2016)	2012b	253 days	NAIS	45
Pushpawela et al (2018a)	2015-18	232 days	NAIS	37
Present	2022-23	8 months	SEMS	26

Table 1: Details of the six studies investigated.

Three different instruments were used in these studies - the TSI scanning mobility particle sizer (SMPS), the Airel Neutral cluster and Air Ion Spectrometer (NAIS) and the Brechtel scanning electrical mobility sizer (SEMS). The instruments were located on the sixth floor of a building on the Queensland University of Technology (QUT) campus at Gardens Point. The sampling location was about 100 m away from a busy motorway carrying about 120,000 vehicles per day.

In Table 1, the last column shows the percentage of days on which an NPF event was observed. These numbers are not precise as there are several factors that affected the results. In the various studies, the monitoring periods varied from 22 days to 1 year. However, Pushpawela et al (2018a) did not find a systematic annual variation in NPF frequency. Therefore, we have included the short-term study of Guo et al (2008) too in the analysis.

During a typical NPF event, the particle number concentration (PNC) can increase from about 10^3 cm^{--3} to about 10^5 cm^{-3} within a period of 2 hours. However, this may also occur during controlled hazard reduction burning events when smoke is carried to the monitoring site. The detection of an NPF event is strongly dependent on the smallest size of particle that can be detected by the instrument. In this respect, there is a vast difference between the SMPS (10-15 nm) and the NAIS (2 nm). This prompted Pushpawela et al (2018b) to conclude that many of the NPF events reported by the SMPS were in fact merely growth events. Hygroscopic growth of particles (without actual formation) occurs on most nights when the temperature falls and the humidity increases. The identification of an NPF event is also subjective. For example, in the NAIS studies, NPF events were classified in accordance with the method provided by Zhang et al (2004) using the particle formation rate, dN/dt, where N is the PNC in the size range 2-10 nm. Events with a PNC greater than 5000 cm^{-3} for a period of at least 1 h and dN/dt > 5000 cm^{-3} h^{-1} were classified as NPF events.

RESULTS

The present study using a SEMS has been on-going since July 2022. This comprised nearly eight months of good data. NPF events were observed on 56 of the 215 days for which complete data were available. In agreement with previous studies (Pushpawela et al, 2018a), almost all of the NPF events began between 8 am and 12 noon, reached a peak PNC between 10 am and 1 pm, and gradually decreased over the afternoon until about 4-5 pm. The percentage of days on which NPF was observed was 26%. This is lower than in all other studies with the exception of Cheung et al (2011) who found the same value. The result, compared to previous years are shown in Figure 1.

It is clear that the frequency of NPF has not changed significantly over the last 17 years. One possible explanation is that the competition between PM and SO_2 over the years has balanced out. However, this is not borne out by the variation of PM concentrations over the years. Figure 2 presents the annual

average PM_{10} and $PM_{2.5}$ concentrations observed in Brisbane (DES, 2022). The unusually high concentrations in 2009 and 2019 were due to smoke from bush fires. The relatively low concentrations in 2020 and 2021 were due to the Covid lockdown. The corresponding SO_2 concentrations between 2006 and 2021 remained at the threshold value of 1.0 ppb right through (DES 2022) and are, thus, not shown here.

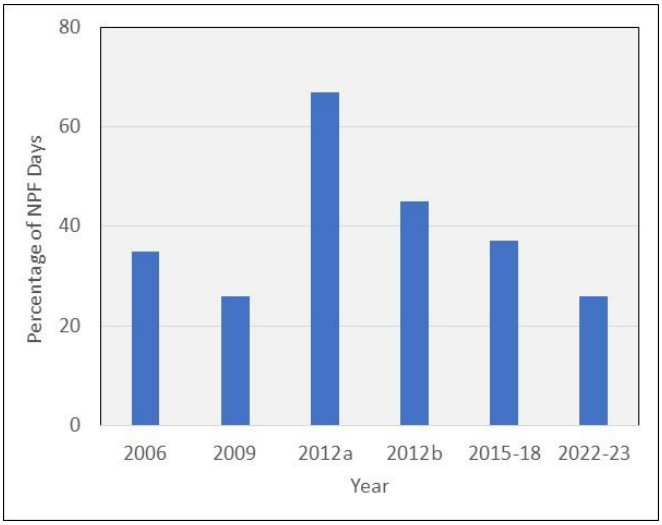

Figure 1: The frequency of NPF events observed in Brisbane. Refer to Table 1 for details.

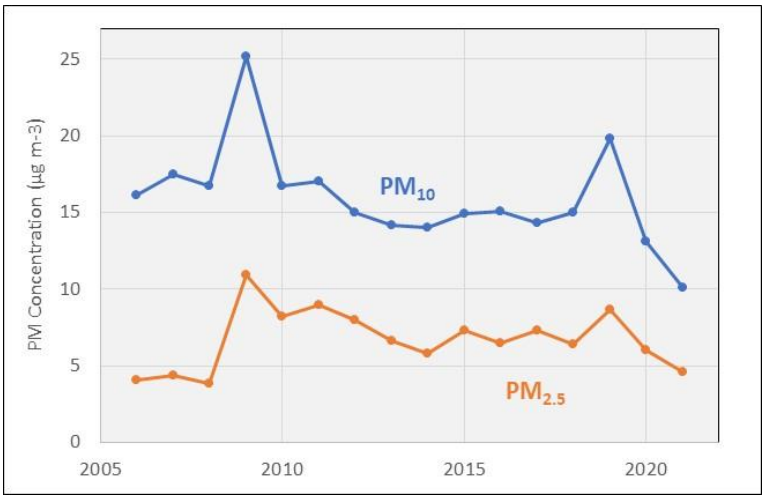

Figure 2: Annual average PM_{10} and $PM_{2.5}$ concentrations observed in Rocklea, Brisbane (DES, 2022).

CONCLUSIONS

This analysis of past and present studies of NPF in Brisbane shows that the frequency of NPF has not changed significantly over the last 17 years (Fig 1). One possible explanation is that the competition between PM and SO_2 has balanced out. However, the annual average PM concentrations measured in Brisbane has not changed significantly (Fig 2), while the SO_2 concentration has been too low to show any discernible temporal trend (DES 2022). There may be other factors in play.

ACKNOWLEDGEMENTS

This study was carried out under Australian Research Council Linkage Grant ARC LP180100516. We are grateful to the Queensland Department of Environment and Science for providing the PM data.

REFERENCES

Cheung, H., Morawska, L., Ristovski, Z. (2011). Observation of new particle formation in subtropical urban environment, *Atmos. Chem. Phys.* **11**, 3823-3833.

DES (2022). Queensland Air Monitoring Report 2021. Department of Environment and Science. Queensland Government.

Guo, H., Ding, A., Morawska, L., He, C., Ayoko, G., Li, Y. S., and Hung, W. T. (2008) Size distribution and new particle formation in subtropical eastern Australia, *Environ. Chem.*, **5**, 382-390.

Jayaratne, E. R., Pushpawela, B., and Morawska, L. (2016) Temporal evolution of charged and neutral nanoparticle concentrations during atmospheric new particle formation events and its implications for ion-induced nucleation, *Front. Environ. Sci. Eng*. **10**, 13-22.

Kerminen, V., Chen, X., Vakkari, V., Pertaja, T., Kulmala, M. (2018). Atmospheric new particle formation and growth: review of field observations. *Environ Res Lett.* **13**, 103003.

Kulmala, M., Kontkanen, J., Junninen, H., Lehtipalo, K., Manninen, H. E., Nieminen, T., Petäjä, T., Sipilä, M., Schobesberger, S., and Rantala, P. (2013). Direct observations of atmospheric aerosol nucleation, *Science*, **339**, 943-946.

Morawska L, Ristovski Z, Jayaratne ER, Keogh DU, Ling X. (2008). Ambient nano and ultrafine particles from motor vehicle emissions: Characteristics, ambient processing and implications on human exposure. *Atmos. Environ*. **42**: 8113-8138.

Pushpawela, B., Jayaratne, R., and Morawska, L. (2018a). Temporal distribution and other characteristics of new particle formation events in an urban environment, *Environ. Pollution*, **233**, 552-560.

Pushpawela, B., Jayaratne, R., Morawska, L. (2018b). Differentiating between particle formation and growth events in an urban environment. *Atmos Chem Phys.* **18**, 11171-11183.

Salimi, F., Rahman, M., Clifford, S., Ristovski, Z., and Morawska, L (2017). Nocturnal new particle formation events in urban environments, *Atmos. Chem. Phys*. **17**, 521-530.

Zhang, Q., Stanier, C., Canagaratna, M., Jayne, J., Worsnop, D., Pandis, S., and Jiminez, J. (2004). Insights into the Chemistry of New Particle Formation and Growth Events in Pittsburgh Based on Aerosol Mass Spectrometry, *Environ Sci Tech*, **38**, 4797-4809.

OBSERVATIONS OF AEROSOL-INDUCED FOG THICKENING OVER NORTH INDIA

N. ARUN[1], CHANDAN SARANGI[1*], VIJAY P. KANAWADE[2], and RITESH GAUTAM[3]

[1] Department of Civil Engineering, Indian Institute of Technology Madras, Chennai, India
[2] Centre for Earth, Ocean, and Atmospheric Sciences, University of Hyderabad, Hyderabad, Telangana, India
[3] Environmental Defense Fund, Washington DC, USA

Keywords: RADIATION FOG, AEROSOL-FOG INTERACTION, WINTER HAZE, INDO-GANGETIC PLAINS

INTRODUCTION

Fog formation and its persistence over the IGP are prime examples of radiation fog, where low-level moisture, calm winds, temperature inversion, and night-time radiative cooling are the main prerequisites for its development (Duynkerke, 1990). The characterization of a 'moderate fog' or 'dense fog' is directly inferred from the horizontal visibility parameter (Ghude et al., 2017) rather than the vertical extent of the fog (such as geometrical thickness). Hence, the estimates of fog macro properties, such as the fog's top and thickness, including their variations and the processes involved, are poorly understood. The IGP also experiences high aerosol loading in the winter months (Babu et al., 2013; Dey and Di Girolamo, 2011; Kumar et al., 2017). These aerosols can impact the growth and dissipation of fog via competitive radiative and microphysical pathways (Bharali et al., 2019; Gautam et al., 2007; Jia et al., 2019; Maalick et al., 2016). In this study, we have used long-term simultaneous aerosols and fog observations from spaceborne Cloud-Aerosol Lidar and Infrared Pathfinder Satellite Observation (CALIPSO) to understand the potential physical associations between aerosol loading and fog macrophysics.

METHODOLOGY AND DATA

CALIPSO

The Cloud-Aerosol Lidar and Infrared Pathfinder Satellite Observations (CALIPSO) mission was developed as part of the National Aeronautics and Space Administration (NASA) Earth System Science Pathfinder (ESSP) program in collaboration with Centre National d'Études Spatiales (CNES), the French space agency to probe the vertical structure and microphysical properties of clouds and aerosols over the globe (Winker et al., 2007). The daytime winter months (December through February) for the last 15 years (2006-2021), exclusively over the IGP, have been chosen in this study. The CALIOP lidar observations can effectively differentiate cloud and aerosol layers at a vertical resolution of 60 m and horizontal resolution of 5 km during the day using the backscatter intensity measurements; hence can be utilized to constrain the base and top height of the cloud samples to identify the fog layer. The cloud top and base height estimates enable us to calculate the fog thickness, which can be used to infer the persistence of a fog event, as the thicker fog can prolong the dissipation phase. We have devised a strategy that will only isolate fog if the detected layer's base height is less than 0.075 km and the top height is less than 0.8 km. Simultaneous to the identified fog layer, we also found the co-existence of aerosol loading above the fog (hereafter AOD_{FOG}). Thus, for any corresponding fog layer, AOD_{FOG} is calculated by vertically integrating the extinction coefficient above the identified fog layer from its top height to (top height + 1) km.

CONCLUSION

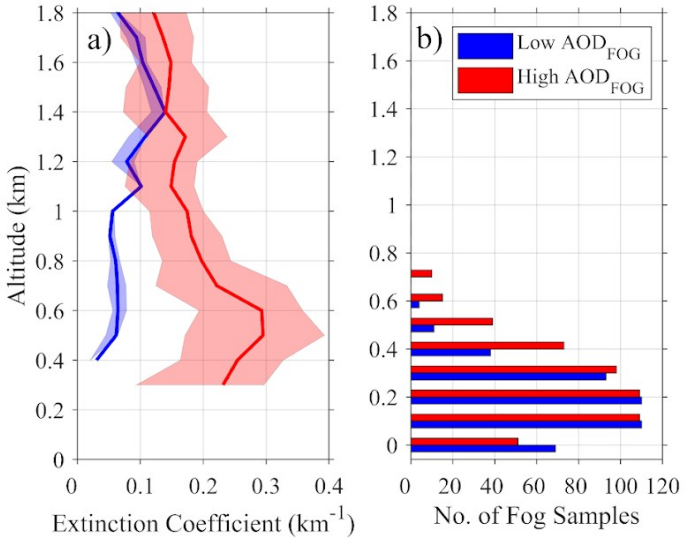

Figure 1: Vertical distribution of aerosol extinction and fog layers over IGP. (a) Vertical profiles of extinction coefficient (altitude above ground) and (b) the number of fog samples (altitude above ground) over IGP corresponding to low AOD_{FOG} (0 – 0.02; 110 profiles) and high AOD_{FOG} (0.06 – 0.28; 109 profiles) scenarios. The bounds in figure 2a represent the 25th and 75th percentile values.

A total of 1501 fog profiles were obtained over the entire IGP domain from 15 years (2006 - 2021) of CALIPSO data, and out of these, 671 profiles found AOD_{FOG}. To isolate the effects of aerosols on the macro-physical changes in the fog, we restrict our subsequent analyses to the area with the largest fog occurrence and higher AOD_{FOG} concentration. We see that the aerosol extinction profiles for the high AOD_{FOG} bin are 2-3 times greater than the profile for the low AOD_{FOG} bin near the surface, and this difference, however, reduces with the altitude (figure 1a). Subsequently, this high aerosol loading is characterized by increased fog layers with fog tops between 0.3 – 0.8 km (figure 1b). However, in the low AOD_{FOG} scenario, the fog samples increased only near the ground (~0 km). These results suggest a relative vertical growth of the fog layer under a high aerosol loading regime.

ACKNOWLEDGEMENT

C.S. and N.A. want to acknowledge research support from the Department of Science and Technology (DST), India. N. A acknowledges the usage of HPC resources of IIT Madras for this work.

REFERENCES

Babu, S.S., Manoj, M.R., Moorthy, K.K., Gogoi, M.M., Nair, V.S., Kompalli, S.K., Satheesh, S.K., Niranjan, K., Ramagopal, K., Bhuyan, P.K., Singh, D., 2013. Trends in aerosol optical depth over indian region: Potential causes and impact indicators. **118**, 11,794-711,806, DOI: 10.1002/2013jd020507.

Bharali, C., Nair, V.S., Chutia, L., Babu, S.S., 2019. Modeling of the effects of wintertime aerosols on boundary layer properties over the indo gangetic plain. **124**, 4141-4157, DOI: 10.1029/2018jd029758.

Dey, S., Di Girolamo, L., 2011. A decade of change in aerosol properties over the indian subcontinent. **38**, DOI: 10.1029/2011gl048153.

Duynkerke, P.G., 1990. Radiation fog: A comparison of model simulation with detailed observations. *Monthly Weather Review* **119**, 324-341, DOI: 10.1175/1520-0493(1991)119<0324:RFACOM>2.0.CO;2.

Gautam, R., Hsu, N.C., Kafatos, M., Tsay, S.-C., 2007. Influences of winter haze on fog/low cloud over the indo-gangetic plains. *Journal of Geophysical Research* **112**, DOI: 10.1029/2005jd007036.

Ghude, S.D., Bhat, G.S., Prabhakaran, T., Jenamani, R.K., Chate, D.M., Safai, P.D., Karipot, A.K., Konwar, M., Pithani, P., Sinha, V., Rao, P.S.P., Dixit, S.A., Tiwari, S., Todekar, K., Varpe, S., Srivastava, A.K., Bisht, D.S., Murugave, P., Ali, K., Mina, U., 2017. Winter fog experiment over the indo-gangetic plains of india. *Current Science (00113891)* **112**, 767-784, DOI: 10.18520/cs/v112/i04/767-784.

Jia, X., Quan, J., Zheng, Z., Liu, X., Liu, Q., He, H., Liu, Y., 2019. Impacts of anthropogenic aerosols on fog in north china plain. *Journal of Geophysical Research: Atmospheres* **124**, 252-265, DOI: 10.1029/2018JD029437.

Kumar, M., Raju, M.P., Singh, R.K., Singh, A.K., Singh, R.S., Banerjee, T., 2017. Wintertime characteristics of aerosols over middle indo-gangetic plain: Vertical profile, transport and radiative forcing. *Atmospheric Research* **183**, 268-282, DOI: https://doi.org/10.1016/j.atmosres.2016.09.012.

Maalick, Z., Kühn, T., Korhonen, H., Kokkola, H., Laaksonen, A., Romakkaniemi, S., 2016. Effect of aerosol concentration and absorbing aerosol on the radiation fog life cycle. *Atmospheric Environment* **133**, 26-33, DOI: https://doi.org/10.1016/j.atmosenv.2016.03.018.

Winker, D.M., Hunt, W.H., McGill, M.J., 2007. Initial performance assessment of caliop. *Geophysical Research Letters* **34**, DOI: 10.1029/2007GL030135.

MODELING APPROACHES FOR ATMOSPHERIC ION-DIPOLE COLLISIONS

I. NEEFJES[1], R. HALONEN[2], H. VEHKAMÄKI[1] and B. REISCHL[1]

[1] *Institute for Atmospheric and Earth System Research / Physics, Faculty of Science, University of Helsinki, P.O. Box 64. FI-00014, Helsinki, Finland.*

[2] *Center for Joint Quantum Studies and Department of Physics, School of Science, Tianjin University, 92 Weijin Road, Tianjin 300072, China.*

Keywords: molecular dynamics, collision rate coefficient, ion, dipole, central field model.

INTRODUCTION

Collisions between ions and dipolar molecules can facilitate the formation of atmospheric aerosol particles and play an important role in their detection in chemical ionization mass spectrometers. Conventionally, analytical models or simple parametrizations have been used to calculate rate coefficients of ion-dipole collisions in the gas phase. Such models, however, neglect the atomistic structure and charge distribution of the collision partners.

METHODS

To determine the accuracy and applicability of these theoretical approaches, we calculated collision cross sections and rate coefficients from all-atom molecular dynamics collision trajectory simulations, sampling a relevant range of impact parameters and relative velocities, and from a central field model using an effective attractive interaction fitted to the long-range potential of mean force between the collision partners (Halonen *et al.*, 2019). We considered collisions between various atmospherically relevant molecular ions and dipoles, as well as charged and neutral dipolar clusters.

System	$\beta_{\mathrm{MD}}/\beta_{\mathrm{CF}}$	$\beta_{\mathrm{MD}}/\beta_{\mathrm{SC}}$
H_2SO_4 – HSO_4^-	1.04	1.20
H_2SO_4 – $(CH_3)_2NH_2^+$	0.92	1.11
H_2SO_4 – NH_4^+	1.05	1.14
H_2SO_4 – NO_3^-	1.04	1.16
H_2SO_4 – $[H_2SO_4 \cdot HSO_4^-]$	0.98	1.16
$[HSO_4^- \cdot (CH_3)_2NH_2^+]$ – HSO_4^-	0.93	1.39
$[HSO_4^- \cdot (CH_3)_2NH_2^+]$ – $(CH_3)_2NH_2^+$	0.90	1.32
$[HSO_4^- \cdot (CH_3)_2NH_2^+]$ – $[H_2SO_4 \cdot HSO_4^-]$	1.01	1.31

Table 1: Comparison between collision rate coefficients obtained from molecular dynamics simulations β_{MD}, central field model with parameters fitted to the PMF curve β_{CF}, and Su and Chesnavich parametrization β_{SC}.

CONCLUSIONS AND OUTLOOK

We find excellent agreement between the collision cross sections and rate coefficients obtained from the molecular dynamics trajectory simulations and the central field model (Tab. 1; Fig. 1). Therefore, we conclude that the effective interactions between the collision partners are highly

isotropic, and the central field model is able to capture the relevant physicochemical properties of the system.

Comparing the molecular dynamics trajectory simulations with the often-used parametrization by Su and Chesnavich (1982), we find that the latter can predict the collision rate coefficient quite well for systems with a molecular dipole, but the agreement worsens for systems with a dipolar cluster (Tab. 1).

Based on our results, we propose the combination of potential of mean force calculation and central field model as a viable and elegant alternative to brute force sampling of individual collision trajectories over a large range of impact parameters and relative velocities (Neefjes *et al.*, 2022).

We are currently using the combination of potential of mean force calculation and central field model, as well as the atomistic trajectory simulations, to understand the relatively large increase in rate coefficient observed in chemical ionization mass spectrometers when sulfuric acid is charged with acetate, as compared to nitrate (Fomete *et al.*, 2022).

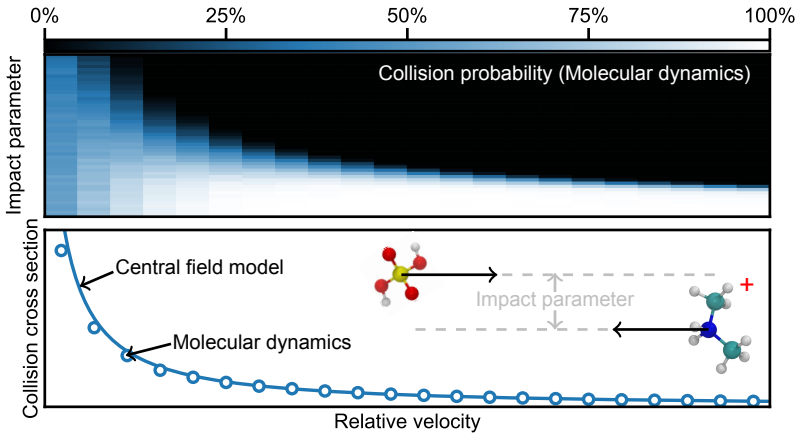

Figure 1: The collision probability from molecular dynamics simulations as a function of the impact parameter and relative velocity (top) and the collision cross section from molecular dynamics simulations and central field model with parameters fitted to the PMF curve as a function of relative velocity for the H_2SO_4–$(CH_3)_2NH_2^+$system (bottom).

ACKNOWLEDGEMENTS

This work was supported by the European Research Council (Project No. 692891 DAMOCLES), the Academy of Finland flagship program (Grant No. 337549), the Centers of Excellence Program (Project No. 1346368 VILMA), and the University of Helsinki, Faculty of Science ATMATH project. Computational resources were provided by the CSC-IT Centre for Science Ltd., Finland.

REFERENCES

Fomete, S. K. W., Johnson, J. S., Myllys, N., Neefjes, I., Reischl, B. and Jen, C. N., (2022). Ion-Molecule Rate Constants for Reactions of Sulfuric Acid with Acetate and Nitrate Ions. *J. Phys. Chem. A*, **126**, 8240–8248.

Halonen, R., Zapadinsky, E., Kurtén, T., Vehkamäki, H. and Reischl, B., (2019). Rate enhancement in collisions of sulfuric acid molecules due to long-range intermolecular forces. *Atmos. Chem. Phys.*, **19**, 13355–13366.

Neefjes, I., Halonen, R., Vehkamäki, H. and Reischl, B., (2022). Modeling approaches for atmospheric ion–dipole collisions: all-atom trajectory simulations and central field methods. *Atmos. Chem. Phys.*, **22**, 11155–11172.

Su, T, and Chesnavich. W. J., (1982). Parametrization of the ion–polar molecule collision rate constant by trajectory calculations. *J. Chem. Phys.*, **69**, 2243–2250.

HUMIDITY-DEPENDENT SURVIVAL OF AIRBORNE RESPIRATORY SYNCYTIAL VIRUS

S. NIAZI [1], R. GROTH [1], K. SPANN [2] AND Z. RISTOVSKI [1]

[1]International Laboratory for Air Quality and Health (ILAQH), School of Earth and Atmospheric Sciences, Queensland University of Technology (QUT), Brisbane, QLD 4000, Australia

[2]Centre for Immunology and Infection Control (CIIC), School of Biomedical Sciences, Queensland University of Technology (QUT), Brisbane 4006, Australia

Keywords: AIRBORNE VIRUS SURVIVAL, RSV, INDOOR AIR, RELATIVE HUMIDITY

INTRODUCTION

Respiratory syncytial virus (RSV) is a significant cause of respiratory infection in both adults and children, causing mild to severe disease including pneumonia, bronchiolitis and exacerbating chronic respiratory conditions such as asthma (Lewnard et al., 2022). The airborne route of transmission has been identified as a primary mode of respiratory virus spread (Niazi et al., 2021b). However, there is limited understanding of airborne RSV survival and transmission. We have utilised transdisciplinary techniques in aerosol physics, atmospheric chemistry and virology to deliver an innovative and transformative approach to fundamentally understand airborne RSV survival in different indoor air conditions. We determined how ambient relative humidity (RH) can interact with physicochemical properties of exhaled respiratory particles and impact airborne RSV survival. This study offers practical new knowledge for reducing the infectivity of airborne RSV in built environments.

METHOD

We measured the hygroscopic behaviour of particles nebulized from the virus carrier fluid at a dry diameter of 100 nm using a humidification tandem differential mobility analyzer (H-TDMA). Three static different indoor ambient RH scenarios, including sub-dry (RH<39%), hysteresis (40%<RH<67%) and super-wet air (RH>67%) were defined based on the hygroscopic behaviour of the virus-laden particles **(figure 1)**. We determine RH-dependence survival of airborne RSV in three static indoor air conditions as well as in three dynamic indoor air conditions (transitions between the static conditions) over timescales spanning 5 min to 45 minutes. We tested our previously hypothetical model known as the Efflorescence and Deliquescence Divergent Infectivity (EDDI) model to explain the RH-dependent survival of airborne RSV at different ranges of RH. The EDDI model suggests that saline respiratory-borne particles can be either effloresced (crystalized) or deliquesced (aqueous) within intermediate (hysteresis) RH zone depending on RH history, which coincides largely with the recommended ergonomically comfortable RH for built environments (30-60%). This means the survival of embedded viruses in such particles can be either promoted or diminished, depending on the state of the particles and their RH history. We used a 400 L aerosol aging drum equipped with RH and temperature control systems to model and precisely maintain various indoor air conditions.

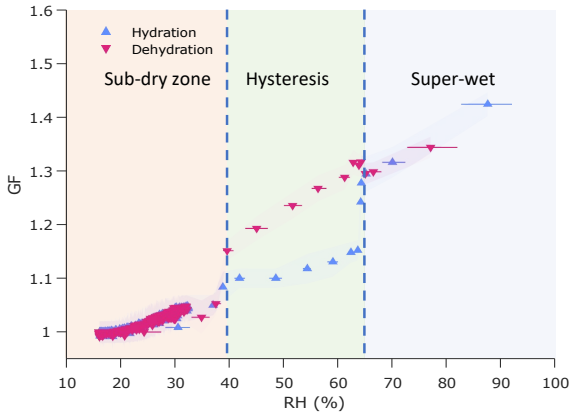

Figure 1. Hygroscopic growth factor (GF) of particles nebulised from the virus carrier fluid across the whole RH range (D0=100 nm).

CONCLUSIONS

The static indoor air conditions modelled in the drum and measured airborne virus infectivity are summarized in **figure 2**. Experiments were performed in triplicate.

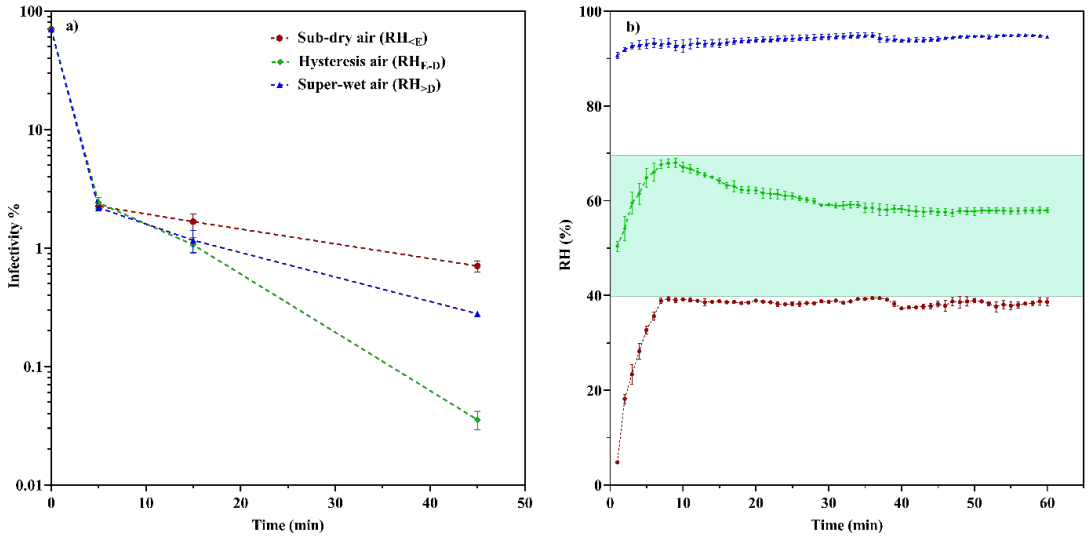

Figure 2. a) Airborne RSV infectivity % loss over 45 minutes particle aging (means ± standard errors of three experiments) in static experiments of sub-dry, hysteresis, and super-wet indoor air scenarios and b) Ambient RH measurements for these three indoor air scenarios (average of three experiments). Initial infectivity (t = 0) is measured to be 70% ± 1.63%. Initial infectivity rate considers the effects of the nebulizer and sampler on RSV at time zero.

We tested three dynamic scenarios (transitions between the static conditions) to investigate the airborne RSV infectivity rates due to RH transition to the final hysteresis air scenario (intermediate RH). **Figure 3b** shows the conditions inside the rotating drum for examining these scenarios. For effloresced particles, the virus carrier fluid was nebulized in the lowest reachable RH (4.6%) in the drum and after reaching equilibrium the RH was raised to the hysteresis range by nebulizing ultrapure DNase/RNase-free distilled water. For the deliquesced state, the virus-laden particles were introduced into hysteresis RH (56.6%) and then water was nebulized into the drum, increasing the RH from 56.6% to 82.83%. In the next step, dry HEPA-filtered compressed air was injected to bring back the RH to hysteresis air. We tested another scenario named as deliquesced control treatment case as the control for previous two states. In this case, the virus-laden particles were introduced into a high RH (91%) and by introducing dry HEPA-filtered compressed air the RH declined to the hysteresis range. The samples were collected at 15, 25, 55 minutes aging time in the hysteresis air for all these three scenarios.

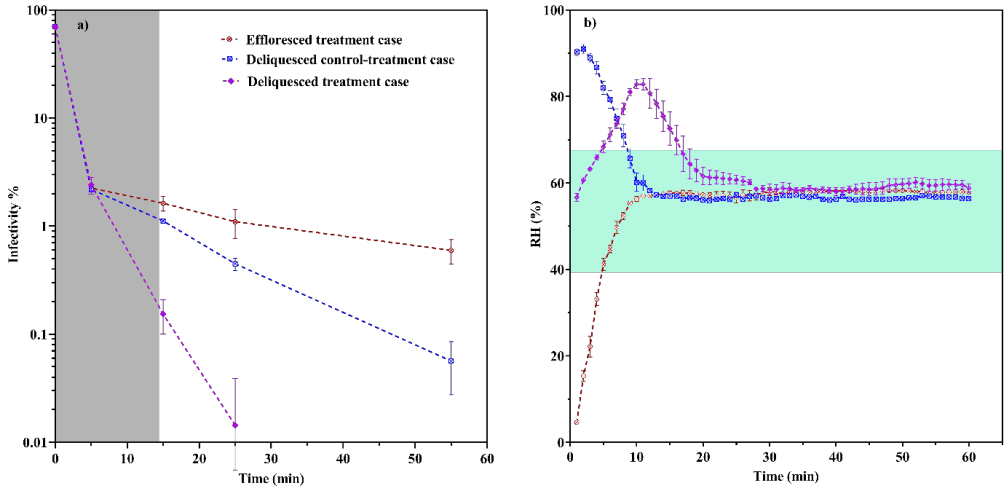

Figure 3. EDDI model ability in predicting airborne RSV survival in hysteresis indoor air scenario. a) presents RSV infectivity % (means ± standard errors of three experiments) for effloresced and deliquesced carrier particles after gradual change of the RH to 56% and subsequent prolonged aging for 5, 15, and 45 min at 56% RH. Gray and green shadings show the gradual RH shift before the first sampling and the hysteresis air RH range. The infectivity percentage at 5 min was acquired from the direct nebulization of virus-laden particles into sub-dry and super-wet indoor air scenarios.

Our results indicate that the majority of airborne RSV is inactivated in the first 5 min aging time in all three static indoor air scenarios. This initial rapid viability loss happened within the first 5 min particles aging time when the particles were introduced as a plume into sub-dry, hysteresis and super-wet air conditions. These particles were subjected to an extensive change in RH from 100% to sub-dry RH (4.6%), hysteresis RH (50%) and super-wet RH (90%) in several seconds. These scenarios also occur in the real world when the virus-laden particles are expired into a heated dry air plume, into comfortable intermediate RH in indoor air or into humid air resulted from outdoor rainfall.

Although airborne RSV infectivity rates following aerosolization into sub-dry and super-wet static air scenarios were similar, this changed when the RH was adjusted to intermediate RH or hysteresis air setting (**figure 3**). Airborne RSV infectivity fractions after 5 min aging time in both sub-dry and super-wet RHs were ~2.2%. However, following the RH adjustment to hysteresis air setting, the infectivity for effloresced particles was more preserved, maintaining 1.62% out of 2.24% infectivity fraction after aerosolization. For the deliquesced control-treatment case (where the RH was adjusted from high to intermediate level), the virus viability fraction declined from 2.19% to 1.11%. We have previously reported the same behaviour for non-enveloped human rhinovirus (Niazi et al., 2021a), and enveloped influenza (Niazi et al., 2021c), however, the viability reductions for these two viruses were much higher than RSV following the RH adjustment from high to intermediate level. The observed trend of infectivity loss for effloresced particles realigned with that for the dried particles (nebulized in sub-dry air), highlighting that the virus inactivation mechanism had the largest impact during the slow water evaporation process, and it intensely decelerated after reaching equilibrium with surrounding ambient indoor RH. Our results indicated that the virus decay rate becomes stable earlier for effloresced particles compared to deliquesced control treatment particles due to the rapid equilibration and particle eater content. This means pre-drying the carrier particles inhabited virus deactivation even with adjusting the RH from low to intermediate level.

Figure 4 summarized airborne RSV infectivity declines due to abrupt and gradual changes in ambient RH at t=45 min. These results presented that the infectivity of airborne RSV adheres a V-shaped curve in its response to different indoor air RH scenarios over 45 min, similar to that described for airborne influenza virus (an enveloped virus). While the virus infectivity at sub-dry air scenario or low RH is similar to that for intermediate and high RHs after 5 min aging time, it is increased during the aging in this condition.

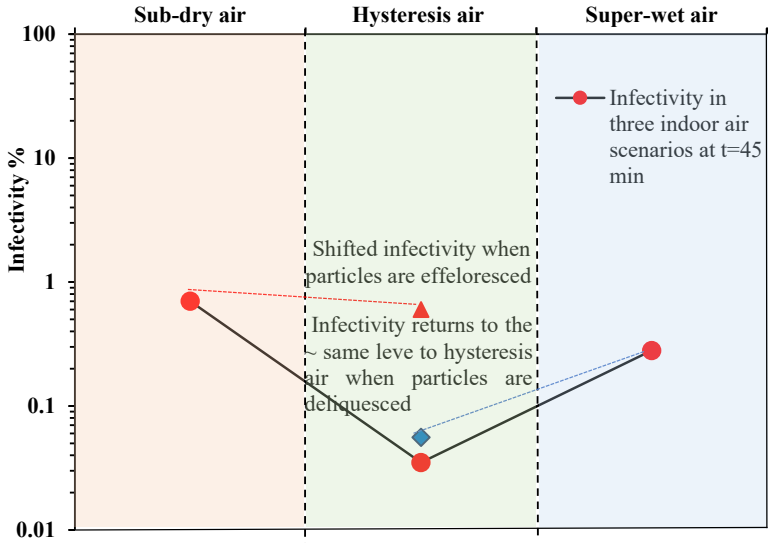

Figure 4. Outcomes of EDDI model in predicting airborne RSV survival over 45 min.

The infectivity in the intermediate RH range preferred for human comfort, is significant and is greatly enhanced (red dash line with triangle) if the particles become effloresced by interacting with dry air immediately after particles production. Conversely, the infectivity in the intermediate RH range is greatly decreased (blue dash with diamond) if the particles pass the deliquescence RH by coming from a humid air into a drier air (intermediate range). Our findings can propose intervention strategies for the improved virus infectivity through the EDDI mechanism. As it discussed above, a part of ambient room air recommended RH (30-60%) overlaps with the hysteresis RH zone of respiratory-borne particles. This means human respiratory exhaled particles efficiently detain a memory of last ambient RH experienced. In low ambient indoor air RH, below the efflorescence RH (39%), aerosolized virus-laden particles undergo a crystal mode, expelling the water content and preserving the virus. These particles can become saturated if the RH exceeds the deliquescence RH (67%). This phenomenon, becoming efflorescence, happens regularly in real-world settings e.g., coughing or sneezing in dry air plume of air conditioning vents or entering cold air into room air during cold seasons. Furthermore, gradual cycling the air between hysteresis and above the deliquescence RH resulted in zero virus survival after 15 min. This finding can be incorporated in future national and international guidelines to provide new insights for the better control of respiratory viruses. We finally propose to maintain the ambient indoor RH between above the efflorescence RH (39%) and below the deliquescence RH (67%) where outside of this range the embedded virus does not benefit from crystallized salt or supportive vitreous shell.

ACKNOWLEDGEMENTS

This study was funded by the Australian Research Council discovery grant no. DP210103284.

REFERENCES

LEWNARD, J. A., FRIES, L. F., CHO, I., CHEN, J. & LAXMINARAYAN, R. 2022. Prevention of antimicrobial prescribing among infants following maternal vaccination against respiratory syncytial virus. *Proceedings of the National Academy of Sciences,* 119**,** e2112410119.

NIAZI, S., GROTH, R., CRAVIGAN, L., HE, C., TANG, J. W., SPANN, K. & JOHNSON, G. R. 2021a. Susceptibility of an Airborne Common Cold Virus to Relative Humidity. *Environmental Science & Technology,* 55**,** 499-508.

NIAZI, S., GROTH, R., SPANN, K. & JOHNSON, G. R. 2021b. The role of respiratory droplet physicochemistry in limiting and promoting the airborne transmission of human coronaviruses: A critical review. *Environmental Pollution,* 276**,** 115767.

NIAZI, S., SHORT, K. R., GROTH, R., CRAVIGAN, L., SPANN, K., RISTOVSKI, Z. & JOHNSON, G. R. 2021c. Humidity-Dependent Survival of an Airborne Influenza A Virus: Practical Implications for Controlling Airborne Viruses. *Environmental Science & Technology Letters,* 8**,** 412-418.

Measure/Model the Effects of Phase States on Deposition Ice Nucleation

ZHENLI LAI[1], ISABELLE STEINKE[2,+], XIAOHAN LI[3], MARTIN WOLF[4], SINING NIU[1], ZHENFA ZHANG[5], JASON D. SURRATT[5,6], DANIEL CZICZO[7], SUSANNAH BURROWS[2,*], YUE ZHANG[1,*]

[1]*Department of Atmospheric Sciences, Texas A&M University, College Station, TX, United States 77843*

[2]*Pacific Northwest National Laboratory, Richland, WA, United States 99354*

[3] *Department of Civil and Environmental Engineering, Princeton University, Princeton, NJ 08544*

[4]*Yale School of Environment, New Haven, CT, United States 06511*

[5]*Department of Environmental Sciences and Engineering, University of North Carolina at Chapel Hill, Chapel Hill, NC, United States 27599*

[6]*Department of Chemistry, University of North Carolina at Chapel Hill, Chapel Hill, NC, United States 27599*

[7]*Department of Earth, Atmospheric, and Planetary Sciences, Purdue University, West Lafayette, IN, United States 47907*

[+]*Now at* Delft University of Technology

Keywords: SOA, 2-Methyltetrols, Deposition Ice Nucleation, Phase State

INTRODUCTION

Aerosol-cloud interactions, including the formation of ice clouds, is the largest uncertainty in predicting future climate based on the reports from Intergovernmental Panel on Climate Change (IPCC). Ice clouds are often formed with the aid of ice nucleating particles (INPs) through heterogeneous ice nucleation. Recent studies show that secondary organic aerosols (SOA), a major component of atmospheric fine particulate matter, may facilitate the heterogeneous ice nucleation by changing its phase state from liquid to semi-solid or glass. Such change of the phase state can lead to enhancement of ice nucleation from previous studies of organic aerosol surrogates. However, there have been limited studies to examine the effects of phase state on the heterogeneous ice nucleation properties of real atmospheric aerosol components. There are also few model parameterizations that are established to describe the heterogeneous ice nucleation properties of SOA by considering the environmental parameters and their phase state.

METHODS

In this study, we first generated 2-methyltetrol (2-MT) particles through homogeneous nucleation. 2-MT is a major component of the isoprene-derived SOA. The 2-MT particles are then size selected by a differential mobility analyzer before passing through a pre-cooling apparatus. The pre-cooling apparatus is used to condition the aerosols to selected temperatures so as to vary the phase state of the 2-MT particles. The pre-condition 2-MT particles were then passed to a Spectrometer for Ice Nucleation (SPIN) to measure the deposition ice nucleation frozen fraction as a function of pre-cooling temperature and frozen temperature. The results show the frozen fraction of 2-MT particles have a strong dependence on the phase state.

Hence, we also develop a parameterization framework based on a stochastic ice nucleation model to describe the deposition ice nucleation process of SOA at various phase states and environmental conditions. This framework takes experimentally measured ice nucleation parameters from organic aerosols under selected phase states, and output the heterogeneous ice nucleation rate coefficient, J_{het}, as a function of

temperature, ice supersaturation, and aerosol phase state (viscosity). The simulated J_{het} isolines follow u-shaped curves in the ice supersaturation–temperature diagram at temperatures between 227-239 K, agreeing well with existing experimental data.

CONCLUSIONS

Our experimental results demonstrate that the phase state of 2-MT particles have strong influence on the deposition ice nucleation abilities. A lower pre-cooling temperature with more viscous 2-MT particles lead to an increase of the deposition ice nucleation property. Our simulated results shows that including the phase state will more accurately predict the heterogeneous ice nucleation abilities for 2-MT particles, as shown in Figure 1. In addition, the model results further suggest that certain SOA species are potentially important INP sources in the tropical troposphere region and the updraft rate of the air is also important in altering the ice nucleation ability of SOA by affecting the cooling rate. We estimate that the isoprene-epoxydiol-derived SOA (IEPOX-SOA) can increase the number concentration of INP by 30 L^{-1} at 10-12 km in altitude based on field measurements from the Amazon rainforest. These results imply that the interplay between INP and aerosol phase state may need to be considered in regional- and global-scale climate models in order to further understand the aerosol-cloud interaction processes and global radiative forcing.

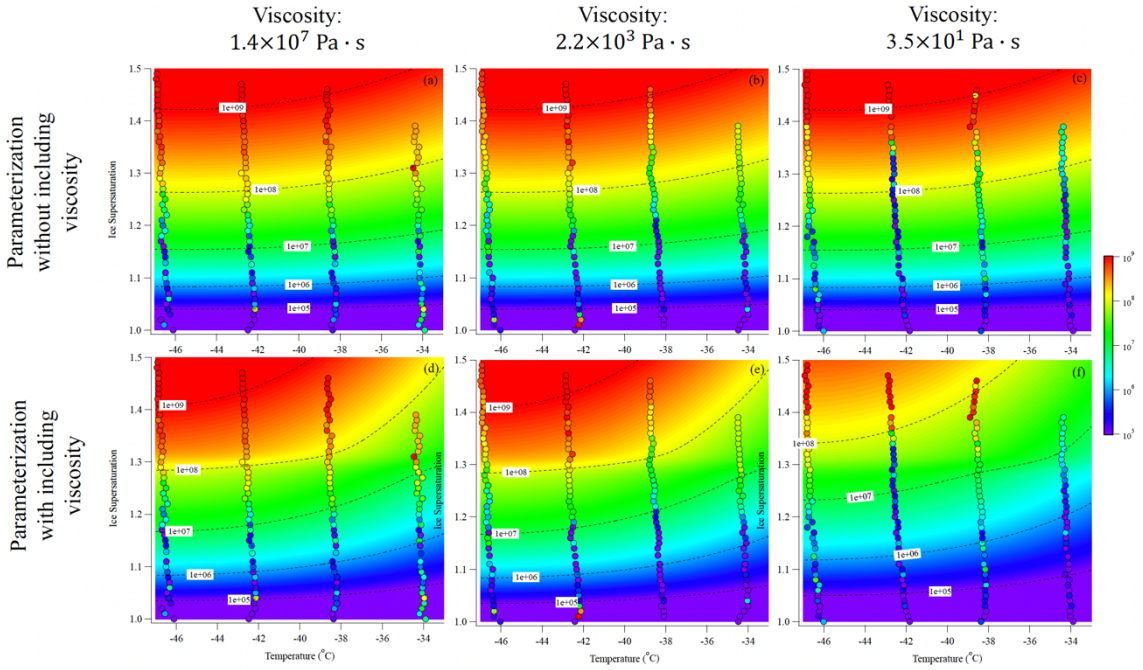

Figure 1: (a-c): fitted J_{het} of 2-MT as a function of only supersaturation and temperature at different pre-cooling conditions. (d-f): fitted J_{het} of 2-MT as a function of viscosity, supersaturation, and temperature at different pre-cooling conditions

ACKNOLWEDGEMENT

This work was supposed by the U.S. National Science Foundation (NSF) Grant Nos. AGS-2131369 (Zhang), AGS-2131371 (Cziczo), AGS-2131370 (Surratt).

REFERENCES

Knopf, D. A.; Alpert, P. A.; Wang, B., The Role of Organic Aerosol in Atmospheric Ice Nucleation: A Review. ACS Earth and Space Chemistry 2018, 2 (3), 168-202.

The Effects of Acid-Catalyzed Multiphase Chemistry on the Cloud Condensation and Ice Nucleation of Secondary Organic Aerosols

SINING NIU[1], YEASEUL KIM[1], ZEZHEN CHENG[2], GREGORY VANDERGRIFT[2], GOURIHAR KULKARNI[3], ALLA ZELENYUK[3], SWARUP CHINA[2], YUE ZHANG[1]

[1]*Department of Atmospheric Sciences, College of Geosciences, Texas A&M University, College Station, 77843, USA*

[2]*Environmental Molecular Sciences Laboratory, Pacific Northwest National Laboratory, Richland, WA, 99354, USA*

[3]*Atmospheric Sciences and Global Change Division, Pacific Northwest National Laboratory, Richland, WA, 99354, USA*

Keywords: SOAs, Multiphase Chemistry, Cloud Condensation Nucleus, Ice Nucleation Particles

INTRODUCTION

Aerosols are ubiquitous in the atmosphere and the aerosol-cloud interactions are one of the largest uncertainties in estimating the radiative forcing and predicting future climate. The physicochemical properties of aerosols can significantly alter their cloud condensation and ice nucleation properties, as well as cloud microphysics. Among atmospheric aerosols, a significant fraction is coming from the multiphase reactions of biogenic volatile organic compounds (BVOCs) with anthopogenic acidic sulfate particles. Previous studies have shown that specific organosulfate (OS) compounds could potentially enhance the ice nucleation properties of aerosol particles from both field sampling and laboratory measurements. Additionally, the phase states of the particles may also hsve critical impacts on their ice nucleation activities.

This study aims to bridge the scientific gap by investigating the impact of multiphase reactions on the phase state, mixing state, and morphology of the particles, and examining how the modification of the physicochemical properties would jointly affect the cloud condensation and ice nucleation activities.

METHODS

The SOAs derived from four BVOCs are generated from a potential aerosol mass (PAM, Aerodyne Research INC.) reactor, with both neutral ammonium sulfate (AS) and acidic ammonium bisulfate (ABS) seed particles. The impacts of the oxidized low volatility organic compounds condensed onto the seed particles are eliminated with the neutral AS seed particle system, and the influences from reactive uptake are isolated, as an acidic environment would promote the multiphase reactions.

Both online and offline techniques are utilized to monitor the change of the chemical composition, specifically, the formation of OS through multiphase oxidation. Filter samples are collected, and the concentration and chemical composition of OS is determined by high resolution aerosol mass spectrometer and Nanospray Desorption Electrospray Ionization coupled with Orbitrap mass spectrometer. The SOAs are also collected onto the TEM grids with their morphology and phase state being analyzed with a Scanning Electron Microscope. The cloud condensation and ice nucleation (IN) activities of the SOAs undergoing multiphase reactions are measured by the PNNL Cloud Condensation Nucleus (CCN) Counter and the Continuous Flow Diffusion Chamber (CFDC) in real-time to derive hygroscopicity parameter κ and ice nucleation onset RH, respectively.

CONCLUSIONS

As shown in Figure 1, the hygroscopicity of the OS containing IEPOX SOA drastically decreased compared with the inorganic ABS seed particles, indicating a reduction of CCN activity during the multiphase reaction. The analogous analyses are conducted for other BVOC systems for both CCN and IN activities. The role multiphase reaction from BVOCs on the CCN and IN properties of SOAs are symmetrically examined in this study.

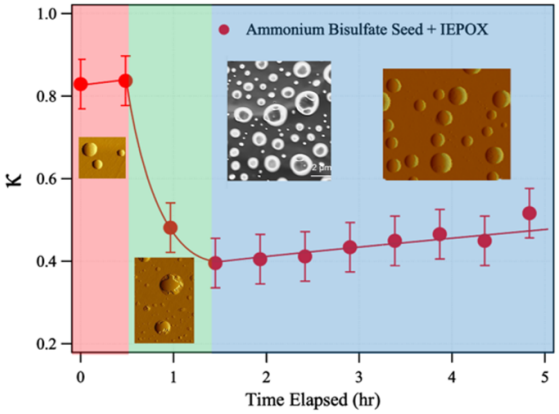

Figure 1: The change of hygroscopicity and morphology of the SOA particles before (red), during (green), and after (blue) IEPOX injection.

ACKOWLEDGEMENTS

This study is funded by NSF AGS 2131369 and DOE EMSL Large-Scale Research 51942.

REFERENCES

Wolf, M. J.; Zhang, Y.; Zawadowicz, M. A.; Goodell, M.; Froyd, K.; Freney, E.; Sellegri, K.; Rösch, M.; Cui, T.; Winter, M.; Lacher, L.; Axisa, D.; DeMott, P. J.; Levin, E. J. T.; Gute, E.; Abbatt, J.; Koss, A.; Kroll, J. H.; Surratt, J. D.; Cziczo, D. J. (2020) A biogenic secondary organic aerosol source of cirrus ice nucleating particles. Nat. Commun., 11 (1), 4834.

China, S.; Alpert, P. A.; Zhang, B.; Schum, S.; Dzepina, K.; Wright, K.; Owen, R. C.; Fialho, P.; Mazzoleni, L. R.; Mazzoleni, C.; Knopf, D. A. (2017). Ice cloud formation potential by free tropospheric particles from long-range transport over the Northern Atlantic Ocean. J. Geophys. Res. (Atmos.), 122 (5), 3065-3079.

LAGRANGIAN VERSUS EULERIAN PERSPECTIVES OF NEW PARTICLE FORMATION EVENTS

S.E. O'DONNELL[1], B. CROFT[2], S.H. JATHAR[3], J.R. PIERCE[1]

[1]Department of Atmospheric Science, Colorado State University,
Fort Collins, Colorado, 80521, United States

[2]Department of Physics and Atmospheric Science, Dalhousie University,
Halifax, Nova Scotia, B3H 4R2, Canada

[3]Department of Mechanical Engineering, Colorado State University,
Fort Collins, Colorado, 80521, United States

Keywords: Aerosols, Nucleation, NPF, CCN.

INTRODUCTION

New particle formation (NPF) in the atmosphere, the process by which new ultrafine-particles are formed from gas-phase precursors, is the dominant source of global aerosol number. In environments with low existing aerosol and/or sufficient condensable material, newly formed particles can grow by condensation to sizes where they can readily act as cloud condensation nuclei (CCN); this process of NPF and growth is a major contributor (~50%; Gordon et al., 2017) to global CCN concentrations. NPF events have been observed in cities and the remote atmosphere, and the study of these events has greatly enhanced our understanding of the underlying processes that govern NPF in different environments. The majority of NPF observations occur at stationary sites; however, the stationary site may not adequately observe the isolated effects of aerosol chemistry and physics due to gradual or rapid changes in the air masses passing over the site. In this work, we will compare and contrast modeled aerosol size distributions at a stationary site and along Lagrangian trajectories crossing the site throughout event days, and we will examine any discrepancies and implications therein.

METHODS

In this work, we ran a 3-D chemical transport model (GEOS-Chem) over the central United States during the HI-SCALE campaign in 2016, which took place at the Southern Great Plains (SGP) observatory in northern Oklahoma. The model uses the TwO Momen Aerosol Sectional (TOMAS; Adams and Seinfeld, 2002) aerosol microphysics, which represents changes in aerosol number and species mass due to condensation, coagulation, and nucleation across 40 size bins ranging from 1 nm to 10 μm. To assess the Lagrangian perspective of NPF events, we ran the HYbrid Single-Particle Lagrangian Integrated Trajectory (HYSPLIT) model (Draxler and Rolph, 2012) to obtain air mass trajectories that pass over the SGP site. We then compare the modeled aerosol size distributions derived along the trajectory paths with the modeled size distribution from the SGP site.

RESULTS

Figure 1. shows a comparison between the modeled aerosol size distributions at the stationary site (SGP) and 5 Lagrangian trajectories passing over the SGP site each at a different time. The stationary size distribution shows particles appearing already grown to sizes ~10 nm, which would indicate that the initial particle growth is not being captured at the stationary site. Contrarily, the aerosol size distributions along the Lagrangian trajectories show more consistent 'banana' shaped NPF events. However, even some of

these trajectories show the particles showing up having grown to several nm, which is due to nucleation and growth occurring at the top of the boundary layer prior to mixing to the surface (not shown) The contrast between the stationary size distribution and the Lagrangian size distributions indicates that an analysis of the stationary size distribution may lead to inaccurate conclusions about the underlying mechanisms driving the NPF event. In this work, we will present an analysis of several NPF events with discrepancies between the stationary and moving size distributions, and we will examine some of the implications of these discrepancies.

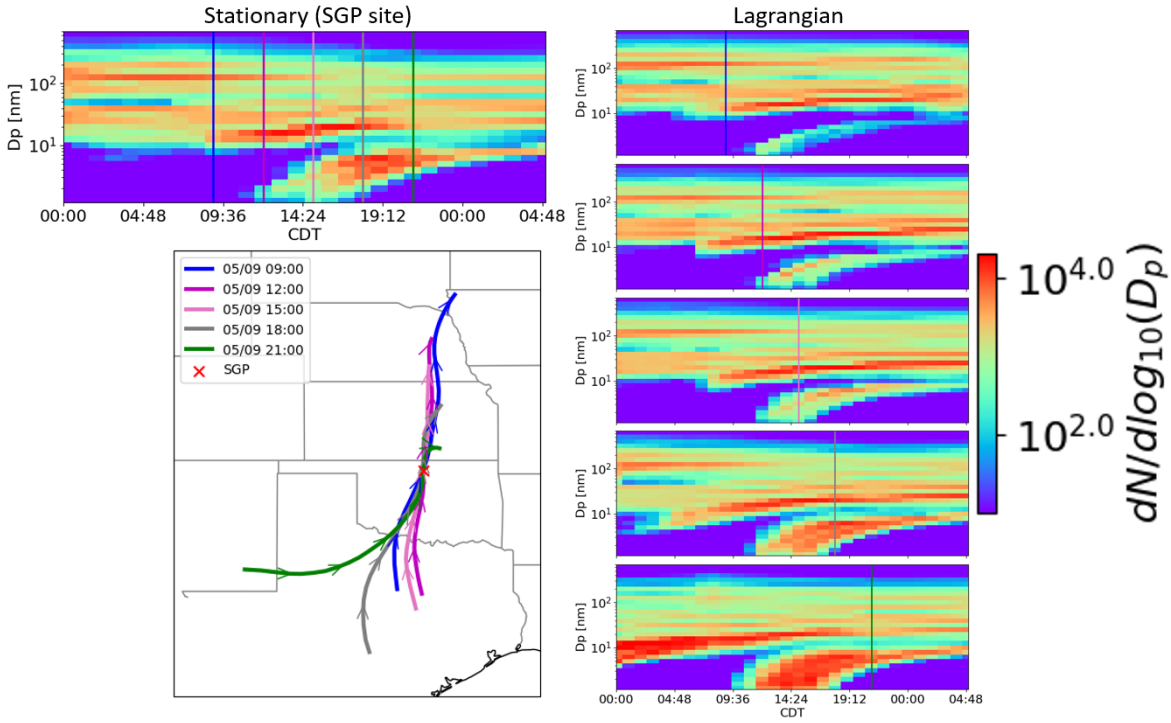

Figure 1. The top left panel shows the aerosol size distribution from GEOS-Chem at the stationary site (SGP). The vertical lines indicate the times at which the Lagrangian trajectories pass over the site. The panels on the right show the aerosol size distributions as observed along the trajectories. The vertical line on each panel indicates the time at which the parcel passes over the SGP site. The panel on the bottom left shows the trajectory path of each of the air parcels, and the colors of the lines correspond to the vertical lines on the aerosol size distribution panels. The SGP site is indicated by the red 'X'.

ACKNOWLEDGEMENTS

This work is supported by the Atmospheric System Research (ASR) program, part of the US Department of Energy's Office of Biological and Environmental Research within the Office of Science, under grants DE-SC0021208 and DE-SC0019000.

REFERENCES

Gordon, H.; Kirkby, J.; Baltensperger, U.; Bianchi, F.; Breitenlechner, M.; Curtius, J.; Dias, A.; Dommen, J.; Donahue, N. M.; Dunne, E. M.; Duplissy, J.; Ehrhart, S.; Flagan, R. C.; Frege, C.; Fuchs, C.; Hansel, A.; Hoyle, C. R.; Kulmala, M.; Kürten, A.; Lehtipalo, K.; Makhmutov, V.; Molteni, U.; Rissanen, M. P.; Stozkhov, Y.; Tröstl, J.; Tsagkogeorgas, G.; Wagner, R.; Williamson, C.; Wimmer, D.; Winkler, P. M.; Yan, C.; Carslaw, K. S.: Causes and Importance of New Particle Formation in the

Present-Day and Preindustrial Atmospheres. *J. Geophys. Res.: Atmos.*, *122* (16), 8739–8760. doi:10.1002/2017JD026844, 2017.

Draxler, R. R. and Rolph, G. D.: HYSPLIT (HYbrid Single-Particle Lagrangian Integrated Trajectory) Model access via NOAA ARL READYWebsite, NOAA Air Resources Laboratory, Silver Spring, MD, 2012.

Adams, P. J.; Seinfeld, J. H.: Predicting Global Aerosol Size Distributions in General Circulation Models. J. Geophys. Res.: Atmos., 107 (D19), AAC 4-1-AAC 4-23. doi:10.1029/2001JD001010, 2002

REMOTE SENSING OF CLOUD MICROPHYSICAL PERTURBATIONS IN SUPER-COOLED STRATUS CLOUDS

K. OHNEISER[1], P. SEIFERT[1], J. HENNEBERGER[2], R. SPIRIG[2], F. RAMELLI[2], C. FUCHS[2], F. SENF[1], W. SCHIMMEL[1], and ULRIKE LOHMANN[2]

[1]Leibniz Institute for Tropospheric Research, Leipzig, Germany

[2]Institute for Atmospheric and Climate Science, ETH Zurich, Zurich, Switzerland.

Keywords: CLOUD MICROPHYSICS, SEEDING, REMOTE SENSING, RADAR.

ABSTRACT

A multitude of processes is involved in the evolution of cloud systems under slightly supercooled conditions down to -10°C. The interaction of thermodynamics, water vapour and aerosol particles controls the phase partitioning, precipitation formation and radiative properties, but the associated pathways can hardly be disentangled. The project PolarCAP Polarimetric Radar Signatures of Ice Formation Pathways from Controlled Aerosol Perturbations (PolarCAP) aims at tackling this complex problem by exploring the evolution of the ice phase at slightly supercooled conditions in a thermodynamically and aerosol-controlled natural environment using radar polarimetry and spectral-bin modelling. The targets of the study are predominantly liquid supercooled stratiform cloud layers which frequently form during wintertime in the temperature range from -10 to 0°C over the Swiss Plateau. In the frame of the external ERC research project CLOUDLAB, drones are used to seed these clouds with defined amounts of ice nucleating particles, i.e. silver iodide. The subsequent formation of ice phase and decay of the liquid phase will be characterized within CLOUDLAB using in-situ measurements and a standard set of remote sensing instrumentation such as lidar and LDR-mode cloud radar, with the goal to improve 1-moment and 2-moment ice-phase parameterisations of the numerical weather prediction model ICON. PolarCAP collaborates with the CLOUDLAB project in order to enhance and utilize the unique dataset by means of the application of cutting-edge polarimetric radar- and lidar-based remote sensing techniques for the determination of cloud microphysical properties, as well as the application of cloud-resolving spectral-bin modelling. Synergistic, multi-wavelength and polarimetric ground-based remote sensing with scanning radar and lidar are used to monitor the transition of supercooled liquid stratiform clouds into mixed-phase clouds. The observations yield new insights into the interplay of contact and immersion freezing, secondary ice formation and ice multiplication, by investigating clouds in the supercooled temperature regimes which are presumed to be either affected or unaffected by specific ice-phase processes.
Within the PolarCAP project the remote sensing equipment of LACROS (Leipzig Aerosols and Clouds Remote Observations System) is installed in Eriswil, Switzerland during three winter campaigns 2022-2025. We will present the main goals of the PolarCAP project, the experimental setup of LACROS that is located side by side with the CLOUDLAB experimental setup. We will further present first results of our cloud microphysical measurements regarding ice crystal detection.

AUSTRALIAN WILDFIRE SMOKE IN THE STRATOSPHERE (2020/2021) AND SELF-LOFTING OF TROPOSPHERIC SMOKE DURING THE SIBERIAN FIRES 2019

K. OHNEISER[1], A. ANSMANN[1], B. KAIFLER[2], A. CHUDNOVSKY[3], B. BARJA[4], D. KNOPF[5], N. KAIFLER[2], H. BAARS[1], P. SEIFERT[1], D. VILLANUEVA[1], C. JIMENEZ[1], M. RADENZ[1], R. ENGELMANN[1], I. VESELOVSKII[6], F. ZAMORANO[4], J. WITTHUHN[1], H. DENEKE[1], G. WALTER[1] and F. SENF[1]

[1]Leibniz Institute for Tropospheric Research, Leipzig, Germany.

[2]Institut für Physik der Atmosphäre, Deutsches Zentrum für Luft- und Raumfahrt, Oberpfaffenhofen, Germany.

[3]Porter School of Earth Sciences and Environment, Tel Aviv University, Tel Aviv, Israel.

[4]Atmospheric Research Laboratory, University of Magallanes, Punta Arenas, Chile.

[5]School of Marine and Atmospheric Sciences, Stony Brook University, Stony Brook, NY 11794-5000, USA.

[6]Prokhorov General Physics Institute, Russian Academy of Sciences, Moscow, Russia.

Keywords: SMOKE, STRATOSPHERE.

ABSTRACT

Smoke in the stratosphere has severe impact on the Earth's climate system. Stratospheric smoke influences radiation, temperature distribution, chemical composition, dynamics, ozone depletion and cirrus evolution. Typically, smoke reaches the stratosphere via the well-known pathway of pyrocumulonimbus convection as it was observed during the record-breaking wildfires that raged in southeastern Australia in late December 2019 and early January 2020.

Rather strong pyrocumulonimbus (pyroCb) convection developed over the fire areas and lofted enormous amounts of biomass burning smoke into the tropopause region and caused the strongest wildfire-related stratospheric aerosol perturbation ever observed around the globe. We discuss the geometrical, optical, and microphysical properties of the stratospheric smoke layers and the decay of this major stratospheric perturbation (Ohneiser et al., 2020, 2022). A multiwavelength polarization Raman lidar at Punta Arenas (53.2°S, 70.9°W), southern Chile, and an elastic backscatter Raman lidar at Río Grande (53.8°S, 67.7°W) in southern Argentina, were operated to monitor the major record-breaking event until the end of 2021. These lidar measurements can be regarded as representative for mid to high latitudes in the Southern Hemisphere. A unique dynamical feature, an anticyclonic, smoke-filled vortex with 1000 km horizontal width and 5 km vertical extent, which ascended by about 500 m d^{-1}, was observed over the full last week of January 2020. The key results of the long-term study are as follows. The smoke layers extended, on average, from 9 to 24 km in height. The smoke partly ascended to more than 30 km height as a result of self-lofting processes. Clear signs of a smoke impact on the record-breaking ozone hole over Antarctica in September–November 2020 were found. A slow decay of the stratospheric perturbation detected by means of the 532 nm aerosol optical thickness (AOT) yielded an e-folding decay time of 19–20 months. The maximum smoke AOT was around 1.0 over Punta Arenas in January 2020 and thus 2 to 3 orders of magnitude above the stratospheric aerosol background of 0.005. After 2 months with strongly varying smoke conditions, the 532 nm AOT decreased to 0.03-0.06 from March–December 2020 and to 0.015–0.03 throughout 2021. The particle extinction coefficients at 532 nm were in the range of 10–75 Mm−1 in January 2020 and, later on, mostly between 1 and 5 Mm^{-1}. An ozone reduction of 20 % – 25 % in the 15–22 km height range was observed over Antarctica and New Zealand ozonesonde stations in the smoke-polluted air.

In contrast to the Australian wildfires, smoke from Siberian wildfires was observed in the lower stratosphere in 2019-2020 during the MOSAiC campaign (Multidisciplinary drifting Observatory for the Study of ArctIc Climate) in the absence of previous pyroCb convection (Ohneiser et al., 2021). The absorption of Sun light by optically thick smoke layers results in heating of the ambient air. This heating is translated into self-lofting of the smoke up to more than 1 km in altitude per day. The main goal is to demonstrate for the first time that radiative heating of intense smoke plumes is capable of lofting them from the lower and middle free troposphere (injection heights) up to the tropopause without the need of pyrocumulonimbus (pyroCb) convection (Ohneiser et al., 2022b). The further subsequent ascent within the lower stratosphere (caused by self-lofting) is already well documented in the literature. Simulations of heating rates which are then converted into lofting rates are conducted by using the ECRAD (European Centre for Medium-Range Weather Forecasts Radiation) scheme. As input parameters thermodynamic profiles from CAMS (Copernicus Atmosphere Monitoring Service) reanalysis data, aerosol profiles from ground-based lidar observations, radiosonde potential temperature profiles, CALIOP (Cloud Aerosol Lidar with Orthogonal Polarization) aerosol measurements, and MODIS (Moderate Resolution Imaging Spectroradiometer) aerosol optical depth retrievals were used.
The sensitivity analysis revealed that the lofting rate strongly depends on aerosol optical thickness (AOT), layer thickness, layer height, and black carbon (BC) fraction. We also looked at the influence of different meteorological parameters such as cloudiness, relative humidity, and potential temperature gradient.
Lofting processes in the stratosphere observed with CALIOP after major pyroCb events (Canadian fires, 2017, Australian fires 2019-2020) are compared with simulations to demonstrate the applicability of our self-lofting model. We analyzed long-term CALIOP observations of Siberian smoke layers and plumes evolving in the troposphere and UTLS (upper troposphere and lower stratosphere) region over Siberia and the adjacent Arctic during the summer season of 2019 and found several indications (fingerprints) that self-lofting contributed to the vertical transport of smoke. We hypothesize that the formation of a near-tropopause aerosol layer, observed with CALIOP over several months, was the result of self-lofting processes because this is in line with the self-lofting simulations.
We will show a detailed analysis of tropospheric and stratospheric smoke lofting rates based on simulations and observations as well as a detailed overview over the decay phase of the Australian wildfire smoke in the stratosphere in 2020-2021.

REFERENCES

Ohneiser, K., A. Ansmann, H. Baars, P. Seifert, B. Barja, C. Jimenez, M. Radenz, A. Teisseire, A. Floutsi, M. Haarig, A. Foth, A. Chudnovsky, R. Engelmann, F. Zamorano, J. Bühl, and U. Wandinger (2020). Smoke of extreme Australian bushfires observed in the stratosphere over Punta Arenas, Chile, in January 2020: optical thickness, lidar ratios, and depolarization ratios at 355 and 532 nm, *Atmos. Chem. Phys.*, **20**, 8003–8015.

Ohneiser, K., A. Ansmann, A. Chudnovsky, R. Engelmann, C. Ritter, I. Veselovskii, H. Baars, H. Gebauer, H. Griesche, M. Radenz, J. Hofer, D. Althausen, S. Dahlke and M. Maturilli (2021). The unexpected smoke layer in the High Arctic winter stratosphere during MOSAiC 2019–2020, *Atmos. Chem. Phys.*, **21**, 15783–15808.

Ohneiser, K., A. Ansmann, B. Kaifler, A. Chudnovsky, B. Barja, D. Knopf, N. Kaifler, H. Baars, P. Seifert, D. Villanueva, C. Jimenez, M. Radenz, R. Engelmann, I. Veselovskii and F. Zamorano (2022). Australian wildfire smoke in the stratosphere: the decay phase in 2020/2021 and impact on ozone depletion, *Atmos. Chem. Phys.*, **22**, 7417–7442.

Ohneiser, K., A. Ansmann, J. Witthuhn, H. Deneke, A. Chudnovsky and G. Walter (2022b). Self-lofting of wildfire smoke in the troposphere and stratosphere caused by radiative heating: simulations vs space lidar observations, *Atmos. Chem. Phys. Discuss. [preprint]*.

FACTORS INFLUENCING THE AIRBORNE STABILITY OF SARS-COV-2 OVER SHORT TIMESCALES.

H.P. OSWIN[1], A. HADDRELL[2*], M.O. FERNANDEZ[2], J. MANN[3], T. HILDITCH[2], J. TIAN[2], D. HARDY[2], D. HILL[4], A. FINN[4], A. DAVIDSON[4], and J. P. REID[2*]

[1]*School of Earth & Atmospheric Sciences, Queensland University of Technology,, Brisbane, Australia*

[2]*School of Chemistry, Cantock's Close, University of Bristol, Bristol, UK*

[3]*Bristol Veterinary School, University of Bristol, Langford House, Langford, Bristol, UK*

[4]*School of Cellular and Molecular Medicine, University of Bristol, Bristol, UK*

.

Keywords: Aerobiology, Virology, Epidemiology, Chemistry.

INTRODUCTION

The physicochemical processes that take place within airborne droplets of respiratory fluid are complex and the impacts they have on the stability of airborne pathogens remain poorly understood, particularly within the first few seconds after aerosolisation. Understanding these processes may help to improve our understanding of the airborne spread of disease and to develop improved infection control strategies.

METHODS

Using the Controlled Electrodynamic Levitation and Extraction of Bioaerosols onto a Substrate (CELEBS) instrument (Oswin *et al* 2022) we studied the airborne stability of the Delta variant of SARS-CoV-2 over very short timescales, manipulating the composition of both the droplet containing the virus and the gas surrounding the droplet, to gain insights into the mechanisms driving losses of viral infectivity at different relative humidities (RH).

CONCLUSIONS

Increasing the concentration of CO2 around the droplets improved the short-term survival of SARS-CoV-2 across all RHs, but with the largest impact being seen at high RH, where the droplet was still likely to be liquid. Increasing the salt content of the droplet had a different effect, with no impact being seen on the stability of the virus at high RH, but an increase in survival being seen when the RH was low enough for phase change to occur in the droplet. These experiments provide further evidence that different physicochemical processes determine airborne viral stability at different RHs and demonstrate that different combinations of host and environmental factors can account for large differences in the stability of airborne viral pathogens.

ACKNOWLEDGEMENTS

This work was supported by grants from EPSRC and The Elizabeth Blackwell Institute.

REFERENCES

Oswin, H.P. *et al* (2022). The dynamics of SARS-CoV-2 infectivity with changes in airborne microenvironment, *Proceedings of the National Academy of Sciences*, 119(27), p.e2200109119.

ESTIMATING GLOBAL ACCUMULATION MODE PARTICLE CONCENTRATIONS WITH MACHINE LEARNING METHODS

A. OVASKA[1], E. RAUTH[1], D. HOLMBERG[1], B. BERGMANS[2], D. COLLINS[3], A. DING[4], M. A. FRANCO[5], S. GANI[1], T. HUSSEIN[1,6], A. HYVÄRINEN[7], R. LEAITCH[8], N. MIHALOPOULOS[9], C. O´DOWD[10], M. SPORRE[11], P. TUNVED[12], V. ULEVICIUS[13], A. WIEDENSOHLER[14], V. ZDIMAL[15], R. MAKKONEN[1,7], K. PUOLAMÄKI[1], T. NIEMINEN[1] AND P. PAASONEN[1]

[1]Institute for Atmospheric and Earth System Research (INAR)/Physics, University of Helsinki, Finland; [2]Institut Scientifique de Service Public (ISSeP), Liege, Belgium; [3]University of California, Riverside, U.S.; [4]School of Atmospheric Sciences, Nanjing University, China; [5]Institute of Physics, University of São Paulo, Brazil; [6]Departmenf of Physics, School of Science, University of Jordan, Amman, Jordan; [7]Finnish Meteorological Institute (FMI), Helsinki, Finland; [8]Environment and Climate Change Canada [9]Department of Chemistry, University of Crete, Greece; [10]School of Physics, National University of Ireland, Galway, Ireland; [11]Deparment of Physics, Lund University, Sweden; [12]Department of Environmental Science, Stockholm University, Sweden; [13]State research institute Center for Physical Sciences and Technology, Vilnius, Lithuania; [14]Leibniz Institute for Tropospheric Research (TROPOS), Leipzig, Germany; [15]Institute of Chemical Process Fundamentals of the CAS, Prague, Czech Republic

Keywords: Aerosol-cloud interactions, Cloud condensation nuclei, Machine learning.

INTRODUCTION

Constraining uncertainties related to aerosol-cloud interactions require a better understanding of global cloud condensation nuclei (CCN) concentrations (Rosenfeld *et al.*, 2014; Quaas *et al.*, 2020). While direct in-situ measurements of CCN exist, observations are scarce and localized. Therefore, estimating global CCN concentrations requires parametrizations and models. Previously developed methods have commonly utilized remote sensing retrievals but achieving sufficient accuracy has proven challenging (Rosenfeld *et al.*, 2014, Stier 2016). In our approach, we used in-situ aerosol measurements and reanalysis data combined with machine learning methods. The aim was to produce models that can estimate global CCN concentrations based on reanalysis data. The results can be used to validate Earth system models.

METHODS

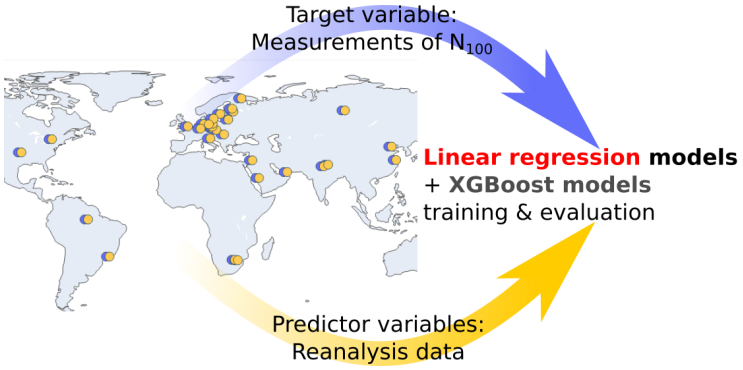

Figure 1. We train and test Linear Regression and XGBoost models using N_{100} measurements and CAMS reanalysis data variables from 30 stations.

The in-situ aerosol measurements contained the number concentration of accumulation mode particles (dry diameter larger than 100 nm), called N_{100}. We used N_{100} as a substitute for CCN measurements. The N_{100} measurements were collected from 30 measurement stations across five continents. Additionally, we used Copernicus Atmosphere Monitoring System (CAMS) reanalysis data (Inness *et al.*, 2019) containing aerosol, gas, and meteorological variables related to CCN formation. We retrieved these for the

coordinates of each station. Combined, N_{100} and CAMS reanalysis data formed a dataset that we used for training and evaluating the models.

We trained Linear Regression (LR) and extreme gradient boosted (XGBoost) models with daily N_{100} measurements as target and CAMS reanalysis data as predictors (Figure 1). We evaluated the model performance against observations at the measurement stations. In particular, we were interested in the model performance at a station when said station was excluded from model training.

Using the trained models, we produced global N_{100} estimates. Our models (XGBoost or LR) take daily averaged full model area CAMS variable fields as input and produced a global N_{100} estimate (Figure 2).

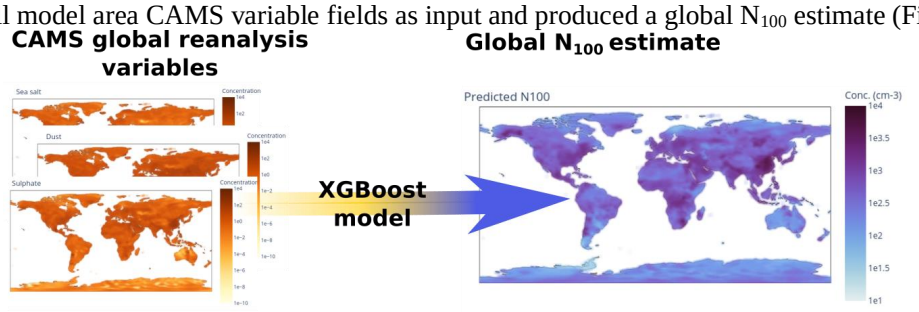

Figure 2. Schematic figure showing how XGBoost data takes daily global CAMS data fields as input and produces a global N_{100} estimate for an example day.

RESULTS

The overall performance for all stations combined is quite good, especially for the XGBoost model, which indicates that the models can capture the range of N_{100} values observed at measurement stations (Figure 3). However, if we look at individual stations, the model performance varies depending on how well the training set represents that station. When we exclude each station from training and analyze performance at the excluded station, we see that some stations have worse performance (Figure 4). These stations are typically in some way unique compared to the rest of the dataset. Even though we include all stations in the final models, this test indicates that there are locations where our global models may perform poorly due to not being represented in our set of measurement stations. Furthermore, there are some differences in the performance between LR and XGBoost. We see that typically XGBoost performs better, but LR is better at stations that are different from the rest of the dataset, possibly because it is better at extrapolating.

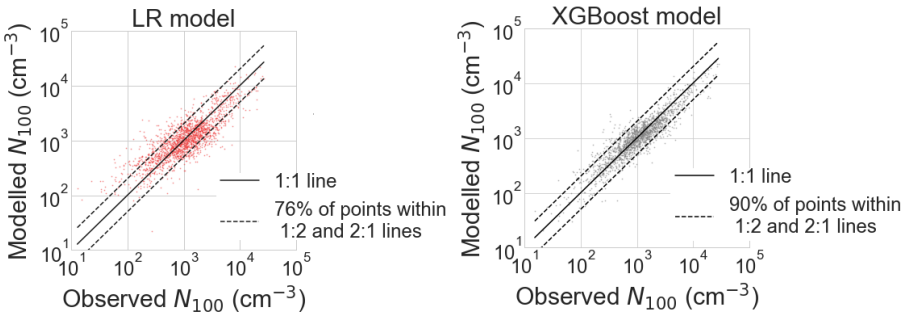

Figure 3. The overall performance of Linear Regression (LR) and XGBoost models with modelled N_{100} compared against observations from all measurement stations.

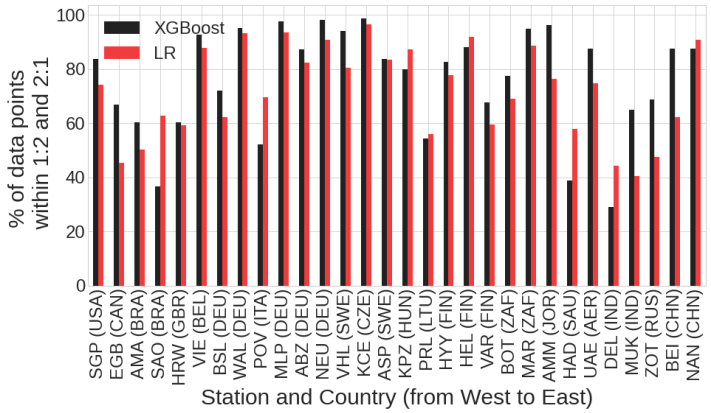

Figure 4. Model performance at each measurement station when said station was excluded from training. Black bars show XGBoost model result, red bars show Linear Regression model result. The model performance metric is the percentage of datapoints within factor of two from observations, where larger number indicates better result.

Using the trained models and CAMS reanalysis variables, we produced global N_{100} estimates. The estimates have daily temporal resolution and 0.75 degrees spatial resolution.

CONCLUSIONS

We used CAMS reanalysis variables and measured N_{100} from 30 measurement stations to train Linear Regression and XGBoost models. The performance of these models was evaluated against measurement data. The evaluation indicates that the models can capture the range of N_{100} observed at the stations. However, outside the training stations the performance varies depending on how well our training set represents the location.

We used the trained models to produce global N_{100} estimates. We will further investigate the behavior and accuracy of the global estimates in different locations outside the measurement stations. Based on our analysis, it is possible that while XGBoost yields better results at training stations, LR may be a more suitable method for spatial extrapolation and producing reliable global estimates.

ACKNOWLEDGEMENTS

This work is supported by Academy of Finland (337549 and 311932), European Union's Horizon 2020 research and innovation program (821205) and European Regional Development Fund (UIA03-240). The model is generated using Copernicus Atmosphere Monitoring Service information 2021. CAMS reanalysis dataset was downloaded from the CAMS Atmosphere Data Store (ADS).

REFERENCES

Inness, A. *et al.* (2019). The CAMS reanalysis of atmospheric composition. *Atmos. Chem. Phys.*, *19*(6), 3515–3556.

Quaas, J. *et al.* (2020). Constraining the Twomey effect from satellite observations: Issues and perspectives, *Atmos. Chem. Phys*, 20(23), 15079–15099.

Rosenfeld, D. *et al.* (2014). Global observations of aerosol-cloud-precipitation- climate interactions, *Rev. Geophys.*, 52, 750–808.

Stier, P. (2016). Limitations of passive remote sensing to constrain global cloud condensation nuclei, *Atmos. Chem. Phys*, 16(10), 6595–6607.

TRENDS IN AMBIENT AEROSOLS AT LULIN ATMOSPHERIC BACKGROUND STATION, TAIWAN

S.K. PANI[1] and N.H. LIN[1]

[2]Department of Atmospheric Sciences, National Central University, Taoyuan, Taiwan.

Keywords: PARTICULATE MATTER, BLACK CARBON.

SYNOPSIS

Aerosols play an important role in the radiation balance of the earth-atmosphere system. Black carbon (BC), a prominent particle-phase light absorber, is exclusively produced by the incomplete combustions of fossil fuel, biofuel, and biomass. BC-related research has received significant global focus due to its notable impact on regional-to-global climate change. However, the knowledge about long-term changes in PM_{10}, $PM_{2.5}$, and BC aerosols in the western North Pacific is very limited. Lulin Atmospheric Background Station (LABS; 23.47°N, 120.87°E; 2862 m above sea level) on the summit of Lulin Mountain in central Taiwan is the only high-altitude background station in the western Pacific region and still operational since the spring of 2006 to study the impact of various air pollutants through long-range transport. Continuous real-time measurements of PM_{10} (2006-2016)/$PM_{2.5}$ (2013-2020) and BC (2008-2020) at LABS were carried out by using the tapered element oscillating microbalances (TEOM 1405; Thermo Fisher Scientific, USA) and an aethalometer (AE-31, Magee Scientific, USA), respectively, in order to investigate their temporal variations, characteristics, and the important factors controlling long-term trend. The influence of meteorological parameters on their monthly/seasonal burden was extensively studied through correlation analysis. Multi-year annual mean mass concentrations of PM_{10}, $PM_{2.5}$, and BC were 9.2, 7.2, and 0.4 $\mu g\ m^{-3}$, respectively. Based on concentration weighted trajectory analyses, important contributory long-distant source regions for all aerosols at LABS were northern peninsular Southeast Asia and mainland China, particularly during spring (March-May) and northeast-monsoon (October-November), respectively. A slightly downward trend in PM_{10} (-0.35% $year^{-1}$), $PM_{2.5}$ (-0.24% $year^{-1}$), and BC (-0.63% $year^{-1}$) mass concentrations was observed at LABS. This might be due to the decline in the contribution of biomass-burning smoke emissions from peninsular Southeast Asia to the western North Pacific, recent energy policy change in China, and also changes in regional atmospheric boundary layer dynamics.

ACKNOWLEDGEMENTS

This work was supported by the National Science and Technology Council, Taiwan and the Taiwan Environmental Protection Administration.

CCN activation of aerosols from different combustion emissions sources

A.S. Panicker[1] , V. Anil Kumar[1] , M.P. Raju[1] , G. Pandithurai[1] , P.D. Safai[1] , G. Beig[1], S.Das[2]

[1]Indian Institute of Tropical Meteorology, Pune, India

[2] Stockholm University, Sweden

Key words: Carbonaceous aerosols, black carbon, CCN

Introduction and Method

It is necessary to understand the cloud condensation nuclei (CCN) activation of aerosols (especially carbonaceous aerosols) from various combustion sources. In this regard, the CCN activation of aerosols has been studied from various sources of emissions such as combustion of wood, cow dung cake, wood-coal burning and diesel generator (DG) in a laboratory environment at the High Altitude Cloud Physics Laboratory (HACPL) in Mahabaleshwar, India. Different instruments such as Cloud particle counter, CCN counter; Aethalometer, OC/EC analyser etc. were used for this purpose. The combustion from various sources was separately carried out inside a chamber and the outlet from the charmer was connected to all the other instruments for simultaneous measurements.

Results and conclusion

The CCN activation was found to be faster in carbonaceous aerosol emission from combustion of cow dung cake (complete CCN activation of particles was observed at 0.3% super saturation (SS). Wood burning showed an activation at 0.4% SS and the wood coal burning showed CCN activation at 0.7% SS. However the activation of particles from DG exhaust found to be a higher super saturation (SS) of 0.9% (100.9% RH). Compared to Black carbon and Elemental carbon, Organic carbon was found to be the dominant carbon

component in all four emission sources. The OC/EC rati was higher for wood burning (8.35) and was lowest for DG emissions (2.03). For the same number of BC particles, BC mass concentration was higher for DG emissions. The Organic species was found to be dominant compared to inorganic species in all the emissions. The study suggests that the carbonaceous aerosols from direct emissions can undergo CCN activations at high super saturations.

IN-SITU MEASUREMENTS OF MORPHOLOGICAL VARIABLES AND GROWTH OF ICE CRYSTALS

S. PARK[1], J. UM[1], E. JÄRVINEN[2], M. SCHNAITER[2], G.M. MCFARQUHAR[3], J. KIM[1], C. H. JUNG[4]

[1]BK21 School of Earth and Environmental Systems, Division of Earth Environmental System, Department of Atmospheric Sciences, Pusan National University, Republic of Korea.
[2]Karlsruhe Institute of Technology, Germany.
[3]Cooperative Institute for Severe and High Impact Weather Research and Operations, School of Meteorology, University of Oklahoma, USA.
[4]Department of Health Management, Kyungin Women's University, Republic of Korea.

Keywords: Ice crystal, Growth, PHIPS, ACLOUD, SOCRATES.

INTRODUCTION

Morphological variables (e.g., maximum dimension D_{max}, projected area, perimeter, width, and roundness) of ice crystals are fundamental information needed to represent microphysical and radiative properties of ice clouds in numerical models. These variables can be derived via in-situ aircraft measurements using cloud probes. Conventional airborne cloud probes are limited to a single observation angle to measure morphological variables. Non-spherical ice crystals may have different measured morphological variables depending on the observation angle, which causes uncertainties in the representations of the microphysical and radiative properties of ice clouds. Thus, it is required to quantify uncertainties that depend on observation angles for determining morphological variables of ice crystals.

METHODS

In this study, the differences in determining morphological variables of ice crystals depending on observation angles were quantified using measurements of the Particle Habit Imaging and Polar Scattering (PHIPS) probe that were acquired during the 2017 Arctic Cloud Observation Using airborne measurements during polar Day (ACLOUD) field campaign and the 2018 Southern Ocean Clouds Radiation Aerosol Transport Experimental Study (SOCRATES) field campaign. The PHIPS provides bright-field stereo-microscopic images at two different observation angles that are 120° apart for the sampled ice crystals. Figure 1 shows the example PHIPS stereo images of a quasi-spherical ice crystal and a non-spherical ice crystal. Morphological variables and habits of ice crystals were determined based on the stereo images. Detailed information on the PHIPS can be found in Abdelmonem *et al*. (2016), Schnaiter *et al*. (2018), and Waitz *et al*. (2021). The uncertainty in determining a morphological variable of an ice crystal was quantified using the relative difference between two morphological variables acquired at two different observation angles, which is represented by

$$Relative\ Diff\ V = \frac{|V_{angle1} - V_{angle2}|}{Max(V_{angle1}, V_{angle2})},$$

where V_{angle1} and V_{angle2} are morphological variables of ice crystals depending on the observation angle 1 and 2, respectively, and *Max* (V_{angle1}, V_{angle2}) is the maximum value of V_{angle1} and V_{angle2}. Larger *Relative Diff V* indicates larger impacts of nonsphericity of ice crystals on the determined morphological variables. The statistics of the *Relative Diff V* were calculated for different temperature and D_{max} ranges.

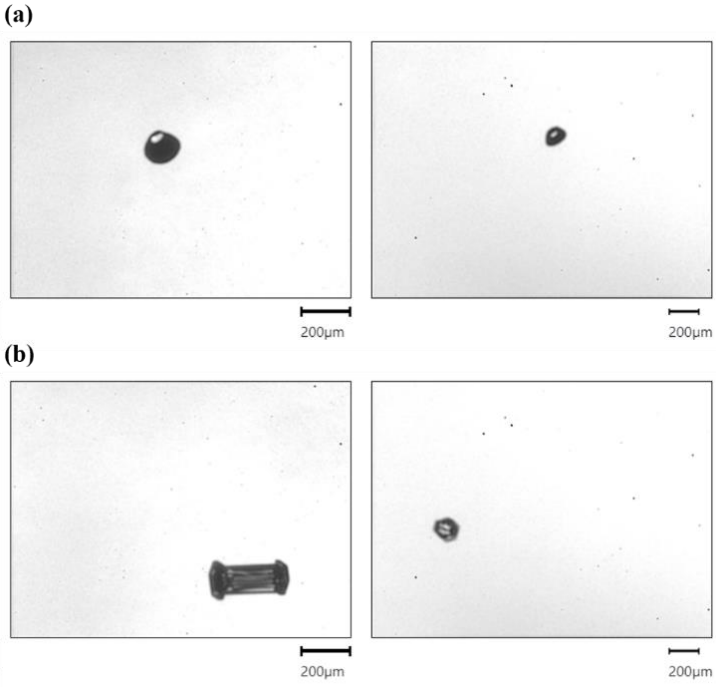

Figure 1. The stereo images of (a) a quasi-spherical ice crystal and (b) a non-spherical (capped column) ice crystal acquired via the PHIPS.

RESULTS

Figure 2 shows the habits and mean roundness of ice crystals sampled by the PHIPS during the ACLOUD and SOCRATES in different temperature and D_{max} ranges. Small irregulars (49.9%) and needles (13.1%) are dominant habits of the measured 5517 ice crystals. The roundness (nonsphericity) of needle ice crystals that have elongated shapes is smaller (larger) than that of small irregular ice crystals that have a quasi-spherical shape (Fig. 3). Thus, the increase in the percentage of needle ice crystals with the increase in temperature (D_{max}) mainly caused the decrease in mean roundness. In particular, the mean roundness of ice crystals depended strongly on D_{max}.

Figure 4 shows the differences in morphological variables of ice crystals depending on the observation angles (i.e., *Relative Diff V*) as functions of different temperature and D_{max} ranges. A positive correlation was found between the *Relative Diff V* and temperature (D_{max}). Particularly, the *Relative Diff V* depended strongly on D_{max}, which was caused by the notable decrease in roundness with increasing D_{max}. The mean *Relative Diff* D_{max} (projected area; perimeter; width; roundness) of all ice crystals was 14.69% (22.75%; 14.57%; 16.67%; 18.76%), and the maximum was 69.95% (95.32%; 75.87%; 95.19%; 89.95%).

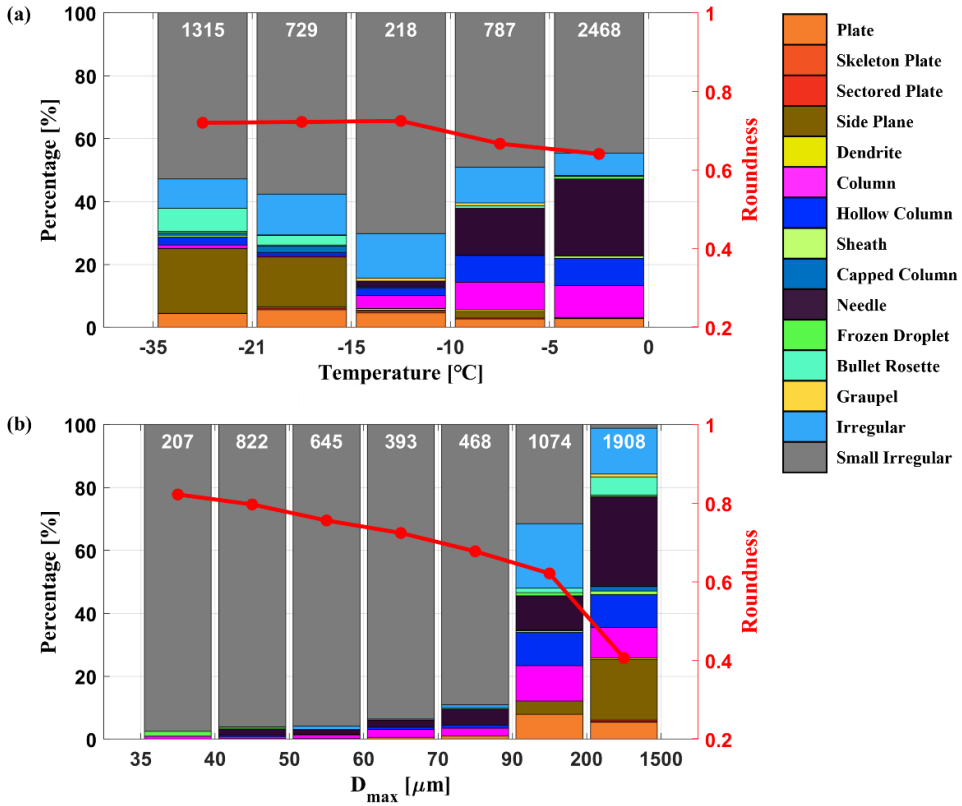

Figure 2. The habits and roundness of ice crystals in different (a) temperature and (b) D_{max} ranges. The maximum of D_{max} was determined at two observation angles and the corresponding roundness was used for statistical analysis. The red lines indicate the mean roundness. The number of ice crystals in different temperature and D_{max} ranges is indicated in each panel.

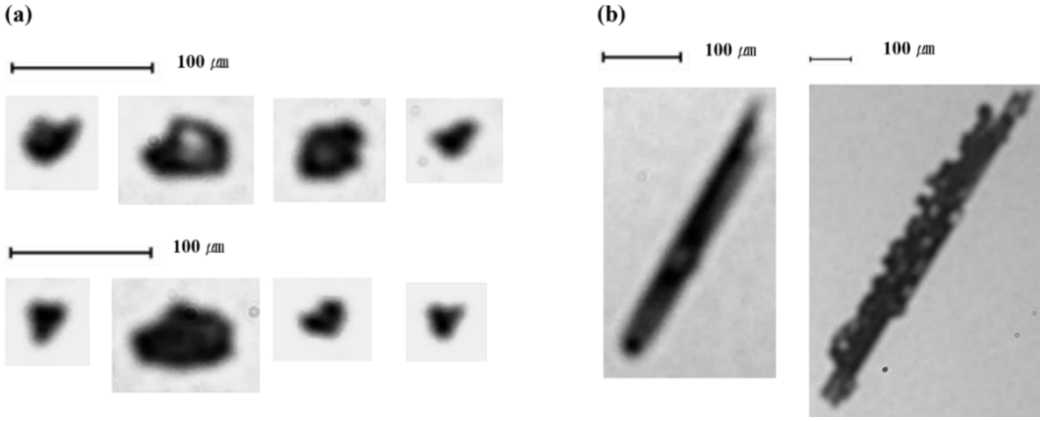

Figure 3. Examples of (a) small irregular ice crystals and (b) needle ice crystals acquired at a single observation angle of PHIPS.

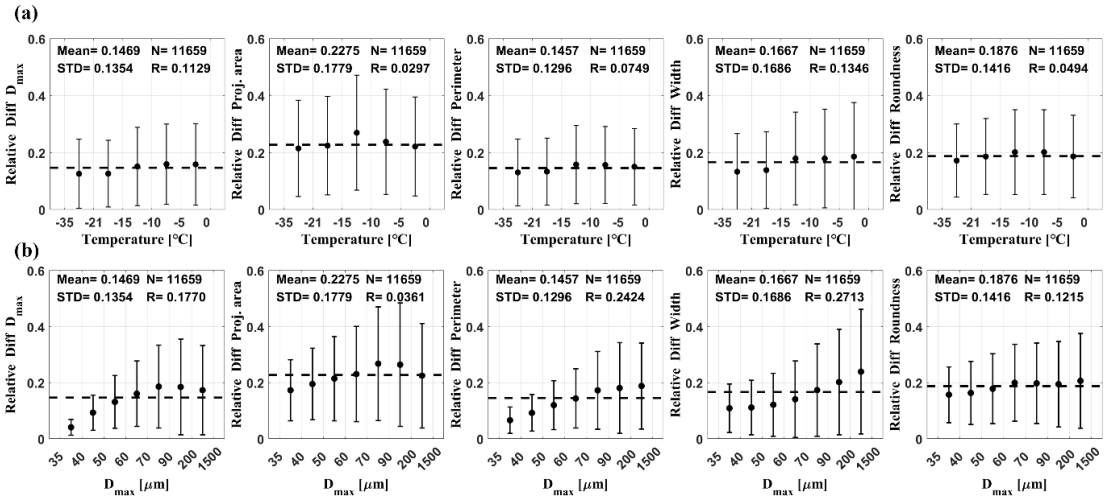

Figure 4. The *Relative Diff V* depending on different (a) temperature and (b) D_{max} regimes. The D_{max} is the maximum of values determined at two observation angles. The dashed lines are the mean *Relative Diff V* of ice crystals. Mean, standard deviation, correlation coefficient (R), and the number of ice crystals are indicated in each panel.

CONCLUSIONS

In this study, the uncertainties in determining morphological variables of ice crystals were quantified by calculating the differences in morphological variables of ice crystals depending on observation angles for -35℃ < T < 0℃ and 35 μm < D_{max} < 1500 μm. The nonsphericity of ice crystals increased with the increase in temperature and D_{max}, which caused the increase in uncertainties in determining morphological variables of ice crystals. The nonsphericity of ice crystals caused the mean 14.69% (22.75%; 14.57%; 16.67%; 18.76%) uncertainty and the maximum 69.95% (95.32%; 75.87%; 95.19%; 89.95%) uncertainty in determining D_{max} (projected area; perimeter; width; roundness).

ACKNOWLEDGEMENTS

This work was supported by the National Research Foundation of Korea (NRF) grant funded by the Korea government (MSIT) (No. 2020R1A2C1013278). This work was funded by the Korea Meteorological Administration Research and Development Program “Research on Weather Modification and Cloud Physics” under Grant (KMA2018-00224).

REFERENCES

Abdelmonem, A., E. Järvinen, D. Duft, E. Hirst, S. Vogt, T. Leisner, and M. Schnaiter (2016). PHIPS–HALO: the airborne Particle Habit Imaging and Polar Scattering probe–Part 1: Design and operation, *Atmospheric Measurement Techniques*, **9**(7), 3131-3144.

Schnaiter, M., E. Järvinen, A. Abdelmonem, and T. Leisner (2018). PHIPS-HALO: the airborne particle habit imaging and polar scattering probe–Part 2: Characterization and first results, *Atmospheric measurement techniques*, **11**(1), 341-357.

Waitz, F., M. Schnaiter, T. Leisner, and E. Järvinen (2021). PHIPS-HALO: the airborne Particle Habit Imaging and Polar Scattering probe–Part 3: Single-particle phase discrimination and particle size distribution based on the angular-scattering function, *Atmospheric Measurement Techniques*, **14**(4), 3049-3070.

New particle formation (NPF) events in various environments

H. LEE[1], H. CHO[1], and K. PARK[1]

[1]*School of Earth Sciences and Environmental Engineering, Gwangju Institute of Science and Technology,*

123 Cheomdangwagiro, Buk-gu, Gwangju, Republic of Korea

Keywords: NPF, URBAN, ARCTIC, AGRICULTRUAL, LIVESTOCK.

INTRODUCTION

Atmospheric nanoparticles can be produced by direct emission from various combustion sources and/or be indirectly formed by gas-to-particle conversion process. New particle formation (NPF) usually refers to the secondary formation of nanoparticles from precursor molecules through nucleation, condensation, and coagulation processes (Kerminen et al., 2018). The newly formed particles will grow and affect the Earth's climate system. They act as significant contributor to the number-based aerosol population in the ambient atmosphere (Kulmala et al., 2016) and serve as cloud condensation nuclei (CCN) affecting cloud formation (Kerminen et al., 2018). The NPF has been frequently observed in many locations and times with various precursor species, pollution levels, and meteorological conditions (Kerminen et al., 2018). In this study, characteristics of NPF parameters such as particle formation rate (J), growth rate (GR), condensation sink (CS), occurrence frequency, and occurrence criteria (L_gamma) were compared among different environments (urban, agricultural (livestock and cropland), and the Arctic) to better understand underlying mechanism of NPF under various environments.

METHODS

NPF measurements have been conducted at various locations. The number size distributions of particles from 3 nm to 10 μm were continuously measured by using a nano-scanning mobility particle sizer (SMPS) consisting of a nano-differential mobility analyzer (nano-DMA) (model 3085, TSI, USA) and a condensation particle counter (CPC) (model 3776, TSI, USA), a regular- SMPS consisting of a DMA (Model 3081, TSI, USA) and a CPC (Model 3772, TSI, USA)., a nanoscan-SMPS, and/or optical particle counter (OPC) (1.108, Grimm, Germany). The urban site is located on the Gwangju Institute of Science and Technology (GIST) campus in Gwangju, Korea (35.13° N and 126.50° E). The site is surrounded by residential, commercial, and agricultural areas, and is located 1.8 km to the east of the Honam highway. The agricultural sites are selected in livestock and cropland areas. The livestock site is located in Yongji-myeon, Gimje-si (35.84° N, 126.99° E), Jeollabuk-do, Korea, close to numerous livestock farms (swine and chicken) and fertilizer production facilities. The area is home to 120,134 swine heads and 2,456,931 chicken heads and contains 11 fertilizer facilities which are also sources of ammonia emissions. The concentrated animal feeding operations (CAFOs) are located to the southwest and north of the site, hosting ~64,000 swine heads and ~590,000 chicken heads and ~43,000 swine heads and ~1,310,000 chicken heads, respectively. The estimated ammonia emissions from swine and chicken feedlots in this area are 1.8 Gg year–1, accounting for 5.5% of Jeollabuk-do's total ammonia emission or 0.6% of the country's total ammonia emission (Top 3: agriculture > manure treatment > swine and chicken feedlots (Gimje-si)). The cropland site is located in Seongdeok-myeon, Gimje-si (35.81° N, 126.79° E), Jeollabuk-do, Korea, and is surrounded by cultivated areas such as rice paddies. The area has a high density of rice paddy fields and is the largest contributor of ammonia emissions from fertilizer use in Jeollabuk-do,

ranking 4th in the country. The Arctic site is in the Zeppelin Observatory which is located in Ny-AlesundÅ lesund, Svalbard, Norway (78.54° N and 11.53° E). The site is elevated approximately 474 m above sea level. This site is positioned a few kilometers away from a small scientific village and is located at the northernmost point of the warm Atlantic inflow within the west Spitsbergen current.

CONCLUSIONS

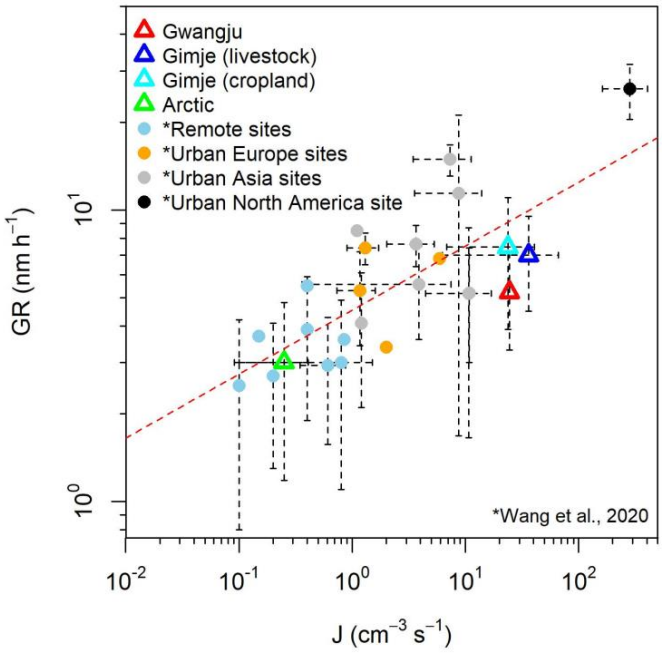

Figure 1. Comparison of J and GR during NPF event days among sites.

The highest NPF occurrence frequency was observed at agricultural (livestock) site in summer even with high CS and temperature, compared to urban, agricultural (cropland), and arctic sites, due to the highest source rates of ammonia and other gases emitted from pig and chicken farms. The lowest GR and J were observed at the Arctic site with the least condensable vapors, but the ratio of other condensable vapors to H2SO4 was the highest at the Arctic site, suggesting the importance of biological organic vapors in the Arctic NPF.

ACKNOWLEDGEMENTS

This research was supported by National Research Foundation of Korea (NRF) and the

Samsung Advanced Institute of Technology (SAIT).

REFERENCES

Kerminen, V.-M., Chen, X., Vakkari, V., Petäjä, T., Kulmala, M., and Bianchi, F. (2018).

Atmospheric new particle formation and growth: review of field observations, *Environ. Res. Lett.*, **13**, 103003.

Kulmala, M., Petäjä, T., Kerminen, V.-M., Kujansuu, J., Ruuskanen, T., Ding, A., Nie, W., Hu, M., Wang, Z., Wu, Z., Wang, L., and Worsnop, D. R. (2016) On secondary new particle formation in China, Front. *Environ. Sci. Eng*., **10**, 8.

Wang, M., Kong, W., Marten, R., He, X.-C., Chen, D., Pfeifer, J., Heitto, A., Kontkanen, J., Dada, L., Kürten A., Yli-Juuti, T., Manninen, H. E., Amanatidis, S., Amorim, A., Baalbaki, R., Baccarini, A., Bell, D. M., Bertozzi, B., Bräkling, S., Brilke, S., Murillo, L. C., Chiu, R., Chu, B., Menezes, D. L.-P., Duplissy, J., Finkenzeller, H., Carracedo, L. G., Granzin, M., Guida, R., Hansel, A., Hofbauer, V., Krechmer, J., Lehtipalo, K., Lamkaddam, H., Lampimäki, M., Lee, C. P., Makhmutov, V., Marie, G., Mathot, S., Mauldin, R. L., Mentler, B., Müller, T., Onnela, A., Partoll, E., Petäjä, T., Philippov, M., Pospisilova, V., Ranjithkumar, A., Rissanen, M., Rörup, B., Scholz, W., Shen, J., Simon, M., Sipilä, M., Steiner, G., Stolzenburg, D., Tham, Y. J., Tomé, A., Wagner, A. C., Wang, D. S., Wang, Y., Weber, S. K., Winkler, P. M., Wlasits, P. J., Wu, Y., Xiao, M., Ye, Q., Zauner-Wieczorek, M., Zhou, X., Volkamer, R., Riipinen, I., Dommen, J., Curtius, J., Baltensperger, U., Kulmala, M., Worsnop, D. R., Kirkby, J., Seinfeld, J. H., El-Haddad, I., Flagan, R. C., and Donahue, N. M. (2020). Rapid growth of new atmospehric particles by nitric acid and ammonia condensation, *Nature*, **581**, 184–189.

THE COMPOSITION OF AMBIENT PARTICULATE FROM MOBILE MONITORING CAMPAIGNS

H. PATEL[1,2], C. TOLLERMACHE[3], P. DAVY[4], J. SALMOND[1], D. WILLIAMS[2,3]

[1]School of Environment, Faculty of Science, University of Auckland, Private Bag 92019, Auckland, New Zealand

[2]Mote Limited, 40a George Street, Mount Eden, Auckland

[3]School of Chemical Sciences, Faculty of Science, University of Auckland, Private Bag 92019, Auckland, New Zealand

[4]GNS Science, 40 Gracefield Road, Lower Hutt

Keywords: Particulate Matter, Raman, X-ray Fluorescence, Personal Exposure

INTRODUCTION

Particulate matter (PM) is one of the greatest risks to human health and the environment. PM is emitted into the atmosphere via a series of different emission pathways, both anthropogenic and natural and is comprised of a series of different elements and compounds varying in size, morphology and chemistry (Groma et al. 2022; de Jesus et al. 2019; World Health Organization 2021; Gong et al. 2016). Most commonly quantified using gravimetric mass estimates fails to identify the chemical and elemental properties of PM (O'Connor et al. 2014). Most studies also use data collected from fixed monitoring stations which are well known to underestimate commuter exposure (O'Connor et al. 2014; Kaur, Nieuwenhuijsen, and Colvile 2005) These methods are therefore limiting in providing an accurate assessment of personal exposure to PM, impacting contributions to policy initiatives like traffic calming measures to mitigate this hazardous air pollutant. A series of mobile monitoring campaigns were devised to collect ambient particulate along a customised route to understand the potential impact of road dust and exhaust emissions on personal exposure.

METHODS

A 5km walking route was devised through Central Auckland covering roads of differing traffic intensities and land uses. Using a small vacuum pump, samples were collected onto PTFE filters. Total sample volume was recorded, and blanks were collected for quality assurance purposes. Samples were then analysed using a combination of x-ray fluorescence (XRF) and Raman spectroscopy (RS).

RESULTS & DISCUSSION

XRF analyses indicated the presence of soil components (Al, Si, Fe), sea salt (Na, Cl) and heavy metals (Cr, Fe, Co, Ni, As, Mo, Cd, Sn, Sb, Ba). RS identified carbon black and diesel soot along with the presence of other chemicals. Peak fitting of carbonaceous soot particles exhibited differing intensities within the D and G bands, revealing the presence of soot particles of different crystallinities. RS coupled with XRF provided a powerful technique to identify ambient particulate's elemental and chemical composition from a series of mobile monitoring campaigns. Such studies allow for the continued characterisation of ambient particulate to contribute to toxicology studies and policy initiatives to mitigate the impacts of air pollution.

REFERENCES

Gong, Xianda, Ci Zhang, Hong Chen, Sergey A. Nizkorodov, Jianmin Chen, and Xin Yang. 2016. "Size

Distribution and Mixing State of Black Carbon Particles during a Heavy Air Pollution Episode in Shanghai." *Atmospheric Chemistry and Physics* 16 (8): 5399–5411. https://doi.org/10.5194/acp-16-5399-2016.

Groma, Veronika, Bálint Alföldy, Endre Börcsök, Ottó Czömpöly, Péter Füri, Annamária Horváthné Kéri, Gabriella Kovács, Szabina Török, János Osán, and Gabriella Kov. 2022. "Sources and Health Effects of Fine and Ultrafine Aerosol Particles in an Urban Environment." *Atmospheric Pollution Research* 13 (2). https://doi.org/10.1016/j.apr.2021.101302.

Jesus, Alma Lorelei de, Md Mahmudur Rahman, Mandana Mazaheri, Helen Thompson, Luke D. Knibbs, Cheol Jeong, Greg Evans, et al. 2019. "Ultrafine Particles and PM2.5 in the Air of Cities around the World: Are They Representative of Each Other?" *Environment International* 129 (May): 118–35. https://doi.org/10.1016/j.envint.2019.05.021.

Kaur, S., M. Nieuwenhuijsen, and R. Colvile. 2005. "Personal Exposure of Street Canyon Intersection Users to PM2.5, Ultrafine Particle Counts and Carbon Monoxide in Central London, UK." *Atmospheric Environment* 39 (20): 3629–41. https://doi.org/10.1016/j.atmosenv.2005.02.046.

O'Connor, Sean, Paula Fey O'Connor, H. Amy Feng, and Kevin Ashle. 2014. "Gravimetric Analysis of Particulate Matter Using Air Samplers Housing Internal Filtration Capsules." *Gefahrst Reinhalt Luft* 74 (10): 403–10. https://pubmed.ncbi.nlm.nih.gov/27165699%0Ahttps://www.ncbi.nlm.nih.gov/pmc/articles/PMC5664198/%0Afile:///C:/Users/Carla Carolina/Desktop/Artigos para acrescentar na qualificação/The impact of birth weight on cardiovascular disease risk in the.pdf.

World Health Organization. 2021. *WHO Global Air Quality Guidelines. Particulate Matter (PM2.5 and PM10), Ozone, Nitrogen Dioxide, Sulfur Dioxide and Carbon Monoxide*. Geneva.

AIRBORNE ICE NUCLEATING PARTICLES IN CONVECTIVE MID-LATITUDE CLOUDS

RYAN J. PATNAUDE[1], KATHRYN A. MOORE[1], RUSSELL J. PERKINS[1], THOMAS C. J. HILL[1], CARSON C. HUME[1], CHRISTINA S. MCCLUSKEY[2], PAUL LAWSON[3], PAUL J. DEMOTT[1], GREG M. MCFARQUHAR[4], PAVLOS KOLLIAS[5], MENGISTU WOLDE[6], and SONIA M. KREIDENWEIS[1]

[1]Department of Atmospheric Science, Colorado State University, Fort Collins, CO, USA.

[2]National Center for Atmospheric Research, Boulder, CO, USA

[3]Stratton Park Engineering Company, Inc., Boulder, CO, USA

[4]School of Meteorology, University of Oklahoma, Norman, OK, USA

[5]Division of Atmospheric Sciences, Stony Brook University, Stony Brook, NY, USA

[6]National Research Council Canada, Ottawa, Ontario, Canada

Keywords: ICE NUCLEATING PARTICLES, PRIMARY NUCLEATION, SECONDARY ICE PRODUCTION

INTRODUCTION

Ice crystal formation in mixed-phase and ice clouds plays an important role in the physical processes that subsequently control the cloud lifetime, precipitation formation, and Earth's radiative balance. Formation of ice in mixed phase clouds (MPCs) strongly depends initially on the presence of aerosols, specifically ice nucleating particles (INPs), which facilitate freezing by lowering the energy that needs to be overcome for the formation of a critical ice embryo. In the mixed-phase cloud regime, heterogeneous nucleation is the primary ice nucleation process, as opposed to homogeneous nucleation that occurs readily at temperatures < -38 ºC, and depending on the environmental conditions and INP composition, can proceed via a number of different nucleation pathways (Kanji et al., 2017; Vali et al., 2015). Because coincident collection of INP data along with cloud microphysical measurements has been so rare, only limited comparisons have been possible to explore the consistency or lack thereof between INP concentrations and ice crystal concentrations in clouds. Finding agreement between INPs and initiation of ice crystals by primary nucleation processes in convective MPCs is further complicated due to the occurrence of secondary ice processes (SIP) proceeding through various mechanisms (Field et al., 2017). Unfortunately, most models oversimplify SIP leading to large uncertainties in the simulated evolution of the ice phase. Here we report on targeted measurement campaigns that collected data on INPs at the surface, as well as making airborne measurements of both INPs and ice crystal concentrations in cumulus congestus clouds over the Central Great Plains and the Gulf Coast of the United States of America. These data allow for comparison of INP concentrations with in-cloud ice crystal concentrations to deduce whether SIP was active.

METHODS

Airborne observations used in this study were obtained aboard the NSF-NCAR Gulfstream-V (GV) aircraft in May and June of 2021 during the Secondary Production of Ice in Cumulus Experiment (SPICULE) campaign over the Central Great Plains and aboard the National Research Council Canada (NRC) Convair-580 aircraft in May and June of 2022 during the Experiment of Sea Breeze Convection, Aerosols, Precipitation and Environment (ESCAPE) campaign in the Houston metro area. For both studies, ice nucleation measurements were obtained through two methods. Real-time observations were

made using the Colorado State University (CSU) continuous flow diffusion chamber (CFDC) (Barry et al., 2021; Rogers, 1988) to provide high-resolution INP measurements in the immersion freezing mode. Offline measurements of INPs activating via immersion freezing were made using the CSU Ice Spectrometer (IS) from suspensions of aerosol particles in pure water following collections on polycarbonate membrane filters in inline filter units (sampling from the same ambient inlet as the CFDC) (Barry et al., 2021). While CFDC measurements recorded INP concentrations at one temperature at a time, IS measurements provided temperature spectra of INP concentrations, integrated over a ~20-min sampling interval. CFDC sampling during SPICULE and ESCAPE occurred through different methods when in vs. out of cloud. During SPICULE ambient, clear-air sampling used the HIAPER Modular Inlet (HIMIL) in the boundary layer (BL) and out-of-cloud, and a similar isokinetic inlet was used during ESCAPE. For in-cloud measurements during both campaigns, sampling was instead downstream of a counterflow virtual impactor (CVI; Twohy et al., 1997) inlet, which selectively captures cloud hydrometeors. The flow containing the remaining residual aerosol particles after cloud particle evaporation was sent to the CFDC for detection of INPs. Ground-based INP measurements were collected during ESCAPE as part of the US Department of Energy's Tracking Aerosol Convection Interactions Experiments (TRACER) campaign, which had intensive operations around Houston during the same time as ESCAPE. Open-faced filters were collected at the location of the first ARM Mobile Facility (AMF1) in Laporte, TX and processed identically to the filters collected on the aircraft, to obtain INP spectra. Multiple flights during ESCAPE were designed to fly near or directly over the Laporte site for direct comparison of INP observations between the surface and aloft.

During both the SPICULE and ESCAPE campaigns, cloud microphysical data were collected on the GV and Convair-580 and additionally aboard the Stratton Park Engineering Company (SPEC Inc.) Learjet which flew in coordination with the GV and Convair-580. The Learjet typically probed supercooled cloud levels at the tops of ascending cumuli while the other aircraft captured sub-cloud and warm-phase cloud data. Cloud hydrometeors were measured aboard the Learjet using a suite of instruments including the Cloud Droplet Probe (CDP), a two-dimensional stereo probe (2DS), and the High-Volume Precipitation Spectrometer (HVPS). This suite measures the complete range of cloud hydrometeor sizes, from 3 μm up to several centimeters. Ice crystal number concentrations during SPICULE cloud passes were estimated by analyzing the high-resolution images from the cloud imaging probe (CPI) on the Learjet and separating the composite size distributions from all hydrometeor probes into the liquid and ice phases, similar to methods employed by Lawson et al. (2017, 2022).

RESULTS

In this section, we will present selected results from the campaigns described above. INP concentrations at various temperatures, as measured by the CFDC are shown in Figure 1 for each of the ESCAPE research flights, and generally show concentrations between 1 and 100 L^{-1} in the temperature range –18 to –34 ºC. There was also a fairly wide range in INP concentrations, more than a factor of 10, during each flight. Additionally, during the last four flights of ESCAPE, a strong Saharan dust intrusion was observed, denoted by the tan shaded region in Figure 1, which was reflected in the large increase in INP concentrations, especially for temperatures below -20 ºC. Saharan dust is known to possess effective ice nuclei at temperatures below -20 ºC (DeMott et al., 2003), and was present throughout much of the BL and aloft, as observed in independent aerosol measurements. INP spectra during the dust intrusion showed strong log-linear increases as temperatures decreased from ~-20 ºC down to -30 ºC. Similar behaviors were observed in the IS spectra (not shown) from samples obtained at the surface at the AMF1 site, those obtained from flights in the BL, and those observed at higher altitudes, indicating INP concentrations are consistent throughout the lower troposphere and would likely be ingested into the clouds forming in these air masses.

In Figure 2, we present results from the SPICULE campaign comparing ice crystal concentrations in the cold phase region of a cumulus congestus cloud to INP concentrations. Figure 2a shows the estimated ice crystal concentration and size distribution from a cloud pass in the Learjet during RF08 of SPICULE. The GV and Learjet penetrated the same cloud within a minute of each other, but at different vertical levels, at ~11k and 23k ft, respectively. Figure 2b shows the estimated ice concentrations during the Learjet cloud pass overlaid on the INP temperature spectra from the filters collected in the BL, and the CFDC measurements on the CVI. Strong agreement is observed between -17 ºC and -20 ºC in the ice concentrations and the number of INPs observed by both the CFDC and from one of the BL filter samples during this particular cloud pass, indicating the likelihood that the aircraft were observing the cloud soon after primary ice nucleation. In contrast, analyses of additional cloud passes during other research flights in SPICULE (not shown) showed disagreement between ice crystal and INP concentrations, suggesting that SIP were active.

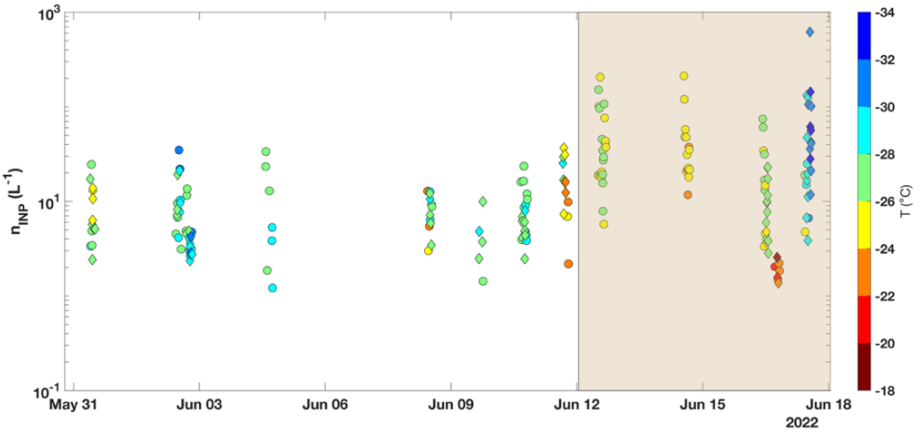

Figure 1. Time series of the number of INPs measured by the CFDC during ESCAPE. The colored markers denote the temperature of the CFDC column during collection, circles indicate sampling on the isokinetic inlet in clear sky conditions, and diamonds indicate sampling on the CVI during cloud passes. The tan shaded region indicates the period during the Saharan dust intrusion into the sampling region.

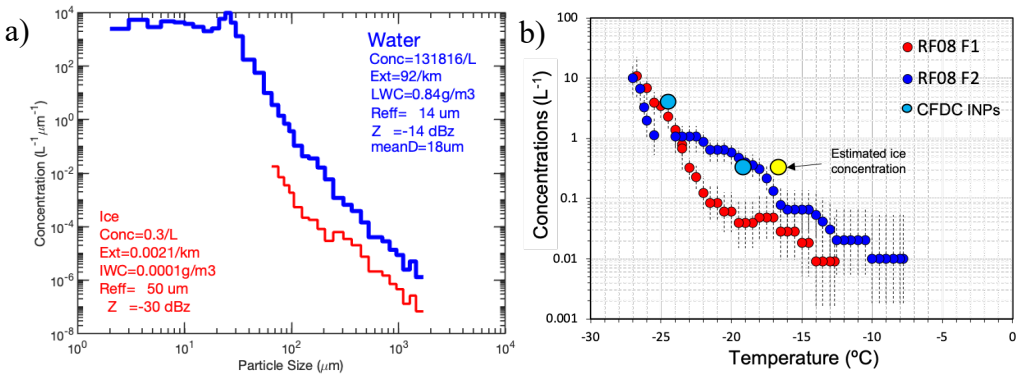

Figure 2. (a) Composite size distributions from the Learjet separated into the liquid (blue line) and ice phase (red line) from a cloud pass during SPICULE RF08 and (b) cumulative INP concentrations as a function of temperature from IS filters 1 and 2 collected in the BL (red and blue markers, respectively) and from the CFDC (light blue markers) during the same SPICULE flight. The estimated ice concentrations from (a) is also shown at the ambient temperature during the Learjet cloud pass, and denoted by the yellow marker.

CONCLUSIONS

This study used both ground-based and airborne observations of INP concentrations and cloud microphysical properties to provide insight into the vertical distributions of INPs and their role in the ice

phase of convective clouds. The wide variability in INP concentrations during both the SPICULE and ESCAPE flight campaigns illustrates the difficulty in constraining and parameterizing INPs in convective environments. Good agreement between ground and airborne INP concentrations showed that for the case presented, INPs appeared to be well mixed in the lower atmosphere and could be readily ingested into convective clouds. The dataset also enabled comparison of ice crystal concentrations in convective clouds to INP concentrations collected in the BL which was used to help elucidate whether and when primary or secondary ice processes were occurring. Modeling of emissions of INPs from their source regions and of their transport to locations where they can nucleate ice in clouds remains a difficult task. The observations from SPICULE and ESCAPE may help play a role in improving the understanding of the distribution of INPs in the lower troposphere and their role in primary and secondary ice processes in numerical simulations, leading to better prediction of precipitation and Earth's radiative balance.

ACKNOWLEDGEMENTS

This work was supported by the US National Science Foundation under grants AGS-1917510 (SPICULE) and AGS-2019947 (ESCAPE). We thank the research and support staff of NCAR EOL and the NRC Convair-580 group for vital assistance in field preparations and conduct of flights. We also knowledge Kevin Barry for his help with filter preparation for both field campaigns.

REFERENCES

Barry, K. R., Hill, T. C. J., Levin, E. J. T., Twohy, C. H., Moore, K. A., Weller, Z. D., et al. (2021). Observations of Ice Nucleating Particles in the Free Troposphere From Western US Wildfires. *Journal of Geophysical Research: Atmospheres*, *126*(3). https://doi.org/10.1029/2020JD033752

DeMott, P. J., Sassen, K., Poellot, M. R., Baumgardner, D., Rogers, D. C., Brooks, S. D., et al. (2003). African dust aerosols as atmospheric ice nuclei. *Geophysical Research Letters*, *30*(14), 26–29. https://doi.org/10.1029/2003GL017410

Field, P. R., Lawson, R. P., Brown, P. R. A., Lloyd, G., Westbrook, C., Moisseev, D., et al. (2017). Chapter 7. Secondary Ice Production - current state of the science and recommendations for the future. *Meteorological Monographs*. https://doi.org/10.1175/amsmonographs-d-16-0014.1

Kanji, Z. A., Ladino, L. A., Wex, H., Boose, Y., Burkert-Kohn, M., Cziczo, D. J., & Krämer, M. (2017). Overview of Ice Nucleating Particles. *Meteorological Monographs*, *58*(1), 1.1-1.33. https://doi.org/10.1175/amsmonographs-d-16-0006.1

Lawson, P., Gurganus, C., Woods, S., & Bruintjes, R. (2017). Aircraft observations of cumulus microphysics ranging from the tropics to midlatitudes: Implications for a "new" secondary ice process. *Journal of the Atmospheric Sciences*, *74*(9), 2899–2920. https://doi.org/10.1175/JAS-D-17-0033.1

Lawson, R. P., Korolev, A. V., DeMott, P. J., Heymsfield, A. J., Bruintjes, R. T., Wolff, C. A., et al. (2022). The Secondary Production of Ice in Cumulus Experiment (SPICULE). *Bulletin of the American Meteorological Society*, *104*(1), E51–E76. https://doi.org/10.1175/bams-d-21-0209.1

Rogers, D. C. (1988). Development of a continuous flow thermal gradient diffusion chamber for ice nucleation studies. *Atmospheric Research*, *22*(2), 149–181. https://doi.org/10.1016/0169-8095(88)90005-1

Twohy, C. H., Schanot, A. J., & Cooper, W. A. (1997). Measurement of condensed water content in liquid and ice clouds using an airborne counterflow virtual impactor. *Journal of Atmospheric and Oceanic Technology*, *14*(1), 197–202. https://doi.org/10.1175/1520-0426(1997)014<0197:MOCWCI>2.0.CO;2

Vali, G., DeMott, P. J., Möhler, O., & Whale, T. F. (2015). Technical Note: A proposal for ice nucleation terminology. *Atmospheric Chemistry and Physics*, *15*(18), 10263–10270. https://doi.org/10.5194/acp-15-10263-2015

CONNECTING COASTAL EMISSIONS TO AEROSOL FORMATION AT THE BALTIC SEA

M. PELTOLA[1], R. THAKUR[1], K. SPENCE[2], J. LAMPILAHTI[1], S. HAAPANALA[3], A. VÄHÄ[1], I. MAMMARELLA[1], J. NORKKO[2], A. NORKKO[2], M. KULMALA[1], and M. EHN[1]

[1]*Institute for Atmospheric and Earth System Research/Physics, University of Helsinki, 00014 Helsinki, Finland.*

[2]*Tvärminne Zoological Station, University of Helsinki, 10900, Hanko, Finland.*
[3]*Suvilumi Ltd., Helsinki, Finland.*

Keywords: AEROSOL FORMATION, MARINE, COASTAL.

INTRODUCTION

Even though marine aerosols can play an important role in regulating the climate, most aerosol measurements are from continental sites. Coastal regions are of particular interest, since they are highly productive and at the same time heavily impacted by human activities. The Baltic Sea is a good example, with a long history of eutrophication and with a complex coastline with high habitat and species diversity. Nevertheless, the role of the Baltic Sea in general and the coastal zones in particular for aerosol formation and thus climate is poorly understood. Earlier work has shown that coastal areas can act as hotspots for new particle formation (NPF) through emissions of iodine species from macroalgae (He et al. 2021; McFiggans et al. 2004). In the Baltic Sea, cyanobacterial blooms have been shown to influence NPF (Thakur et al. 2022) and emissions of greenhouse gases in coastal areas have been shown to be highly variable both seasonally and between habitat types (Roth et al. 2022). Connecting the coastal emissions to aerosol formation is therefore of importance for understanding and for mitigating climate change.

The recently founded Centre for Coastal Ecosystem and Climate Change Research (CoastClim) connects expertise in atmospheric sciences, marine biogeochemistry and marine ecology to understand how the state of the Baltic Sea is connected to the climate. Part of this effort is focused on understanding how emissions of different chemical species from the sea surface influence aerosol formation and thus the climate. To achieve this, we have established extensive aerosol and air chemistry measurements at the southern coast of Finland. Here, we present first results from these measurements with a focus on aerosol formation, compare the data to similar data from the Hyytiälä Forestry Station in southern Finland and connect it to marine biological processes by investigating the relationship between the smallest negative ions and CO_2 fluxes.

METHODS

Permanent atmospheric measurements were started at Tvärminne Zoological Station, on the southern coast of Finland in 2022 (Fig. 1). So far we have installed a Neutral Air cluster and Ion Spectrometer (NAIS, S. Mirme and A. Mirme 2013) and a Particle Size Magnifier (PSM, Vanhanen et al. 2011) to study the smallest aerosols and during 2023 we will install a Differential Mobility Particle Size (DMPS) and an Aerodynamic Particle Sizer (APS) to extend the aerosol size distribution measurements up to 20 μm. In addition to aerosol measurements, we are conducting comprehensive measurements on air chemistry to understand the chemical precursors of aerosol particles and the connection of these precursors to the state of the Baltic Sea. To study the chemical composition of

molecular clusters that can form aerosols, we use an Atmospheric pressure interface time of flight mass spectrometer (APi-TOF) with a Multi-scheme chemical ionization inlet (MION, Rissanen et al. 2019) using both nitrate and bromide ionisation as well as measuring ambient anions. Additionally, in summer 2022 we performed a campaign with a Vocus PTR-TOF mass spectrometer (Krechmer et al. 2018) to study the volatile organic compounds emitted from the sea. In addition to these instruments, our measurements include basic trace gases (CO, O_3, SO_2, NO, NO_2), CO_2 fluxes measured using eddy covariance and basic seawater properties such as salinity, temperature, pH, chlorophyll-a and coloured dissolved organic matter. With these comprehensive measurements and supporting campaigns, involving characterization of biodiversity, we aim to understand how the Baltic Sea will interact with the climate.

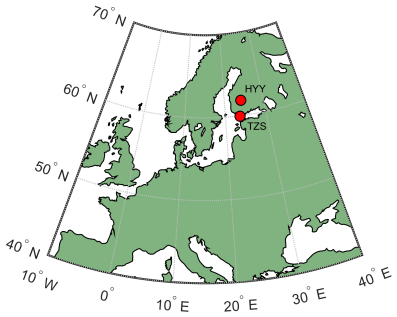

Figure 1: Map of the locations of the Tvärminne Zoological Station (TZS) and the Hyytiälä Forestry station (HYY).

To obtain a first impression of the importance of aerosol formation at Tvärminne and to understand how the coastal environment differs from the boreal forest, first we focus on the NAIS data and compare it to NAIS measurements from the Hyytiälä Forestry station, located 235 km northeast from Tvärminne (see Fig. 1). For this we use data measured between 25.2.-11.4.2022 and 31.5.-8.10.2022 from both stations and focus on NPF events. To understand the origins of the events, we used 72 h air mass back trajectories from the HYSPLIT model (Rolph et al. 2017; Stein et al. 2015). Furthermore, we study the differences in concentrations of small ambient ions over land and over the sea and connect these ions to biological activity in the sea using CO_2 fluxes.

RESULTS AND DISCUSSION

During the time when NAIS data is available for Tvärminne, we observed NPF events on 9.9% of the days for Tvärminne and 8.7% of the days for Hyytiälä. Even though the event frequencies are similar, only one third of the events occur on the same days at both stations. Figure 2 shows particle size distributions for one of the days when a clear NPF event was observed at both stations. During this day, the air mass back trajectories had crossed first over the Baltic Sea from the west and then over Southern Finland. This means that these events occurred likely over land. Future work will look deeper into the events observed at Tvärminne and focus on coastal air masses.

Comparing concentrations of ions and particles in different size ranges at the two stations showed that the differences in concentrations between Hyytiälä and Tvärminne were smaller than differences between two different instruments in Hyytiälä, so no definitive conclusions of the comparison could be made yet. On the other hand, comparing the concentrations of negative ions in different size ranges in Tvärminne when the wind direction was either from land ($> 250°$ or < 90 °) or from the sea (90-250°) showed interesting results. In size ranges <2 nm, 2-3 nm and 2-4 nm, negative ion concentrations were statistically significantly higher in coastal air compared to continental air

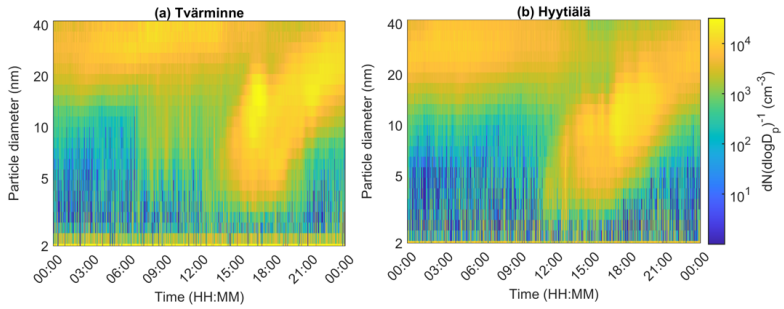

Figure 2: An example of particle size distributions measured in a) Tvärminne and b) Hyytiälä on 3 March 2022 .

where as for larger 3-6 nm negative ions no significant difference was observed (Fig. 3). The difference was largest for the sub-2 nm range, which had 20% higher ion concentrations in coastal air compared to continental air.

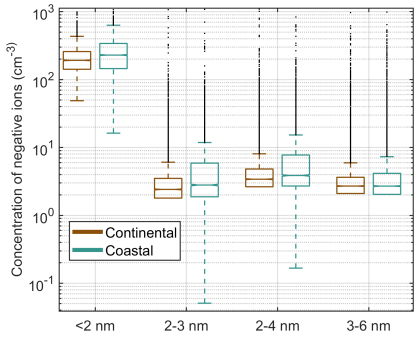

Figure 3: Concentrations of negative ions in different size ranges when the winds are coastal or crossing over land. The boxes show the medians and 25th and 75th percentiles.

To further understand how aerosol formation is connected to biological processes at the coast, we compared concentrations of the smallest negative ions to CO_2 fluxes. Here we used data from March 2022 to January 2023. This work showed that in coastal air there is a weak positive correlation between the CO_2 flux and sub 2 nm ions (Spearman correlation coefficient 0.2, $p << 0.01$). This could indicate that when the Baltic Sea is emitting CO_2 it is also emitting other gases that act as aerosol precursors. No similar positive correlations were observed in the larger size ranges or in continental air.

Our future work will aim to identify the composition of these ions by using MION data. This way we could understand what chemical species the biological processes in the Baltic sea are emitting and how this connects to aerosol formation. We will also use air mass back trajectories to quantify the time that the air mass has spent around the coast before reaching the station to make our analysis more quantitative.

CONCLUSIONS

A new permanent atmospheric measurement station has been set up at the Tvärminne Zoological station at the Baltic Sea coast as a part of the CoastClim project. With these measurements we aim to understand how the Baltic Sea and its ecosystem state can interact with climate. The preliminary results show that aerosol concentrations at the station are similar to those observed

at the Hyytiälä Forestry Station and new particle formation frequencies at the two stations are similar. We also showed that air coming from the sea has higher concentrations of sub-4 nm ions and that sub-2 nm ions have a positive correlation with CO_2 fluxes over the sea, indicating a possible marine source for these ions. Our future work will investigate the effect of coastal sources on aerosol formation and its chemical precursors.

ACKNOWLEDGEMENTS

This work was funded by Jane and Aatos Erkko Foundation, Ella and Georg Ehrnrooth Foundation and Academy of Finland flagship ACCC (337549) The authors gratefully acknowledge the NOAA Air Resources Laboratory (ARL) for the provision of the HYSPLIT transport and dispersion model and READY website (https://www.ready.noaa.gov) used in this publication.

REFERENCES

He, X.-C., Tham, Y. J., Dada, L., Wang, M., Finkenzeller, H., Stolzenburg, D., Iyer, S., Simon, M., Kürten, A., Shen, J., et al. (2021). Role of iodine oxoacids in atmospheric aerosol nucleation. *Science*, *371*(6529), 589–595.

Krechmer, J., Lopez-Hilfiker, F., Koss, A., Hutterli, M., Stoermer, C., Deming, B., Kimmel, J., Warneke, C., Holzinger, R., Jayne, J., et al. (2018). Evaluation of a new reagent-ion source and focusing ion–molecule reactor for use in proton-transfer-reaction mass spectrometry. *Analytical Chemistry*, *90*(20), 12011–12018.

McFiggans, G., Coe, H., Burgess, R., Allan, J., Cubison, M., Alfarra, M. R., Saunders, R., Saiz-Lopez, A., Plane, J., Wevill, D., et al. (2004). Direct evidence for coastal iodine particles from laminaria macroalgae–linkage to emissions of molecular iodine. *Atmospheric Chemistry and Physics*, *4*(3), 701–713.

Mirme, S., & Mirme, A. (2013). The mathematical principles and design of the nais-a spectrometer for the measurement of cluster ion and nanometer aerosol size distributions. *Atmospheric Measurement Techniques*, *6*(4), 1061.

Rissanen, M. P., Mikkilä, J., Iyer, S., & Hakala, J. (2019). Multi-scheme chemical ionization inlet (mion) for fast switching of reagent ion chemistry in atmospheric pressure chemical ionization mass spectrometry (cims) applications. *Atmospheric Measurement Techniques Discussions*, *2019*, 1–11. https://doi.org/10.5194/amt-2019-159

Rolph, G., Stein, A., & Stunder, B. (2017). Real-time environmental applications and display system: Ready. *Environmental Modelling & Software*, *95*, 210–228.

Roth, F., Sun, X., Geibel, M. C., Prytherch, J., Brüchert, V., Bonaglia, S., Broman, E., Nascimento, F., Norkko, A., & Humborg, C. (2022). High spatiotemporal variability of methane concentrations challenges estimates of emissions across vegetated coastal ecosystems. *Global Change Biology*, *28*(14), 4308–4322.

Stein, A., Draxler, R. R., Rolph, G. D., Stunder, B. J., Cohen, M., & Ngan, F. (2015). Noaa's hysplit atmospheric transport and dispersion modeling system. *Bulletin of the American Meteorological Society*, *96*(12), 2059–2077.

Thakur, R. C., Dada, L., Beck, L. J., Quéléver, L. L. J., Chan, T., Marbouti, M., He, X.-C., Xavier, C., Sulo, J., Lampilahti, J., Lampimäki, M., Tham, Y. J., Sarnela, N., Lehtipalo, K., Norkko, A., Kulmala, M., Sipilä, M., & Jokinen, T. (2022). An evaluation of new particle formation events in helsinki during a baltic sea cyanobacterial summer bloom. *Atmospheric Chemistry and Physics*, *22*(9), 6365–6391. https://doi.org/10.5194/acp-22-6365-2022

Vanhanen, J., Mikkilä, J., Lehtipalo, K., Sipilä, M., Manninen, H., Siivola, E., Petäjä, T., & Kulmala, M. (2011). Particle size magnifier for nano-cn detection. *Aerosol Science and Technology*, *45*(4), 533–542.

OBSERVATIONS OF CONTINENTAL-SCALE BIOSPHERE – ATMOSPHERE INTERACTIONS IN BOREAL ENVIRONMENT

T. PETÄJÄ[1], E. EZHOVA[1], M. RÄTY[1], D. MOISSEEV[1], V.-M. KERMINEN[1], J. BÄCK[2], H. KOKKOLA[3], T. MIELONEN[3], T. YLI-JUUTI[3], A. VIRTANEN[3] and M. KULMALA[1]

[1]Institute for Atmospheric and Earth System Research / Physics, Faculty of Science, University of Helsinki, Helsinki, 00560, Finland

[2]Institute for Atmospheric and Earth System Research / Forest Sciences, Faculty of Agriculture and Forestry, University of Helsinki, Helsinki, 00560, Finland

[3]Department of Technical Physics, University of Eastern Finland, Kuopio, 70211, Finland

Keywords: atmosphere-biosphere interactions, feedbacks, atmospheric aerosol particles, biogenic volatile organic compounds, clouds, precipitation

INTRODUCTION

Biogenic emissions of volatile organic compounds facilitate aerosol formation and growth in the boreal environment. This phenomenon is regional, and with ground-based observations the formed aerosols are observed to reach sizes where they are large enough to contribute to Cloud Condensation Nuclei (CCN) concentrations (Kerminen et al. 2012). At the same time, evapotranspiration from the land and biosphere increases the amount of water vapour available for formation of clouds and precipitation. While these processes are typically driven by meteorological conditions and synoptic weather systems, it is plausible that the biogenic secondary aerosols can affect cloud droplet formation in a critical manner if they are transported into the cloud layer.

The boreal forest provides an ideal locale to study biosphere-atmosphere interactions, aerosol and cloud microphysical processes in a biogenically dominated environment. The key infrastructure is Station for Measuring Ecosystem – Atmosphere Relations, SMEAR II (Hari and Kulmala, 2005) in Hyytiälä, Finland, where biosphere-aerosol-cloud-climate research has been conducted during the last twenty years. The existing work has identified a connection between the aerosol particles formed from the gaseous precursors (Kulmala et al. 2013) and their subsequent growth to CCN sizes (Kerminen et al. 2012), as observed at the ground level. Tunved et al. (2006) showed that the long-term data from a fixed measurement site in a boreal environment can be represented in such a way that each measured data point represents a certain exposure time to biogenic emissions during transport to the observation site. In practice, for SMEAR II this can be simplified to a residence time over land because the surrounding terrestrial region is dominated by the boreal forest. In this work, we summarize recent findings connecting biosphere-atmosphere interactions and aerosol-cloud-precipitation interactions in the boreal environment.

RESULTS AND DISCUSSION

Biogenic Aerosols – Effects on Clouds and Climate (BAECC, Petäjä et al. 2016) was an intensive eight-month campaign in Hyytiälä, Finland. It provided unique ground-based remote sensing data to explore aerosol-cloud interactions. We applied the time-over-land concept to this data set. In the analysis we concentrated on clean, Arctic air masses arriving to Hyytiälä predominantly from North-West direction, where the influence of anthropogenic sources was minimal. Petäjä et al. 2022 showed that there was a clear difference in physical, chemical, and optical character of aerosol particles at the surface, when comparing fast and slow moving airmasses, which were exposed short or extended times, respectively, to biogenic

emissions from the boreal forest. With the aid of ground-based remote sensing, we were able to confirm that the influence of time-over-land difference was visible in the aerosol population not only at the surface level but throughout the boundary layer. Furthermore, we expanded the analysis to the properties of clouds with radars. In order to differentiate the meteorological impacts to cloud properties, we studied only non-precipitating liquid clouds. We showed that these clouds in the slow-moving air masses tended to have higher cloud droplet number concentrations than in the fast moving air masses. For the first time, Petäjä et al. (2022) was able to show with observations that the newly formed secondary organic aerosol particles in fact influenced the cloud properties in the boreal environment.

We expanded the analysis with long-term observational data available from the SMEAR II station. Räty et al. (2022) utilized more than ten years of data from the site and applied the time-over-land concept to the data set. The results confirmed the differences between the rapid and slow air masses in their aerosol characteristics. Furthermore, we were able to show that also the precipitation intensity was influenced by the biosphere-atmosphere interactions.

The work of Yli-Juuti et al. (2021) explored the role of warming climate to aerosol-cloud interactions. Their results showed that the warmer summers typically had larger organic aerosol mass concentrations and the satellite-derived cloud albedo was higher than the values obtained during cooler summers. Putting this into perspective, the warmer summers are a proxy for the future conditions in the boreal environment. Therefore, the warmer climate seems to lead to higher biogenic volatile organic emissions, organic aerosol mass concentrations, and consequently higher cloud condensation nuclei concentrations. This will decrease the cloud effective radius while the clouds tend to be thicker. Overall, the satellite-derived data indicates higher cloud albedo as the function of warming. Such cooling feedback could help to slow down climate change.

As a summary, biospheric emissions of volatile organic compounds and their atmospheric processing first to condensable vapors and then to new aerosol particles is a relevant feature contributing to the properties of clouds and likely also spatial variability of precipitation on a continental scale. It is crucial to maintain the comprehensive observational capacity (in-situ, ground-based and satellite-borne remote sensing) in order to better understand the feedbacks and interactions on a continental scale. The historical data will provide benchmarking opportunities for the new data. Overall, the combination will be critical in assessing the impact of climate change to the emissions, aerosols and clouds.

ACKNOWLEDGEMENTS

Financial support through Academy of Finland Flagship Atmosphere and Climate Competence Center (ACCC), through projects 337549, 337550, 334792 and 325681.

REFERENCES

Hari, P. and Kulmala, M. (2005) Station for Measuring Ecosystem – Atmosphere Relations (SMEAR II), *Boreal Environ. Res.,* 10, 315-322.

Kerminen, V.-M., Paramonov, M., Anttila, T., Riipinen, I., Fountoukis, C., Korhonen, H., Asmi, E., Laakso, L., Lihavainen, H., Swietlicki, E., Svenningsson, B., Asmi, A., Pandis, S.N., Kulmala, M. and Petäjä, T. (2012) Cloud condensation nuclei production associated with atmospheric nucleation: a synthesis based on existing literature and new results, *Atmos. Chem. Phys.*, 12, 12037-12059.

Kulmala, M., Kontkanen, J., Junninen, H., Lehtipalo, K., Manninen, H.E., Nieminen, T., Petäjä, T., Sipilä, M., Schobesberger, S., Rantala, P., Franchin, A., Jokinen, T., Järvinen, E., Äijälä, M., Kangasluoma, J., Hakala, J., Aalto, P.P., Paasonen, P., Mikkilä, J., Vanhanen, J., Aalto, J., Hakola, H., Makkonen, U., Ruuskanen, T.M., Mauldin III, R.L., Duplissy, J., Vehkamäki, H., Bäck, J., Kortelainen, A., Riipinen, I., Kurtén, T., Johnston, M.V., Smith, J.N., Ehn, M., Mentel,

T.F., Lehtinen, K.E.J., Laaksonen, A., Kerminen, V.-M. and Worsnop, D.R. (2013) Direct observations of atmospheric nucleation, *Science,* 339, 943-946, doi:10.1126/science.1227385.

Petäjä, T., O'Connor, E.J., Moisseev, D., Sinclair, V.A., Manninen, A.J., Väänänen, R., von Lerber, A., Thornton, J.A., Nicoll, K., Petersen, W., Chandrasekar, V., Smith, J.N., Winkler, P.M., Krüger, O., Hakola, H., Timonen, H., Brus, D., Laurila, T., Asmi, E., Riekkola, M.-L., Mona, L., Massoli, P., Engelmann, R., Komppula, M., Wang, J., Kuang, C., Bäck, J., Virtanen, A., Levula, J., Ritsche, M. and Hickmon, N. (2016) BAECC, A field campaign to elucidate the impact of Biogenic Aerosols on Clouds and Climate, *Bull. Am. Met. Soc,.* 97, 1909-1928, https://doi.org/10.1175/BAMS-D-14-00199.1

Petäjä, T., Tabakova, K., Manninen, A., Ezhova, E., O'Connor, E., Moisseev, D., Sinclair, V.A., Backman, J., Levula, J., Luoma, K., Virkkula, A., Paramonov, M., Räty, M., Äijälä, M., Heikkinen, L., Ehn, M., Sipilä, M., Yli-Juuti, T., Virtanen, A., Ritsche, M., Hickmon, N., Pulik, G., Rosenfeld, D., Worsnop, D.R., Bäck, J., Kulmala, M. and Kerminen, V.-M. (2022) Influence of biogenic emissions from boreal forests on aerosol–cloud interactions, *Nature Geosci.* 15, 42-47, doi.org/10.1038/s41561-021-00876-0.

Räty, M., Sogacheva, L., Keskinen, H.-M., Kerminen, V.-M., Petäjä, T., Ezhova, E. and Kulmala, M. (2022) Transformation of marine air mass in the Fennoscandian Boreal forest – changes in aerosol, humidity, and clouds, *Atmos. Chem. Phys. Discuss.,* https://doi.org/10.5194/acp-2022-264.

Tunved, P., Hansson, H.-C., Kerminen, V.-M., Ström, J., Dal Maso, M., Lihavainen, H., Viisanen, Y., Aalto, P.P., Komppula, M. and Kulmala, M. (2006). High natural aerosol loading over boreal forests. *Science,* 312, 261–263.

Yli-Juuti, T., Mielonen, T., Heikkinen, L., Arola, A., Ehn, M., Isokääntä, S., Keskinen, H.M., Kulmala, M., Laakso, A., Lipponen, A., Luoma, K., Mikkonen, S., Nieminen, T., Paasonen, P., Petäjä, T., Romakkaniemi, S., Tonttila, J., Kokkola, H. And Virtanen, A. (2021) Significance of the organic aerosol driven climate feedback in the boreal area, *Nature Comm.* 12, 5637.

ON THE EVOLUTION OF AEROSOL PROPERTIES IN BIOMASS BURNING PLUMES

J.R. PIERCE[1]

[1]Department of Atmospheric Science, Colorado State University, Fort Collins, Colorado, 80521, United States

Keywords: Aerosols, biomass burning, smoke, climate.

**Invited keynote lecture*

Open biomass burning, such as wild and prescribed fires, is a significant source of aerosols to the atmosphere, greatly influencing both climate and human health. These biomass burning particles evolve in both size and composition within the smoke plumes, affecting the particles' abilities to act as cloud condensation nuclei, interact with radiation, and impact climate. However, this particle evolution differs between fires, being strongly influenced by aerosol mass concentrations in the plumes. Aerosol mass concentrations in a plume of a small fire (think agricultural field) will dilute to <1 $\mu g\, m^{-3}$ in seconds or minutes due to the short dilution length scale. On the other hand, the PM in large wildfires may remain >100 $\mu g\, m^{-3}$ or even >1000 $\mu g\, m^{-3}$ for hours or days. How does this wide range of concentrations influence the aerosol chemical and physical processes, and how does it affect the evolving size distribution?

In this talk, I will show recent results that use measurement from recent biomass burning field campaigns (FIREX-AQ, WE-CAN, BBOP) with plume and 3D models to understand the roles of fire size, initial concentrations, and dilution rates on the evolution of biomass burning aerosol size and composition. Particles in plumes that maintain high concentrations (high initial concentration with slow dilution) grow to larger sizes but are less oxidized than particles in dilute plumes. I will also show how accounting the concentration/dilution-controlled evolution in climate models can greatly change the estimated aerosol direct and indirect effects of biomass burning aerosol.

THE EFFECT OF SECONDAY ORGANIC AEROSOL FORMATION PATHWAYS ON CLIMATE AND HUMAN HEALTH

L. QI[1], K. Y. CHEUNG[1], C. P. LEE[1], D. Y. WANG[1], Z. Y. LI[2], W. K. RAN[2], Y. F. HAO[1], G. CHEN[1], W. Q. XU[3], Q. Q. WANG[3], Y. L. GE[4], Q. CHEN[4], T. Q. CUI[1], K. LI[1], Y. M. HAN[2], Q. Y. WANG[2], Z.F. WANG[3], Y. L. SUN[3], U. BALTENSPERGER[1], R. L. MODINI1, E. I. IMAD[1], J. J. CAO[2,3], A. S. H. PREVOT[1] & J. G. SLOWIK[1]

[1]Laboratory of Atmospheric Chemistry, Paul Scherrer Institute, 5232 Villigen PSI, Switzerland.
[2]Key Laboratory of Aerosol Chemistry and Physics, Institute of Earth Environment, Chinese Academy of Sciences, Xi'an, 710061, China.
[3]Key Laboratory of Atmospheric Boundary Layer Physics and Atmospheric Chemistry, Institute of Atmospheric Physics, Chinese Academy of Sciences, Beijing, 100029, China.
[4]State Key Joint Laboratory of Environmental Simulation and Pollution Control, College of Environmental Sciences and Engineering, Peking University, Beijing 100871, China.

Keywords: SOA sources, formation pathways, AqSOA, aerosol health effect.

INTRODUCTION

Atmospheric aerosols significantly affect visibility, air quality and climate. Exposure to atmospheric aerosols has been associated with increased cardiopulmonary mortality and morbidity(Pye et al., 2021; Daellenbach et al., 2020). Directly emitted hydrocarbon components are referred to as primary organic aerosol (POA) and secondary organic aerosols (SOA) can be formed via gas-phase reactions and the subsequent condensation of semi-volatile vapour, as well as by multiphase and heterogeneous processes.

SOA accounts for as much as 50 – 90 % of the total organic aerosol (OA) burden and has recently received much attention. Moreover, SOA also contributes importantly to the Earth's radiation balance through its absorption and scattering of solar radiation and by altering cloud microphysical properties since it contains not only colorless carbon, which merely scatters light, but also colored carbon, which can absorb light(Pani et al., 2021).

However, the quantification of SOA sources and/or pathways and the climatic effect of SOA are more challenging mostly due to poor understanding and measurement of the SOA species, consisting of thousands of multifunctional, oxygenated species to a highly varing degree and including high molecular weight species and oligomers. Limitations in SOA source apportionment are tied directly to limitations of the measuring instruments nowadays around the world, which either involve thermal decomposition, or have low time and mass resolution. In consequence, the exact SOA sources and PM chemical composition along with its mass concentrations at molecular level for predicting the overall health impacts associated with aerosol exposure remain unknown at present.

In the present study, we use field observations to derive the brown carbon optical properties and OP parameters impacted by SOA sources. We demonstrate that the SOA contributions to BrC and OP are both considerable and strongly source-dependent. These results highlight the urgent need for source-based treatments of SOA in addressing aerosol impacts on climate and human health.

METHODS

Measurements were performed from 26 January to 20 February 2021 (covered the Chinese New Year, CNY) at the Tower Site of the Institute of Atmospheric Physics (IAP). The site is located between the

third ring and the forth ring roads in northern Beijing, surrounded by residential infrastructure and is characterized as an urban background site.

Here we utilize the recently developed extractive electrospray ionization (EESI) inlet, coupled to both high-resolution time-of-flight and ultra-high resolution orbitrap mass spectrometries (EESI-LTOF and EESI-Orbitrap, respectively), to elucidate wintertime SOA sources/pathways in Beijing, China. EESI-based instruments provide highly time-resolved measurements of organic molecules without thermal decomposition, overcoming the measurement based obstacles described above. Combined with co-located aerosol mass spectrometer (AMS) measurements and advanced source apportionment techniques, this allows identification and quantification of key SOA (and other OA) sources and processes.

RESULTS AND DISCUSSION

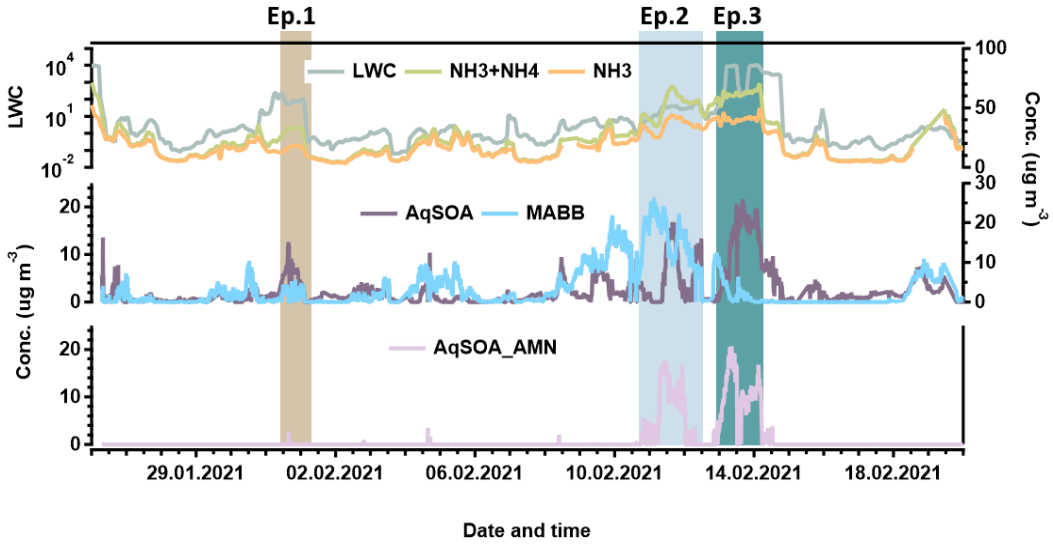

Figure 1. Time series of chemical species (NH_4^+-, NH_3), liquid water content (LWC), AqSOA chemistry, AqSOA_AMN chemistry and MABB pathways.

The measurement period includes three high pollution episode (denoted Ep. 1, Ep. 2, and Ep. 3; see Fig. 1), featuring strong contributions of secondary aerosol, with SOA comprising ~80% of OA in all events. Traditional source apportionment analysis utilizing only an aerosol mass spectrometer (AMS) would suggest these events to be similar. However, we here combine with measurements by an extractive electrospray ionization mass spectrometer (EESI-MS), which greatly improves the chemical resolution at molecular level, enabling identification of specific sources and processes.

The EESI-MS-based SOA source apportionment reveals that the three high pollution events are in fact quite dissimilar. This is summarized in Fig. 1, which shows the time series of three key factors resolved from source apportionment, together with supporting data. These factors include aged biomass burning (MABB), a factor related to aqueous-phase SOA production characterized by small, highly oxygenated molecules (AqSOA), and a second aqueous-derived factor with enhanced concentrations of N-containing molecules consistent with imidazoles (AqSOA_AMN). The different temporal behaviour of these factors largely defines the differences in the pollution episodes. Specifically, Ep. 1 is driven by a mix of aqueous-phase oxidation and aged biomass burning emissions, Ep. 2 is dominated by aged biomass burning, and Ep. 3 is driven by aqueous chemistry influenced by high levels of particulate ammonium and gaseous ammonia. As shown in Fig. 1, AqSOA correlates with aerosol liquid water content (LWC), whereas AqSOA_AMN is related to both LWC and high concentrations of particle-phase NH_4^+, gaseous NH_3, or

both. This is consistent with imidazole formation, which can occur from aqueous reactions of glyoxal in the presence of NH_4^+-containing seed.

SOA source apportionment results were analysed in conjunction with online measurements of brown carbon and dithiothreitol-based oxidation potential (OP^{DTT}). The MLR analysis of the SOA source results against BrC suggest that AqSOA-AMN is strongly light absorbing, consistent with products such as imidazoles. Indeed, the aged biomass burning-driven Ep. 2 and the NH_3/NH_4^+- mediated Ep. 3 show similar contributions to BrC, while Ep. 1 is much lower. Ep. 3 also exhibits far higher OP than either Ep. 1 or Ep. 2, both in terms of total OP and on a per mass basis. This highlights the implications of NH_3/NH_4^+-mediated aqueous chemistry for climate and health.

CONCLUSIONS

We find that the differences in SOA composition and production pathways between these high pollution events considerably alter the associated radiative impacts and health risks. More generally, our results highlight the shortcomings of treating SOA as a bulk or non-source-specific quantity. Determining the sources and pathways drives the effects of OA on climate and health. This highlights the need for source-specific treatments of SOA in air quality studies and policy design.

ACKNOWLEDGEMENTS

This work was supported by the Sino-Swiss cooperation on the Clean Air China program funded by Swiss DEZA under grand 7F-09802.01.03.

REFERENCES

Daellenbach, K. R., Uzu, G., Jiang, J., Cassagnes, L. E., Leni, Z., Vlachou, A., Stefenelli, G., Canonaco, F., Weber, S., Segers, A., Kuenen, J. J. P., Schaap, M., Favez, O., Albinet, A., Aksoyoglu, S., Dommen, J., Baltensperger, U., Geiser, M., El Haddad, I., Jaffrezo, J. L., and Prevot, A. S. H.: Sources of particulate-matter air pollution and its oxidative potential in Europe, Nature, 587, 414-419, 10.1038/s41586-020-2902-8, 2020.

Pani, S. K., Lin, N. H., Griffith, S. M., Chantara, S., Lee, C. T., Thepnuan, D., and Tsai, Y. I.: Brown carbon light absorption over an urban environment in northern peninsular Southeast Asia, Environ Pollut, 276, 116735, 10.1016/j.envpol.2021.116735, 2021.

Pye, H. O. T., Ward-Caviness, C. K., Murphy, B. N., Appel, K. W., and Seltzer, K. M.: Secondary organic aerosol association with cardiorespiratory disease mortality in the United States, Nat Commun, 12, 7215, 10.1038/s41467-021-27484-1, 2021.

SECONDARY AEROSOLS AT MARAMBIO STATION:

FROM GASES TO CLOUD CONDENSATION NUCLEI

L. L. J. QUÉLÉVER[1], M. BOYER[1], Z. BRASSEUR[1], A-K GOßMANN[2], S. SOFIEVA[3], G. MARINCOVICH[4], L. BARREIRA[3], M. AURELA[3], D. WORSNOP[4], E. ASMI[3] and M. SIPILÄ[1]

[1] Institute for Atmospheric and Earth System Research / INAR-Physics, P.O. Box 64, FI-00014 University of Helsinki, Finland.
[2] Palas GmbH, Technische Universität Darmstadt, Greschbachstraße 3B, 76229 Karlsruhe, Germany.
[3] Finnish Meteorological Institute / FMI, Erik Palmenin aukio 1, FI-00560 Helsinki, Finland.
[4] Servicio Meteorológico Nacional / SMN, Av. Dorrego, 4019, Buenos Aires, Argentina.
[5]Aerodyn Research Inc., Billerica, MA 01821, USA.

Keywords: Marambio, Antarctic Peninsula, New Particle Formation, Aerosol Particles, Precursor gases.

INTRODUCTION

Secondary particles contribute significantly to the cloud condensation nuclei (CCN) budget and therefore can impact the climate. Many chemical processes can be involved in new particle formation (NPF), and they depend on gases that are either emitted locally or transported. Antarctica remains the most pristine place on Earth due to the lack of direct anthropogenic emissions which make it the best place to study atmospheric processes that occurred before the industrial era. The Marambio station (64°14'S, 56°37'W) is located North of the Antarctic Peninsula and is characterized (1) the absence human activity - else than the station maintenance, (2) the total lack of land vegetation, (3) the influence of the marine ecosystem surrounding the island – either from the Southern Ocean or from the Weddell Sea. Herein, we are presenting our imminent measurement campaign on aerosol and their gas precursors from Dec. 2022 to ~Apr. 2023 at the Marambio station. This campaign occurring along the austral summer highlights the different synoptic and chemical processes occurring with the ice state, the bird-breading season, and the blooming ocean.

METHODS

Supported by pernanent measurement of aerosol size distribution (Differential Mobility Particle Sizer – DMPS, University of Helsinki and Neutral Cluster and Air Ion Spectrometer – NAIS, Airel Ltd.), meteorological parameters, and collections of particles onto filters for offline chemical composition characterisation, this season deployment targets multiscale processes from (1) NPF-precursor identification, (2) chemical characterisation of the aerosol phase, (3) cloud droplets and the CCN evaluation and (4) ice nucleation particles (INP) quantification.

Specifically for the gas phase, a multi-scheme ionization (MION, Kärsä Oy.) atmospheric pressure interface time of flight (APi-TOF, Tofwerk) mass spectrometer will be set to measure precursor gases such as sulfuric acid, methane sulfonic acid, iodic acid or possibly highly oxygenated organic compounds and ammonia concentration will be measured with a quantum cascade tuneable infrared laser differential absorption spectrometer (QC-TILDAS, Aerodyne Inc.). Additionally, the chemical composition of the particle will be characterized with an aerosol chemical speciation monitor (ASCM, Aerodyne Inc.). The potential CCN will be estimated with a cloud condensation nuclei counter (CCN-100, Droplet Measurement Technologies) with several supersaturation ratio while the quantification of INP will be determined using cold stage analysis particles collected on filters. The cloud droplet number size distribution in the cloudy atmosphere will be measured online with a cloud droplet analyser (CDA, Palas GmbH).

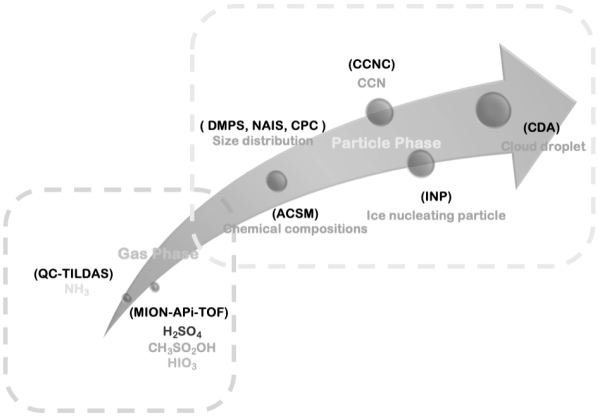

Figure 1. Instrument deployment at Marambio station for the Austral summer campaign 2022-2023. The instrumentation will cover multi-phase processes from new particle formation to cloud droplet stage, including the detection precursor vapours, atmospheric clusters, aerosol particle up to CCN sizes.

CONCLUSION

We aim to present this on-going work that promises an irrefutable assessment of NPF mechanism in the Antarctic peninsula region that would complete the previous work done by Quéléver et al. (2022) and Brean et al. (2021) who concluded on a significant role of amine and ammonia - that will now be quantified. Beside a comparison with Quéléver et al. (2022) on NPF mechanistic in the same place and same season, this deployment period extends to the melting onset and terminates after the refreezing possibly catching additional processes that can trigger new NPF (e.g., Sipilä et al 2016). Finally, with measurement of the aerosol size distribution up to CCN sizes, we assess the significance of the secondary aerosol particles to climate where even small changes in particle population can result in significant climate impact for clouds and the cryosphere.

ACKNOWLEDGEMENTS

This work was supported by the Academy of Finland (project no 335844 - Antarctic Climate Forcing Aerosol- ACFA, and Flagship funding no 337552), and the European Research Council (ERC-GASPACON). We are grateful for the collaboration of the Servicio Meteorológico Nacional – SMN, Fuerza Aerea Argentina – FAA and the FINNish Antarctic Research Program – FINNARP.

REFERENCES

Brean et al. (2021): Open Ocean and coastal new particle formation from sulfuric acid and amines around the Antarctic Peninsula. *Nat. GeoSci., 14, 383-388, 2021.*

Quéléver et al. (2022): Investigation of new particle formation mechanisms and aerosol processes at Marambio station, Antarctic Peninsula. *Atmos. Chem. Phys., 22, 8417-8437, 2022.*

Sipilä et al. (2016): Molecular -scale evidence of aerosol particle formation via sequential addition of HIO3. *Nature, 537, 532-534, 2016*

FREE ENERGY OF CRITICAL DROPLETS – FROM THE BINODAL TO THE SPINODAL

A. AASEN[1], Ø. WILHELMSEN[1,2], M. HAMMER[1,2], and D. REGUERA[3,4]

[1] *SINTEF Energy Research, NO-7465 Trondheim, Norway.*

[2] *Norwegian University of Science and Technology, Department of Chemistry, NO-7491 Trondheim, Norway.*

[3] *Departament de Física de la Matèria Condensada, Universitat de Barcelona, Martí i Franquès 1, 08028 Barcelona, Spain.*

[4] *Universitat de Barcelona Institute of Complex Systems (UBICS), Martí i Franquès 1, 08028 Barcelona, Spain.*

Keywords: Classical Nucleation Theory, Umbrella Sampling simulations, Tolman length, Scaling relations.

INTRODUCTION

Arguably, the main challenge of nucleation theory is to accurately evaluate the work of formation of the critical embryo of the new phase. Since the nucleation rate depends exponentially on this quantity, a small error will cause the predicted nucleation rate to deviate by orders of magnitude from experimental results or simulations. In Classical Nucleation Theory (CNT) this work of formation is estimated using the capillarity approximation, which relies on the value of the planar surface tension. For pure fluids, CNT is qualitatively correct. However, it does not account for the expected vanishing of the nucleation barrier at the spinodal, and the predicted rates show systematic deviations from experiments, with errors reaching 20 orders of magnitude for the simple case of argon condensation (Iland *et al.*, 2007).

The capillary approximation has been blamed for the large discrepancies between predictions from CNT and experiments. Thus, the incorporation of curvature corrections to the surface tension seems one of the most promising routes to solve the problems of CNT. The second order curvature expansion of the surface tension in terms of the curvature $1/R$

$$\gamma(R) = \gamma_0 - 2\gamma_0\delta/R + k_s/R^2 \tag{1}$$

is called the Helfrich expansion, where the coefficients of the first- and second-order corrections are given by the Tolman length δ and the rigidity constant k_s, respectively.

Recently, it was shown how the Tolman length and rigidity constants can be calculated by using Density Gradient Theory (DGT) (Wilhelmsen *et al.*, 2015; Wilhelmsen *et al.*, 2015b; Aasen *et al.*, 2020) or Density Functional Theory (DFT) (Blokhuis and van Giessen, 2013). Incorporating this expansion into CNT, one obtains a curvature corrected expression (c-CNT) for the work of formation of critical clusters (Aasen *et al.*, 2020)

$$W_{\text{c-CNT}} \approx \frac{4\pi\gamma_0 R_{\text{CNT}}^2}{3}\left(1 - \frac{6\delta}{R_{\text{CNT}}}\right) + 4\pi k_{\text{s}}, \tag{2}$$

where $R_{\text{CNT}} = 2\gamma_0/\Delta P$ is the CNT prediction for the radius of the critical cluster.

This c-CNT has been shown to significantly improve agreement with experimental results for water (Wilhelmsen *et al.*, 2015). It has also solved some of the inconsistencies that arise when CNT is extended to multi-component systems (Aasen *et al.*, 2020).

In this work, we present a comprehensive study of the free energy of formation of critical clusters of the Lennard-Jones fluid truncated and shifted at 2.5σ using Umbrella Sampling Monte Carlo simulations, density gradient theory (DGT), and density functional theory (DFT). The aim was to test the accuracy of classical nucleation theory (CNT) and curvature corrected CNT (c-CNT).

METHODS

For a spherical critical cluster, the work of formation is given by the formally exact relation (Gibbs, 1961)

$$W = \frac{16\pi\gamma^3}{3(\Delta P)^2}, \tag{3}$$

where γ is the surface tension of the cluster with the surface of tension as dividing surface, and $\Delta P = P^\ell(T,\mu) - P^{\rm v}(T,\mu)$ is the pressure difference of the (stable) bulk liquid and (metastable) bulk vapor having the same intensive properties (T,μ). For CNT the nucleation barrier is obtained by using the capillarity approximation, which assumes that the surface tension γ is the same as that of the bulk liquid with a planar interface γ_0. Accordingly, the ratio of the exact work of formation of a spherical critical droplet to that of the CNT-approximation is

$$\frac{W}{W_{\rm CNT}} = \left(\frac{\gamma}{\gamma_0}\right)^3. \tag{4}$$

We have calculated the free energy of formation W for the Lennard-Jones fluid truncated and shifted at 2.5σ using three different methods. First, we used density gradient theory with a constant influence parameter chosen to reproduce the correct value of the planar surface tension. Second, we used density functional theory based on a weighted density average approach (Sauer *et al.*, 2011) and the White Bear fundamental measure theory to model the hard sphere contribution (Roth *et al.*, 2002). For both DFT and DGT, the bulk behavior is governed by the PeTS equation of state (Heier *et al.*, 2018), and the density profiles are obtained by solving the corresponding Euler–Lagrange equations. Finally, we have performed Umbrella Sampling Monte Carlo simulations to calculate the free energy of critical droplets of the Lennard-Jones fluid truncated and shifted at 2.5σ at two different temperatures: $T = 0.625$ and $T = 0.900$. Simulation results of (ten Wolde Frenkel, 1998) for a third intermediate temperature $T = 0.741$ were also included in our comparison.

Since the pioneering work of (McGraw Laaksonen, 1996) on scaling relations, there is increasing evidence suggesting that the work of formation of critical clusters normalized by the CNT prediction, $f \equiv W/W_{CNT}$, may be a universal function of the degree of metastability, depending only weakly on the temperature and of the details of the intermolecular potential. Accordingly, many expressions for this scaling function f have been proposed in the literature.

In this work, we have formulated a new scaling function $f(\Delta P)$, using all the ingredients that we know, namely (i) $f(0) = 1$, since CNT is expected to be valid at the binodal, (ii) the slope at the binodal given by the Tolman length δ, (iii) the spherical rigidity $k_{\rm s}$, (iv) zero work of formation at the vapor spinodal $f(\Delta P^{\rm v}_{\rm sp}) = 0$ and (v) the liquid spinodal $f(\Delta P^{\ell}_{\rm sp}) = 0$. An accurate scaling function that satisfies these five conditions is a fourth-order polynomial in the Laplace pressure:

$$f(\Delta P) = \frac{(\Delta P - \Delta P^{\ell}_{\rm sp})(\Delta P - \Delta P^{\rm v}_{\rm sp})(1 + b\Delta P + c(\Delta P)^2)}{\Delta P^{\ell}_{\rm sp}\Delta P^{\rm v}_{\rm sp}} \tag{5}$$

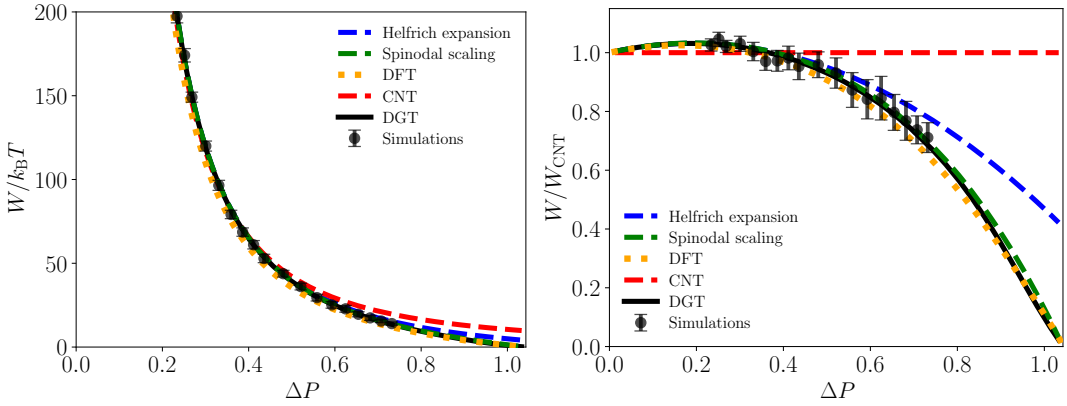

(a) Work of formation.

(b) Work of formation ratio.

Figure 1: Comparison of theories and simulations for $T = 0.625$ as a function of the Laplace pressure ΔP, where the x-axes are delimited by the binodal on the left and the vapor spinodal on the right. Helfrich coefficients were computed with DGT.

where

$$b = \frac{-3\delta}{\gamma_0} + \frac{1}{\Delta P_{\mathrm{sp}}^{\mathrm{v}}} + \frac{1}{\Delta P_{\mathrm{sp}}^{\ell}} \tag{6}$$

$$c = \frac{-(3b\Delta P_{\mathrm{m}} + 2)\Delta P_{\mathrm{m}} + (\Delta P_{\mathrm{sp}}^{\ell} + \Delta P_{\mathrm{sp}}^{\mathrm{v}})(2b\Delta P_{\mathrm{m}} + 1) - \Delta P_{\mathrm{sp}}^{\ell}\Delta P_{\mathrm{sp}}^{\mathrm{v}} b}{4(\Delta P_{\mathrm{m}})^3 - 3(\Delta P_{\mathrm{sp}}^{\ell} + \Delta P_{\mathrm{sp}}^{\mathrm{v}})(\Delta P_{\mathrm{m}})^2 + 2\Delta P_{\mathrm{sp}}^{\ell}\Delta P_{\mathrm{sp}}^{\mathrm{v}}\Delta P_{\mathrm{m}}} \tag{7}$$

The first two factors in the numerator of Eq. 5 warrant that the work of formation vanishes at both spinodals. The coefficients of the parabolic third factor are obtained from the slope at the binodal given by the Tolman length and the location of the maximum of the work of formation at $\Delta P_{\mathrm{m}} = \frac{2\delta\gamma_0^2}{k_{\mathrm{s}}}$.

Fig. 1 compares the work of formation predicted from all theories considered in this work against simulations for the temperature $T = 0.625$. We can observe that Eq. 5 accurately reproduces results from simulations, DGT, and DFT. The same excellent agreement is observed at the all the temperatures studied.

CONCLUSIONS

In this work, we have performed a careful analysis of the work of formation of critical clusters of the truncated and shifted Lennard-Jones fluid at three different temperatures and a wide range of pressures from the binodal to the spinodal.

We find that density gradient theory and density functional theory accurately reproduce molecular simulation results of critical droplet sizes and their free energies. The capillarity approximation grossly overestimates the free energy of small droplets. The incorporation of curvature corrections up to second order with the Helfrich expansion greatly remedies this and performs very well for most of the experimentally accessible region. However, it is imprecise for the smallest droplets and largest metastabilities, since it does not account for a vanishing nucleation barrier at the spinodal. To remedy this, we have proposed a scaling function for the nucleation barrier that incorporates both the coefficients of the Helfrich expansion and the requirement of vanishing nucleation barriers at the spinodals as corrections of CNT. The scaling function reproduces accurately the free energy

of formation of critical droplets for the entire metastability range and all temperatures examined, and deviates from density gradient theory by less than one $k_{\mathrm{B}}T$.

Our results suggest that c-CNT and the new scaling function constitute an accurate, yet simple model to predict accurately nucleation rates and solve the limitations of CNT. Here, we have confirmed this for the work of formation of droplets. However, the new scaling function is expected to be equally accurate for bubbles, and could also possibly be extended to crystallization and nucleation in multicomponent systems of interest in atmospheric processes. Thus, the proper incorporation of curvature corrections and the location of the spinodals might open the door to quantitatively accurate predictions of nucleation rates for other substances and a wide range of problems of scientific and technological interest.

ACKNOWLEDGEMENTS

This work received funding from Norwegian Research Council, project number 328679. AA, ØW and MH acknowledge funding from the Research Council of Norway (RCN), the Center of Excellence Funding Scheme, Project No. 262644, PoreLab. DR acknowledges funding from the Spanish government through grants PGC2018-098373-B-I00 and PID2021-126570NB-I00 (MINECO/FEDER, UE).

REFERENCES

Aasen, A., Reguera, D. Wilhelmsen, Ø. (2020). Curvature Corrections Remove the Inconsistencies of Binary Classical Nucleation Theory. *Phys. Rev. Lett.*, **124**, 045701.

Blokhuis, E. M. and van Giessen, A. E. (2013). Density functional theory of a curved liquid-vapour interface: evaluation of the rigidity constants. *J. Phys. Cond. Mat.*, **25**, 225003.

Gibbs, J. W.(1961).*The scientific papers of J. Willard Gibbs*. (Dover, New York).

Heier, M. et al. (2018). Equation of state for the Lennard-Jones truncated and shifted fluid with a cut-off radius of 2.5σ based on perturbation theory and its applications to interfacial thermodynamics. *Mol. Phys.*, **116**, 2083.

Iland, K., Wölk, J., Strey, R. Kashchiev, D. (2007). Argon nucleation in a cryogenic nucleation pulse chamber. *J. Chem. Phys.*, **127**, 154506.

McGraw, R. Laaksonen, A. (1996). Scaling properties of the critical nucleus in classical and molecular-based theories of vapor-liquid nucleation. *Phys. Rev. Lett.*, **76**, 2754.

Roth, R., Evans, R., Lang, A. Kahl, G. (2002). Fundamental Measure Theory for Hard-Sphere Mixtures Revisited: The White Bear Version. *J. Phys. Condens. Matter*, **14**, 12063.

Sauer, E. Gross, J. (2017). Classical density functional theory for liquid–fluid interfaces and confined systems: A functional for the perturbed-chain polar statistical associating fluid theory equation of state. *Ind. & Eng. Chem. Res.*, **56**, 4119.

ten Wolde, P. R. Frenkel, D. (1998). Computer simulation study of gas–liquid nucleation in a Lennard-Jones system. *J. Chem. Phys.*, **109**, 9901.

Wilhelmsen, Ø., Bedeaux, D. and Reguera, D. (2015). Communication: Tolman length and rigidity constants of water and their role in nucleation. *J. Chem. Phys.*, **142**, 171103

Wilhelmsen, Ø., Bedeaux, D. and Reguera, D. (2015). Tolman length and rigidity constants of the Lennard–Jones fluid. *J. Chem. Phys.*, **142**, 64706.

DIRECT RADIATIVE EFFECTS OF AIRBORNE MICROPLASTICS

L. E. REVELL[1], P. KUMA[1,3], E. C. LE RU[2], W. R. C. SOMERVILLE[2], and S. GAW[1]

[1]School of Physical and Chemical Sciences, University of Canterbury, Christchurch, New Zealand

[2]The MacDiarmid Institute for Advanced Materials and Nanotechnology, School of Chemical and Physical Sciences, Victoria University of Wellington, Wellington, New Zealand

[3]Now at: Department of Meteorology, Stockholm University, Stockholm, Sweden

Keywords: AIRBORNE MICROPLASTICS, NANOPLASTICS, RADIATIVE FORCING

INTRODUCTION

Since large-scale production of plastics began in the 1950s, around 5 Gt of plastic waste has accumulated in landfills or the environment (Geyer et al., 2017). Plastics become brittle as they age and may break down to produce microplastics and nanoplastics, typically defined as particles 1–5,000 μm and <1 μm in size, respectively. Microplastics and nanoplastics are widespread contaminants in the atmosphere, where, due to their small size and low density, they can be transported with winds around the Earth (Allen et al., 2022). As a relatively recently discovered source of airborne particulate matter, little is known about the climate impacts of airborne microplastics and nanoplastics. They are hypothesized to act as ice nucleating particles and potentially as cloud condensation nuclei when aged, and thus may impact climate indirectly in remote and unpolluted regions (Aeschlimann et al., 2022). Here, we present calculations of airborne microplastics' optical properties and direct radiative effects.

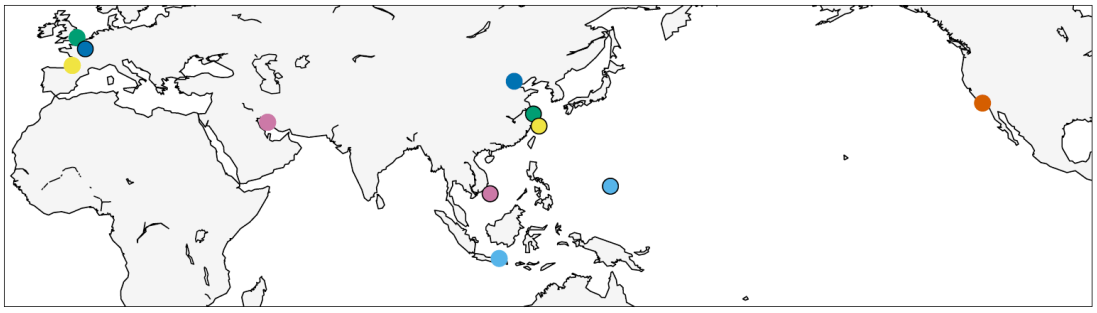

Location	Concentration (MP m^{-3})	Analytical method
Beijing, China[13]	5,650	SEM-EDX
London, UK[12]	2,502	Raman spectral imaging
Surabaya, Indonesia[20]	109	FTIR
Bushehr Port, Iran (dusty days)[1]	10.3	μRaman
French Atlantic Coast (offshore wind)[3]	9.6	μRaman
Southern California[9]	6.2	μRaman and μFTIR
French Atlantic Coast (onshore wind)[3]	2.9	μRaman
Bushehr Port, Iran (normal days)[1]	2.1	μRaman
Shanghai, China[14]	1.42	μFTIR
Paris, France[8]	0.9	μFTIR
East China Sea[15]	0.13	μFTIR
South China Sea and West Pacific Ocean[17]	0.11	μFTIR
West Pacific Ocean[15]	0.01	μFTIR

Figure 1. Concentrations of airborne microplastics (MP) reported in previous studies. All studies relied on pumped air (active) sampling rather than deposition collection (passive sampling), and all studies confirmed polymer composition spectroscopically via either micro-Fourier Transform Infrared (μFTIR), micro-Raman (μRaman) or scanning electron microscopy-energy dispersive X-ray (SEM-EDX) spectroscopy. The mean and median concentrations are 638 and 2.9 MP m^{-3}, respectively (Revell et al., 2021).

METHODS

Typical airborne microplastic morphotypes, size distributions and compositions were summarized according to a literature survey (Revell et al., 2021). The optical properties of microplastic fragments and fibres, the two most common morphotypes, were calculated separately. Scattering and absorption cross-sections, single-scattering albedos and asymmetry factors were calculated and weighted by the incoming solar spectrum to calculate integral properties in each spectral band. These were then used to prepare volume scattering, absorption coefficients, and asymmetry factors for use in the Hadley Centre Global Environment Model version 3 (HadGEM3). The absorption and scattering coefficients of microplastics were added to the model's coefficients calculated for atmospheric gases, aerosols and clouds using HadGEM3's EasyAerosol scheme. We assume a uniform surface concentration of 1 MP m^{-3}: approximately the median concentration from previous studies (Fig. 1). However, to clearly isolate signal from noise, HadGEM3 simulations were performed using 100× scaling (i.e., a uniform surface concentration of 100 MP m^{-3}: close to the mean concentration from Fig. 1) to clearly isolate signal from noise. Twenty-year simulations were performed with and without microplastics to calculate effective radiative forcing (ERF; Fig. 2).

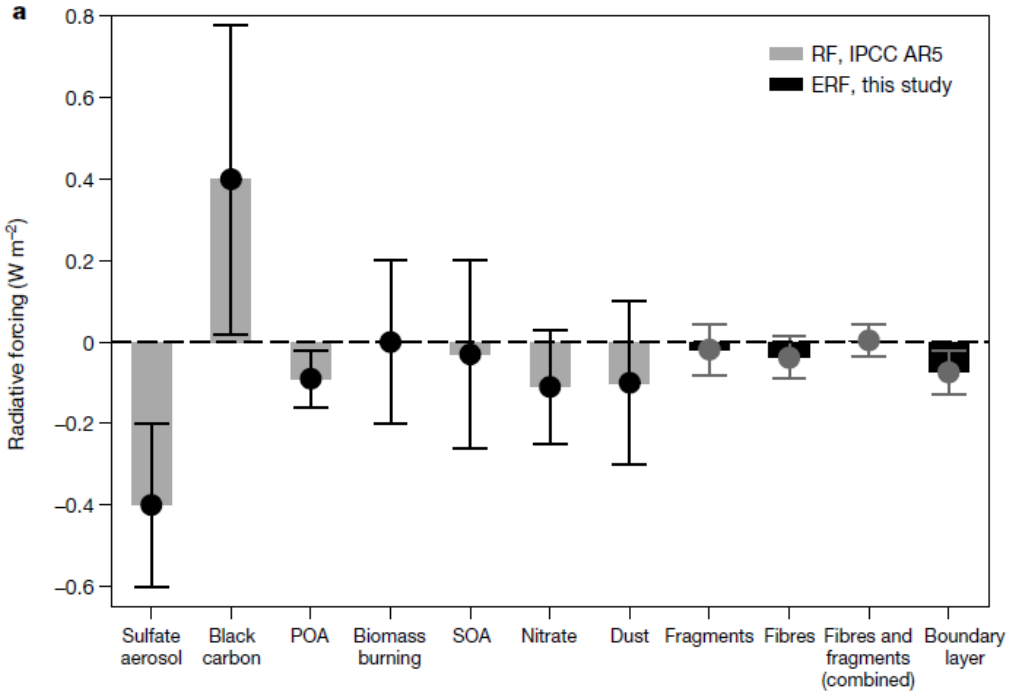

Figure 2. Global-, annual-mean ERF for non-pigmented microplastics, averaged over 20-year global climate model simulations for microplastic fragments and fibres (Revell et al., 2021). Microplastics are assumed to be present up to 10 km altitude with a surface concentration of 100 MP m^{-3}. Also shown is a simulation in which microplastics are assumed to be in the boundary layer only (bottom 2 km of the atmosphere). Error bars indicate the 90% confidence interval. For comparison, the global- and annual mean radiative forcing due to aerosol-radiation interactions between 1750 and 2011 of seven aerosol components are included (Myhre et al., 2013).

CONCLUSIONS

The ERF of airborne microplastics is computed to be 0.044 ± 0.399 mW m^{-2} in the present-day atmosphere assuming a uniform surface concentration of 1 MP m^{-3} and a vertical distribution up to 10 km altitude (Fig. 2). However, there are large uncertainties in the geographical and vertical distribution of microplastics. Assuming that they are confined to the boundary layer, shortwave effects dominate and the microplastic ERF is approximately -0.746 ± 0.553 mW m^{-2}. Compared with the total ERF due to aerosol–radiation interactions (-0.71 to -0.14 W m^{-2}; Bellouin et al., 2020), the microplastic ERF is small. Uncertainties arise due to a current lack of data; the magnitude of ERF is influenced by the concentration of microplastics, and the sign is subject to uncertainties in the wavelength-dependent refractive index, which depends on properties such as composition and colour. Airborne microplastic pollution will become more severe in future—not only are microplastics durable but, based on current production and waste management trends, the abundance of plastic accumulated in landfills and the environment is projected to double over the next three decades (Geyer et al., 2017). Since plastic degrades through age and exposure to UV light to produce secondary microplastics, we expect microplastics to be present in Earth's atmosphere for many years to come.

ACKNOWLEDGEMENTS

This research has been supported by the Royal Society of New Zealand Marsden Fund (contract number MFP-UOC1903).

REFERENCES

Aeschlimann, M., G. Li, Z. A. Kanji and D. M. Mitrano (2022), Potential impacts of atmospheric microplastics and Nano plastics on cloud formation processes, *Nature Geoscience* 15(12): 967-975.

Allen, D., S. Allen, S. Abbasi, A. Baker, M. Bergmann, J. Brahney, T. Butler, R. A. Duce, S. Eckhardt, N. Evangeliou, T. Jickells, M. Kanakidou, P. Kershaw, P. Laj, J. Levermore, D. Li, P. Liss, K. Liu, N. Mahowald, P. Masque, D. Materić, A. G. Mayes, P. McGinnity, I. Osvath, K. A. Prather, J. M. Prospero, L. E. Revell, S. G. Sander, W. J. Shim, J. Slade, A. Stein, O. Tarasova and S. Wright (2022), Microplastics and nanoplastics in the marine-atmosphere environment, *Nature Reviews Earth & Environment* 3(6): 393-405.

Bellouin, N., J. Quaas, E. Gryspeerdt, S. Kinne, P. Stier, D. Watson-Parris, O. Boucher, K. S. Carslaw, M. Christensen, A.-L. Daniau, J.-L. Dufresne, G. Feingold, S. Fiedler, P. Forster, A. Gettelman, J. M. Haywood, U. Lohmann, F. Malavelle, T. Mauritsen, D. T. McCoy, G. Myhre, J. Mülmenstädt, D. Neubauer, A. Possner, M. Rugenstein, Y. Sato, M. Schulz, S. E. Schwartz, O. Sourdeval, T. Storelvmo, V. Toll, D. Winker and B. Stevens (2020), Bounding Global Aerosol Radiative Forcing of Climate Change, *Reviews of Geophysics* 58(1): e2019RG000660.

Geyer, R., J. R. Jambeck and K. L. Law (2017), Production, use, and fate of all plastics ever made, *Science Advances* 3(7): e1700782.

Myhre, G. et al. in *Climate Change 2013: The Physical Science Basis* (eds Stocker, T. F. et al.) Ch. 8 (IPCC, Cambridge Univ. Press, 2013).

Revell, L. E., P. Kuma, E. C. Le Ru, W. R. C. Somerville and S. Gaw (2021), Direct radiative effects of airborne microplastics, *Nature* 598(7881): 462-467.

SOUTHERN OCEAN EMISSIONS OF DMS IN A GLOBAL ATMOSPHERIC MODEL

YUSUF A. BHATTI[1], LAURA E. REVELL[1], ALEX SCHUDDEBOOM[1], ADRIAN J. MCDONALD[1,2], ALEX ARCHIBALD[3,4], JONNY WILLIAMS[5], AND ERIK BEHRENS[5]

[1]School of Physical and Chemical Sciences, University of Canterbury, Christchurch, New Zealand
[2]Gateway Antarctica, University of Canterbury, Christchurch, New Zealand
[3]National Centre for Atmospheric Science, Cambridge, United Kingdom
[4]Yusuf Hamied Department of Chemistry, University of Cambridge, Cambridge, United Kingdom
[5]National Institute of Water and Atmospheric Research (NIWA), Wellington, New Zealand

Keywords: DMS, Southern Ocean, Global climate modeling

INTRODUCTION

Dimethyl sulfide (DMS) is the dominant source of natural sulfur over the Southern Ocean, formed from biogenic processes involving marine phytoplankton. DMS is oxidized to sulfur dioxide in the atmosphere and eventually forms sulfate aerosol. However, the processes involving the emission of DMS to the atmosphere and subsequent oxidation to sulfate aerosol are highly uncertain. Here, we evaluate the variability in oceanic DMS, DMS emissions, and atmospheric DMS in global model simulations performed with four seawater DMS data sets and three sea-to-air flux parameterizations.

METHODS

Using a nudged configuration of the UK atmosphere-only Earth System Model, UKESM1, we performed nine 10-year simulations using forcings from 2009 – 2018. One set of simulations used four different seawater DMS data sets: a climatology of DMS compiled from simulations performed with the coupled UKESM1 (Anderson et al. 2001), two data sets compiled from seawater DMS observations (Lana et al. 2011, Hulswar et al. 2022), and a DMS data set calculated from MODIS chlorophyll-a concentrations using the same approach as Anderson et al. (2001). The other set of simulations tested three DMS sea-to-air flux parameterizations: Liss and Merlivat (1986), Blomquist et al. (2017), and Wannkinhof (2014).

CONCLUSIONS

Using a quadratic sea-to-air flux parameterization (Wanninkhof 2014) provides fast transfer velocities in DMS, creating a positive bias across most areas of the Southern Ocean except for biologically productive areas, such as the Chatham Rise and high latitude regions. Although quadratic formulas are able to capture elevated Southern Ocean atmospheric DMS concentrations seen in observations, large areas of the Southern Ocean have lower measured atmospheric DMS than simulated by the model when using a quadratic sea-to-air flux parameterization. Linear relationships between wind and DMS flux (Liss and Merlivat 1986, Blomquist et al. 2017) are shown to be more realistic. The variability across all simulations with different oceanic DMS datasets using the same sea-to-air flux parameterizations (Fig. 1) is 112% (6.92 to 3.27 TgS Yr^{-1}). The variability in simulations using the same oceanic DMS dataset but differing sea-to-air flux parameterizations is 50-60% (4.69 to 2.9 TgS Yr^{-1}). Simulations that implement a quadratic sea-to-air show 35% higher DMS mixing ratios than simulations using a linear sea-to-air flux. This work highlights the need for Earth System Models to include a sea-to-air flux parameterization that is appropriate for DMS, and for oceanic DMS datasets to capture the time-varying nature of the marine biogenic activity. Such improvements would help provide more accurate simulations of oceanic and atmospheric DMS in the Southern Ocean.

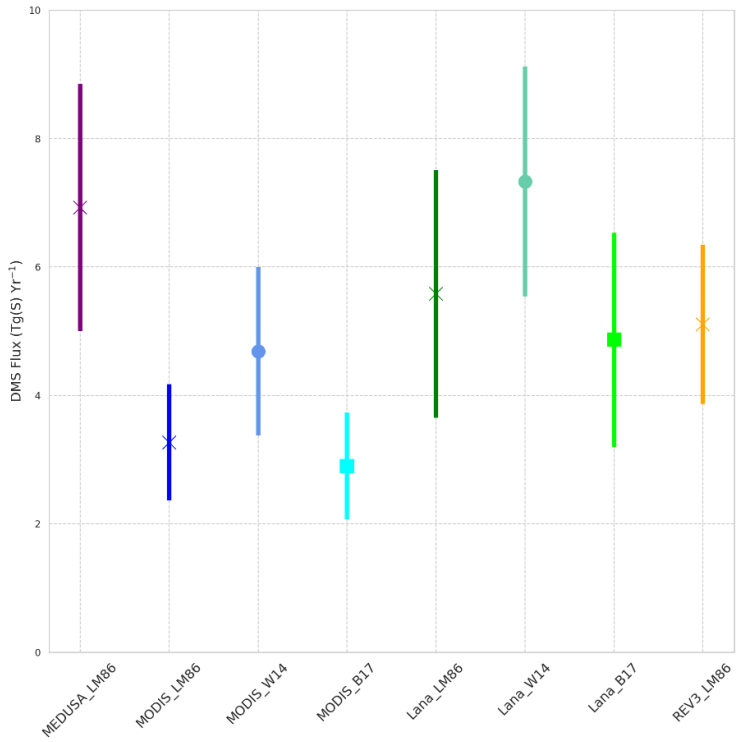

Figure 1. Summertime (December – February) Southern Ocean sulfur emissions in Tg year^{-1} in all model simulations performed. The error bars represent the spatial and temporal standard deviation. The different colors represent different oceanic DMS climatologies (Purple: MEDUSA (Sellar et al., 2019; Anderson et al., 2001), Green: Lana et al., (2011) and Orange: REV3 (Hulswar et al., 2022), and time series (Blue: derived from MODIS chlorophyll-a) used in this work. The x marker represents simulations performed with the Liss and Merlivat (1986) sea-to-air flux, the dot marker represents Wanninkhof 2014, and square marker represents Blomquist et al. (2017).

ACKNOWLEDGEMENTS

This research has been supported by the Deep South National Science Challenge (grants C01X1412 and C01X1901).

REFERENCES

Blomquist, B. W., Brumer, S. E., Fairall, C. W., Huebert, B. J., Zappa, C. J., Brooks, I. M., Yang, M., Bariteau, L., Prytherch, J., Hare, J. E., et al.: Wind speed and sea state dependencies of air-sea gas transfer: Results from the High Wind speed Gas exchange Study (HiWinGS), Journal of Geophysical Research: Oceans, 122, 8034–8062, 2017.

Hulswar, S., Simó, R., Gali Tapias, M., Bell, T. G., Lana, A., Inamdar, S., Halloran, P. R., Manville, G., and Mahajan, A. S.: Third revision of the global surface seawater dimethyl sulfide climatology (DMS-Rev3), Earth System Science Data, 14, 2963–2987, 2022

Lana, A., Bell, T., Simó, R., Vallina, S., Ballabrera-Poy, J., Kettle, A., Dachs, J., Bopp, L., Saltzman, E., Stefels, J., et al.: An updated climatology of surface dimethlysulfide concentrations and emission fluxes in the global ocean, Global Biogeochemical Cycles, 25, 2011.

Liss, P. S. and Merlivat, L.: Air-sea gas exchange rates: Introduction and synthesis, pp. 113–127, Springer, 1986.

Sellar, A. A., Jones, C. G.,Mulcahy, J. P., Tang, Y., Yool, A.,Wiltshire, A., O'connor, F.M., Stringer,M., Hill, R., and Palmieri, J.: UKESM1: Description and evaluation of the UK Earth System Model, Journal of Advances in Modeling Earth Systems, 11, 4513–4558, 2019.

Wanninkhof, R.: Relationship between wind speed and gas exchange over the ocean revisited, Limnology and Oceanography: Methods, 12, 351–362, 2014.

HIGH-TIME-RESOLUTION CARBONACEOUS AEROSOLS FINGERPRINT USING AN ADVANCED TOTAL CARBON–BLACK CARBON (TC-$BC_{7\text{-}\lambda}$) METHOD

M. RIGLER[1], M. IVANČIČ[1], G LAVRIČ[1] , B. ALFÖLDY[1], I. JEŽEK[1], S. HASHEMINASSAB[2], P. PAKBIN[2], F. AHANGAR[2], M. SOWLAT[2] , S. BODDEKER[2], A. GREGORIČ[1,3]

[1]Aerosol d.o.o., Research & Development Department, Kamniška 39a, SI-1000 Ljubljana, Slovenia
[2]South Coast Air Quality Management District, 21865 Copley Dr, Diamond Bar, CA 91765, USA
[3]Centre for Atmospheric Research, University of Nova Gorica, Vipavska 13, SI-5000 N. Gorica, Slovenia

Keywords: Brown carbon, Primary organic aerosol, Secondary organic aerosol, Aethalometer Total carbon analyzer, Carbonaceous aerosol speciation system

INTRODUCTION

Due to carbonaceous aerosol (CA) complex chemical and physical properties, the underlying processes controlling the overall impact of CA on climate and human health are still not fully understood. A lack of long-term, highly time-resolved data of CA components represents a limiting factor when studying the impact of specific constituents and their synergistic effects. Thus, adequate online and high-time resolution apportionment methods of CA are needed to identify their main sources and formation mechanisms and point out the components with the highest impact on public health and climate forcing. In this study we present an advanced TC-BC approach (Ivančič et al., 2022) in which CA are measured by the CASS system (Carbonaceous Aerosol Speciation System), which combines the Total Carbon Analyzer TCA08 (Rigler et al., 2020) and the Aethalometer AE33 (Drinovec et al., 2015), providing high time-resolved data on the carbonaceous aerosol composition and optical properties in real-time.

METHODS

Advanced apportionment of the carbonaceous aerosol is based on the simplified CASS method, where the organic carbon (OC) content is calculated as the difference between total carbon (TC) and black carbon (BC). The multiple-wavelength analysis of the Aethalometer AE33 data allows apportionment of the optical absorption into two components: black carbon (BC) and brown carbon (BrC). Furthermore, the BC tracer method separates organic carbon into the primary and secondary OC (Wu and Yu, 2016). Integrating numerical algorithms to high-time-resolution measurements with CASS, an advanced method is introduced to apportion CA into six components based on their optical absorption properties and their primary or secondary origin:

$$CA = BC_{ff} + BC_{bb} + POA_{BrC} + POA_{non\text{-}abs} + SOA_{BrC} + SOA_{non\text{-}abs},$$

where BC_{ff} and BC_{bb} represent fossil fuel and biomass burning related BC components, POA_{BrC} and SOA_{BrC} are the primary emitted and secondarily formed light-absorbing organic aerosols, and $POA_{non\text{-}abs}$ and $SOA_{non\text{-}abs}$ non-light-absorbing aerosols (Figure 1).

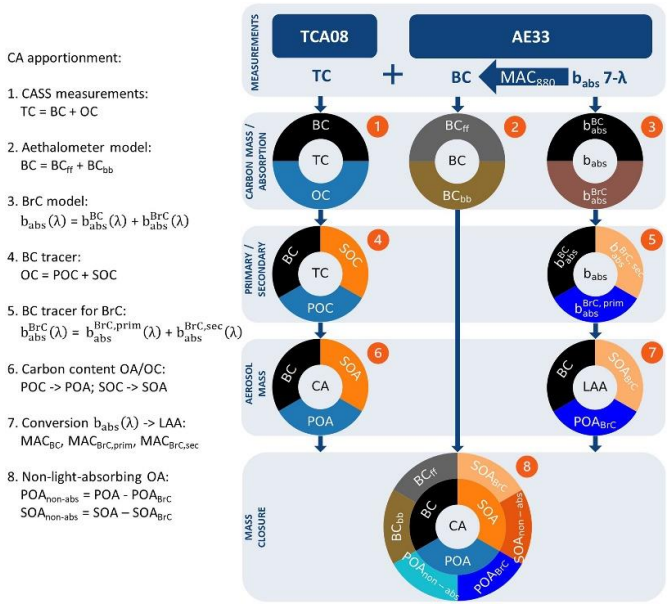

Figure 1. Flowchart for CA apportionment to six components using the advanced TC-BC method.

CONCLUSIONS

The advanced TC-BC method was validated on a 2-year measurement campaign in Los Angeles Basin (LA Central and LA Riverside measurement sites, CA, USA, Figure 2). The high-time-resolution approach allowed to study the diurnal and seasonal evolution of different components as a function of sources, transformation, and meteorology (Fig. 3).

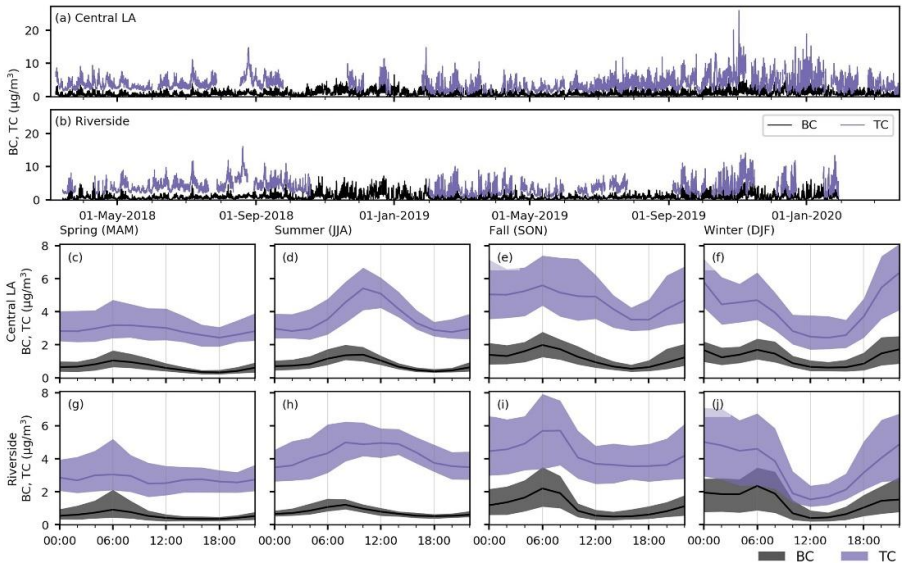

Figure 2. Two-year-long measurements with CASS in Central LA (a) and Riverside (b) and diurnal profiles of BC and TC by season in Central LA (c-f) and Riverside (g-j). The lines represent median values, and the borders of the shaded area are the first and third quartiles in diurnal plots.

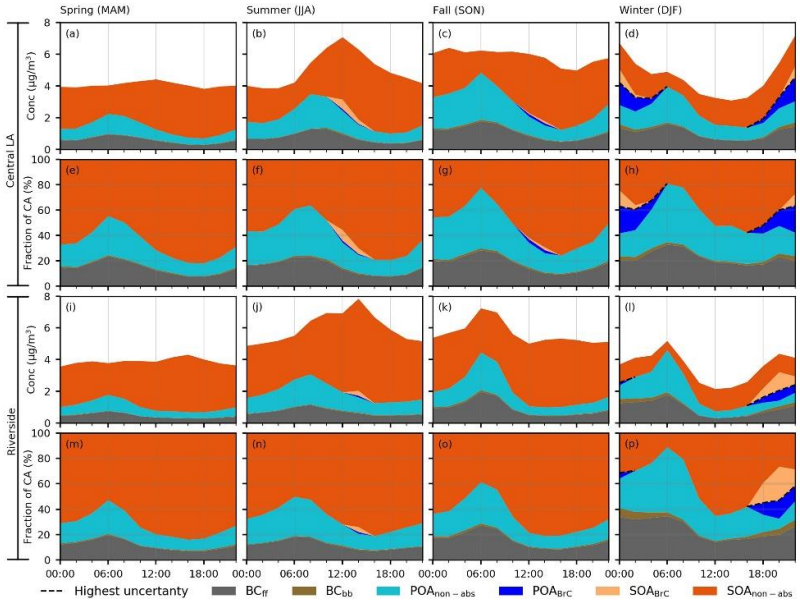

Fig. 3. Diurnal profiles of CA apportioned to BC_{ff}, BC_{bb}, $POA_{non\text{-}abs}$, POA_{BrC}, $SOA_{non\text{-}abs,}$ and SOA_{BrC} in Central LA (a-h) and Riverside (i-p). Results are separated into seasons: (a, e, i and m) for spring, (b, f, j and n) for summer, (c, g, k and o) for fall, and (d, h, I and p) for winter. Graphs (a-d) and (i-l) contain medians, and relative fractions are shown in (e-h) and (m-p). The black dashed line represents the split between POA_{BrC} and SOA_{BrC} during winter nights, where the highest uncertainty is expected to appear.

Road transport (all over the year) and biomass burning (winter) are confirmed here as the main sources of primary emitted carbonaceous aerosols, this latter fraction being significant in winter. On the other hand, secondary formed SOA is dominant in summer afternoons when their contribution can reach 70 % of CA but is also important during nights in the colder months. The results were validated with complementary air quality measurements (e.g., gaseous pollutants, ultrafine particles, PM2.5, offline OC/EC).

Finally, we compared the average CA fingerprint from LA basin to other locations, illustrating the interest of applying our high time-resolution CA source apportionment to provide important information for the adaptation of air pollution abatement strategies in different environments.

REFERENCES

Drinovec, L., Močnik, G., Zotter, P., Prévôt, A. S. H., Ruckstuhl, C., Coz, E., Rupakheti, M., Sciare, J., Müller, T., Wiedensohler, A., and Hansen, A. D. A.: The dual-spot Aethalometer: an improved measurement of aerosol black carbon with real-time loading compensation, Atmospheric Measurement Techniques, 8, 1965–1979, https://doi.org/10.5194/amt-8-1965-2015, 2015.

Ivančič, M., Gregorič, A., Lavrič, G., Alföldy, B., Ježek, I., Hasheminassab, S., Pakbin, P., Ahangar, F., Sowlat, M., Boddeker, S., and Rigler, M.: Two-year-long high-time-resolution apportionment of primary and secondary carbonaceous aerosols in the Los Angeles Basin using an advanced total carbon–black carbon (TC-BC(λ)) method, Science of The Total Environment, 848, 157606, https://doi.org/10.1016/j.scitotenv.2022.157606, 2022.

Rigler, M., Drinovec, L., Lavrič, G., Vlachou, A., Prévôt, A. S. H., Jaffrezo, J. L., Stavroulas, I., Sciare, J., Burger, J., Kranjc, I., Turšič, J., Hansen, A. D. A., and Močnik, G.: The new instrument using a TC–BC (total carbon–black carbon) method for the online measurement of carbonaceous aerosols, Atmospheric Measurement Techniques, 13, 4333–4351, https://doi.org/10.5194/amt-13-4333-2020, 2020.

Wu, C. and Yu, J. Z.: Determination of primary combustion source organic carbon-to-elemental carbon (OC / EC) ratio using ambient OC and EC measurements: secondary OC-EC correlation minimization method, Atmos. Chem. Phys., 16, 5453–5465, https://doi.org/10.5194/acp-16-5453-2016, 2016.

VERTICAL DISTRIBUTION OF AEROSOLS OVER THE SOUTHERN GREAT BARRIER REEF

ROBERT G. RYAN[1], LILANI TOMS-HARDMAN[2], ROBYN SCHOFIELD[1]

[1]*School of Geography, Earth and Atmospheric Sciences, The University of Melbourne, Victoria, Australia*
[2]*Defence Science and Technology Group, HMAS Stirling, Western Australia, Australia*

INTRODUCTION

The fundamental role of atmospheric aerosols in the climate system of the Great Barrier Reef (GBR) has been examined in several recent field campaigns. One of the limiting factors for incorporating aerosol information in atmospheric models is that while a large amount of surface information exists, vertically resolved aerosol data is more limited. In this study we present vertical aerosol extinction profiles from a two-month field campaign at One Tree Island, a small coral cay in the Capricorn Bunker Group of the Southern GBR.

METHODS

The measurement campaign at One Tree Island was conducted from mid-January to early April 2023. We compare measured aerosol extinction profiles derived from both Mini Micro Pulse LiDAR (MiniMPL) backscatter profiles and Multi-Axis Differential Optical Absorption Spectrometer (MAX-DOAS) O_4 absorption spectra to aerosol profiles simulated with the WRF-Chem chemical transport model. This dataset, including Microtops sun-photometer aerosol optical depth results, meteorological observations and sea-surface wind and wave-height measurements from a wave-ride buoy, was collected as part of the Reef Restoration and Adaptation's 2023 Cooling and Shading fieldwork program. MiniMPL data gathered on One Tree Island was also used to estimate atmospheric boundary layer (ABL) top height, as the presence of atmospheric aerosols can both enhance and suppress ABL stability, making ABL height an important parameter for determining the vertical distribution of atmospheric aerosols.

CONCLUSIONS

Using the vertical extinction profiles, ABL height estimations, and other relevant data we examine the sources and vertical mixing of aerosols through the marine boundary layer in this unique, pristine region, and recommend improvements needed in modelling aerosol distributions over the GBR.

CIGAS-UHEL AIMS AT OPEN-ACCESS, SUSTAINABLE, TRACEABLE, HIGH-QUALITY DATA OF IN-SITU MEASURED CONDENSABLE VAPOURS

N. SARNELA[1], T. JOKINEN[2], T. PETÄJÄ[1] and S. HÄME[1]

[1]Institute for Atmospheric and Earth System Research, University of Helsinki, Helsinki, 00560, Finland

[2] Climate and Atmosphere Research Center, The Cyprus Institute, Nicosia, 2121, Cyprus

Keywords: condensable vapours, secondary particle formation, calibration, quantitative measurements

INTRODUCTION

Secondary particle formation and aerosol precursors have been studied intensively during the last decade. The method to measure sulfuric acid and methane sulfonic acid in-situ with chemical ionization mass spectrometry using nitrate ion as a reagent ion was presented already twenty years ago (Eisele & Tanner, 1993). Since then, a significant leap in the characterization of aerosol precursors happened when the measurements of condensable vapours started with time-of-flight mass spectrometers enabling simultaneous measurements of vast number of vapours (Junninen et al., 2010, Jokinen et al., 2012). Second advancement in condensable vapour measurements has been the diversification of the reagent ions enabling different selectivities for the methods (Riva et al., 2019) and conducting successive measurements with different reagent ions with one instrument (Huang et al., 2021, Rissanen et al., 2019).

Last decade has brought several new measurement techniques for general use in atmospheric measurement stations and chamber experiments and our understanding of new particle formation on molecule and cluster level has become significantly more detailed. The condensable vapours have been studied qualitatively in different environments and conditions, and also their concentrations or approximations of them have been published. The quantitative analysis of condensable vapours has still large uncertainties and there are just a few calibration methods in use. In addition to that, no standardization of the methods, nor general guidelines for measurements have been done. We are establishing a new unit CiGas-UHEL, as a part of Topical Centre ACTRIS CiGas (The Aerosol, Clouds and Trace Gases Research Infrastructure, Centre for Reactive Trace Gases In Situ Measurements), which will aim at open-access, sustainable, traceable, high-quality data of in-situ measured condensable vapours.

METHODS

The goal of producing high-quality data of condensable vapours will be executed by several actions put into practice together with the associated scientific community. One of the first tasks is to assembly a standard operation procedure (SOP) including measurement guidelines and clear processes for quality control and data processing. The SOP will focus especially on condensable vapour measurements conducted with chemical ionization atmospheric pressure interface mass spectrometry. SOP includes topics such as description of different kind inlets and their best practices; maintenance and troubleshooting; description of the mass spectrometer itself, tuning of the voltages and their effect on fragmentation and transmission and things to consider when measuring in field, laboratory, on aircraft or from chamber experiments. The calibration procedures, determination of limit of detection, blank measurements and quality control during normal operation will be described. Data treatment will be one of the core topics as the data from ACTRIS National Facilities (such as measurement stations and atmospheric simulation chambers) will be processed based on the guidelines and submitted to the ACTRIS data base from where they are openly available for all.

As a Topical Centre Unit of ACTRIS, CiGas-UHEL is responsible for providing standardization, training and consultancy, intercomparison workshops, calibrations and doing method development for the measurements of condensable vapours. The standardization will be executed by providing SOP for users and labelling and auditing the ACTRIS National Facilities. Calibration, training, and consultancy are offered as operation support for the instrument users within ACTRIS but also as services for other users. One way to understand the operation of instruments and the functionality of individual instruments better, is to arrange intercomparison workshops where instruments can be measuring the same sample side by side. CiGas-UHEL will arrange its first intercomparison campaign in co-operation with OrGanic Tracers and Aerosol Constituents - Calibration Centre (OGTAC-CC) at TROPOS, Germany in spring 2023. The first intercomparison workshop will gather together around ten instruments and their operators using different methods to detect the condensable vapours. Comparison of the data from these measurements will give more insight about the transmission, sensitivity and selectivity of different methods and individual instruments. In future CiGas-UHEL can arrange intercomparison workshops focusing also on different themes. The method development is one of the tasks of our Unit and in that we mean especially calibration methods for condensable vapours. The development work will be done in co-operation with other users and altogether the co-operation with associated scientific communities and the transfer of knowledge to them is a crucial part of everything that our Unit does.

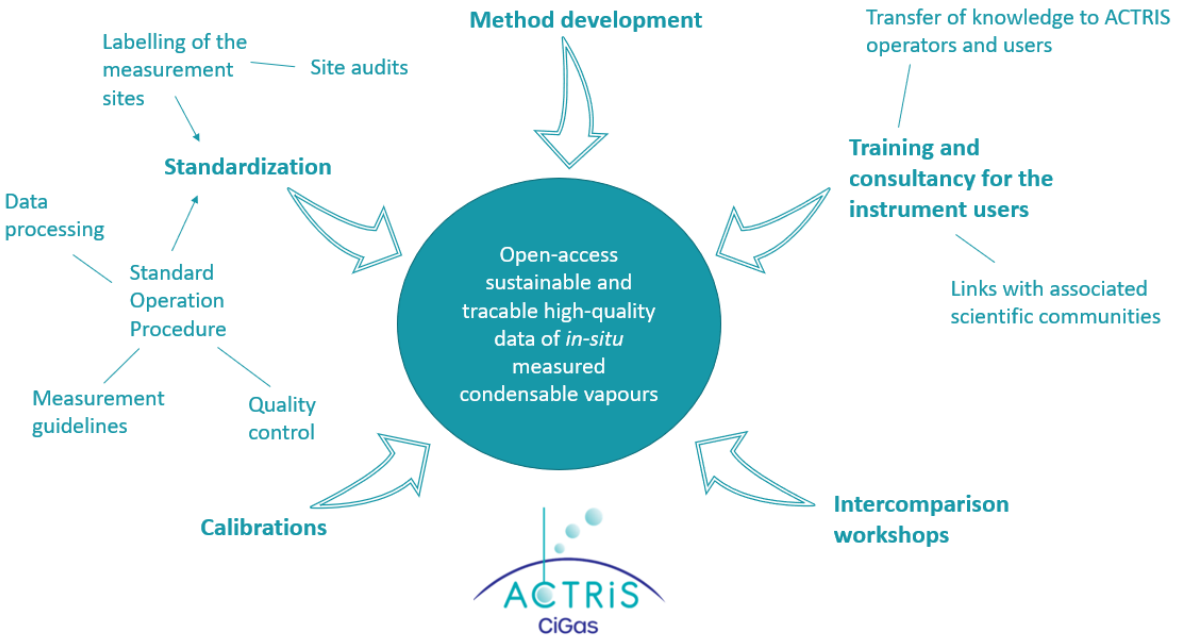

Figure 1. The core operations of CiGas-UHEL to achieve its goal to enable production of high-quality data of condensable vapours

SUMMARY

A new calibration center called CiGas-UHEL, as part of ACTRIS Centre for Reactive Trace Gases In Situ Measurements, is focusing on the quantitative measurements of condensable vapours with chemical ionization mass spectrometry. The goal of supporting the production of open-access, sustainable, traceable, high-quality data of in-situ measured condensable vapours is achieved by several operations that include offering calibrations, training and consultancy, arranging intercomparison workshops, conducting method development and leading the standardization of the measurements.

ACKNOWLEDGEMENTS

We thank OrGanic Tracers and Aerosol Constituents - Calibration Centre (OGTAC-CC) and Leibniz Institute for Tropospheric Research for valuable co-operation. The work has been supported by University of Helsinki hosting the ACTRIS CiGas-UHEL Unit, Academy of Finland (projects no. 329274, 328616) and the European Commission (ACTRIS IMP, H2020-INFRADEV-2019-2, Grant Agreement no.: 871115).

REFERENCES

Eisele, F. L. & Tanner, D. J. (1993) Measurement of the gas phase concentration of H_2SO_4 and methane sulfonic acid and estimates of H_2SO_4 production and loss in the atmosphere, *J. Geophys Res. Atmos.*, 98, 9001-9010.

Huang, W., Li, H., Sarnela, N., Heikkinen, L., Tham, Y. J., Mikkilä, J., Thomas, S. J., Donahue, N. M., Kulmala, M., and Bianchi, F. (2021) Measurement report: Molecular composition and volatility of gaseous organic compounds in a boreal forest – from volatile organic compounds to highly oxygenated organic molecules, *Atmos. Chem. Phys.*, **21**, 8961–8977.

Jokinen, T., Sipilä, M., Junninen, H., Ehn, M., Lönn, G., Hakala, J., Petäjä, T., Mauldin III, R. L., Kulmala, M., and Worsnop, D. R. (2012) Atmospheric sulphuric acid and neutral cluster measurements using CI-APi-TOF, *Atmos. Chem. Phys*., **12**, 4117–4125.

Junninen, H., Ehn, M., Petäjä, T., Luosujärvi, L., Kotiaho, T., Kostiainen, R., Rohner, U., Gonin, M., Fuhrer, K., Kulmala, M., and Worsnop, D. R. (2010) A high-resolution mass spectrometer to measure atmospheric ion composition, *Atmos. Meas. Tech*., **3**, 1039–1053.

Rissanen, M. P., Mikkilä, J., Iyer, S., and Hakala, J. (2019) Multi-scheme chemical ionization inlet (MION) for fast switching of reagent ion chemistry in atmospheric pressure chemical ionization mass spectrometry (CIMS) applications, *Atmos. Meas. Tech.*, **12**, 6635–6646.

Riva, M., Rantala, P., Krechmer, J. E., Peräkylä, O., Zhang, Y., Heikkinen, L., Garmash, O., Yan, C., Kulmala, M., Worsnop, D., and Ehn, M. (2019) Evaluating the performance of five different chemical ionization techniques for detecting gaseous oxygenated organic species, *Atmos. Meas. Tech.*, **12**, 2403–2421.

DETERMINING THE ACIDITY OF TROPOSPHERIC SUB-MICRON AEROSOL OVER RURAL OKLAHOMA

S. SCHOBESBERGER[1,2], T. YLI-JUUTI [1], J.E. SHILLING[3] , R.A. ZAVERI[3], J.D. FAST[3], AND J.A. THORNTON[2]

[1]Department of Technical Physics, University of Eastern Finland, Kuopio, Finland.

[2]Department of Atmospheric Sciences, University of Washington, Seattle, WA, U.S.A.

[3]Pacific Northwest National Laboratory, Richland, WA, U.S.A.

Keywords: AMMONIA, ACIDITY, AIRBORNE MEASUREMENTS, THERMODYNAMIC MODELING.

INTRODUCTION

Acidity, typically defined by pH, is a key property of atmospheric aerosol particles (Pye *et al.*, 2020). Aerosol pH can control the uptake of semi-volatile vapors, e.g., via the gas-particle partitioning of acids and bases, or via the acid-catalyzed reactive uptake of species such as isoprene epoxydiols (Gaston *et al.*, 2014). It also catalyzes condensed-phase chemistry such as many organic accretion reactions (Hallquist *et al.*, 2009). As a consequence, aerosol pH can modulate atmospheric aerosol loading and composition, and thereby important aerosol properties such as volatility, hygroscopicity and toxicity. It also plays important roles in atmosphere-ecosystem relations, as it affects the acidity of precipitation and governs the dry deposition of inorganic reactive nitrogen (Nenes *et al.*, 2021), a major nutrient for plant growth.

The pH of ambient fine aerosol is extremely challenging to measure directly. Typically, it needs to be inferred by thermodynamic modeling. Commonly used modeling tools calculate a thermodynamic equilibrium of an aqueous aerosol system under given boundary conditions. The aerosol system will contain at least the most important inorganic ions (e.g., H^+, NH_4^+, NO_3^- and SO_4^{2-}) and their respective gases. Often, organic components can be considered as well. For assessing the pH of ambient aerosol, model input is based on measurements of aerosol particle composition and of gas-phase mixing ratios of relevant semi-volatile vapors. A particular challenge is often the measurement of gaseous ammonia (NH_3), as it is prone to interact with instrument surfaces, causing losses, high backgrounds and slow response times. However, knowledge of NH_3 mixing ratios is particularly useful for thermodynamic modeling, as ammonium (NH_4^+) is usually the dominant cation in fine aerosol, while its partitioning is pH-sensitive in typical ambient conditions.

In this study, we use airborne online measurements of sub-micron aerosol composition and trace vapor mixing ratios to infer sub-micron aerosol pH via thermodynamic modeling. The state-of-the-art airborne instrumentation provided for a formidable dataset for that purpose, in particular as trace gas observations included precise measurements of NH_3 as well as nitric acid (HNO_3), albeit alternatingly. The airborne deployment enabled a vertically resolved investigation of the ambient aerosol: throughout the mixed boundary layer as well as in the lower free troposphere.

METHODS

The airborne observations used in this study were made aboard the Gulfstream I aircraft of the U.S. Department of Energy's Atmospheric Radiation Measurement (ARM) Aerial Facility. They were part of the Holistic Interactions of Shallow Clouds, Aerosols, and Land-Ecosystems (HI-SCALE) field campaign that took place in Oklahoma, USA, during the spring and summer/fall of 2016. An overview of the campaign is given in Fast *et al.* (2019). Most of the flying was conducted within a 50-km radius of the

ARM Southern Great Plains field site (SGP) in northern Oklahoma. Vertically, the flying focused on altitudes from the mid boundary layer to the lower free troposphere. The non-refractory composition of sub-micron aerosol particles was measured at 0.08 Hz by a high-resolution time-of-flight aerosol mass spectrometer (AMS; Aerodyne Research, Billerica, MA, USA) (DeCarlo *et al.*, 2006). Ambient air was sampled through an isokinetic inlet that permitted aerosol with aerodynamic diameters < 5 µm. Via a pressure-controlled inlet and an aerodynamic lens, the AMS sub-sampled aerosol particles < 1 µm and flash-vaporized non-refractory components for chemical analysis via electron impact ionization and time-of-flight mass spectrometry. Trace gas mixing ratios were measured at 2 Hz by a high-resolution time-of-flight chemical ionization mass spectrometer CIMS; Tofwerk, Thun, Switzerland, and Aerodyne Research). The sampling and ionization setup included some modifications to enhance quantification of airborne measurements (Lee *et al.*, 2018). Sample was drawn with a large sheath flow into a short ion-molecule reaction region, where trace gases were ionized at 100 mbar via forming adducts with admixed reagent ions, followed by transfer to the high-vacuum mass spectrometer. By switching instrument voltage polarities, iodide anions and deuterated benzene cations were used alternatingly to quantify HNO_3 and NH_3 mixing ratios based on $HNO_3.I^-$ and $NH_3.C_6D_6^+$ adducts, respectively (Schobesberger *et al.*, 2023). For calculating thermodynamic equilibria, including aerosol liquid water and pH, we use primarily the Extended Aerosol Inorganics Model (E-AIM; e.g., Clegg *et al.*, 1998). E-AIM is considered a very accurate thermodynamic model for predicting aerosol pH, at least for inorganic solutions (Pye *et al.*, 2020), while its relatively high computational demands are not an issue for our application. Other models are explored as well, such as the Model for Simulating Aerosol Interactions and Chemistry (MOSAIC; Zaveri *et al.*, 2008), which can provide particle size-resolved pH, and ISORROPIA (Kakavas *et al.*, 2022), which is computationally efficient and is seeing widespread use in chemical transport models.

RESULTS & CONCLUSIONS

Figure 1 presents an example observational dataset obtained during the HI-SCALE research flights, including NH_3 mixing ratio measurements by CIMS (center panel) and AMS measurements of sub-micron aerosol composition (bottom panel). The excerpt spans 15 min of flight time. The first 10 min represent a straight-and-level leg within the mixed boundary layer and cover a horizontal distance of 16 km. Then, a climb was initiated, upon which air temperature first dropped, which may have caused the concurrent increase in particulate nitrate and ammonium, despite gas-phase NH_3 levels staying broadly constant, consistent with lower temperatures favoring the formation of ammonium nitrate. After ~18:27, the climb proceeded into the free troposphere, marked by a temperature inversion and sharp drops in humidity, [NH_3] and aerosol loading. In relative terms, the amount of particulate ammonium dropped only mildly, thereby decreasing the gas-particle partitioning ratio from ~6:1 to ~2.5:1. Assuming aqueous aerosol particles, this ratio can also be directly used to derive aerosol pH values, if equilibrium constants and in particular aerosol liquid water content are known (Hennigan *et al.*, 2015). As the latter was not constrained by measurements during HI-SCALE, it still needs to be estimated by thermodynamic modeling. Similarly, the hygroscopicity and activity of the organic particle phase need to be assessed, along with other possible biases. In any case, the ammonia partitioning ratios as observed in Fig. 1 imply that the aerosol was more acidic in the free troposphere than in the boundary layer below. More robust results for aerosol pH are achieved via detailed thermodynamic modeling with consideration of constraints provided by the simultaneous gas-phase measurements of NH_3 and HNO_3. For instance, a preliminary E-AIM calculation in 'forward mode', based on a set of measurements 300 m above the SGP ground site (13-s average at 18:20; Fig. 1), yields an aerosol pH of 2.4, with the predicted NH_3 partitioning ratio deviating from observations by only 15%, corresponding to an expected error in pH of less than ±0.1. Note that our particle composition measurements have a resolution of 13 s, corresponding to distances of ~1.2 km. But averaging over larger swaths of time, and hence distances, is clearly required to obtain compositions that are more likely to correspond to thermodynamic equilibrium conditions (Fig. 1). Beyond the ability to obtain vertical profiles, the aircraft measurements also give access to the horizontal spatial variabilities in aerosol properties that were indeed observed during HI-SCALE (Fast *et al.*, 2022). Given expected aerosol heterogeneities in all dimensions, we explore the suitability of averaging strategies across horizontal, vertical and time domains.

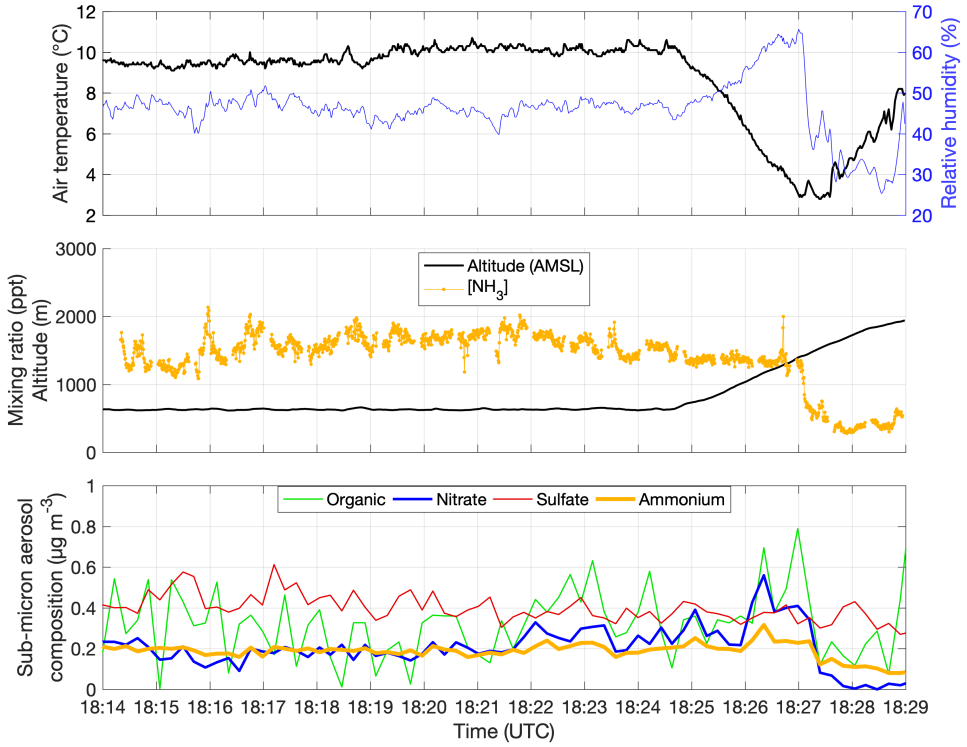

Figure 1. Excerpt of observations during HI-SCALE research flight #13 in the afternoon of 14 May 2016. Times are given in coordinated universal time (UTC), which was 5 h ahead of local time. The top panel shows air temperature (black), and relative humidity (blue) calculated from dew point temperature measurements. The center panel shows altitude above mean sea level (AMSL) in black; ground elevation was between 300 and 350 m. Gas-phase ammonia (NH_3) mixing ratio measurements are shown in orange. The bottom panel shows measured contributions of nitrate, sulfate, ammonium and non-refractory organic material to the mass concentration of sub-micron aerosol particles.

ACKNOWLEDGEMENTS

This study has been supported by the European Commission H2020 Marie Skłodowska-Curie Actions, (grant no. 701958), the Academy of Finland (grant nos. 310682 and 337550), the U.S. Department of Energy (DOE) Office of Science (grant nos. DE-SC0021097 and DE-SC0011791), the Pacific Northwest National Laboratory (grant no. 243766 T.O. 276416) and the National Science Foundation (grant no. DGE-1256082). Pacific Northwest National Laboratory (PNNL) is operated for DOE by Battelle Memorial Institute under contract DE-AC05-76RL01830.

REFERENCES

Clegg S.L., P. Brimblecombe, A.S. Wexler (1998). Thermodynamic Model of the System H+−NH4+−SO42-−NO3-−H2O at Tropospheric Temperatures, *J. Phys. Chem. A* **102**, 2137-2154.

DeCarlo P.F., J.R. Kimmel, A. Trimborn, M.J. Northway, J.T. Jayne, A.C. Aiken, M. Gonin, K. Fuhrer, T. Horvath, K.S. Docherty, D.R. Worsnop, J.L. Jimenez (2006). Field-Deployable, High-Resolution, Time-of-Flight Aerosol Mass Spectrometer, *Anal. Chem.* **78**, 8281-8289.

Fast J.D., L.K. Berg, L. Alexander, D. Bell, E. D'Ambro, J. Hubbe, C. Kuang, J. Liu, C. Long, A. Matthews, F. Mei, R. Newsom, M. Pekour, T. Pinterich, B. Schmid, S. Schobesberger, J. Shilling, J.N. Smith, S. Springston, K. Suski, J.A. Thornton, J. Tomlinson, J. Wang, H. Xiao, A. Zelenyuk

(2019). Overview of the HI-SCALE Field Campaign: A New Perspective on Shallow Convective Clouds, *Bull. Am. Meteorol. Soc.* **100**, 821-840.

Fast J.D., D.M. Bell, G. Kulkarni, J. Liu, F. Mei, G. Saliba, J.E. Shilling, K. Suski, J. Tomlinson, J. Wang, R. Zaveri, A. Zelenyuk (2022). Using aircraft measurements to characterize subgrid-scale variability of aerosol properties near the Atmospheric Radiation Measurement Southern Great Plains site, *Atmos. Chem. Phys.* **22**, 11217-11238.

Gaston C.J., T.P. Riedel, Z. Zhang, A. Gold, J.D. Surratt, J.A. Thornton (2014). Reactive Uptake of an Isoprene-Derived Epoxydiol to Submicron Aerosol Particles, *Environ. Sci. Technol.* **48**, 11178-11186.

Hallquist M., J.C. Wenger, U. Baltensperger, Y. Rudich, D. Simpson, M. Claeys, J. Dommen, N.M. Donahue, C. George, A.H. Goldstein, J.F. Hamilton, H. Herrmann, T. Hoffmann, Y. Iinuma, M. Jang, M.E. Jenkin, J.L. Jimenez, A. Kiendler-Scharr, W. Maenhaut, G. McFiggans, T.F. Mentel, A. Monod, A.S.H. Prevot, J.H. Seinfeld, J.D. Surratt, R. Szmigielski, J. Wildt (2009). The formation, properties and impact of secondary organic aerosol: current and emerging issues, *Atmos. Chem. Phys.* **9**, 5155-5236.

Hennigan C.J., J. Izumi, A.P. Sullivan, R.J. Weber, A. Nenes (2015). A critical evaluation of proxy methods used to estimate the acidity of atmospheric particles, *Atmos. Chem. Phys.* **15**, 2775-2790.

Kakavas S., S.N. Pandis, A. Nenes (2022). ISORROPIA-Lite: A Comprehensive Atmospheric Aerosol Thermodynamics Module for Earth System Models, *Tellus B* **74**, 1-23.

Lee B.H., F.D. Lopez-Hilfiker, P.R. Veres, E.E. McDuffie, D.L. Fibiger, T.L. Sparks, C.J. Ebben, J.R. Green, J.C. Schroder, P. Campuzano-Jost, S. Iyer, E.L. D'Ambro, S. Schobesberger, S.S. Brown, P.J. Wooldridge, R.C. Cohen, M.N. Fiddler, S. Bililign, J.L. Jimenez, T. Kurtén, A.J. Weinheimer, L. Jaegle, J.A. Thornton (2018). Flight Deployment of a High-Resolution Time-of-Flight Chemical Ionization Mass Spectrometer: Observations of Reactive Halogen and Nitrogen Oxide Species, *J. Geophys. Res. Atmos.* **123**, 7670-7686.

Nenes A., S.N. Pandis, M. Kanakidou, A.G. Russell, S. Song, P. Vasilakos, R.J. Weber (2021). Aerosol acidity and liquid water content regulate the dry deposition of inorganic reactive nitrogen, *Atmos. Chem. Phys.* **21**, 6023-6033.

Pye H.O.T., A. Nenes, B. Alexander, A.P. Ault, M.C. Barth, S.L. Clegg, J.L. Collett Jr, K.M. Fahey, C.J. Hennigan, H. Herrmann, M. Kanakidou, J.T. Kelly, I.T. Ku, V.F. McNeill, N. Riemer, T. Schaefer, G. Shi, A. Tilgner, J.T. Walker, T. Wang, R. Weber, J. Xing, R.A. Zaveri, A. Zuend (2020). The acidity of atmospheric particles and clouds, *Atmos. Chem. Phys.* **20**, 4809-4888.

Schobesberger S., E.L. D'Ambro, L. Vettikkat, B.H. Lee, Q. Peng, D.M. Bell, J.E. Shilling, M. Shrivastava, M. Pekour, J. Fast, J.A. Thornton (2023). Airborne flux measurements of ammonia over the southern Great Plains using chemical ionization mass spectrometry, *Atmos. Meas. Tech.* **16**, 247-271.

Zaveri R.A., R.C. Easter, J.D. Fast, L.K. Peters (2008). Model for Simulating Aerosol Interactions and Chemistry (MOSAIC), *J. Geophys. Res. Atmos.* **113**.

SEASONALITY IN SIZE-SEGREGATED PARTICLE NUMBER CONCENTRATIONS IN AN URBAN LOCATION

M. SEBASTIAN[1], V. KANAWADE[1], P. CHERIAN[1]

[1]*Centre for Earth, Ocean and Atmospheric Sciences, University of Hyderabad, Hyderabad, India*

Keywords: ULTRAFINE PARTICLES, NUCLEATION, GROWTH. PRIMARY EMISSIONS

INTRODUCTION

Atmospheric aerosols vary in a wide size range with four orders of magnitude difference between the smallest and the largest particle. The spatial and temporal variability in aerosol emissions strongly modulates the dynamical behaviour and associated properties of aerosols [Costabile et al., 2009; Kerminen et al., 2018; Zhang et al., 2015]. The primary emissions and secondary formation via gas-to-particle conversion are the major contributors to the total aerosol numbers in the atmosphere[Rönkkö et al., 2017; Wu et al., 2008]. The aim of this work is to quantify the contribution of different aerosol modes to the total aerosol mass, and thereby haze formation.

METHODS

In this study, we have used long-term (2019-2012) observations of particle number size distribution from the nano Condensation Nucleus Counter (nCNC) in the size range from 1 to 3 nm and Scanning Mobility Particle Sizer (SMPS) from 10 nm to 600 nm in an urban location, Hyderabad, in India. We have calculated size-segregated particle number concentrations in four major modes such as cluster mode (sub-3nm), nucleation mode (<25 nm), Aitken mode (25-100 nm) and accumulation mode (100-600 nm). We further used in-situ measured particulate matter of less than 2.5 µm ($PM_{2.5}$) to deduce hazy and non-hazy days.

CONCLUSIONS

Size-segregated particle number concentrations showed a distinct seasonal variation, with the highest concentrations in spring (March-May) and the lowest concentrations during winter (December-February). Our results also show that the concentrations of cluster mode particles were the highest at low $PM_{2.5}$ levels and the lowest at high $PM_{2.5}$ levels, indicating that cluster mode particles are efficiently scavenged by high concentrations of pre-existing particles. Seasonal variation in particle number concentrations is highly related to planetary boundary layer evolution, temperature (which determines the oxidation extent of the atmosphere), and pre-existing particles (efficient scavenging of smaller particles). We will further show

analyses on seasonal variability in size-segregated particle number concentrations on hazy and non-hazy days.

ACKNOWLEDGEMENTS

VPK acknowledge financial support from the Department of Science & Technology (DST)-Science Engineering Research Board (SERB; ECR/2016/001333) and DST-Climate Change Division Program (Aerosol/89/2017). MS acknowledge the Institute of Eminence, University of Hyderabad (sanction no. UoH/IoE/RC1/RC1-20-014).

REFERENCES

Costabile, F., W. Birmili, S. Klose, T. Tuch, B. Wehner, A. Wiedensohler, U. Franck, K. König, and A. Sonntag (2009), Spatio-temporal variability and principal components of the particle number size distribution in an urban atmosphere, *Atmos. Chem. Phys.*, *9*(9), 3163-3195.

Kerminen, V. M., X. Chen, V. Vakkari, T. Petäjä, M. Kulmala, and F. Bianchi (2018), Atmospheric new particle formation and growth: review of field observations, *Environmental Research Letters*, *13*(10), 103003.

Rönkkö, T., et al. (2017), Traffic is a major source of atmospheric nanocluster aerosol, *Proceedings of the National Academy of Sciences*, 201700830.

Wu, Z., M. Hu, P. Lin, S. Liu, B. Wehner, and A. Wiedensohler (2008), Particle number size distribution in the urban atmosphere of Beijing, China, *Atmospheric Environment*, *42*(34), 7967-7980.

Zhang, R., G. Wang, S. Guo, M. L. Zamora, Q. Ying, Y. Lin, W. Wang, M. Hu, and Y. Wang (2015), Formation of Urban Fine Particulate Matter, *Chemical Reviews*, *115*(10), 3803-3855.

AEROSOLS AND CCN MEASURED IN SEOUL FROM 2019 TO 2021

PYOSUK SEO[1], SEONG SOO YUM[1], MINSU PARK[1] and CHANWOO AHN[1]

[1]*Department of Atmospheric Sciences, Yonsei University, Seoul, Republic of Korea.*

Keywords: Aerosol, Cloud Condensation Nuclei, New Particle Formation events, Back trajectory.

INTRODUCTION

The rapid industrial development of the East Asian region since the late 20th century has led to a significant increase in anthropogenic aerosol emissions, which have been a major cause of health and climate issues in the region (e.g., Andreae and Rosenfeld, 2008). However, there have been many efforts to restrict aerosol emissions in the region, leading to a significant decrease in aerosol concentrations in recent decades. In this study, we present data on atmospheric aerosol and cloud condensation nuclei (CCN) concentrations measured in Seoul, South Korea from 2019 to 2021, which includes the COVID-19 social lockdown period. We compare these recent measurements to those from previous decades. Since Seoul is a representative megacity in East Asia, the data from this region may provide insights into the overall trend of aerosol concentration in urban regions.

DATA and METHODS

The aerosol number concentration (N_{CN}) and size distribution were measured using a condensation particle counter (CPC; TSI 3772) and a scanning mobility particle sizer (SMPS; TSI SMPS), respectively. The CCN number concentration (N_{CCN}) was measured by a cloud condensation nuclei counter (CCNC; DMT CCN-100). A ceilometer is used to determine the planetary boundary. Surface meteorological parameters were obtained from the Korea Meteorological Administration's weather station data, and traffic volume data were obtained from the Korean Transport Operation & Information Service (TOPIS). Finally, air mass back trajectories were obtained from NOAA HYSPLIT model and the Potential Source Contribution Function (PSCF) (Herenz et al., 2019) is applied to understand the transport of air masses to Seoul.

CONCLUSIONS

The annual average N_{CN} and N_{CCN} at 0.6% supersaturation were compared between 2019, a non-COVID-19 year, and 2020 and 2021, which were affected by COVID-19 social lockdowns. The results showed that both N_{CN} and N_{CCN} were lower in 2020 and 2021 compared to 2019. Specifically, in 2019, the average N_{CN} was 14090 ± 7045 and the average N_{CCN} was 3098 ± 1940, while in 2020, they were 12007 ± 6402 and 2717 ± 1838, respectively, and in 2021, they were 10980 ± 5873 and 2349 ± 1414, respectively. When these three year data were analyzed together, we found that N_{CN} and N_{CCN} were lower during the summer season compared to the winter season, as a result of the monsoon and reduced anthropogenic emissions. The factors that affected N_{CN} varied by season. In the summer, traffic volume was the most significant factor in determining aerosol number concentration. However, during the winter season, temperature, wind speed, and relative humidity also played an important role in N_{CN}. PBL height showed significant influence on the average diurnal variation of N_{CN}, but its effect on the overall trend was relatively small. PSCF analysis indicated that the aerosols in Seoul originated from diverse regional air mass inflows, which

varied by season. During the summer season, N_{CN} decreased when the air mass originated from the ocean. However, in winter, N_{CN} tended to be higher when the air mass originated from the north of Mongolia due to the occurrence of New Particle Formation (NPF) events. To see a long term trend, N_{CN} and N_{CCN} from previous studies conducted in Seoul (Kim et al., 2014, Kim et al., 2017, Kim et al., 2018) were combined together as shown in Fig. 1. We see a generally declining trend of N_{CN} and N_{CCN} from 2004 to 2021, which is likely due to a decrease in air pollutant emissions. Further detailed results will be presented at the conference.

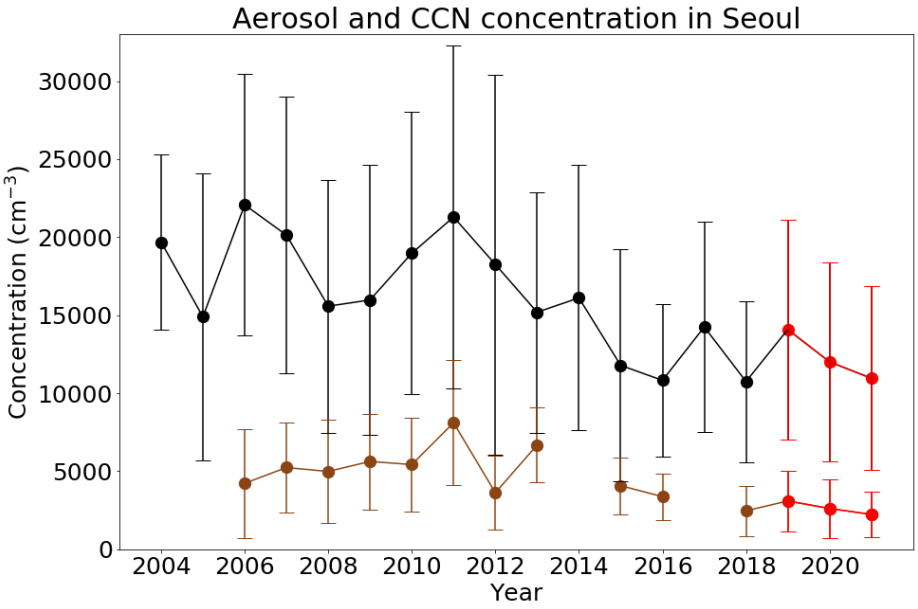

Figure 1. Aerosol (Black) and CCN (Brown) number concentration in Seoul, Red color indicates the data analyzed in this study.

ACKNOWLEDGEMENTS

This work was supported by the National Research Foundation of Korea (NRF) grant funded by the Korea government (MSIT) (NO.NRF-

2021R1A2B5B02002458).

REFERENCES

Andreae, M. O. and Rosenfeld, D., Aerosol-cloud-precipitation interactions. Part 1. The nature and sources of cloud-active aerosols, Earth-Science Reviews, 13-41, 10.1016/j.earscirev.2008.03.001, 2008.

Herenz, P., Wex, H., Mangold, A., Laffineur, Q., Gorodestkaya, I., Fleming, Z., Panagi, M., and Stratmann, F., CCN measurements at the Princess Elisabeth Antarctica Research Station during three austral summers. Atmos. Chem. Phys., 19, 275-294, https://doi.org/10.5194/acp-19-275-2019, 2019.

Kim, J. H., Yum, S. S., Shim, S., Kim, W. J., Park, M., Kim, J.-H., Kim, M.-H., and Yoon, S.-C.: On the submicron aerosol distributions and CCN number concentrations in and around the Korean Peninsula, Atmos. Chem. Phys., 14, 8763-8779, https://doi.org/10.5194/acp-148763-2014, 2014.

Kim, N., Park, M., Yum, S.S., Park, J.S., Song, I.H., Shin, H.J., Ahn , J.Y., Kwak, K.-H., Kim, H., Bae, G.-N., and Lee, G., Hygroscopic properties of urban aerosols and their cloud condensation nuclei activities measured in Seoul during the MAPS-Seoul campaign. Atmos. Environ. 153, 217-232. http://dx.doi.org/10.1016/j.atmosenv.2017.01.034, 2017.

Kim, N., Park, M., Yum, S. S., Park, J. S., Shin, H. J., and Ahn , J. Y., Impact of urban aerosol properties on cloud condensation nuclei (CCN) activity during the KORUS-AQ field campaign, Atmos. Environ. 185, 221-236, https://doi.org/10.1016/j.atmosenv.2018.05.019, 2018.

HIGH GASEOUS METHANESULFONIC ACID PRODUCTION FROM DIMETHYL SULFIDE OXIDATION AND INVESTIGATE ITS CONTRIBUTION TO AEROSOL FORMATION IN REMOTE REGIONS

J. SHEN[1], R. BAALBAKI[1], W. SCHOLZ[2], X-C. HE[1,3], J. KIRKBY[4], M. KULMALA[1], F. BIANCHI[1], K. LEHTIPALO[1,3], D.R. WORSNOP[1,5], and THE CLOUD COLLABORATION

[1]Institute for Atmospheric and Earth System Research/Physics, Faculty of Science, University of Helsinki, 00014 Helsinki, Finland

[2]Institute of Ion Physics and Applied Physics, University of Innsbruck, 6020 Innsbruck, Austria

[3]Finnish Meteorological Institute, 00560 Helsinki, Finland

[4]CERN, the European Organization for Nuclear Research, 1211 Geneva, Switzerland

[5]Aerodyne Research, Inc., Billerica, 01821 MA, USA

Keywords: DMS oxidation, H_2SO_4 to MSA ratio, remote regions, free troposphere, new particle formation.

INTRODUCTION

In the remote marine atmosphere, dimethyl sulfide (DMS) oxidation is essential to new particle formation and initial particle growth as the sole source of sulfuric acid (H_2SO_4) and methanesulfnic acid (MSA; CH_3SO_3H) (Kreidenweis *et al.*, 1988; Covert *et al.*, 1992; Dawson *et al.*, 2012; Beck *et al.*, 2012) in the absence of anthropogenic and volcanic emission of sulfur dioxide (SO_2) (Dawson *et al.*, 1998; Bardouki *et al.*, 2003; Nowak *et al.*, 2001; Edtbauer *et al.*, 2020). However, estimating H_2SO_4 and MSA concentrations from DMS oxidation with the current widely used mechanism has remained highly uncertain. For example, ambient observations by Beck *et al.* (2021) and Jokinen *et al.* (2018) have shown high gas-phase MSA concentrations larger than H_2SO_4 in polar regions, indicating that MSA production from DMS oxidation is underestimated at subzero temperatures. Thus, investigating the DMS oxidation mechanism under the conditions relevant to polar regions is critical to better predict MSA and H_2SO_4 from DMS oxidation and further understand aerosol formation in remote marine environments.

Besides in the marine atmosphere, high MSA concentrations were also observed in the free tropospheric air at 5420 m altitude in the Bolivian Andes, 330 km away from the Pacific coast, which is plausibly related to the DMS-containing air masses that originated from the Pacific Ocean after convective lifting. All these pieces of evidence indicate the relevance of MSA in remote regions (e.g., polar regions and the free troposphere), where temperatures and condensation sink are low. Although MSA nucleation mechanisms have been investigated for decades (Hoppel *et al.*, 1987; Kreidenweis *et al.*, 1988), many aspects are still unclear, especially under atmospherically relevant conditions. Therefore, understanding the MSA nucleation mechanism and its contribution to initial particle growth becomes important in estimating the impact of DMS on the formation of aerosols and cloud condensation nuclei (CCN) in remote regions.

METHODS

In this study, we conducted experiments in the CERN Cosmics Leaving Outdoor Droplets (CLOUD) chamber to investigate the OH-initiated DMS oxidation mechanism for polar regions conditions

with an array of state-of-art chemical ionization mass spectrometers. With the CLOUD chamber, we were able to lower the concentration of vapor precursors to atmospherically representative conditions and experimentally investigate DMS oxidation under subzero conditions (-10 °C). The different chemical ionization mass spectrometers were used to quantify numerous DMS oxidation products like H_2SO_4, MSA, dimethyl sulfoxide (DMSO; $CH_3S(O)CH_3$), dimethyl sulfone ($DMSO_2$; $CH_3S(O)_2CH_3$), and methanesulfinic acid ($CH_3S(O)OH$, MSIA), as well as to identify several intermediate products including hydroperoxymethyl thioformate (HPMTF; $HOOCH_2SCHO$), methyl thioformate (CH_3SCHO), CH_3SOH and $CH_3S(O)_2OOH$. The measured DMS and its oxidation products were then used to evaluate and constrain the oxidation mechanism via a numeric kinetic model.

We also investigated the role of MSA in the nucleation and early growth of aerosol particles in the CLOUD chamber at different temperatures (+10 °C, -10 °C, -30 °C, and -50 °C). A wide range of aerosol instrumentation including a nano Condensation Nucleus Counter (nCNC, Airmodus Ltd.), a nano Scanning Mobility Particle Sizer (nanoSMPS, TSI Inc.), and a Neutral cluster and Air Ion Spectrometer (NAIS, Airel Ltd.) were deployed for a full-size range (1.3-1000 nm) measurement of particle and ion size distribution. The composition of particles was examined using a Filter Inlet for Gases and AEROsols (FIGAERO) iodide (I^-) chemical ionization mass spectrometer (CIMS).

A similar suite of chemical ionization mass spectrometers was deployed to study the composition of different air masses at the *Chacaltaya Global Atmosphere Watch (GAW) Station* in the Bolivian Andes (5240 m) between December 2017 and the beginning of June 2018. The location of the station is unique, where the air masses can be influenced by the free tropospheric air that originates from the Pacific ocean. It is, therefore, possible to observe DMS and its oxidation products and investigate their contribution to aerosols.

CONCLUSIONS

During the experiments in the CLOUD chamber, we noticed a significant production of MSA from OH-initiated DMS oxidation under atmospherically-relevant conditions, especially at low temperatures. The results showed that the production of gas-phase MSA was highly dependent on temperature, increasing dramatically as the temperature decreased. This is because MSA formation involves thermal decomposition reactions for which the reaction rate coefficient is exponentially dependent on temperature. As shown in Figure 1, the observed ratio of gas-phase H_2SO_4 to MSA was small (below one) at low temperatures. The impact of NO_x on this ratio was less pronounced compared to the temperature effect. We also investigated heterogeneous reactions that occur on the chamber walls, with only DMS and O_3 in the chamber, showing that heterogeneous reactions influence the distribution of DMSO and $DMSO_2$ but is predominant only for $DMSO_2$ production. With the above findings, we developed a numerical model to constrain specific mechanisms, determining that MSIA is the key precursor dominating MSA production, consistent with observations in polar regions. This emphasizes the significance of MSA in the natural sulfur cycle and highlights the need to update the atmospheric chemistry modules in aerosol simulation models with the new mechanism to enhance the accuracy of aerosol simulation in marine remote areas.

During the measurements at the Global Atmosphere Watch (GAW) station Chacaltaya in the Bolivian Andes, we extracted the periods influenced by free tropospheric air from the Pacific region that may contain DMS and its oxidation products. The air masses that reach the station have been transported over long distances but still contained large amounts of DMS and its oxidation products, including DMSO, $DMSO_2$, MSIA, CH_3SCHO, CH_3SOH, MSA, and H_2SO_4. As shown in Figure 2, the measured MSA shows much higher concentrations in the free tropospheric air than in the boundary layer, up to 4×10^6 cm^{-3}. The back trajectory calculations show that DMS and relevant compounds in free tropospheric air masses originated from above the ocean (distance >330 km)

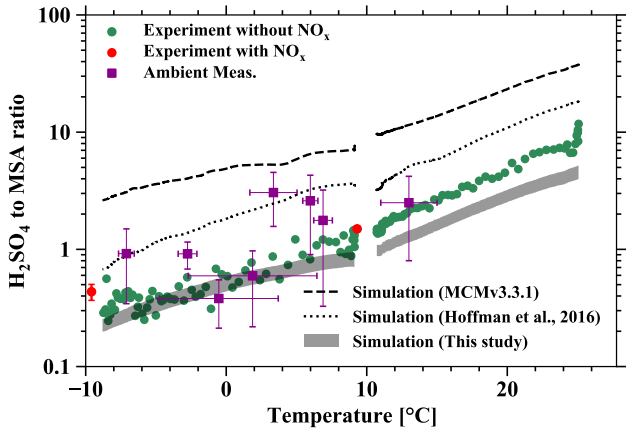

Figure 1: Temperature dependence of the H_2SO_4 to MSA ratio in the CLOUD chamber. The NO_2 and NO differences between the red and green circles are around 400 pptv and 8 pptv. Purple square symbols are the daytime average of ambient measurement from Beck *et al.* (2021), Jokinen *et al.* (2018), and Berresheim *et al.* (2002). The simulation results in this study are presented as gray rectangles by varying the reaction rate coefficient of the isomerization of methylthiomethylperoxy radical (CH_3SCH_2OO, MSP).

without local surface contact. All these pieces of evidence are indicative of the potential impact of marine DMS emissions on the distribution of sulfur-containing vapors in the free troposphere far away from the ocean.

Both the chamber experiments and ambient observation show that MSA concentration is highly possible to reach high values in remote regions. To further investigate its contribution to aerosol formation in these remote regions, MSA(-NH_3) nucleation and growth experiments under atmospheric representative conditions were performed in the CLOUD chamber. The ratio of MSA to H_2SO_4 varied depending on DMS oxidation, reaching a value as high a factor of 15 at -30 °C, which reduced the contribution of H_2SO_4 to nucleation. We will present the results of our MSA-(NH_3) nucleation and growth experiments in this presentation.

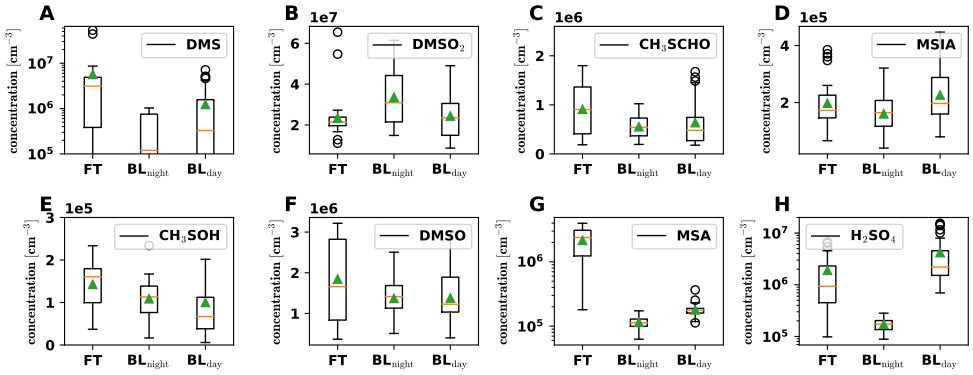

Figure 2: DMS oxidation products in the gas phase, detected by PTR3 and nitrate-CIMS at Chacaltaya in FT (free troposphere without boundary layer influence), BL_{night}(within boundary layer during night time), BL_{day} (within boundary layer during day time) air masses.

ACKNOWLEDGEMENTS

This work was supported by European Organization for Nuclear Research (CERN), the EU H2020 programme Marie Sklodowska Curie ITN 'CLOUD-TRAIN' (764991), CHAPAs (grant no. 850614). We thank everyone for contributing to the measurements at CLOUD and at Chacaltaya.

REFERENCES

Kreidenweis, S. & Seinfeld, J. (1988). Nucleation of sulfuric acid-water and methanesulfonic acid-water solution particles: Implications for the atmospheric chemistry of organosulfur species. *Atmospheric Environment*, **22**, 283-296.

Covert, D., Kapustin, V.N and et al. (1992). New particle formation in the marine boundary layer. *Journal of Geophysical Research: Atmospheres*, **97**, 20581–20589.

Dawson, M.L., Varner, M.E and et al. (2012). Simplified mechanism for new particle formation from methanesulfonic acid, amines, and water via experiments and ab initio calculations. *Proceedings of the National Academy of Sciences*, **109**, 18719–18724.

Beck, L.J., Sarnela, N and et al. (2021). Differing Mechanisms of New Particle Formation at Two Arctic Sites. *Geophysical Research Letters*, **48**, e2020GL091334.

Davis, D., Chen, G and et al. (1998). DMS oxidation in the Antarctic marine boundary layer: Comparison of model simulations and held observations of DMS, DMSO, $DMSO_2$, H_2SO_4(g), MSA(g), and MSA(p) *Journal of Geophysical Research: Atmospheres*, **103**, 1657–1678.

Bardouki, H., Berresheim, H and et al. (2003). Gaseous (DMS, MSA, SO_2, H_2SO_4 and DMSO) and particulate (sulfate and methanesulfonate) sulfur species over the northeastern coast of Crete. *Atmospheric Chemistry And Physics*. **3**, 1871-1886.

Nowak, J., Davis, D and et al. (2001). Airborne observations of DMSO, DMS, and OH at marine tropical latitudes. *Geophysical Research Letters*. **28**, 2201-2204.

Edtbauer, A., Stonner, C and et al. (2020). A new marine biogenic emission: methane sulfonamide (MSAM), dimethyl sulfide (DMS), and dimethyl sulfone ($DMSO_2$) measured in air over the Arabian Sea. *Atmospheric Chemistry And Physics*. **20**, 6081-6094.

Jokinen, T., Sipila, M and et al. (2018). Ion-induced sulfuric acid-ammonia nucleation drives particle formation in coastal Antarctica. *Science Advances*. **4**, eaat9744.

Berresheim, H., Elste, T and et al. (2002). Gas-aerosol relationships of H_2SO_4, MSA, and OH: Observations in the coastal marine boundary layer at Mace Head, Ireland. *Journal Of Geophysical Research: Atmospheres*. **107**, PAR 5-1-PAR 5-12.

Hoppel, W. A. (1987). Nucleation in the MSA-water vapor system. *Atmospheric Environment*. **21**, 2703-2709.

Degradation of PAHs during long range transport based on simultaneous measurements in East Asia with the use of international observational network on isolated islands

K. Shimada[1,5,2*], M. Nohchi[2], X. Yang [3], T. Sugiyama[4], K. Miura[5], A. Takami[6], K. Sato[6], X. Chen[3], S. Kato[7], Y. Kajii[4], F. Meng[3] and S. Hatakeyama[1,5,9]

[1] Global Innovation Research Organization, Tokyo University of Agriculture and Technology, 3-5-8 Saiwaicho, Fuchu, Tokyo, 183-8509, Japan
[2] University of the Ryukyus, Okinawa, Japan, 1 Senbaru, Nishihara-cho, Nakagami-gun, Okinawa, Japan
[3] State Key Laboratory of Environmental Criteria and Risk Assessment, Chinese Research Academy of Environmental Sciences, 8 Dayangfang, Beiyuan Road, Chaoyang, Beijing, 100012, China
[4] Graduate School of Engineering, Kyoto University, Kyoto, 606-8501, Japan
[5] Graduate School of Agriculture, Tokyo University of Agriculture and Technology, 3-5-8 Saiwaicho, Fuchu, Tokyo, 183-8509, Japan
[6] Center for Regional Environmental Research, National Institute for Environmental Studies, 16-2 Onogawa, Tsukuba, Ibaraki, 305-8506, Japan
[7] Department of Applied Chemistry, Faculty of Urban Environmental Sciences, Tokyo Metropolitan University, 1-1 Minami-oosawa, Hachioji, Tokyo, 192-0397, Japan
[8] Department of Natural Resources, Graduate School of Global Environmental Studies, Kyoto University, Yoshida-honmachi, Sakyoku, Kyoto, Kyoto, 606-8501, Japan
[9] Present address: Asia Center for Air Pollution Research, 1182, Sowa, Nishiku, Niigatashi, Niigata, 950-2144, Japan

Keywords: PAHs, CHAAMS, Tuoji Island, PAH, degradation, coal combustion

ABSTRACT

The abstracts produced should be camera-ready, and from ONE to FOUR pages long on separate sheets of paper. On the first page of the abstract, start typing text here (about 7cm from the top of the typing area). Text on the next pages can start at the top of the typing area (where the title is on this page). All parts of the abstract should lie in a box 240 mm high and 165 mm wide. There should be a top margin of 29 mm depth and a left margin 23 mm wide. Times New Roman font is preferred, and you should use a character size of 11pt. The title should be in bold capitals, the authors' names should be in capitals, and the addresses of authors should be in lower case. All these should be centred.

We investigated the degradation of polycyclic aromatic hydrocarbons (PAHs) during long-range transport. Aerosols were collected simultaneously at remote sites on Tuoji Island, China; Fukue Island, Japan; and the Cape Hedo Atmosphere and Aerosol Measurement Station (CHAAMS), Okinawa, Japan in April, October, and December from 2012 to 2013. These remote sites were convenient for investigating the degradation of PAHs during long-range transport. PAHs were analyzed via gas chromatography/mass spectrometry. We identified air masses that passed over all sites and combined our measurements with a chemical transport model. We estimated the relative contributions of the PAHs at the three sites by normalizing the PAH concentrations to elemental carbon. Benzo[a]pyrene persisted in 5–16% of samples. The results of this study are consistent with laboratory studies in which secondary organic aerosol (SOA) coatings protected PAHs from degradation by ozone. We detected an inhibition of the degradation PAHs by SOA coatings by collecting PAHs simultaneously at the three sites. To elucidate the major sources of the SOAs, we carried out a positive matrix factorization analysis to identify the major sources of SOA coating, which controls the lifetime of PAHs. In spring and winter, the contribution of vehicle emissions was higher (46%) at Tuoji Island than at CHAAMS (13%). In contrast, the contribution of coal combustion was higher at CHAAMS (59%) than at Tuoji Island (28%). This result implies that during long-range transport, PAHs derived from coal combustion are more slowly degraded than PAHs derived from vehicle emissions. We

found that the viscosity of SOA coatings derived from vehicle emissions in China was low, and the corresponding PAHs were rapidly degraded. In contrast, the viscosity of SOA coatings derived from coal combustion was high, and degradation of the corresponding PAHs was relatively slow. These results imply that PAHs derived from coal combustion have long lifetime.

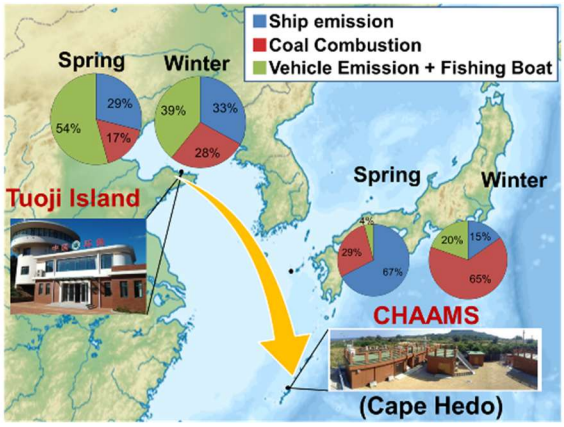

TIGHT COUPLING OF SURFACE AND IN PLANT BIOCHEMISTRY AND CONVECTION GOVERNS KEY FINE PARTICULATE COMPONENTS OVER THE AMAZON

M. SHRIVASTAVA[1], Q.Z. RASOOL[1], A. ZELENYUK[1], B.ZHAO[1], M.OCTAVIANI[1], R.A.ZAVERI[1], A.ZELENYUK[1], B.GAUDET[1], Y.LIU[1], J.E.SHILLING[1] J.SCHNEIDER[2], C.SCHULZ[3], M.ZOGER[4], S.T.MARTIN[5], J.YE[6], A.GUENTHER[7], R.F.SOUZA[8], M.WENDISCH[9], U.POSCHL[10]

[1]Pacific Northwest National Laboratory, Richland, WA, USA 99352
[2]*Particle Chemistry Department, Max Planck Institute for Chemistry, Mainz 55128, Germany*
[3]Leibniz Centre for Agricultural Landscape Research; Müncheberg 15374, Germany
[4]*Flight Experiments, German Aerospace Center (DLR), Oberpfaffenhofen 82234, Germany*
[5]*Department of Earth and Planetary Sciences, Harvard University, Cambridge, Massachusetts 02138*
[6]Southern University of Science and Technology; Shenzhen, Guangdong, 518055, China
[7]*University of California Irvine, Irvine, California 92697, United States*
[8]*Amazonas State University, Av Darcy Vargas, Manaus, Amazonas 69050020, Brazil*
[9]*Leipzig Institute for Meteorology, University of Leipzig, Stephanstr. 3, Leipzig 04103, Germany*
[10]*Multiphase Chemistry Department, Max Planck Institute for Chemistry, Mainz 55128, Germany*

Keywords: SECONDARY ORGANIC AEROSOL, PLANT BIOCHEMISTRY, ISOPRENE EPOXYDIOLS, AMAZON RAINFOREST, CONVECTION

INTRODUCTION

Combining unique high-altitude aircraft measurements and detailed regional model simulations, we show that in-plant biochemistry plays a central but previously unidentified role in fine particulate-forming processes and atmosphere–biosphere–climate interactions over the Amazon rainforest. Isoprene epoxydiol secondary organic aerosols (IEPOX-SOA) are key components of sub-micrometer aerosol particle mass throughout the troposphere over the Amazon rainforest and are traditionally thought to form by multiphase chemical pathways. Here, we show that these pathways are strongly inhibited by the solid thermodynamic phase state of aerosol particles and lack of particle and cloud liquid water in the upper troposphere. Strong diffusion limitations within organic aerosol coatings prevailing at low temperatures and low relative humidity in the upper troposphere strongly inhibit the reactive uptake of IEPOX to inorganic aerosols. We find that direct emissions of 2-methyltetrol gases formed by in-plant biochemical oxidation and/or oxidation of deposited IEPOX gases on the surfaces of soils and leaves and their transport by cloud updrafts followed by their condensation at low temperatures could explain over 90% of the IEPOX-SOA mass concentrations in the upper troposphere. Our simulations indicate that even near the surface, direct emissions of 2-methyltetrol gases represent a ubiquitous, but previously unaccounted for, source of IEPOX-SOA. Our results provide compelling evidence for new pathways related to land surface–aerosol–cloud interactions that have not been considered previously.

METHODS

Measurements of IEPOX-SOA were made onboard the German HALO aircraft both near the surface and the upper troposphere using an Aerosol Mass Spectrometer (AMS) over the entire atmospheric column from 0-14 km altitudes over the Amazon (Schulz et al. 2018). These high-altitude measurements of IEPOX-SOA are especially important, providing a unique opportunity to evaluate our knowledge of processes governing IEPOX-SOA formation. Here, we conduct detailed regional model simulations using the Weather Research and Forecasting Model coupled to Chemistry (WRF-Chem) over the Amazon at a horizontal grid spacing of 10 km covering 1500 km x1000 km centered on the Manaus urban area in the Amazon. We implemented detailed mechanisms and equations governing the multiphase reactive uptake of IEPOX and the role of viscous SOA coatings limiting IEPOX-SOA formation. Combining unique high-altitude aircraft measurements, laboratory-based process modeling, and detailed regional model

simulations, we show that in-plant biochemistry plays a central but previously unidentified role in fine particulate-forming processes and atmosphere–biosphere–climate interactions over the Amazon rainforest (Shrivastava et al. 2022).

CONCLUSIONS

IEPOX-SOA are key components of ultrafine aerosol particle mass throughout the atmospheric column over the Amazon rainforest and are traditionally thought to form by multiphase chemical pathways. We showed that these pathways are strongly inhibited by the solid phase of aerosol particles and lack of cloud liquid water in the cold and dry regions of the upper troposphere. Using detailed regional model simulations, we found that using traditional multiphase chemistry underpredicts the IEPOX-SOA observed by aircraft at high altitudes by more than an order of magnitude. Incorporating newly discovered processes related to the release of 2-methyltetrol gases formed by in-plant biochemistry on the surfaces of soils and leaves, their transport by clouds to the upper troposphere, and condensation to particles closed the large model-measurement gaps and helped explain the aircraft measurements of IEPOX-SOA in the upper troposphere. The results provide compelling evidence for new pathways related to land surface–aerosol–cloud interactions that have not been previously considered.

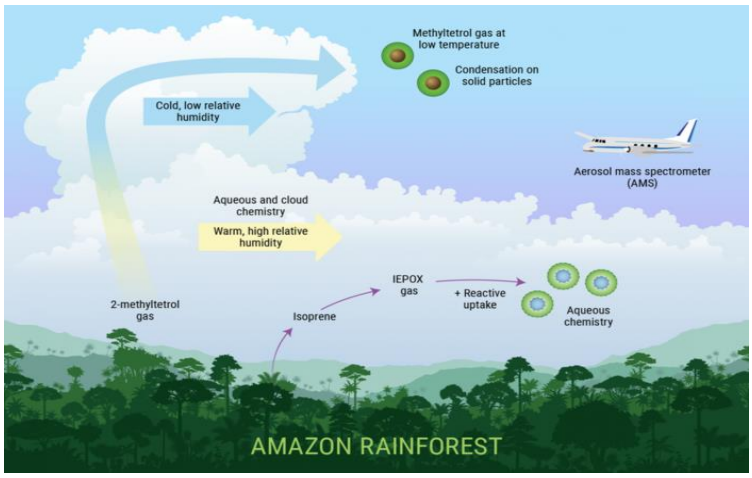

Fig. 1. In-plant biochemistry and/or surface chemistry causes the release of methyltetrol gases. Cloud updrafts then transport the gases to the upper troposphere where they condense to particles at low-temperatures. This uniquely explains the IEPOX-SOA mass loadings observed by aircraft over the Amazon rainforest. These key land-atmosphere-cloud interactions are not included in current atmospheric models.

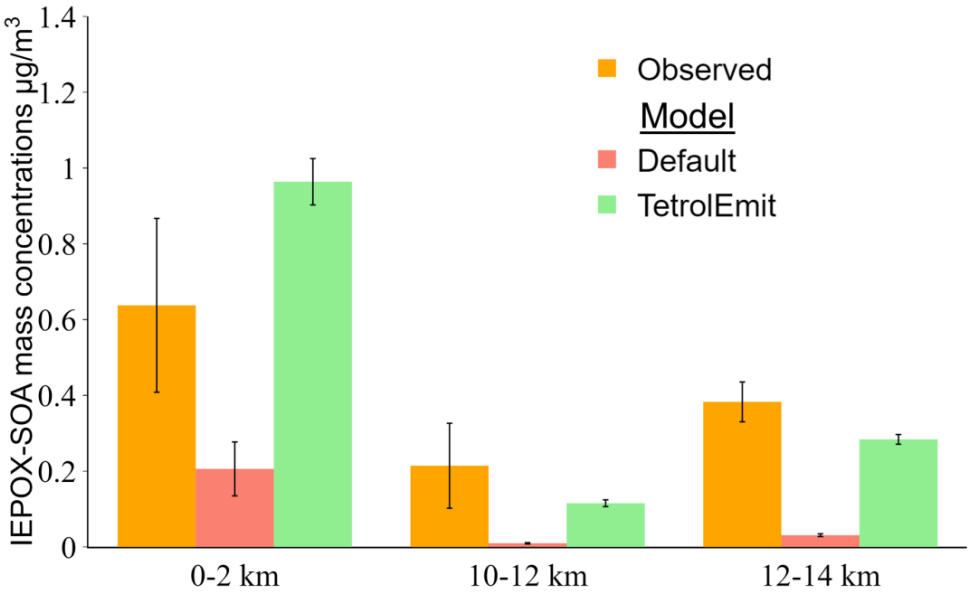

Fig. 2. HALO aircraft-measured (gray) and WRF-Chem-simulated (colored) IEPOX-SOA mass concentrations (µg m^{-3}, at standard temperature and pressure: 300 K and 995 hPa) are averaged across the same latitude–longitude ranges and times at three altitude ranges, the surface (0–2 km), and upper troposphere (10–12 and 12–14 km), on September 21, 2014. The bars represent averages of IEPOX-SOA at each altitude range, while the whiskers denote standard deviations showing the extent of spatial variations. Above figure is adapted from Shrivastava et al. (Shrivastava et al. 2022).

We compare results from different IEPOX-SOA model sensitivity simulations with HALO-measured average IEPOX-SOA for September 21, 2014 (Figure 2). The Default model simulation (Figure 2) representing the current state of knowledge of IEPOX-SOA moderately underpredicts the observed IEPOX-SOA of ~0.6 µg m^{-3} near the surface (0–2 km altitude) by a factor of 3. However, it greatly underpredicts IEPOX-SOA in the upper troposphere by over an order of magnitude (factor of ~12–22), that is, the measured IEPOX-SOA is 0.2–0.4 µg m^{-3}, while the Default-simulated value is negligible, ~0.01–0.03 µg m^{-3}. In the Default model formulation, IEPOX reactive uptake is negligible at upper troposphere altitudes (10–14 km) since viscosity calculations as a function of temperature, RH, and OA composition predict a solid OA shell due to the cold and moderately dry conditions. The solid OA shell shuts off the reactive uptake of IEPOX. In addition, aqueous and cloud chemistry processes do not occur in the upper troposphere due to low RH (20–40%) and cold temperatures (~225 K), which leads to the absence of particle and cloud liquid water needed for aqueous chemistry of IEPOX-SOA. In contrast, the mostly warm and moist near-surface conditions (temperature ~ 300 K, RH ~ 75%) result in a liquid-like OA shell below 2 km altitudes. The Default simulation represents the current state of knowledge in IEPOX-SOA formation and shows a key gap in our understanding of IEPOX-SOA formation in the upper troposphere. Direct emissions of gas-phase methyltetrols by in-plant chemistry and their vertical convective transport represent a previously unconsidered pathway of IEPOX-SOA formation (green, Figure 2). More than 99% of these gases partition to the particle-phase OA in the upper troposphere due to extremely cold temperature, thus, these gases represent the major source of IEPOX-SOA in the upper troposphere. While our current study focuses on IEPOX-SOA, there is clear evidence that in-plant biochemistry causes emissions of other compounds as well (e.g., methyl vinylketone and methacrolein), which were assumed to be produced only by oxidation of isoprene in the atmosphere. We showed that clouds and convective transport couple the surface-level biosphere to the upper troposphere and that the upper tropospheric SOA formation holds crucial insights into key biosphere processes that had been previously overlooked.

ACKNOWLDEGEMENTS

This research was supported by the U.S. Department of Energy (DOE) Office of Science, Office of Biological and Environmental Research (BER) through the Early Career Research Program and DOE BER's Atmospheric System Research (ASR) program. Funding for data collection onboard the G-1 aircraft and at the ground sites was provided by the Atmospheric Radiation Measurement (ARM) Climate Research Facility, a DOE user facility sponsored by BER. HALO-related work was supported by the Max Planck Society, the DFG (Deutsche Forschungsgemeinschaft, German Research Foundation) Priority Program SPP 1294, the German Aerospace Center (DLR), the BMBF program ROMIC (01LG1205E), the Max Planck Society, the Brazilian foundations FAPESP (São Paulo Research Foundation) Grants 2009/15235-8 and 2013/05014-0 and FAPEAM, and a wide range of other institutional partners. The Pacific Northwest National Laboratory (PNNL) is operated for the DOE by Battelle Memorial Institute under contract DE-AC06-76RL01830. Computational resources for the simulations were provided by EMSL (a DOE Office of Science User Facility sponsored by the Office of Biological and Environmental Research located at PNNL).

REFERENCES

Schulz, C., J. Schneider, B. Amorim Holanda, O. Appel, A. Costa, S. S. de Sá, V. Dreiling, D. Fütterer, T. Jurkat-Witschas, T. Klimach, C. Knote, M. Krämer, S. T. Martin, S. Mertes, M. L. Pöhlker, D. Sauer, C. Voigt, A. Walser, B. Weinzierl, H. Ziereis, M. Zöger, M. O. Andreae, P. Artaxo, L. A. T. Machado, U. Pöschl, M. Wendisch, and S. Borrmann. 2018. 'Aircraft-based observations of isoprene-epoxydiol-derived secondary organic aerosol (IEPOX-SOA) in the tropical upper troposphere over the Amazon region', *Atmospheric Chemistry and Physics*, 18: 14979-5001.

Shrivastava, Manish, Quazi Z Rasool, Bin Zhao, Mega Octaviani, Rahul A Zaveri, Alla Zelenyuk, Brian Gaudet, Ying Liu, John E Shilling, and Johannes Schneider. 2022. 'Tight Coupling of Surface and In-Plant Biochemistry and Convection Governs Key Fine Particulate Components over the Amazon Rainforest', *ACS Earth and Space Chemistry*.

SOURCE AND EMISSION STRENGTH OF BLACK CARBON AEROSOLS IN ASIA

SINGH M[1], SINHA P[1], LIN N[2], PANI S[2], SUBRAHAMANYAM D[3], MADHAVAN B[4], SAHU L[5], ANSARI K[5], SHERIDAN P[6], OGREN J[6] and AISWARYA [1,7]

[1]*Indian Institute of Space Science and Technology, Thiruvananthapuram, Kerala, India*
[2]*Department of Atmospheric Sciences, National Central University, Taoyuan City , Taiwan*
[3]*Space Physics Laboratory, Vikram Sarabhai Space Centre, Thiruvananthapuram, Kerala, India*
[4]*National Atmospheric Research Laboratory, Gadanki, Andhra Pradesh , India*
[5]*Physical Research Laboratory (PRL), Navrangpura Ahmedabad, Gujarat, India*
[6]*National Oceanic and Atmospheric Administration/Earth System Research Laboratory, Boulder Colorado, USA*
[7]*Indian Institute of Technology Bombay, Mumbai, Maharastra, India*

Keywords: BLACK CARBON, ASIA, TRAJECTORY, PONMUDI, MT. LULIN

INTRODUCTION

The black carbon particles (BC) are light-absorbing carbonaceous aerosols that are emitted during incomplete combustion of fossil fuels, biofuels, and biomass burning. The BC concentration can have an impact on health, climate, radiation balance, and hydrological cycle. The measurement of BC aerosols is therefore very important. We can assess the contribution from long-range vs local transport by measuring BC aerosol at high altitudes. In our study, equivalent BC was measured by Aethalometer (AE-31) at two high altitude sites. The measurement at two different wavelengths was used to attribute EBC into biomass and anthropogenic fraction. The study of diurnal variation and seasonality of EBC provided us insights into local emission while the HYSPLIT model for air mass back trajectories provided us insight into long-range transport. The observations were then compared with the model output of MRI-ESM2.

METHODS

The Ponmudi Climate Observatory (PCO, 8.76°N, 77.12°E; 1.0 km a.m.s.l.) is located on the hills of Western Ghats about 65 Km from Thiruanantpuram, Kerala, India. This high altitude site is apt to study the role of long-range transport. The unique location also offers a peek into seasonality effects arising from Indian Summer Monsoon. Since August 2019, BC concentration have been measured using Aethalometer (AE-31) at PCO.
The Lulin Atmospheric Background Station (LABS, 23.47°N, 120.87°E, 2.86 km a.m.s.l.) is located at the peak of Mt. Lulin, Taiwan. LABS is a two-story

building in Yushan National Park in central Taiwan. This site is around 2 km from a minor traffic road. It is located at high altitudes and is largely influenced by Asian air masses.

Aethalometer was used at both sites for measuring the BC concentration. Aethalometer has seven distinct wavelengths operated at a sampling interval of 5 minutes at PCO and 1 minute at LABS. The flow rate was kept constant at 4 LPM from August 2019 to April 2020. Aethalometer uses a filter-based absorption technique to measure BC mass concentration and it is proportional to the change in transmittance through the quartz filter tape due to the particle deposition,

$$ATN = -100 \times \ln\left(\frac{I}{I_o}\right) \tag{1}$$

where I and I_o are the intensity of light beam passing through aerosol laden and an unloaded spot of filter tape. After incorporating the flow rate and sampling interval, the b_{ATN} is given as follows,

$$b_{ATN} = \frac{\Delta ATN}{100\,\Delta t} \times \frac{A}{Q} \tag{2}$$

where A is aerosol loading spot area (1.67 cm^2) on the filter and Q is the volumetric flow rate of the instrument.

To take account of multiple scattering and loading effects, C and R corrections Weingartner et al., (2003) are applied. The values of C and R are taken from Schmid et al. (2006) and Sandradewi et al. (2008).

$$b_{abs}(\lambda) = \frac{b_{ATN}(\lambda)}{C(\lambda) \times R(\lambda)} \tag{3}$$

Finally this absorption coefficient b_{abs} (Mm^{-1}) is converted into equivalent BC concentration using wavelengthdependent MAC (m^2g^{-1}).

$$eBC(\lambda) = \frac{b_{abs}(\lambda)}{MAC(\lambda)} \tag{4}$$

To correct the actual volume aspirated based on ambient temperature and pressure, the following adjustments were made.

$$EBC = eBC \times \left[\frac{P_o \times T}{P \times T_o}\right]^{-1} \tag{5}$$

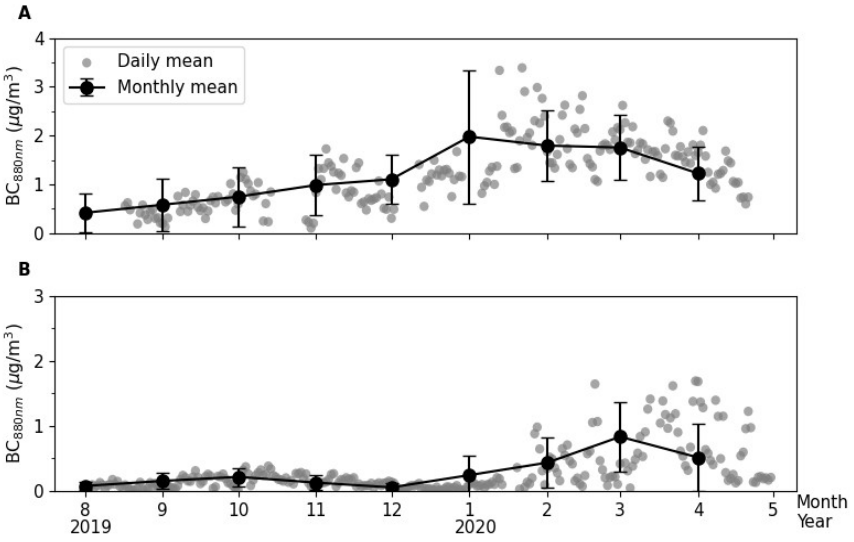

Figure 1: Daily and Monthly mean of EBC (λ=880nm) at (A) Ponmudi (B) Lulin. Vertical bar indicate ± 1σ from the mean.

To access performance of AE-31 (Ponmudi), an intercoparison between AE-31

and AE-33 was carried out later at Space Physics Laboratory, Thiruvananthapuram, India. It was found that the two measurements were highly correlated ($r^2 = 0.96$) and the slope agreed within 19% (m = 1.19).

The estimation of biomass burning and fossil fuel BC mass fracction was carried out by using 2α-model Sandradewi et al. (2008). The principle of attribution is based on the fact that the b_{abs} is directly proportional to λ^{-AAE} where AAE is the absorption Angstrom exponent and can be determined using following equation,

$$AAE = -\frac{\ln\left(\frac{b_{abs}(\lambda_1)}{b_{abs}(\lambda_2)}\right)}{\ln\left(\frac{\lambda_1}{\lambda_2}\right)} \quad (6)$$

In this study we assumes that AAE_{FF} (fossil fuel) and AAE_{BB} (biomass burning) are 1.8 and 1.0 (Herich et al.,(2011); Dumka et al., (2018,2019). Source apportionment was performed to estimate the percentage contribution of BB to and FF EBC Sandradewi et al., (2008b); Zotter et al., (2017); Helin et al., (2018).

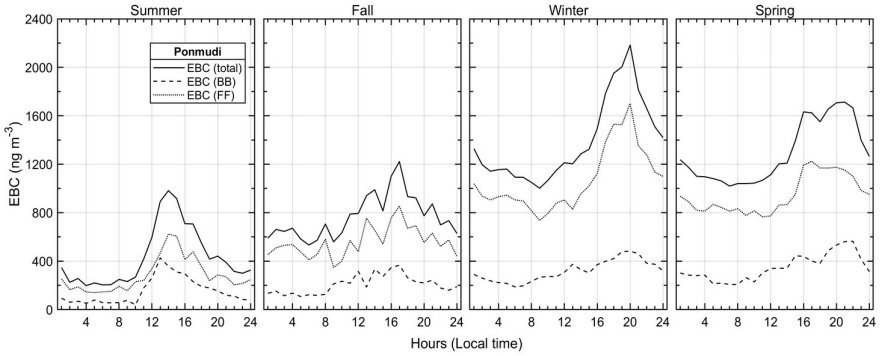

Figure 2: Diurnal variation of EBC and its contribution from FF and BB at Ponmudi

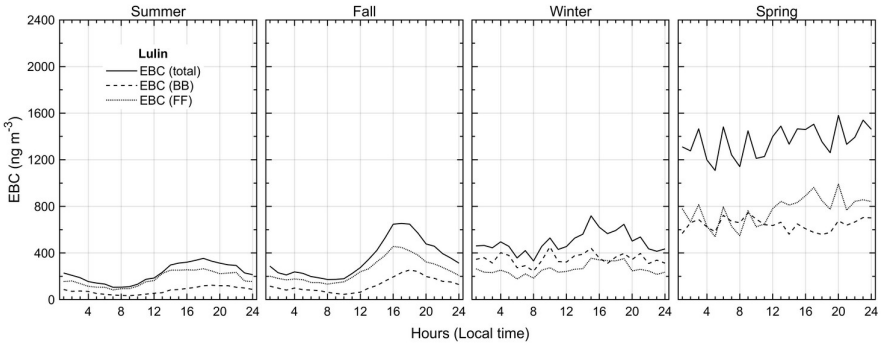

Figure 3: Diurnal variation of EBC and its contribution from FF and BB at Lulin

BB plays a significant role throughout the year at Ponmudi and increases in winter and spring, whereas at Lulin, the BB and FF fractions are equally important for total EBC.

The Hybrid Single Particle Lagrangian Integrated Trajectory (HYSPLIT) model was used to trace the hourly 7 days back trajectories of air mass arrivng at the two sites. In regions nearby the study site, trajectories were clustered based on 80% residence time while in regions not immediately adjacent, trajectories were clustered based on 50% criteria. There is a significant contribution of the free troposphere (air mass above 700 hpa) at Ponmudi, and precipitation suppresses the BC concentration during monsoon months.

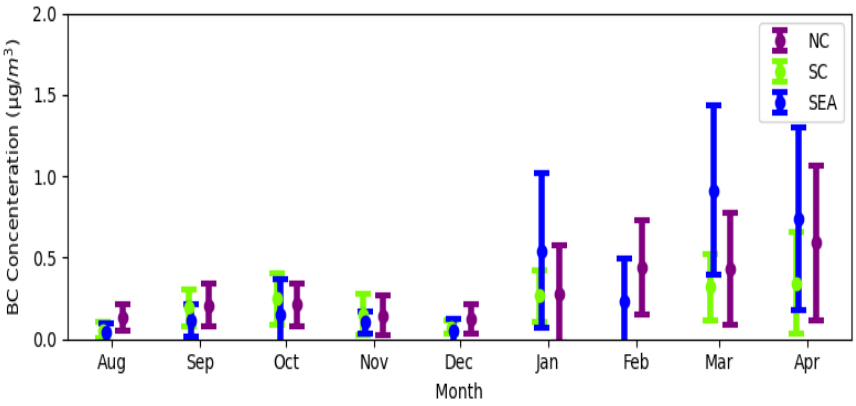

Figure 4: Monthly variation of BC concenteration from IO (Indian Ocean), ME (Middle East) and FT (Free Troposphere) are shown for Ponmudi.

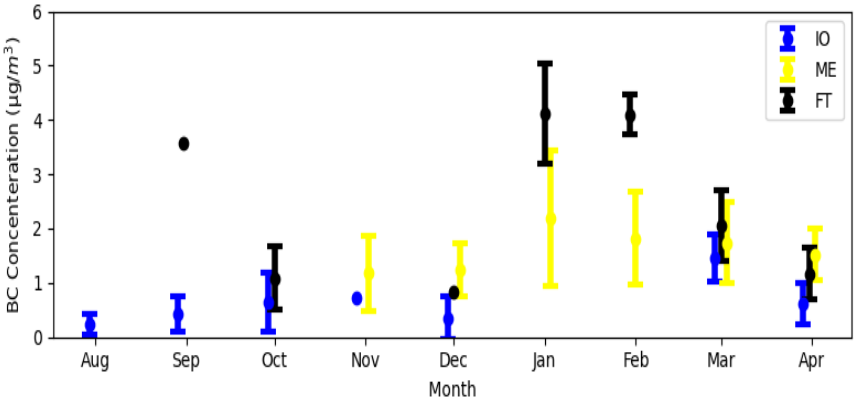

Figure 5: Monthly variation of BC concenteration from NC (North China), SC (South China) and SEA (South East Asia) are shown for Lulin.

For Ponmudi and Lulin, MRI-ESM2 correctly predicts the peak seasons, although it overestimates BB fractions for Lulin.

CONCLUSIONS

Ponmudi has influence from local as well as long range transport and majority of emissions in winter and spring is from fossil fuel. Lulin on the other hand is influenced by North China, South China and South-east Asia and both FF and BB has comparable influence throughout the year.

REFERENCES

Kanaya, Y. et al. (2016). Long-term observations of black carbon mass concentrations at Fukue Island, western Japan, during 2009–2015: constraining wet removal rates and emission strengths from East Asia, Atmos. Chem. Phys., 16, 10689–10705.

Liu, X. et al. (2013). Seasonal Variations of Black Carbon Observed at the Remote Mountain Site Happo in Japan. Journal of Geophysical Research: Atmospheres 118.9 (2013): 3709–3722. Web.

Pani, S. K. et al (2020). Black carbon over an urban atmosphere in northern peninsular Southeast Asia: Characteristics, source apportionment, and associated health risks.Environ Pollut. 2020;259:113871.

Weingartnera, E. Et et al. (2003). Absorption of light by soot particles: determination of the absorption coeffcient by means of aethalometers. J.Aerosol Sci., Vol:34,pp:1445-1463.

Estimates of mass absorption cross-section of Aethalometers in the Arctic

SINGH M[1], SINHA P[1], KONDO Y[2], OSHIMA N[3], ANDREWS E[4], HYVÄRINEN A[5]

[1] *Indian Institute Of Space Science And Technology, Trivandrum Kerala, India*
[2] *Ice Core Research Center, National Institute of Polar Research, Tachikawa Tokyo, Japan*
[3] *Department of Atmosphere, Ocean and Earth System Modeling Research, Meteorological Research Institute, Osaka, Japan*
[4] *NOAA Earth System Research Laboratory , Boulder Colorado, USA*
[5] *Finnish Meteorological Institute, Helsinki, Finland*

Keywords: MASS ABSORPTION CROSS SECTION, AETHALOMETER , COSMOS, ARCTIC

INTRODUCTION

A filter-based optical technique, mainly an Aethalometer (Magee Scientific, Berkeley, CA, USA) has been extensively used to provide climatology of equivalent BC (Black carbon) mass concentration (E_{BC}) at several sites in the Arctic to determine its potential sources, transport pathways, and also to validate model simulations. However, site, as well as season-independent constant mass absorption cross-section (MAC) values, have been used to derive E_{BC} from light absorption coefficient (b_{abs}) ($E_{BC} = b_{abs}/MAC$). However, differences in aerosol properties including mixing states of BC, variations in other co-existing light-absorbing aerosols such as brown carbon and mineral dust, and measurement artifacts by light scattering aerosols on depositing filter largely contribute to different MACs and thus induce a large bias in E_{BC} (Aethalometer). To date, accuracy of MAC (Aethalometer) was not estimated mainlyZdue to lack of reference MBC measurement. We measured b_{abs} using Aethalometer (b_{abs} (Aethalometer)), and reference MBC by a COSMOS (MBC (COSMOS)) with particle diameters less than 1 μm (PM1) at four sites, Alert (2018-2019), Barrow (2012-2021), Ny-Alesund (2012-2019) and Pallas (2019-2022). The b_{abs} (Aethalometer), and MBC (COSMOS) were tightly correlated (r^2 = 0.83-0.96), allowing necessary condition to reliably estimate MAC corr at these sites using simple b_{abs} (Aethalometer) - MBC (COSMOS) correlation method.

METHODS

An Aethalometer was used to measure Black Carbon (BC) mass concentration (babs) at four distinct sites - Alert (82.5°N, 62.5°W), Barrow (71.3°N, 156.6°W), Ny-Ålesund (78.9°N, 11.9°E), and Pallas (68.0°N, 24.0°E) located in Canada, Alaska, Svalbard, and Finland respectively. The Aethalometer has seven wavelength channels (370, 470, 520, 590, 660, 880, and 950 nm). The data availability in Alert is from January 2018 to December 2019. In Barrow, AE-31 data is available from January 1st, 2012 to August 18th, 2016, while AE-33 data is available from August 25th, 2014 to August 8th, 2022. The

collocated COSMOS data is available from August 8th, 2012 to February 23rd, 2021. Ny-Alesund data is only available for 590 nm from 2012 to 2019 for both AE-31 and COSMOS. In Pallas, AE-33 data is available from March 25th, 2019 to November 21st, 2022 and COSMOS data is available from July 22nd, 2019 to March 31st, 2022.

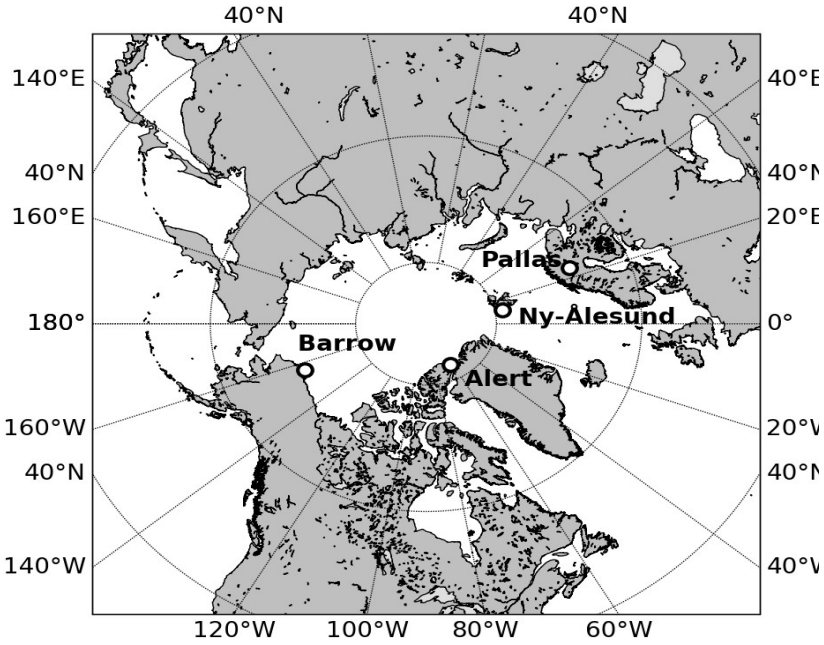

Figure 1: Location of the Arctic sites

The Aethalometer utilizes a filter-based absorption method to determine the mass concentration of Black Carbon (BC). The measurement is proportional to the change in transmittance that occurs through a quartz filter tape, as a result of particle deposition.

$$ATN = -100 \times \ln\left(\frac{I}{I_o}\right) \tag{1}$$

where I and I_o are the intensity of light beam passing through aerosol laden and an unloaded spot of filter tape. After incorporating the flow rate and sampling interval, the b_{ATN} is given as follows,

$$b_{ATN} = \frac{\Delta ATN}{100\,\Delta t} \times \frac{A}{Q} \tag{2}$$

where A is aerosol loading spot area (0.5 cm^2) on the filter and Q is the volumetric flow rate of the instrument.

To take account of multiple scattering and loading effects, C and R corrections are used. Here in our study we have used C=3.5 recommended by the World Meteorological Organization/Global Atmosphere Watch (WMO/GAW, 2016) and R=1 as filter loading effect is not significant in Arctic, Backman et al. (2017).

$$b_{abs}(\lambda) = \frac{b_{ATN}(\lambda)}{C(\lambda) \times R(\lambda)} \tag{3}$$

Finally this absorption coefficient b_{abs} (Mm^{-1}) is converted into equivalent BC concentration using wavelengthdependent MAC (m^2g^{-1}).

$$MAC(\lambda) = \frac{b_{abs}(\lambda)}{M_{BC}(COSMOS)} \tag{4}$$

Here we evaluate the accuracy and stability of conversion of b_{abs} into M_{BC}. The measurement by COSMOS is to measure M_{BC}. In this instrument, we have a

heated inlet (300°C), which removes non-refractory components. COSMOS M_{BC} values have been compared with single particle soot photometer (SP2) and it was found that the measurement of M_{BC}(COSMOS) and M_{BC}(SP2) agree within 10% Kondo et al., (2009, 2011); Ohata et al., (2019).

CONCLUSIONS

Data has been analyzed on a daily and hourly basis for all four sites.

Table 1: MAC (Aethalometer - AE-31 ;λ and r^2 at Alert from 2018-2019

Wavelength (nm)	MAC (Hourly)	R^2	MAC (Daily)	R^2
370	18.51	0.84	18.75	0.9
470	15.38	0.88	15.6	0.93
520	13.86	0.88	14.07	0.94
590	12.49	0.89	12.68	0.94
660	11.42	0.87	11.61	0.94
880	8.82	0.85	8.98	0.94
950	8.09	0.84	8.26	0.94

Table 2: MAC (Aethalometer - AE31 ;λ) and r^2 at Barrow from 2012-2016

Wavelength (nm)	MAC (Hourly)	R^2	MAC (Daily)	R^2
370	16.6	0.79	15.93	0.83
470	13.84	0.81	13.31	0.85
520	12.33	0.82	11.88	0.87
590	11.19	0.74	10.77	0.86
660	10.33	0.82	10.01	0.87
880	7.92	0.82	7.74	0.87
950	7.23	0.81	7.09	0.86

Table 3: MAC (Aethalometer - AE33 ;λ) and r^2 at Barrow from 2014-2016

Wavelength (nm)	MAC (Hourly)	R^2	MAC (Daily)	R^2
370	18.66	0.92	18.96	0.94
470	13.75	0.92	14.22	0.95
520	11.74	0.93	12.14	0.96
590	10.23	0.94	10.58	0.96
660	8.87	0.96	9.18	0.97
880	6.43	0.94	6.64	0.97
950	6.12	0.94	6.32	0.97

Table 5: MAC (Aethalometer - AE-31 ;λ and r^2 at Ny-Alesund from 2012-2019

Wavelength (nm)	MAC (Hourly)	R^2	MAC (Daily)	R^2
590	10.21	0.9	10.06	0.9

Table 6: MAC (Aethalometer - AE33 ;λ) and r^2 at Pallas from 2019-2022

Wavelength (nm)	MAC (Hourly)	R^2	MAC (Daily)	R^2
370	21.32	0.96	21.37	0.96
470	16.91	0.96	16.95	0.96
520	14.54	0.96	14.57	0.96
590	12.59	0.96	12.62	0.96
660	10.65	0.96	10.68	0.96
880	7.45	0.95	7.47	0.95
950	6.84	0.95	6.86	0.95

The MAC values has a spectral as well as temporal variation. The accuracy of MAC_{corr} showed spectrally weak variation and similar values at these four sites. The MAC_{corr} estimated by this method at 590 nm varied 10.21 - 12.59 m^2g^{-1} for 1-hr and from 10.06 - 12.68 m^2g^{-1} for 24-hr data at these sites. The mean and median values at each location were as follows: Alert - 16.73 ± 3.21 m^2g^{-1} and 16.16 m^2g^{-1} ; Barrow (AE-31) - 13.14 ± 2.81 m^2g^{-1} and 12.93m^2g^{-1} ; Barrow (AE-33) - 10.97 ± 1.89 m^2g^{-1} and 10.32 m^2g^{-1} ; Ny-Alesund - 15.14 ± 4.16 m^2g^{-1} and 14.71 m^2g^{-1} ; and Pallas - 13.89 ± 2.43 m^2g^{-1} and 13.37 m^2g^{-1} , respectively exhibiting weak seasonal and year-to-year variations (within 30% of the seasonal or annual mean values). We recommend scaling E_{BC} measured with Aethalometer with the corrected MAC presented in this study to provide error-constraint E_{BC} at these sites.

REFERENCES

Asmi, E., Backman, J., Servomaa, H., Virkkula, A., Gini, M. I., Eleftheriadis, K., Müller, T., Ohata, S., Kondo, Y., and Hyvärinen, A.: Absorption instruments inter-comparison campaign at the Arctic Pallas station, Atmos. Meas. Tech., 14, 5397–5413.

Backman, J., Schmeisser, L., Virkkula, A., Ogren, J. A., Asmi, E., Starkweather, S., Sharma, S., Eleftheriadis, K., Uttal, T., Jefferson, A., Bergin, M., Makshtas, A., Tunved, P., and Fiebig, M.: On Aethalometer measurement uncertainties and an instrument correction factor for the Arctic, Atmos. Meas. Tech., 10, 5039–5062.

Kondo, Y., Sahu, L., Kuwata, M., Miyazaki, Y., Takegawa, N., Moteki, N., Imaru, J., Han, S., Nakayama, T., Oanh, N. T. K., Hu, M., Kim, Y. J., and Kita, K.: Stabilization of the mass absorption cross section of black carbon for filter-based absorption photometry by the use of a heated inlet, Aerosol Sci. Tech., 43, 741–756.

Ohata, S. et al. (2021). Estimates of mass absorption cross sections of black carbon for filter-based absorption photometers in the Arctic, Atmos. Meas. Tech., 14, 6723–6748, 2021

Sharma, S., Leaitch, W. R., Huang, L., Veber, D., Kolonjari, F., Zhang, W., Hanna, S. J., Bertram, A. K., and Ogren, J. A.: An evaluation of three methods for measuring black carbon in Alert, Canada, Atmos. Chem. Phys., 17, 15225–15243.

WMO/GAW: World Meteorological Organization/Global Atmosphere Watch: WMO/GAW aerosol measurement procedures, guidelines, and recommendations, GAW Report No. 227, 2016.

DISTINCT ROLES OF ATMOSPHERIC BUFFERS IN CLOUDS AND AEROSOLS

GUANGJIE ZHENG[1], HANG SU[1], YAFANG CHENG[1]

[1] *Max Planck Institute for Chemistry, Mainz 55128, Germany*

Keywords: Acidity of aerosols and clouds, atmospheric multiphase reactions, organic acids, carbon dioxide (CO_2), ammonia, multiphase buffering, cloud chemistry

INTRODUCTION

Acidity is one central parameter in atmospheric multiphase reactions, influencing aerosol formation and its effects on climate, health and ecosystems. Weak acids and bases, mainly CO_2, organic acids and ammonia, are long considered to play a role in regulating atmospheric acidity. However, unlike the strong acids and bases, their importance and influencing mechanisms in a given aerosol or cloud droplet system remain to be clarified.

METHODS

Here, we investigate this issue with new insights provided by recent advances in the field, in particular the multiphase buffer theory *(Zheng et al., 2020, Science)*.

CONCLUSIONS

We show that, in general, aerosol acidity is primarily buffered by ammonia, with a negligible contribution from CO_2 and a potential contribution from organic acids under certain conditions. For fogs, clouds and rains, CO_2, organic acids, and ammonia may all provide certain buffering under higher pH levels (pH>~4). Despite the 10^4~10^7 lower abundance of ammonia and organic weak acids, their buffering effect can still be comparable with that of CO_2. This is due to that the cloud pH is at the very far end of the CO_2 multiphase

buffering range. This study highlights the need for more comprehensive field observations under different conditions, and further studies in the interactions among organic acids, acidity and cloud chemistry.

ACKNOWLEDGMENT

The research was supported by the Max Planck Society (MPG). Y.C. acknowledges the Minerva Program of MPG.

REFERENCES

Zheng, G.; Su, H.; Wang, S.; Andreae, M. O.; Pöschl, U.; Cheng, Y., Multiphase buffer theory explains contrasts in atmospheric aerosol acidity. *Science* **2020,** *369* (6509), 1374-1377.

PHYSICOCHEMICAL PROCESSES BEHIND NEW PARTICLE FORMATION AT PO VALLEY

J. SULO[1], J. CAI[1], S. HOLM[1], Y. GU[1,] K. LEHTIPALO[1,2], F. BIANCHI[1], D. STOLZENBURG[1,3]

[1]Institute for Atmospheric and Earth System Research/Physics, University of Helsinki, 00014 Helsinki, Finland
[2]Finnish Meteorological Institute, 00560 Helsinki, Finland
[3]Institute for Materials Chemistry, TU Wien, 1060 Vienna, Austria.

Keywords: FORMATION RATE, NEW PARTICLE FORMATION, PARTICLE SIZE DISTRIBUTION

INTRODUCTION

New particle formation (NPF) is estimated to produce between 40 and 80 % of all aerosol loading in the atmosphere and is therefore an important source of aerosol loading in the atmosphere (Dunne et al., 2016). If the pre-existing aerosol sink is large, such as in polluted areas, NPF is often suppressed to a significant degree. However, recent studies have concluded that NPF occurs even in the most polluted areas if the conditions are right. Po Valley is considered one of the most polluted areas in Europe as the area has many sources of anthropogenic pollutants, from industrial sites and power plants to agricultural activities and ship emissions from the Adriatic Sea. The surrounding mountains also modulate the air flows in the area and often trap pollution. In this study, we investigate the formation of new particles at Po Valley during spring 2022 by measuring the size distribution of aerosol particles and the concentrations of aerosol precursor vapors with a set of instrumentation specifically designed to study NPF.

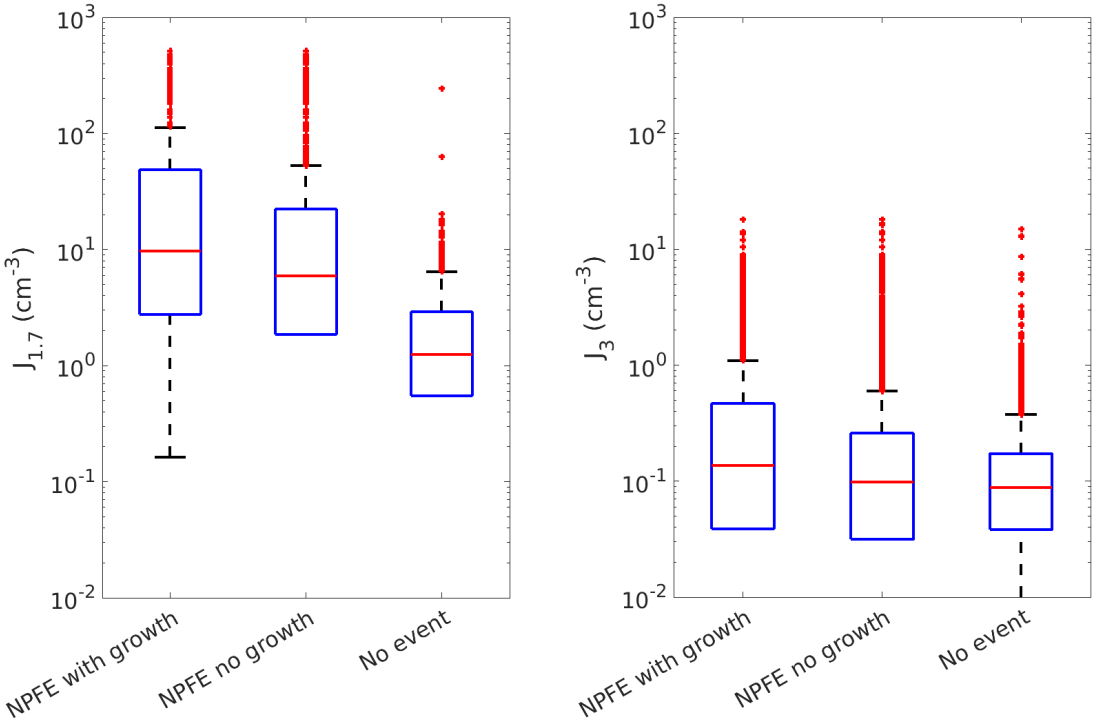

Figure 1. The formation rates of 1.7 nm (left) and 3 nm (right) particles in Po Valley between March 1st and April 30th. The red line shows the median concentration for each month and the blue box contains 50

percent (25th to 75th percentile) of all data points. The whiskers mark the location of the 95th and 5th percentile data points.

METHODS

We measured the size distribution of atmospheric aerosols between 1 and 800 nm by using a combination of instruments: A half-mini DMPS (Kangasluoma et al., 2018) to measure aerosols between 2-15 nm, a Hauke-type DMPS for measurements from 10 to 800 nm in size and a Particle Size Magnifier (PSM) (Vanhanen et al., 2011) to measure the smallest clusters between 1 and 3 nm in size. The measurements took place on a field at the San Pietro Capiofume meteorological station, about 25 km north-east of Bologna in the Po Valley and lasted between February 17th and May 7th, 2022. Formation rates were calculated as presented in Kulmala et al (2012) for both $J_{1.7}$ and J_3. Days were classified based on the particle size distributions from the DMPS and PSM so that if a growing mode was visible in the DMPS it was considered a new particle formation event with growth (NPFE with growth) while those days where a growing mode was visible only in the sub-3 nm size distribution and no growing mode was visible in the DMPS, it was a new particle formation event with no growth (NPFE no growth). When neither instrument showed elevated nucleation mode concentrations, the day was considered a non-event.

CONCLUSIONS

Our analysis shows (Figure 1) that the median formation rate of 1.7 nm particles during growing event days is 10 cm^{-3} and during clustering event days the median formation rate is 6 cm^{-3}. During non-event days the median formation rate is even lower, 1 cm^{-3}. The formation rate of 3 nm particles is an order of magnitude lower, with the median formation rates being 0.14, 0.1 and 0.09 for growing events days, clustering event days and non-event days respectively. $J_{1.7}$ has a maximum during midday, during both clustering and growing events, but shows no maximum during non-event days (Figure 2). However, the median formation rate during the daily maximum is over two times larger for growing events, showing that sufficient formation of clusters is required for particles to survive to larger sizes. As expected, the formation rate of 3 nm particles J_3 has a clear diurnal cycle only during growing event days, while there is no clear diurnal cycle otherwise (Figure 2). We investigate the physicochemical processes behind growing and clustering events by analyzing gas-phase precursor measurements done with a nitrate-CI-APi-ToF and naturally charged cluster measurements done with an APi-ToF, which were simultaneously operated. We find that the specific precursor patterns and meteorology (mainly the seasonal pattern between polluted winter and cleaner spring) determine whether the clustering can turn into a growing NPF event with potential relevance to the atmospheric system.

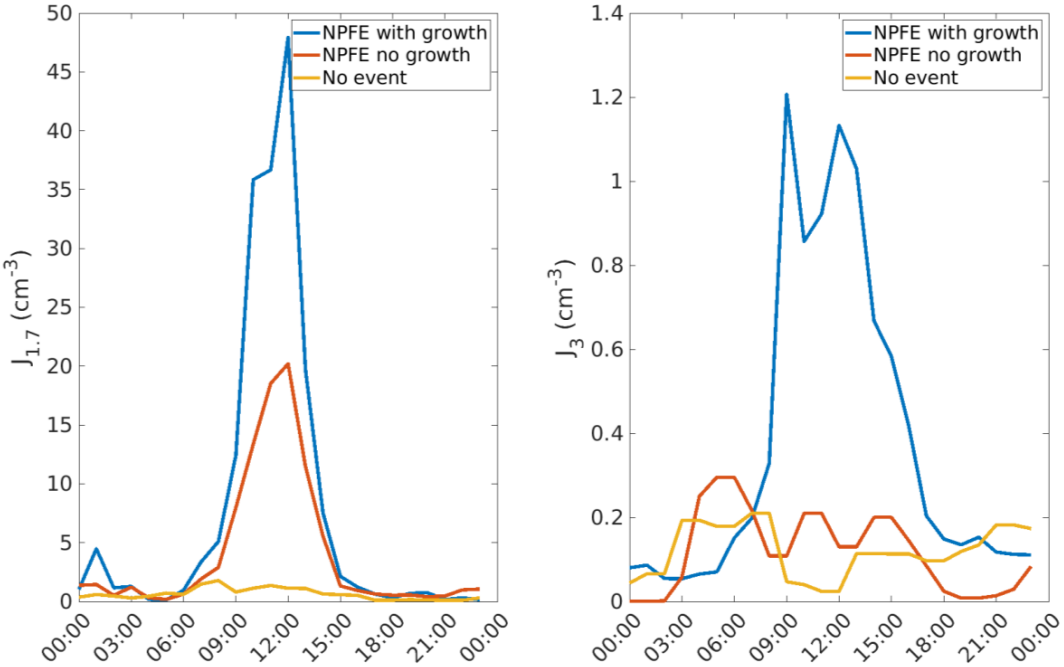

Figure 2. The median diurnal cycles of the formation rate of 1.7 nm particles (left) and 3 nm particles (right) between March 1st and April 30th.

ACKNOWLEDGEMENTS

This research has been supported by the Academy of Finland (grant nos. 337549, 302958, 325656) and the European Research Council, H2020 European Research Council (grant no. ATM-GTP (742206)). This research has received funding from the European Union's Horizon 2020 research and innovation programme under the Marie Sklodowska-Curie grant agreement no. 895875 ("NPF-PANDA").

REFERENCES

Dunne, E. M., Gordon, H., Kürten, A., Almeida, J., Duplissy, J., Williamson, C., Ortega, I. K., Pringle, K. J., Adamov, A., Baltensperger, U., Barmet, P., Benduhn, F., Bianchi, F., Breitenlechner, M., Clarke, A., Curtius, J., Dommen, J., Donahue, N. M., Ehrhart, S., Flagan, R. C., Franchin, A., Guida, R., Hakala, J., Hansel, A., Heinritzi, M., Jokinen, T., Kangasluoma, J., Kirkby, J., Kulmala, M., Kupc, A., Lawler, M. J., Lehtipalo, K., Makhmutov, V., Mann, G., Mathot, S., Merikanto, J., Miettinen, P., Nenes, A., Onnela, A., Rap, A., Reddington, C. L. S., Riccobono, F., Richards, N. A. D., Rissanen, M. P., Rondo, L., Sarnela, N., Schobesberger, S., Sengupta, K., Simon, M., Sipilä, M., Smith, J. N., Stozkhov, Y., Tomé, A., Tröstl, J., Wagner, P. E., Wimmer, D., Winkler, P. M., Worsnop, D. R., & Carslaw, K. S. (2016). Global atmospheric particle formation from CERN CLOUD measurements. Science, 354 (6316), 1119–1124. https://doi.org/10.1126/science.aaf2649

Kangasluoma, J., Ahonen, L. R., Laurila, T. M., Cai, R., Enroth, J., Mazon, S. B., Korhonen, F., Aalto, P. P., Kulmala, M., Attoui, M., & Petäjä, T. (2018). Laboratory verification of a new high flow differential mobility particle sizer, and field measurements in Hyytiälä. *Journal of Aerosol Science*, *124*, 1–9. https://doi.org/10.1016/j.jaerosci.2018.06.009

Kulmala, M., Petäjä, T., Nieminen, T., Sipilä, M., Manninen, H. E., Lehtipalo, K., Dal Maso, M., Aalto, P. P., Junninen, H., Paasonen, P., Riipinen, I., Lehtinen, K. E., Laaksonen, A., & Kerminen, V.-M. (2012). Measurement of the nucleation of atmospheric aerosol particles. *Nature Protocols*, *7*(9), 1651–1667. https://doi.org/10.1038/nprot.2012.091

Vanhanen, J., Mikkilä, J., Lehtipalo, K., Sipilä, M., Manninen, H. E., Siivola, E., Petäjä, T., & Kulmala, M. (2011). Particle size magnifier for nano-cn detection. Aerosol Science and Technology, 45 (4), 533–542. https://doi.org/10.1080/02786826. 2010.547889

BIOMASS BURNING ORGANIC AEROSOL CV-TOF-ACSM MEASUREMENTS FROM THE AUSTRALIAN 2020 BUSHFIRES

A.R. Sutresna[1,2*], M. Keywood[2], C. Paton-Walsh[3], J.B. Simmons[3], Q. Dang[3], M. Mochida[4], S. Ohata[4], S. Afsana[4], B. Kunwar[5], K. Kawamura[5], C. Mynard[2], R.S. Humphries[2], K. Emmerson[2], A. Griffiths[6], R. Schofield[1], P.J. Rayner[1]

[1] *School of Geography, Earth & Atmospheric Sciences, University of Melbourne, Parkville, VIC 3010, Australia*
[2] *Climate Science Centre, CSIRO Oceans and Atmosphere, Aspendale, VIC 3195, Australia*
[3] *Centre for Atmospheric Chemistry, School of Earth, Atmospheric and Life Sciences, University of Wollongong, Wollongong, NSW 2522, Australia*
[4] *Nagoya University, Nagoya, Aichi 464-8601, Japan*
[5] *Chubu University, Kasugai, Aichi 487-8501, Japan*
[6] *Australian Nuclear Science & Technology Organisation, Lucas Heights, NSW 2234*

Keywords: biomass burning, organic aerosols, ToF-ACSM

INTRODUCTION

The Time-of-Flight Aerosol Chemical Speciation Monitor (ToF-ACSM) is a mass spectrometry instrument that uses fragmentation calculations to estimate the amount of nitrates, sulfates, ammonium, chlorides, and organics in non-refractory particles smaller than 1 micron in diameter (PM_1). In recent years, development of the capture vapouriser (CV) has drastically reduced uncertainties in the ToF-ACSM associated with particle bounce, though its use has led to some unintended side effects. Firstly, the CV's different construction to the standard vapouriser (SV) means it is possible for the ToF-ACSM to detect refractory particles such as sea salt at lower temperatures compared to the SV. The other major side effect is that it changes the fragmentation patterns of many organic molecules (Hu et al., 2017) compared to that using the SV, meaning that marker ions for such molecules identified using the SV may not be useful when using the CV.

This study analyses field CV-ToF-ACSM data from the Characterising Organic Aerosols Loading over Australia (COALA-2020) campaign located approximately 50 km southwest of Sydney, New South Wales, Australia between January and March 2020 during the historic Black Summer bushfires. Along with a range of collocated instruments, the data collected using the CV-ToF-ACSM during this campaign was used to evaluate how biomass burning organic aerosols (BBOA) in the field fragment when using an instrument with a CV.

METHODS

Different sources of organic aerosols (OA) are identified using the statistical receptor model Positive Matrix Factorisation (PMF), which decomposes the CV-ToF-ACSM OA measurements into a defined number of factors consisting of strongly correlated species. These factors are then correlated against concentrations of marker species measured by other instruments. The primary identifier of BBOA is filter measurements of levoglucosan, which was used alongside other biomass burning tracers like black carbon, carbon monoxide, and acetonitrile.

As the measurement site is close to the coast and the instrument has the potential to easily detect sea salt, marker ions of sea salt identified by Freney et al. (2021) were also included in the CV-ToF-ACSM's fragmentation table for organic species. If substantial concentrations of sea salt are detected in the instrument, a factor consisting of sea salt marker ions would be expected to appear in the PMF solution. Radon-222 measurements were also used to verify the presence of a sea salt factor, as a negative correlation with radon suggests a marine particle source.

CONCLUSIONS

An oxygenated OA (OOA) factor as well as a sea salt factor were identified in a four-factor PMF solution, with the OOA factor accounting for a large majority of OA mass (47.11 %). The OOA factor, characterised by a dominant peak at 44 amu, was also the factor that correlated best with levoglucosan (r = 0.85). With OOA representing aged particles produced by the oxidation of fresh OA particles from a range of sources including biomass burning, this result suggests that the presence of OOA was so ubiquitous that it was difficult to distinguish their physical sources from fresh BBOA. This is consistent with the conditions during the collection period, where the amount and intensity of the bushfires were so high that even after the worst of the bushfires had subsided, a large amount of smoke remained in the area. To investigate marker ions for BBOA using a CV-ToF-ACSM more reliably, it is likely that measurements from more typical biomass burning events will be required.

The sea salt factor was identified by the peaks at 23, 35, 36, 37, 38, 58, and 60 amu; with the ratios of 35:37, 36:38, and 58:60 reflecting the isotopic ratio of ^{35}Cl to ^{37}Cl. This factor contributed 11.68 % to the total OA mass and was the only factor to be negatively correlated with radon (r = -0.27).

REFERENCES

Freney, E., Sellegri, K., Nicosia, A., Williams, L. R., Rinaldi, M., Trueblood, J. T., . . . Guieu, C. (2021). Mediterranean nascent sea spray organic aerosol and relationships with seawater biogeochemistry. *Atmospheric Chemistry and Physics, 21*(13), 10625-10641. doi:10.5194/acp-21-10625-2021

Hu, W., Day, D. A., Campuzano-Jost, P., Nault, B. A., Park, T., Lee, T., . . . Jimenez, J. L. (2018). Evaluation of the new capture vaporizer for aerosol mass spectrometers: Characterization of Organic Aerosol Mass Spectra. *Aerosol Science and Technology, 52*(7), 725-739. doi:10.1080/02786826.2018.1454584

CASE STUDY OF HIGH PM CONCENTRATION IN FUKUOKA, JAPAN DURING SPRING SEASON, AND ESTIMATION OF PM SOURCES

A. YOSHINO[1], A. TAKAMI[1], A. SHIMIZU[1], K. SATO[1], K. HAYAKAWA[2], N. TANG[2], Y. INOMATA[2], T. SETO[3], H. NAKAMURA[4], A. HARA[4] and H. ODAJIMA[5]

[1]Regional Environment Conservation Division, National Institute for Environmental Studies, Tsukuba, Ibaraki, 305-8506, Japan.

[2]Institute of Nature and Environmental Technology, Kanazawa University, Kanazawa, Ishikawa, Japan.

[3]Institute of Science and Engineering, Kanazawa University, Kanazawa, Ishikawa, Japan.

[4]Faculty of Medicine, Institute of Medical, Pharmaceutical and Health Sciences, Kanazawa University, Kanazawa, Ishikawa, Japan.

[5]Department of Pediatrics, National Hospital Organization, Fukuoka National Hospital, Fukuoka, Fukuoka, Japan.

Keywords: $PM_{2.5}$, PAHs, sulphate, trans-boundary air pollution.

INTRODUCTION

The western part of Japan, especially the Kyushu region, is located downwind of the monsoon from the Asian continent from winter to spring, which transports air pollutants such as $PM_{2.5}$. In recent years, $PM_{2.5}$ concentrations in East Asia have been decreasing due to environmental measures taken by China and other countries. In Japan as well, $PM_{2.5}$ concentrations are decreasing due to the decrease of transboundary transport and the annual average concentration of $PM_{2.5}$ in Japan in 2020 was 9.5 μgm^{-3} for the monitoring station located at the residential areas. However, the World Health Organization (WHO) lowered the recommended value for the annual average from 10 to 5 μgm^{-3} in September 2021, and in comparison, the annual average concentration in Japan is still high. It is also not yet clear whether it is particulate matter such as $PM_{2.5}$ or the chemical composition contained in particulate matter that affect human health. We observed $PM_{2.5}$ and its chemical composition in Fukuoka, Japan. In this study, we analyzed cases of high concentrations of $PM_{2.5}$ and its chemical components in the spring of 2020 and 2021 using data on ionic components, polycyclic aromatic hydrocarbons (PAHs), trace metal elements, carbon components, and gas components. The sources were also estimated using backward trajectory analysis and factor analysis methods.

METHODS

Located in the western part of Japan, Fukuoka is one of the largest cities with a population of approximately 1.5 million people, including various local sources *i.e.* a commercial district, a port and an airport, and an urban highway within the area. Its location in the western part of Japan is affected by transboundary air pollution due to the monsoon from the Asian continent from winter to spring.

The PM and gas observation methods and the data used in this analysis are similar ones as was used in the previously published paper (Yoshino *et al*, 2022). We analyzed the data in spring 2020 and 2021. A brief description of the observation methods and data is given below. PM was collected by a high-volume air sampler (HV-RW, Sibata Scientific Technology, Ltd) with a slit-type $PM_{2.5}$ separator installed on the roof of the National Hospital Organization Fukuoka Hospital (Minami-ku, Fukuoka City) at a flow rate of 1000 $Lmin^{-1}$ on a fluoroplastic binder glass fiber filter (TX40HI20WW, Pall Corporation). Atmospheric samples were collected for 24 hours. The filter was cut for PAHs and ion analysis, and PAHs were analyzed by

Kanazawa University (Pham *et al.*, 2022), and ions were analyzed by the National Institute for Environmental Studies (NIES). For ion analysis, the filters were immersed in ultrapure water, sonicated, and filtered through a disk filter (pore size 0.45 μm), and the ion components were analyzed by ion chromatography (Prominence, Shimadzu Corporation) (Yoshino *et al*, 2022).
For $PM_{2.5}$ mass concentration, the data measured by the Fukuoka City Hall monitoring station was used. Data published by the Ministry of the Environment Japan were used for metal elements and carbon components (organic carbon (OC) and elemental carbon (EC)). Meteorological data were from the Fukuoka District Meteorological Observatory. Ozone was measured at Fukuoka University by NIES using an ozone monitor (Model 49i, Thermo Fisher Scientific Inc.) (Yoshino *et al*, 2022).
NOAA's HYSPLIT (The Hybrid Single-Particle Lagrangian Integrated Trajectory model) system (Stein *et al.*, 2015, Rolph *et al.*, 2017) was used to investigate air mass transport pathways. The Chemical Weather FORecasting System (CFORS) was also used to analyze the transport of sulphate ions and dust in East Asia.

RESULTS AND DISCUSSION

Mass concentrations of major ionic components in $PM_{2.5}$ observed in spring 2020 and 2021 are shown in Figure 1. The variability of $PM_{2.5}$ and chemical components such as SO_4^{2-} was generally consistent, while PAHs and SO_4^{2-} sometimes showed different variability.

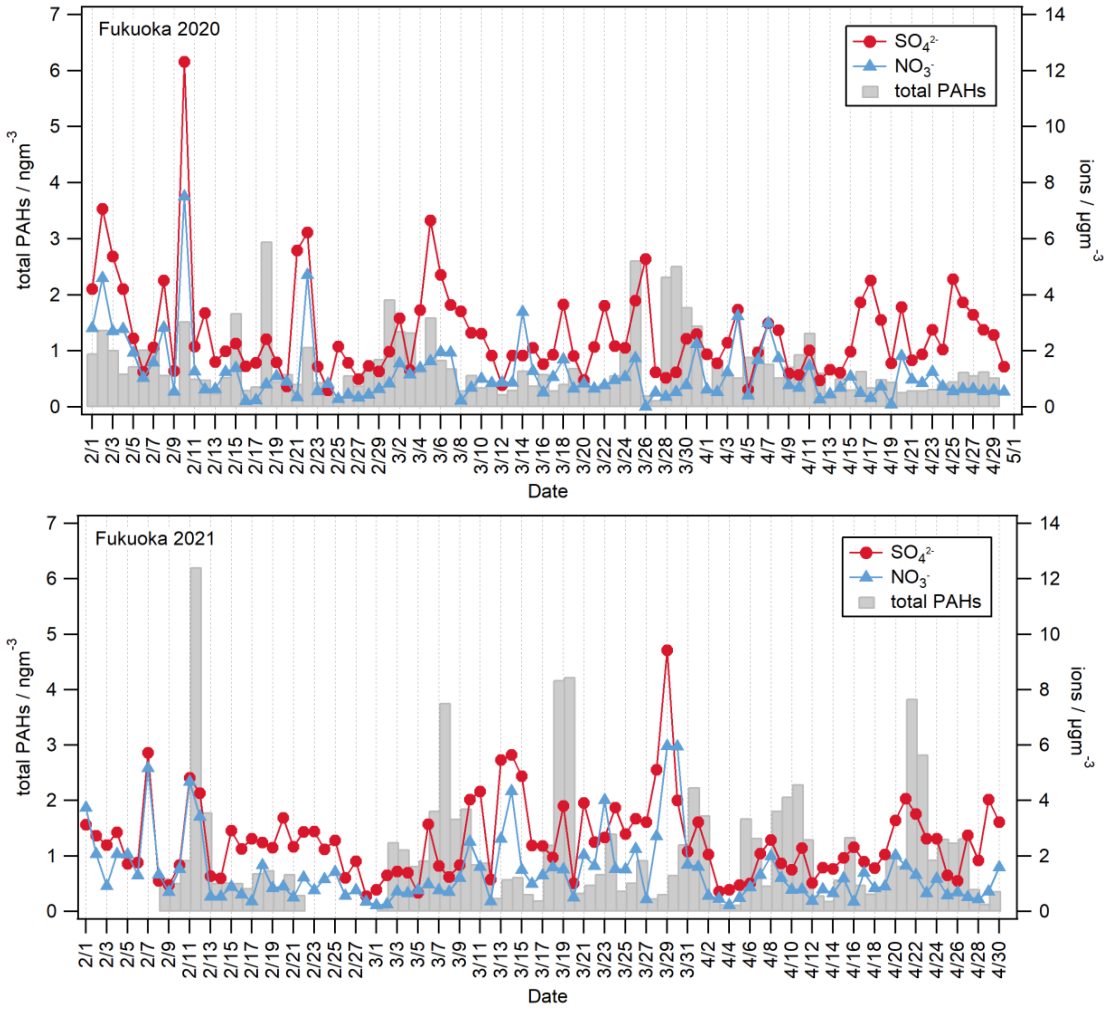

Figure 1. Time series of ionic and PAHs components in $PM_{2.5}$ observed in Fukuoka City, Japan in spring 2020 (upper) and 2021 (lower).

The mean concentration and standard deviation (σ) were calculated for $PM_{2.5}$ and chemical components for February-April 2020 and 2021, and high concentration days were defined as days with a concentration greater than the mean concentration + 1σ value. The average concentrations of $PM_{2.5}$ and major chemical components are summarized in Table 1.

Year	$PM_{2.5}$ /μgm^{-3}	Nitrate /μgm^{-3}	Sulphate /μgm^{-3}	Total Ions /μgm^{-3}	Total PAHs /ngm^{-3}	Total metals /μgm^{-3}
2020	12.4	1.20	2.62	5.60	0.75	1.32
2020 (high conc.)	25.2	3.76	6.07	13.4	1.85	3.14
2021	12.7	1.41	2.52	5.57	1.11	1.46
2021 (high conc.)	24.2	4.27	4.98	12.3	3.91	4.00

Table 1. The average concentrations of $PM_{2.5}$ and major chemical components observed from February to April and on high concentration days (high. conc.).

For the high concentration days for each component, the pathways along which air masses were transported were examined by backward trajectory analysis using HYSPLIT to investigate whether there was a relationship between concentration fluctuations and transport pathways (Figure 2). The results for spring 2020 and 2021 are summarized below, in which the trends are same for both 2020 and 2021.

- ✓ On most of high concentration days of $PM_{2.5}$ and chemical components, air masses were arriving in Fukuoka via China and Korea (Figure 2 (a)).
- ✓ When PAHs were at high concentrations, they were often transported to Fukuoka via the East China Sea and the Korean Peninsula, but when only PAHs were at high concentrations, they reached Fukuoka via the Seto Inland Sea and Kitakyushu City in Japan (Figure 2 (b)).
- ✓ On days when only sulphate ions were high, the air masses reached Fukuoka by moving northward from the southern seas of Japan. It is thought that this was influenced by volcanoes such as Sakurajima and Suwanosejima (Figure 2 (c)).

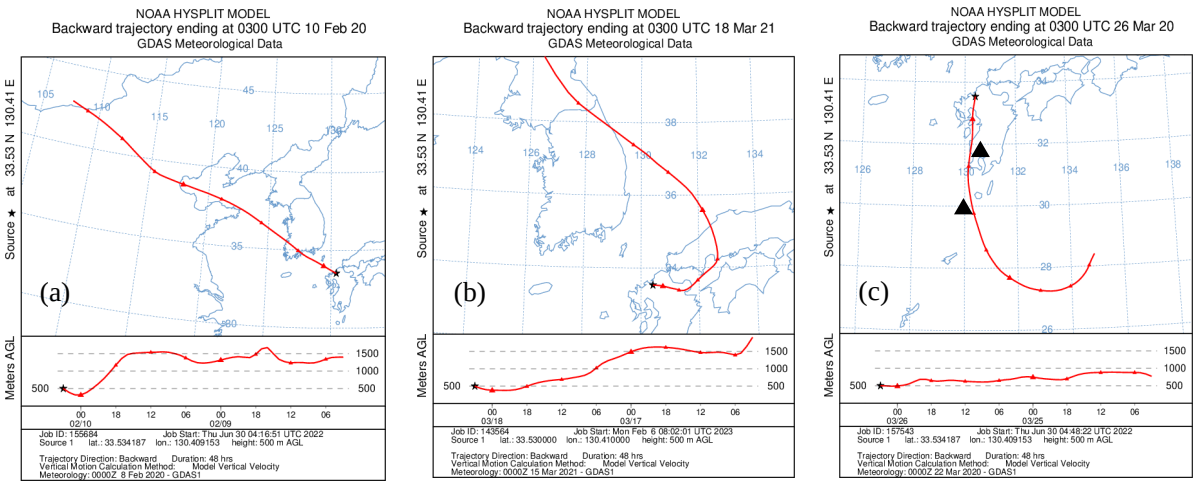

Figure 2. Examples of backward trajectory analysis on high concentration days of (a) $PM_{2.5}$ and chemical components, 10 February, 2020, (b) PAHs, 18 March, 2021, and (c) sulphate, 26 March, 2020. Closed triangles indicate volcanoes.

Thus, PAHs and sulphate ions could have higher concentrations due to different sources than each component of $PM_{2.5}$. The presentation will include a more detailed analysis of the spring 2021 data and source estimation using factor analysis such as the Positive Matrix Factorization (PMF) method. The air quality model will also be used to estimate the contribution of transboundary air pollution and local pollution.

CONCLUSIONS

We observed concentrations of $PM_{2.5}$ and its chemical composition in Fukuoka in the spring of 2020 and 2021. $PM_{2.5}$ and many chemical components showed similar concentration variations, but PAHs and sulphate sometimes showed different variations. We defined high concentration days of $PM_{2.5}$ and chemical components and analyzed air mass pathways on high concentration days. On high concentration days of $PM_{2.5}$ and chemical components, air masses reached Fukuoka from China and Korea. On days of high concentrations of only PAHs, the air masses sometimes passed through the Seto Inland Sea and Kitakyushu City in Japan. On days of high sulphate concentration only, the air masses reached Fukuoka over the southern seas of Japan and was probably influenced by volcanoes such as Suwanosejima and Sakurajima.

ACKNOWLEDGEMENTS

This study was supported by the Environment Research and Technology Development Fund (JPMEERF20195051, JPMEERF20225M02) of the Environmental Restoration and Conservation Agency provided by the Ministry of Environment of Japan.
We would like to thank Ms. M. Oda, Ms. N. Takeyama, Ms. Y. Shigeoka and Ms. K. Kojima of Fukuoka National Hospital for collecting samples of $PM_{2.5}$ every day.

REFERENCES

Pham, K.-O., Hara, A., Zhao, J., Suzuki, K., Matsuki, A., Inomata, Y., Matsuzaki, H., Odajima, H., Hayakawa, K., and Nakamura, H. (2022) Different transport behaviors between Asian Dust and polycyclic aromatic hydrocarbons in urban areas: Monitoring in Fukuoka and Kanazawa, Japan. *Appl. Sci.*, **12**, 5404.

Rolph, G., Stein, A., and Stunder, B. (2017) Real-time Environmental Applications and Display sYstem: READY. *Environ. Model. Softw.* **95**, 210–228.

Stein, A.F., Draxler, R.R., Rolph, G.D., Stunder, B.J.B., Cohen, M.D., and Ngan, F. (2015) NOAA's HYSPLIT atmospheric transport and dispersion modeling system. *Bull. Am. Meteorol. Soc.*, **96**, 2059–2077.

Yoshino, A, Takami, A., Shimizu, A., Sato, K., Hayakawa, K., Tang, N., Pham, K-O., Hara, A., Nakamura, H., and Odajima, H. (2022) Analysis of chemical components of fine particulate matter observed at Fukuoka, Japan, in spring 2020 and their transport paths. *Appl. Sci.*, **12**, 11400.

DUST-SURFACE PROMOTES THE FORMATION OF SULFURIC ACID AND ITS EFFECT ON NPF

TingYu Liu[1], ChenJie Hua[2] and Chao Yan[*]

[1] Beijing University of Chemical Technology.Beijing Adcanced Innovation Ceter for Soft Matter Science and Engineering

Keywords: Dust, gaseous H_2SO_4, NPF, Aerosol.

INTRODUCTION

The phenomenon of NPF event occurs widely in various atmospheric environments all over the world (Nieminen et al., 2018; Lee et al., 2019).. The key role of sulfuric acid in this process has been extensively studied and a variety of different models have been proposed, while gaseous sulfuric acid concentrations above 10^5 molecules per cubic centimeter have been shown to be necessary for atmospheric NPF induction(Berndt, T et al 2010)

Dust is an important factor affecting the quality of atmospheric environment, especially in northern China. In recent years, although the frequency of sand-dust weather in Beijing has decreased, its impact on people's life and atmospheric environment can not be ignored. At the same time, dust will also react with trace gases in the atmosphere, changing the chemical and physical properties of aerosols(Usher, C. R. et al 2003).

In previous studies, it was thought that there was no correlation between NPF events and dust, because high background aerosol concentration would lead to high condensing sink and coagulation sink, which would more quickly remove low-volatile vapors (such as sulfuric acid) and small clusters.(Wei Nie et al 2014) However, some recent observations have shown that NPF events occur under high aerosol background conditions.

METHODS

Our observation site is located at the top of the fifth floor of the West Campus of Beijing University of Chemical Technology, Haidian District, Beijing. It is located in the West Third Ring road of Beijing, near the road and residential areas, and there is no emission from heavy industry nearby. It is a typical urban site.

For the selection of dust cases, we used the PMF particle source analysis method to select in 2019. The PNSD were obtained from a PSM system and a DMPS system(Markku Kulmala et al 2012). At present, the uncertainty range of PSM measurement is acceptable, mainly measuring aerosol particle size spectrum below 3nm. The DMPS used at the site were developed by the University of Helsinki to measure aerosol particle size spectrum at 6-840nm. For the observation of sulfuric acid, the main use(T. Jokinen1 et al 2011) of chemical ionization atmospheric pressure interface time-of-flight mass spectrometer (CI-APi-TOF), this kind of mass spectrometry time resolution can be as low as one second, its detection limit can also reach $3.6*10^4$ per cubic centimeter. Metal concentration of particulate matter in air was obtained by heavy metal analyzer.

RESULTS AND COBCLUSION

For the Beijing in 2019, we found a total of 10 dust events. Among these 10 events, there were 12 NPF events related to dust, and 11 of them were events that grew to about 100nm. Further, the influence of dust on NPF events is divided into two types: NPF occurring simultaneously with dust and NPF occurring after dust. Among the 10 dust events, 6 new particle generation events occur at noon of the day when dust is about to end (Type 1), and 4 occur during dust. It is accompanied by a higher condensing sink (Type2). Meanwhile, in some cases, we also found abnormal peaks in PM coarse along with sulphuric acid and particulate matter below 3nm (Type 3) during the analysis. All these phenomena suggest that there may be some heterogeneous chemical reactions on the dust surface, which promote the formation of sulfuric acid and particles below 3nm. Previously, some studies have reported that Biwu Chu, who used pure TiO_2 in the smoke box and

connected it with SO_2, detected the promoting effect on NPF events. For example, Yoan Dupart, who used purchased artificial dust samples in the flow pipe, detected the change of particle number concentration.

In Type1, the new particle generation event occurs at the end of the dust, and the comparison between inorganic salts of the day and inorganic salts of the dust period can be seen (FIG. 1), indicating that this type of NPF event is due to the transit of the cold front, the existing particles and pollutants in the atmosphere are blown away by the wind, and the concentration is reduced. However, this clean condition is more suitable for the generation and growth of new particles. This type of new particle generation event has nothing to do with the dust itself.

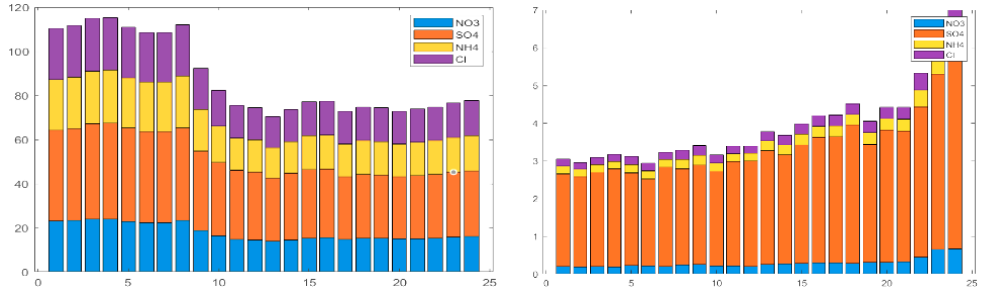

Fig.1 Comparison of inorganic salts in dust and NPF days

Although Type3 has the peak value of sulfuric acid and the particles, due to the high background aerosol concentration brought by dust, the newly formation particles are easy to be captured by large particles due to coagulation, so it is difficult to form a complete NPF event. However, it can also be found that, dust, sulfuric acid and particles below 3nm have good coincidence peaks (FIG. 2).

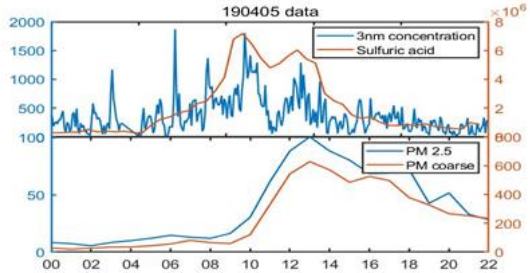

Fig.2 Correlation of PM coarse with sulfuric acid and 3nm particulate

In Type2, a complete NPF process is formed in the dust process (FIG. 3), which is often accompanied by high condensing sinks and coagulation sinks, which is contrary to our previous understanding. This phenomenon may indicate that sulfuric acid and new particle are being created on the dust surface at a rate that exceeds their loss rate and is sufficient to form a complete NPF. This kind of phenomenon was also found in the article of Nie Wei before, but due to the limitation of technical means at that time, there was no better in-depth study. And follow-up research is under way.

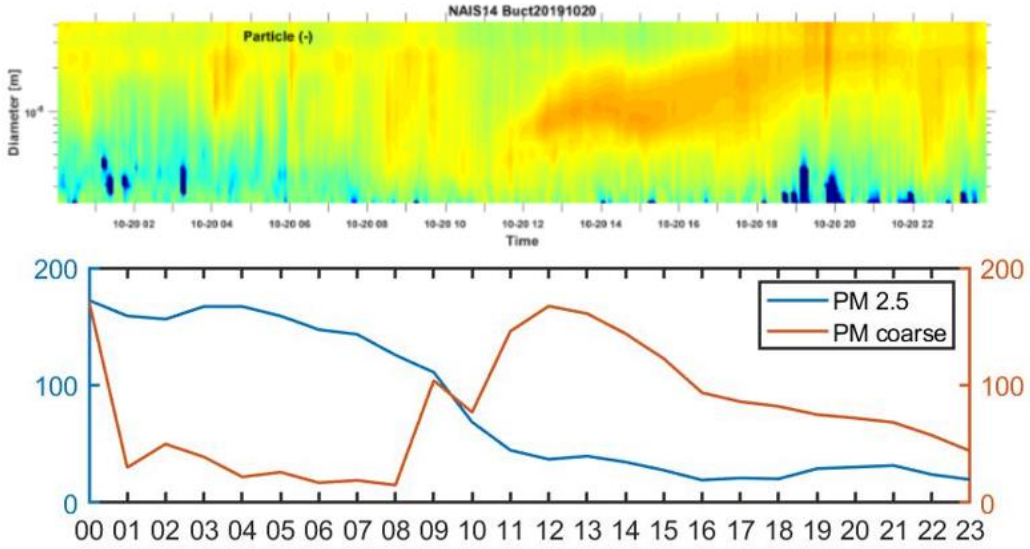

Fig.3 NPF events and dust occur simultaneously

ACKNOWLEDGEMENTS

This work was financially supported the Ministry of Science and Technology of the People's Republic of China (2019YFC0214701). We thank the Beijing University of Chemical Technology for providing the measurement platform for this campaign。

REFERENCES

Nieminen, T., Kermine(2018).Global analysis of continental boundary layer new particle formation based on long-term measurements, *Atmos. Chem. Phys.*, 18, 14737–14756
Lee, S.-H., Gordon, H.(2019) .New Particle Formation in the Atmosphere: From Molecular Clusters to Global Climate, *J. Geophys. Res.-Atmos*., 124, 7098–7146
Berndt, T.; Stratmann, F.;(2010) J. Laboratory study on new particle formation from the reaction OH + SO2: influence of experimental conditions, H_2O vapour, NH_3 and the amine tert-butylamine on the overall process. *Atmos. Chem. Phys.* 10, 7101−7116.
Usher, C. R., Michel;(2003) Reactions on mineral dust. *Chem.Rev*. 103, 4883–4939
Wei Nie, Aijun Ding(2014) Polluted dust promotes new particle formation and growth*,science reports,* 6634
T. Jokinen1 , M. Sipila(2011) Atmospheric sulphuric acid and neutral cluster measurements using CI-APi-TOF,*Atmos. Chem. Phys*.4117-4125
Markku Kulmala, Tuukka Petäjä(2012) Measurement of the nucleation of atmospheric aerosol particles,*nature protocols,*1651-1667

CCN CLIMATOLOGY OF THE GREAT BARRIER REEF

TROUNCE[1*], H., RISTOVSKI[1], Z.D., CRAVIGAN, L., ALROE[1], J., MILJEVIC[1], B., HORCLHER[1], E.J., HUMPHRIES[2], R., HARRISON[3], D.

[1] School of Earth and Atmospheric Sciences, Queensland University of Technology, Brisbane, 4000, Australia

[2] CSIRO Oceans and Atmosphere, Aspendale, 3195, Australia

[3] National Marine Science Centre, Southern Cross University, Coffs Harbour, 2450, Australia

Keywords: aerosols, clouds, CCN, great barrier reef

*corresponding author: Haydn Trounce [h.trounce@qut.edu.au]

Atmospheric aerosols play an important role in the global energy balance by absorbing or scattering solar radiation in what is known as "aerosol-radiation interactions", and by acting as cloud condensation nuclei (CCN) in "aerosol-cloud interactions" (Boucher et al., 2013). CCN concentrations affect cloud albedo, fraction and lifetime, which in turn affects surface temperatures, and is important for ecosystems such as the Great Barrier Reef (GBR) Marine Park. Despite this, characterisation of aerosols in the GBR remains incomplete (Cropp et al., 2018).

This work aims to characterise sources and transport of CCN over the GBR Marine Park. The work combines measurements collected during six voyages – two aboard Australia's RV Investigator (IN2016_v05, IN2019_T02), one aboard Schmidt Ocean Institute's RV Falkor (FK201122) and one taken as part of the Reef Restoration and Adaptation Program (RRAP) Cooling and Shading sub-program. The voyage details are shown in Table 1.

Table 1: Details of voyages analysed by this work. Aside from Darwin (located in the Northern Territory, Australia), all locations are in Queensland, Australia.

Voyage Code	Vessel	Dates	Location
IN2016_V05	RV Investigator	26/09/2016 – 26/10/2016	Brisbane – Cairns
IN2019_T02	RV Investigator	04/10/2019 – 14/10/2019	Brisbane – Darwin
FK201122	RV Falkor	22/11/2020 – 22/12/2020	Brisbane – Gladstone
2022_02_CS02	RV Magnetic /RV Guardian	27/01/2022 – 22/02/2022	Broadhurst Reef

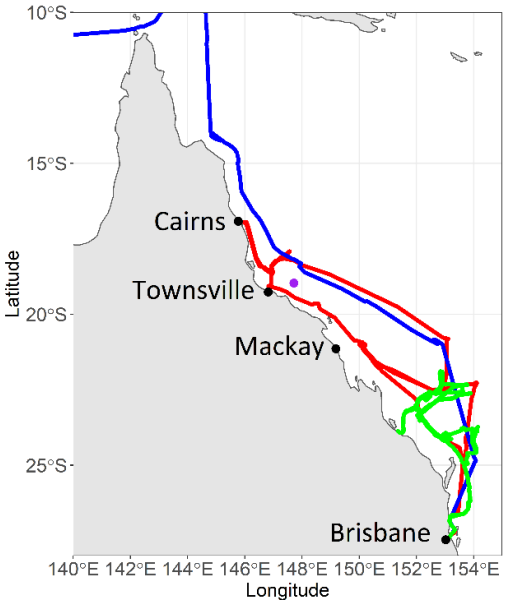

Figure 1 (right): Voyage track Voyage tracks of campaigns analysed by this work. The red, blue, and green tracks represent IN2016_v05, IN2019_T02 and FK201122, respectively. The purple dot shows the location of Broadhurst Reef (2021_03_C02, 2021_12_CS07, 2022_02_CS02)

Aerosol-cloud interactions have a large uncertainty in climate models (Boucher et al., 2013). Observations collected during these campaigns can be used to improve climate models in the region and predictions of the longevity of the reef. In addition, data collected over the GBR will be utilised within the RRAP to examine the inherent sensitivity in cloud radiative forcing over the GBR to CCN.

The RRAP is a collaboration of Australia's leading experts to create a suite of innovative and targeted measures to help preserve and restore the Great Barrier Reef. One such innovation is the Cooling and Shading subprogram, which aims at increasing local cloud albedo over the GBR by increasing the amount of available CCN for cloud formation. It is important for this subprogram that the existing CCN climatology be well understood, so that the effects of any interventions can be understood and quantified.

Particle number concentration, size distributions, CCN concentrations and activation diameters, and particle composition measurements are analysed across the four campaigns to develop a CCN climatology of the Great Barrier Reef marine park. The four campaigns take place in the southern hemisphere spring/summer months spanning six years, allowing temporal changes and changes due to effects such as La Nina or El Nino to be investigated.

ACKNOWLEDGEMENTS

The authors would like to acknowledge the CSIRO Marine National Facility and their role in undertaking this research. The authors would like to acknowledge the crew of the Marine National Facility RV *Investigator* and all personnel who took part in this voyage, and the fieldwork at Garners Beach. The fieldwork was supported by the ARC Discovery Project (DP150101649).

The authors would like to acknowledge the Schmidt Ocean Institute and the crew of the Research Vessel Falkor, for their role in the FK201122 voyage of this work.

REFERENCES

Boucher, O., D. Randall, P. Artaxo, C. Bretherton, G. Feingold, P. Forster, V.-M. Kerminen, Y. Kondo, H. Liao, U. Lohmann, P. Rasch, S.K. Satheesh, S. Sherwood, B. Stevens and X.Y. Zhang, 2013: Clouds and Aerosols. In: Climate Change 2013: *The Physical Science Basis. Contribution of Working Group I to the Fifth Assessment Report of the Intergovernmental Panel on Climate Change* [Stocker, T.F., D. doi:10.1017/CBO9781107415324.016.

Cropp, R., Gabric, A., van Tran, D., Jones, G., Swan, H., & Butler, H. (2018). Coral reef aerosol emissions in response to irradiance stress in the Great Barrier Reef, Australia. *Ambio, 47*(6), 671-681.

ON REPRESENTATION OF LOCAL NEW PARTICLE FORMATION BY AIR IONS

S. TUOVINEN[1], J. LAMPILAHTI[1], V.-M. KERMINEN[1] and M. KULMALA[1]

[1]*Institute for Atmospheric and Earth System Research, University of Helsinki, Helsinki, 00014, Finland*

Keywords: NEW PARTICLE FORMATION, CLUSTERING, AIR IONS, BOREAL FORESTS.

INTRODUCTION

Atmospheric aerosol particles affect climate through direct radiative effects and by acting as cloud condensation nuclei (CCN) (IPCC, 2021). In Hyytiälä, Finland, atmospheric new particle formation, the formation and growth of aerosol particles due to gas-to-particle conversion (Kulmala *et al.*, 2004; Dal Maso *et al.*, 2005), has been observed to increase CCN concentrations by more than 70% (Sihto *et al.*, 2011), demonstrating how aerosol production of an area or environment due to NPF can have a considerable impact on its total climate impact. Thus, to asses the potential climate effects and feedbacks of for example, a boreal forest area, the aerosol production due to NPF in that area should be quantified in addition to factors such as carbon sink and surface albedo (Kulmala *et al.*, 2020). To be able to accurately describe and combine the influence of these different factors, we want to represent local NPF with footprint area of similar magnitude as for CO_2 fluxes measured by eddy covariance measurements.

In this study we consider the suitability of atmospheric ions of different sub-3 nm sizes for indication of limited scale new particle formation using air number size distribution data measured by Neutral cluster and Air Ion Spectrometer (NAIS) (Mirme and Mirme, 2013) from SMEAR II station in Hyytiälä (Hari and Kulmala, 2005). Our aim is to find an atmospheric ion size that well represents local particle production due to NPF, while having minimal influence on the concentrations due to transport of ions.

METHODS

Ion number size distribution data from 2016 to 2020 measured by NAIS (Mirme and Mirme, 2013) at the SMEAR II measurement station in Hyytiälä, southern Finland (Hari and Kulmala, 2005), were used in the analysis. The site is surrounded by boreal, relatively homogeneous Scots pine forest.

Data was used from all seasons and all days, regardless of whether NPF had been observed to occur during the day. Concentrations from four different size bins of the instrument were investigated. The median diameters and approximate ranges of the investigated size bins were $d_{bin} \approx 1.868$ (1.733–2.008), 2.158 (2.008–2.32), 2.493 (2.32–2.68), and 2.88 (2.68–3.096) nm.

Median diurnal curves of the ion concentrations were determined by dividing the data into 30 minute time bins based on which the median values for each 30 minute of a day were determined. Based on these diurnal curves we could estimate how well ions of different sizes statistically represent particle formation. In addition, the correlation between ion concentrations in the different size bins and neutral particles between 3-6 nm measured with negative charging was evaluated.

CONCLUSIONS

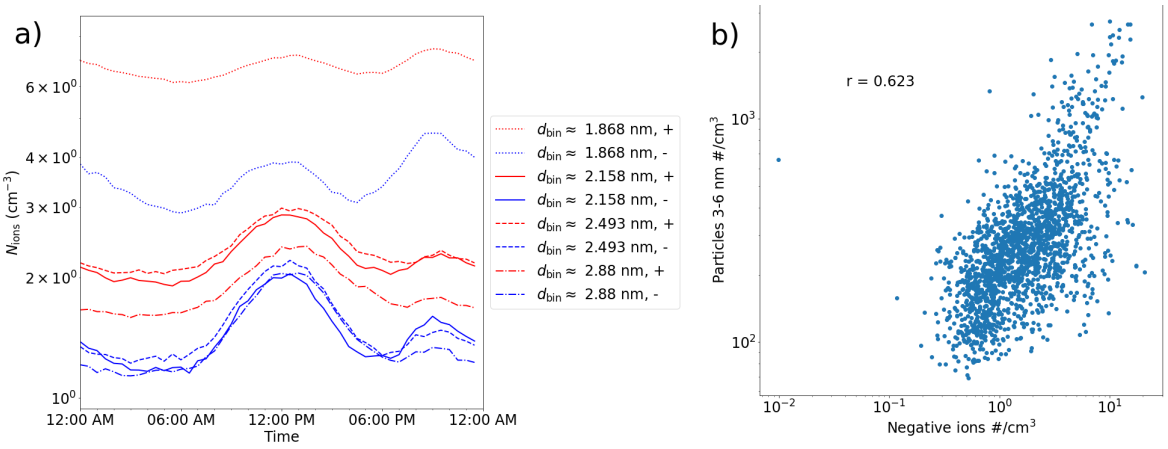

Figure 1: a) The median diurnal number concentrations of ions of diameters $d_{bin} \approx$ 1.868, 2.158, 2.493, and 2.88 nm in Hyytiälä, southern Finland. b) Median daily (08:00-16:00, local time) concentrations of negative ions with diameter $d_{bin} \approx$ 2.158 nm versus concentrations of particles with diameters between 3 and 6 nm. Spearman correlation coefficient r has been included, showing high correlation between the two concentrations.

We have found that negative ions of diameter $d_{bin} \approx$ 2.158 nm are best suited for representing local aerosol production. The influence of constant background ion concentrations for this size is much lower than for smaller sizes, and ions of smaller sizes do not accurately show the relative strength of NPF, which is important for estimating the climate impact of aerosol production. In addition, the influence of transport on ion concentrations in $d_{bin} \approx$ 2.158 nm is estimated to be considerably lower than for larger sizes, and the ions of this size are estimated to be on average mostly originating from within a one kilometer radius. Finally, negative ion concentrations in $d_{bin} \approx$ 2.158 nm show strong correlation with 3-6 nm particles, indicating that they can be applied to predict the production of particles with diameters larger than themselves. Next step will be estimating the relationship between negative ions of $d_{bin} \approx$ 2.158 nm with particles eventually growing to CCN sizes.

ACKNOWLEDGEMENTS

We acknowledge ACCC Flagship funded by the Academy of Finland grant number 33754 and University of Helsinki doctoral programme (ATM-DP).

REFERENCES

Dal Maso *et al.* (2005). Formation and growth of fresh atmospheric aerosol: eight years of aerosol size distribution data from SMEAR II, Hyytiälä, Finland. *Boreal Env. Res.* **10**, 323-336.

Hari and Kulmala (2005). Station for measuring Ecosystem-Atmosphere relations (SMEAR II). *Boreal Env. Res.* **10**, 315–322.

IPCC (2021). Summary for Policymakers. In *Climate Change 2021: The Physical Science Basis. Contribution of Working Group I to the Sixth Assessment Report of the Intergovernmental Panel on Climate Change.* (Cambridge University Press, Cambridge, UK and New York, NY, USA), doi:10.1017/9781009157896.001.

Kulmala *et al.* (2004). Formation and growth rates of ultrafine atmospheric particles: A review of observations. *J. Aerosol Sci.* **35**, 143-176.

Kulmala *et al.* (2020). CarbonSink+ -Accounting for multiple climate feedbacks from forests. *Boreal Env. Res.* **25**, 145–159.

Mirme and Mirme (2013). The mathematical principles and design of the NAIS — a spectrometer for themeasurement of cluster ion and nanometer aerosol size distributions. *Atmospheric Measurement Techniques* **6**, 1061–1071.

Sihto *et al.* (2011). Seasonal variation of CCN concentrations and aerosol activation properties in boreal forest. *Atmos. Chem. Phys* **11**(24), 13269–13285. https://doi.org/10.5194/acp-11-13269-2011

Increased contribution to $PM_{2.5}$ from traffic-influenced road dust in Shanghai over recent years and predictable future

MENG WANG[1], YUSEN DUAN[2], QINGYAN FU[2], SHUN-CHENG LEE[1, *]

[1]Department of Civil and Environmental Engineering, The Hong Kong Polytechnic University, Hung Hom, Hong Kong SAR, China

[2]Shanghai Environmental Monitoring Center, Shanghai, China

Keywords: Random Forest; Traffic; Air pollution; Non-exhaust emission

INTRODUCTION

Vehicular emissions contribute to ambient fine particulate matter ($PM_{2.5}$) through engine exhaust and non-exhaust emissions e.g., road dust (An et al., 2019; Fuzzi et al., 2015). Exposure to emissions from heavily trafficked roadways can lead to adverse health effects, including dementia, Parkinson's disease, lung cancer, cardiovascular and respiratory diseases (Annavarapu and Kathi, 2016; Chen et al., 2017; Halonen et al., 2016). Road dust caused by traffic-generated turbulence has attracted considerable research interest in recent years (Chen et al., 2019; Kong et al., 2011; Niu et al., 2019; Shakya et al., 2017). Most of these studies were based on filter measurements, influenced by artificial artifacts occurring during filter sampling and poor temporal resolution (e.g., 24 h mean), which have failed to provide sufficient information e.g., the diurnal variation. Moreover, lack of long-term roadside measurements of road dust limits our understanding of its recent trend and our ability to predict future emissions. In particular, as the number of vehicles is increasing (Jin and He, 2019; Wang et al., 2019), the corresponding road dust is expected to increase however, this remain poorly investigated in real-world conditions because of the lack of long-term roadside data.

In this study, markers for engine exhaust (EC), and road dust (calcium; Ca), were measured, along with the major components of $PM_{2.5}$, at an hourly resolution at a roadside near a highway in Shanghai from 2016 to 2019. A random forest-based machine learning algorithm (Grange and Carslaw, 2019; Grange et al., 2018) was applied to train the model to rebuild the measured EC, Ca, $PM_{2.5}$, and NO_x using meteorological and temporal variables as the model input. The SHapley Additive explanation (SHAP) algorithm (Lundberg et al., 2020; Oukawa et al., 2022) was used to understand the physical and chemical processes that govern the measured EC, Ca, and $PM_{2.5}$. Finally, a trend analysis was performed after meteorological normalization to reveal the deweathered changes over the four years.

METHODS

2 Methods

2.1 Sampling site

Hourly samples of EC and Ca in $PM_{2.5}$ were collected for four years at the Dianshan Lake (DSL)

supersite (31.09° N,120.98° E, approximately 15 m above ground), located in Qingpu District in western Shanghai.

2.3 Data analysis

2.3.1 Random Forest modeling set-up and validation

A decision-tree-based random forest model was developed to understand the trends of the observed EC, Ca, $PM_{2.5}$, and NO_x individually over the four years (2016–2019). EC was used as a marker of traffic exhaust emissions as traffic was its main contributor in Shanghai (Jia et al., 2021), whereas Ca was used as a marker of non-exhaust emissions (i.e., road dust) (Chang et al., 2018). The diurnal patterns of EC, and Ca show elevated concentrations during rush hour, which is consistent with its traffic-induced emission pattern. However, Ca may be occasionally associated with dust storms in spring, leading to the observed spikes.

Four random forests were developed, when the meteorological (ws, wd, air_temp, RH, rainfall, and pressure) and, time (date_unix, day of the year (day_julian), weekday, hour of the day, and day of the lunar year) variables for each random forest were used as model inputs. Eighty percent of the dataset was randomly selected as the training dataset, whereas the remaining 20% used to validate the models using the latest "rmweather" R package (Grange et al., 2018). To develop a tree, the number of independent/explanatory variables was set to three. The number of trees in the forest was set to 300, following Grange et al. (2018).

2.3.2 Meteorological normalization

For each target pollutant, meteorological normalization was performed by repeatedly resampling the explanatory variables (only meteorological variables included) and predicting the values at a specific time on a rolling basis over four years using deweathering techniques (Vu et al., 2019). The input meteorological variables (ws, wd, air_temp, RH, rainfall, and pressure) were randomly resampled from the original dataset (Vu et al., 2019). The resampled meteorological variables were subsequently fed to the random forest model to predict the dependent variables (EC, Ca, $PM_{2.5}$, and NO_x). This process was repeated 1000 times for each target variable. The corresponding 1000 predictions were arithmetically averaged to obtain meteorologically normalized or deweathered pollutants (Dai et al., 2021; Shi et al., 2021), i.e., the deweathered pollutants were not affected by a specific meteorological condition at a particular time.

2.3.3. Feature importance analysis

SHAP can be used to explain the output of any machine learning model (Lundberg et al., 2020; Oukawa et al., 2022). The SHAP (https://github.com/slundberg/shap) method was applied to evaluate the importance of the meteorological variables in predicting each target pollutant. SHAP uses an additive feature attribution method to produce an interpretable model (Lundberg et al., 2020), which quantified the contribution of the input meteorological variables to a single prediction at a specific time, producing a SHAP value in the same unit as the target pollutant. In this study, only the morning rush hour data (6:00–10:00) of the study period were used as model input to minimize the impact of daily variation on the pollutants.

CONCLUSIONS

In this study, hourly EC and Ca in $PM_{2.5}$ from highway sampling site in Shanghai were collected from 2016 to 2019, and were analyzed using a random forest-based machine learning algorithm. Four random forests were developed with satisfactory performances. Based on machine learning, the predicted values agreed well with the observed values, with R^2 >0.70. The effects of temperature and RH, as well as ws and wd on the observed values were revealed through the SHAP algorithm. After meteorological normalization, we showed that $PM_{2.5}$, decreased by -6.4% $year^{-1}$ over four years (Figure1). As an important source of $PM_{2.5}$, vehicular exhaust emissions, i.e., EC, also decreased but at a rate slower than that of $PM_{2.5}$. Thus, direct particulate emissions from traffic were suggested to become increasingly important, despite the decrease in traffic emissions. Moreover, road dust, as opposed to engine exhaust, which cannot be directly controlled by aftertreatment technology, was suggested to be become increasingly important. The fraction of Ca in $PM_{2.5}$ showed an increasing rate of 6.1% $year^{-1}$, roughly twice that of BC. The results from this study suggest that road dust will not abate even with cleaner on-road traffic owing to advances in aftertreatment technology and stricter emission standards. Such a trend may be exacerbated by global warming, leading to a drier atmosphere (i.e., low RH) in certain areas, inducing higher emissions of road dust from on vehicles.

ACKNOWLEDGEMENTS

This work was supported by the Environment and Conservation Fund-Environmental Research, Technology Demonstration and Conference Projects (ECF 63/2019), the RGC Theme-based Research Scheme (T24-504/17-N), the RGC Theme-based Research Scheme (T31-603/21-N).

REFERENCES

An Z, Huang R-J, Zhang R, Tie X, Li G, Cao J, et al. Severe haze in northern China: A synergy of anthropogenic emissions and atmospheric processes. Proceedings of the National Academy of Sciences 2019; 116: 8657.

Annavarapu RN, Kathi S. Cognitive disorders in children associated with urban vehicular emissions. Environmental Pollution 2016; 208: 74-78.

Chang Y, Huang K, Xie M, Deng C, Zou Z, Liu S, et al. First long-term and near real-time measurement of trace elements in China's urban atmosphere: temporal variability, source apportionment and precipitation effect. Atmos. Chem. Phys. 2018; 18: 11793-11812.

Chen H, Kwong JC, Copes R, Tu K, Villeneuve PJ, van Donkelaar A, et al. Living near major roads and the incidence of dementia, Parkinson's disease, and multiple sclerosis: a population-based cohort study. The Lancet 2017; 389: 718-726.

Chen S, Zhang X, Lin J, Huang J, Zhao D, Yuan T, et al. Fugitive Road Dust PM(2.5) Emissions and Their Potential Health Impacts. Environ Sci Technol 2019; 53: 8455-8465.

Dai Q, Hou L, Liu B, Zhang Y, Song C, Shi Z, et al. Spring Festival and COVID-19 Lockdown: Disentangling PM Sources in Major Chinese Cities. Geophysical Research Letters 2021; 48: e2021GL093403.

Fuzzi S, Baltensperger U, Carslaw K, Decesari S, Denier Van Der Gon H, Facchini M, et al. Particulate matter, air quality and climate: lessons learned and future needs. Atmospheric Chemistry and Physics 2015; 15: 8217-8299.

Grange SK, Carslaw DC. Using meteorological normalisation to detect interventions in air quality time series. Science of The Total Environment 2019; 653: 578-588.

Grange SK, Carslaw DC, Lewis AC, Boleti E, Hueglin C. Random forest meteorological normalisation models for Swiss PM10 trend analysis. Atmos. Chem. Phys. 2018; 18: 6223-6239.

Halonen JI, Blangiardo M, Toledano MB, Fecht D, Gulliver J, Anderson HR, et al. Long-term exposure to traffic pollution and hospital admissions in London. Environmental Pollution 2016; 208: 48-57.

Jia H, Pan J, Huo J, Fu Q, Duan Y, Lin Y, et al. Atmospheric black carbon in urban and traffic areas in Shanghai: Temporal variations, source characteristics, and population exposure. Environmental Pollution 2021; 289: 117868.

Jin L, He H. Comparison of the electric car market in China and the United States. https://theicct.org/sites/default/files/publications/ICCT_US-China_EV-mkt-%20comp_20190523.pdf (last access: April 01 2022), 2019.

Kong S, Ji Y, Lu B, Chen L, Han B, Li Z, et al. Characterization of PM10 source profiles for fugitive dust in Fushun-a city famous for coal. Atmospheric Environment 2011; 45: 5351-5365.

Lundberg SM, Erion G, Chen H, DeGrave A, Prutkin JM, Nair B, et al. From local explanations to global understanding with explainable AI for trees. Nature Machine Intelligence 2020; 2: 56-67.

Niu XY, Ho KF, Hu TF, Sun J, Duan J, Huang Y, et al. Characterization of chemical components and cytotoxicity effects of indoor and outdoor fine particulate matter (PM2.5) in Xi'an, China. ENVIRONMENTAL SCIENCE AND POLLUTION RESEARCH 2019; 26: 31913-31923.

Oukawa GY, Krecl P, Targino AC. Fine-scale modeling of the urban heat island: A comparison of multiple linear regression and random forest approaches. Science of The Total Environment 2022; 815: 152836.

Shakya KM, Rupakheti M, Shahi A, Maskey R, Pradhan B, Panday A, et al. Near-road sampling of PM2. 5, BC, and fine-particle chemical components in Kathmandu Valley, Nepal. Atmos. Chem. Phys. 2017; 17: 6503-6516.

Shi Z, Song C, Liu B, Lu G, Xu J, Vu TV, et al. Abrupt but smaller than expected changes in surface air quality attributable to COVID-19 lockdowns. Science Advances 2021; 7: eabd6696.

Vu TV, Shi Z, Cheng J, Zhang Q, He K, Wang S, et al. Assessing the impact of clean air action on air quality trends in Beijing using a machine learning technique. Atmos. Chem. Phys. 2019; 19: 11303-11314.

Wang J, Wu Q, Liu J, Yang H, Yin M, Chen S, et al. Vehicle emission and atmospheric pollution in China: problems, progress, and prospects. PeerJ 2019; 7: e6932-e6932.

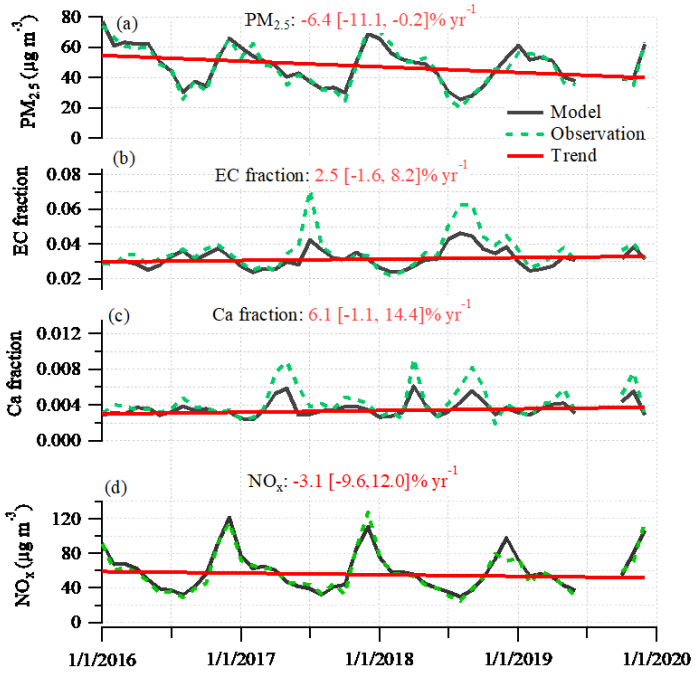

Figure 1. Monthly average (a) PM2.5 (μg m-3) (b) fraction of EC in PM2.5; and (c) fraction of Ca in PM2.5, and (d) NOx before (i.e., observation) after meteorological normalization (i.e., model). The red line represents the trend analysis of PM2.5 using the Theil-Sen estimator, with values above representing the modelled trend and the 95% confidence level.

Properties of supercooled water determined from homogeneous ice nucleation in solution droplets

A. WELTI[1], A.A. PIEDEHIERRO[1], Y.VIISANEN[1] and A. LAAKSONEN[1,2]

[1] Finnish Meteorological Institute, Helsinki, Finland

[2]Department of Applied Physics, University of Eastern Finland, Kuopio, Finland

Keywords: Homogeneous ice nucleation, supercooled water saturation, cirrus clouds.

INTRODUCTION

Due to the homogeneous freezing of water, the properties of supercooled water are difficult to measure at temperatures below 233 K. Previous experiments to study the properties of supercooled water use very rapid cooling, small droplet volumes, or high pressures to keep the probability of freezing low. Here we explore the approach of determining the saturation pressure of water below 233 K from measurements of homogeneous ice nucleation in aqueous solution droplets. Measurements of the probability of homogeneous ice nucleation as a function of relative humidity with respect to ice (RH_{ice}) and temperature, as well as solute specific water uptake, are used in the theoretical framework of Koop *et al.* (2000) to find solutions for water saturation pressure that bring Koop's approach into agreement with measurements.

METHODS

Homogeneous freezing data from salts without any heterogeneous ice nucleation ability are used for the analysis. Ice nucleation experiments are conducted using a modified version of the SPectrometer for Ice Nucleation (SPIN) chamber (Welti, 2020) capable of exposing test particles to temperatures down to 208 K and variable humidity. Particles are prepared using a combination of atomizer, dryer, and size selection with a differential mobility analyzer. Salt particles introduced into the SPIN chamber absorb water and equilibrate to the thermodynamic conditions inside the chamber. Towards lower temperatures, more concentrated solution droplets that are in equilibrium at lower supersaturation are expected to start freezing. To account for various solute effects and droplet size, the growth factors of the salt particles used are measured with a humidified tandem differential mobility analyzer or taken from the literature.
The results of experiments on homogeneous nucleation are shown in Fig. 1(a) in terms of 1% frozen fractions of solution droplets. The derived conditions of supercooled water saturation are shown in Fig. 1(b).

CONCLUSIONS

When using the estimated water saturation pressure of Murphy and Koop (2005), the measured isolines of homogeneous freezing probability diverge slightly from the theoretical estimates based on Koop *et al.* (2000). Using the measured isolines of homogeneous freezing as input for solving the equations for water saturation pressure, the results follow estimations, e.g., of Holten *et al.* (2012), shown in Fig. 1(b) , which account for a high- to low-density liquid-liquid phase transition in the homogeneous freezing regime, visible as a dip and change in slope of the water saturation line. The use of updated estimates of the saturation pressure of supercooled water can improve the

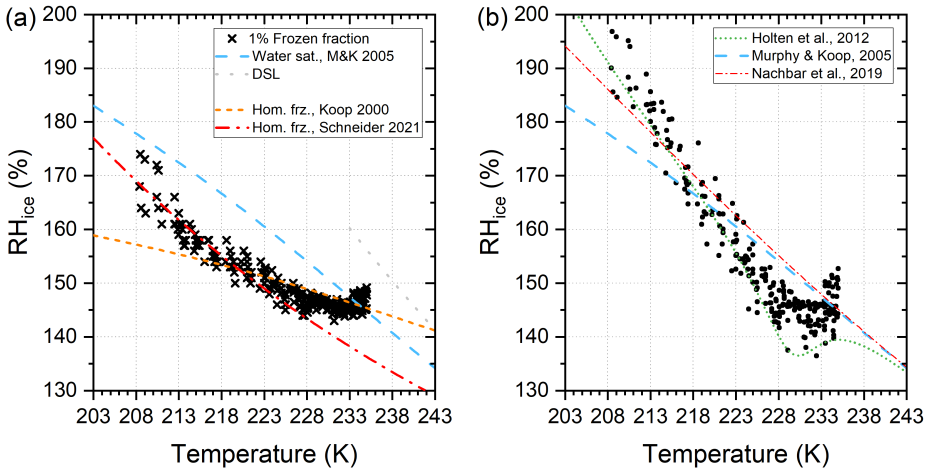

Figure 1: (a) Measured conditions (RH_{ice}, temperature) at which 1% of solution droplets freeze. For comparison, the freezing conditions predicted by Koop *et al.* (2000) and the homogeneous freezing line of aqueous sulfuric acid aerosol particles proposed by Schneider *et al.* (2021) are shown. DSL indicates conditions above which droplets interfere with the detection of the activated fraction. Water saturation from Murphy and Koop (2005) is shown in (a) and (b) as reference line. (b) Water saturation conditions derived from the measurements shown in (a). For comparison, the water saturation lines from Holten *et al.* (2012), Murphy and Koop (2005), and Nachbar *et al.* (2019) are shown.

discrimination between homogeneous and heterogeneous ice nucleation in experiments and refine the simulation of homogeneous ice nucleation in high-altitude cirrus clouds.

ACKNOWLEDGEMENTS

This work was supported by the Academy of Finland, project MEDICEN (grant no. 345125), and the ACCC Flagship programme (grant no. 337552).

REFERENCES

Holten, V., et al. (2012). Thermodynamics of supercooled water *J. Chem. Phys* , **136**, 094507.

Koop, T., et al. (2000). Water activity as the determinant for homogeneous ice nucleation in aqueous solutions *Nature*, **406**, 611-614.

Murphy, D.M. and Koop, T. (2005). Review of the vapour pressures of ice and supercooled water for atmospheric applications *Q. J. R. Meteorol. Soc.*, **131**, 1539-1565.

Schneider, J., et al. (2021). High homogeneous freezing onsets of sulfuric acid aerosol at cirrus temperatures *Atmos. Chem. Phys.*, **21**, 14403-14425.

Nachbar, M., et al. (2019). The vapor pressure of liquid and solid water phases at conditions relevant to the atmosphere *J. Chem. Phys.*, **151**, 064504.

Welti, A., et al. (2020). SPIN modification for low-temperature experiments *Atmos. Meas. Tech.*, **13**, 7059-7067.

DIRECT OBSERVATION OF CLOUD SEED AEROSOLS VIA AIRBORNE AMS MEASUREMENTS

M. KONWAR[1], B.S. WERDEN[2], E. C. FORTNER[2], S. PATIL[1], S. CHOWDHURI[1], J. SANDEEP[1], M. VARGHESE[1], N. MALAP[1], S. BERA[1], P. CROTEAU[2], J. JAYNE[2], M. CANAGARATNA[2], K. HIBERT[3], D. AXISA[4], D. BAUMGARDNER[5], P.F. DECARLO[6], D. WORSNOP[2], AND THARA PRABHAKARAN[1]

[1] *Indian Institute of Tropical Meteorology, Ministry of Earth Sciences, Pune, India, 411008*
[2] *Aerodyne Research Inc, Billerica, MA, USA, 01821*
[3] *Weather Modification Inc., Fargo, ND, USA, 58102*
[4] *Center for Western Weather and Water Extremes, Scripps Institution of Oceanography, La Jolla, CA 92037, USA*
[5] *Droplet Measurement Technologies, Longmont, CO, USA, 80503*
[6] *Department of Environmental Health and Engineering, Johns Hopkins University, Baltimore, MD USA 21218*

Keywords: Cloud Seeding, AMS, Residuals, Tracing

INTRODUCTION

Cloud seeding to control precipitation and manage drought has been well-documented (Bowen, 1952; Mather, 1997; Bruintjes, 1999). Direct observation of tracing material in seeded clouds has been an elusive challenge in cloud modification experiments (Rosenfeld, 2010), undermining the efficacy of such programs (Ryan, 1997; Silverman, 2003). Here we show novel measurements made by a mini Aerosol Mass Spectrometer (mAMS, Aerodyne Research Inc, Billerica, MA, USA; Jayne, 2000; Decarlo, 2006; Canagaratna, 2007; Drewnick, 2015) on board a research aircraft tracing flare particles. This study observed increased large-diameter droplet concentration, with seed flare aerosol as cloud residuals, lofted up to 2.25 km above the cloud base in convective clouds.

The Indian Institute of Tropical Meteorology, Pune, in collaboration with Aerodyne Research Inc., USA, and Droplet Measurement Technologies, carried out this experiment during the Cloud Aerosol Interaction and Precipitation Enhancement EXperiment (CAIPEEX; Gayatri, 2023) phase IV in 2019, in Solapur, India. This portion of the CAIPEEX project studied the effects of seeding on Monsoon clouds. This work observed cloud seeding effects and the chemical signature of cloud seeding flares by a mAMS on an airborne platform.

Cloud seeding, a widely used geoengineering technique to induce precipitation and seeding impacts, is well-studied (Flossman, 2019). Typically, SF_6, as a tracer, identifies the base of seeded clouds (WMO, 2000; Stith, 1986; Bruintjes, 1995); however, SF_6 has a multi-century lifetime in the atmosphere and is the most potent greenhouse gas (Ravishankara, 1993; Hodnebrog, 2013; Ray, 2017). This work is driven by the need for a low-impact means to study the effect of flare aerosol (Tessendorf, 2012). Using a mAMS we directly measured seed particles as cloud residuals in real-time.

METHODS

A research aircraft characterized cloud microphysical properties through wing-mounted liquid water content, cloud droplet, and particle imaging probes (LWC, CDP, PIP; Droplet Measurement Technologies, Longmont, CO, USA) and chemical composition by an onboard mAMS. The mAMS sampled interstitial non-cloud aerosol through a traditional inlet and cloud residuals through a counterflow virtual impactor (CVI; Brechtel Inc.; Shingler, 2012). Due to limited field calibrations, the concentrations presented here are nitrate equivalent.

These experiments launched flares from aircraft to measure their cloud seeding effect. Potassium perchlorate ($KClO_4$) was the flare's oxidizing agent, and calcium chloride ($CaCl_2$) was the hygroscopic seed (Hindman,

1978; Bruintjes, 2012). mAMS aircraft measurements identified cloud residual ions of the oxidant (K) and seed agent (Cl). These measurements are the first observations of hygroscopic flare particles in a seeded cloud without a tracer gas.

In laboratory experiments of atomized $CaCl_2$, shown in Figure 1, we observed slow vaporization of refractory chloride. This slow vaporizing Cl, traditionally non-refractory, can be used as an indicator of the cloud seed material. K measured in this study within hypothesized seeded clouds was also semi-refractory, with similar slow vaporization.

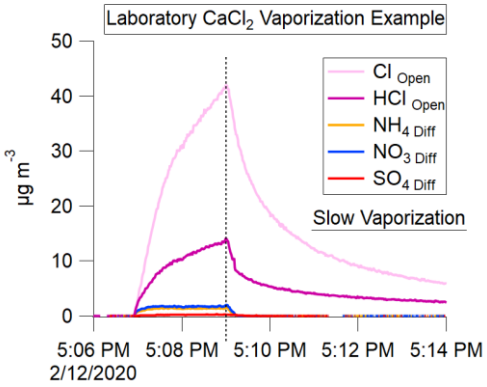

Figure 1: Example of slow vaporization of $CaCl_2$ from laboratory experiments.

The slow vaporization of these semi-refractory ions, K and Cl, in the mAMS is corrected by their specific e-folding time to match the timing of the physical cloud space intercept for NO_3, SO_4, and liquid water content (LWC) (Giordano, 2018). The e-folding times, found experimentally, were 6.7 ± 2.3 for K and 3.3 ± 0.8 for Cl. Figure 2 exhibits the correction for Cl during a seeded cloud intercept example on August 23rd, 2019.

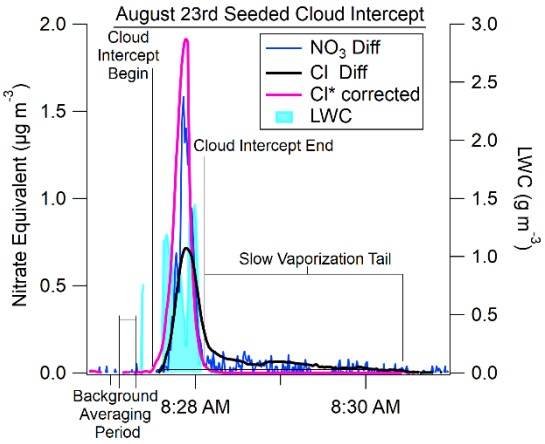

Figure 2: Example of slow vaporization correction for refractory Cl during CAIPEEX 2019.

Repeated intercepts through the same, identifiable cloud at differing altitudes by the research aircraft provide a framework for comparing the chemical composition and physical attributes before and after seeding (Hindman, 1978; Bruintjes, 2012). Observation of slow vaporizing K and Cl in known seeded clouds allows for experimental verification of this technique. Thus, with this methodology, and known flare precursors, the mAMS can, in real-time, identify seeded clouds.

RESULTS

The mAMS observed an enhancement of sulfate (SO_4), nitrate (NO_3), potassium (K), and chloride (Cl) ions in seeded cloud intercepts (SCI) over non-seeded cloud intercepts (NSCI) in over 70 successful cloud

intercepts (Figure 3). The concentration of K and Cl in SCI increased by over ten-fold compared to NSCI. This increase in the chemical signature of seed ions was only observed in clouds downwind of the flare launch site and often lofted well above the launch altitude. This lofting is the expected result of successful cloud seeding (Mather, 1997).

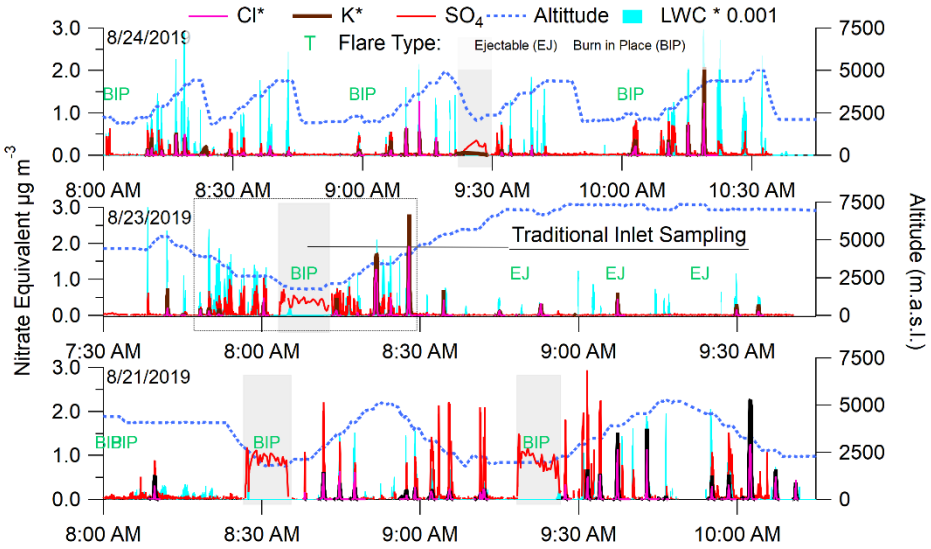

Figure 3: Time series of seed intercept chemical signatures and altitude from cloud passes in Solapur India, from CAIPEEX 2019.

Observations of an example cloud interaction from 7:49-8:28 AM on 8/23/2019 exhibit a pre- and post-seed cloud change (Figure 4), with a significant increase in tracer concentration. The cloud had minimal droplets larger than 100nm before seeding. The cloud underwent rapid hygroscopic growth immediately after the flare launch. We measure an increase in the chemical signature of the flare as refractory K and Cl in the cloud after seeding. Hygroscopic seed and oxidant aerosols from the flare, launched at ~2500 m a.s.l., were observed lofted over 2km vertically in the cloud. The top SCI had a 400% increase in large droplets and a greater than ten-fold increase in nitrate, Cl, and K compared to NSCI.

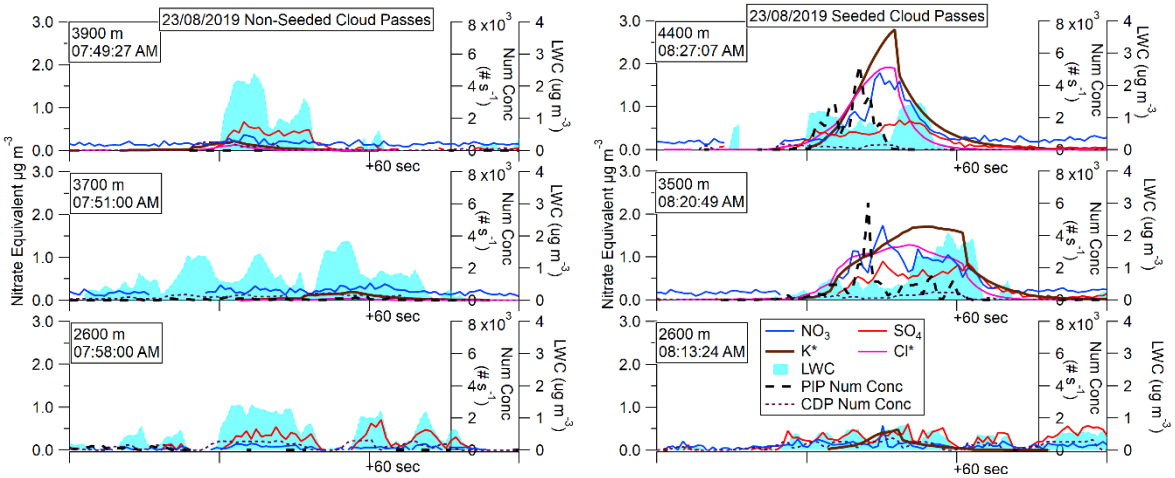

Figure 4: Six passes through the same cloud at various altitudes before and after cloud seed flare release showing aerosol background, flare seed aerosol, and droplet concentration from CAIPEEX IV 2019 in Solapur India.

CONCLUSIONS

After multiple seeding experiments, an airborne mAMS measured an enhancement of refractory K and Cl ions in convective clouds. K and Cl are components of the seed and oxidant in the flare used for this study

and, thus, are ready tracer ions for seeded cloud experiments. This work supports that this cloud seeding signature is traceable by mAMS. These seed aerosols were carried to higher altitudes by updrafts, implying active seeding effects even after cloud processing of the aerosols. This implementation can lower costs and greenhouse emissions associated with traditional SF_6 trace and release. Using a mAMS in cloud seeding experiments allows for the real-time tracking of flare plumes, which can inform the application and measure the impact of cloud geoengineering.

ACKNOWLEDGEMENTS

The Ministry of Earth Sciences, Govt. of India, funded the CAIPEEX project and this experiment. We thank the Director of IITM for their continuous support, V.Ruge of M/S Tesscorn AeroFluid, Inc., and the pilots.

REFERENCES

Bowen EG, A new method of stimulating convective clouds to produce rain and hail. Q. J. Royal Meteorol. Soc. 78, 37–45 (1952).

Bruintjes RT, A review of cloud seeding experiments to enhance precipitation and some new prospects. Bull. Am. Meteorol. Soc. 80, 805-820 (1999).

Bruintjes RT, et al., Evaluation of hygroscopic cloud seeding flares. J. Of Weather. Modif. 44, (2012).

Bruintjes RT, *et al*., The dispersion of tracer plumes in mountainous regions in central Arizona: Comparisons between observations and modeling results. J. Appl. Meteorol. 34, (1995).

Canagaratna MR, *et al*., Chemical and microphysical characterization of ambient aerosols with the aerodyne aerosol mass spectrometer. Mass Spectrom. Rev. 26, 185–222 (2007).

DeCarlo PF, *et al*., Field-deployable, high-resolution, time-of-flight aerosol mass spectrometer. Anal Chem 78, 8281-8289 (2006).

Drewnick F, *et al*., Aerosol mass spectrometry: particle vaporizer interactions and their consequences for the measurements. Atmospheric Meas. Technol. 8, 3811-3830 (2015).

Flossmann A, *et al*., Review of advances in precipitation enhancement research. Bull. Am. Meteorol. Soc. 100, 1465–1480 (2019).

Gayatri K *et al*., Physical evaluation of hygroscopic cloud seeding in convective clouds using in situ observations and numerical simulations during CAIPEEX Atmos. Research. 284 (2023)

Giordano MR, *et al*., The importance of blowing snow to halogen-containing aerosol in coastal antarctica: Influence of source region versus wind speed. Atmospheric Chem. Phys. 18 (2018).

Hindman EE, Water droplet fogs formed from pyrotechnically generated condensation nuclei. J. Of Weather. Modif. 10, 77-96 (1978).

Hodnebrog, *et al*., Global warming potentials and radiative efficiencies of halocarbons and related compounds: A comprehensive review. Rev. Geophys. 51, 300-378 (2013).

Jayne JT, *et al*., Development of an aerosol mass spectrometer for size and composition analysis of submicron particles. Aerosol Sci. Tech. 33, (2000).

Mather GK, DE Terblanche, FE Steffens, L Fletcher, Results of the south African cloud seeding experiments using hygroscopic flares. J. Appl. Meteorol. 36, 1433-1447 (1997).

Ravishankara AR, *et al*., Atmospheric lifetimes of long-lived halogenated species. Science 259, 194-199 (1993).

Ray EA, *et al*., Quantification of the sf6 lifetime based on mesospheric loss measured in the stratospheric polar vortex. J. Geophys. Res. Atmosphere 122, 4626-4638 (2017).

Rosenfeld D, *et al*., A quest for effective hygroscopic cloud seeding. J. Appl. Meteorol. Climatol. 49, 1548-1562 (2010).

Ryan BF, King WD, A critical review of the Australian experience in cloud seeding. Bull. Am. Meteorol. Soc. 78, 239-254 (1997).

Shingler T, *et al*., Characterisation and airborne deployment of a new counterflow virtual impactor inlet. Atmospheric Meas. Tech. 5, (2012).

Silverman BA, A critical assessment of hygroscopic seeding of convective clouds for rainfall enhancement. Bull. Am. Meteorol. Soc. 84, (2003).

Stith JL, *et al*., Aircraft observations of transport and diffusion in cumulus clouds. J. Appl. Meteorol. Climatol. 25, 1959-1970 (1986).

Tessendorf SA, *et al*., Investigating transport, mixing, and the formation of ice in cumuli with gaseous tracer techniques. Bull. Am. Meteorol. Soc. 93, 75-88 (2012).

WMO, Report on the WMO international workshop on hygroscopic seeding: Experimental results, physical processes, and research needs. WMP Rep 35, WMO/TD Rep 1006 36, 68pp (2000).

HETEROGENEOUS NUCLEATION ONTO PLASTIC-DERIVED NANOPARTICLES

P.J. WLASITS[1,2], R. KONRAT[1] and P.M. WINKLER[1]

[1] *Faculty of Physics, University of Vienna, Vienna, Austria.*

[2] *Vienna Doctoral School in Physics, University of Vienna, Vienna, Austria.*

Keywords: heterogeneous nucleation, Size Analyzing Nuclei Counter, nucleation probability, nanoplastics.

INTRODUCTION

In recent years nanoplastics, i. e. plastic-derived nanoparticles with diameters smaller than 1 μm (Velimirovic *et al.*, 2021), have been identified to be novel pollutants of anthropogenic origin (Materić *et al.*, 2022). Nanoplastic dispersion across various ecosystems indicates that pollution arising from these particles is a global-scale problem (Amobonye *et al.*, 2021; Materić *et al.*, 2022). As research interest is growing, new sampling and characterization methods are urgently needed to yield first insights into fundamental properties of nanoplastic aerosols (Wlasits *et al.*, 2023). Recent research has shown that aerosolized nanoplastics can be reproducibly generated from the controlled evaporation-condensation of macroplastics (Wlasits *et al.*, 2022). The presented method enabled research on heterogeneous nucleation onto airborne nanoplastic particles (Wlasits *et al.*, 2023).

Here we present the results of a set of experiments on the heterogeneous nucleation of supersaturated water vapor onto seed particles originating from Polyethylene Terephthalate (PET).

METHODS

Figure 1 shows a schematic of the experimental setup used for the presented study. PET pellets of known composition and PET platelets harvested from a water bottle were used as particle materials. Seed particles were generated by controlled evaporation-condensation using a tube furnace (Nabertherm R50/250/13) as described in Wlasits *et al.* (2022). Downstream of the furnace the aerosol was put into charge equilibrium using a soft X-ray charger (TSI Advanced Aerosol Neutralizer 3088) and size selected using a Vienna-type nano-DMA (Winkler *et al.*, 2008; Wlasits *et al.*, 2020).

Subsequent to humidification using a double-walled glass tube, the aerosol was fed into the Size Analyzing Nuclei Counter (Winkler *et al.*, 2006), an expansion-type CPC developed at the University of Vienna. Following vapor supersaturation, vapor nucleates onto and grows the seeds inside a thermostated chamber. The newly formed particles are illuminated by a laser beam and the scattered as well as the transmitted light fluxes are monitored as a function of time. The particle number concentration and particle size are determined by comparison to theoretical scattered light fluxes as a function of size, calculated from Mie theory (CAMS method, Wagner *et al.*, 1985; Winkler *et al.*, 2006).

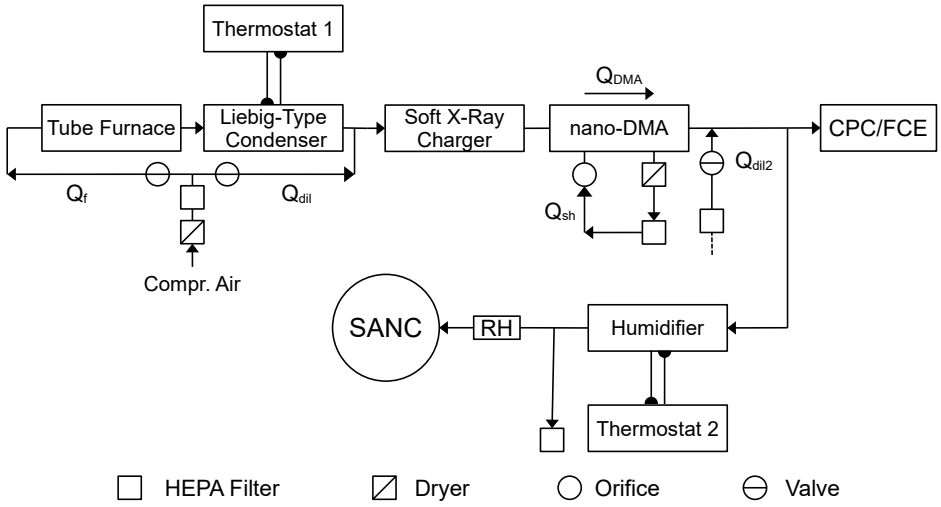

Figure 1: Schematic of the experimental setup (Wlasits et al., 2023)

CONCLUSIONS

We were able to determine the onset saturation ratios of heterogeneous nucleation occurring on the surface of sub-10 nm aerosol particles originating from PET of known composition and commodity PET. Figure 2 shows the nucleation probability as a function of the saturation ratio. The onset

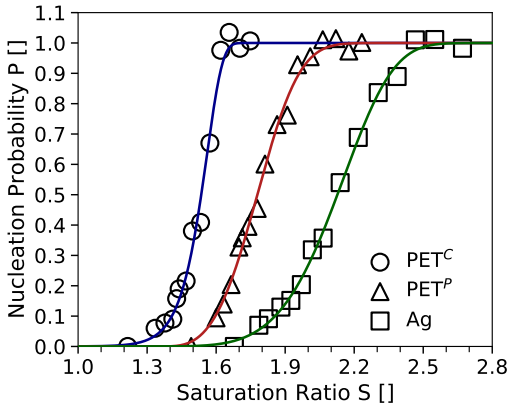

Figure 2: The figure shows the nucleation probability as a function of the saturation ratio of water vapor for PET-derived seeds of known composition (PET^P), seeds from commodity PET (PET^C) and Ag seeds. Seeds with mobility diameters of approximately 6 nm were used and the nucleation temperature was kept at 7.5 °C. (Figure and caption are based on Figure 3a in Wlasits *et al.* (2023))

saturation ratios correspond to a nucleation probability of 50 %. The activation of PET-derived seeds was compared to the activation of Ag seeds. We found, that the nanoplastic seeds are activated at lower onset saturations compared to Ag seeds having the same diameter (Wlasits *et al.*, 2023). Clearly, heterogeneous nucleation shows a significant material dependence that needs

further investigation by chemical analysis of the seeds. Furthermore the influence of the nucleation temperature was investigated and increasing onset saturation ratios for PET-derived seeds were recorded for increasing nucleation temperatures (Wlasits *et al.*, 2023). Our study reveals that condensation techniques can be used for the characterization of nanoplastic aerosols. Based on the observed temperature trend together with the size dependent behavior we conclude that nanoplastic particles may become candidates for CCNs at cold conditions despite their usually hydrophobic behavior in macroscopic state (Wlasits *et al.*, 2023).

REFERENCES

Amobonye, A., P. Bhagwat, S. Raveendran, S. Singh and S. Pillai. (2021) Environmental Impacts of Microplastics and Nanoplastics: A Current Overview. *Front. Microbiol.*, **12**, 768297.

Materić, D., H.A. Kjær, P. Vallelonga, J.-L. Tison, T. Röckmann and R. Holzinger. (2022). Nanoplastics measurements in Northern and Southern polar ice. *Environ. Res.*, **208**, 112741.

Velimirovic, M., K. Tirez, S. Verstraelen, E. Frijns, S. Remy, G. Koppen, A. Rotander, E. Bolea-Fernandez and F. Vanhaecke. (2021). Mass spectrometry as a powerful analytical tool for the characterization of indoor airborne microplastics and nanoplastics. *J. Anal. At. Spectrom.*, **36**, 695-705.

Wagner, P.E. (1985). A Constant-Angle Mie Scattering Method (CAMS) for Investigation of Particle Formation Processes. *J. Colloid Interface Sci.*, **105**, 456-467.

Winkler, P.M., A. Vrtala, R. Rudolf, P.E. Wagner, I. Riipinen, T. Vesala, K.E.J. Lehtinen, Y. Viisanen and M. Kulmala. (2006). Condensation of water vapor: Experimental determination of mass and thermal accommodation coefficients. *J. Geophys. Res.: Atmos.*, **111**, D19202.

Winkler, P.M., G. Steiner, A. Vrtala, H. Vehkamäki, M. Noppel, K.E.J. Lehtinen, G.P. Reischl, P.E. Wagner and M. Kulmala. (2008). Heterogeneous Nucleation Experiments Bridging the Scale from Molecular Ion Clusters to Nanoparticles. *Science*, **5868**, 319, 1374-1377.

Wlasits, P.J., D. Stolzenburg, C. Tauber, S. Brilke, S.H. Schmitt, P.M. Winkler and D. Wimmer. (2020). Counting on chemistry: laboratory evaluation of seed-material-dependent detection efficiencies of ultrafine condensation particle counters. *Atmos. Meas. Tech.*, **13**, 3787-3798.

Wlasits, P.J., A. Stoellner, G. Lattner, K. Maggauer, and P.M. Winkler. (2022). Size characterization and detection of aerosolized nanoplastics originating from evaporated thermoplastics. *Aerosol Sci. Technol.*, **56**, 176-185.

Wlasits, P.J., R. Konrat and P.M. Winkler. (2023). Heterogeneous Nucleation of Supersaturated Water Vapor onto Sub-10 nm Nanoplastic Particles. *Environ. Sci. Technol.*, doi:10.1021/acs.est.2c07643.

SIMULATING AEROSOL SEA-SPRAY INJECTION OVER THE GREAT BARRIER REEF

M.T. WOODHOUSE[1] and R.L. JACKSON[2]

[1]Environment, Commonwealth Scientific and Industrial Research Organisation, Aspendale, Victoria, Australia

[2] Environment, Commonwealth Scientific and Industrial Research Organisation, Black Mountain, Canberra, Australia

Keywords: reef, marine, regional modelling, clouds.

INTRODUCTION

The predicted increase in the frequency and severity of coral bleaching events, even under optimistic future emission scenarios, means that additional interventions may be needed to conserve coral reefs. The Reef Restoration and Adaptation Program (RRAP) aims to develop and assess interventions to help restore the health of the Great Barrier Reef (GBR) and prevent further degradation. Marine cloud brightening via sea-spray injection is one such intervention which may prevent coral bleaching by reducing acute heat and light stress in corals during high-risk bleaching periods.

Simulations of the impacts of sea-spray injection can be useful in many ways. They can be used to assess the impact of marine club brightening over wide areas; assess potential undesirable outcomes; and help optimize brightening strategies and timing.

METHODS

We have configured a nested atmospheric modelling system (Gordon et al., 2020) with an outer domain spanning north-eastern Australia, and a smaller higher resolution inner domain that can be relocated to focus interest on a particular area of the GBR.

The atmospheric model uses the two-moment modal aerosol scheme GLOMAP-mode (Mann et al., 2010; 2012), and simulates the full lifecycle of both natural and anthropogenic aerosol. GLOMAP-mode is coupled to the model cloud and radiation scheme, and thus can simulate aerosol direct and indirect effects.

CONCLUSIONS

Using this nested regional atmospheric model, we show that sea-spray injections over the GBR can increase the amount of solar radiation reflected away from the sea surface through aerosol direct and indirect effects, leading to a decline in surface short-wave radiation.

Sea-spray injection activities at different scales can be evaluated for their efficacy and any undesired outcomes (e.g. on precipitation, temperature, cloud cover etc)

ACKNOWLEDGEMENTS

The Reef Restoration and Adaptation Program is funded by the partnership between the Australian Governments Reef Trust and the Great Barrier Reef Foundation.

REFERENCES

Gordon, H., Field, P. R., Abel, S. J., Barrett, P., Bower, K., Crawford, I., Cui, Z., Grosvenor, D. P., Hill, A. A., Taylor, J., Wilkinson, J., Wu, H., Carslaw, K. S., 2020. Development of aerosol activation in the double-moment Unified Model and evaluation with CLARIFY measurements. *Atmospheric Chemistry and Physics* **20**: 10997-11024.

Mann, G. W., Carslaw, K. S., Spracklen, D. V., Ridley, D. A., Manktelow, P. T., Chipperfield, M. P., Pickering, S. J., Johnson, C. E., 2010. Description and evaluation of GLOMAP-mode: a modal global aerosol microphysics model for the UKCA composition-climate model. *Geoscientific Model Development* **3**: 519-551.

Mann, G. W., Carslaw, K. S., Ridley, D. A., Spracklen, D. V., Pringle, K. J., Merikanto, J., Korhonen, S., Schwarz, J. P., Lee, L. A., Manktelow, P. T., Woodhouse, M. T., Schmidt, A., Breider, T. J., Emmerson, K. M., Chipperfield, M. P., Pickering, S. J., 2012. Intercomparison of modal and sectional aerosol microphysics representations within the same 3-D global chemical transport model. *Atmospheric Chemistry And Physics* **12**: 4449-4476.

A new oxidation flow reactor: characterisation and a case study

C. WU [a,b], R. A. BROWN [a], Z. E. BROWN [a], H. TROUNCE [a], E. J. HORCHLER [a], L. WANG [e], B. MILJEVIC [a], C. ZHANG [b,c], H. WANG [b,c], B. WANG [b,c], Z. RISTOVSKI [a,b], S. STEVANOVIC [d]

[a] International Laboratory for Air Quality and Health, School of Earth and Atmospheric Sciences, Queensland University of Technology, Brisbane, Australia

[b] JNU-QUT Joint Laboratory for Air Quality Science and Management, Jinan University, Guangzhou, China

[c] Institute for Environmental and Climate Research, Jinan University, Guangzhou, China

[d] School of Engineering, Deakin University, Waurn Ponds, Australia

[e] Shanghai Key Laboratory of Atmospheric Particle Pollution and Prevention (LAP3), Department of Environmental Science and Engineering, Fudan University, Shanghai, China

Keywords: Oxidation flow reactor, secondary organic aerosol, flaming, biomass burning

Presenting author email: changda.wu@hotmail.com / c64.wu@hdr.qut.edu.au

INTRODUCTION

Oxidation flow reactors (OFRs) have been extensively used to investigate secondary aerosol formation mechanisms of the ambient air or emission sources such as biomass burning or vehicular emissions, and they can provide useful information on the mechanisms of secondary aerosol formation. Compared with smog chambers, OFRs have a few advantages, being: (1) short residence time, (2) higher degrees of aging and (3) portability (Simonen et al., 2017). However, there has been speculation that OFR chemistry may be irrelevant to the troposphere due to the dissimilarity of its initial oxidant generation to the stratosphere (Peng and Jimenez, 2020). Despite this, OFR can still provide valuable information for studying the oxidation of VOCs, SOA formation and ageing in addition to smog chambers.

In this study, we present the characterisation results of a custom-built OFR called Rapid Aerosol Ageing Device (RAAD). OH radicals are the main oxidant in the RAAD that is formed by the photolysis of externally generated O_3 and water molecules under the radiation from 254 nm UV lamps. The flow rate of the RAAD was experimentally optimised with the pulses of carbon dioxide (CO_2) and 100 nm ammonium sulphate (AS) particles, respectively. The determined optimal flow rate was then applied for the characterisation experiments, which included residence time distribution (RTD) of particles and gases, particle wall losses and OH exposure levels under varying relative humidity and ozone conditions. The performance of the reactor was further evaluated by measuring aged emissions from laboratory-generated biomass burning emissions. Results from the ageing degree of aerosols, such as enhancement ratios of organic aerosols (OA_{ER}) and the average carbon oxidation state ($\overline{OS_C}$) will be presented.

DESCRIPTION OF RAAD

The RAAD was designed at the International Laboratory of Air Quality and Health (ILAQH), Queensland University of Technology, in collaboration with Fudan University. The reactor (Fig. 1) is a 1 m long stainless-steel cylinder with an inner diameter of 25.4 cm. With a total volume of 48.76 L, the RAAD has a surface-area-to-volume ratio of 26.52 m^{-1}.

An inlet metal plate with uniformly distributed perforations was installed to create a pre-mixing compartment, while the buffer plate forces the flow to enter the compartment radially with high turbulence. This design will ensure the sample is well mixed before being drawn into the main chamber for ageing. Another metal plate was placed at the outlet to ensure the two side flows are equally drawn from the walls of the chamber. Four UV lamps with wavelengths at 185 and 254 nm housed in quartz

sheaths were placed inside the RAAD. A large volume of compressed air (~100 LPM) is pushed through these housings to remove the heat generated by the lamps, and a temperature of 26±2 °C can be achieved while in operation. Only the central flow (about 50% of the total flow) through the reactor is used for measurements. This flow passes through the stainless-steel plate at the exit and then converges through a cone-shaped exit. The side flows, on the other hand, are influenced by the walls of the reactor and the quartz sheaths and can cause an unrealistic ageing process. Hence, this flow will not be taken into account for measurements and will be removed through two side exits close to the quartz sheaths.

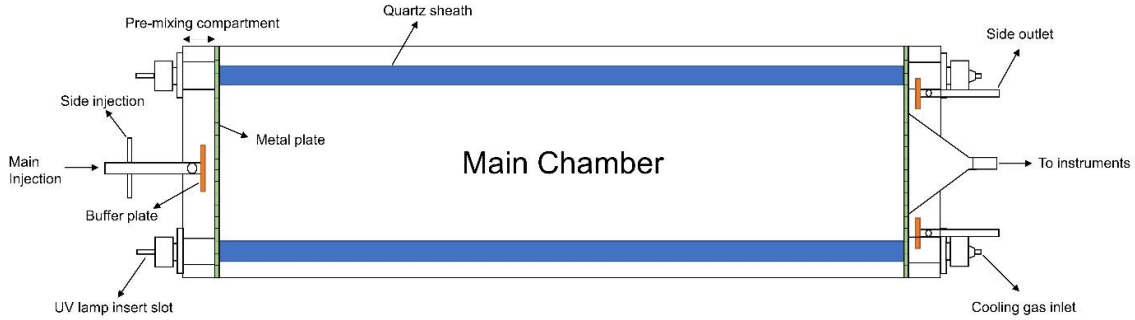

Fig. 1 Schematic of the RAAD.

RESULTS

RTDs of AS particles and CO_2 in the RAAD and the comparison with other OFRs are presented in Fig. 2. Results show that the RTDs of both gas and particles in the RAAD are close to the laminar flow, although the pulses are slightly broader than the laminar flow. The particle residence time in the RAAD is somewhat longer than that of the gas, possibly because particles are "stickier" than the inert gas and may have more interaction with the inner surface of the reactor. Both pulses are narrower than the PAM and CPOT, and a shorter tail can be observed for the RAAD. The average RTD was calculated to be 68 s at the flow rate of 45 SLPM (the optimal flow rate determined experimentally) based on the laminar flow condition.

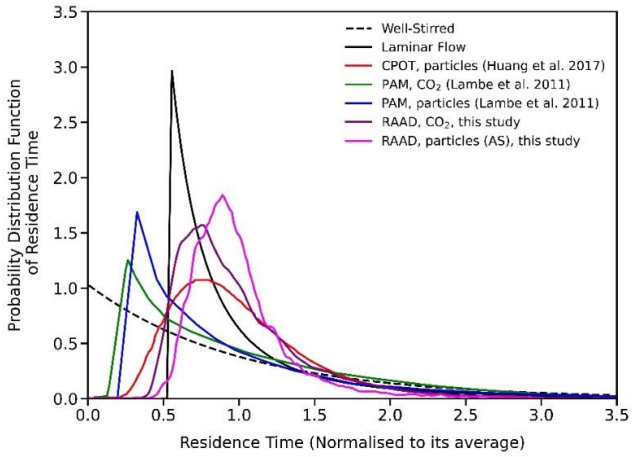

Fig. 2 Probability distribution functions of residence times for different flow reactors as a function of normalised residence time (Caltech Photooxidation Flow Tube (CPOT, (Huang et al., 2017)); Potential Aerosol Mass (PAM) chamber, (Lambe et al., 2011))

The particle transmission efficiency of the RAAD and the comparison with other OFRs are shown in Fig. 3. Overall, OFRs constructed with stainless steel generally have lower particle transmission

efficiency compared to those made of glass, possibly due to its minimal electrostatic loss property. Similar low particle wall losses were also discovered in the RAAD, with roughly 11% loss for small size particles with a mobility diameter of 30 nm. Another factor of the small losses discovered in the RAAD is that only the central flow was used for measurements, and there is no surface for particles to deposit on in this flow.

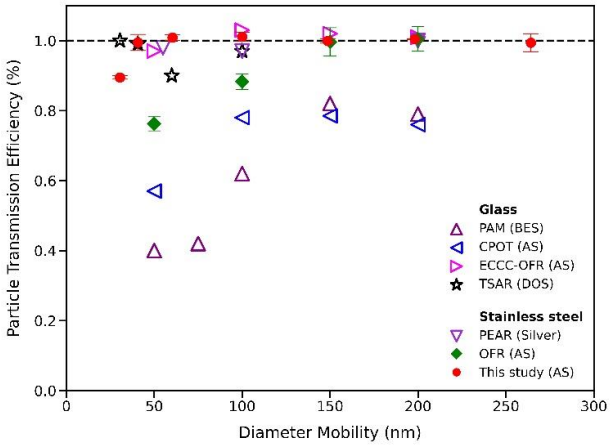

Fig. 3 Particle transmission efficiency for the RAAD and comparison with PAM (Lambe et al., 2011)), CPOT (Huang et al., 2017), ECCC-OFR (Li et al., 2019), TSAR (Simonen et al., 2017), PEAR (Ihalainen et al., 2019) and OFR (Zhao et al., 2021). Error bars are standard deviations. The generated particles in the literature include a solution of BES (bis(2-ethylhexyl) sebacate), DOS (dioctyl sebacate) and silver, respectively.

The OH exposure time (OH_{exp}) was also determined by injecting a fixed concentration of SO_2 with various ozone and relative humidity levels under UV irradiation (Fig. 4). The maximum OH_{exp} at 30% RH reached about 1.25 x 10^{12} molecule s cm^{-3}, equivalent to approximately 9 days of atmospheric ageing. In a drier condition, 15% RH, for example, the OH radicals were not efficiently produced, leading to a relatively low OH_{exp}. OH_{exp} noticeably increased under a humid condition (45% RH), reaching up to 14 days of equivalent atmospheric exposure.

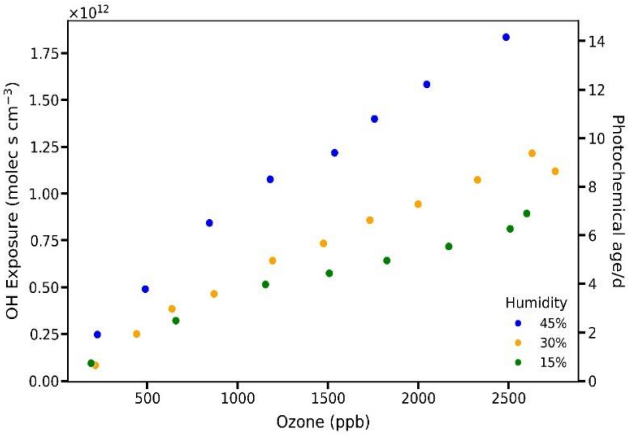

Fig. 4 OH exposures as a function of O_3 concentrations under three humidity conditions.

CONCLUSIONS

In this work, we characterised a new custom-built oxidation flow reactor named RAAD. The characterisation results demonstrate that a near-laminar flow profile can be obtained at a total flow rate of 45 slpm (25/20, centre/side), and negligible wall losses were observed in the reactor for particles with an aerodynamic diameter above 40 nm. The RTDs of gas and particles further proved that the RAAD has a near-laminar flow, with a residence time of 68s. O_3- and RH-dependent OH_{exp} were evaluated and found to have an equivalent atmospheric ageing of approximately 10 d with 30% RH. The performance of the RAAD was then evaluated by oxidising laboratory-generated biomass burning emissions with OH radicals, and reasonable OA_{ER} and $\overline{OS_C}$ were achieve.

ACKNOWLEDGEMENT

The design and construction of the RAAD was supported by the National Natural Science Foundation of China (NSFC) grant (Grant No. 21650110455). This study was also partially supported by the Australian Research Council (ARC) Discovery grant (DP180102632).

REFERENCE

Huang, Y.L., Coggon, M.M., Zhao, R., Lignell, H., Bauer, M.U., Flagan, R.C., Seinfeld, J.H., 2017. The Caltech Photooxidation Flow Tube reactor: design, fluid dynamics and characterization. Atmospheric Measurement Techniques 10, 839-867. https://doi.org/10.5194/amt-10-839-2017.

Ihalainen, M., Tiitta, P., Czech, H., Yli-Pirila, P., Hartikainen, A., Kortelainen, M., Tissari, J., Stengel, B., Sklorz, M., Suhonen, H., Lamberg, H., Leskinen, A., Kiendler-Scharr, A., Harndorf, H., Zimmermann, R., Jokiniemi, J., Sippula, O., 2019. A novel high-volume Photochemical Emission Aging flow tube Reactor (PEAR). Aerosol Science and Technology 53, 276-294. https://doi.org/10.1080/02786826.2018.1559918.

Lambe, A.T., Ahern, A.T., Williams, L.R., Slowik, J.G., Wong, J.P.S., Abbatt, J.P.D., Brune, W.H., Ng, N.L., Wright, J.P., Croasdale, D.R., Worsnop, D.R., Davidovits, P., Onasch, T.B., 2011. Characterization of aerosol photooxidation flow reactors: heterogeneous oxidation, secondary organic aerosol formation and cloud condensation nuclei activity measurements. Atmospheric Measurement Techniques 4, 445-461. https://doi.org/10.5194/amt-4-445-2011.

Li, K., Liggio, J., Lee, P., Han, C., Liu, Q.F., Li, S.M., 2019. Secondary organic aerosol formation from alpha-pinene, alkanes, and oil-sands-related precursors in a new oxidation flow reactor. Atmospheric Chemistry and Physics 19, 9715-9731. https://doi.org/10.5194/acp-19-9715-2019.

Peng, Z., Jimenez, J.L., 2020. Radical chemistry in oxidation flow reactors for atmospheric chemistry research. Chemical Society Reviews 49, 2570-2616. https://doi.org/10.1039/c9cs00766k.

Simonen, P., Saukko, E., Karjalainen, P., Timonen, H., Bloss, M., Aakko-Saksa, P., Rönkkö, T., Keskinen, J., Dal Maso, M., 2017. A new oxidation flow reactor for measuring secondary aerosol formation of rapidly changing emission sources. Atmospheric Measurement Techniques 10, 1519-1537. https://doi.org/10.5194/amt-10-1519-2017.

Zhao, R., Zhang, Q., Xu, X., Zhao, W., Yu, H., Wang, W., Zhang, Y., Zhang, W., 2021. Effect of experimental conditions on secondary organic aerosol formation in an oxidation flow reactor. Atmospheric Pollution Research 12, 205-213. https://doi.org/10.1016/j.apr.2021.01.011.

Secondary aerosol formation in summertime Antarctica: A model-measurement comparison at ABOA and Neumayer

CARLTON XAVIER[1,2], LISA BECK[3], ROBIN WOLLESEN DE JONGE[1], TUIJA JOKINEN[3,4], MIKKO SIPILÄ[3], TINJA OLENIUS[2], and PONTUS ROLDIN[1]

[1]*Division of Nuclear Physics, Department of Physics, Lund University, P. O. Box 118, 221 00 Lund, Sweden.*
[2] *Swedish Meteorological and Hydrological Institute, 60176 Norrköping, Sweden.*
[3] *Institute for Atmospheric and Earth Systems Research, University of Helsinki, P.O. Box 64, 00014 Helsinki, Finland*
[4]*Climate & Atmosphere Research Centre (CARE-C), Cyprus Institute, P.O. Box 27456, Nicosia, 1645, Cyprus*

Keywords: New particle formation (NPF), secondary aerosols, Antarctica, polar regions.

INTRODUCTION

Atmospheric new particle formation (NPF) significantly influences climate by providing seed aerosols for cloud condensation nuclei (CCN), thereby affecting the surface albedo and radiative balance (Dall'Osto et al., 2017). Characterizing the important chemical processes that lead to the formation of these atmospheric aerosols is crucial to better our prediction of the future climate. This is especially important in the pristine polar regions, which are observed to be warming at least twice as fast as the global average (Stucker et.al 2018). In this study, we attempt to improve our understanding of processes governing secondary aerosol formation in summertime remote Antarctic environments, specifically at ABOA (*73º03'S, 13º25'W, 7th-9th January 2015*) and Neumayer III (*70º40'S, 8º17'W, 12th-18th January 2019*).

METHODS

Aerosol Dynamics, gas and particle phase CHEMistry and radiative transfer model (ADCHEM) (Roldin et al., 2011) is used to model the concentrations of gases and particles along the air mass trajectories ending at ABOA (73º03'S, 13º25'W) and Neumayer III (70º40'S, 8º17'W). ADCHEM is used as a one-dimensional column model that solves the diffusion equation, with 40 linear vertical grid cells of height 100m extending up to 2500 m a.g.l. (Xavier et al., 2022). We utilize the most common and widely used Master Chemical Mechanism (MCM), an explicit chemical scheme detailing the gas phase processes involved in the tropospheric reactions of volatile organic compounds (http://chmlin9.leeds.ac.uk/MCM/roots.htt), which was coupled to the recently developed comprehensive dimethyl sulfide (DMS) and halogen multi-phase oxidation chemistry scheme(Wollesen de Jonge et al., 2021). The chemistry scheme was further updated to include the formation of gas-phase HIO_3 based on the study by Finkenzeller et al., 2022.

The air mass trajectories were calculated using the Lagrangian particle dispersion model FLEXPART Version 10.4 (Pisso et al., 2019) with meteorological input from European Center for Medium-Range Weather forecasts (ECMWF) integrated forecast systems (IFS). The air-mass trajectories were calculated for 7 days backwards in time and ending ABOA and Neumayer at 00:00, 03:00, 09:00, 12:00, 15:00, 18:00, and 21:00 UTC. The biogenic emissions (α-pinene, β-pinene, limonene, carene) were calculated using Model of Emissions of Gases and Aerosols from Nature (MEGAN v2.04). The primary biogenic ocean and anthropogenic emissions were obtained from Copernicus Atmosphere Monitoring Service (CAMS) global (CAMS-GLOB-ANT and CAMS-GLOB-OCE), which aggregates reported emissions to 246 different combinations of sectors and fuels, with a spatial resolution of 0.1º x 0.1º (lon x lat) (Granier et al., 2019).

In this work, we simulate new-particle formation by a molecular cluster plugin which explicitly couples cluster and aerosol dynamics to simulate gas-cluster-aerosol interactions and feedbacks (Olenius and Roldin, 2022). To assess the roles of different NPF mechanisms, we apply the most recent available data sets for molecular cluster thermochemistry, using all combinations of 3 different clustering chemistries involving sulfuric acid (H_2SO_4), methanesulfonic acid (MSA), ammonia (NH_3) and dimethylamine (DMA), including neutral and ion-induced H_2SO_4-NH_3 and H_2SO_4-DMA (AN, AD) pathways (ionization rate of 1.7 cm^{-3} s^{-1}) (Besel et al., 2020; Myllys et al., 2019), and neutral H_2SO_4-MSA-DMA (AMsD) (Rasmussen et al., 2022). All data sets apply the DLPNO-CCSD(T)/aug-cc-pVTZ//ωB97X-D/6-31++G(d, p) quantum chemical level of theory, but the AMsD data also involves the quasi-harmonic correction, thus not being quantitatively comparable to the other data sets. Future simulations will include also HIO_3-HIO_2. The modeled particle size distributions are compared to available DMPS and SMPS measurements at ABOA and Neumayer respectively.

CONCLUSIONS

Figure 1 shows the measured and simulated median size distribution for different combinations of clustering chemistries e.g. H_2SO_4-NH_3 (AN), H_2SO_4-DMA (AD) and H_2SO_4-MSA-DM (AMsD). These preliminary results indicate the following: first, the combination of the AN and AD chemistries can produce elevated levels of Aitken-mode particles at the Antarctic conditions. These data sets compare reasonably well with laboratory data with some underprediction of particle formation rates (Besel et al., 2020; Myllys et al., 2019) suggesting that the results of Figure 1 are likely within the lower end of realistic predictions for these pathways. Second, the AMsD and AN-AMsD cases show lower concentrations with dominance of the AN mechanism, even with enhancement of MSA for the AMsD pathway. This is likely due to the lower predicted cluster stability and absence of ions for the AMsD data set. However, as complete multi-component data sets for A-Ms-N-D are not yet available, the pathways may only be treated separately which can also cause under-prediction (Olenius et al., 2023). The inclusion of additional, e.g. iodine-driven, pathways and multi-component data sets, when available, in future simulations is expected to increase the NPF intensity.

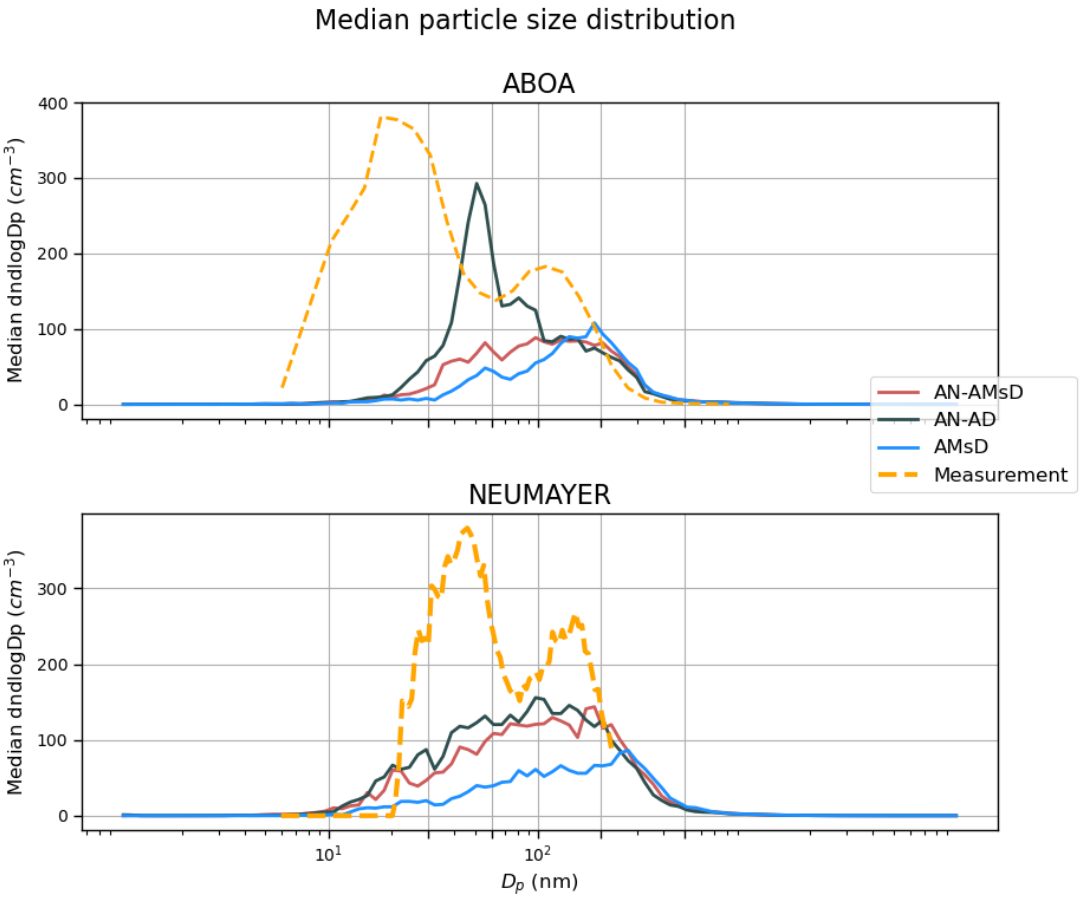

Figure 1: Measured and simulated median particle size distribution at ABOA (upper panel) and Neumayer (lower panel). The figure depicts the simulated median size distribution using combinations of different clustering chemistries, namely H_2SO_4 (A), NH_3 (N), DMA (D) and MSA (Ms). The black, red, and blue lines indicate the median size distribution using the H_2SO_4-NH_3 / H_2SO_4-DMA (AN-AD) system, the H_2SO_4-NH_3 / H_2SO_4-MSA-DMA (AN-AMsD) system, and the H_2SO_4-MSA-DMA (AMsD) system, respectively.

ACKNOWLEDGEMENTS

This project has received funding from the Swedish Research Councils Formas (projects no. 2018-01745-COBACCA, 2019-01433) and VR (projects no. 2019-05006, 2019-04853)) and the Crafoord foundation (project no. 20210969).

REFERENCES

Besel, V., Kubečka, J., Kurtén, T., and Vehkamäki, H.: Impact of Quantum Chemistry Parameter Choices and Cluster Distribution Model Settings on Modeled Atmospheric Particle Formation Rates, Journal of Physical Chemistry A, 124, 5931–5943, https://doi.org/10.1021/acs.jpca.0c03984, 2020.

Dall'Osto, M., Beddows, D. C. S., Tunved, P., Krejci, R., Ström, J., Hansson, H. C., Yoon, Y. J., Park, K. T., Becagli, S., Udisti, R., Onasch, T., Ódowd, C. D., Simó, R., and Harrison, R. M.: Arctic sea ice melt leads to atmospheric new particle formation, Sci Rep, 7, 1–10, https://doi.org/10.1038/s41598-017-03328-1, 2017.

Finkenzeller, H., Iyer, S., He, X.-C., Simon, M., Koenig, T. K., Lee, C. F., Valiev, R., Hofbauer, V., Amorim, A., Baalbaki, R., Baccarini, A., Beck, L., Bell, D. M., Caudillo, L., Chen, D., Chiu, R., Chu, B., Dada, L., Duplissy, J., Heinritzi, M., Kemppainen, D., Kim, C., Krechmer, J., Kürten, A., Kvashnin, A., Lamkaddam, H., Lee, C. P., Lehtipalo, K., Li, Z., Makhmutov, V., Manninen, H. E., Marie, G., Marten, R., Mauldin, R. L., Mentler, B., Müller,

T., Petäjä, T., Philippov, M., Ranjithkumar, A., Rörup, B., Shen, J., Stolzenburg, D., Tauber, C., Tham, Y. J., Tomé, A., Vazquez-Pufleau, M., Wagner, A. C., Wang, D. S., Wang, M., Wang, Y., Weber, S. K., Nie, W., Wu, Y., Xiao, M., Ye, Q., Zauner-Wieczorek, M., Hansel, A., Baltensperger, U., Brioude, J., Curtius, J., Donahue, N. M., Haddad, I. el, Flagan, R. C., Kulmala, M., Kirkby, J., Sipilä, M., Worsnop, D. R., Kurten, T., Rissanen, M., and Volkamer, R.: The gas-phase formation mechanism of iodic acid as an atmospheric aerosol source, Nat Chem, https://doi.org/10.1038/s41557-022-01067-z, 2022.
Granier, C., Darras, S., Gon, H. D. van der, Jana, D., Elguindi, N., Bo, G., Michael, G., Marc, G., Jalkanen, J.-P., Kuenen, J., Liousse, C., Quack, B., Simpson, D., and Sindelarova, K.: The Copernicus Atmosphere Monitoring Service global and regional emissions (April 2019 version), 2019.
Myllys, N., Kubečka, J., Besel, V., Alfaouri, D., Olenius, T., Norman Smith, J., and Passananti, M.: Role of base strength, cluster structure and charge in sulfuric-acid-driven particle formation, Atmos Chem Phys, 19, 9753–9768, https://doi.org/10.5194/acp-19-9753-2019, 2019.
Olenius, T. and Roldin, P.: Role of gas–molecular cluster–aerosol dynamics in atmospheric new-particle formation, Sci Rep, 12, 1–13, https://doi.org/10.1038/s41598-022-14525-y, 2022a.
Olenius, T. and Roldin, P.: Role of gas–molecular cluster–aerosol dynamics in atmospheric new-particle formation, Sci Rep, 12, https://doi.org/10.1038/s41598-022-14525-y, 2022b.
Olenius, T., Kupiainen-Määttä, O., Ortega, I. K., Kurtén, T., and Vehkamäki, H.: Free energy barrier in the growth of sulfuric acid–ammonia and sulfuric acid–dimethylamine clusters, J Chem Phys, 139, 084312, https://doi.org/10.1063/1.4819024, 2013.
Olenius, T., Bergström, R., Kubečka, J., Myllys, N., and Elm, J.: Reducing chemical complexity in representation of new-particle formation: Evaluation of simplification approaches, Environmental Science: Atmospheres, https://doi.org/10.1039/d2ea00174h, 2023.
Pisso, I., Sollum, E., Grythe, H., Kristiansen, N. I., Cassiani, M., Eckhardt, S., Arnold, D., Morton, D., Thompson, R. L., Groot Zwaaftink, C. D., Evangeliou, N., Sodemann, H., Haimberger, L., Henne, S., Brunner, D., Burkhart, J. F., Fouilloux, A., Brioude, J., Philipp, A., Seibert, P., and Stohl, A.: The Lagrangian particle dispersion model FLEXPART version 10.4, Geosci Model Dev, 12, 4955–4997, https://doi.org/10.5194/gmd-12-4955-2019, 2019.
Rasmussen, F. R., Kubečka, J., and Elm, J.: Contribution of Methanesulfonic Acid to the Formation of Molecular Clusters in the Marine Atmosphere, Journal of Physical Chemistry A, 126, 7127–7136, https://doi.org/10.1021/acs.jpca.2c04468, 2022.
Roldin, P., Swietlicki, E., Schurgers, G., Arneth, A., Lehtinen, K. E. J., Boy, M., and Kulmala, M.: Development and evaluation of the aerosol dynamics and gas phase chemistry model ADCHEM, Atmos Chem Phys, 11, 5867–5896, https://doi.org/10.5194/acp-11-5867-2011, 2011.
Roldin, P., Ehn, M., Kurtén, T., Olenius, T., Rissanen, M. P., Sarnela, N., Elm, J., Rantala, P., Hao, L., Hyttinen, N., Heikkinen, L., Worsnop, D. R., Pichelstorfer, L., Xavier, C., Clusius, P., Öström, E., Petäjä, T., Kulmala, M., Vehkamäki, H., Virtanen, A., Riipinen, I., and Boy, M.: The role of highly oxygenated organic molecules in the Boreal aerosol-cloud-climate system, Nat Commun, 10, 4370, https://doi.org/10.1038/s41467-019-12338-8, 2019.
Wollesen de Jonge, R., Elm, J., Rosati, B., Christiansen, S., Hyttinen, N., Lüdemann, D., Bilde, M., and Roldin, P.: Secondary aerosol formation from dimethyl sulfide – improved mechanistic understanding based on smog chamber experiments and modelling, Atmos Chem Phys, 21, 9955–9976, https://doi.org/10.5194/acp-21-9955-2021, 2021.
Xavier, C., Baykara, M., Wollesen De Jonge, R., Altstädter, B., Clusius, P., Vakkari, V., Thakur, R., Beck, L., Becagli, S., Severi, M., Traversi, R., Krejci, R., Tunved, P., Mazzola, M., Wehner, B., Sipilä, M., Kulmala, M., Boy, M., and Roldin, P.: Secondary aerosol formation in marine Arctic environments: a model measurement comparison at Ny-Ålesund, Atmos Chem Phys, 22, 10023–10043, https://doi.org/10.5194/acp-22-10023-2022, 2022a.
Xavier, C., Baykara, M., Jonge, R. W. de, Altstädter, B., Petri Clusius, Vakkari, V., Thakur, R., Beck, L., Becagli, S., Severi, M., Traversi, R., Wehner, B., Mikko Sipilä, Kulmala, M., Boy, M., and Roldin, P.: Secondary aerosol formation in marine Arctic environments: A model measurement comparison at Ny-Ålesund, Atmos. Chem. Phys. Discuss. [preprint], https://doi.org/10.5194/acp-2022-200, in review, 2022., 2022.

EVALUATION ON ENHANCING POTENTIAL OF PRECURSORS FOR IODIC ACID-INDUCED NUCLEATION

H.-B. XIE[1], F.F. MA[1], and X.-C. HE[2]

[1]KEY LABORATORY OF INDUSTRIAL ECOLOGY AND ENVIRONMENTAL ENGINEERING, DALIAN UNIVERSITY OF TECHNOLOGY, DALIAN, CHINA
[2]INAR/PHYSICS, UNIVERSITY OF HELSINKI, HELSINKI, FINLAND

Keywords: MARINE PARTICLE FORMATION, IODIC ACID, QSAR, DIETHYLAMINE, QUANTUM CHEMICAL CALCULATION, ATMOSPHERIC CLUSTER DYNAMICS SIMULATION

INTRODUCTION

Iodic acid (IA) has recently been recognized as a key driver for new particle formation (NPF) in marine atmospheres (Sipilä *et al*., 2016; He *et al*., 2021). However, the knowledge of which atmospheric vapors can enhance IA-induced NPF remains limited. The unique halogen bonds (XBs) forming capacity of IA (Rong *et al*., 2020; Ning *et al*., 2022) makes it difficult to evaluate the enhancing potential (EP) of target compounds on IA-induced NPF based on widely studied sulfuric acid systems.

Herein, we employed a three-step procedure to evaluate the EP of potential atmospheric nucleation precursors on IA-induced NPF. Firstly, we evaluated the EP of 63 precursors by calculating the formation free energies (ΔG) of the IA-containing dimer clusters. All the selected 63 compounds including iodine and sulfur oxoacids, NH_3, amines, carbonyl compounds, organic acids, sulfides, thiol, etc. were detected in the marine atmosphere. Based on the calculated ΔG values, a quantitative structure-activity relationship (QSAR) model was constructed. Secondly, we evaluated the atmospheric concentrations of 63 $(IA)_1(X)_1$ dimer clusters. Finally, based on the concentrations of the $(IA)_1(X)_1$ dimer clusters, the compounds with the highest dimer concentration (Diethylamine (DEA)) was selected as the representative to investigate its exact enhancing potential on IA-induced nucleation by considering larger $(IA)_x(DEA)_y$ ($0 \leqslant x \leqslant 3$, $0 \leqslant y \leqslant 3$) clusters.

METHODS

A multistep global minimum sampling scheme was employed to search for the global minima of the $(IA)_1(X)_1$ dimer clusters and the $(IA)_x(DEA)_y$ (x = 1-3, y = 1-3) clusters. We calculated the concentrations of 63 $(IA)_1(X)_1$ dimer clusters ($[(IA)_1(X)_1]$) based on the ΔG values and the concentrations of IA and X. The $[(IA)_1(X)_1]$ can be written as (McGrath *et al*., 2012; Ortega *et al*., 2012):

$$[(IA)_1(X)_1] = k_{coll}[X] \times [IA]/(k_{evap} + k_{coag})$$

where k_{coll} is the kinetic gas theory collision rate coefficient between IA and X; k_{evap} and k_{coag} are the evaporation rate coefficient and coagulation sink rate coefficient of the $(IA)_1(X)_1$ dimer cluster, respectively; [X] and [IA] are the atmospheric concentrations of the X and IA, respectively.

The Atmospheric Cluster Dynamics Code (ACDC) (McGrath *et al*., 2012) was used to simulate the time evolution of the cluster formation rates (J), steady-state concentrations and growth pathways of $(IA)_x(DEA)_y$ (x = 0-3, y = 0-3) clusters.

Additionally, the calculated ΔG values of the 63 $(IA)_1(X)_1$ dimer clusters were used to construct a QSAR model by stepwise multiple linear regression (MLR).

RESULTS AND CONCLUSIONS

Among all dimer clusters, 44 contain XBs, demonstrating that XBs are frequently formed. The results reveal the important contribution of XBs to the ΔG values, distinct from the sulfuric acid (SA)/ methane sulfonic acid (MSA)-organics systems.

The QSAR model can predict the ΔG values of other $(IA)_1(X)_1$ dimer clusters and provides a foundation for the future evaluation of the collective contribution of all potential atmospheric nucleation precursors within the model applicability domain on the IA-induced nucleation.

By considering the atmospheric concentrations of 63 precursors and the ΔG values of the corresponding $(IA)_1(X)_1$ dimer clusters, DEA was found to have the highest potential to enhance IA-induced nucleation. The ACDC simulation of larger $(IA)_{1-3}(DEA)_{1-3}$ clusters revealed that [DEA] > 2.5×10^6 cm^{-3} (0.1 ppt) can lead to a notable J value when [IA] > 10^6 cm^{-3}. DEA reaches an enhancement comparable to iodous acid (HIO_2) in IA-induced nucleation (Zhang *et al*., 2022).

IA can strongly bind with S-atoms-containing (in-)organic acids and certain O-atoms-containing organic acids (OAs) besides amines and HIO_2. Since iodine oxoacids, S-atoms-containing (in-)organic acids, O-atoms-containing OAs and amines can coexist in the polluted atmosphere, the synergistic nucleation of multi-components may occur.

ACKNOWLEDGEMENTS

This work was supported by the National Natural Science Foundation of China (22236004, 22176022 and 21876024); the National Key Research and Development Program of China (2022YFC3701000, Task1); the Academy of Finland project no. 349659. F.F.M. thanks the National Natural Science Foundation of China (22206020) and the China Postdoctoral Science Foundation (2022M720640). X.-C.H. thanks Jenny and Antti Wihuri foundation for providing funding to this study.

REFERENCES

M. Sipilä, N. Sarnela, …, M. Kulmala, C. O'Dowd, Molecular-scale evidence of aerosol particle formation via sequential addition of HIO_3. *Nature*. **537**, 532-534 (2016).

X.-C. He, Y. J. Tham, …, D. R. Worsnop, M. Sipilä, Role of iodine oxoacids in atmospheric aerosol nucleation. *Science*. **371**, 589-595 (2021).

H. Rong, J. Liu, …, X. Zhang, Z. Li, Nucleation Mechanisms of Iodic Acid in Clean and Polluted Coastal Regions. *Chemosphere.* **253**, 126743 (2020).

A. Ning, L. Liu, L. Ji, X. Zhang, Molecular-Level Nucleation Mechanism of Iodic Acid and Methanesulfonic Acid. *Atmos. Chem. Phys.* **22**, 6103-6114 (2022).

M. J. McGrath, T. Olenius, …, M. Kulmala, H. Vehkamäki, Atmospheric Cluster Dynamics Code: A Flexible Method for Solution of the Birth-Death Equations. *Atmos. Chem. Phys.* **12**, 2345-2355 (2012).

I. K. Ortega, O. Kupiainen, …, V. Loukonen, H. Vehkamäki, From Quantum Chemical Formation Free Energies to Evaporation Rates. *Atmos. Chem. Phys.* **12**, 225-235 (2012).

R. Zhang, H.-B. Xie, …, M. Kulmala, X.-C. He, Critical Role of Iodous Acid in Neutral Iodine Oxoacid Nucleation. *Environ. Sci. Technol.* **56**, 14166-14177 (2022).

Aviation soot particle emissions and contrail formation under high-altitude simulation

Zheng XU[1], Meiyin ZHU[1], Zhenhong YU[1], Kang PAN[1], Bin ZHANG[1], Xuehuan HU[2], Shenghui ZHONG[1] and Longfei CHEN[2]

[1] Beihang Hangzhou Innovation Institute Yuhang, Beihang University,
Xixi Octagon City, Yuhang District, Hangzhou, China
[2] School of Energy and Power Engineering, Beihang University,
Xueyuan road No.37, Haidian district, Beijing, China.

Keywords: Aviation particulate emission, High altitude, Contrail formation, Sustainable aviation fuel

INTRODUCTION

Aviation soot particle emissions at cruise altitudes are dominant if not the only anthropogenic particle source. They can form contrail and cirrus clouds under certain ambient conditions, which may affect the earth's radiation balance and thus climate pattern. Related studies have shown that contrails and induced cirrus clouds may have a greater impact on global climate than aviation CO_2 emissions [Kärcher, 2018]. Regarding aviation particulate matter emissions, the current International Civil Aviation Organization (ICAO) database is relatively mature and complete, but they are based on ground tests under LTO cycle. There are few high-altitude emission data available in the literature, which involves real flight tests. There are inevitable limitations in the high-altitude real flight tests because the sampling airplane had to be at least several hundred meters behind the test airplane due to safety reasons, hence the plume dilution and evolution process could not be controlled or even measured and the early stage of contrail formation near the engine nozzle cannot be determined at all. Therefore, we have built a high-altitude environmental chamber and a miniature aero-engine can operate on ground to simulate its cruise operation including intake air and contrail evolution under cruise-like conditions. In this paper, we will report well-controlled experimental data focusing on the early stage of contrail formation and elucidate how sustainable aviation fuel (SAF) alters the contrail formation.

METHODS

In this study, the high-altitude environmental simulation system was used to carry out the high-altitude turbofan aero-engine tests, focusing on the soot particle emissions and the early stage of contrail formation. The test fuel was conventional kerosene and SAF originated from waste cooking oil. The high-altitude test system can simulate the ambient air conditions from ground all the way up to cruise altitudes (0 km – 15 km), such as temperature (-60℃-50℃), low pressure (0.2 bar-1.0 bar), relative humidity (20%-100%), wind speed (0 m/s-100 m/s) and wind direction. Thus, the combustion and emission of the engine would be similar to the real high-altitude data. The experimental apparatus includes a visualized high-altitude environment chamber (Figure 1), which allows the engine exhaust plume to enter, and to be visualized so that the macroscopic shape of the contrail formation, and the micron-sized ice crystals can be obtained through an adjustable microscopic optical system. The experimental system can be used to predict the radiative forcing of contrail under different conditions as well. Furthermore, the aviation soot particulate measurement system (nvPM-MS, ICAO standards), scanning electric mobility particulate size spectrometer (SMPS) and continuous Flow Diffusion Chamber-Ice Activation Spectrometer (CFDC-IAS) were used as well. The measured number and mass, particulate size distribution and the ice nucleating capability of soot particulates emitted under high-altitude environments, could facilitate the understanding of the influence factors and the microphysics mechanism of contrail formation.

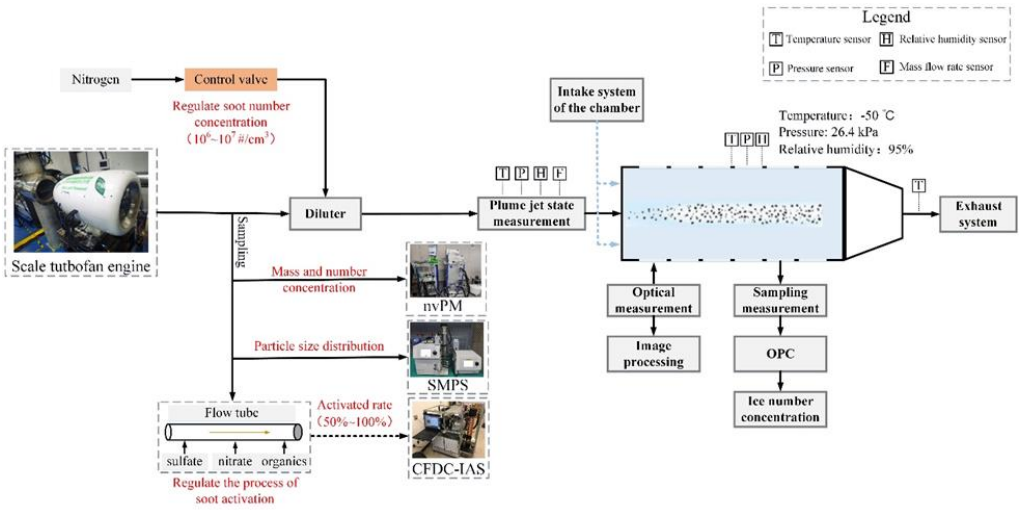

Figure 1 High-altitude contrail formation observation system

CONCLUSIONS

Some preliminary conclusions are as follows:

Under the high-altitude environment, the soot particulate produced by SAF combustion are about 25% and 20% less than RP3 in number and mass, respectively. Moreover, high-altitude SAF combustion tends to produce nano-particulate with smaller particulate sizes. For example, the average particulate sizes of RP3 and SAF under aero-engine 50% thrust condition are 29nm and 20nm, respectively (Figure 2), which theoretically reduces their ability to become cloud nucleation.

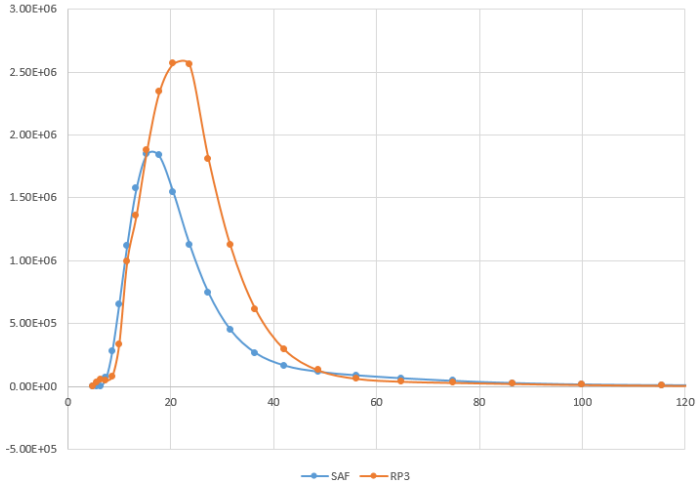

Figure 2 Soot particulate size distribution of SAF and RP3 under cruise conditions

Under the conditions of temperature and pressure at an altitude of 12km, as well as a relative humidity of 70%, the shape of the contrail (Figure 2) formed by SAF from waste cooking oil is slightly less obvious than that of RP3 (Figure 3), that means, less ice crystals and higher light transmittance. Although SAF can reduce the emission of soot particulate, the amount of water vapor emission may increase at the same time. Whether all types of SAF can reduce the formation of contrail under high-altitude environments needs further investigation.

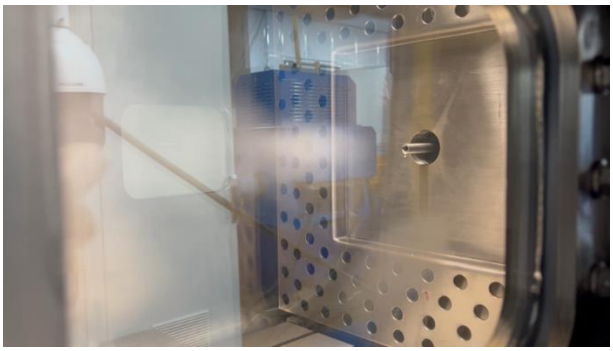

Figure 3 Shape of contrail formation under high-altitude originated from RP3 soot particulate

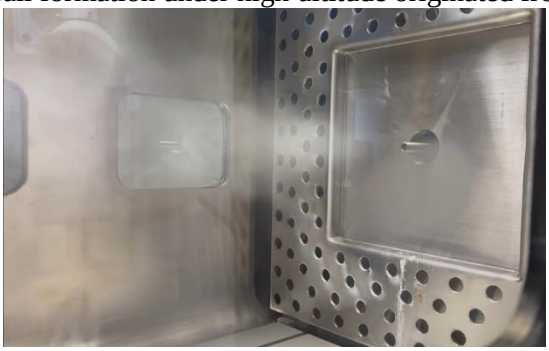

Figure 4 Shape of contrail formation under high-altitude originated from SAF soot particulate

ACKNOWLEDGEMENTS

This work was supported by the Basic Research Program of the National Nature Science Foundation of China under grant 52206131, and Zhejiang Provincial Natural Science Foundation of China under grant LQ22E060004 and LQ23E060007.

REFERENCES

Undavalli, V., Olatunde, O. B. G., Boylu, R., Wei, C., Haeker, J., Hamilton, J., & Khandelwal, B. (2023). Recent advancements in sustainable aviation fuels.*Progress in Aerospace Sciences*,*136*, 100876.

Kärcher, B. (2018). Formation and radiative forcing of contrail cirrus. Nature communications, 9(1), 1824.

Aygun, H., & Turan, O. (2023). Analysis of cruise conditions on energy, exergy and NOx emission parameters of a turbofan engine for middle-range aircraft. *Energy*, *267*, 126468.

ILLUMINATING AN OBSCRUED SOURCE FOR MARINE CLOUD NUCLEI

W. XU[1,2], J. OVADNEVAITE[2], K. FOSSUM[2], C, O'DOWD[2], D. CEBURNIS[2]

[1]*College of Ocean and Earth Sciences, Xiamen University, Xiamen, China*

[2]*Center for Climate and Air Pollution Studies, University of Galway, Galway, Ireland*

Keywords: sea spray aerosol, cloud condensation nuclei, hygroscopicity, number size distribution

INTRODUCTION

It has been suggested that the sea spray aerosol (SSA) contributes a small fraction to marine cloud condensation nuclei (CCN), due to the low number concentration of SSA. However, the SSA number concentration remains poorly constrained and often extrapolated from super-micrometre sizes.

METHODS

Here we analyse long-term observations of aerosol concentrations and compositions in the Northeast Atlantic. We derive SSA number size distribution from ambient by combining aerosol hygroscopicity growth measurement and number size distribution.

CONCLUSIONS

Our results showed that the number concentration of sub-micron SSA has been greatly underestimated, and SSA contributed significantly to the marine CCN budget, exceeding previous estimates by up to 50% to 500% at moderated marine cloud supersaturations. Given the impact of marine clouds on the Earth's radiative budget, accounting for sub-micron SSA is essential to better constrain the aerosol-cloud interaction and future climate. We derived SSA extraction method based on humidified tandem differential mobility analyser combined with scanning mobility particle sizer(denoted as HTDMA-SMPS), compared to the widely used single-sea-spray lognormal mode fitting (denoted as SSLMF), our method indicates that a large fraction of SSA has been obscured. As shown in Figure 1, the HTDMA-SMPS revealed SSA number concentrations approaching 500 cm-3 when wind speed (U10) increased up to 25 m/s.

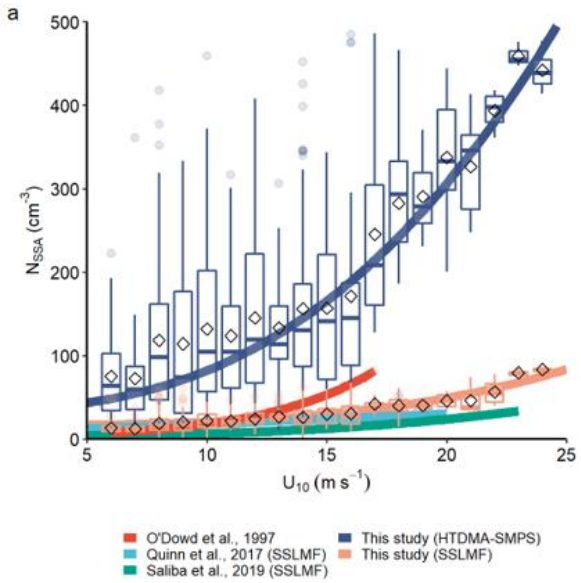

Figure 1. **Wind speed (U_{10}) versus N_{SSA}. (a)** N_{SSA} as a function of U_{10} derived by HTDMA-SMPS (dark blue line and boxes) and conventional used method(orange line and boxes), the hourly data are binned to the U_{10} intervals equal to 1 m s^{-1}, the horizontal lines represent the median value, the boxes represent 25th to 75th percentile, the whiskers represent 1.5 inter-quartile range, the points represent outliers and the cubic markers represent mean values. Also shown are previous parametrisations: O'Dowd et al., 2019[33] (red line), Quinn et al., 2017[16] (sky blue line) and Saliba et al., 2019[17] (green line).

ACKNOWLEDGEMENTS

This work was supported by the EPA Research Programme 2021-2030 (AEROSOURCE project 2016-CCRP-MS-31). The EPA Research Programme is a Government of Ireland initiative funded by the Department of Environment, Climate and Communications.

REFERENCES

Xu, W. et al. Sea spray as an obscured source for marine cloud nuclei. Nat Geosci 15, 282–286 (2022).

Quinn, P. K., Coffman, D. J., Johnson, J. E., Upchurch, L. M. & Bates, T. S. Small fraction of marine cloud condensation nuclei made up of sea spray aerosol. Nat. Geosci. 10, 674–679 (2017).

Saliba, G. et al. Factors driving the seasonal and hourly variability of sea-spray aerosol number in the North Atlantic. Proc. Natl Acad. Sci. USA 116, 20309–20314 (2019).

O'Dowd, C. D., Smith, M. H., Consterdine, I. E., and Lowe, J. A.: Marine aerosol, sea-salt, and the marine sulphur cycle: a short review, Atmos Environ, 31, 73 80, https://doi.org/10.1016/s1352-2310(96)00106-9, 1997.

WRF-WxMod®: a comprehensive model for cloud seeding research and applications

Luiln Xue1 (xuel@uar.edu), Roy Rasmussen1, Sarah Tessendorf1, Sisi Chen1, Jamie Wolff1, Thomas Chubb2, Andrew Peace2, Suzanne Kenyon2, Johanna Speirs2, Luis Ackermann3, Artur Gevorgyan3,5, Yi Huang4,6, and Steven Siems3

1 NCAR, Boulder, CO, USA
2 Snowy Hydro Ltd., Cooma, NSW, Australia
3 Monash University, Melbourne, Victoria, Australia
4 University of Melbourne, Melbourne, Victoria, Australia
5 Hydrometeorology and Monitoring Center, Climate Service Division, Yerevan, Armenia
6 Australian Research Council (ARC) Centre of Excellence for Climate Extremes, Melbourne, Victoria, Australia

The discovery of cloud microphysical responses to artificial ice nucleating particles by Schaefer and Vonnegut in the late 1940s set the stage for glaciogenic cloud seeding as a technology to increase water supplies especially in mountainous regions during wintertime. It is extremely difficult to evaluate cloud seeding effects based on observations only due to a lack of repeatability, small signal to noise ratio, and large variability in natural clouds and precipitation. Numerical models that reasonably reproduce natural cloud and precipitation processes and represent physical processes related to cloud seeding are useful for assessing cloud seeding impacts quantitatively.

The development of the novel WRF-WxMod® model system makes it a useful tool to evaluate the impacts of cloud seeding on precipitation, design new or optimize existing cloud-seeding programs, and/or forecast cloud-seeding opportunities in a real-time forecast mode.

An observation-constrained ensemble seeding simulation approach is introduced to provide a transferrable framework/tool for quantitative seeding effect assessment with uncertainty estimate based on the SNOWIE field experiment in the USA. The approach is now applied to evaluate historical seeding operations conducted by Snowy Hydro Ltd. in Australia.

Cloud-top generating cells formation in WRF-LES of two SNOWIE cases

Lulin Xue1, Sisi Chen1, Courtney Weeks1, Sarah Tessendorf1, Kyoko Ikeda1, Amanda Siems-Anderson1, Roy Rasmussen1, Nick Dawson2, Derek Blestrud2, Melvin Kunkel2, Melinda Meadows2, and Shaun Parkinson2

National Center for Atmospheric Research, Boulder, Colorado
Idaho Power Company, Boise, Idaho

Cloud-top generating cells (GCs) are ubiquitous in many types of cloud, such as the deep winter storms, post-frontal stratiform, and supercooled orographic clouds. Radar observations and in-situ measurements of cloud-top GCs show that these fine-scale cloud structures generally have higher reflectivity and stronger turbulence than the surrounding areas, and produce drizzle drops or ice particles that lead to precipitation fall streaks. Idealized numerical simulations of cloud-top GCs over the deep winter storms indicate that these strutures are caused and regulated by the instability release induced by the environmental convective instability, cloud-top radiative cooling, and shear. Recent field observations during the Seeded and Natural Orographic Wintertime clouds: the Idaho Experiment (SNOWIE) field campaign showed that cloud-top GCs were formed in a stable environment in many Intensive Observed Periods (IOPs).

Detailed analysis of high-resolution (grid spacing of 20 m) WRF Large Eddy Simulations (LES) revealed that cloud-top GCs formed only when the radiative cooling is simulated. If radiation is shut down during the active GC period, GCs quickly disappear in the simulation. It is also found that the unstable layers above the cloud top caused by dry-cold air intrusions do not facilitate GC formation. The model results indicate that the simulation of the full history of winter orographic clouds is crtical to capture the GC formation and its impact on precipitation. It is important to parameterize such ice-formation mechnisms in coarser resolution NWP models.

CHARACTERISTICS OF NEGATIVE CLUSTER IONS IN AN URBAN ENVIRONMENT

R. YIN[1,2], X. LI[1,2], C. YAN[2,4], R. CAI[2], Y. ZHOU[4], J. KANGASLUOMA[2], N. SARNELA[2], J. LAMPILAHTI[2], T. PETÄJÄ[2], V. KERMINEN[2], F. BIANCHI[2], M. KULMALA[2,4] and J. JIANG[1]

[1]Institute for Atmospheric and Earth System Research/Physics, Faculty of Science, University of Helsinki, 00014 Helsinki, Finland

[2]State Key Joint Laboratory of Environment Simulation and Pollution Control, School of Environment, Tsinghua University, Beijing, 100084, China

[3]School of Resources and Environmental Sciences, Wuhan University, 430072 Wuhan, China

[4]Aerosol and Haze Laboratory, Beijing Advanced Innovation Center for Soft Matter Science and Engineering, Beijing University of Chemical Technology, 100029 Beijing, China

Keywords: NEGATIVE CLUSTER IONS, ION COMPOSITION, URBAN ATMOSPHERE

INTRODUCTION

Atmospheric cluster ions are important constituents in the atmosphere that are mainly formed through a series of ion-molecule reactions between neutral gaseous molecules and charged atoms, molecules, and molecular clusters in the atmosphere (Carslaw *et al.*, 2002). The newly formed cluster ions will subsequently undergo more ion-molecule reactions, ion-ion recombination, or deposition on particles. Characteristics of cluster ions including their concentrations and compositions continually evolve during these processes and affect their implications on atmospheric chemistry, air quality, and human health (Jiang *et al.*, 2018; Shuman *et al.*, 2015). However, quantitative research on cluster ion compositions is still rare, especially in urban areas. In this study, we demonstrate the feasibility of an *in-situ* quantification method of atmospheric ion compositions by performing field measurements of negative ions using an atmospheric pressure interface high-resolution time-of-flight mass spectrometer (APi-TOF) and a neutral cluster and air ion spectrometer (NAIS) simultaneously in urban Beijing. Further, the governing factors of cluster ion composition and concentration in an urban atmosphere are revealed.

METHODS

A filed measurement is deployed at the Aerosol and Haze Laboratory of Beijing University of Chemical Technology Station (AHL/BUCT station), Beijing, China. There are two main traffic roads around the sampling site within 0.5 km. There are also some residential buildings around it. Fig.1 shows the location of the sampling site. It has been continuously running since 2018, and the period analyzed in this study is from Jan 14th to Sep 16th, 2018. In comparison, the measurement results of a boreal forest site Hyytiälä are used as a representative of the pristine environment.

An atmospheric pressure interface time-of-flight high-resolution mass spectrometer (APi-HTOF, Tofwerk AG) was used to measure the atmospheric negative ion compositions. In order to improve the signal-to-noise of the instrument, the 1 h average of raw signals is used for analysis. The relative mass-dependent transmission efficiency of APi-HTOF is obtained by adding a chemical ionization inlet (CI-inlet) in front of the APi-TOF (Heinritzi *et al.*, 2016). It should be noted that the voltage settings were kept the same as when APi-mode is running and were adjusted to minimize the fragmentation inside HTOF. The ion mobility distribution of atmospheric ions is measured by a neutral cluster and air ion spectrometer (NAIS, Airel Ltd.) with a mobility range of 3.2-0.0013 $cm^2 \cdot V^{-1} \cdot s^{-1}$.

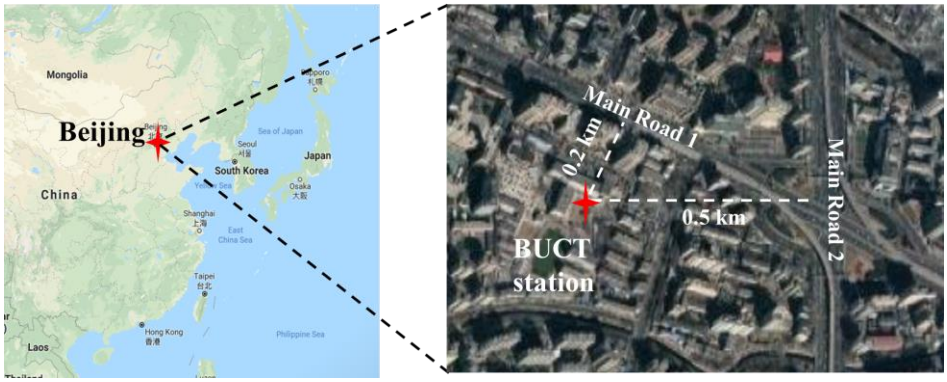

Figure 1. Map of the sampling site and the surrounding two main roads

By connecting the *m/z* of ions and ion mobilities, the concentrations of atmospheric negative cluster ions within a certain *m/z* range measured by APi-HTOF and a certain mobility range measured by NAIS are compared. The results show that their synchronous measurements are highly consistent. The derived slope between these two sets of data is taken as the detection efficiency of APi-HTOF for ions with a certain *m/z*. After correcting the sampling losses, an absolute mass-dependent transmission efficiency of APi-HTOF is obtained and shows good consistency with the relative one obtained by adding CI-inlet. This good coincidence between transmission efficiencies obtained through two independent methods show that the *in-situ* comparison between APi-HTOF and NAIS can help to well calibrate the atmospheric ions measured by APi-HTOF.

CONCLUSIONS

The concentrations of atmospheric negative ions with different compositions are quantified through the *in-situ* comparison between APi-HTOF and NAIS. Then their composition and concentrations are found to be largely affected by the high concentrations of aerosol surface area and nitrogen oxides in urban Beijing. Compared with Hyytiälä, the concentration of cluster ions is much lower in urban Beijing and shows a clear decreasing trend with an increase in condensation sink, which is mainly due to the high ion loss rate on large particles.

ACKNOWLEDGEMENTS

We gratefully acknowledge the support of the research teams in AHL/BUCT laboratory and SMEAR II station.

REFERENCES

Carslaw, K. S., Harrison, R. G., and Kirkby, J. (2002). Cosmic Rays, Clouds, and Climate, *Science* **298**, 1732-1737.

Heinritzi, M., Simon, M., Steiner, G., Wagner, A. C., Kürten, A., Hansel, A., and Curtius, J. (2016). Characterization of the mass-dependent transmission efficiency of a CIMS, *Atmos. Meas. Tech.* **9**, 1449-1460.

Jiang, S.-Y., Ma, A., and Ramachandran, S. (2018). Negative Air Ions and Their Effects on Human Health and Air Quality Improvement, *Int. J. Mol. Sci.* **19**, 2966.

Shuman, N. S., Hunton, D. E., and Viggiano, A. A. (2015). Ambient and Modified Atmospheric Ion Chemistry: From Top to Bottom, *Chem. Rev.* **115**, 4542-4570.

DETERMINING SULFURIC ACID PROXY PERFORMANCES AT SMEAR II, SOUTHERN FINLAND

I. YLIVINKKA[1,2], T. NIEMINEN[1], L. DADA[3], N. SARNELA[1], L. BECK[1], T. JOKINEN[1,4], H. JUNNINEN[5], K. PUOLAMÄKI[6] and M. KULMALA[1]

[1]Institute for Atmospheric and Earth System Research INAR / Physics, Faculty of Science, University of Helsinki, P.O. Box 64, 00014 Helsinki, Finland.
[2]SMEAR II station, University of Helsinki, 35500 Korkeakoski, Finland.
[3]Paul Scherrer Institute, Forschungsstrasse 111, 5232 Villigen PSI Switzerland.
[4]Climate & Atmosphere Research Centre (CARE-C), Cyprus Institute, P.O. Box 27456, Nicosia, 1645, Cyprus
[5]Institute of Physics, University of Tartu, W. Ostwaldi 1, 50411, Tartu, Estonia.
[6]Department of Computer Science, Faculty of Science, University of Helsinki, P.O. Box 68, 00014 Helsinki, Finland.

Keywords: SULFURIC ACID, PROXY, MODEL, BOREAL FOREST.

INTRODUCTION

Sulfuric acid is a key component of atmospheric new particle formation (NPF) due to its low saturation vapor pressure and capability to form strong bonds between molecules. NPF is a common phenomenon observed almost all around the world, and it is a large source of nanometer-sized particles. The particles can diminish air quality and affect the radiative balance of the Earth by scattering and absorbing solar radiation and acting as cloud condensation nuclei, altering cloudiness and cloud properties (Kerminen et al., 2018). Though the role of sulfuric acid in NPF is well established, the mechanisms behind NPF are still not fully understood, leading to a need for knowing the atmospheric concentrations of NPF precursor gases, such as sulfuric acid (Kerminen et al., 2018).

Long-term sulfuric acid concentration measurements are sparse, because sulfuric acid has low atmospheric concentration and therefore the measurements require specialized instrumentation and experts to operate the instruments and process the data. To fill the gap in knowledge, several proxies estimating the atmospheric concentration of sulfuric acid have been derived based on its known source and sink reactions (Petäjä et al., 2009; Mikkonen et al., 2011; Dada et al., 2020).

In this work we introduce detailed analysis on the proxies developed by Dada et al. (2020) using data from the SMEAR II (Station for Measuring Ecosystem-Atmosphere Relations) site in Hyytiälä, Finland. The aim is to understand the importance of different source and sink terms in the light of finding the best possible proxy and a simplest proxy with reasonable performance. We analyze the data also seasonally and determine the conditions when the proxies perform the most accurately.

METHODS

The most detailed proxy accounts for formation of sulfuric acid from oxidation of sulfur dioxide by OH radicals and stabilized Criegee intermediates, and loss of sulfuric acid by condensing on preexisting particles and formation of molecular dimers. Due to lack of measured OH concentration, OH is estimated using UVB or global radiation as was also done in Petäjä et al. (2009). The Criegee intermediates are formed in the ozonolysis of alkenes (Mauldin et al., 2012). In boreal forests monoterpenes (MT) form a significant share of emitted organic compounds, and are thus used here as a proxy for alkenes (Hellén et al., 2018). Loss on preexisting particles is determined with condensation sink (CS) from aerosol number

size distribution data (Kulmala et al., 2012). When including all the above mentioned processes, the rate of change in sulfuric acid concentration is

$$\frac{d[H_2SO_4]}{dt} = k_{RAD}[RAD][SO_2] + k_{sCI}[O_3][MT][SO_2] - CS[H_2SO_4] - k_{DIM}[H_2SO_4]^2. \quad (1)$$

Assuming steady state conditions, we get a formula for the concentration of sulfuric acid

$$[H_2SO_4] = \frac{-CS}{2k_{DIM}} + \sqrt{\left(\frac{CS}{2k_{DIM}}\right)^2 + \frac{[SO_2]}{k_{DIM}}\left(k_{RAD}UVB + k_{sCI}[O_3][MT]\right)}. \quad (3)$$

By minimizing the difference between the formula (Eq. 3) and measured sulfuric acid concentration, we gained values for the empirical scaling coefficients k_{RAD}, k_{sCI} and k_{DIM} related to different terms. We minimized the sum of squared logarithm of the ratio between values given by the formula and measured sulfuric acid, since the large variation in sulfuric acid concentration requires logarithmic data processing for optimal results. For the minimization we used global optimization function *fmincon* of MATLAB with *sqp* algorithm.

The proxy was developed with measurement data from years 2013, 2018-2020, and 2022. Condensation sink was obtained from the number size distribution from combined measurements of differential mobility particle sizer (DMPS) and aerodynamic particle sizer (APS; Aalto et al., 2001). Ozone, sulfur dioxide and radiation are measured in continuous basis at the station. Alkenes represented by monoterpenes were measured with proton-transfer-reaction quarupole mass spectrometer (Taipale et al., 2008) and sulfuric acid with chemical ionization ambient pressure interface time-of-flight mass spectrometer (Jokinen et al., 2012). Sulfuric acid concentration was measured at 35 m high tower, and other gas concentrations at the close-by mast from 16.8 m height above the ground level.

RESULTS

The scaling coefficients for the detailed proxy using UVB or global radiation (Eq. 3) are shown in Table 1. The correlation between proxy and measured sulfuric acid concentration are shown in Figure 1, and diurnal variation in Figure 2. The plots show good correlation between proxy and measured sulfuric acid concentration and the proxy also follows well the diurnal cycle of measured sulfuric acid concentration. Both UVB and global radiation can be used for estimating OH concentration since they produce nearly identical results.

In Figure 2 the diurnal cycle of proxies by Petäjä et al. (2009) are compared with the new detailed proxy. The comparison highlights, in accordance with Dada et al. (2020), the importance of new source and sink terms for the performance of proxies in producing diurnal variation correctly. Here, the presented scaling coefficients for the proxy using global radiation differs slightly from those presented in Dada et al. (2020) since the data set is partly different, we used CS calculated from the combined DMPS and APS data, and in finding the scaling coefficients we used global optimization, which is more accurate in large optimization problems (Nocedal & Wright, 2006).

Table 1. Scaling factors for boreal forest determined minimizing the sum of squared difference between measured and modeled sulfuric acid data.

	k_{RAD} ($m^2\ W^{-1}\ s^{-1}$)	k_{sCI} ($\cdot 10^{-29}\ cm^6\ s^{-1}$)	k_{DIM} ($\cdot 10^{-9}\ cm^3\ s^{-1}$)
UVB	$7.7 \cdot 10^{-6}$	8.6	2.6
Global radiation	$6.7 \cdot 10^{-9}$	7.5	2.9

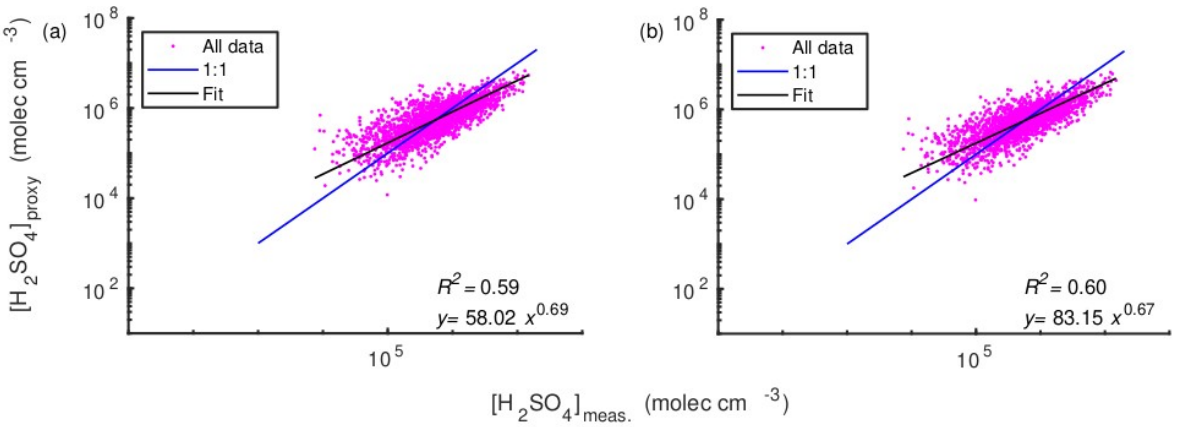

Figure 1. Scatter plot between measured sulfuric acid concentration and (a) sulfuric acid proxy using UVB radiation and (b) sulfuric acid proxy using global radiation. Blue line shows 1:1 line and black line fitted bivariate regression.

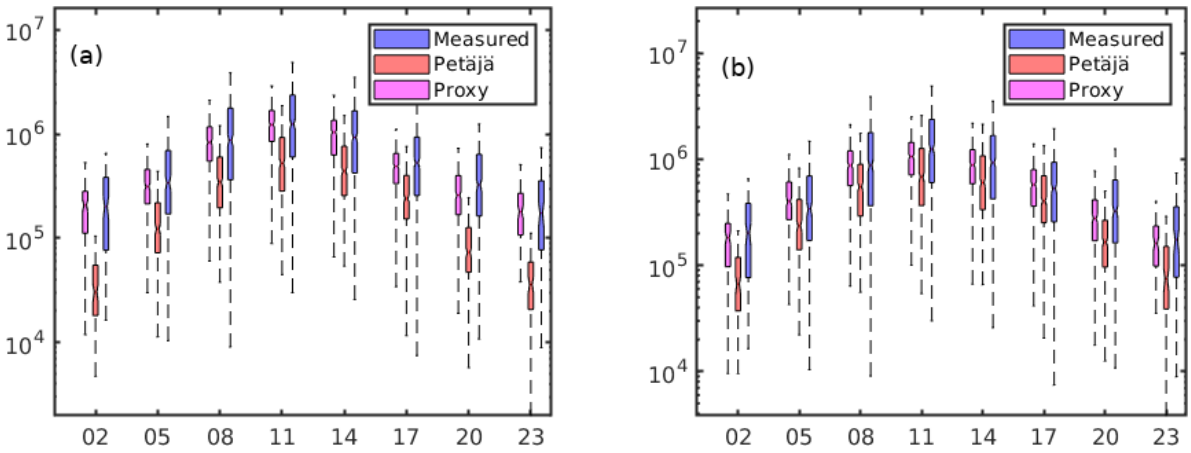

Figure 2. Diurnal variation in (a) sulfuric acid proxy using UVB radiation (pink) and UVB proxy by Petäjä et al. (2009; red) and (b) sulfuric acid proxy using global radiation (pink) and global radiation proxy by Petäjä et al. (2009; red). Measured sulfuric acid concentration is presented with blue in both subplots.

FUTURE OUTLOOK

The analysis indicates that stabilized Criegee intermediates are important oxidants for sulfur dioxide, and thus needed in sulfuric acid proxies in order to reproduce the diurnal cycle correctly. As shown also by Dada et al. (2020), the formation of molecular dimers is not a significant sink for sulfuric acid in the boreal environment. However, the analysis will be continued by quantifying the role of different terms seasonally since the first results indicate that the performance of the proxies is better during spring and summer and worse during autumn and winter. The difference might stem from the seasonality observed in the nature – during autumn the radiation intensity decreases, leading to, for example, growth cessation of vegetation, and thus to decreased monoterpene concentration, but also changes in atmospheric chemistry and concentrations of many compounds in general.

ACKNOWLEDGMENTS

This work was supported by the Academy of Finland The ACCC Flagship (337549).

REFERENCES

Aalto, P., Hämeri, K., Becker, E. D. O., Weber, R., Salm, J., Mäkelä, J. M., ... & Koponen, I. K. (2001). Physical characterization of aerosol particles during nucleation events. *Tellus B: Chemical and Physical Meteorology*, *53*(4), 344-358.

Dada, L., Ylivinkka, I., Baalbaki, R., Li, C., Guo, Y., Yan, C., ..., & Kulmala, M. (2020). Sources and sinks driving sulfuric acid concentrations in contrasting environments: implications on proxy calculations. *Atmospheric Chemistry and Physics*, 20(20):11747–11766.

Hellén, H., Praplan, A. P., Tykkä, T., Ylivinkka, I., Vakkari, V., Bäck, J., ... & Hakola, H. (2018). Long-term measurements of volatile organic compounds highlight the importance of sesquiterpenes for the atmospheric chemistry of a boreal forest. *Atmospheric Chemistry and Physics*, *18*(19), 13839-13863.

Jokinen, T., Sipilä, M., Junninen, H., Ehn, M., Lönn, G., Hakala, J., ... & Worsnop, D. R. (2012). Atmospheric sulphuric acid and neutral cluster measurements using CI-APi-TOF. *Atmospheric Chemistry and Physics*, *12*(9), 4117-4125.

Kerminen, V.-M., Chen, X., Vakkari, V., Petäjä, T., Kulmala, M., & Bianchi, F. (2018). Atmospheric new particle formation and growth: review of field observations. *Environmental Research Letters*, 13(10):103003.

Kulmala, M., Petäjä, T., Nieminen, T., Sipilä, M., Manninen, H. E., Lehtipalo, K., ..., & Kerminen, V.-M. (2012). Measurement of the nucleation of atmospheric aerosol particles. *Nature Protocols*, 7(9):1651–1667.

Mauldin III, R. L., Berndt, T., Sipilä, M., Paasonen, P., Petäjä, T., Kim, S., ... & Kulmala, M. (2012). A new atmospherically relevant oxidant of sulphur dioxide. *Nature*, *488*(7410), 193.

Mikkonen, S., Romakkaniemi, S., Smith, J. N., Korhonen, H., Petäjä, T., Plass-Duelmer, C., ... & Hamed, A. (2011). A statistical proxy for sulphuric acid concentration. *Atmospheric Chemistry and Physics*, *11*(21), 11319-11334.

Nocedal, J. & Wright, S. J. 2006. Sequential Quadratic Programming. In *Numerical Optimization*, pages 529–562. Springer New York, New York, NY.

Petäjä, T., Mauldin III, R. L., Kosciuch, E., McGrath, J., Nieminen, T., Paasonen, P., ... & Kulmala, M. (2009). Sulfuric acid and OH concentrations in a boreal forest site. Atmospheric Chemistry and Physics, 9(19), 7435-7448.

Taipale, R., Ruuskanen, T. M., Rinne, J., Kajos, M. K., Hakola, H., Pohja, T., & Kulmala, M. (2008). Quantitative long-term measurements of VOC concentrations by PTR-MS–measurement, calibration, and volume mixing ratio calculation methods. *Atmospheric Chemistry and Physics*, *8*(22), 6681-6698.

URBAN AEROSOL NUMBER SIZE DISTRIBUTION: SOURCES AND VISIBILITY IMPACT

L.-H. YOUNG[1], C.-S. HSU[1]., T.-C. HSIAO[2]., N.-H. LIN[3], S.-C. TSAY[4]., T.-H. LIN[5], W.-Y. LIN[6], C.-R. JUNG[7]

[1] Department of Occupational Safety and Health, China Medical University, Taichung, Taiwan.

[2] Graduate Institute of Environmental Engineering, National Taiwan University, Taipei, Taiwan.

[3] Department of Atmospheric Sciences, National Central University, Taoyuan, Taiwan.

[4] NASA Goddard Space Flight Center, Maryland, USA.

[5] Center for Space and Remote Sensing Research, National Central University, Taoyuan, Taiwan.

[6] Institute of Environmental Engineering and Management, National Taipei University of Technology, Taipei, Taiwan.

[7] Department of Public Health, China Medical University, Taichung, Taiwan.

Keywords: SOURCE APPORTIONMENT, SUBMICROMETER PARTICLES, SIZE DISTRIBUTION, TRANSPORT, LIGHT EXTINCTION

INTRODUCTION

Atmospheric submicrometer (< 1 μm) particles are linked to adverse impacts on human health (Pope et al., 2020) and atmospheric visibility (Hand et al., 2002). Due to the complex sources and dynamic nature of submicrometer particles, the particle number size distributions (PNSDs) for this category often exhibit a multimodality that varies widely in sizes and by environment (Morawska et al., 1999) and commonly being described by three modes, namely nucleation (< 25 nm), Aitken (25 – 100 nm), and accumulation (100 – 1000 nm) mode. Of special interests are the nucleation and accumulation mode particles that play a decisive role in the particle number and mass budget, respectively. Most of the visibility studies have relied on the bulk aerosol mass (viz., of the $PM_{2.5}$ and PM_{10}) and chemical composition to establish the potential links between aerosols and visibility (Pitchford et al., 2007). In contrast, the role of PNSDs has been less considered due to the lack of information on size-resolved compositions. Nevertheless, numerous source apportionment studies have attempted to resolve the source-dependent PNSD profiles using receptor models. In the latest global review, Hopke et al. (2022) identified 55 peer-reviewed journal articles on the source apportionment of particles contributing to PNSDs in 102 locations/time periods. Those studies, however, did not further investigate the link between the sources and atmospheric visibility, and none were reported from Taiwan. With that in mind, this study used positive matrix factorization (PMF) to analyze measurements obtained between 2017 and 2021 of the submicrometer PNSDs, aerosol light extinction (b_p), air pollutants, and meteorology in an urban area of central Taiwan. The PMF results were further linked and discussed in relation to their contribution to impaired visibility.

METHODS

This conference presentation is based on Young et al. (2023) with a few new analyses and the detailed methodology can be found therein. In brief, the study area was in the urban basin of Taichung City, which is the second most populous city in central Taiwan. Measurements were made at a height of 17.5 m above ground level and adjacent to one of Taiwan EPA's air quality monitoring stations. PNSD measurements in the size range of 10 – 1,094 nm with a sequential mobility particle sizer and condensation particle counter

(SMPS/CPC) system (Model 5.500, GRIMM), whereas aerosol light scattering (b_{sp}) and absorption (b_{ap}) were measured with an integrating nephelometer (Model 3563, TSI) and a seven-wavelength aethalometer (AE33, Magee Scientific), respectively. Other supplemental data, including $PM_{2.5}$, PM_{10}, SO_2, CO, NO_x, O_3, T, RH, wind speed (WS) and direction (WD), were obtained from the EPA station. The collected hourly data were then analyzed with PMF with the Multilinear Engine (ME-2; v1.345) developed by Paatero (1999) using an IGOR-based Source Finder package (SoFi; v8) developed by Canonaco et al. (2013). The Hybrid Single Particle Lagrangian Integrated Trajectory (HYSPLIT v.5.0.0) model was used to calculate the 72-hr back trajectories of air masses arriving at study area and to assess the impact of long-range transport on the measured PNSDs.

CONCLUSIONS

The PMF resolved six PNSD source profiles and the the measured PNSDs and bp were reasonably reconstructed. The Nucleation factor (factor 1, F1), the key contributor to total particle number (TPN; 35.0%), represented nucleation (< 25 nm) particles associated with fresh traffic emission and secondary new particle formation, which were transported from the west-southwest by stronger winds (> 2.2 m s–1). F2 represented the large Aitken (50 – 100 nm) particles transported regionally via northerly winds, whereas F3 represented large accumulation (300 – 1000 nm) particles, which showed elevated concentrations under stagnant conditions (< 1.1 m s–1). F4 represented small Aitken (25 – 50 nm) particles arising from the growth and transport of the nucleation particles (F1) via west-southwesterly winds. F5 represented large Aitken particles originating from combustion-related SO_2 sources and carried by west-northwesterly winds. F6 represented small accumulation (100 – 300 nm) particles emitted both by local sources and by the remote SO_2 sources found for F5. Overall, large accumulation particles (F3) played the greatest role in determining the total particle volume (TPV; 66.4%) and surface (TPS; 34.8%), and their contribution to b_p increased markedly from 17.3% to 40.7% as visibility decreased (Figure 1), indicating that TPV and TPS are better metrics than TPN for estimating b_p. Furthermore, slow-moving air masses—and therefore stagnant conditions—facilitate the build-up of accumulation mode particles (F3+F6), resulting in the poorest visibility (Figure 2).

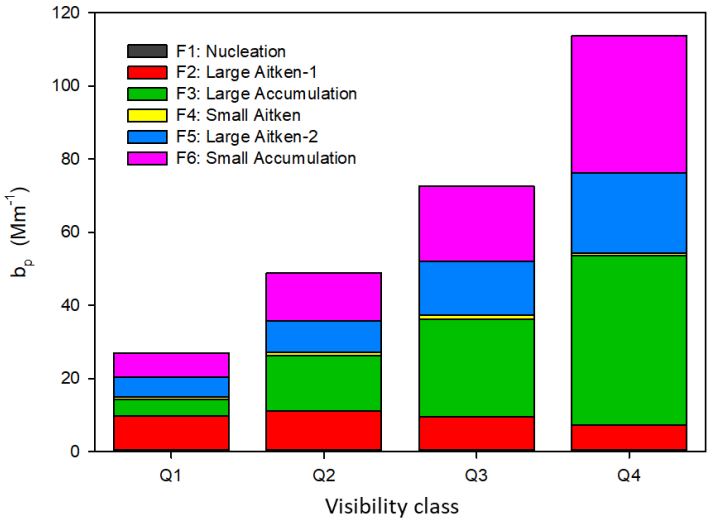

Figure 1. The aerosol extinction coefficient (b_p) associated with the six PMF-resolved factors across four visibility classes, with Q1 represents the best visibility and Q4 represents the worst.

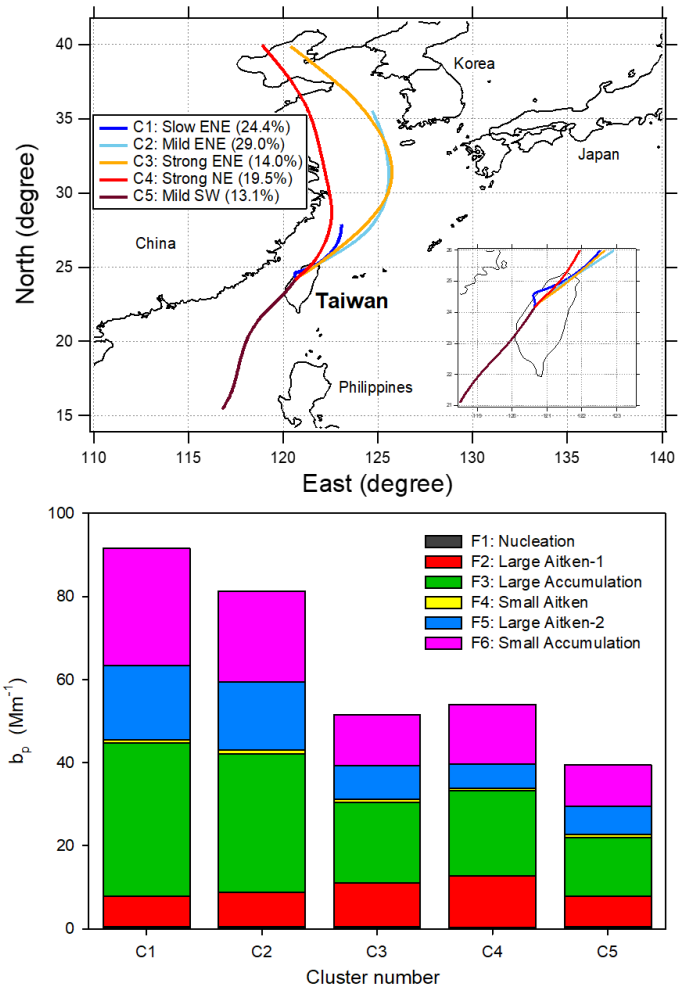

Figure 2. The five-representative back-trajectory clusters and their associated b_p and six PMF-resolved factors.

ACKNOWLEDGEMENTS

This work was supported by the Taiwan's Environmental Protection Administration under grants MOST-106-EPA-F-005-004, MOST-107-EPA-F-004-003, MOST-107-EPA-F-018-001, MOST-108-2813-C-039-006-E and 109A266.

REFERENCES

Canonaco, F., Crippa, M., Slowik, J.G., Baltensperger, U. and A.S.H. Prevot (2013). SoFi, an IGOR-based interface for the efficient use of the generalized multilinear engine (ME-2) for the source apportionment: ME-2 application to aerosol mass spectrometer data. *Atmos. Meas. Tech.* **6**, 3649–3661.

Hand, J.L., Kreidenweis, S.M., Sherman, D.E., Jr., J.L.C., Hering, S.V., Day, D.E. and W.C. Malm (2002). Aerosol size distributions and visibility estimates during the Big Bend regional aerosol and visibility observational (BRAVO) study. *Atmos. Environ.* **36**, 5043–5055.

Hopke, P.K., Feng, Y. and Q. Dai (2022). Source apportionment of particle number concentrations: A global review. *Sci. Total Environ.* **819**, 153104.

Morawska, L., Thomas, S., Jamriska, M. and G. Johnson (1999). The modality of particle size distributions of environmental aerosols. *Atmos. Environ.* **33**, 4401–4411.

Paatero, P. (1999). The multilinear engine—A table-driven, least squares program for solving multilinear problems, including the n-way parallel factor analysis model. *J. Comput. Graph. Stat.* **8**, 854–888.

Pitchford, M., Maim, W., Schichtel, B., Kumar, N., Lowenthal, D. and J. Hand (2007). Revised algorithm for estimating light extinction from IMPROVE particle speciation data. *J. Air Waste Manage.* **57**, 1326–1336.

Pope, C.A., Coleman, N., Pond, Z.A. and R.T. Burnett (2020). Fine particulate air pollution and human mortality: 25+ years of cohort studies. *Environ. Res.* **183**, 108924.

Young, L.-H., Hsu, C.-S., Hsiao, T.-C., Lin, N.-H., Tsay, S.-C., Lin, T.-H., Lin, W.-Y. and C.-R. Jung (2023). Sources, transport, and visibility impact of ambient submicrometer particle number size distributions in an urban area of central Taiwan. *Sci. Total Environ.* **856**, 159070.

Present: Source apportionment, Submicrometer particle, Size distribution, Transport, Light extinction.

Inter-correlation of Port and Urban $PM_{2.5}$: Chemical Characteristics and Source Resolution

Chung Shin Yuan[1,2*], Yu-Lun Tseng[1], I-Chieh Du[1], Po-Hsuan Yen[1]

[1] Institute of Environmental Engineering, National Sun Yat-sen University, Kaohsiung, Taiwan

[2]Aeroaol Science Research Center, National Sun Yat-sen University, Kaohsiung, Taiwan

Keywords: $PM_{2.5}$, port and urban areas, chemical characteristics, local emissions, source apportionments

INTRODUCTION

Kaohsiung Harbor (KH) is the largest international seaport in Taiwan, located at the southwestern coast of Taiwan Island. It nears the leading ocean-going trade line through the Taiwan Strait and the Bashi Channel. More than 36,000 inbound and outbound vessels berthed in the harbor annually (Tseng et al., 2022). Its container traffic volume ranked 15th in the world. The sea-going vessels are particularly becoming a significant contributor to SO_2, NOx, and $PM_{2.5}$ with increasing global trade in the coastal and harbor cities with an industrial complex (Lee et al., 2021; Wang et al., 2019; Lindstad et al., 2011). It contributes considerable $PM_{2.5}$ emissions from the port areas (Kirrane et al., 2019). Accordingly, it would be crucial for exploring the effects of ship emissions on particulate air quality in harbor fields. This study aims to explore the temporal variation and the spatial distribution of $PM_{2.5}$ levels and characterize the chemical fingerprints of $PM_{2.5}$ in the port and urban areas CMB and PMF receptor models were further applied to resolve the source identification and apportionment of $PM_{2.5}$ in the Kaohsiung Harbor and Metro Kaohsiung.

METHODS

This study conducted $PM_{2.5}$ sampling at two sites in Kaohsiung Harbor (Qihou (QH) and Zhonghe (ZH) Checkpoints) and other two sites in Metro Kaohsiung (Mincyuan (MC) Elementary School and Fengshan (FS) High School) in four seasons (Fig. 1). The quartz filters of 47 mm were used to collect $PM_{2.5}$ samples for consecutive seven days in each season. Diurnal sampling of $PM_{2.5}$ was conducted in the daytime (08:00–20:00) and at nighttime (20:00–08:00). A total of 224 $PM_{2.5}$ samples were collected to explore the diurnal variation of $PM_{2.5}$ concentrations.

Fig.1. Location of $PM_{2.5}$ sampling sites selected for collecting $PM_{2.5}$.

Fig. 2. $PM_{2.5}$ sampling.

RESULTS AND DISCUSSION

The results showed that the concentration of $PM_{2.5}$ in the Kaohsiung Harbor was mainly higher than those in Metro Kaohsiung (Figs. 3 and 4). The prevailing winds were mainly blown from the west and the northwest to the harbor. The winds in the urban area were mainly blown from the west, which caused the $PM_{2.5}$ concentration decreased gradually from the port to the urban areas. It showed that the air quality of

Metro Kaohsiung was not only affected by vehicular exhausts, but also affected by ship emissions from the Kaohsiung Harbor, resulting in the deterioration of particulate air quality in the Metro Kaohsiung.

The average concentration of SO_4^{2-} in the port area was generally higher than that of NO_3^-, indicating that harbor area is mainly affected by ship emissions and industrial boilers (Fig. 5). In contrast, urban area was primarily influenced by vehicular exhausts. The V/Ni ratios in the port area were much higher than those in the urban area. In addition, the concentrations of V, Ni, and Cr were significantly high in the harbor area due to the influence of ship emissions from inbound and outbound vessels (Fig. 6). The carbonaceous content of $PM_{2.5}$ was dominated by organic carbon (OC), indicating that nighttime environment in the port area was favorable for the formation of secondary organic aerosols (SOA) (Fig. 7).

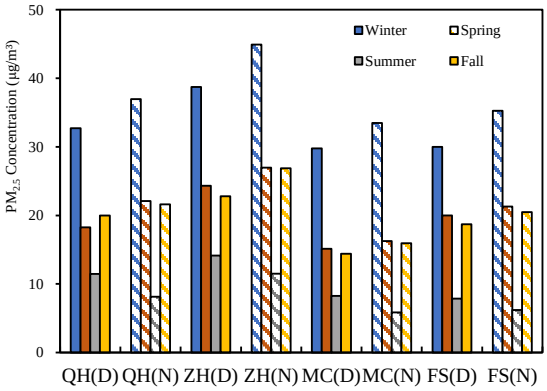

Fig.3 Seasonal variation of $PM_{2.5}$ concentration in the port and urban areas.

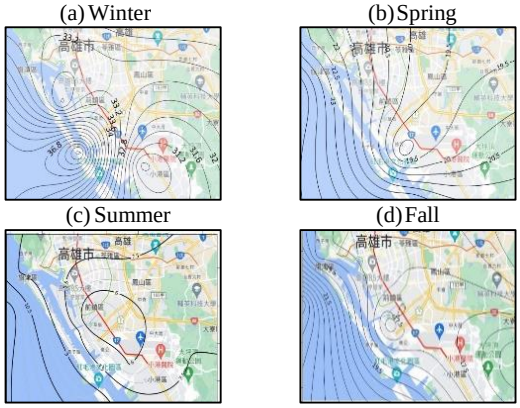

Fig. 4. Seasonal contours of $PM_{2.5}$ concentration in the port and urban areas.

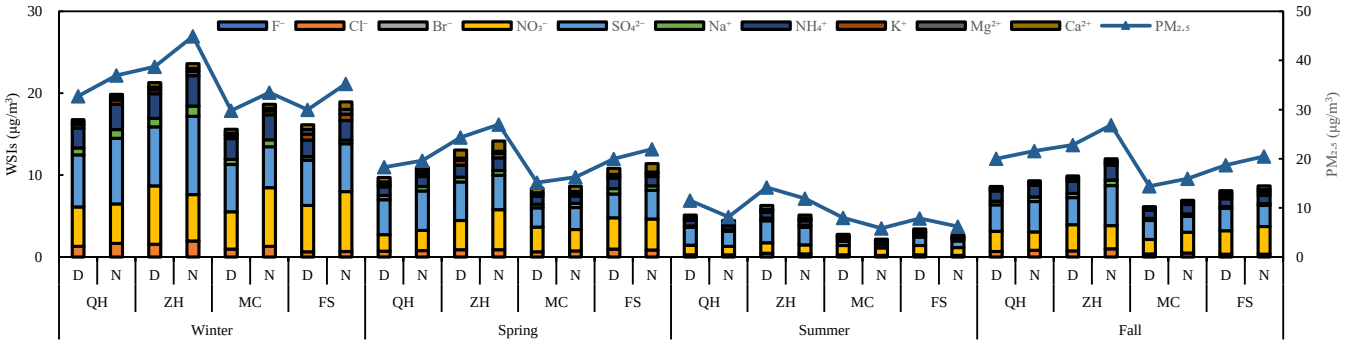

Figure 5. Water-soluble ions in $PM_{2.5}$ in the port and urban areas.

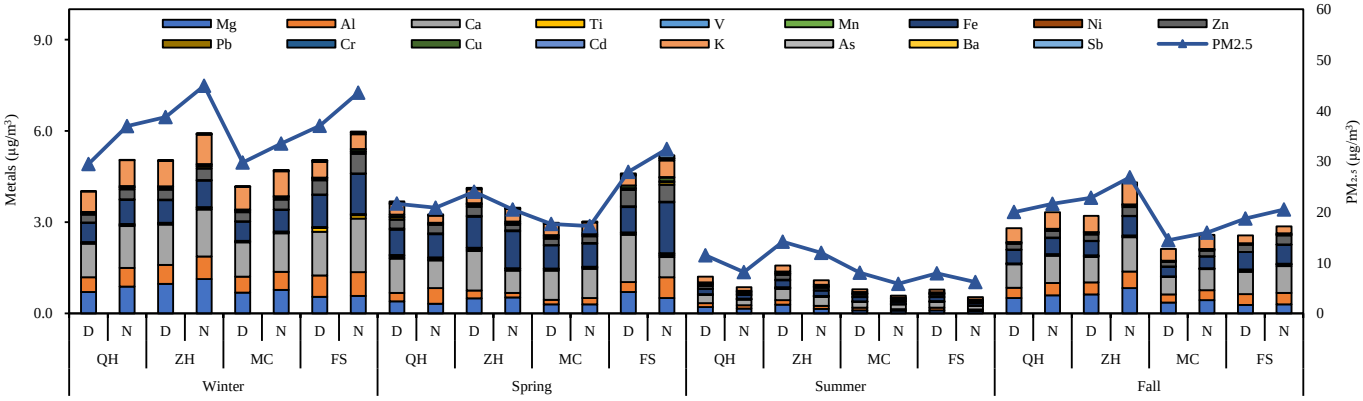

Fig. 6. Metallic elements in $PM_{2.5}$ in the port and urban areas.

The diurnal concentrations of organic acids showed nighttime > daytime (Fig. 8). Strong solar radiation in the daytime reduced organic acids due to atmospheric photochemical reactions. The major source of Kaohsiung Port was ship emissions, but the urban area was primarily from vehicular exhausts and road dust. The contributions of secondary aerosols in the port and urban areas were relatively high in winter and spring, indicating that air pollutants from long-range transport (LRT) also increased the concentration of secondary aerosols (Fig. 9).

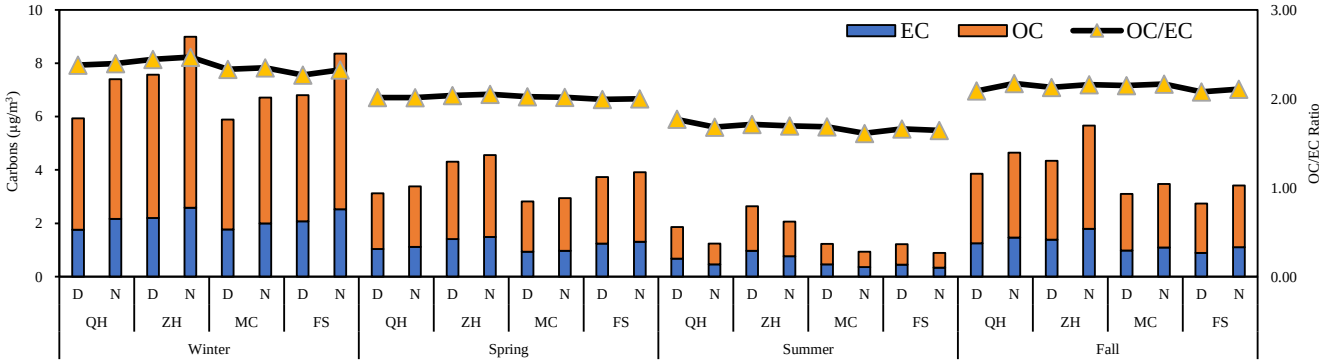

Fig.7. Carbonaceous content and OC/EC ratios of $PM_{2.5}$ in the port and urban areas.

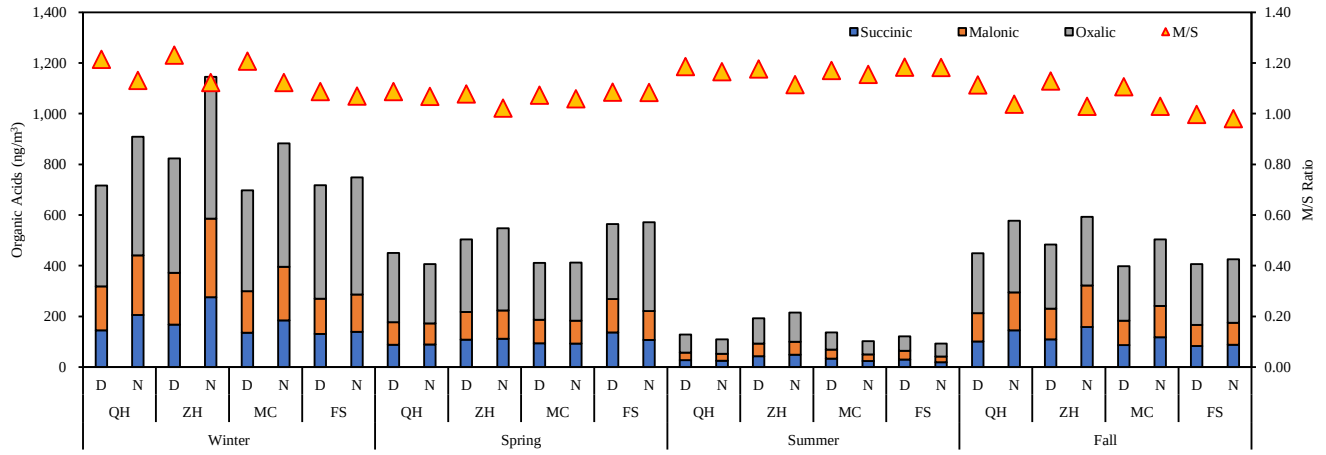

Fig. 8. Organic acids and M/S ratios of $PM_{2.5}$ in the port and urban areas.

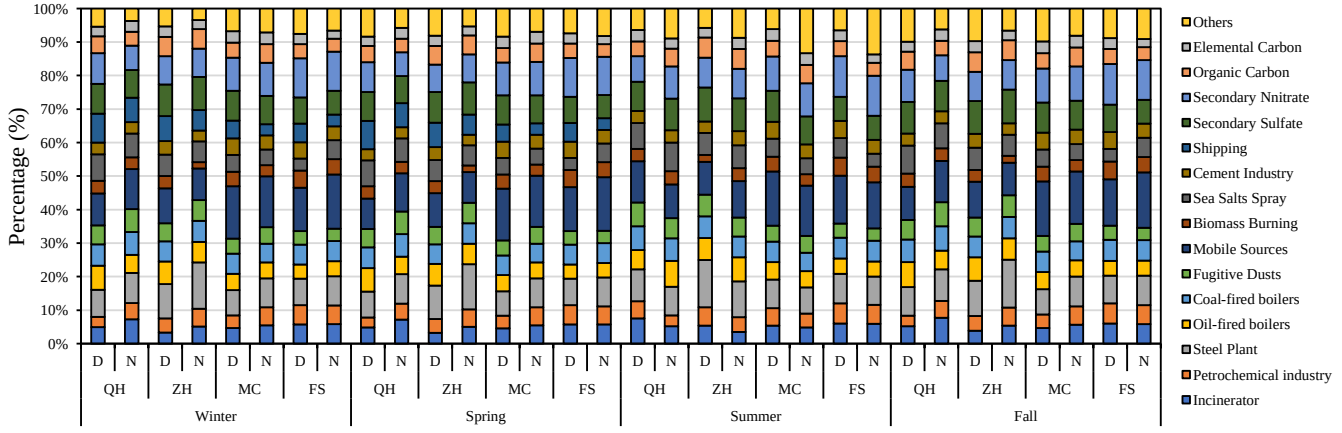

Fig. 9. Source apportionment of $PM_{2.5}$ in the port and urban areas.

CONCLUSIONS

This study concluded that the wind field in the Kaohsiung Harbor was mainly blown from the west and the northwest, while that in Metro Kaohsiung was mainly blown from the west. Additionally, Kaohsiung Area is located at the leeward of the Central Mountains, and the sea-land breeze caused relatively stable atmosphere. As a result, the worse dispersion resulted in the deterioration of air quality in Kaohsiung Area. $PM_{2.5}$ concentrations in the port and urban areas showed the spatiotemporal variation of nighttime > daytime and port > urban. The V/Ni ratios of $PM_{2.5}$ at the QH and ZH sites in the Kaohsiung Harbor were higher than those at the MC and FS sites in Metro Kaohsiung. The enrichment factor (EF) of V, Ni, and Cr were significantly higher in the Kaohsiung Harbor, which was mainly influenced by ship emissions in the port area. The major source of Kaohsiung Harbor was ship emissions, while Metro Kaohsiung was primarily from vehicular exhausts and road dust.

ACKNOWLEDGEMENTS

This study was performed under the auspices of Environmental Protection Administration of Executive Yuan, Taiwan. The authors are grateful to its constant financial support. Special thanks go to Kaohsiung Port of Taiwan International Ports Corporation, Ltd. and Taiwan Coast Guard for their administrative assistance during the $PM_{2.5}$ sampling periods.

REFERENCES

Kirrane, E. F., Luben, T., Benson, A., Owens, E., Sacks, J., Dutton, S., Madden, M., & Nichols, J. (2019). A systematic review of cardiovascular responses associated with ambient black carbon and fine particulate matter. Environment International., 127, 305-316.

Lee, H., Pham, H. T., Chen, M., & Choo, S. (2021). Bottom-up approach ship emission inventory in Port of Incheon based on VTS data. Journal of Advanced Transportation, vol 2021, 16.

Lindstad, H., Asbjørnslett, B. E., & Strømman, A. H. (2011). Reductions in greenhouse gas emissions and cost by shipping at lower speeds. Energy Policy, 39(6), 3456-3464.

Tseng, Y. L., Yuan, C. S., Bagtasa, G., Chuang, H. L., & Li, T. C. (2019). Inter-correlation of Chemical Compositions, Transport Routes, and Source Apportionment Results of Atmospheric $PM_{2.5}$ in Southern Taiwan and the Northern Philippines. Aerosol and Air Quality Research., 9(12), 2645-2661.

Wang, X., Shen, Y., Lin, Y., Pan, J., Zhang, Y., Louie, P. K. K., Li, M., & Fu, Q. (2019). Atmospheric pollution from ships and its impact on local air quality at a port site in Shanghai. Atmospheric Chemistry and Physics, 19(9), 6315-6330.

DIRECT OBSERVATIONS OF OXIDIZED ORGANIC MOLECULES IN THE TROPICAL FREE TROPOSPHERE AT A HIGH-ALTITUDE RESEARCH STATION CHACALTAYA IN THE BOLIVIAN ANDES (5240M A.S.L.)

Qiaozhi Zha[1], Diego Aliaga[1], Radovan Krejci[2], Victoria Sinclair[1], Cheng Wu[2], Douglas Worsnop[1,3], Claudia Mohr[2], and Federico Bianchi[1]

[1]Institute for Atmospheric and Earth System Research /Physics, University of Helsinki, Helsinki, Finland

[2]Department of Environmental Science & Bolin Centre for Climate Research, Stockholm University, Stockholm, Sweden

[3]Aerodyne Research, Inc., Billerica, MA, USA

Keywords: Oxidized organic molecule, New particle formation, Tropical free troposphere, Amazon.

INTRODUCTION

Atmospheric aerosol particles can affect the Earth's radiative balance and modify cloud properties by acting as cloud condensation nuclei (CCN). New particle formation (NPF) is the largest source (in number) of aerosol particles, contributing more than half of the global CCN (Gordon et al., 2017). Intensive NPF events have been constantly observed in the free troposphere (FT) on a global scale. High concentrations of small particles (diameter $\leqslant$50 nm) have been observed by several recent aircraft-based aerosol studies in the FT over the Amazon Basin (Wang et al., 2016; Andreae et al., 2018). These particles may descend to the Amazon boundary layer, acting as an important source sustaining the aerosol population in the boundary layer over the Amazon. They may also contribute to the stratospheric aerosol population by ascending to the stratosphere. While increasing evidence shows that the oxygenated molecules originating from biogenic sources may be a critical contributor to NPF in the Amazon FT (Andreae et al., 2018; Palmer et al., 2022), direct molecular-level observations of such oxidized organic molecules (OOMs) are still absent.

METHODS

The present study focuses on measurements in January 2018 during the austral summer months (wet season), as part of the Southern hemisphere high ALTitude Experiment on particle NucleAtion and growth (SALTENA) campaign (Bianchi et al., 2022). A set of state-of-the-art mass spectrometers (including an atmospheric pressure interface time-of-flight mass spectrometer (APi-TOF) and a nitrate-based chemical ionization atmospheric pressure interface time-of-flight mass spectrometer (nitrate CI-APi-TOF)), detecting the chemical composition of gaseous precursors and cluster ions, were deployed at the Global Atmospheric Watch (GAW) station Chacaltaya (CHC; 5240 m a.s.l.) at the summit of Mount Chacaltaya in the Bolivian Andes. The station is ~18 km away from the city area of La Paz. These measurements were complemented by numerous long-term (and permanent) observations, such as particle number size distribution and black carbon (BC).

CONCLUSIONS

During the study period, CHC was primarily under the influence of air masses from Amazonia. Based on trace gas and in-situ aerosol observations during the wet season, combined with estimation of air mass origin using FLEXPART-WRF air mass history analysis, we find that OOMs presented in this part of the tropical FT are dominated by the oxidation products of isoprene. Such molecular-level observations of the OOMs are unprecedented at high altitudes in the Southern Hemisphere. Our results thus contribute an observational

piece to the puzzle of the source of the large number of organic aerosol particles observed in the FT over Amazonia.

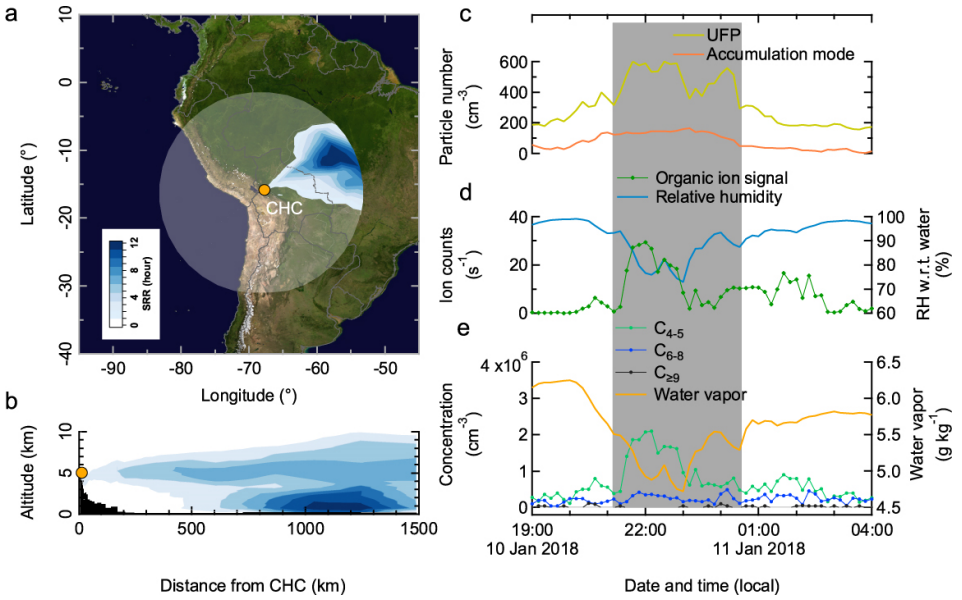

Figure 1. An Amazon FT event observed at CHC in the night of 10 January 2018. **a**, Horizontal profile of the vertically integrated source-receptor relationship (SRR, units of hours) derived from the FLEXPART-WRF model and averaged from 21:00 to 00:00 (local date and time, UTC-4). The semi-transparent circle indicates the horizontal output domain of the model. The model output is in 1-hour time resolution. The color bar denotes the SRR values of the passive air tracers. **b**, Vertical profile of the SRR integrated over the radial direction, averaged from 21:00 to 00:00. Black shading indicates the topography near the station. **c**, Concentrations of WVMR and eBC. The grey shaded area denotes the exact period of the FT event, identified with WVMR $\leqslant$5.5 g kg^{-1} and eBC $\leqslant$0.08 µg m^{-3}. **d**, Concentrations of UFPs (10 - 50 nm diameter) and accumulation mode particles (100 - 500 nm diameter). **e**, Concentrations of oxidized organic molecules (OOMs) measured by a nitrate-based CI-APi-TOF; grouped based on their number of carbon atoms ($C_{4\text{-}5}$, $C_{6\text{-}8}$, and $C_{\geqslant 9}$). $C_{\geqslant 9}$ OOM concentration is below the detection limit of the CI-APi-TOF for most of the time during this FT event.

ACKNOWLEDGEMENTS

The authors would like to thank all staff at Chacaltaya GAW station for technical support. This study is supported by the European Union (EU) H2020 program via the findings European Research Council (ERC; project CHAPAs no. 850614 and ATM-GTP no. 742206) and the Marie Skłodowska Curie (CLOUD-MOTION no. 764991), the Finnish Centre of Excellence as well as the Academy of Finland (project no. 311932, 315203 and 337549), and the Knut and Alice Wallenberg Foundation (WAF project CLOUDFORM no. 2017.0165).

REFERENCES

Andreae, M. O., Afchine, A., Albrecht, R., Holanda, B. A., Artaxo, P., Barbosa, H. M. J. J., Borrmann, S., Cecchini, M. A., Costa, A., Dollner, M., Fütterer, D., Järvinen, E., Jurkat, T., Klimach, T., Konemann, T., Knote, C., Krämer, M., Krisna, T., Machado, L. A. T. T., Mertes, S., Minikin, A., Pöhlker, C., Pöhlker, M. L., Pöschl, U., Rosenfeld, D., Sauer, D., Schlager, H., Schnaiter, M., Schneider, J., Schulz, C., Spanu, A., Sperling, V. B., Voigt, C., Walser, A., Wang, J., Weinzierl, B., Wendisch, M., and Ziereis, H.: Aerosol characteristics and particle production in the upper troposphere over the Amazon Basin, Atmospheric Chem. Phys., 18, 921–961, https://doi.org/10.5194/acp-18-921-2018, 2018.

Bianchi, F., Sinclair, V. A., Aliaga, D., Zha, Q., Scholz, W., Wu, C., Heikkinen, L., Modini, R., Partoll, E., Velarde, F., Moreno, I., Gramlich, Y., Huang, W., Koenig, A. M., Leiminger, M., Enroth, J., Peräkylä, O., Marinoni, A., Xuemeng, C., Blacutt, L., Forno, R., Gutierrez, R., Ginot, P., Uzu, G., Facchini, M. C., Gilardoni, S., Gysel-Beer, M., Cai, R., Petäjä, T., Rinaldi, M., Saathoff, H., Sellegri, K., Worsnop, D., Artaxo, P., Hansel, A., Kulmala, M., Wiedensohler, A., Laj, P., Krejci, R., Carbone, S., Andrade, M., and Mohr, C.: The SALTENA Experiment: Comprehensive Observations of Aerosol Sources, Formation, and Processes in the South American Andes, Bull. Am. Meteorol. Soc., 103, E212–E229, https://doi.org/10.1175/BAMS-D-20-0187.1, 2022.

Gordon, H., Kirkby, J., Baltensperger, U., Bianchi, F., Breitenlechner, M., Curtius, J., Dias, A., Dommen, J., Donahue, N. M., Dunne, E. M., Duplissy, J., Ehrhart, S., Flagan, R. C., Frege, C., Fuchs, C., Hansel, A., Hoyle, C. R., Kulmala, M., Kürten, A., Lehtipalo, K., Makhmutov, V., Molteni, U., Rissanen, M. P., Stozkhov, Y., Tröstl, J., Tsagkogeorgas, G., Wagner, R., Williamson, C., Wimmer, D., Winkler, P. M., Yan, C., and Carslaw, K. S.: Causes and importance of new particle formation in the present-day and preindustrial atmospheres, J. Geophys. Res. Atmospheres, 122, 8739–8760, https://doi.org/10.1002/2017JD026844, 2017.

Palmer, P. I., Marvin, M. R., Siddans, R., Kerridge, B. J., and Moore, D. P.: Nocturnal survival of isoprene linked to formation of upper tropospheric organic aerosol, 6, https://doi.org/10/gpcd74, 2022.

Wang, J., Krejci, R., Giangrande, S., Kuang, C., Barbosa, H. M. J., Brito, J., Carbone, S., Chi, X., Comstock, J., Ditas, F., Lavric, J., Manninen, H. E., Mei, F., Moran-Zuloaga, D., Pöhlker, C., Pöhlker, M. L., Saturno, J., Schmid, B., Souza, R. A. F., Springston, S. R., Tomlinson, J. M., Toto, T., Walter, D., Wimmer, D., Smith, J. N., Kulmala, M., Machado, L. A. T., Artaxo, P., Andreae, M. O., Petäjä, T., and Martin, S. T.: Amazon boundary layer aerosol concentration sustained by vertical transport during rainfall, Nature, 539, 416–419, https://doi.org/10.1038/nature19819, 2016.

Multicomponent Vaper Condensation on Nanoparticles

Zichen Zhang[1], Liuyong Chang and Guangze Li[1] Longfei Chen[1],

[1]Beihang Hangzhou Innovation Institute (Yuhang District),
Hangzhou, Zhejiang, 310023, China

Keywords: Condensation, Aerosol, Multicomponent vapor, Stefan flow.

INTRODUCTION

Multicomponent vapor condensation on aerosol particles plays an important role in secondary aerosol formation. For instant, primary particles emitted from aero-engines are surrounded by a great variety of volatile organic components (VOCs) and water vapor, so that their secondary evolution such as contrail formation is truly multi-component heterogeneous condensation onto nascent nanoparticles[1].
However, most heterogeneous nucleation models consider only mono-component condensation for the sake of simplicity, yet it may deviate significantly from the reality if the condensing vapor contains various species with differing molecular polarities due to non-ideality effects. Furthermore, Stefan flow effects significantly affect evaporation process yet whether the reverse Stefan flow could influence the multi-component condensation has rarely been reported[2]. This study aims to evaluate the importance of non-ideality and reverse Stefan flow in multicomponent condensation via experiments and theoretical analysis.

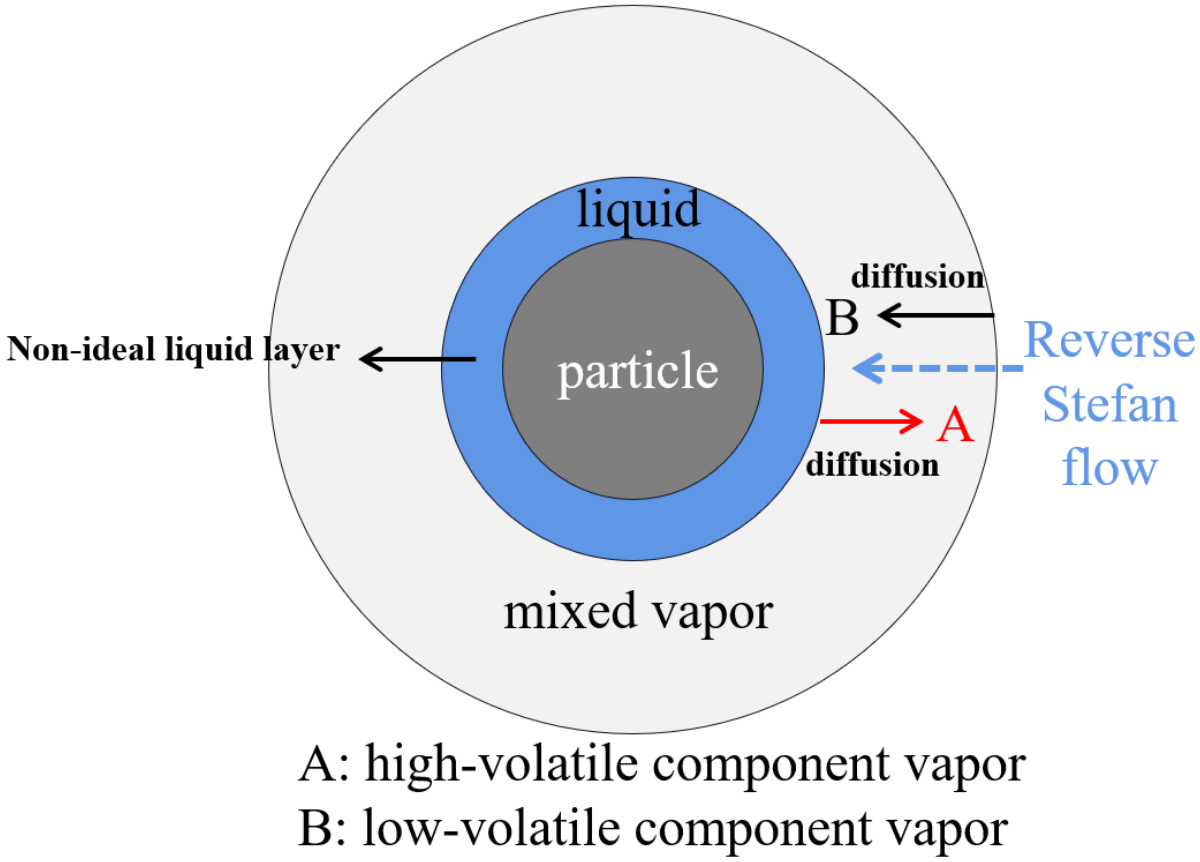

Figure 1. multi-component vapor condensation on ultrafine particles

METHODS

Environmental scanning electron microscopy (ESEM) will be used to characterize the condensation on nanoparticles. ESEM was adopted with a vapor generator to inject vapor into ESEM. A high-precision Peltier cooler was installed in ESEM to control the surface temperature and to allow the condensation of multi-component vapor (see Fig. 2). The Peltier cooler was wrapped by a thick layer of thermal insulation foam to avoid condensation on the cooling stage. A small thermal conductor was attached to the Peltier cooler to cool down the sample surface which was covered by nanoparticles. The time-resolved condensation on nanoparticles could be clearly observed when the particle pressure of multi-component vapor is a little above the saturated pressure of it. Lv et al.[3] successfully used the similar method to observe the water condensation on particles but multi-component condensation has not been investigated using this method yet.

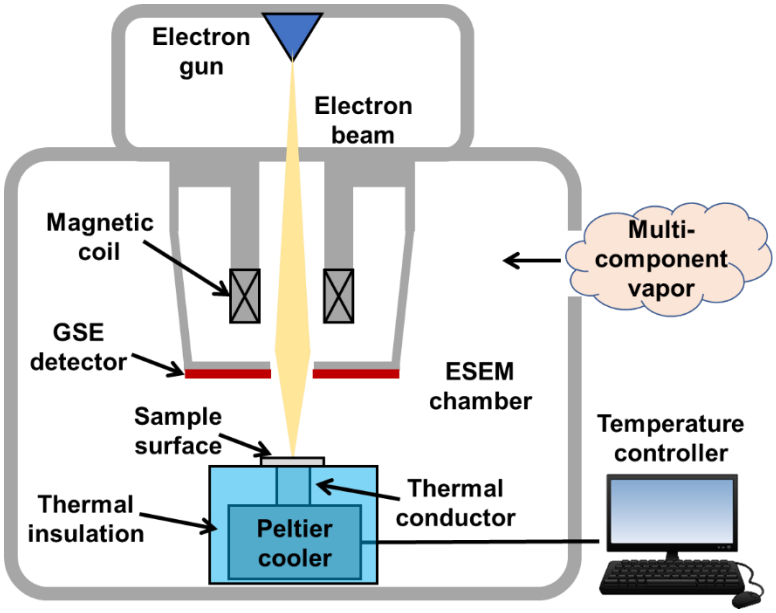

Figure 2. Sketch of the experimental setup for multi-component condensation using ESEM

The multi-component condensation on flying nanoparticles will be investigated in a condensation particle counter (CPC). CPC is a machine that detects and counts aerosol particles by enlarging them using the condensation theorem. The hot supersaturated vapor flow was mixed with the aerosol flow in CPC before entering a cooling tube where vapor is condensed on particles to enlarge the particle size. CPC can detect only particles larger than a specific size. In this way, the condensation rate and the growth rate of particles can be analyzed quantitively by identifying the counting efficiency (the ratio of the number of detected particles to the number of total particles). This experiment will inject multi-component vapor into CPC to investigate the underlying physics of multi-component condensation on flying nanoparticles.

CONCLUSIONS

Some preliminary results are given bellow:

1) The reverse stefan flow induced by the difference of component concentration play a non-negligible role on the condensation of multi-component vapor on nano-particles, it enhances the thermal resistance of condensation and leads to the hysteresis phenomenon.

2) The non-ideality of the mixing vapor has a big influence on the heterogenous condensation process, reducing the high-volatile component of the mixing vapor significantly promote the condensation rate of the particle.

ACKNOWLEDGEMENTS

This authors acknowledge the support of National Science Foundation of China.

REFERENCES

[1] B. Kärcher, Formation and radiative forcing of contrail cirrus, Nat. Commun. 9 (2018) 1–17. https://doi.org/10.1038/s41467-018-04068-0.

[2] Y. Li, Z. Gan, X. Zhang, M. Nie, H. Zhang, Mechanism of stefan flow in the collection of particles on evaporating/condensing surfaces: A review, Ind. Eng. Chem. Res. 60 (2021) 4766–4776. https://doi.org/10.1021/acs.iecr.0c06076.

[3] L. Lv, J. Zhang, J. Xu, J. Yin, Heterogeneous condensation process observed by environmental scanning electron microscopy (ESEM): On smooth single aerosol particle, Aerosol Sci. Technol. 54 (2020) 1515–1526. https://doi.org/10.1080/02786826.2020.1796460.

RADIOCARBON-BASED SOURCE APPORTIONMENT FOR THE SIZE-RESOLVED AEROSOLS IN NORTHERN THAILAND

YAN-LIN ZHANG[1], WENHUAI SONG[1,2]

[1]School of Applied Meteorology, Nanjing University of Information Science and Technology. Nanjing 210044, China

[2]Department of Chemistry, Biochemistry and Pharmaceutical Sciences & Oeschger Centre for Climate Change Research, University of Bern, Bern, 3012, Switzerland

Keywords: Biomass burning, Carbonaceous aerosols, Biogenic secondary organic aerosols, Machine learning

To study the role of biomass burning (BB) in air pollution at upper-northern Thailand, the quantitative analysis for the sources of size-resolved carbonaceous aerosols from Chiang Mai was carried out by using the radiocarbon (^{14}C) based source apportionment. BB-derived aerosol contributed the most to carbonaceous aerosols and is majorly distributed in fine particles (Dp < 2.1 μm). Fossil fuel-derived carbonaceous aerosol shows an unexpectedly even distribution in fine and coarse particles (2.1 < Dp < 10 μm). BB-derived organic carbon (OC_{bb}) and elemental carbon (EC_{bb}), as well as fossil fuel-derived EC (EC_f) showed unimodal size distribution with a peak at 0.43-0.65 μm. While OC_f displayed a bimodal mode with the major peak at 2.1-10 μm, and the minor one at 0.43-0.65 μm, which indicates different sources in different size ranges. The enhanced biogenic secondary organic aerosols (eBSOA) caused by the open burning during high BB (HBB) season were assessed by coupling machine learning and ^{14}C datasets. The results show that open burning enhanced the production of BSOA by

189 ± 80% on average, and the eBSOA was predominantly distributed in sub-micron particles. In general, the fine particle loading is controlled by combustion sources and BSOA, and is significantly aggravated during HBB. The coarse particle level is mainly affected by biogenic primary organic aerosols (BPOA) and vehicle emissions. Our results highlight the critical importance of controlling open fires to reduce air pollutants and the potential exposure risk.

ACKNOWLEDGEMENTS

This work was supported by the National Natural Science Foundation of China (grant numbers: 42192512, 41977305) and Thailand Science Research and Innovation (TSRI, formerly the Thailand Research Fund, TRF) (grant number: RDG 6030019). The authors would also like to thank the China Scholarship Council for the support to Wenhuai Song.

SIMULATING THE IMPACTS OF POLLEN ON CLOUD FORMATION THROUGH HETEROGENEOUS ICE NUCLEATION

YINGXIAO ZHANG[1], TAMANNA SUBBA[2], BRIANNA N. HENDRICKSON[3], SARAH D. BROOKS[3], ALLISON L. STEINER[1]

[1] *University of Michigan, Ann Arbor, Department of Climate and Space Sciences and Engineering*

[2] *Brookhaven National Laboratory, Environmental and Climate Sciences Department*

[3] *Texas A&M University, Department of Atmospheric Sciences*

Keywords: PRIMARY BIOLOGICAL AEROSOL, ICE NUCLEATION

INTRODUCTION

Primary biological aerosol particles (PBAPs) are emitted from Earth's biosphere, including pollen, fungal spores, virus, bacteria, and plant debris. PBAPs are linked to adverse health effects and have the potential to influence ice nucleation at warmer temperatures, further impacting overall climate and hydrological cycles. Anemophilous (or wind-driven) pollen is one type of PBAP, their emission is driven by climate factors (including temperature, precipitation, and CO_2) (Wozniak and Steiner, 2017; Zhang and Steiner, 2022). The emitted pollen grains can rupture under high humidity to form smaller sub-pollen particles (SPP). Both pollen and SPP can be lifted to the upper troposphere under convective conditions, readily take up water and serve as cloud condensation nuclei (CCN) and ice nucleating particles (INPs), and therefore impact cloud formation and reflectivity (Kanji *et al*., 2017). Depending on the amount of SPPs produced by one pollen grain, SPPs can exert different magnitude of effects on the precipitation (Wozniak *et al.*, 2018). Although biological aerosol have been observed frequently in clouds (Pratt *et al*., 2009) and have proven to be effective INPs in previous studies (Testa *et al*., 2021), they are typically not included in emission inventories. Thus, it is difficult to quantify their effects on cloud formation and local climate.

Here, we include the emission and rupture of pollen in Weather Research and Forecast model (WRF-Chem; Grell *et al*. 2005) simulations and investigate the impacts of pollen and SPP on both warm and ice clouds in the South Great Plains (SGP) region of the United States. We update the Morrison microphysics scheme inside WRF-Chem using aerosol-aware INP parameterizations for heterogeneous freezing (immersion, contact, and deposition freezing) and homogeneous freezing. The updated microphysics scheme simulates ice nucleation from other anthropogenic and natural aerosol (dust, soot, sulfate etc.) as well as pollen and SPP. The INP parametrizations for pollen and SPP are obtained from laboratory experiments, and we include these new parameterizations to evaluate pollen and SPP effects on cold cloud formation in a suite of WRF-Chem simulations. Overall, this work combines lab experiments and model simulations to provide insight into understanding biological aerosol-cloud interactions and aerosol climate effects.

METHODS

MODEL DEVELOPMENT

Pollen emissions are simulated by Pollen Emissions for Climate Models version 2.0 (PECMv2.0) (Wozniak and Steiner, 2017; Zhang and Steiner, 2022), which is a climate-flexible model that simulate gridded daily pollen emissions for 13 different types of pollen emitting vegetation (Fig. 1). We incorporate the simulated total daily pollen emission into a modal aerosol module in WRF-Chem, the Modal Aerosol Dynamics Model for Europe (MADE) aerosol model with the Secondary Organic Aerosol Model (SORGAM). Pollen is added as a new tracer in WRF-Chem to simulate pollen emission,

rupture, transport, and their fate in the atmosphere (Subba et al., under review). To evaluate the effects of pollen and other aerosol on cloud microphysics, we update the Morrison microphysics scheme (Morrison *et al.,* 2005) within WRF-Chem. The original Morrison scheme is a two-moment bulk stratiform cloud microphysics scheme that tracks number concentration and mass mixing ratio for five hydrometeors (cloud droplets, raindrops, snow, ice and graupel) (Morrison *et al*., 2005). The main heterogeneous ice formation processes include immersion, contact, and condensation/deposition freezing and are simulated by temperature-dependent only INP parametrizations (Bigg, 1953; Cooper, 1986; Meyers *et al*., 1992). Here, we replace these previous parameterizations with aerosol-aware parameterizations from previous literature that show improved agreement of ice number-temperature correlations observed in natural environment (DeMott *et al.*, 2010). For mixed-phase cloud, we utilize the DeMott *et al.* (2010) parametrization (hereafter D10) to simulate the immersion and contact freezing from aerosol with diameters larger than 0.5 μm, including soil dust, sea salt, and anthropogenic aerosol. Additionally, we include INP parametrizations obtained from laboratory experiment (Hendrickson *et al*. under review; hereafter H23), which quantified the contact and immersion freezing temperatures of pollen grains and the immersion freezing temperatures of SPP, as well as updated rupture rates for pollen to SPP. For cirrus cloud (with temperature lower than -40℃), we add homogeneous freezing of aqueous solution aerosol (Koop et al., 2000) and heterogenous freezing of dust and soot (Ullrich *et al.*, 2017). The aerosol impacts on cirrus clouds depends on the competition between these two freezing mechanisms, which is determined by both the number of homogeneous and heterogenous freezing particles and the updraft velocity (Liu and Penner, 2005). All aerosol implemented in the aerosol-aware microphysics are determined prognostically from the aerosol chemistry component of the model.

MODEL DOMAIN AND CONFIGURATION

The WRF-Chem model simulation domain is centered on the Southern Great Plains (SGP) of the United States bounded by 33.4-39.6ºN and 93.5-101.5ºW (as shown in Fig.1). The domain has 224 × 224 grid cells horizontally with 3 km spacing. The 45 vertical layers range from 1000-50mb. Because the SGP region frequently experiences severe weather, we select this domain to conduct a case study based on one convective event from 17-18 April 2013. During these high convective days, pollen can be transported to the upper atmosphere and has the potential to impact cloud formation (Subba *et al*., under review). Prior work by Subba *et al*., (under review) analyzing this event found the model can represent the convective system and regional aerosol concentrations. For all simulations, initial and boundary meteorological condition are produced from the National Centers for Environment Prediction (NECP) North America Mesoscale Forecast System (NAM) data. The gas-phase and aerosol chemistry are simulated with the RADM2-MADE-SORGAM models for gas and aerosol-phase chemistry. Anthropogenic emissions are derived from the 2011 US EPA National Emissions Inventory (NEI) and biogenic emissions are simulated by the Model of Emissions of Gases and Aerosols from Nature version MEGAN v2.1 biogenic emissions. The chemical initial and boundary conditions are simulated by MOZBC from the Model for Ozone and Related chemical Tracers (MOZART) model.

SIMULATION DESIGN

To test pollen and SPP effects on mixed-phase cloud formation, we designed 5 different sensitivity experiments (Table 1). Five ensemble members are conducted for each sensitivity experiment from April 11-20, 2013, with a 6-hr difference in the start time to alter initial conditions. The first experiment 'Control' is simulated using the updated Morrison microphysics scheme described above, where the mixed-phased cloud scheme (D10) includes all aerosol except pollen and SPPs. Experiment 'POL_p' adds primary pollen only (no pollen rupture) to the anthropogenic and natural aerosol in the D10 scheme to simulate immersion and contact freezing from pollen. Experiment 'POL_{p+s}' turns on pollen rupture and includes both pollen and SPP in the D10 scheme. Experiment 'H23' simulates contact and immersion freezing from pollen and SPPs using a newly developed pollen INP parametrization (H23). Experiment 'H23+rup' also use H23 scheme to simulate pollen and SPP ice nucleation and increases the pollen rupture rate from 1000 SPPs/grain to 1.25×10^5 SPPs/grain based on the recent lab study

(Hendrickson *et al*. under review). The model simulation results from experiment 'Control' are evaluated using observation data from Atmospheric Radiation Measurement (ARM) SGP sites, indicating the improved Morrison scheme has a better representation of convective system vertical structure than the original Morrison scheme.

Experiment Name	Description
Control	Updated Morrison Microphysics scheme (including D10) without pollen.
POL_p	Adds primary pollen (POL_p) in D10 scheme
POL_{p+s}	Adds both primary pollen and SPPs in D10 scheme
H23	Revises freezing temperatures for primary pollen and SPP based on H23 laboratory experiments
H23+rup	H23 freezing rates + H23 rupture rates

Table 1. WRF-Chem cloud microphysics sensitivity experiments

CONCLUSIONS

We select one study region (region R) over the model simulation domain to evaluate different model experiments (Fig.1). This selected region has high primary pollen and SPPs concentrations, and the convective system passes through region from 17-18 April 2013. We compare spatially averaged vertical ice number concentration for the Control simulation in region R (Fig. 2a) and compare the percent change in ice-phase hydrometeors between different simulations and the Control simulation (Fig. 2b-e). As simulated by the Control simulation (Fig. 2a), the convective system passes through R1 from 17 April 2013 18:00:00 to 18 April 2013 09:00:00, forming ice phase hydrometeors up to 1000 per g dry air at about 9-14km. Lower concentrations (200-400 per g dry air) are present at lower altitudes (4-8km). After adding primary pollen grains in the ice nucleation simulated by D10 parameterization (POL_p experiment), more ice (up to 90%) are simulated in the mixed-phase cloud (at around -30°C) and less ice (up to -70%) are simulated in the ice cloud after the convective system. However, these changes are relatively small and occurs in a short time duration. When adding SPPs in the simulation (experiment POL_{p+s}; Fig. 2c), there are larger changes in the ice cloud (increase up to 100%) with a longer time duration. Revising the pollen freezing rates (experiment H23) increases the ice number concentration about 60% (Fig.2d) at 4-8km altitude. Increasing the rupture rates (H23+rup) increases the SPP concentration by a factor of 2, which increases both ice cloud (>100%) and mixed phase cloud (up to 80%) ice number concentrations at the end of the convective system (18 April 2013 9-12:00:00), potentially extending the duration of the convective system.

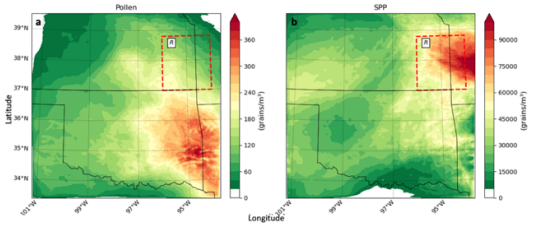

Figure 1. WRF-Chem simulation domain with the averaged (11-20 April 2013) spatial concentration of (a) pollen ($grains/m^3$) and (b) SPPs ($grains/m^3$). Red dashed square (region R) bounds the study region for the following analysis of different experiments.

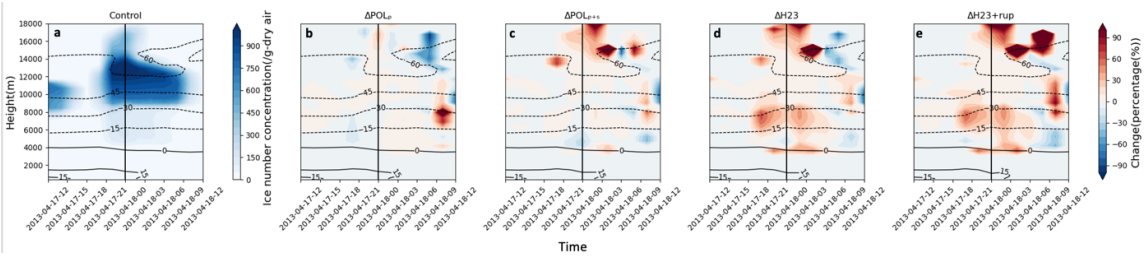

Figure 2. Spatial (region R) averaged vertical ice number concentrations (g-dry air^{-1}) of (a) experiment Control. b-e show the difference between experiment Control and experiment (b) POL_p, (c) POL_{p+s}, (d) H23, and (e) H23+rup, respectively (Δ experiment = experiment-Control). X-axis is time duration, ranging from 17 April 2013 12:00:00 to 18 April 2013 12:00:00, and y-axis is height (m). The results showing here are 5-ensemble member averages.

Overall, our results highlight that the addition of PBAPs such as pollen and SPPs can alter hydrometeors in a convective system, with .more SPP leading to greater increases in ice concentrations. Although new laboratory results indicate that pollen grains are more effective INPs than SPPs, the concentration of SPP is higher and more SPPs can be lifted to the upper atmosphere. Additionally, the newly developed pollen-specific parametrizations simulate more ice from pollen in the mixed-phased cloud than the previous parametrizations that do not distinguish the aerosol composition, suggesting that methods do not specifically account for the freezing properties of primary biological aerosol such as pollen may underestimate pollen effects in ice and mixed phase clouds.

ACKNOWLEDGEMENTS

This work is supported by National Science Foundation grant AGS-1821173 and NASA FINESST grant 80NSSC22K1434.

REFERENCES

Bigg, E. K. (1953). The formation of atmospheric ice crystals by the freezing of droplets. *Quarterly Journal of the Royal Meteorological Society*, *79*(342), 510–519.

Cooper, W. A. (1986). Ice Initiation in Natural Clouds. *Precipitation Enhancement—A Scientific Challenge*, 29–32.

DeMott, P. J., Prenni, A. J., Liu, X., Kreidenweis, S. M., Petters, M. D., … Rogers, D. C. (2010). Predicting global atmospheric ice nuclei distributions and their impacts on climate. *Proceedings of the National Academy of Sciences of the United States of America*, *107*(25), 11217–11222.

Grell, G. A., Peckham, S. E., Schmitz, R., McKeen, S. A., Frost, G., … Eder, B. (2005). Fully coupled "online" chemistry within the WRF model. *Atmospheric Environment*, *39*(37), 6957–6975.

Hendrickson, B. et al. (2023) Pollen effects on health and cloud formation. under review

Kanji, Z. A., Ladino, L. A., Wex, H., Boose, Y., Burkert-Kohn, M., Cziczo, D. J., & Krämer, M. (2017). Overview of Ice Nucleating Particles. *Meteorological Monographs*, *58*(1), 1.1-1.33.

Koop, T., Luo, B., Tsias, A., & Peter, T. (2000). Water activity as the determinant for homogeneous ice nucleation in aqueous solutions. *Nature 2000 406:6796*, *406*(6796), 611–614.

Liu, X., & Penner, J. E. (2005). Ice nucleation parameterization for global models. *Meteorologische Zeitschrift*, *14*(4), 499–514.

Meyers, M. P., Demott, P. J., & Cotton, W. R. (1992). New primary ice-nucleation parameterizations in an explicit cloud model. *Journal of Applied Meteorology*, *31*(7), 708–721.

Morrison, H., Curry, J. A., & Khvorostyanov, V. I. (2005). A new double-moment microphysics parameterization for application in cloud and climate models. Part I: Description. *Journal of the Atmospheric Sciences*, *62*(6), 1665–1677.

Pratt, K. A., Demott, P. J., French, J. R., Wang, Z., Westphal, D. L., … Prather, K. A. (2009). In situ detection of biological particles in cloud ice-crystals. *Nature Geoscience 2009 2:6*, *2*(6), 398–401.

Subba, T., Zhang, Y. and Steiner, A. (2023). Modeling of pollen rupture mechanisms and their role in chemistry-climate-interactions. under review

Testa, B., Hill, T. C. J., Marsden, N. A., Barry, K. R., Hume, C. C., … DeMott, P. J. (2021). Ice Nucleating Particle Connections to Regional Argentinian Land Surface Emissions and Weather During the Cloud, Aerosol, and Complex Terrain Interactions Experiment. *Journal of Geophysical Research: Atmospheres*, *126*(23), e2021JD035186.

Ullrich, R., Hoose, C., Möhler, O., Niemand, M.,…Leisner, T.(2017). A New Ice Nucleation Active Site Parameterization for Desert Dust and Soot. *Journal of the Atmospheric Sciences*, *74*(3), 699–717.

Wozniak, M. C., Steiner, A. L., & Solmon, F. (2018). Pollen Rupture and Its Impact on Precipitation in Clean Continental Conditions. *Geophysical Research Letters*, *45*(14), 7156–7164.

Wozniak, Matthew C, & Steiner, A. L. (2017). A prognostic pollen emissions model for climate models (PECM1.0). *Geosci. Model Dev*, *10*, 4105–4127.

Zhang, Y., & Steiner, A. L (2022). Projected climate-driven changes in pollen emission season length and magnitude over the continental United States.*Nature Communications 2022 13:1*, *13*(1), 1–10.

DUST POLLUTION CLASSIFICATION AND ITS EFFECTS IN BEIJING

FEIXUE ZHENG[1], JING CAI[1,2], ZEMIN FENG[1,4], ZHUOHUI LIN[1], XIAOLONG FAN[1,5,6], CHANG LI[1], YUSHENG ZHANG[1], CHAO YAN[2,7], KASPAR R. DAELLENBACH[2,3], YONGCHUN LIU[1], MARKKU KULMALA[1,2]

1 Aerosol and Haze Laboratory, Beijing Advanced Innovation Center for Soft Matter Science and Engineering, Beijing University of Chemical Technology, Beijing 100029, China

2 Institute for Atmospheric and Earth System Research, Faculty of Science, University of Helsinki, Helsinki 00014, Finland

3 Laboratory of Atmospheric Chemistry, Paul Scherrer Institute, Villigen, Switzerland
4 College of Chemical Engineering, North China University of Science and Technology, Tangshan 063021, China
5 Center for Excellence in Regional Atmospheric Environment, Institute of Urban Environment, Chinese Academy of Sciences, Xiamen 361021, China
6 Key Lab of Urban Environment and Health, Institute of Urban Environment, Chinese Academy of Sciences, Xiamen 361021, China
7 Joint International Research Laboratory of Atmospheric and Earth System Sciences, School of Atmospheric Sciences, Nanjing University, Nanjing 210023, China

Keywords: $PM_{2.5}$, Dust pollution, Classification method, Principal Component Analysis (PCA), Ozone.

INTRODUCTION

Dust aerosol is a key concern for air quality at the global scale (Houghton et al., 2001; Tegen and Schepanski, 2009). Most of the previous studies of dust are based on satellite observations, model calculations, and laboratory experiments, including dust transport pathways (Bozlaker et al., 2013; Jin et al., 2022), aerosol optical and physical properties (Gui et al., 2022; Yus-Díez et al., 2021), chemical compositions and morphology (Bora et al., 2021; Engelbrecht et al., 2016). Traditionally, dust is defined by meteorological parameters, such as dust aerosol optical depth in satellite observations (Remer et al., 2005; Song et al., 2022). Observations suggested that dust can carry a large number of mineral elements, such as transition metal oxides and carbonates (Gao et al., 1992) with a sharp decrease in relative humidity and fine particle concentrations (Zhu et al., 2020). Meanwhile, dust particles can also react with acidic gaseous pollutants in polluted areas and participate in the physical and chemical reactions in the atmosphere (Shang et al., 2010; Zhao et al., 2018). However, to our best knowledge, studies related to the full characterizations of dust influence on the changes in meteorological conditions, air quality, and $PM_{2.5}$ chemical components in megacities are still limited.

METHODS

In this study, we applied a Principal Component Analysis (PCA) model (Bartlett, 1951) to construct a dust pollution determination based on a year-long measurements of various urban PM species (Mn, Pb, Ti, K, Si, Br, Ca, Fe, Ba, Cl, NH_4, OA, NO_3, SO_4, BC, $PM_{2.5}$, and PM_{10}) in Beijing. We compared our method to other two common dust definitions: calculating the coarse fraction of PM_{10} (Guan et al., 2018) and using the crustal matter equation of $PM_{2.5}$ to determine the dust fraction (Liu et al., 2022). Through this analysis, we evaluated the strengths and limitations of each approach and identified different types of dust pollution. Furthermore, we discuss the influence of dust particles on the other secondary pollutants during the selected dust pollution type days and the seasonal variations for dust pollution in Beijing.

CONCLUSIONS

We found that regional dust pollution can be effectively identified by PCA model. As shown in Fig.1, the coarse fraction method and the dust fraction method are affected by the measurement of $PM_{2.5}$ and PM_{10}, especially when the mass concentration of PM is very low, some data points that do not belong to the dust types will be selected out. Additionally, the dust fraction method is also affected by high ratio of $PM_{2.5}$ to PM_{10}, further reducing the accuracy to identity dust types. These two methods are not suitable for specific identification of regional dust pollution, but can screen suspended dust events. Finally, we divided dust into three types: regional dust comes from northern or north-western regions (N-regional dust); regional dust comes from southern regions (S-regional dust); and suspended dust (Tab.1).

Under regional dust pollution, the mass concentration of PM_{10} and $PM_{2.5}$ increased by 5.6 times and 2.1 times, respectively, when compared to clean days (Fig.2). At the same time, the mass concentration of metal elements related to dust, such as Si, Ti, Ca, and Fe, increased significantly by 17.6 times, 10.6 times, 8.3 times, and 5.6 times, respectively. O_3 increased about 20% that can be influenced by the transport of O_3 in the residual layer following the air mass of dust. In contrast, Nitrate, sulphate, ammonium, and organic pollutants were reduced by 89%, 47%, 68%, and 61%, respectively. This suggest that the dust air mass affected the generation of secondary pollutants. The present study provides a comprehensive analysis of the effects of dust aerosols on changes in meteorological conditions, air quality, and $PM_{2.5}$ chemical components in megacities, thereby advancing the understanding of the chemical and physical properties of dust aerosols.

Dust type	PM_{10} max ($\mu g/m^3$)	Dust frequency (time)				Method
		Winter	Spring	Summer	Autumn	
N-regional dust	697	3	2	0	4	PCA
S-regional dust	729	0	1	0	0	PCA
Suspended dust	< 100	/	/	/	/	Others

Note: N-regional dust means regional dust from northern or north-western regions;
S-regional dust means regional dust from southern regions.
Others include the coarse fraction method and the dust fraction method.

Table 1. The different dust types in Beijing in 2019.

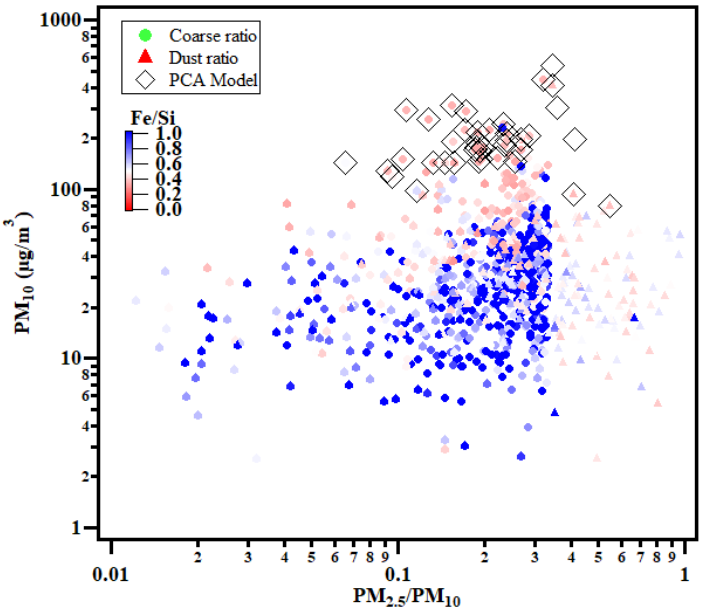

Figure 1. The comparison of different dust selection methods. Coarse ratio is the calculated coarse fraction of $PM_{2.5}$ (> 0.4); Dust ratio is the dust fraction calculated by dust equation in $PM_{2.5}$ (> 0.6); PCA model is selected by the calculated scores of PCA results.

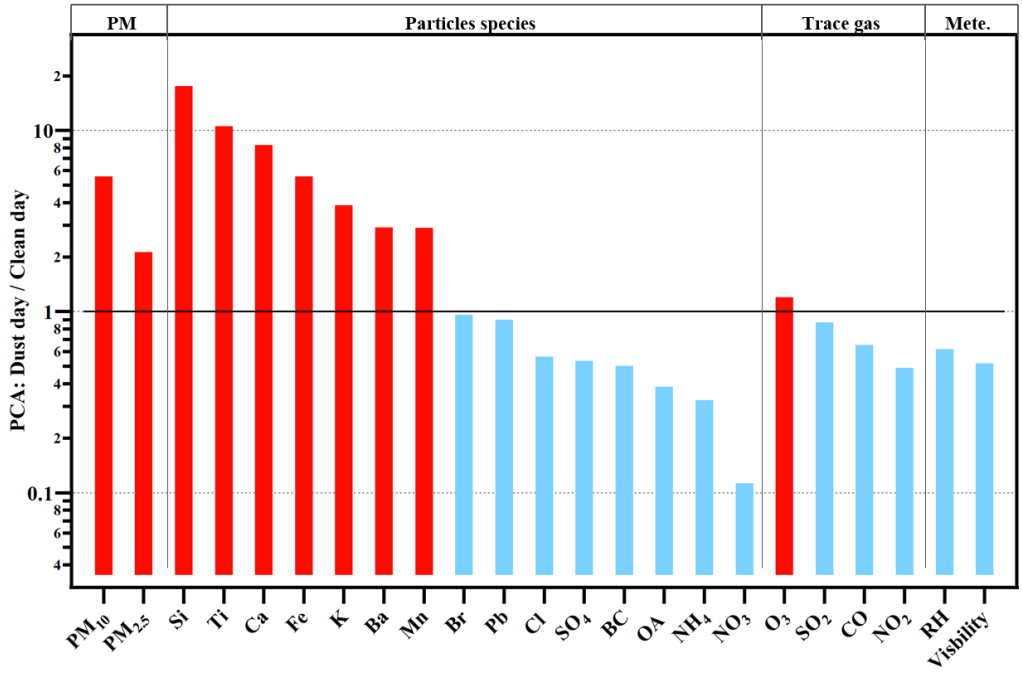

Figure 2. Comparison of PM_{10}, $PM_{2.5}$, and 15 species of $PM_{2.5}$, four trace gases (NO_2, SO_2, O_3 and CO), and two parameters (RH and visibility) between dust and clean type.

ACKNOWLEDGEMENTS

This work was financially supported the National Natural Science Foundation of China (41877306, 42275117, 92044301), and the Ministry of Science and Technology of the People's Republic of China (2019YFC0214701).

REFERENCES

Bartlett, M.S.J.B. (1951). The effect of standardization on a χ 2 approximation in factor analysis. *38*, 337-344.
Bora, J., Deka, P., Bhuyan, P., Sarma, K.P., and Hoque, R.R. (2021). Morphology and mineralogy of ambient particulate matter over mid-Brahmaputra Valley: application of SEM–EDX, XRD, and FTIR techniques. SN Applied Sciences *3*.
Bozlaker, A., Prospero, J.M., Fraser, M.P., and Chellam, S. (2013). Quantifying the contribution of long-range Saharan dust transport on particulate matter concentrations in Houston, Texas, using detailed elemental analysis. Environ Sci Technol *47*, 10179-10187.
Engelbrecht, J.P., Moosmüller, H., Pincock, S., Jayanty, R.K.M., Lersch, T., and Casuccio, G. (2016). Technical note: Mineralogical, chemical, morphological, and optical interrelationships of mineral dust re-suspensions. Atmospheric Chemistry and Physics *16*, 10809-10830.
Gao, Y., Arimoto, R., Duce, R.A., Lee, D.S., and Zhou, M.Y. (1992). Input of atmospheric trace elements and mineral matter to the Yellow Sea during the spring of a low-dust year. *97*, 3767-3777.
Guan, Q., Li, F., Yang, L., Zhao, R., Yang, Y., and Luo, H. (2018). Spatial-temporal variations and mineral dust fractions in particulate matter mass concentrations in an urban area of northwestern China. J Environ Manage *222*, 95-103.
Gui, K., Yao, W., Che, H., An, L., Zheng, Y., Li, L., Zhao, H., Zhang, L., Zhong, J., Wang, Y., *et al.* (2022). Record-breaking dust loading during two mega dust storm events over northern China in March 2021: aerosol optical and radiative properties and meteorological drivers. Atmospheric Chemistry and Physics *22*, 7905-7932.

Houghton, J.T., Ding, Y., Griggs, D.J., Noguer, M., van der Linden, P.J., Dai, X., Maskell, K., and Johnson, C. (2001). Climate change 2001: the scientific basis: contribution of Working Group I to the third assessment report of the Intergovernmental Panel on Climate Change (Cambridge university press).
Jin, J., Pang, M., Segers, A., Han, W., Fang, L., Li, B., Feng, H., Lin, H.X., and Liao, H. (2022). Inverse modeling of the 2021 spring super dust storms in East Asia. Atmospheric Chemistry and Physics *22*, 6393-6410.
Liu, X., Turner, J.R., Hand, J.L., Schichtel, B.A., and Martin, R.V. (2022). A Global-Scale Mineral Dust Equation. J Geophys Res Atmos *127*, e2022JD036937.
Remer, L.A., Kaufman, Y.J., Tanré, D., Mattoo, S., Chu, D.A., Martins, J.V., Li, R.-R., Ichoku, C., Levy, R.C., Kleidman, R.G., *et al.* (2005). The MODIS Aerosol Algorithm, Products, and Validation %J Journal of the Atmospheric Sciences. *62*, 947-973.
Shang, J., Li, J., and Zhu, T. (2010). Heterogeneous reaction of SO2 on TiO2 particles. Science China Chemistry *53*, 2637-2643.
Song, Q., Zhang, Z., Yu, H., Kok, J.F., Di Biagio, C., Albani, S., Zheng, J., and Ding, J. (2022). Size-resolved dust direct radiative effect efficiency derived from satellite observations. Atmospheric Chemistry and Physics *22*, 13115-13135.
Tegen, I., and Schepanski, K. (2009). The global distribution of mineral dust. IOP Conference Series: Earth and Environmental Science *7*.
Yus-Díez, J., Ealo, M., Pandolfi, M., Perez, N., Titos, G., Močnik, G., Querol, X., and Alastuey, A. (2021). Aircraft vertical profiles during summertime regional and Saharan dust scenarios over the north-western Mediterranean basin: aerosol optical and physical properties. Atmospheric Chemistry and Physics *21*, 431-455.
Zhao, D., Song, X., Zhu, T., Zhang, Z., Liu, Y., and Shang, J. (2018). Multiphase oxidation of SO₂ by NO₂ on CaCO₃ particles. Atmospheric Chemistry and Physics *18*, 2481-2493.
Zhu, J., Zhang, X., He, W., Yan, X., Yu, Q., Xu, C., Jiang, Q., Huang, H., and Wang, R. (2020). Response of plant reflectance spectrum to simulated dust deposition and its estimation model. Sci Rep *10*, 15803.